

Finite-Rate Chemistry Effects in Turbulent Premixed Combustion

by

Matthew John Dunn

A thesis submitted in fulfilment of
the requirements for the degree of
Doctor of Philosophy

School of Aeronautical, Mechanical and Mechatronic Engineering
The University of Sydney



2008

© Matthew John Dunn 2008

Declaration

I hereby declare that the work presented in this thesis is solely my own work and that to the best of my knowledge the work is original except where otherwise indicated in the text of this thesis by reference to the author or by acknowledgement of the source of the work. No part of this work has been submitted for any other degree or diploma.

(Matthew John Dunn)

Acknowledgements

I was fortunate enough to have Prof. Assaad R. Masri as my supervisor and Prof. Robert W. Bilger as my associate supervisor for my PhD, both are world leaders in the field of combustion science. I am grateful to have had two supervisors who are so passionate about the field of combustion science; discussions with them have always been a source of inspiration for me. I would particularly like to thank them for their time and effort that they have invested in me during my studies.

I would like to thank all my co-workers in the Sydney combustion group throughout my PhD studies for their friendship and help whenever needed. I would especially like to thank Dr. Sten H. Stärner for “showing me the ropes” in the combustion lab.

Part of the work involved my PhD involved an experimental campaign at Sandia National Laboratories in collaboration with Dr. Robert S. Barlow. It was a pleasure to work in one of the finest combustion laboratories in the world and to learn from one of the great combustion experimentalist in the field. The hospitality that my wife and I received combined with the science conducted on this trip made the Sandia adventure unforgettable. The help of Dr. Guanghua Wang and Bob Harmon in setting up and conducting experiments at Sandia National Laboratories is gratefully acknowledged.

The continual encouragement and support from my mother, father and brother made the completing my PhD that little bit easier. Thank you for your encouragement and support.

Most importantly, I would like to thank my wife Sandra and my daughter Nisha, they have both had to endure large sacrifices in order for me to complete my studies, and for this, their never ending love, encouragement and support, I am eternally grateful.

Preface

In recent times significant public attention has been drawn to the topic of combustion. This has been due to the fact that combustion is the underlying mechanism of several key challenges to modern society: climate change, energy security (finite reserves of fossil fuels) and air pollution. The further development of combustion science is undoubtedly necessary to find improved solutions to manage these combustion science related challenges in the near and long term future. Combustion is essentially an exothermic process, this exothermicity or heat release essentially occurs at small scales, by small scales it meant these scales are small relative to the fluid length scales, for example heat release layer thicknesses in flames are typically much less than the fluid integral length scales. As heat release occurs at small scales this means that in turbulent combustion the small scales of the turbulence (which can be of the order of the heat release layer thickness) can possibly interact and influence the heat release and thus chemistry of the flame reaction zone. Premixed combustion is a combustion mode where the fuel and oxidiser are completely premixed prior to the flame reaction zone, this mode of combustion has been shown to be a promising method to maximise combustion efficiency and minimise pollutant formation. The continued and further application of premixed combustion to practical applications is limited by the current understanding of turbulent premixed combustion, these limitations in understanding are linked to the specific flame phenomena that can significantly influence premixed combustion in a combustion device, examples of such phenomena are: flame flashback, flame extinction and fuel consumption rate – all phenomena that are influenced by the interaction of the small scales of turbulence and chemistry. It is the study and investigation of the interaction of turbulence and chemistry at the small scales (termed finite-rate chemistry) in turbulent premixed flames that is the aim of this thesis which is titled “Finite-rate chemistry effects in turbulent premixed combustion”.

Two very closely related experimental burner geometries have been developed in this thesis: the Piloted Premixed Jet Burner (PPJB) and the Premixed Jet Burner (PJB). Both feature an axisymmetric geometry and exhibit a parabolic like flow field. The PPJB and PJB feature a small 4mm diameter central jet from which a high velocity lean-premixed methane-air mixture issues. Surrounding the central jet in the PPJB is a 23.5mm diameter pilot of stoichiometric methane-air products, the major difference between the PPJB and the PJB is that the PJB does not feature a stoichiometric pilot. The pilot in the PPJB provides a rich source of combustion intermediates and enthalpy which promotes initial ignition of the central jet mixture. Surrounding both the central jet and pilot is a large diameter hot coflow of combustion products. It is possible to set the temperature of the hot coflow to the adiabatic flame temperature of the central jet mixture to simulate straining and mixing against and with combustion products without introducing complexities such as quenching and dilution from cold air. By parametrically increasing the central jet velocity in the PPJB it is possible to show that there is a transition from a thin conical flame brush to a flame that exhibits extinction and re-ignition effects. The flames that exhibit extinction and re-ignition effects have a luminous region near the jet exit termed the initial ignition region. This is followed by a region of reduced luminosity further downstream termed the extinction region. Further downstream the flame luminosity increases this region is termed the re-ignition region. For the flames that exhibit extinction and re-ignition it is proposed that intense turbulent mixing and high scalar dissipation rates drives the initial extinction process after the influence of the pilot has ceased ($x/D > 10$). Re-ignition is proposed to occur downstream where turbulent mixing and scalar dissipation rates have decreased allowing robust combustion to continue. As the PJB does not feature a pilot, the flame stabilisation structure is quite different to the PPJB. The flame structure in the PJB is essentially a lifted purely premixed flame, which is an experimental configuration that is also quite unique.

A suite of laser diagnostic measurements has been parametrically applied to flames in the PPJB and PJB. Laser Doppler Velocimetry (LDV) has been utilised to measure the mean and fluctuating radial and axial components of velocity at a point, with relevant time and length scale information being extracted from these measurements. One of the most

interesting results from the LDV measurements is that in the PPJB the pilot delays the generation of high turbulence intensities, for flames that exhibit extinction the rapid increase of turbulence intensity after the pilot corresponds to the start of the extinction region. Using the LDV derived turbulence characteristics and laminar flame properties and plotting these flames on a traditional turbulent regime diagram indicates that all of the flames examined should fall in the so call distributed reaction regime.

Planar imaging experiments have been conducted for flames using the PPJB and PJB to investigate the spatial structure of the temperature and selected minor species fields. Results from two different simultaneous 2D Rayleigh and OH PLIF experiments and a simultaneous 2D Rayleigh, OH PLIF and CH₂O PLIF experiment are reported. For all of the flames examined in the PPJB and PJB a general trend of decreasing conditional mean temperature gradient with increasing turbulence intensity is observed. This indicates that a trend of so called flame front thickening with increased turbulence levels occurs for the flames examined. It is proposed that the mechanism for this flame front thickening is due to eddies penetrating and embedding in the instantaneous flame front. In the extinction region it is found that the OH concentration is significantly reduced compared to the initial ignition region. In the re-ignition region it is found that the OH level increases again indicating that an increase in the local reaction rate is occurring. In laminar premixed flames CH₂O occurs in a thin layer in the reaction zone, it is found for all of the flames examined that the CH₂O layer is significantly thicker than the laminar flame. For the high velocity flames beyond $x/D=15$, CH₂O no longer exist in a distinct layer but rather in a near uniform field for the intermediate temperature regions. Examination of the product of CH₂O and OH reveals that the heat release in the initial ignition region is high and rapidly decreases in the extinction region, an increase in the heat release further downstream is observed corresponding to the re-ignition region. This finding corresponds well with the initial hypothesis of an extinction region followed by a re-ignition region that was based on the mean chemiluminescence images.

Detailed simultaneous measurement of major and minor species has been conducted using the line Raman-Rayleigh-LIF technique with CO LIF and crossed plane-OH PLIF

at Sandia National Laboratories. By measuring all major species it is also possible to define a mixture fraction for all three streams of the PPJB. Using these three mixture fractions it was found that the influence of the pilot in the PPJB decays very rapidly for all but the lowest velocity flames. It was also found that for the high velocity flames exhibiting extinction, a significant proportion of the coflow fluid is entrained into the central jet combustion process at both the extinction region and re-ignition regions. The product of CO and OH conditional on temperature is shown to be proportion to the net production rate of CO₂ for certain temperature ranges. By examining the product of CO and OH the hypothesis of an initial ignition region followed by an extinction region then a re-ignition region for certain PPJB flames has been further validated complementing the [CH₂O][OH] imaging results.

Numerical modelling results using the transported composition probability density function (TPDF) method coupled to a conventional Reynolds averaged Navier Stokes (RANS) solver are shown in this thesis to successfully predict the occurrence of finite-rate chemistry effects for the PM1 PPJB flame series. To calculate the scalar variance and the degree of finite-rate chemistry effects correctly, it is found that a value of the mixing constant (C_ϕ) of approximately 8.0 is required. This value of C_ϕ is much larger than the standard expected range of 1.5-2.3 for C_ϕ that has been established for non-premixed combustion. By examining the results of the RANS turbulence model in a non-reacting variable density jet, it is shown that the primary limitation of the predictive capability of the TPDF-RANS method is the RANS turbulence model when applied to variable density flows.

NOMENCLATURE

Roman Symbols

<i>Symbol</i>	<i>Definition</i>	<i>Units</i>
a	stretch rate	s^{-1}
A_{ij}	Einstein coefficient for spontaneous emission between states i and j	s^{-1}
B_{ij}	Einstein coefficient for absorption or stimulated emission between states i and j	s^{-1}
c	speed of light in a vacuum (2.998×10^8)	$m.s^{-1}$
cm^{-1}	wave number	
C_T	reaction progress variable based on temperature	
C_ϕ	Mixing model constant	
C_μ	turbulent viscosity constant	
$C_{\varepsilon 1}, C_{\varepsilon 2}$	constants in the transport equation for ε	
D	diameter of central jet	mm
Da	Damköhler number	
f_B	Boltzmann fraction	
f_{QE}	quadratic exponential function form	
F	LIF signal	
$f_\#$	f number	
g	acceleration due to gravity	$m.s^{-2}$
h	Planck's constant (6.626×10^{-34})	J.s
i	complex number ($i = \sqrt{-1}$)	

I	laser irradiance	$\text{W.cm}^{-2}.\text{s}$
I_ν	laser spectral irradiance	$\text{W.cm}^{-2}.\text{s}$
I_ν^0	normalised laser spectral irradiance	$\text{W.cm}^{-2}.\text{s}$
J	rotational quantum number	
k	turbulent kinetic energy	$\text{m}^{-2}.\text{s}^{-2}$
k_B	Boltzmann constant (1.381×10^{-23})	$\text{J.K}^{-1}.\text{molec}^{-1}$
Ka	Karlovitz number	
l_0	Integral length scale	m
L	quenching loss factor	
Le	Lewis number	
M	magnification number	
n_i	concentration in level i	molec.cm^{-3}
n_{OH}	total OH concentration	molec.cm^{-3}
N_i	normalised concentration in level i	
N_A	Avogadro's number (6.022×10^{23})	molec.mole^{-1}
N_0	Loschmidt number	
P	pressure	Pa
Q	volumetric flow rate	$\text{m}^3.\text{s}^{-1}$
Q_{ij}	Quenching rate from level i to j	s^{-1}
r	radius	m
R_{ij}	rotational transfer rate from level i to level j	s^{-1}
R_{mix}	mixture specific ideal gas constant	
R_u	universal gas constant (8.314)	
Re	Reynolds number	
Re_T	turbulence Reynolds number	
Re_λ	Reynolds number based on the Taylor microscale	
S_L	laminar flame speed	m.s^{-1}
S_T	turbulent flame speed	m.s^{-1}
t	time	s
T	temperature	K

T_{ij}	total transfer rate from level i to level j	s^{-1}
T_{ad}	adiabatic temperature	K
u, U	axial velocity	$m.s^{-1}$
u'	RMS fluctuation of axial velocity	$m.s^{-1}$
v, V	radial velocity	$m.s^{-1}$
V_{ij}	vibration transfer from levels i to j	s^{-1}
v'	RMS fluctuation of radial velocity	$m.s^{-1}$
W_{ij}	transfer rate from level i to level j due to laser coupling	s^{-1}
X_i	mole fraction of species i	
Y_i	mass fraction of species i	
Z_i	mass fraction of elemental mass fraction i	
x	x-axis of Cartesian coordinate system or laser propagation direction	
y	y-axis of Cartesian coordinate system or direction in the height of laser sheet	
z	z-axis of Cartesian coordinate system or direction in the thickness of the laser sheet or complex variable	

Greek symbols

<i>Symbol</i>	<i>Definition</i>	<i>Units</i>
α	Angle local flame normal is from the measurement axis	rad
δ	Flame thickness	mm, m
δ_L	Laminar flame thickness	mm, m
δ_{th}	Thermal flame thickness	mm, m

ε	Turbulent kinetic energy dissipation	$\text{m}^2.\text{s}^{-1}$
λ	Wavelength of light	nm
μ	Dynamic viscosity	$\text{kg}.\text{m}.\text{s}^{-3}.\text{K}^{-1}$
ν	Kinematic viscosity	$\text{m}^2.\text{s}^{-1}$
	or wavelength	cm^{-1}
	or vibrational quantum number	
ξ_i	Mixture fraction of the i^{th} stream	
σ_i	Differential Rayleigh cross section of species i	$\text{m}^2.\text{sr}^{-1}$
η	Optical collection efficiency	
	or sample space variable for the mean mixture fraction	
θ	Angle cross plane is tilted from vertical axis	
ρ	Density	$\text{kg}.\text{m}^{-3}$
ξ	Sample space variable for temperature	
	or sample space variable for C_T	
Σ	Flame surface density	m^{-1}
Λ	The component of the electronic orbital angular momentum along the diatomic molecular internuclear axis	
τ	Heat release parameter	
τ_1, τ_2, τ_3	Simplifying constants	
ϕ	Equivalence ratio	
ϕ_L	Spectral bandwidth of laser	
ϕ_A	Spectral bandwidth of absorption transition	
Π	Shortened notation for $\Lambda = 1$	
Σ	The component of the electronic spin along the diatomic molecular internuclear axis	
	or shortened notation for $\Lambda = 0$	
Ω	Optical detection solid angle	sr

Diacriticals

<i>Symbol</i>	<i>Definition</i>
—	Reynolds or ensemble mean
~	Favre or mass-weighted mean

Subscripts

<i>Symbol</i>	<i>Definition</i>
b	burnt gas value
coflow	referring to the coflow stream of the PPJB or PJB
i	value for species i or arbitrary Cartesian coordinate
jet	referring to the central jet stream of the PJB or PPJB
jet-CL	referring to the centreline value of central jet stream of the PJB or PPJB
L	laminar flame case
mix	property of the mixture
T	temperature
p	product
pilot	referring to the pilot stream of the PPJB
r	reactant
u	unburnt gas value
x	x-axis of Cartesian coordinate system
y	y-axis of Cartesian coordinate system
z	z-axis of Cartesian coordinate system

Superscripts

<i>Symbol</i>	<i>Definition</i>
'	Fluctuation about the Reynolds mean or laser excited state value
"	Fluctuation about the Favre mean or laser pumped level value
*	Excited state

Operators

<i>Symbol</i>	<i>Definition</i>
d	Differential
∇	Gradient operator
Δ	Discrete difference
\otimes	Convolution operator
\Leftrightarrow	Fourier transformation
∂	Partial differential
	Modulus operator

ABBREVIATIONS

1D	One Dimensional
2D	Two Dimensional
3D	Three Dimensional
ANN	Artificial Neural Network
AR	Anti Reflection
ASE	Amplified Spontaneous Emission
BD	Beam Dump
CA	California
CARS	Coherent Anti-stokes Raman Scattering
CC	Concave
CCD	Charge Coupled Device
CDS	Central Differencing Scheme
CFD	Computational Fluid Dynamics
CFM	Coherent Flame Model
CL	Cylindrical Lens
CMC	Conditional Moment Closure
CNG	Compressed Natural Gas
CPDF	Conditional Probability Density Function
CPU	Central Processing Unit
CSP	Computational Singular Perturbation
CX	Convex
DME	Density Matrix Equations
DNS	Direct Numerical Simulation
EBU	Eddy Break-Up
EET	Electrical Energy Transfer

EMST	Euclidean Minimum Spanning Tree
EOA	Ellipsoid Of Accuracy
FD	Finite Difference
FDS	Forward Difference Scheme
FFT	Fast Fourier Transform
FWHM	Full Width Half Maximum
HCCI	Homogenous Charge Compression Ignition
ICCD	Intensified Charge Coupled Device
IEM	Interaction by Exchange with the Mean
ILDm	Intrinsically Low Dimensional Manifold
IQSS	Integrated Quasi Steady State
IR	Infra-Red
ISAT	In-Situ-Adaptive-Tabulation
ISATPD	In-Situ-Adaptive-Tabulation based on Principle Directions
JPDF	Joint Probability Density Function
KDP	Potassium Dihydrogen-Phosphate
LDV	Laser Doppler Velocimetry
LES	Large Eddy Simulation
LHS	Left Hand Side
LIF	Laser Induced Fluorescence
LIPF	Laser Induced Predissociative Fluorescence
LSF	Line Spread Function
LPG	Liquefied Petroleum Gas
MC	Modified Curl
MCP	Micro-Channel Plate
MTF	Modulation Transfer Function
MOLEC	molecule
Nd:YAG	Neodymium doped Yttrium Aluminium Garnet
NO _x	Oxides of Nitrogen
ODE	Ordinary Differential Equation
PAH	Polycyclic Aromatic Hydrocarbons

PDE	Partial Differential Equation
PDF	Probability Density Function
PDPA	Phase Doppler Particle Anemometry
PISO	Pressure-Implicit with Splitting of Operators
PIV	Particle Image Velocimetry
PL	Planar
PLIF	Planar Laser Induced Fluorescence
PMT	Photo Multiplier Tube
POD	Proper Orthogonal Decomposition
PJB	Premixed Jet Burner
PPJB	Piloted Premixed Jet Burner
PRESTO	Pressure Staggering Option
PSF	Point Spread Function
QUICK	Quadratic Upwind Interpolation for Convective Kinematics
QSS	Quasi-Steady State
RAM	Random Access Memory
RANS	Reynolds Averaged Navier Stokes equations
RHS	Right Hand Side
RNG	Re-Normalised Group
RS	Reynolds Stress
RET	Rotational Energy Transfer
RMS	root mean square
SDE	Stochastic Differential Equation
SHG	Second Harmonic Generator
SI	Spark Ignition
SIU	Standard International system of Units
SIMPLE	Semi-Implicit Method for Pressure-Linked Equations
SIMPLEC	Semi-Implicit Method for Pressure-Linked Equations Consistent
SIMPLER	Semi-Implicit Method for Pressure-Linked Equations Revised
SL	Spherical lens
SLM	Standard Litres per Minute

SNL	Sandia National Laboratories
SNR	Signal to Noise Ratio
SRF	Step Response Function
SS	Steady State
STP	Standard Temperature and Pressure
TCL	Turbulent Combustion Laboratory
THG	Third Harmonic Generator
TOPLIF	Two Optical Path Laser Induced Fluorescence
TPDF	Transported Probability Density Function
UDS	Upwind Difference Scheme
UV	Ultra-Violet
VET	Vibrational Energy Transfer

CONTENTS

Declaration.....	iii
Acknowledgments.....	v
Preface.....	vii
Nomenclature.....	xi
Abbreviations.....	xvii
List of Tables.....	xxv
List of Figures.....	xxvii
CHAPTER 1 INTRODUCTION	1
CHAPTER 2 BACKGROUND	9
2.1 Turbulent Premixed Combustion	9
2.2 Laser Diagnostics	15
2.2.1 Rayleigh scattering.....	15
2.2.2 Raman Scattering.....	17
2.3 Numerical Modelling	22
2.3.1 An Overview of the Probability Density Function Method.....	22
2.3.2 Previous work using the PDF Method.....	25
2.3.3 Equations for the Probability Density Function Method	31
2.3.4 Efficient Chemistry Methods for PDF Calculations.....	34
2.3.5 Mixing Models for PDF Calculations.....	39
CHAPTER 3 BURNER DEVELOPMENT AND CHARACTERISATION.....	45
3.1 PPJB Burner	47
3.1.1 PPJB Burner Design	47
3.1.2 PPJB Stability Characteristics.....	50
3.1.3 PPJB Flow-Field Measurements.....	54
3.2 PJB Burner and Stability Characteristics	60
3.2.1 PJB Burner Design and Characterisation.....	62
3.2.2 PJB Flow-Field Measurements.....	65
CHAPTER 4 LIF QUANTIFICATION	71
4.1 Non-Linear LIF Background.....	72
4.2 Detailed six-level model.....	75

4.2.1	Model Overview	77
4.2.2	Assessment of RET and Final State Effects	81
4.2.3	Effects of Laser Temporal Pulse Distribution	88
4.2.4	Spatial Irradiance Distribution	91
4.3	The Reduced Model	94
4.3.1	Steady State and Quasi-Steady State Assumptions	94
4.3.2	Explicit Model Formulation	98
4.3.3	IQSS Model Numerical Validation	100
4.4	Experimental Comparison	106
4.5	Discussion	108
CHAPTER 5 PPJB 2D IMAGING RESULTS		111
5.1	Large Image Region Rayleigh OH PLIF Imaging	113
5.1.1	Experimental Setup	114
5.1.2	Data Processing	116
5.1.3	Results and Discussion	122
5.2	High Resolution Rayleigh OH PLIF Imaging	126
5.2.1	Experimental Setup and Characterisation	127
5.2.2	Data Processing	131
5.2.3	Results and Discussion	135
5.3	Simultaneous Rayleigh, OH and CH ₂ O PLIF Imaging	141
5.3.1	Experimental Setup	143
5.3.2	Data Processing	148
5.3.3	Results and Discussion	150
CHAPTER 6 PPJB RAMAN-RAYLEIGH-LIF RESULTS		159
6.1	Experimental Setup	162
6.1.1	Experimental Facility Overview	162
6.1.2	Excitation Laser Setup and Optics	164
6.1.3	Signal Collection	170
6.1.4	PPJB Burner	172
6.1.5	Calibrations	174
6.2	Data Processing and Experimental Characterisation	176
6.2.1	Processing methodology	176
6.2.2	Spatial Resolution	177
6.2.3	Accuracy and Precision	181
6.3	Results and Discussion	181
6.3.1	Mean and RMS Temperature Profiles	181
6.3.2	Scalar Profiles	184
6.3.3	Mixture Fraction Profiles	185
CHAPTER 7 PJB 2D IMAGING RESULTS		193
7.1	Experimental Setup	195
7.2	Data Reduction	198
7.3	Results and Discussion	200

CHAPTER 8 FINITE RATE CHEMISTRY	207
8.1 Flame Thickness.....	208
8.2 Reaction Rate	211
8.2.1 Mean Flame Chemiluminescence.....	211
8.2.2 Minor Species	213
8.2.3 CO ₂ Net Production Rate	217
8.2.4 Heat Release.....	220
8.3 Discussion: Flame Characterisation	222
CHAPTER 9 EXPERIMENTAL AND NUMERICAL INVESTIGATIONS OF NON- REACTING VARIABLE DENSITY JETS	227
9.1 Selected Cases and Experimental Measurements	230
9.2 Numerical Solution Problem Setup.....	231
9.3 RANS Based Turbulence Modelling.....	233
9.4 Constant Density Case Results.....	247
9.5 Variable Density Case Results	251
CHAPTER 10 RANS TPDF SIMULATION RESULTS.....	257
10.1 The PDF Method in Premixed Combustion.....	259
10.2 Numerical Algorithm and Numerical Models	264
10.3 Numerical Error Analysis and Validation.....	267
10.4 Velocity and Scalar Predictions	272
10.5 Finite-Rate Chemistry Predictions.....	279
10.6 Discussion and Further Results.....	281
CHAPTER 11 CONCLUSIONS AND RECCOMENDATIONS	293
11.1 Conclusions	293
11.2 Discussion of Future Work and Recommendations.....	296
CHAPTER 12 REFERENCES	303
APPENDIX A.....	349
APPENDIX B	357
APPENDIX C	361
APPENDIX D.....	377
APPENDIX E	403

LIST OF TABLES

Table 3-1. Summary of the flame conditions for the NPM flames stabilised on the PJB.	64
Table 3-2. Freely propagating laminar flame characteristics for the three central jet CNG/air compositions used for the NPM flames. d_{th} is taken to be the laminar flame thermal thickness based on the maximum gradient. t_f is defined as the laminar flame thermal time scale (d_{th}/S_L).	64
Table 6-1. Cold flow and heated flow calibrations flow rates and primary calibration purpose for the Sandia experiments.	175
Table 6-2. Summary of the methane-air flat flames used for high temperature Raman-Rayleigh-LIF calibrations.	176
Table 6-3. Elemental mass fractions for each of the three streams at the exit plane for all of the flames examined.	187
Table 8-1. Laminar flame characteristics for an unstrained premixed methane-air flame of equivalence ratio (Φ) equal to the central jet composition of the PM1 flames investigated. T_{ad} is the adiabatic flame temperature. S_L is the laminar flame speed. δ_{th} is the laminar flame thermal thickness based on the maximum gradient. t_f is defined as the laminar flame thermal time scale (δ_{th}/S_L).	223
Table 8-2. Non-dimensional parameters for the flames examined. q' is the total turbulence intensity, η is the Kolmogorov length scale, l_0 is the integral length scale, Re_t is the turbulent Reynolds number and Da is the Damköhler number.	224
Table 9-1. Summary of the flow conditions examined in this chapter for non-reacting flows of constant and variables densities.	230
Table 9-2. Turbulence model constants used for the standard $k-\epsilon$ model.	236
Table 9-3. Values for the turbulence model constants for the RNG $k-\epsilon$ model in the high Reynolds number limit.	238
Table 9-4. Turbulence model constants used for the realizable $k-\epsilon$ model.	239
Table 9-5. Turbulence model constants used for the standard $k-\omega$ model.	241
Table 9-6. Turbulence model constants used for the $k-\omega$ SST model.	244

Table 9-7. Turbulence model constants used for the stress- ω model.	245
Table 9-8. Turbulence model constants used for the quadratic pressure strain Reynolds stress turbulence model.	247
Table 10-1. Mechanism details for the additional reactions added to the DRM22 mechanism to calculate the C_2H and CH^* concentrations as well as the CH^* spontaneous emission rate. The forward rate coefficient is assumed to be expressed as $k_j = AT^b \exp(-E_a/R_u T)$. The units for the k_j expression are consistent with standard CHEMKIN notation for chemical mechanisms, that is A ($gmol/cm^3$) and E_a ($cal/gmol$).	287

LIST OF FIGURES

Fig. 3-1. Sectioned view of the PPJB, with significant features given a balloon callout.	49
Fig. 3-2 Characterisation map for the PPJB, a constant coflow temperature of 1500K is used for all cases. The location of the selected flame conditions studied further in this study is shown for reference.	52
Fig. 3-3. Time averaged images taken with a conventional colour digital camera of the selected flames, A: PM1-50, B: PM1-100, C: PM1-150, D: PM1-200. Note: A, B, C and D correspond to the respective regimes in Fig. 3-2.	53
Fig. 3-4. Axial variation of the mean and RMS u component of velocity for the PM1 flame series. Values for both the selected flames (FL) and the corresponding non-reacting cases (NR) are shown.....	56
Fig. 3-5. Radial variation of velocity for the selected flames, showing the increased turbulence intensity in the shear layer.	57
Fig. 3-6. Measured lift-off heights as a function of jet velocity for three different PJB flame series. It should be noted that for the NPM2 ($\phi=0.6$) flames the coflow is 1650K, whilst for the NPM1 ($\phi=0.5$) and NPM4 ($\phi=0.8$) flames the coflow temperature is 1500K.....	62
Fig. 3-7. Cross sectional view of the PJB, with all major features labelled	63
Fig. 3-8. Mean flame luminosity images of the NPM2-40 a), and NPM2-200 b) flames. The small red region to the right of the central jet is the coflow pilot; this pilot flame in way influences the central jet combustion process.	65
Fig. 3-9. LDV velocity measurements for the NPM2-40 flame. The centreline velocity statistics are presented in a) with the normalized mean velocity shown with a solid black line with data points demarked by triangles and the normalized turbulent kinetic energy is shown with a dashed blue with data points demarked with asterisks. The radial traverse velocity statistics are presented in b) for three axial stations, the solid black line represents the normalized mean velocity data and the dashed thin blue represents the normalized turbulent kinetic energy. All data points in a) and b) are joined with a linear line to guide the eye, it is not implied that intermediate points will lie on this straight line.....	66

Fig. 3-10. LDV velocity measurements for the NPM2-100 flame. An identical data identification scheme is used in this figure as in Fig. 3-9.....	67
Fig. 4-1. Energy transfer diagram for the six-level detailed model. All spontaneous emission paths from the excited $A^2\Sigma^+$ state as well as EET and VET pathways to and from levels 1 and 2 are not shown in this diagram for clarity.	77
Fig. 4-2. Relative sensitivities of the temporally integrated LIF signal, F , as a function of the normalized spectral irradiance (I_ν^0). Dashed line shows the relative sensitivity of F to the rotational energy transfer rate ($S_{F,R}^{rel}$). Solid line shows the relative sensitivity of F to the quenching loss factor ($S_{F,L}^{rel}$).	82
Fig. 4-3. The effect of three different temporal pulse distributions as a function of the normalized spectral irradiance, I_ν^0 : a) The variation of the temporally integrated LIF signal F and b) the variation of the relative sensitivity of F to the normalized spectral irradiance ($S_{F,I_\nu^0}^{rel}$).....	90
Fig. 4-4. A comparison of the temporally and spatially integrated LIF signals, F , for four different spatial spectral irradiance distributions as a function of the normalized spectral irradiance I_ν^0 . The variation of F is given in a) and the variation of the relative sensitivity of F to the normalized spectral irradiance ($S_{F,I_\nu^0}^{rel}$) is given in b).93	
Fig. 4-5. Energy transfer diagram for the four-level model, spontaneous emission pathways from the excited $A^2\Sigma^+$ state are not shown for clarity.....	95
Fig. 4-6. Relative sensitivity of the temporally integrated fluorescence, F , to the normalized spectral irradiance, I_ν^0 . Results for the detailed six-level model are compared with the four-level model for two different assumptions: quasi-steady state (QSS) and steady state (SS)......	98
Fig. 4-7. Energy transfer diagram for the two-level model.	101
Fig. 4-8. Relative sensitivity of the spatially and temporally integrated fluorescence, F , to the normalized spectral irradiance, I_ν^0 . Results for the detailed six-level model are compared with the four-level model for two different assumptions: quasi-steady state (QSS) and steady state (SS). Also shown are the results for the two-level model assuming steady state (SS)......	102
Fig. 4-9. Relative sensitivity of F , temporally and spatially integrated, to the local Electronic quenching rate, Q , as a function of the normalized spectral irradiance, I_ν^0 . Results for the detailed six-level model are compared with the four-level model for two different assumptions: quasi-steady state (QSS) and steady state (SS). Also shown are the results for the two-level model assuming steady state (SS).	103

Fig. 4-10. Relative sensitivity of F , temporally and spatially integrated, to temperature as a function of the normalized spectral irradiance, I_{ν}^0 . Results for the detailed six-level model are compared with the four-level model for two different assumptions: quasi-steady state (QSS) and steady state (SS). Also shown are the results for the two-level model assuming steady state (SS).....	105
Fig. 4-11. Comparison of the IQSS model predictions and experimental measurements for the relationship between F , spatially and temporally integrated, and the normalized spectral irradiance, I_{ν}^0	107
Fig. 5-1. An overview of the experimental layout for the large image region Rayleigh OH PLIF experiment including lasers, optics and signal collection.	114
Fig. 5-2. Variation of the line of best fit for the relative Rayleigh cross section as a function of the normalised Rayleigh signal.	118
Fig. 5-3. Variation of lines of best fit for the electronic energy transfer (Q_{13}) and vibration energy transfer (V_{34}) in the temperature range 300K to 1500K.	120
Fig. 5-4. Simultaneous temperature (top image) and OH mole fraction images (bottom image) centred at $x/D=15$ and $r/D=0$ for increasing central jet velocities. a) PM1-50, b) PM1-100, c) PM1-150, d) PM1-200.	123
Fig. 5-5. Simultaneous temperature (top image) and OH mole fraction images (bottom image) at for flame PM1-150 (150 m/s central jet velocity) at four axial locations, centred at $r/D=0$. a) $x/D=7$, b) $x/D=15$, c) $x/D=27$, d) $x/D=38$. Note the temperature colour scale is different to the one used in Fig. 5-4.	125
Fig. 5-6. An overview of the experimental setup for the high resolution imaging setup.	129
Fig. 5-7. Relative Rayleigh cross section vs. Rayleigh signal normalised by air for the PM1 flame series.	132
Fig. 5-8. OH quenching rates vs. Rayleigh signal normalised by air.	133
Fig. 5-9. Comparison of mean temperature dissipation error using three different image smoothing schemes.	135
Fig. 5-10. Simultaneous imaging results of OH, temperature and $ \nabla T _{2D}$ for PM1-50 (top row), PM1-100 (middle row) and PM1-150 (bottom row).....	136
Fig. 5-11. Temperature gradient conditional on temperature for flames PM1-50, PM1-100 and PM1-150, data taken at $x/D=10$	137
Fig. 5-12. Laminar flame temperature gradient vs. temperature data for freely propagating central jet reactants and opposed flow simulations of fresh central jet reactants vs. hot coflow products for a range of strain rates.	138

Fig. 5-13. Conditional mean X_{OH} for flames PM1-50, PM1-100 and PM1-150. The results presented here are data taken at $x/D=10$.	139
Fig. 5-14. Conditional mean X_{OH} conditioned on the local value of the 2D temperature gradient for flames PM1-50, PM1-100 and PM1-150. The results presented here are data taken at $x/D=10$.	140
Fig. 5-15. An overview of the experimental setup showing lasers, beam paths, beam optics, burner, signal collection optics and cameras used for the simultaneous imaging of temperature, OH and CH_2O .	148
Fig. 5-16. Randomly selected instantaneous imaging of temperature, CH_2O , OH and the reaction rate indicator CH_2OxOH for the PM1-150 flame at $x/D=5$ (left column), 10 (middle column) and 15 (right column).	152
Fig. 5-17. Randomly selected instantaneous imaging of temperature, CH_2O , OH and the reaction rate indicator CH_2OxOH for the PM1-150 flame at $x/D=30$ (left column), 45 (middle column) and 60 (right column).	154
Fig. 6-1. Schematic diagram of the four frequency doubled Nd:YAG lasers and pulse stretcher used for the Raman-Rayleigh system. This figure is used with permission from Dr. R. S. Barlow.	164
Fig. 6-2. Temporal variation of the laser power at the exit of the Nd:YAG pulse stretcher. This figure is used with permission from Dr. R. S. Barlow.	166
Fig. 6-3. a) Example image of the 532nm Raman-Rayleigh beam for a single realization in a uniform medium, note this image is not to scale, the vertical height of the image is approximately 1mm and the length 7mm. b) Sectional profile of the imaged beam intensity distribution through the section A-A shown in a), note the FWHM for this profile is $110\mu m$ and the $1/e^2$ width is $225\mu m$.	168
Fig. 6-4. a) Example image of the resultant single-shot CO LIF signal in a uniform medium of post flame gases, note this image is not to scale as the vertical height of the image is approximately 2.8mm and the length 6.5mm. b) Sectional profile of the imaged beam intensity distribution through the section A-A shown in a), note the FWHM for this profile is $133\mu m$ and the $1/e^2$ width is $320\mu m$.	169
Fig. 6-5. A pictorial overview of the TCL at Sandia showing the six lasers, beam paths, test section and five cameras. This figure is used with permission from Dr. R. S. Barlow.	170
Fig. 6-6. An overview of the Sandia Raman-Rayleigh-LIF measurement system focusing on the final laser sheet formation, signal collection optics and signal recording cameras. This figure is used with permission from Dr. R. S. Barlow.	171
Fig. 6-7. Photograph of the PPJB in the Sandia measurement test section. Surrounding the burner is the filtered air wind tunnel adapter that was made specifically for the	

PPJB. Also note the burner in this image features the standard height collar (65mm).	173
Fig. 6-8. An example realisation of temperature gradient through the reaction zone of a lean-premixed laminar Bunsen flame. The experimental results using different processing techniques are compared with the numerically calculated profile.....	180
Fig. 6-9. Radial profiles at a number of axial locations of the Reynolds mean temperature for the four PM1 flames ((a) PM1-50, b).PM1-100, c) PM1-150 and PM1-200)..	182
Fig. 6-10. Radial profiles at a number of axial locations of the Reynolds RMS temperature for the four PM1 flames ((a) PM1-50, b).PM1-100, c) PM1-150 and PM1-200).	184
Fig. 6-11. Radial profiles at a number of axial locations of the Reynolds mean CO ₂ mass fraction for the four PM1 flames ((a) PM1-50, b).PM1-100, c) PM1-150 and PM1-200).	185
Fig. 6-12. Radial profiles at a number of axial locations of the Reynolds mean coflow mixture fraction for the four PM1 flames ((a) PM1-50, b).PM1-100, c) PM1-150 and PM1-200).	188
Fig. 6-13. Radial profiles at a number of axial locations of the Reynolds RMS coflow mixture fraction for the four PM1 flames ((a) PM1-50, b).PM1-100, c) PM1-150 and PM1-200).	189
Fig. 6-14. Radial profiles at a number of axial locations of the Reynolds mean pilot mixture fraction for the four PM1 flames ((a) PM1-50, b).PM1-100, c) PM1-150 and PM1-200).	189
Fig. 6-15. Radial profiles at a number of axial locations of the Reynolds RMS pilot mixture fraction for the four PM1 flames ((a) PM1-50, b).PM1-100, c) PM1-150 and PM1-200).	190
Fig. 6-16. Radial profiles at a number of axial locations of the Reynolds mean central jet mixture fraction for the four PM1 flames ((a) PM1-50, b).PM1-100, c) PM1-150 and PM1-200).	191
Fig. 6-17. Radial profiles at a number of axial locations of Reynolds RMS central jet mixture fraction for the four PM1 flames.	191
Fig. 7-1. Experimental schematic showing lasers, laser beam paths, laser and collection optics, imaging collection system and the PJB.	197
Fig. 7-2. Numerical simulation results for the Rayleigh cross section variation vs. normalised Rayleigh signal. The normalised Rayleigh signal is taken to be the numerically calculated Rayleigh signal divided by the corresponding Rayleigh signal of ambient air. The error bars show the bounds for low strain and high strain rate simulations.	199

Fig. 7-3. Mean Temperature and OH images combined with a representative instantaneous realisation of temperature, OH and the computed temperature gradient for the NPM2-40 flame a centred at $x/D=5$ a), $x/D=15$ b) and $x/D=25$ c).	201
Fig. 7-4. Mean Temperature and OH images combined with a representative instantaneous realisation of temperature, OH and the computed temperature gradient for the NPM2-200 flame a centred at $x/D=5$ a), $x/D=25$ b) and $x/D=50$ c).	202
Fig. 7-5. Radial Profiles of the Reynolds mean OH and temperature at $x/D=5$, 15 and 25 for the NPM2-40 flame.	203
Fig. 7-6. Radial Profiles of the Reynolds mean OH and temperature at $x/D=5$, 25 and 50 for the NPM2-200 flame.	204
Fig. 7-7. Comparison of the ensemble Reynolds mean 2D temperature gradient conditional on temperature for the NPM2-40 flame computed from images at $x/D=5$, 15 and 25.	204
Fig. 7-8. Comparison of the ensemble Reynolds mean 2D temperature gradient conditional on temperature for the NPM2-200 flame computed from images at $x/D=5$, 25 and 50.	205
Fig. 8-1. Conditional mean temperature gradients taken at $\xi=1200\text{K}$ for the PM1 flame series at a number of axial stations.	209
Fig. 8-2. PDF of $\nabla T_{3D} \xi$ for the PM1 flame series, the probability density is proportional to the shade of grey, light corresponds to a low probability and dark a high probability. The conditional mean is shown as a black solid line.	210
Fig. 8-3. The spatial structure of heat release (HR), CH, CH* and temperature (T (K)) in a freely-propagating laminar premixed flame of methane-air with an equivalence ratio of 0.5. Curves for the mass fractions of CH and CH* as well as the heat release have been normalized by their respective peak value.	212
Fig. 8-4. PDF of CO mole fraction for the PM1 flame series, the probability density is proportional to the shade of grey, light corresponds to a low probability and dark a high probability. The conditional mean is shown as a black solid line.	216
Fig. 8-5. PDF of OH mole fraction for the PM1 flame series, the probability density is proportional to the shade of grey, light corresponds to a low probability and dark a high probability. The conditional mean is shown as a black solid line.	217
Fig. 8-6. Variation of the ratio of $[\text{CO}][\text{OH}]$ to the net CO_2 production rate as a function of strain rate. $\sum \dot{\omega}_{i,\text{CO}_2}$ is taken to be the net reaction rate for CO_2 summed over the i^{th} reaction, for all evaluated reactions.	218
Fig. 8-7. Conditional mean values for the product of CO and OH, taken at $\xi=1400\text{K}$ at a number of axial stations, for the PM1 flame series.	219

Fig. 8-8. PDF of [CO][OH] the PM1 flame series, the probability density is proportional to the shade of grey, light corresponds to a low probability and dark a high probability. The conditional mean is shown as a black solid line.	220
Fig. 8-9. A comparison of the product [CO][OH] and [CH ₂ O][OH] conditional on a temperature of 1400K for the PM1-150 flame.	221
Fig. 8-10. The premixed combustion regime diagram similar to that proposed by Chen and Bilger [9], the locations of the four PM1 flames in terms of the central jet velocity is shown. The integral length scales and turbulence intensity values necessary to locate the selected flames on the regime diagram were taken from the values at $x/D=15$	226
Fig. 9-1. a) (Top) Close up view of the central jet exit highlighting the mesh density and cell aspect ratio, note the jet radius is 2mm making the area of interest for this figure ~7mm x 3.75mm. b) (Bottom) gives an overview of the computational domain and boundary conditions utilised for the simulations.	232
Fig. 9-2. a) Mean axial velocity and RMS velocity b) (right) at $r/D=0$ for the cold flow case with a central jet velocity of 50m/s.	248
Fig. 9-3. a) Mean axial velocity and RMS axial velocity b) (right) at $x/D=5$ for the cold flow case with a central jet velocity of 50m/s.	249
Fig. 9-4. a) Mean axial velocity and RMS axial velocity b) (right) at $x/D=15$ for the cold flow case with a central jet velocity of 50m/s.	249
Fig. 9-5. a) Mean axial velocity and RMS axial velocity b) (right) at $x/D=25$ for the cold flow case with a central jet velocity of 50m/s.	250
Fig. 9-6. a) Mean axial velocity and RMS axial velocity b) (right) at $x/D=35$ for the cold flow case with a central jet velocity of 50m/s.	250
Fig. 9-7. a) Mean axial velocity and RMS axial velocity b) (right) at $r/D=0$ for the cold flow case with a central jet velocity of 150m/s.	251
Fig. 9-8. a) Mean axial velocity and RMS axial velocity b) (right) at $x/D=25$ for the cold flow case with a central jet velocity of 150m/s.	251
Fig. 9-9. a) Mean axial velocity and RMS axial velocity b) (right) at $r/D=0$ for the 1500K coflow case with a central jet velocity of 50m/s.	253
Fig. 9-10. a) Mean axial velocity and RMS axial velocity b) (right) at $x/D=5$ for the 1500K coflow case with a central jet velocity of 50m/s.	253
Fig. 9-11. a) Mean axial velocity and RMS axial velocity b) (right) at $x/D=15$ for the 1500K coflow case with a central jet velocity of 50m/s.	254
Fig. 9-12. a) Mean axial velocity and mean RMS axial velocity b) (right) at $r/D=0$ for the 1500K coflow case with a central jet velocity of 150m/s.	254

Fig. 9-13. a) Mean axial velocity and RMS axial velocity b) (right) at $x/D=5$ for the 1500K coflow case with a central jet velocity of 150m/s.	255
Fig. 9-14. a) Mean axial velocity and RMS axial velocity b) (right) at $x/D=15$ for the 1500K coflow case with a central jet velocity of 150m/s.	255
Fig. 10-1. Convergence of the axial velocity as a function of the inverse number of grid cells at $x/D=60$, $r/D=0$ for the PM1-150 flame.	269
Fig. 10-2. Convergence of the mean static temperature as a function of the inverse number of grid cells at $x/D=22.5$, $r/D=0$ for the PM1-150 flame.	269
Fig. 10-3. Convergence of the mean static temperature as a function of the inverse number of particles per cell at $x/D=22.5$, $r/D=0$ for the PM1-150 flame.	270
Fig. 10-4. Convergence of the axial velocity as a function of the inverse number of particles per cell at $x/D=60$, $r/D=0$ for the PM1-150 flame.	270
Fig. 10-5. Variation of the peak Favre mean mass fraction for six species along the centreline ($r/D=0$) as a function of the ISAT error tolerance. Data points for each species are shown as diamond symbols, the expected $\pm 2\%$ bounds around the expected error-free value obtained by Richardson extrapolation is shown as two dashed horizontal lines in each figure.	271
Fig. 10-6. Variation of three flame brush parameters along the centreline ($r/D=0$) as a function of the ISAT error tolerance, a) Favre mean flame brush length in central jet diameters, b) Favre mean flame brush thickness in central jet diameters and c) peak Favre RMS temperature fluctuation. Data points are shown as diamond symbols, the expected $\pm 2\%$ bounds around the expected error-free value obtained by Richardson extrapolation is shown as two dashed horizontal lines in each figure.	271
Fig. 10-7. Variation of three flame brush parameters along the centreline ($r/D=0$) as a function of the number of particles per cell, a) Favre mean flame brush length in central jet diameters, b) Favre mean flame brush thickness in central jet diameters and c) peak Favre RMS temperature fluctuation. Data points are shown as diamond symbols, the expected $\pm 2\%$ bounds around the expected error-free value obtained by Richardson extrapolation is shown as two dashed horizontal lines in each figure.	272
Fig. 10-8. Comparison of LDV measurements with the $k-\omega$ and $k-\epsilon$ model results for the axial velocity statistics along the centreline $r/D=0$ for the PM1-50 flame. The mean velocity profile is reported in a), and the RMS velocity is reported in b).	273
Fig. 10-9. Comparison of LDV measurements with the $k-\omega$ and $k-\epsilon$ model results for the axial velocity statistics along the centreline $r/D=0$ for the PM1-100 flame. The mean velocity profile is reported in a), and the RMS velocity is reported in b).	273
Fig. 10-10. Comparison of LDV measurements with the $k-\omega$ and $k-\epsilon$ model results for the axial velocity statistics along the centreline $r/D=0$ for the PM1-150 flame. The mean velocity profile is reported in a), and the RMS velocity is reported in b).	274

- Fig. 10-11. Comparison of LDV measurements with the $k-\omega$ and $k-\epsilon$ model results for the axial velocity statistics along the centreline $r/D=0$ for the PM1-200 flame. The mean velocity profile is reported in a), and the RMS velocity is reported in b). 274
- Fig. 10-12. Comparison of LDV measurements with the $k-\omega$ and $k-\epsilon$ model results for the radial velocity statistics at $x/D=5$ for the PM1-100 flame. The mean velocity profile is reported in a), and the RMS velocity is reported in b). 275
- Fig. 10-13. Comparison of LDV measurements with the $k-\omega$ and $k-\epsilon$ model results for the radial velocity statistics at $x/D=15$ for the PM1-100 flame. The mean velocity profile is reported in a), and the RMS velocity is reported in b). 275
- Fig. 10-14. Comparison of LDV measurements with the $k-\omega$ and $k-\epsilon$ model results for the radial velocity statistics at $x/D=25$ for the PM1-100 flame. The mean velocity profile is reported in a), and the RMS velocity is reported in b). 276
- Fig. 10-15. Comparison of LDV measurements with the $k-\omega$ and $k-\epsilon$ model results for the radial velocity statistics at $x/D=35$ for the PM1-100 flame. The mean velocity profile is reported in a), and the RMS velocity is reported in b). 276
- Fig. 10-16. Comparison of Raman-Rayleigh-LIF measurement of temperature with the $k-\omega$ and $k-\epsilon$ model results for the temperature statistics at $x/D=2.5$ for the PM1-150 flame. The Favre mean temperature profile is reported in a), and the Favre RMS temperature is reported in b). 277
- Fig. 10-17. Comparison of Raman-Rayleigh-LIF measurement of temperature with the $k-\omega$ and $k-\epsilon$ model results for the temperature statistics at $x/D=7.5$ for the PM1-150 flame. The Favre mean temperature profile is reported in a), and the Favre RMS temperature is reported in b). 277
- Fig. 10-18. Comparison of Raman-Rayleigh-LIF measurement of temperature with the $k-\omega$ and $k-\epsilon$ model results for the temperature statistics at $x/D=15$ for the PM1-150 flame. The Favre mean temperature profile is reported in a), and the Favre RMS temperature is reported in b). 278
- Fig. 10-19. Comparison of Raman-Rayleigh-LIF measurement of temperature with the $k-\omega$ and $k-\epsilon$ model results for the temperature statistics at $x/D=30$ for the PM1-150 flame. The Favre mean temperature profile is reported in a), and the Favre RMS temperature is reported in b). 278
- Fig. 10-20. Comparison of Raman-Rayleigh-LIF measurement of temperature with the $k-\omega$ and $k-\epsilon$ model results for the temperature statistics at $x/D=45$ for the PM1-150 flame. The Favre mean temperature profile is reported in a), and the Favre RMS temperature is reported in b). 278
- Fig. 10-21. Axial variation of $[CO][OH]_{\xi, 1400 > \xi > 1350 (K)}$ for the PM1 flame series using the $k-\epsilon$ turbulence model with $C_{\epsilon 1}=1.6$ and the EMST mixing model with $C_{\phi}=1.5$. Particle data is presented as small blue dots, with the conditional mean being shown as the thick black line. 279

- Fig. 10-22. Axial variation of $[CO][OH]_{\xi, 1400 > \xi > 1350 (K)}$ for the PM1 flame series using the $k-\omega$ turbulence model and the EMST mixing model with $C_\phi=1.5$. Particle data is presented as small blue dots, with the conditional mean being shown as the thick black line. 280
- Fig. 10-23. Axial variation of $[CO][OH]_{\xi, 1400 > \xi > 1350 (K)}$ for the PM1-150 flame using the $k-\omega$ turbulence model and the EMST mixing model with different values of C_ϕ . Particle data is presented as small blue dots, with the conditional mean being shown as the thick black line. 282
- Fig. 10-24. Axial variation of $[CO][OH]_{\xi, 1400 > \xi > 1350 (K)}$ for the PM1-150 flame using the $k-\omega$ turbulence model and the MC mixing model with different values of C_ϕ . Particle data is presented as small blue dots, with the conditional mean being shown as the thick black line. 283
- Fig. 10-25. Axial variation of $[CO][OH]_{\xi, 1400 > \xi > 1350 (K)}$ for the PM1-150 flame as a function of C_ϕ using the $k-\omega$ turbulence model and the IEM mixing model. Particle data is presented as small blue dots, with the conditional mean being shown as the thick black line. 284
- Fig. 10-26. A comparison of the calculated and experimentally measured peak Favre RMS temperature as a function of axial location for the PM1-150 flame using three different mixing models a) EMST, b) MC and c) IEM. The results for each mixing model are reported for values of C_ϕ equal to 2, 6, 8 and 10. The representative peak Favre RMS temperature is determined at each axial location by taking the peak value in the radial profile at the given axial location. 285
- Fig. 10-27. Comparison of the radially averaged CH^* emission for the PM1-150 flame as a function of axial location for the experimental measurements and the numerically calculated CH^* field from the PDF calculations. 289

CHAPTER 1 INTRODUCTION

Fire has been used by mankind for many thousands of years. The origin and nature of fire were often thought to be attributed to mystical or divine origins. Evidence of this can be found in the mythology of many cultures, one such an example is the ancient Greek myth by Hesiod [1] of how Prometheus stole fire from Zeus and gave it to mankind. The use of fire by early mankind was an important method for cooking food and keeping warm. Fire was also an instrumental tool in the progression from the stone to the bronze and then to the iron ages. Without fire as a heat source, the various smelting and heating processes required for making bronze and iron would not have been possible. The required level of understanding of fire (or combustion) for these early uses were small, basically limited to knowledge of suitable ignition and fuel sources. This illustrates how it was relatively easy to use fire as a tool without a great depth of understanding of the fundamentals behind the process.

Some of the earliest attempts to obtain a deeper understanding of the nature of fire were proposed by the ancient Greeks who proposed that fire was one of the four fundamental elements of matter. This description of matter and fire although wrong, did provide some guidance and predictive capability to the prevention of fire. Uncontrolled fires have been a considerable threat throughout history to man, whether this has been from bush fires in the wild or uncontrolled fires in cities such as the great fire of London in 1666. Until modern times the understanding of combustion that was fundamentally relied upon to combat these problems was based on ancient Greek ideas of the classical elements, for

example to make houses from materials that did not contain or had given up the element "fire" or to extinguish the fire with its opposite element: water.

It was left until the development of chemistry as a science and the beginnings of the industrial revolution for combustion science to be placed on a firm footing. The German chemist George Stahl proposed that when a substance burns a substance called phlogiston flowed out of the combusting material [2]. Stahl proposed that upon enclosing a flame such as a candle in an enclosed container the air eventually becomes saturated with phlogiston, thus flame extinguishes because the air can no longer absorb phlogiston from the flame. Although the phlogiston theory was incorrect, it was based on interpretations of carefully controlled qualitative experiments, the phlogiston theory was able to explain certain processes such as the reduction of metal oxides by charcoal; as such the phlogiston theory can be considered to be one of the first theories of combustion arrived at by an approximate scientific methodology. Based on experiments on a gas that was derived and isolated from air Joseph Priestly proposed that a flame in an enclosed container extinguished due to consumption of a component of the air by the flame. The component of the air that was consumed by the flame was isolated by Priestly and was called "dephlogisticated air" [3], this gas was later referred to as oxygen. Antoine Lavoisier carefully measured the mass of gases (as well as liquids and solids) both before and after combustion to reveal that mass is conserved in all chemical reactions, including the highly exothermic reaction of combustion [4]. By use of careful quantitative experimental techniques Lavoisier was also able to prove that the phlogistic interpretation of combustion was incorrect as it violated the principle of conservation of mass. These examples show how the initial development of the fundamental understanding of combustion was significantly aided by the application of a scientific methodology to the interpretation experimental results and design of new experiments to test certain hypothesis.

At approximately the same time as the fundamental studies were made in chemistry and combustion science by Lavoisier, the industrial revolution was taking place powered by the Newcomen steam engine and later by the more efficient steam engine designed by

James Watt [5]. To power the boiler of these steam engines typically the combustion of coal was utilised, this placed interest in the design of efficient boilers and combustion processes hence requiring a greater understanding of the fundamentals of combustion. Most significantly the steam engine established combustion as an important source of power through the combustion of fossil fuels, this utilisation of combustion to generate power continues to be of fundamental importance to the modern world.

The permeation and reliance on combustion into the modern world is astounding. Almost all cars, trucks, boats and airplanes all rely on fossil fuel combustion. 80-90% of the world's electricity is produced from combustion derived processes. This astounding reliance on fossil fuels for transportation and electricity generation makes the study of combustion essential to not only to optimise these devices to minimise costs and pollutants but to enhance energy security of these limited resources.

In the late 19th and early 20th centuries the idea of the earth falling into another ice age was seen to be a possible threat to the continuation of civilised society, Arrhenius [6] suggested one strategy to combat such a problem would be to encourage the emission of CO₂ into the atmosphere encouraging the so called "greenhouse effect" proposed by Fourier [7] in 1824. In modern times the idea that CO₂ influences the green house effect is still accepted, however the idea now is to minimise the greenhouse effect as opposed to maximising it! The common thread that runs throughout the green house debate throughout history is that by far the largest emission of CO₂ over recent centuries is due to combustion of fossil fuels. Based on this pressing need to minimise greenhouse gas emissions, the most pressing challenge in the short term is to ensure that all necessary fossil fuel combustion is done in the most efficient manner. In order for scientists and engineers to maximise the efficiencies of fossil fuel burning combustion devices a deep level of understand of the fundamentals of the combustion process is required. A longer term solution to the global warming issue is to move to renewable energy sources (that would still include combustion); however this fundamental shift in the source of energy will take many decades to implement.

The combustion of many fuels can result in many different types of undesirable pollutants. Combustion of high sulphur petroleum and coal results in SO_x emissions that combine with water vapour and droplets in the atmosphere form sulphuric acid or so called acid rain. This acid rain is almost always highly damaging to natural ecosystems. The urban smog that is encountered around many metropolitan cities around the world is primarily due to a mixture NO_x , unburnt hydrocarbons and soot particulates. Not only is this smog plume unsightly but it is also the source respiratory problems and certain components of the smog have been attributed to be highly carcinogenic such as soot particles in the nanometre size regime. It is clear that there is a pressing need to fundamentally understand the mechanism of the formation of the undesirable pollutants so that their production can be eliminated or at least minimised as much as possible.

It is vital that any modern study in combustion no matter how fundamental or applied address in some form (either fundamental or directly) one or more of the issues related to combustion that are relevant to modern society which have been previously mentioned (- and repeated here): climate change, energy security, pollutant minimisation and combustion device optimisation. The study of combustion science encompasses many diverse areas, it is almost impossible for any modern study of combustion to make meaningful contributions to all of the areas. In an attempt to make a meaningful contribution to modern combustion science this thesis specialises in the area of turbulent premixed combustion.

Almost all turbulent combustion processes can be globally categorised as either non-premixed or premixed combustion. In non-premixed combustion the fuel and oxidiser are separated before the reaction zone of the flame. Examples that can be broadly classified as non-premixed combustion are numerous: bushfires, candle flames, spray combustion in internal combustion engines, coal combustion and non-premixed Bunsen flames. Non-premixed combustion is advantageous in that a stable operating mode is usually easily established and the danger of a flashback event is minimised. For non-premixed combustion to occur, mixing is required to occur between the fuel and oxidiser, essentially this means that among other limiting factors the rate of combustion is limited

by the rate of mixing. In non-premixed flames the maximum temperature will occur approximately along the stoichiometric contour, this high temperature region can be a significant contributor to the NO_x production. Also on the rich side of the reaction zones of non-premixed flames complex Polycyclic Aromatic hydrocarbons (PAH), soot precursors and soot can be formed. Although soot production is usually undesirable, in some circumstances it can be desirable; such examples include the use of soot as an enhanced radiative transfer mechanism, production of carbon black and carbon nanotubes.

The premixed mode of combustion occurs when the fuel and air are mixed before entering the flame front; essentially here the rate of combustion is not limited by mixing as in the non-premixed case but rather by the turbulent flame speed, a parameter that is a function of the flow field turbulence as well as the chemical and transport properties of the mixture. For lean premixed combustion there is no high temperature stoichiometric region which is highly advantageous in terms of minimising NO_x emissions. Emissions of soot from lean premixed combustion are also virtually non-existent. Operation in the premixed mode of combustion is not without drawbacks. Flashback can occur which is a potentially damaging if not catastrophic phenomena for a combustion device. Unsteady oscillations can also develop leading to damage and failure of expensive turbo machinery equipment in gas turbine applications. Unburnt hydrocarbon emissions such as CH_2O and possibly high CO emissions are possible for lean premixed combustion if combustion is not complete, this could be caused by wall quenching or flame extinction from high strain rates or cold air dilution.

The study of turbulent premixed combustion theoretically, numerically and experimentally is arguably not as advanced as non-premixed combustion; this has been likely to have been motivated by the considerably greater practical applications involving non-premixed combustion. It has already been outlined and is further emphasised here that premixed combustion (especially lean premixed combustion) offers a mode of combustion that offers the potential to significantly reduce emissions of NO_x , soot and unburnt hydrocarbons compared to conventional non-premixed combustion. For

increasingly leaner mixtures these advantageous properties are enhanced, however undesirable effects such as flame blow-off, intermittent extinction and combustion induced oscillations also increase with leaner mixtures. The increased propensity for extinction of leaner mixtures can be linked to the greater degree of the interaction of the turbulence with the chemistry. For lean mixtures the chemical time scales can be of the order of the fluid mechanical time scales leading to Damköhler number of the order of unity or even less.

Attempts have been made to globally characterise how turbulence interacts with a premixed flame front using the so called “Borghi” diagram [8] and its many variants [9]. It has been shown Chen and Bilger [9] in a modified regime diagram that very few investigations have been carried out that examine distributed reaction regime or the well stirred reaction regimes, in fact it appears that only the works of Chen *et al.* [10] and Dinkelacker *et al.* [11] have accessed these regions with laboratory burners. Essential to the further understanding of turbulent premixed combustion are the small scale processes, it is the small scale process that control the rate of heat release, chemical reaction and flame speed. Greater understanding of these small scale processes are key to being able to describe turbulent premixed combustion in a generalised diagram such as a premixed regime diagram or for the success of numerical modelling efforts.

Specifically this thesis investigates interaction of turbulence and chemistry in turbulent premixed combustion. The interaction of turbulence and chemistry has often been termed as a finite-rate chemistry effect and is also done so in this thesis, hence this thesis is titled “Finite-rate chemistry effects in turbulent premixed combustion”. To conduct this investigation into finite-rate chemistry effects in turbulent premixed combustion three primary aims of the research are identified, these are:

- The design and characterisation of an experimental turbulent premixed burner that exhibits finite-rate chemistry effects possible through extinction and re-ignition.

- Conduct advanced laser diagnostic measurements on this geometry to gain greater insight into how finite-rate chemistry effects manifest in premixed combustion in terms of spatial structure and minor species concentrations.
- Assess the success or failure of state of the art transported probability density function (TPDF) computational models to predict finite-rate chemistry effects in premixed combustion based on the experimental geometry and measurements made in this thesis.

A brief summary of the contents of each Chapter in this thesis is as follows: A review of the necessary background theory for the material in this thesis is presented in Chapter 2. Chapter 3 outlines the development and characterisation of the piloted premixed jet burner (PPJB) and the piloted jet burner (PJB); these experimental burners are used as the platforms for further advanced laser diagnostics to investigate finite-rate chemistry effects in turbulent premixed combustion. In Chapter 4 a laser diagnostic technique is developed that allows quantitative OH measurements to be made in the non-linear LIF regime. This technique is particularly relevant to conditions where the OH concentration is small and high spatial resolution of the measurement required, such conditions and requirements occur for both the PPJB and the PJB flames. The spatial structure of both the scalar and reaction zone structure of the PPJB flames is examined in Chapter 5 using 2D imaging experiments involving the simultaneous measurement of temperature and OH, also in separate experiments the simultaneous 2D measurement of temperature, OH and CH_2O is reported. Line imaging measurements of the PPJB using the Raman-Rayleigh-LIF technique to simultaneously measure temperature, all major species, CO and OH is presented in Chapter 6. From the measurements reported in Chapter 6 it is possible to derive mixture fractions for each of the three streams, three-dimensional flame orientation and the instantaneous product of CO and OH, the derivation and implementation of these quantities for analysis of the experimental data is explored in Chapters 6 and 8. The PJB is examined in Chapter 7 using 2D PLIF imaging experiments involving the simultaneous measurement of temperature and OH, these experiments are aimed at identifying the flame spatial structure and identifying the differences and similarities to the PPJB flame structure reported in Chapter 5. Finite-rate chemistry

effects based in the experimental results of Chapters 5-7 are examined in Chapter 8. Measurands such as the flame thickness based on the temperature gradient, the product of CO and OH, the product of CH_2O and OH and the mean flame chemiluminescence are all discussed in Chapter 8 with regards to the turbulence chemistry interaction and the occurrence of extinction and re-ignition regions.

To complement the experimental investigation of finite-rate chemistry effects in premixed combustion reported in Chapters 3-8 a numerical investigation of finite-rate chemistry effects in premixed combustion is also examined. To gain confidence and provide further understanding of the turbulence predictions provided by the turbulence models in the reacting case, experiments and numerical simulations have been carried out for non-reacting variable density jets, the results of this preliminary study are reported in Chapter 9. In Chapter 10 the Reynolds averaged Navier Stokes equations (RANS) are coupled with the transported probability density function (TPDF) method to numerically simulate a series of PPJB flames. Finally in Chapter 11, the conclusions of the material presented in this thesis are summarised, a section with recommendations and discussion for future work related to the material in this thesis is also included in Chapter 11.

CHAPTER 2 BACKGROUND

Some of the fundamental background material for the work examined in this thesis is examined in this Chapter. As turbulent premixed combustion is the underlying theme of this thesis a brief introduction and overview is given. Topics in laser diagnostics such as Rayleigh and Raman scattering are reviewed, this material is relevant to the experiments presented in Chapters 5, 6 and 7. Background material relevant to the application of the PDF method is reviewed. This review includes areas such as: previous studies using the PDF method, Monte Carlo methods for PDF simulations, efficient chemistry implementation in PDF methods and molecular mixing models for PDF methods.

2.1 Turbulent Premixed Combustion

For premixed combustion to occur the fuel and oxidiser must be completely and homogeneously mixed prior to any chemical reaction occurring in the flame front. This means that over the flame brush the flame is consuming a constant equivalence ratio mixture. The premixed combustion mode is relevant to many practical applications such as lean premixed gas turbine combustors, spark ignition engines and domestic and industrial burners for heating and cooking. Many other practical applications may also be idealised to be considered to be operating in the premixed mode of combustion, such as cases where the fuel and oxidiser are not completely homogeneously mixed such as in gas

turbine combustors where the liquid fuel is pre-vaporised and the resultant mixture is not completely homogenous.

In premixed combustion a combustible mixture is present before the reaction zone, thus the mixture is in a metastable state before the mixture is consumed by the flame front. The addition of energy via a spark or heat or mass transfer can change this metastable state to be a chemically reacting state. It is the transport of heat and radical species balanced by the fluid velocity through a flame front that creates a statistically stationary flame brush; one such an example of this statistical balance to form a steady flame brush is in a stove top cooking flame. If there is no bulk fluid flow to balance the flame propagation, the flame will propagate through the premixture in an accelerating and uncontrolled manner. In practice this unsteady flame propagation is usually undesirable as it can be the result of unintentional ignition of a flammable gas mixture, commonly resulting in personal and property damage. An example where unsteady premixed flame propagation is desirable is in spark ignition engines; here it is usually desirable for the fuel-air mixture to be burnt as fast as possible. Rapid flame propagation from the spark plug ignition point is encouraged through the use of geometrical and flow field features such tumble and strategically placed fuel and air injection locations.

There have been many attempts to characterise turbulent premixed combustion through the use of a so called “regime diagrams” or “Borghi diagrams” [8, 12, 13, 14]. The parameters that are commonly used for such generalised diagrams are the intensity and length scales of the turbulence in the form of the turbulence intensity and integral length scale, while for the chemistry the laminar flame speed and laminar flame thickness are usually used. The aim of developing the regime diagram is to delineate between the different regimes of premixed combustion. There is considerable controversy over the limits of applicability and definitions for the different areas of the regime diagram as highlighted by Chen and Bilger [9]. Part of this controversy lies in the fact that there needs to be significant assumptions and generalisations made to categorise a premixed flame from the many parameters available. Furthermore, the boundaries for the different premixed combustion regimes are typically based on the particular authors view of the

conceptual interaction of different scales of turbulence (such as the integral and Kolmogorov scales) with the laminar flame length scales (thermal or diffusive length scales). Significant experimental work is still needed to validate the boundaries of these regimes.

In the most simplistic form, turbulent premixed combustion can be viewed as the propagation of a thin front through a turbulent media. Damköhler [15] hypothesised that in a statistically one dimensional flow the mass flow rate or mass flux (\dot{m}) through the instantaneous turbulent flame front could be equated to the mean mass flow rate through the flame front by Eq. (2.1).

$$\dot{m} = \rho_u S_L A_T = \rho_u S_T A \quad (2.1)$$

In Eq. (2.1) ρ_u is the unburnt gas density, S_L is the laminar burning velocity, S_T is the turbulent burning velocity, A_T is the turbulent flame area and A is the mean flame area. By using Eqn. (2.1), Damköhler [15] was able derive an expression for the turbulent burning velocity given by Eqn. (2.2).

$$S_T = S_L A_T / A \quad (2.2)$$

Under the assumption that the action of turbulence is solely to geometrically change the turbulent flame area, Damköhler [15] related the instantaneous area of a turbulent flame to the laminar flame and turbulence properties by Eq. (2.3).

$$A_T / A \propto v' / S_L \quad (2.3)$$

Which leads to the geometric scaling given by Eq. (2.4).

$$S_T \propto v' \quad (2.4)$$

A necessary assumption for Eq. (2.4) is that the turbulence is assumed to be large scale and that v'/S_L is large. With these assumptions and the available experimental data for the turbulent burning velocity Bray [16] it is interesting to see that for large values v'/S_L the scaling proposed by Eq. (2.4) is essentially qualitatively correct.

As shown by the analysis by Damköhler [15] the turbulent burning velocity is a central concept in turbulent premixed combustion. There have been numerous experimental measurements of the turbulent burning velocity from the 1950's to the present day. Correspondingly there have also been numerous review articles that have attempted to collate these experimental results into a single relation for the turbulent burning velocity, typically these relations are in terms of S_T/S_L and v'/S_L . There is typically considerable spread observed in the trends from the experimental data as highlighted by Bradley *et al.* [17] and Bray [16]. This high degree of scatter is not solely from experimental error but rather the many different physical parameters that effect the turbulent burning velocity other than the parameters S_T/S_L and v'/S_L . Examples of such influencing parameters include geometrical layout (e.g. open or enclosed flame), Lewis number of the fuel and the mixture heat release ratio.

Based on the experimentally observed fractal nature of turbulent premixed flames, Gouldin [18] proposed a relation between the flame surface area, the inner (ε_i) and outer (ε_o) cutoff fractal scales and the fractal dimension (D_f) given by Eq. (2.5).

$$A_f/A = (\varepsilon_o/\varepsilon_i)^{D_f-2} \quad (2.5)$$

This method seemed to be promising way to categorise premixed flames as the fractal dimension is easily measured in both imaging experiments and DNS. In a recent review Cintosum *et al.* [19] has shown that the fractal dimension of a flame surface is actually a

poor measure of the turbulent burning velocity and hence is not a good universal measure or predictor of the turbulent burning velocity.

There have been numerous models proposed to numerically simulate turbulent premixed combustion. One of the first and most prevalent models for turbulent premixed combustion is the Bray-Moss-Libby (BML) model [20, 21, 22]. The BML model assumes that the flame front is step like in nature so that the probability of finding an intermediate state is zero. As a result of the BML model formalism the experimental measurement and modelling of gradient and counter gradient diffusion of the reaction progress variable has been examined by numerous investigators. The modelling of scalar diffusion in a RANS perspective is typically done in terms of the gradient transport assumption given by Eq. (2.6).

$$\widetilde{u''c''} = -D_t \nabla \tilde{c} \quad (2.6)$$

For small values of ν' Libby and Bray [21] has shown that gradient transport does not occur but rather countergradient transport occurs. The transition from gradient to counter-gradient has been examined experimentally in detail by Kalt *et al.* [23].

The BML formalism still does not completely solve all of the closure issues in the modelling of turbulent premixed combustion, this can be seen by examining the transport equation for \tilde{c} in Eq. (2.7), where the closure of the reaction rate term is non-trivial.

$$\bar{\rho} \frac{\partial \tilde{c}}{\partial t} + \widetilde{\rho v \cdot \nabla \tilde{c}} + \nabla \cdot (\widetilde{\rho v'' c''}) = \tilde{\omega}_c \quad (2.7)$$

The search for an adequate and universal closure for the reaction rate term in Eq. (2.7) has been the source of significant modelling efforts, models ranging from the flamelet crossing length by Bray and Libby [24], flame surface density by Trouvé and Poinso

[25], and coherent flame models by Candel *et al.* [26] have been proposed to name only a few of the most prevalent closure methods.

The ‘G’ equation or level set method proposed by Williams [27] is an entirely different modelling methodology compared to the BML methodology for turbulent premixed combustion. In the G equation modelling methodology the transport equation for a nonreacting scalar G, that tracks the flame surface is solved. The main initial attraction to the G equation modelling methodology is that by virtue of G being a nonreacting scalar the G equation does not feature the reaction rate term, hence the issues related to the closure of this term are not experienced. However, the reaction rate terms and other new terms must be incorporated into the closure of unclosed terms in the G equation, this difficulty combined with the difficulty of the renormalisation requirement of the G field at each time step has been the primary limitation of the G equation modelling methodology. In addition just like the BML approach the G equation is not able to directly predict pollutant formation such as NO_x as it is a kinematic approach to solving premixed combustion as opposed to a chemical kinetic approach.

It is interesting to note that the modelling strategies outlined above involve the initial assumption of a thin step like premixed flame front. Experimental results have indicated that under high turbulence conditions the flame front structure is far from being step like in nature with considerable variations in the instantaneous flame front flame thickness for many practically relevant regimes of premixed combustion [28, 29]. Experimental results for these regimes are limited, because of this considerable controversy still exists over whether a turbulent premixed flame front is thinned or thickened under high turbulence levels [11, 30]. Furthermore, if the instantaneous flame structure can be influenced by turbulence thickening or, the next question that naturally arises is if the flame chemistry is significantly influenced by turbulence in these regimes.

2.2 Laser Diagnostics

The application of advanced laser diagnostics forms an integral part of the investigative experimental technique applied in this thesis. The use of laser diagnostic techniques is advantageous for several reasons:

- They do not perturb the flow-field like probe or hot-wire measurements.
- Species selective and temperature sensitive techniques are available.
- Techniques with sensitivities of the order of ppm in combustion environments are possible.
- It is possible to have very small measurement volumes, typically of the order of $100\mu\text{m}$, hence high spatial resolution is readily achievable
- The time scale of a typical laser pulse is of the order of 10ns, hence very high temporal resolution is readily achievable.
- It is possible to measure short lived species that would not normally survive suction probe extraction from the flow.

A review of the theory for Rayleigh and Raman diagnostics is presented below. A review of laser induced fluorescence (LIF) is not presented in this Chapter as this material incorporated into the original work on LIF presented in Chapter 4.

2.2.1 Rayleigh scattering

Rayleigh scattering is an elastic scattering process that results from a time varying electro-magnetic field inducing a dipole moment in a molecule or atom. This induced dipole moment is most strongly aligned with the polarisation of the electric field; smaller off diagonal terms do exist in the polarisability matrix (α) that are often referred to as the polarisation coefficients, however these terms are typically two orders of magnitude smaller. A probable outcome after the relaxation of the induced dipole moment is the

emission of an electromagnetic wave at the same frequency as the original oscillating electric field. This process can be termed to elastic because the wavelength of the signal and the excitation fields are equal.

The Rayleigh scattering signal is linearly proportional to the number density and cross section of the scattering molecules or atoms as well as the strength of the incident field. This allows Rayleigh scattering to be particularly useful for determining the temperature in isobaric flows where the cross-section is known. There are a number of ways to determine the Rayleigh scattering cross section in combustion relevant flows, in some flows the mixtures are tailored so that the Rayleigh cross section is approximately constant throughout the temperature range [31, 32]. Another method is to form an explicit functional relation for the variation of the Rayleigh cross section; this is typically based on prior calculations such as laminar flamelets or other zero or one dimensional laminar flame simulations [33]. Another method is to measure the individual species concentrations of the gas and compute the Rayleigh cross-section directly from the individual gas components, this is essentially the Raman-Rayleigh matrix inversion methodology [34].

In this thesis the Rayleigh scattering cross section that is required to calculate temperature has been found using two different methods. For the Line imaging experiments reported in Chapter 6 the cross section is determined using the Raman-Rayleigh-LIF matrix inversion technique, where as for the planar imaging experiments reported in Chapters 5 and 7 the cross-section is determined based on an assumed functional form derived from laminar flame calculations. Equations that are used to calculate the corrections for background reflections, laser energy fluctuations and establish a calibration for the optical collection efficiency of the system are presented in Appendix B.

2.2.2 Raman Scattering

Raman scattering is an inelastic process which means that the signal occurs at a shifted wavelength to that of the incident photon of light. The spectral signature of the shifted signal is unique for a particular molecule, allowing the specific measurement of the concentration of a particular component of a mixture of gases. The mechanism that causes Raman scattering is the interaction of an electro-magnetic wave with dipole that is in motion, this motion can be due to oscillation (vibration) or rotation. This description of the mechanism of Raman scattering reveals why noble gases are not Raman active, noble gases do not feature a vibrating or rotating dipole moment.

It is quite fortuitous in methane-air flames that the Raman lines for all of the major species occur in distinct spectral locations with minimal overlap, a possible exception to this statement depending on the spectral resolution and temperature of the measurement is the mild overlap between CO_2 and O_2 Raman lines. The relatively distinct spectral locations for the major species allow the determination of the major species concentrations with minimal correction for so called major species “cross-talk” factors in methane-air flames.

A general obstacle in hydrocarbon-air flames that must be overcome for quantitative Raman measurements is that certain minor species cause severe interferences over the Raman lines of the major species. Examples of minor species that can cause such interferences are C_2 , C_3 , polycyclic aromatic hydrocarbons (PAH), soot precursors and soot. Strategies to minimise these interferences include a selection of a hydrocarbon fuel that has a low propensity to sooting and forming soot precursors, fuel dilution with air, N_2 or an inert gas, acquiring measurements in regions of the flame that feature low levels of interferences (close to the nozzle) and selection of excitation laser wavelength that minimises the interference.

The most significant obstacle in obtaining high SNR levels in Raman scattering experiments is the very small Raman scattering cross sections for combustion relevant

gases, typically Raman scattering cross-sections are three orders of magnitude smaller than for Rayleigh scattering cross-sections. To gain an appreciation of how small Raman cross sections are, typically ten million excitation photons are required to yield just one Raman photon. Raman scattering cross sections scale very favourably with decreasing laser wavelength displaying a ν^4 dependence on laser frequency. Whilst the Raman cross-section scales favourably with laser wavelength, interferences also rapidly increase with laser frequency. It would seem that the selection of the laser wavelength to maximise the Raman cross section and minimise interferences is a compromise. A justification for the laser wavelength used in the experiments reported in Chapter 6 as well as a discussion of the advantages and disadvantages of the various other laser wavelengths is outlined below.

The approach of utilising the frequency doubled output of Nd:YAG has been shown to have many advantages compared to other excitation sources for Raman-Rayleigh diagnostics, particularly when applied to hydrocarbon-air flame measurements. Masri *et al.* [35] show that interferences in hydrocarbon flames originating from photolysis of PAH and small soot particles as well as C₂ LIF are minimised in the 500-600nm wavelength range by use of 532nm wavelength excitation. This is most fortuitous as this is the output from a frequency doubled Nd:YAG is 532nm. Excitation with wavelengths above 600nm is possible such as with the ruby laser at 694nm but these schemes have not been evaluated primarily due to the ν^4 dependence of the Raman cross section leading to prohibitively small cross sections in the red, NIR and IR. High quantum efficiency detectors with the necessary low readout noise in this spectral range relative to the visible are not yet available further discouraging the use and investigation of this wavelength range.

Due to the Raman cross section of most relevant combustion molecules being very small it is possible to consider shorter wavelengths taking advantage of the ν^4 dependence of the Raman cross section with laser frequency. Typically these shorter wavelengths are accessed with pulsed lasers such as frequency tripled or quadrupled Nd:YAG lasers or one of the many varieties of excimer lasers. Although there is an enormous advantage of

increased Raman cross sections at these shorter wavelengths, all of the mentioned excitation lasers suffer from a common problem of large interferences from PAH LIF, C_2 and C_3 LIF, LIF from photolysis of large carbon species, and laser induced heating from soot precursors and small soot particles. These interference problems increase with decreasing wavelengths and mixtures that have a high propensity of sooting such as equivalence ratios larger than 2.0. Although there has not been an all encompassing study of Raman interferences in hydrocarbon flames such as a study of the interferences through all equivalence ratios for all relevant laser wavelengths, there has been a study by Meier and Keck [36] that examined the background levels in the post flame exhaust of a rich flat flame for a number of wavelengths (266nm, 355nm, 487nm and 532nm). The conclusion was made by Meier and Keck [36] that 532nm delivers the least background interferences and that interferences generally increase at a greater rate than the Raman signal for decreasing wavelengths.

In a review of the applications of excimer lasers to combustion diagnostics Rothe and Andresen [37] highlight the cross-section advantages of deep UV excimer lasers for Raman scattering, however the interferences issues and Raman cross-talk problem with UV excitation are not discussed in detail. Although the background levels from excimer lasers were not trialled in the study of Meier and Keck [36] it can be generalised that one of the conclusions from the study of Meier and Keck [36] that the background interferences increase with decreasing wavelength would not change the conclusion that 532nm is the optimal wavelength to minimise interferences. Furthermore each of the combustion relevant excimer lasers suffer from certain interference problems that make them problematic even in an environment where the expected interferences are low such as in lean premixed combustion.

The XeF excimer laser operates at 351nm and is tuneable with a typical bandwidth of around 3nm. The XeF laser is possibly the least interfering excimer laser in clean environments in terms of PAH LIF, C_2 LIF and photolysis interferences based on the spectra reported by Böckle *et al.* [38]. A likely Raman interference source in hydrocarbon flames for the XeF laser that will occur in fuel rich and intermediate temperatures regions

is CH₂O LIF, due to the broadband absorption features (348-355nm) of the $\tilde{A}^2A_1 \leftarrow \tilde{X}^1A_1, 4_0^1$ & 4_0^2 transitions of CH₂O [39, 40]. Subsequent LIF from these transitions will occur in the spectral region 360-550nm which will cause interferences in varying degrees on all of the major species Raman lines. For hydrogen-air flames the CH₂O LIF interference will not occur. The application of the XeF laser to Raman diagnostics in combustion has not been examined to date, this is probably due to the fact that high energy (>100mJ/shot) XeF lasers have only just become commercially available and the proven applicability of other higher power excimer lasers such as the KrF laser.

The XeCl excimer laser operates around 308nm and is tuneable within a 1nm bandwidth. The XeCl laser suffers from a severe absorption problem from the strong A-X (0,0) band of OH. Interferences on the Raman bands from the excited OH is possible, one such an example is the (0,1) transition of OH at 347nm falling on the predicted H₂O Raman line. Despite the mentioned difficulties, Hassel [41] has demonstrated that Raman scattering in flames using the XeCl laser is possible under certain conditions.

The KrF laser operates around 248.5nm and is tuneable to within a 1nm bandwidth, the KrF laser has been proven to be the most popular excimer laser for the application of Raman-Rayleigh diagnostics in combustion. There are a number of interference and photolysis issues with the use of the KrF laser that has been proven to be difficult to account for in a rigorous manner [42]. Some of these interferences include photolysis and LIF of H₂O, OH LIF excited through the (3,0) transition and LIF of O₂ from the Schumann-Runge bands. As a proof of principle, Wehrmeyer *et al.* [43] and Reckers *et al.* [44] were able to show that the KrF laser could be used in a rich hydrogen-air flame without unacceptable LIF interferences from O₂ and OH, the same experimental configuration was essentially utilised by Cheng *et al.* [45] to investigate the flame stabilisation region of lifted H₂-air flames. There are also numerous other examples of successful investigations of turbulent hydrogen-air flames ranging from the turbulent jet flames examined by Nandula *et al.* [46, 47] and Brockhinke *et al.* [29, 30, 31, 32] to the supersonic reacting flows by Cheng *et al.* [48]. It is also possible to utilise the interferences or LIF processes from O₂, H₂O, NO, C₂ or PAH as a qualitative diagnostic

technique for these species [49, 50, 51, 52, 53, 54, 55, 56] in their own right. The extension of the KrF Raman/Rayleigh diagnostic technique to hydrocarbon flames is complicated by interferences from C_2 and other PAH molecules [57], though Chen *et al.* [10, 58] has reported some degree of success in rich methane-air flames that are far from sooting conditions. A promising method to help reduce the level of LIF interferences particularly relevant for the high levels of interferences in KrF Raman measurements due to C_2 and PAH species is to separate the signal into its polarized components [59], the predominant proportion of the Raman signal will be polarized, whereas the interfering signal from C_2 and PAH LIF will not be polarized. Building upon the success of previous Raman measurements using the KrF laser, Multi-dimensional Raman/Rayleigh/LIF using KrF laser measurements have been presented as a proof of principle in a near stoichiometric methane-air flame by Grünefeld *et al.* [60]. A further example that pushes the envelope of KrF laser Raman measurements are those reported by Grünefeld *et al.* [61] in a spray flow of an oil burning furnace and in the a conventional octane-air fuelled spark ignition (SI) engine, it appears as though distinct Raman lines can be observed in these environments at cold temperatures however it is clear from spectra at high temperatures in these environments that the high levels of interferences would preclude quantitative measurements of major species on a single shot or even an average basis.

Although Raman cross sections are approximately 2 orders of magnitude larger for the ArF excimer laser at 193.3nm compared to the frequency doubled Nd:YAG at 532nm, quantitative Raman scattering with the ArF laser is not feasible because of the numerous absorption, LIF, photolysis and interference processes that occur from O_2 [62], H_2O , CO_2 and H_2 . Other Raman interferences could occur with the use of ArF laser excitation; however they have not yet been reported.

Even after the numerous possible interference problems are acknowledged with UV lasers further disadvantages still exist, excimer lasers typically have very poor beam divergence properties and beam profiles, this means that achieving a tight waist of the order of 150 μ m FWHM at the probe volume virtually impossible without sacrificing an unacceptable amount of energy in a spatial modulator. Furthermore detection in the UV

almost exclusively requires an intensifier which is a large source of noise and spatial blurring, hence increasing the uncertainty in the measurement to levels that the measurements may no longer be considered to be quantitative.

In summary the frequency doubled Nd:YAG is the ideal choice to minimise uncertainties for Raman-Rayleigh diagnostics in hydrocarbon-air flames due to the superior beam profile and divergence qualities, minimal spectral interferences in the Raman spectral regions of combustion relevant species, availability of low noise high quantum efficiency detectors, readily available high quality optical components and negligible absorption occurring for combustion relevant species.

2.3 Numerical Modelling

The background to the numerical modelling that is conducted in Chapter 10 is reviewed in this section. This review is primarily concerned with the PDF method and its numerical implementation. Material relating the RANS turbulence models used for the PDF calculations is examined in Chapter 9.

2.3.1 An Overview of the Probability Density Function Method

PDF methods offer the significant advantage over conventional moment closure methods primarily because the advection and chemical source terms in the PDF equations occur in closed form. Whilst exact treatment of advection is always advantageous, for a hybrid particle-finite-volume scheme, such as that used by the PDF method, the primary source of advection error is due to the systematic error in the RANS turbulence model rather than the linearization and subsequent discretisation of the advection terms in the thermo-chemical transport equations. The exact treatment of the chemical source term by the PDF method is an enormous benefit, as accurate treatment of the chemical source term in

turbulent combustion has been and still is one of the fundamental challenges for accurate and predictive combustion models. Few other modelling methodologies are capable of treating the chemical source term in closed form as the PDF method does. Essentially the only other modelling methodologies that treat the chemical source term in closed form are direct numerical simulation (DNS) and the LES implementation of the PDF method, namely the filtered density function (FDF) method.

Despite its advantages there are a number of challenges that need to be addressed when using the TPDF methodology. By definition, the joint PDF methodology is a high dimensional method. The joint PDF of composition as used in this study has N_s+1 dimensions, where N_s represents the number species and the +1 is due to the enthalpy equation. Finite-volume based methods are not efficient in handling problems with high dimensionality as the computational cost scales to the exponent of the problem dimensionality. Clearly for 22 chemical species and enthalpy transport equations a 23 dimensional problem becomes intractable for finite volume methods.

A solution to the high dimensionality of PDF methods is to recast the PDF transport equations as stochastic differential equations and solve them using a Monte Carlo particle-based methodology. The advantage of Monte Carlo based solution methods is that the computational cost is linearly proportional to the dimensionality of the problem; hence the high dimensionality of PDF methods becomes manageable for Monte Carlo based solution methodologies. There is however a drawback to the recasting of the problem as stochastic differential equations and subsequent solution using a Monte Carlo solution method, two new error sources are created: statistical error and bias. These error sources are not present in finite volume methods and are unique to the Monte Carlo solution technique. The new error sources can be controlled and partially quantified in a simulation. Because of these additional error sources additional work is required for Monte Carlo simulations to gain confidence in the accuracy of the calculations.

Although advection and reaction are treated exactly in the TPDF method a new unclosed problem that does not occur in traditional moment closure based methods arises: this is

the need for a micro mixing model. As the stochastic particles advect and react throughout the domain they must interact or mix in some manner. It is the role of the micro mixing model to govern how and which of the stochastic particles mix. In certain geometries such as the auto-igniting Cabra burner [63], the solution will display very little sensitivity to the mixing model but high sensitivity to the kinetics. In other geometries such as the prediction of extinction and re-ignition in the piloted non-premixed flames (such as Sandia flame F [64]) the sensitivity to the mixing model and the time scale ratio constant C_ϕ is very large. The sensitivity of a particular simulation to the mixing model and chemistry can be evaluated by examining the local stochastic particle sensitivities as shown by Ren and Pope [65].

Another challenge for TPDF methods is the computational cost. For a 2D axisymmetric configuration with detailed chemistry the computational cost in terms of time and memory requirements can be comparable to a non-reacting moderate resolution 3D LES of the same flow. Almost all of the PDF computational cost stems from the exact treatment of the chemical source term. In order for chemical reactions to be treated exactly, they must be explicitly calculated for each particle. This creates an enormous computational burden as the stochastic Monte Carlo methods require many particles per finite volume cell (typically 100) to minimise statistical noise and bias. Chemistry acceleration techniques such as *in situ* adaptive tabulation (ISAT) maybe used to speed up the chemistry computation by up to two to three orders of magnitude in some cases over direct integration. Compounding the overhead due to chemistry computation is the fact that stochastic Monte Carlo particle based methods typically take far longer to converge than standard finite-volume methods and once converged require a time averaging procedure to minimise statistical noise in the final solution. These computational overheads do not make PDF computations insurmountable, but rather in comparison to other RANS based combustion models for the same geometry, PDF methods require at least an order of magnitude greater computational time. For comparative purposes, a reacting 2D symmetric TPDF solution will typically require far less computational time than the corresponding reacting 3D LES of the same geometry, even if a tabulated chemistry method is used in the LES calculation. This is an interesting

comparison to make, as the success of the both of these methods can be roughly gauged from the results of recent TNF workshops. The results from these recent workshops indicate that the current state of the art TPDF simulations predict finite-rate chemistry effects well in non-premixed flames but struggle with the predictions of the turbulence fields, in contrast for non-premixed flames exhibiting strong finite-rate chemistry effects state of the art LES using a tabulated reaction rate approach typically predict the turbulence field well but struggle to predict the finite-rate chemistry effects of the flame sufficiently.

The thermochemical composition PDF simulation methodology utilised in this study requires the velocity and turbulence fields to be accurately solved. It is well known that RANS based turbulence models such as the $k-\varepsilon$ model do not accurately simulate many flow geometries due to the many model deficiencies. Errors in the mean velocities translate into errors in the transport terms for the TPDF method, however so long as the mean velocity field is not grossly in error its impact is typically minimal. The fluid mechanical time scale k/ε is used by the mixing model in the calculation of the scalar time scale. This means that any flow that is sensitive to the mixing model will be equally sensitive to the turbulence model which governs the calculation of the mean turbulent kinetic energy and the mean turbulent kinetic energy dissipation fields. Indeed it is the error in the predicted mean turbulent kinetic energy and the mean turbulent kinetic energy dissipation fields that can often be the weak link in TPDF-RANS simulations.

2.3.2 Previous work using the PDF Method

The application of the PDF method to combustion has received considerable attention with most of the effort focused on non-premixed combustion investigations. Some of the more significant PDF studies and their relation to the progression of the PDF method are reviewed in this section.

The single step reaction of NO with O₃ essentially occurs without significant heat release, this reaction was examined using the PDF method by Givi *et al.* [66] in two fundamental geometries: the plane jet and the axisymmetric jet. Although no experimental comparisons were able to be made, the study was an important precursor to PDF methods that included heat release. Nguyen and Pope [67] present PDF calculations of reacting hydrogen-air jet diffusion flames assuming a conserved scalar approach and infinitely fast chemistry, the mixture fraction PDF equation was solved using a stochastic Monte Carlo approach. Some of the obvious limitations in predicting finite-rate chemistry effects when combined with the conserved scalar approach in the PDF method are highlighted by Wouters *et al.* [68].

An intermediate between the conserved scalar approach with no chemistry computation and more detailed kinetic mechanisms is the ILDM chemistry approach. Norris and Pope [69] use three characteristic scalars to characterise the ILDM and use these three scalars in the joint PDF of composition, velocity and dissipation. By incorporating chemistry with only three characteristic scalars Norris and Pope [69] are able to predict blow-off to within 10% of the experimental blow-off jet velocity of a piloted non-premixed flame with a CO/H₂/N₂ fuel jet [70] as well as predict a degree of finite-rate chemistry effects near blow-off.

The simulation of the Delft piloted burner reported by Peeters *et al.* [71] has been examined by Nooren *et al.* [72] using an elliptic PDF code. Three mixing models were evaluated in this study: the IEM model [73], a revised version of the modified Curl (MC) model [74] and the mapping closure model [75, 76]. Due to the elliptic nature of the solution, constrained equilibrium [71] with low temperature corrections [77] and ILDM [78] chemistry were utilised to allow the flames to be computed at a realistic computation cost. The constrained equilibrium solution was shown to yield good predictions for the temperature PDF in mixture fraction space, whilst the ILDM solution went further in its predictive capabilities so that the OH PDF in mixture fraction space was well predicted including the super-equilibrium concentrations. It should be noted that the solution was reported to be sensitive to the mixing model; both the mapping closure and MC mixing

models produced satisfactory results whilst the IEM were reported to be not as good in certain regions of the flow. A constant value of $C_\phi = 2.0$ was used for all simulations by Nooren *et al.* [72].

In the past ten years recent advances in computing power has allowed PDF simulations using more complex methane chemistry ranging from skeletal mechanisms [79] to augmented reduced mechanisms with steady and quasi steady state species [80], to simulations with full GRI3.0 chemistry [81]. With the subsequent increase in chemical description corresponding increases in the predictive capability of kinetic sensitive parameters such as extinction and re-ignition, fuel rich side kinetics, minor species predictions such as OH and CO and pollutant formation such as NO have been reported [81, 82]. Simulations with more complex fuels than methane such as methanol using a augmented reduced mechanism based on a detailed kinetic mechanism [83] have also been carried out using the PDF method.

Typically PDF simulations have relied on geometrical symmetries allowing the problem to be solved on a 2D axisymmetric grid with a considerable saving in computational cost. An extension of the PDF to 3D practically relevant gas turbine combustors has been reported by James *et al.* [84] with many complicating practical aspects incorporated into the calculation such as sprays, secondary dilution, high pressure (17.6 Bar), preheating of the primary air to 782K and direct modelling of the primary swirler. In order to make such large computations tractable a two-step mechanism is used for propane and jet-A fuels. Good agreement is reported for computed and experimental mean temperature profiles.

To model the unclosed micro-mixing term in the PDF equation there have been a number of models proposed such as: Curl's mixing model [85, 86], the modified Curl (MC) mixing model [74, 87, 88], the interaction exchange with the mean (IEM) mixing model [73, 89], the mapping closure model [75], the ordered pairing model [90] and the Euclidean minimum spanning trees (EMST) mixing model [91]. The specifics of three of these mixing models (MC, IEM and EMST) will be reviewed in greater detail later in this

Chapter in Section 2.3.5. In general each of the above mixing models has certain advantages and shortcomings in different situations. In general for non-premixed combustion the EMST model has been shown by Cao *et al.* [92] to give the best results for the TNF piloted diffusion flame series compared to the MC and IEM mixing models. The MC and IEM mixing models are shown to be able to produce extinction and re-ignition; however the scalar variance values are unacceptably under predicted. In general it is also shown by Cao *et al.* [92] that the MC mixing model outperforms the IEM mixing model. Further difference in the predictions of the EMST, IEM and MC mixing models applied to a partially stirred reactor (PaSR) have been examined by Ren and Pope [93], that confirm the EMST mixing model is more resilient to extinction than the IEM and MC mixing models when applied to the particular PaSR problem examined.

The relative performance of the mixing models in terms of the predicted fields for the mean scalar, scalar variance and finite-rate chemistry effects can be modified by changing the value of the value of C_ϕ which governs the ratio of the scalar to fluid mechanical time scales. In early PDF simulations [67, 94, 95, 96, 97] a value of $C_\phi = 2.0$ was used, this assumes that the ratio of scalar to fluid mechanical time scales is 2. The value of C_ϕ is proposed to be in the range 1.5-2.5 by Beguier *et al.* [98] for a range of shear flows, thereby an average value can be taken to be 2. More recent measurements than those of Beguier *et al.* [98] for the scalar time scale ratio carried out by Panchapakesan and Lumley [99] indicate that for the axisymmetric jet the scalar to velocity time scale ratio is within 15% of 1.5 over the entire radial profile up to $r/r_{1/2} = 2.0$.

By modifying the value of C_ϕ it is possible to increase or decrease the predicted scalar variance (such as ξ''), finite-rate chemistry effects (such as extinction and re-ignition) and mean scalar predictions (such as mean flame length and $\tilde{\xi}$). Generally by increasing C_ϕ more robust burning (less extinction) and decreased variance predictions are found. One of the first parametric investigation of the effect of varying C_ϕ in a turbulent flame

with complex chemistry was conducted by Xu and Pope [79] who found that the optimal value of C_ϕ for the piloted flame series using the EMST mixing model was $C_\phi = 1.5$. Further work by Cao *et al.* [92] on the same piloted non-premixed flame geometry confirmed the results of Xu and Pope [79] for $C_\phi = 1.5$ using the EMST mixing model, but also optimal values of $C_\phi = 3.8$ and $C_\phi = 3.3$ were proposed for the MC and IEM mixing models respectively. In auto-igniting flows where the chemical source term dominates and mixing is as important, Masri *et al.* [100] and later Cao *et al.* [101] find there is very little sensitivity for C_ϕ in the range 1.5-2.5 for the EMST, MC and IEM mixing models, further simulations by Ren and Pope [65] examining the sensitivity to mixing model and C_ϕ at the particle level confirm this finding.

The optimal value of C_ϕ is not necessarily universal between investigations. Lindstedt *et al.* [80] report an optimal value of $C_\phi = 2.3$ using the MC mixing model and complex chemistry [102, 103] based on a reduced version of a 48 species 300 reaction mechanism. Cao *et al.* [101] argue that with the GRI3.0 chemical mechanism, a flame is not able to be stabilised for $C_\phi \leq 3.0$ using the MC mixing model for flame E. Cao *et al.* [101] argue that the success of $C_\phi = 2.3$ by Lindstedt *et al.* [80] is probably not due to the implementation differences in the PDF equations or mixing models, but rather that the chemical mechanism used was significantly faster and more resilient to extinction than GRI 3.0. If the explanation provided by Cao *et al.* [101] were to hold then the methanol mechanism [104] used by Lindstedt and Louloudi [83] must also be too kinetically fast and resilient to extinction, as a value of $C_\phi = 2.3$ was also found to be near optimal for their study of the experimental piloted methanol flame reported by Lindstedt and Louloudi [83].

Further resolution of the controversy regarding the optimal or correct value of C_ϕ for non-premixed combustion may not be possible until identical simulations with a given PDF code is computed with the MC mixing model and both GRI3.0 and the Lindstedt

methane mechanism [102, 103] and compared with the results of Lindstedt *et al.* [80] and those of Cao *et al.* [101]. Such a study is already underway and being examined [105].

Using the joint PDF of velocity, turbulence frequency and composition Liu *et al.* [106] has examined the effect of varying C_ϕ for the EMST mixing model and complex chemistry on the prediction for the Sydney bluff-body burner [107, 108, 109, 110, 111, 112, 113]. The results show that $C_\phi = 1.0$ gives optimal results for the mixture fraction variance but $C_\phi = 2.0$ gives better results for extinction and temperature variance fields, furthermore NO and OH is predicted well only for $C_\phi \leq 1.5$. This shows that the optimal choice of C_ϕ is often a compromise between many variables in a simulation as well as between different geometries (bluff-body and pilot diffusion flame).

Using a joint composition PDF approach coupled with a FV solver for the fluid and turbulence solutions, Merci *et al.* [114, 115, 116, 117, 118, 119, 120, 121] have examined the influence of different mixing models, values of C_ϕ and different turbulence models for the Delft piloted flame and the Sydney bluff body flame. These studies confirm those by Cao *et al.* [101] in that the EMST mixing model was found to be superior to the IEM and MC particularly for flames near extinction and increased values of C_ϕ or pilot heat release were required to obtain a stable flame for the IEM and MC mixing models. Also the comment is made by Merci *et al.* [120] concur with those of Fox [122] that the EMST is sometimes ‘too local’. This means that when predicting extinction, the EMST mixing model does not evolve the particle towards the inert mixing limit at the same rate that the experimental data indicates. The MC mixing model seems to do a better job than the EMST mixing model predicting the beginnings of extinction using a significantly increased value of C_ϕ to obtain good correlation with the experimental results. However, the MC model suffers from an unrealistically rapid transition to total flame blow-off due to the non-localness property of the MC mixing model in composition space. This unrealistically rapid transition to total blow-off is an issue the EMST mixing model does not suffer from.

2.3.3 Equations for the Probability Density Function Method

The equations defining the single point joint probability density function (PDF) have been outlined in a number of publications by Pope [123, 124, 125]. Following Pope [124], the transport equation for the single point PDF f (where $f(x, t, \psi)$, x is the position vector and ψ is the thermo chemical composition vector) can be expressed by Eq. (2.8).

$$\begin{aligned} \rho(\psi) \frac{\partial f}{\partial t} + \rho(\psi) V_j \frac{\partial f}{\partial x_j} + \frac{\partial}{\partial \psi_\alpha} [\rho(\psi) S_\alpha(\psi) f] = \\ - \frac{\partial}{\partial x_j} [\rho(\psi) \langle u_j'' | \psi \rangle f] + \frac{\partial}{\partial \psi_\alpha} \left[\rho(\psi) \left\langle \frac{1}{\rho(\psi)} \frac{\partial J_j^\alpha}{\partial x_j} \middle| \psi \right\rangle f \right] \end{aligned} \quad (2.8)$$

It can be seen from inspection of Eq.(2.8) that $\langle S(\alpha) | \alpha = \psi \rangle = S(\psi)$ leading to the claim that the chemical source term is in closed form for the composition PDF method. As only the joint thermo-chemical composition PDF is considered in this study and not the joint velocity-thermo-chemical composition PDF the first term on the RHS of Eq. (2.8) representing the turbulent scalar flux is not in closed form and needs to be modelled. A standard gradient diffusion RANS model for the turbulent scalar flux term is used in this study. Eq. (2.9) gives the relation that is used for the turbulent scalar flux model.

$$- \frac{\partial}{\partial x_j} [\rho(\psi) \langle u_j'' | \psi \rangle f] = \frac{\partial}{\partial x_j} \left(\frac{\mu_t}{\rho(\psi) Sc_t} \frac{\partial f}{\partial x_j} \right) \quad (2.9)$$

The value of the turbulent Schmidt number Sc_t , for all calculation is set to 0.7. The modelling of the turbulent scalar flux is not only limited by the possible error of the

gradient diffusion assumption but also the predictive capability of the turbulent viscosity μ_t , determined by the turbulence model.

As f is a single point PDF, f contains no information of the local scalar gradients, hence a model is required for the 2nd term on the RHS of Eq. (2.8), this model is called the micro mixing model. The micro mixing model essentially governs the modelling of molecular diffusion. It can be shown that the 2nd term on the RHS of Eq. (2.8) can be recast as a conditional Laplacian $\langle \Gamma \nabla^2 \alpha | \psi \rangle$ or alternatively as the conditional scalar dissipation $\langle 2\Gamma \nabla \alpha \cdot \nabla \alpha | \psi \rangle$. Presentation and detailed discussion of the implementation of three mixing models that are evaluated in this study is left until Section 2.3.5 of this Chapter.

The numerical form of Eq. (2.8) is highly dimensional and not feasibly solved using finite volume methods. To solve Eq. (2.8), it is required to transform Eq. (2.8) into a stochastic differential equation (SDE) to be solved using a Monte Carlo method. The advantage of using a Monte Carlo solution method is that the computational cost of a Monte Carlo solution scales linearly with the dimensionality of the problem, making the solution computationally feasible, even for large number of species. As the Monte Carlo method is a particle method, in the implementation many particles are employed per finite-volume cell, the evolution of each of these particles is governed by reaction, diffusion and advection. The implementation of the reaction, diffusion and advection sub-steps in the SDE solution is by a fractional step method. The fractional step method utilised is outlined by Cao and Pope [126], this method displays a weak second order accuracy.

A second order Lagrangian method presented by Pope [127] is used to evolve the particles over the time step Δt , for the steady state calculation. The method involves two advection steps; the first advection step is given by Eq. (2.10), which governs the advection of the particle to an intermediate position.

$$x_i^{1/2} = x_i^0 + \frac{1}{2} u_i^0 \Delta t \quad (2.10)$$

In Eq. (2.10) x_i is the position vector and the superscript denotes the time step progress (⁰ for the initial location, ^{1/2} for the intermediate location and ¹ for the final location at the end of the time step), u_i is the local Favre mean fluid velocity vector and again the superscript denotes the time step progress. The selection of the size of the local time step Δt in Eq. (2.10) is an important parameter in determining the accuracy, stability and the rate of convergence of the fraction step. The calculation of Δt is based on Eq. (2.11), with the definition of the time sub-steps Δt_{conv} , Δt_{diff} and Δt_{mix} given by Eq. (2.12).

$$\Delta t = \min(\Delta t_{conv}, \Delta t_{diff}, \Delta t_{mix}) \quad (2.11)$$

$$\begin{aligned} \Delta t_{conv} &= C_{conv} \Delta x / u_i^0 \\ \Delta t_{diff} &= C_{diff} (\Delta x)^2 / \mu_t \\ \Delta t_{mix} &= C_{mix} k / \varepsilon \\ \Delta x &= [\text{avg}(\Delta x_{cell}, \Delta y_{cell}, \Delta z_{cell})]^{1/D} \end{aligned} \quad (2.12)$$

In Eq. (2.12), D is the dimensionality of the problem, $\text{avg}(\Delta x_{cell}, \Delta y_{cell}, \Delta z_{cell})$ is effectively a characteristic cell dimension and the constants C_{conv} , C_{diff} and C_{mix} are under relaxation factors that ensure both stability and accuracy, these factors are all set to the value of 0.5 for all simulations.

After the calculation of the first advection step the reaction and diffusion sub steps are calculated for the particles. Following this the second advection step is calculated using Eq.(2.13)

$$x_i^1 = x_i^{1/2} + \Delta t \left(u_i^{1/2} - u_i^0 + \frac{1}{\rho S c_t} \frac{\partial \mu_t}{\partial x_i} + \xi_i \sqrt{\frac{2\mu_t}{\rho \Delta t S c_t}} \right) \quad (2.13)$$

In Eq. (2.13), ξ_i is a standardised normal random vector and the value for ρ is taken to be the local cell mean density.

2.3.4 Efficient Chemistry Methods for PDF Calculations

The most computationally intensive part of reactive TPDF is the calculation of the particle reaction rates. Obtaining the species reaction rates by direct integration is computationally very expensive and for large chemical mechanisms this computational cost becomes prohibitively large. To illustrate the computational cost of direct integration a highly conservative example is outlined. Typical 2D axisymmetric combustion simulations using the TPDF method have over one million stochastic particles for a 10000 grid cell problem, usually more than 5000 iterations are required to obtain convergence and obtain statistically averaged quantities. The chemistry is assumed to be a methane-air system represented by a skeletal methane mechanism such as DRM22. The average time for a direct integration of a single particle for such a system on a modern 3.4GHz computer is around 5ms. This means that using direct integration only, the solution a single processor would take 289 days, which is an unacceptably long period of time. Particle methods scale exceptionally well in parallel so this single core processing time could be reduced, however the example given is extremely conservative and is based on a 2D axisymmetric RANS solution. The computing resources required to reduce the problem solution time to a couple of days is well justified in terms of the other competing computational methods available such as LES.

As illustrated above direct integration is not a feasible approach for practical PDF calculations with an elliptic solver. Possible ways to avoid the large cost of direct integration is to not explicitly compute the reaction-rate but rather look the reaction rate up from a table that is pre-computed or computed on the fly. Advanced tabulation

strategies take advantage of the fact the entire composition space is not accessed in a reactive flow, but rather a subset of that. By reducing the composition space to that of a strained laminar flamelet Masri and Pope [128] show that fast and accurate computations using the JPDF method are possible for mildly strained turbulent flames, where significant turbulence chemistry interactions occur such as extinction and re-ignition. By increasing the tabulated compositional space to be parameterised by three scalars by means of a reduced chemical mechanism, Tiang *et al.* [95] show that finite-rate chemistry effects such as the prediction of blow-off can be predicted within an accuracy of 20%.

The successful tabulation of the compositional space relies on a dramatic reduction in the dimensionality of the governing chemical mechanism. Such reductions in dimensionality are possible using partial equilibrium and steady state assumptions as outlined by Smooke [129]. There are several other notable strategies to dramatically reduce the dimensionality of the chemistry to a level where tabulation becomes feasible. The rate-controlled partial equilibrium method developed by Keck and Gillespie [130] identifies the reduced chemistry dimension based on the number of selected rate-limiting reactions. Computational singular perturbation (CSP) is a mathematical method by which numerous chemical reactions are grouped into characteristic time scales; the number of these time scale groupings is effectively the reduced chemistry dimensionality. It should be noted that the time scale grouping process for CSP is entirely mathematical and no prior knowledge of any optimal parameters or assumption for the particular mechanism is required. By making five such groupings (two fast, two moderate and one slow), Lam and Goussis [131] show that an accurate representation of the hydrogen-air reactive system for a wide range of conditions can be made.

Chemical mechanism reduction by intrinsic low-dimensional manifolds (ILDM) outlined by Maas and Pope [78, 132, 133], is a method that aims to reduce the chemical state space globally, by means of an eigenvector analysis to identify locally the fastest time scales of the chemical system. In many respects ILDM and CSP have many similarities, particularly the local determination of the fastest chemical time scales by means of basis vectors. The main distinguishing characteristics between the two are that CSP has the

ability to reduce the computational stiffness of a mechanism and can categorise a mechanism with a reduced number of variables or groupings (whilst the governing equation system remains large), the ILDM method can also reduce the mechanism stiffness and in addition to reducing the dimensionality of the system the governing equations of the system are also reduced.

After the composition space has been reduced by a reduction of the chemical mechanism, further optimisation can be made in the storage and tabulation phase by examining the sensitivity of the tabulation points so that rather being even distributed in composition space they are distributed such that the error is almost equal in composition space. These tabulation concepts are outlined by Tiang *et al.* [95] and Chen *et al.* [134]. More advanced precomputed tabulation methods such as artificial neural networks (ANN) have been implemented into PDF calculations by Christo *et al.* [135, 136]. ANN methods have been shown to be highly memory efficient and are more advantageous for large chemical systems. Generation of optimal training data sets and optimisation of the network geometry are still hurdles that remain to be solved for this method in order to assure erroneous results are not generated or numerical instabilities initiated. One of the powers of ANN is that the stored data is essentially information relating to an advanced mapping function in contrast to a brute force input output tabulation method. Other advanced mapping function storage methods have been proposed beyond ANN, one such an example is parameterisation by proper orthogonal polynomials outlined by Turanyi [137]. In this method the governing set of differential equations is reduced to a set of Gram-Schmidt ortho-polynomials and a solution generated by solving the multivariate Horner equations.

The schemes outlined above are essentially strategies aimed at solving the chemistry off-line and pre-computing a look-up table for the calculations to avoid direct integration. An alternative to these methods is to build the look-up table on-line or *in situ*, by doing so the table can be populated with the particular composition space unique to the particular flow being simulated; no prior assumptions of the dimensionality or type of manifold are required for this strategy. The storage method error control and retrieval process from

such an *in situ* generated table is examined. The *in situ* adaptive tabulation based on principle directions (ISATPD) method outlined by Yang and Pope [138, 139] is one such method that utilises the *in situ* generated table concept. The ISATPD assumes that the tabulation region in composition space is of fixed size once generated, making error control of the tabulated composition region not possible. An inherent feature in the ISATPD method is that the stored mapping function is a constant, if a composition falls in the tabulated cell the output is still the same no matter where in composition space of the cell the original point was. This means that in the ISATPD method, information on the local sensitivity is not stored or included in the calculated mapping; however information on the local principle directions is used to efficiently store cells in composition space. Whilst the ISATPD method was a powerful concept for chemistry tabulation with initial tests indicating a 1665 speed up factor for large mechanisms over direct integration [139], the ISATPD method was quickly superseded by another superior method termed *in situ* adaptive tabulation (ISAT) developed by Pope [140]. ISAT is the method that is used in this study to efficiently evaluate the chemical source term avoiding direct integration methods.

The mathematical details of the calculations of the ellipsoid of accuracy (EOA), the linearised mapping and the local error the reader is referred to Pope [140], a review involving the mathematical detail would simply involve repeating the equations already presented in Pope [140]. Instead of a mathematical description of the ISAT algorithm a conceptual description is given in the few paragraphs below.

ISAT is essentially a method that given the thermo-chemical state of a system $\phi(t_0)$ and a prescribed time step Δt , the thermo-chemical composition at $t_0 + \Delta t$ is calculated ($\phi(t_0 + \Delta t)$). To determine $\phi(t_0 + \Delta t)$ to within a specified error tolerance ε_{tol} , ISAT utilises a number of strategies that are denoted as: direct integration, primary retrieve, secondary retrieve, grow and add. When a calculation is started ISAT begins to populate a table that stores the solutions to the direct integration of the chemical source term. In addition to directly integrating the chemical source term and storing the solution ISAT also stores a mapping called the ellipsoid of accuracy (EOA), which governs how far in composition

space a query to ISAT can be approximated by the stored direct integration result. For a given direct integration mapping for a certain $\phi(\Delta t)$ the size of the resultant EOA for the entry $\phi(\Delta t)$ is a function of the specified mapping or ISAT error tolerance ε_{tol} .

When ISAT is queried, the binary tree is traversed by evaluating the cutting planes in composition space; this process is continued until a termination node is reached. At the termination node $\phi(\Delta t)$ is examined to see if it lies within the EOA of the termination node. If $\phi(\Delta t)$ lies within the EOA of the termination node, a mapping for $\phi(\Delta t)$ is calculated, this process is computationally very fast and is termed a primary retrieve. If $\phi(\Delta t)$ does not lie within the EOA of the termination node, ISAT searches neighbouring nodes on the binary tree in composition space for a given time. This evaluation of the EOA neighbouring nodes is computationally very fast. If it is possible to use one of the EOA from a nearby node from the termination node this is done and is termed a secondary retrieve. If no neighbouring nodes can be found ISAT calculates $\phi(\Delta t)$ directly from the termination node using direct integration. This is a computationally expensive operation. If the direct integration of $\phi(\Delta t)$ from the termination node results in a solution that is within ε_{tol} from the termination node the EOA of the termination node is grown, this process is termed a growth and is computationally expensive. If the direct integration of $\phi(\Delta t)$ from the termination node results in a solution that is outside the EOA of the termination node ISAT searches nearby nodes in composition space to see if the EOA of nearby nodes can be grown if it is possible to do this ISAT grows the EOA of the neighbouring node, this process is called a secondary growth. If the direct integration of $\phi(\Delta t)$ from the termination node results in a solution that is outside the EOA of the termination node or neighbouring nodes ISAT creates a new leaf, cutting plane and EOA for a new node on the binary tree, this process is computationally intensive and is called an addition. As the calculation progresses the number of entries in the ISAT table increases and the EOA for the table entries become more refined allowing a greater number of queries to be evaluated with the computationally cheap action of a retrieve.

In practical calculations it is not possible to continue to register additions to the ISAT table indefinitely; this is due to the finite constraint of the available computational memory. Ideally once the ISAT table has filled the allocated amount of memory, direct integrations that replace additions only accounts for a very small fraction of the total number of queries, e.g. less than 0.1% are direct integrations. By decreasing ε_{tol} a more accurate table will be grown, however the growth phase of the table building will take longer and a greater number of entries (more machine memory) will be required to cover the same compositional space. Conversely by decreasing ε_{tol} a lower accuracy ISAT table will be built at a faster rate requiring less machine memory, also with large values of ε_{tol} it is possible the table might never fill the available machine memory allowing retrieves to almost be the exclusive result of a query resulting very large speed up times over direct integration.

There have been many investigations that examine the effectiveness of the original ISAT algorithm when applied to reacting flow calculations [141, 142, 143, 144], of particular interest is the use of ISAT in reacting PDF calculations [97, 145, 146]. Further refinements of the ISAT algorithm that indicate a further 2-5 times speed up over the original ISAT algorithm are outlined by Lu and Pope [147].

2.3.5 Mixing Models for PDF Calculations

The modified Curl mixing model is based on an original paper by Curl [85], this version of the model is referred to simply as Curl's mixing model. The modified Curl models are sometimes referred to as a Coalescence/dispersion models or a particle interaction models. Curl [85] introduced the mixing model in PDF form whilst Spielman and Levenspiel [86] introduced a stochastic form of this algorithm that is relevant to stochastic PDF simulations. The concept of Curl's mixing model maybe described by the simplified example of mixing between two particles. Consider that ϕ_a and ϕ_b are the compositions of particles a and b before mixing, after mixing the compositions of

particles a and b are denoted as ϕ_a^* and ϕ_b^* . After mixing ϕ_a^* and ϕ_b^* maybe expressed as Eq. (2.14).

$$\phi_a^* = \phi_b^* = \frac{1}{2}(\phi_a + \phi_b) \quad (2.14)$$

It has been shown by Pope [88] that for Curl's model the mean composition is conserved and the variance decreases based on Eq. (2.14). A flaw in Curl's model is that as the PDF evolves it becomes an infinite sum of delta functions, thus the PDF never converges to a continuous distribution. The Modification of Curl's model to produce a continuous distribution is addressed by Janicka *et al.* [74] and Dopazo [87]. Rather than Eq. (2.14) governing the composition after mixing, Eqs. (2.15)-(2.16) Govern the composition after mixing.

$$\phi_a^* = (1 - C_m)\phi_a + \frac{1}{2}C_m(\phi_a + \phi_b) \quad (2.15)$$

$$\phi_b^* = (1 - C_m)\phi_b + \frac{1}{2}C_m(\phi_a + \phi_b) \quad (2.16)$$

The variable C_m in Eqs. (2.15)-(2.16) controls the extent of mixing, with $C_m = 0$ no mixing occurs and with $C_m = 1$ Curl's original model is recovered. By making C_m a random variable with a continuous distribution Janicka *et al.* [74] and Dopazo [87] have shown that the composition PDF inherits the continuous kernel of C_m , thus making the PDF a continuous function. Pope [88] has noted that the joint scalar PDF for the modified Curl mixing model does not perfectly converge to a joint normal distribution in homogenous turbulence, the high order even moments such as the kurtosis $\hat{\mu}_4$ and super-skewness $\hat{\mu}_6$ diverge and tend to infinity as the PDF evolves time. To remedy this problem Pope [88] proposes a revision to the modified Curl model such that the selection of mixing pairs is biased towards reducing the particle age distribution allowing the high

order standardised moments to be finite. The use of model IIIb from Pope [88] allows the PDF in homogenous turbulence to evolve very closely towards (although not perfectly) to Gaussian.

The issue of variable density hence variable particle weights inherent in reacting flows is addressed by Nooren *et al.* [72] by introducing a particle weighting function. This particle weighting function can be applied to the idealised particle pair mixing situation of Eqs. (2.15)-(2.16), yielding Eqs (2.17)-(2.18) for uneven particle weights where m_a and m_b are the corresponding masses of particles a and b respectively.

$$\phi_a^* = (1 - C_m) \phi_a + C_m \frac{(\phi_a m_a + \phi_b m_b)}{(m_a + m_b)} \quad (2.17)$$

$$\phi_b^* = (1 - C_m) \phi_b + C_m \frac{(\phi_a m_a + \phi_b m_b)}{(m_a + m_b)} \quad (2.18)$$

The modified Curl model with particle age biasing and variable particle weight is essentially the form of the modified Curl model that has been used for the simulations in this study

The interaction by exchange with mean mixing model was proposed by Dopazo and O'Brien [73, 89] this model is also often referred to as the linear mean square estimation (LMSE) mixing model. Essentially the IEM model states that during mixing the particle will evolve towards the mean value thereby ensuring that the mean is conserved and the variance decays by its very definition. The IEM is perhaps one of the simplest mixing models in that the molecular mixing term in the PDF equation maybe expressed directly in terms of the IEM which is given by Eq. (2.19).

$$\langle \Gamma \nabla^2 \phi | \phi \rangle = -\frac{1}{2} C_\phi \frac{\varepsilon}{k} (\phi - \langle \phi \rangle) \quad (2.19)$$

For the hybrid FV-particle methodology used in this study the composition evolution of a single particle ϕ_a in a FV cell can be expressed as per Eq. (2.20).

$$\phi_a^* = \phi_a - \left[1 - \exp\left(\frac{C_\phi}{2} \frac{\varepsilon}{k}\right) \right] (\phi_a - \tilde{\phi}_{cell}) \quad (2.20)$$

The $\tilde{\phi}_{cell}$ term in Eq. (2.20) represents the cell Favre mean composition vector. Although the IEM model is very simple in its implementation it has a major short coming, this deficiency is that the model does not preserve the shape of the PDF. Hence for the IEM model in homogenous turbulence the joint scalar PDF does not tend to a joint normal distribution as would be expected Juneja and Pope [148].

The final mixing model to be examined in this study is the Euclidean Minimum Spanning Tree (EMST) mixing model. The EMST model was developed by Subramaniam and Pope [91] being primarily aimed to address the deficiencies of other mixing models such as IEM and MC when applied to problems that feature simultaneous mixing and reaction by capitalising on the concept of locality that the mapping closure model [75, 76] exploits.

The most significant feature of the EMST model is that mixing occurs locally in composition space. This is a feature that neither the IEM nor MC mixing models satisfy. Localness in composition space is enforced by allowing mixing to only occur between particles that are connected by the edges of a Euclidean minimum spanning tree in composition space. The advantage of mixing occurring locally in composition space is shown by the superior results obtained over other mixing models in the diffusion flame test case proposed by Norris and Pope [90]. The superiority of the EMST mixing model has also been shown in its application to a turbulent diffusion flame by Masri *et al.* [96]. If a mixing model is non-local, when applied to the diffusion flame test case proposed by Norris and Pope [90] mixing could be allowed to occur between the cold air and fuel

which could cause extinction due to the two particles being close in physical space but far in composition space caused by the thin flamelet structure. For the EMST mixing model such an event would not occur as the two particles even though they are close in physical space are not close in composition space therefore will not interact directly in mixing.

It is also shown by Subramaniam and Pope [91] that the EMST mixing model obeys several important mixing model quality criteria such as conservation of the mean, decay of the variance and boundedness of the composition during the mixing process. The EMST model does not however satisfy the invariance properties of linearity and independence [149]. Generally the EMST mixing model is considered to be more complex mathematically and computationally demanding than other mixing models such as IEM and MC. An evolution equation for the composition vector of a particle for the EMST mixing model can be given by Eq. (2.21).

$$w_i \frac{d\phi_i}{dt} = -\alpha \sum_{v=1}^{N_T-1} B_v \left[(\phi_i - \phi_{bv}) \delta_{iav} + (\phi_i - \phi_{av}) \delta_{ibv} \right] \quad (2.21)$$

A similar notation is used in Eq. (2.21) as Subramaniam and Pope [150], where v represents edge that connects the particles a and b on the Euclidean minimum spanning tree, δ is Kronecker delta function, w_i is the weight of the i^{th} particle, α is a model parameter that controls the variance decay rate, β_v is a parameter that is a function of the edge weights for a given particle on the Euclidean minimum spanning tree, this parameter directly controls how close the PDF generated by the EMST mixing model decays to a joint normal distribution in homogenous turbulence. Essentially Eq. (2.21) states that the i^{th} particle will evolve according to the composition of the two particles that are directly connected to it on the Euclidean minimum spanning tree. Further validation of the EMST mixing model beyond that initially presented by Subramaniam and Pope [150] is presented in a later publication by Subramaniam and Pope [91]. Subramaniam and Pope [150] examine the relative performance of the EMST mixing model to other mixing

models and the performance of the EMST mixing model in further combustion relevant test cases.

CHAPTER 3 BURNER DEVELOPMENT AND CHARACTERISATION

One of the primary aims of this thesis is to investigate finite-rate chemistry effects in turbulent premixed combustion. To achieve this it is necessary to design a suitable burner that can stabilise premixed flame with sufficiently high turbulence levels over a broad range of equivalence ratios. Such a burner must have excellent optical access to enable laser diagnostics and relatively simple flows to facilitate numerical computations.

The investigation of the interaction of high turbulence intensities with premixed flame fronts requires careful experimental design to prevent flame blow-off. Stabilisation methods such as: preheating, recirculation, swirl or piloting with an additional stream may be required to prevent blow-off. These stabilisation techniques may not be necessary for lean premixed hydrogen flows; however the added complication of differential diffusion and non-unity Lewis number effects become significant as shown by Chen and Bilger [29]. Some of the significant experimental investigations in low Da premixed combustion using the above methods will now be reviewed. El-Banhawy *et al.* [151] utilise a 2D symmetric reverse step combustor geometry operating with lean methane-air compositions Magre *et al.* [152] utilise a similar geometry with the combustion stabilised by either a pilot or a reverse step. The results of both El-Banhawy *et al.* [151] and Magre *et al.* [152] show that significant thickening of the flame front and super-equilibrium concentrations of CO can occur. Bedat and Cheng [153] present a burner design which enables large values of u'/S_L to be stabilised through the use of a novel low swirl design. There are several significant experimental configurations [154, 155, 156] that utilise

strong swirl, recirculation and wall bounded flow to stabilise low Da premixed combustion, simulating the strongly swirling flow field features typically found in gas turbine combustors. Dinkelacker *et al.* [11] utilised significant preheating and strong swirl to stabilise combustion in a model lean premixed gas turbine combustor, they find a trend of instantaneous flame front thinning with increased turbulence intensity. This is contrary to the findings of O'Young and Bilger [157] who report flame broadening with increased turbulence intensity. [58, Mansour *et al.* [158] and Chen *et al.* [10] employed a piloted Bunsen flame geometry, where the pilot was virtually a combusting coflow with a diameter about 5.7 times the main Bunsen jet exit diameter. Chen *et al.* [10] shows with this geometry increased Bunsen jet velocities hence turbulence intensities are achievable before blow-off, through the use of a large diameter pilot. While the burners used studies are extremely useful to investigate the interaction of high turbulence intensities with premixed flame fronts, they have not been able to sufficiently reduce the Da number to broaden the reaction zone in a turbulent premixed flame and force it close to extinction.

As initial starting point a burner design strongly inspired by the hot coflow burner used initially by Cabra *et al.* [63] for diffusion flame studies was deemed suitable since it enabled the stabilisation of flames with high shear rates. During the initial experimental investigations it became apparent that two geometries might be necessary to cover a broader range of conditions. These two geometries are the piloted premixed jet burner (PPJB) and the premixed jet burner (PJB).

The PPJB aims to investigate finite-rate chemistry effects by examining a selected flame series that features extinction and re-ignition effects. The selection of flame series that feature extinction and re-ignition have been shown to be a very powerful tool to understand turbulent diffusion flames. An example of this is the piloted diffusion flame burner by Masri and Bilger [107] that has been the subject of many experimental and numerical investigations, featuring extinction and re-ignition as an integral feature of the flame series. The PPJB features three streams (hot coflow, pilot and central jet), typically each of these three streams have different equivalence ratios although in certain conditions the coflow and the central jet can have the same equivalence ratio. Because of

the multiple compositions in the PPJB, analysis of experimental data and numerical simulation is considerably more complicated compared to burners that can be categorised by a single reaction progress variable. It is important to realise that without the pilot an initial ignition region in the PPJB is not possible therefore extinction and subsequent re-ignition is not possible.

Finite-rate chemistry effects in the PJB manifest in a different manner to the PPJB, in the PJB the flame brush is essentially lifted and the lift off height is determined by the degree of turbulence chemistry interaction. There is no stoichiometric pilot in the PJB hence it is not possible to immediately stabilise a flame at the jet exit. As the fluid turbulence interacts with the jet prior to the stabilisation region in the PJB mixing with little reaction occurs hence prior to the stabilisation region the turbulence has significantly interacted with the chemistry of the flame. An advantage in terms of experimental analysis and future modelling of the PJB is that it is a two stream problem that can be characterised by a single reaction progress variable.

3.1 PPJB Burner

The detailed design features of the PPJB is introduced in Section 3.1.1 followed in Section 3.1.2 by the stability characteristics based primarily on mean chemiluminescence images of the flames. The velocity measurements using the LDV technique for a selected series of flames in the PPJB is examined using Section 3.1.3.

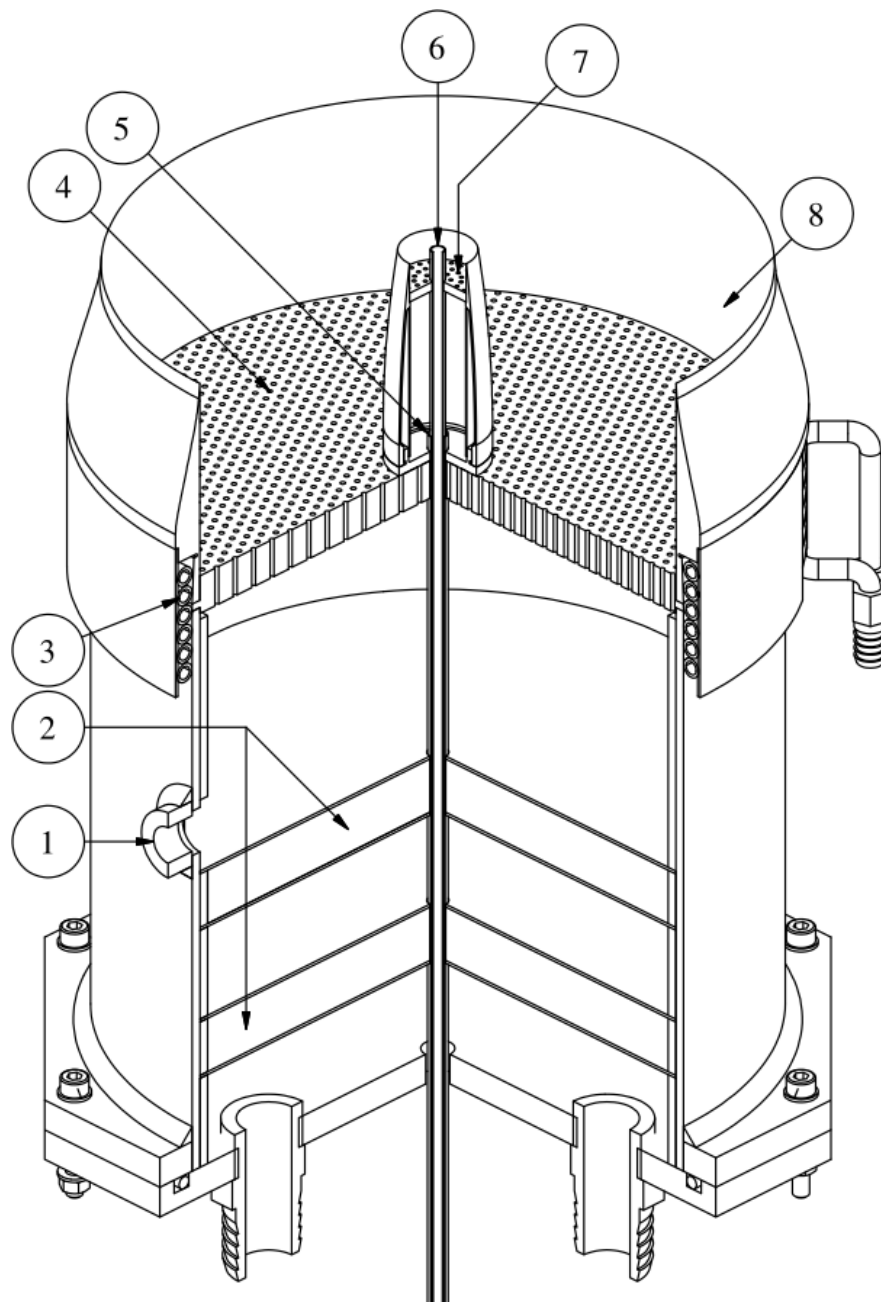
3.1.1 PPJB Burner Design

The current design for the burner, as shown in Fig. 3-1, has been inspired by the success of several antecedents, such as the piloted-jet diffusion flame burner developed at The University of Sydney [159], the burner design of Cabra *et al.* [63] in vitiated coflow auto-ignition investigations, as well the piloted premixed burner designs of Mansour *et al.*

[158] and Frank *et al.* [160]. The axisymmetric design utilises a small diameter high velocity lean-premixed central jet, piloted by a low velocity stoichiometric premixed pilot providing a source of combustion products and intermediates promoting initial ignition of the central jet. Surrounding both the central jet and pilot is a large diameter coflow of hydrogen-air combustion products that shields the central jet combustion process from ambient air entrainment; and hence from reaction quenching and dilution effects.

The premixed central jet and pilot reactants flow through the PPJB body inside concentric stainless steel tubes, as shown in Fig. 3-1. The 4.0mm (D) inside diameter (ID) central jet tube is smooth-walled and unobstructed for more than 100D upstream of the central jet exit, providing well defined and repeatable boundary conditions. The central jet exit plane ($x=0$) is 70mm above the coflow base plate to allow good optical access for laser diagnostics and mixing with a uniform coflow to occur. The pilot premixed gas flows in an annular region around the central jet tube through the burner body, then through the pilot cavity which is filled with stainless steel balls to establish a uniform exit flow through the pilot perforated base plate. The pilot perforated base plate, located 7mm upstream from the central jet exit plane is a 23.5mm outside diameter (OD) and 4.5mm ID disc with 44, 1.3mm holes to stabilise the pilot combustion.

The coflow of the PPJB is stabilised on the coflow perforated base plate, a 12.7mm thick, 197mm OD brass disk with around 1800, 1.6mm diameter evenly spaced holes. A coflow of combustion products uniform in composition and temperature is achieved ~20mm from the perforated base plate. To minimise the effect of a potential flashback through the coflow perforated base plate, two consecutive screens of glass beads have been installed in the burner body, as well as an overpressure switch to turn off the coflow hydrogen supply in the event of a flashback. Thermocouple profiling of the coflow conducted by Dunn *et al.* [161] has shown that the coflow shields the central jet combustion process from ambient air entrainment up to a radius of $r/D=7$ at $x/D=33$. After these thermocouple measurements were conducted an additional 390mm square



Balloon number	Description
1	Flashback over-pressure sensing port
2	Glass bead filled cavities
3	Cooling water coil
4	Coflow perforated baseplate
5	Pilot mixture feed exit
6	Central jet exit
7	Pilot perforated baseplate
8	Coflow collar

Fig. 3-1. Sectioned view of the PPJB, with significant features given a balloon callout.

filtered air coflow and a revised streamlined annular collar extending 65mm above the coflow base plate has been added. Subsequent Rayleigh scattering measurements indicate that with these improvements, the hot coflow shields the central jet combustion process reliably up to a radius of $r/D=5$ at $x/D=60$. Further details of the burner characterisation, geometry and dimensions can be found in Dunn *et al.* [161] and at The University of Sydney Thermofluids web site [162].

3.1.2 PPJB Stability Characteristics

For a given fuel, the parameters that control the stability characteristics of the flames are the equivalence ratios and velocities of the mixtures in the central jet, pilot and hot coflow. For the experiments conducted in this study both the pilot and the central jet run a premixed compressed natural gas (CNG) and air mixture. The approximate CNG composition at the time of the experiment was 88.8% CH₄, 7.8% C₂H₄, 1.9% CO₂ and 1.2% N₂ with the remaining 0.3% being a mixture of propane, propene, butane and pentanes. The velocity of the surrounding co-flowing wind tunnel air does not influence the flame but affects the length of unperturbed cone of hot gases in the coflow. In this study, the velocity of co-flowing wind tunnel air was fixed at 0.8 m/s and the cold-flow velocities of the coflow and pilot were also fixed at 0.8 m/s and 0.7 m/s respectively. The equivalence ratio in the pilot was fixed at stoichiometric to ensure that the flame was always anchored to the burner, giving a constant pilot heat release rate of 1kW for all flames. For a central jet velocity of 100m/s and equivalence ratio of 0.5 the heat release rate of the central jet is 2.4kW. The remaining independent parameters are the equivalence ratio (or temperature) of the coflow as well as the equivalence ratio and velocity in the central jet.

Fig. 3-2 shows the stability characteristics of the flame for the case when the coflow temperature is fixed at 1500K, corresponding to a hydrogen-air equivalence ratio of 0.43 and a heat release rate of 41kW. Based on qualitative observation of the flames, four

regimes are identified parameterised by the velocity and equivalence ratio of the central jet and a representative flame image from each of these regimes is then shown in Fig. 3-3:

- Regime A, where the flame is generally short in length, exhibiting a uniform luminosity along the conical flame brush.
- Regime B, where the flame is longer, showing a neck region downstream from the pilot followed by a slightly broadened and reduced luminosity flame brush above $x/D=25$.
- Regime C, where the flame exhibits a neck structure close to the pilot, followed downstream by an extinction region identified by low flame luminosity around $x/D=25$. Further downstream the flame luminosity increases, indicating the re-ignition region.
- Regime D, where the flame exhibits a short neck structure close to the pilot, whilst for all downstream locations above $x/D=10$ the flame luminosity is uniformly low. No increased luminosity region can be clearly identified further downstream.

The sensitivity of the transition from regime B to regime C in Fig. 3-2 has been examined for a central jet equivalence ratio of 0.5 and coflow temperature of 1500K. We found no discernable change in the location of the B to C transition within the following limits: coflow velocity $\pm 25\%$, coflow temperature $\pm 7\%$ and pilot velocity $\pm 15\%$.

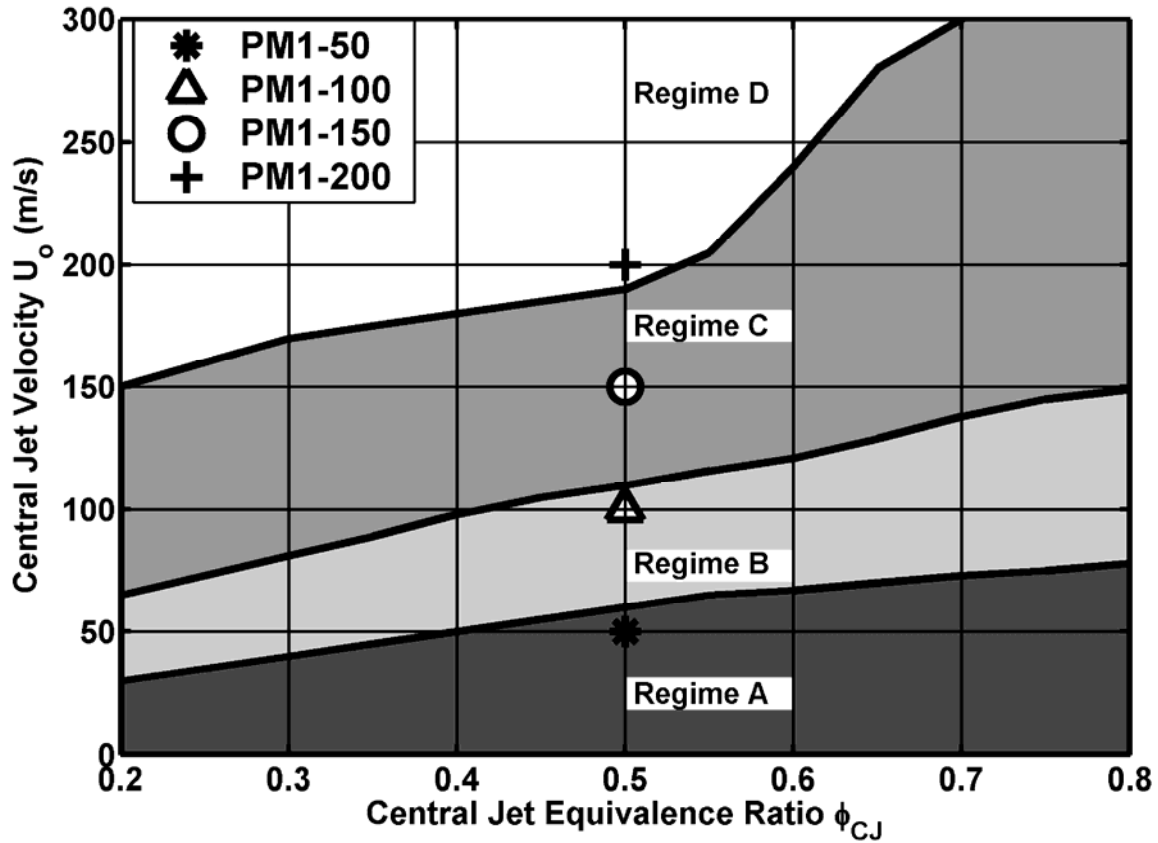


Fig. 3-2 Characterisation map for the PPJB, a constant coflow temperature of 1500K is used for all cases. The location of the selected flame conditions studied further in this study is shown for reference.

Specifically, this study focuses on a central jet equivalence ratio of 0.5 and a coflow temperature of 1500K and examines the effect of increased turbulence intensity achieved via increasing the central jet velocity. By selecting a jet equivalence ratio of 0.5 and a coflow temperature of 1500K allows the coflow to be essentially at the adiabatic temperature of the central jet reactants therefore simulating turbulent mixing and straining against combustion products with complicating factors such as dilution and cold gas quenching. Four flames with central jet velocities of 50, 100, 150 and 200m/s, labelled PM1-50, PM1-100, PM1-150 and PM1-200 respectively, are selected for further investigations. Each of these flames is selected to investigate the four regimes of the stability diagram presented in Fig. 3-2.

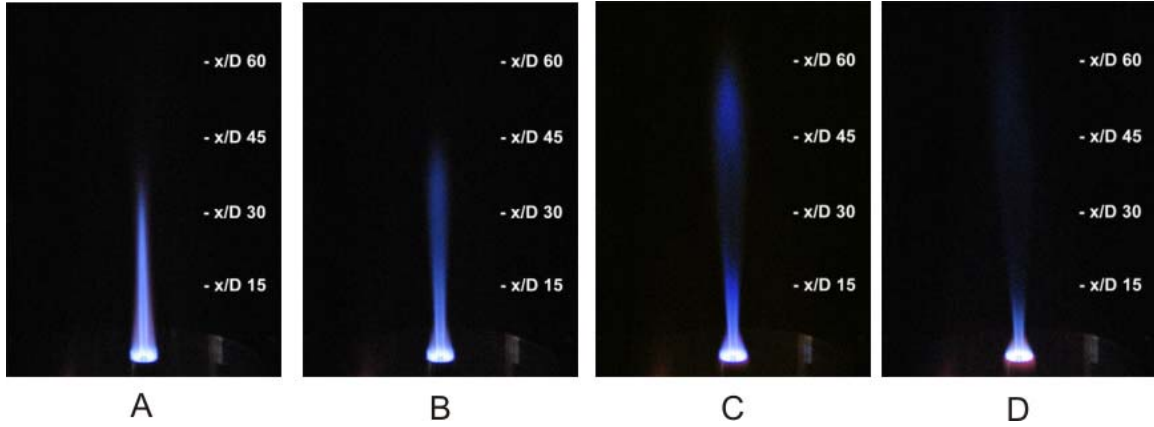


Fig. 3-3. Time averaged images taken with a conventional colour digital camera of the selected flames, A: PM1-50, B: PM1-100, C: PM1-150, D: PM1-200. Note: A, B, C and D correspond to the respective regimes in Fig. 3-2.

The time averaged (over 2 seconds) luminosity of the selected flames illustrating the transition from regimes A to D in Fig. 3-2 is presented in Fig. 3-3. These images were taken using a conventional colour digital camera with a spectral response that is insensitive to any UV chemiluminescence (for example from OH^*), as well as any thermal IR emissions. Extracting the raw red, green, blue channels from the collected images and appropriately weighting the individual channels indicates that most of the luminosity was on the blue channel, implying that the chemiluminescence in these flames is largely due to CH^* emission. This agrees with the findings by Kojima *et al.* [163] that for lean premixed methane-air combustion the overwhelming source of the flame chemiluminescence in the visible spectrum is due to spontaneous emission from CH^* ($\text{CH}^* \rightarrow \text{CH} + h\nu$) occurring at a wavelength around 431nm. It is shown later in Section 8.2.1 that the mean CH^* emission is well correlated to the mean heat release for the PPJB and PJB.

In regimes C and D the axial stream-wise reduction in luminosity, or extinction region, begins around $x/D=20$ and 12 respectively. A characteristic of flames in regime C is the prominent increase in luminosity in the re-ignition zone around $x/D=40$. For flames in regime D, a clear axial location for the re-ignition zone is difficult to define and can only

be approximated as around $x/D=45$: this uncertainty in defining clear re-ignition location is typical of flames situated in regime D.

The transition phenomena highlighted in Fig. 3-2, regime C and Fig. 3-3 C may be explained as follows: at the nozzle exit, the central jet mixture mixes with hot pilot combustion products ensuring initial ignition and flame stabilisation to the burner. Further downstream where the influence of the pilot is diminished, high jet velocities cause high levels of shear to develop between the jet and the coflow leading to the production of high turbulence intensities. High scalar dissipation rates of the reaction progress variable are hence produced, increasing up to a point where the Da is reduced until extinction occurs. It should be noted that the occurrence of extinction here is not due to quenching as is the case with standard piloted non-premixed flames. This is because the coflow gases are hot and in this case have almost the same temperature as the adiabatic temperature of the fuel mixture in the central jet. Further downstream, as the velocity decreases the turbulence intensity decreases and the scalar dissipation rates decay to a point where re-ignition or auto-ignition becomes possible.

3.1.3 PPJB Flow-Field Measurements

Laser Doppler Velocimetry (LDV), is used to measure the mean and RMS velocities for the selected flames as well as for non-reacting cold-flow cases with similar flow-rate conditions. A commercial two channel LDV system (TSI FSA 3500) with phase-Doppler capability and a 7W argon-ion laser (Spectra Physics 2017) is used for all velocity measurements. The central jet is seeded with aluminium oxide particles with a mean diameter of 1 micron, the LDV results are conditioned such that only data with a seed particle diameter less than 10 microns is used in the calculations, preventing spurious data from agglomerated particles that do not follow the flow-field contaminating the results. Data is collected in the forward scatter mode at 30 degrees off axis, with a typical mean data rate of 2-3 kHz being achieved. For each location 10000 data points are taken

to compute the mean and RMS velocity. Based on repeated LDV measurements at the same spatial location, the estimated repeatability over the selected flames for the mean and RMS velocity is 2% and 3% respectively, these values account for flowmeter resetting and spatial relocation mismatch.

All data has been corrected for velocity bias using a gate-time weighted correction function scheme proposed by Buchhave *et al.* [164]. The use of gate-time as a weighting function has been shown by Fuchs *et al.* [165] to be advantageous for moderate data rates compared to velocity weighting [166] and inter-arrival time weighting schemes [167]. Using the gate-time weighted correction scheme, the calculation of the mean and RMS velocity can be found using Eq. (3.1) and Eq. (3.2) respectively.

$$\bar{U} = \frac{\sum_{i=1}^{i=n} u(t_i) \Delta t_i}{\sum_{i=1}^{i=n} \Delta t_i} \quad (3.1)$$

$$u'_{rms} = \sqrt{\frac{\sum_{i=1}^{i=n} [u(t_i) - \bar{U}]^2 \Delta t_i}{\sum_{i=1}^{i=n} \Delta t_i}} \quad (3.2)$$

In Eq. (3.1) and Eq. (3.2) n is taken to be the number of realisations and Δt_i is the gate time for the i^{th} realisation of the velocity.

By effectively weighting each realisation by the corresponding gate time slower velocity realisation will receive a greater weighting (longer gate time) and fast velocity particles will receive a smaller gate time (shorter gate time). To correct the PDF of velocity for velocity bias McLaughlin and Tiederman [166] propose scaling the PDF by a corrected mean, it is found however that this global scaling of the PDF gives erroneous results for a PDF with near zero mean velocity, a prime example of such a PDF in the measurements presented here is the v component of velocity near the centreline. To achieve a more reliable correction for the velocity PDF, a localised slot correction scheme is applied to

the velocity PDF. By dividing the velocity PDF into N slots of width Δu , the corrected value for the velocity PDF in the k^{th} slot $P_u(k\Delta u)$, is given by Eq (3.3).

$$P_u(k\Delta u) = \frac{\sum_{j=1}^{j=n_r} \Delta t_j}{\sum_{j=1}^{j=n_r} \sum_{k=1}^{k=N} \Delta t_{j,k}} \quad (3.3)$$

In Eq. (3.3) k is the slot index and j is the realisation is the realisation index in the k^{th} slot. The number of realisations in the k^{th} slot is n_r and it is implicitly assumed that n_r is a function of the slot index $n_r(k)$. The term $\Delta t_{j,k}$ is now the gate-time for the j^{th} realisation in the k^{th} slot.

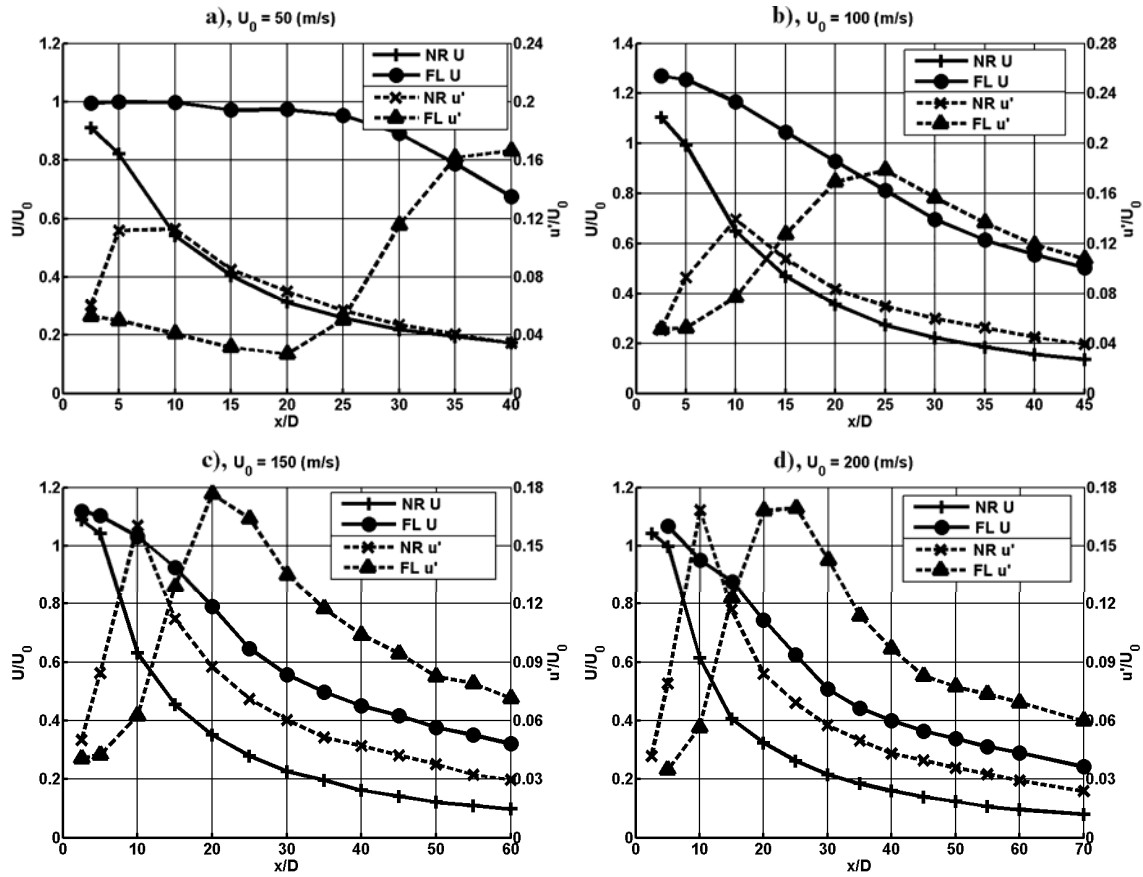


Fig. 3-4. Axial variation of the mean and RMS u component of velocity for the PM1 flame series. Values for both the selected flames (FL) and the corresponding non-reacting cases (NR) are shown.

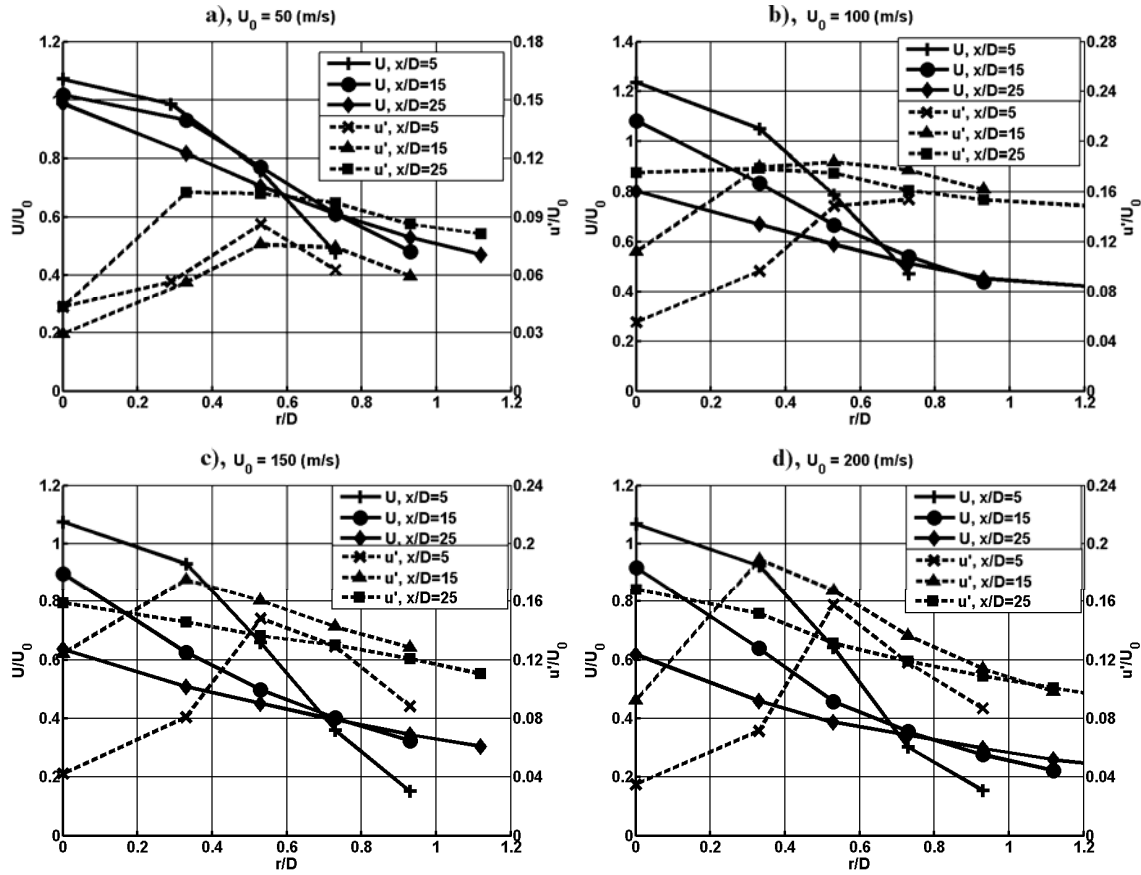


Fig. 3-5. Radial variation of velocity for the selected flames, showing the increased turbulence intensity in the shear layer.

The axial variation in the centreline mean (U) and RMS (u') axial velocities normalised by the average bulk exit velocity (U_0) for both the selected flames and the corresponding non-reacting cold-flow cases are presented in Fig. 3-4. The non-reacting cold-flow cases use exactly the same bulk velocities with air replacing the fuel component in all of the streams. Of particular significance when comparing the reacting and non-reacting cases is the location of the peak RMS velocity. For all of the non-reacting cases the peak RMS velocity occurs close to $x/D=10$, whereas for the reacting cases the location of the peak in RMS velocity depends on the particular flame. For the PM1-50 flame there is insufficient shear to produce an RMS velocity peak inside the flame brush below $x/D=25$. The increased centreline RMS velocity from $x/D=25$ to 40 can be attributed to flame-

generated turbulence, as this region corresponds to the flame brush tip in Fig. 3-3 A. The PM1-100 flame shows an interesting trend for the axial RMS velocity, the peak RMS velocity occurs near $x/D=25$, this is a similar region as an axial reduction in mean flame luminosity as shown in Fig. 3-3 B. The PM1-150 flame is an excellent example featuring extinction and re-ignition as illustrated by Fig. 3-2, regime C and Fig. 3-3 C. The location of reduced mean flame luminosity around $x/D=20$ corresponds well with a peak in RMS velocity around $x/D=20$ as presented in Fig. 3-4c. Flame PM1-200 is an example of a flame with extinction without a readily definable re-ignition region. The extinction region in flame PM1-200 occurs at around $x/D=13$ which corresponds to an RMS velocity of approximately 20 m/s, this is of similar magnitude to the value measured at the beginning of the extinction region of flame PM1-150 of 23m/s. The re-ignition zone in flame PM1-150 occurs where the RMS velocity is approximately 15 m/s, in flame PM1-200 the RMS velocity does not decay to this level until $x/D=60$.

Radial traverses for the measured mean and RMS axial velocities are presented in Fig. 3-5 for the selected flames at axial locations of $x/D=5, 15$ and 25 . For flame PM1-50 the shear layer and flame generated turbulence are illustrated by high turbulent fluctuations located on the mean flame brush contour, similar to the findings for the axial traverse in Fig. 3-4a. For flames PM1-100, PM1-150 and PM1-200 at $x/D=5$ and 15 , the radial traverses show a peak in RMS velocity, the radial location of this peak is close to where the reaction zone and shear layer would be expected to be located. This peak in turbulence shows that there is initially intense mixing occurring between the hot pilot gas and central jet fluid, which is proposed to be the initial ignition mechanism. In Fig. 3-5 at $x/D=25$ and above (not shown) for flames PM1-100, PM1-150 and PM1-200 both the mean and RMS velocity radial profiles show a maximum located on the centreline and become increasingly uniform for radial locations up to $r/D=1.5$. No discernable difference in the mean or RMS velocity are found when radial traverses from either side of the burner at $x/D=5, 15$ and 25 for flames PM1-100 and PM1-150 are compared, indicating no significant flow asymmetries exist.

The integral length scale is a useful quantity to obtain from the LDV measurements, as the integral length scale is required to calculate the Damköhler, Karlovitz and turbulent Reynolds numbers as well as locating the flames on the premixed regime diagram. If Taylor's hypothesis of frozen turbulence is assumed, the integral length scale may be calculated from the single point Eulerian autocorrelation function $\rho(\tau)$. This is done by integrating the autocorrelation function to obtain an integral time scale (T_f) using Eq. (3.4), then this time scale is multiplied by the local mean velocity to obtain an approximate to the integral length scale.

$$T_f = \int_0^{\infty} \rho(\tau) d\tau \quad (3.4)$$

The computation of the single point Eulerian autocorrelation function from the LDV data is non-trivial due to LDV data being randomly sampled in nature, negating the use conventional Fast Fourier Transform (FFT) techniques [168, 169, 170]. A slotting technique with local normalisation similar to the methods described by Tummers and Passchier [171] and Nobach [172] has been utilised to calculate the single point Eulerian autocorrelation function. To account for velocity bias effects that are most prominent in regions of high turbulence intensity, the weighting method proposed by Buchhave *et al.* [164] has been merged with the slotting technique, yielding an expression for the calculation of the autocorrelation function that is given by Eq. (3.5). By merging the two schemes each slot is still normalised by the slot variance thereby ensuring the important property that the value of the auto correlation function remains at or below unity for all values of the time shift parameter τ [173].

$$\rho(k\Delta\tau) = \frac{(k\Delta\tau) \sum_{i=1}^{i=n_s} u_i \Delta t_i \sum_{j=i}^{j=n_s} u_j \Delta t_j}{\sqrt{\sum_{i=1}^{i=n_s} (u_i^2 \Delta t_i \Delta t_j) (k\Delta\tau) \sum_{j=i}^{j=n_s} (u_j^2 \Delta t_i \Delta t_j) (k\Delta\tau)}} \quad (3.5)$$

The repeatability of the integral length scale calculation is assessed based on four independent 10000 sample data sets taken at identical locations and conditions, the calculated sample range normalised by the sample mean is found to be 12%. Comparison with the calculated value of the integral length scale obtained using accepted relations based on the jet velocity half width for non-reacting jets, show significant variation in the regions below $x/D=10$. This is probably caused by the fact that the frozen turbulence assumption is not valid near the potential core region. Further downstream, at $x/D=15$ and above, the error between the two values is at most 30%, an acceptable accuracy for this analysis.

3.2 PJB Burner and Stability Characteristics

In Section 3.1 the piloted premixed jet burner (PPJB) has been shown to be a useful experimental tool to investigate highly turbulent premixed combustion. The PPJB is able to stabilise highly turbulent flames with $u'/S_L \gg 20$ due to the shrouding effect of the hot coflow, preventing dilution and reaction quenching effects. In order to achieve initial ignition in the PPJB a stoichiometric pilot is utilised, this pilot is at a different equivalence ratio to the central jet and the hot coflow. Although the pilot is necessary to enable extinction and re-ignition behaviour in the PPJB, it adds an additional level of complication to the problem by adding a second composition stream. This added composition stream makes the numerical prediction of the PPJB difficult for some numerical models developed for premixed combustion.

By removing the stoichiometric pilot from the PPJB, it is possible to characterize the burner boundary conditions with a single temperature based reaction progress variable c_T . This assumes that the coflow temperature is set to the same temperature as the adiabatic flame temperature of the central jet reactants. This configuration of the PPJB is examined and is referred to as the “premixed jet burner” (PJB).

The configuration of a single premixed jet into a hot coflow has also been examined by Wu *et al.* [174] and also by Chen *et al.* [10] have investigated the structure of premixed flames in a Bunsen burner geometry that have a small pilot and are also referred to in literature as “premixed jet burners”. Such flows are somewhat different from those discussed here since the main jet in the PJB interacts solely with the hot coflow for all relevant axial locations. The premixed jet burners presented by Wu *et al.* [174] and also by Chen *et al.* [10] do not feature such extensive shrouding and only up to a certain axial location in the flame may be considered as undiluted purely premixed combustion. The flame brush geometry of Wu *et al.* [174] and Chen *et al.* [10] are reported to be essentially an elongated form of the “piloted Bunsen” geometry, with the mean flame brush initially anchored close to the exit of the central jet. The flames produced in the PJB all can be described as having a mean flame brush occurring well downstream from the central jet exit, being possibly described as a “lifted premixed jet flame”. Due to the lifted nature of the mean flame brush in the PJB, the classification of the PJB flames as “piloted jet burner” flames maybe limiting. This is because of the finite-rate chemistry effects and ignition delay or initial extinction process forcing the flame to stabilise downstream for the nozzle.

As an addition to examining premixed combustion in a new geometrical configuration, it is possible that further understanding can be gained from the PJB in the controversial area of lifted non-premixed and partially premixed flame stabilization mechanism. Under different conditions it has been argued that lifted flame stabilisation can be due to triple, premixed or auto-igniting flame propagation. Whilst in no way solving the lifted flame controversy, the PJB can help to understand the stabilisation mechanisms in a pure premixed environment where premixed or auto-ignition is the flame stabilisation mechanism. It should be emphasised that since the fuel is premixed, mixing of the two streams is not necessary to stabilise a flame as is the case with the classical lifted diffusion flame

3.2.1 PJB Burner Design and Characterisation

The PJB shown in schematic form in Fig. 3-7, is very similar to the PPJB used in previous investigations; however as previously mentioned the PJB does not have a pilot, essentially making the geometry identical to the burner geometry used for non-premixed combustion investigations in auto-ignition studies by Cabra *et al.* [63]. The central jet of the PJB is a smooth bored stainless steel tube with a 4.0 mm inside diameter (ID) and a 4.5 mm outside diameter (OD), protruding 70mm from the coflow base plate. The hot coflow is produced from the combustion products of a premixed hydrogen-air flame anchored on a 198 mm OD perforated brass disk, with $\sim 2000 \times 1.6$ mm diameter holes. Surrounding the hot coflow is a streamlined collar and a 0.8 m/s filtered air co-flowing wind tunnel to maximise the length of the hot coflow potential core. With these measures it is shown by Dunn *et al.* [175] and also in Section 3.1.1 of this Chapter, that the central jet combustion process is shielded from ambient cold air entrainment at $x/D=60$ up to a normalised radius of $r/D=5$.

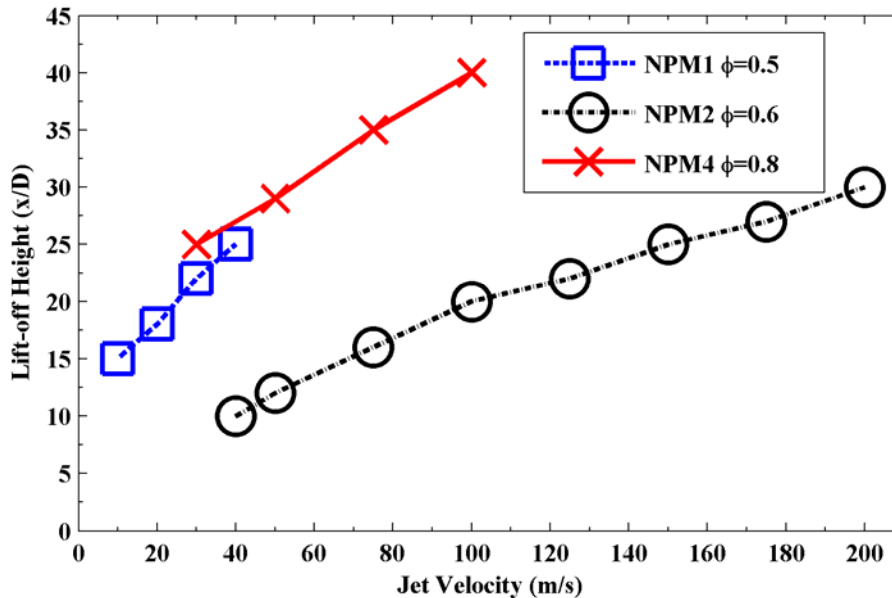


Fig. 3-6. Measured lift-off heights as a function of jet velocity for three different PJB flame series. It should be noted that for the NPM2 ($\phi=0.6$) flames the coflow is 1650K, whilst for the NPM1 ($\phi=0.5$) and NPM4 ($\phi=0.8$) flames the coflow temperature is 1500K.

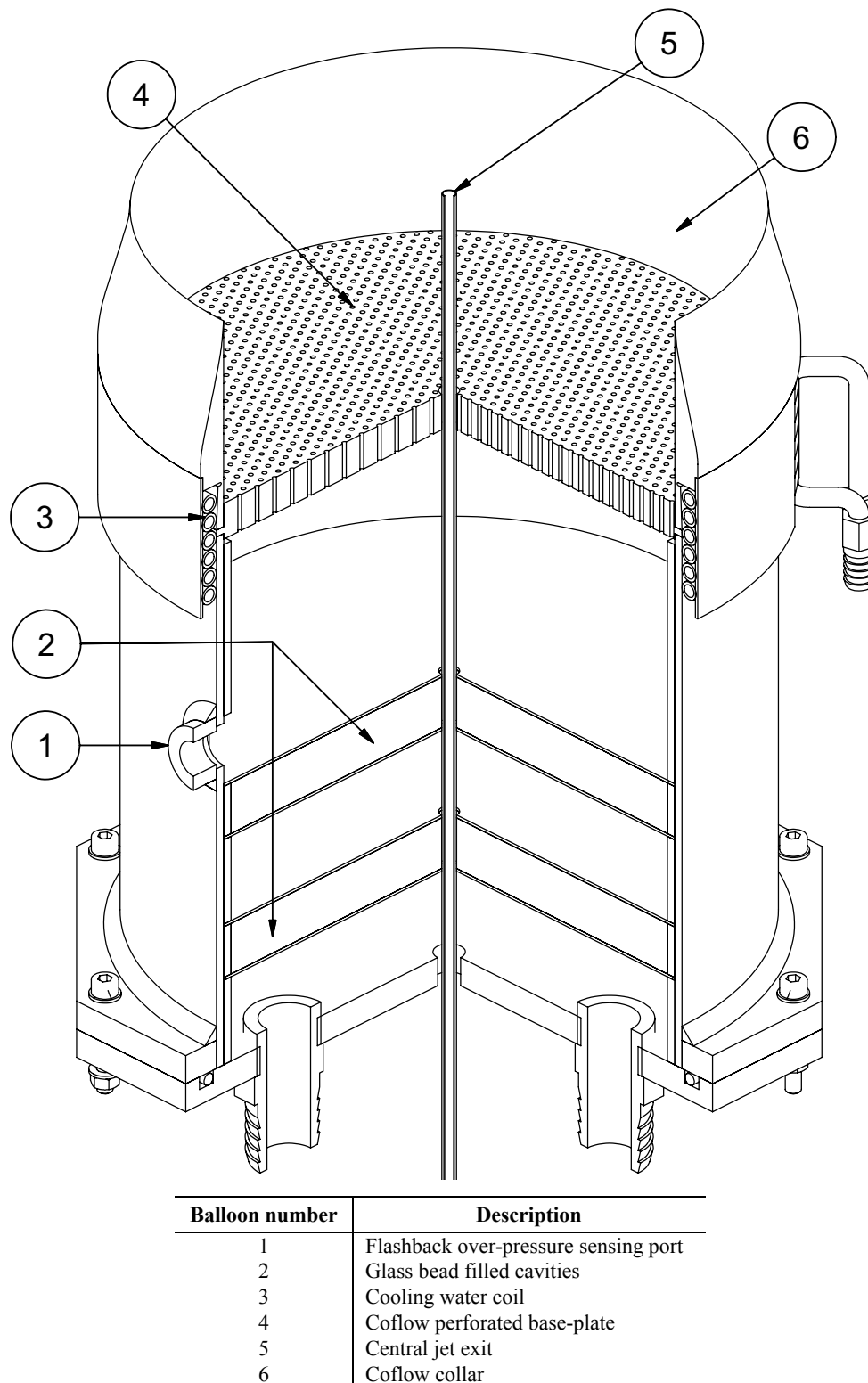


Fig. 3-7. Cross sectional view of the PJB, with all major features labelled

Six flames in the PJB are initially identified for further study. The six flame conditions are summarised in Table 3-1, noting that the NPM1 and NPM2 flames have coflow temperatures equal to the adiabatic flame temperature of the central jet reactants, whilst for the NPM4 flames the coflow temperature is lower than the central jet composition adiabatic flame temperature. The flame selection for the PJB is based on selecting a single central jet composition and finding two central jet velocities that produce a medium lift off and a high lift off flame. The lift-off height ($L.H.$) data for the selected flames is presented in Table 3-1 whilst the detailed lift-off high data as a function of central jet velocity is presented in Fig. 3-6 for the three different NPM flames.

Flame Code	Φ_{CJ}	U_0 (m/s)	Re	T_c (K)	$L.H.$ (x/D)
NPM1-10	0.50	10	2500	1500	15
NPM1-40	0.50	40	10000	1500	25
NPM2-40	0.60	40	10000	1650	10
NPM2-200	0.60	200	50000	1650	30
NPM4-30	0.80	30	7500	1500	25
NPM4-100	0.80	100	25000	1500	40

Table 3-1. Summary of the flame conditions for the NPM flames stabilised on the PJB.

Example mean chemiluminescence images of the low velocity NPM2-40 flame and the high velocity NPM2-200 flame are presented in Fig. 3-8. Although the NPM1 and NPM4 mean chemiluminescence images are not shown, the flame characteristics and appearance are very similar to the NPM2 flames presented in Fig. 3-8. The freely propagating laminar premixed flame parameters for the three central jet compositions are presented in Table 3-2. These results were computed with GRI 3.0 [176] and multi-component diffusion using the open source code Cantera [177].

Φ	T_{ad} (K)	S_L (m/s)	d_{th} (mm)	t_f (ms)
0.50	1490	0.061	1.7	28
0.60	1660	0.12	0.99	8.3
0.80	2000	0.28	0.54	1.9

Table 3-2. Freely propagating laminar flame characteristics for the three central jet CNG/air compositions used for the NPM flames. d_{th} is taken to be the laminar flame thermal thickness based on the maximum gradient. t_f is defined as the laminar flame thermal time scale (d_{th}/S_L).

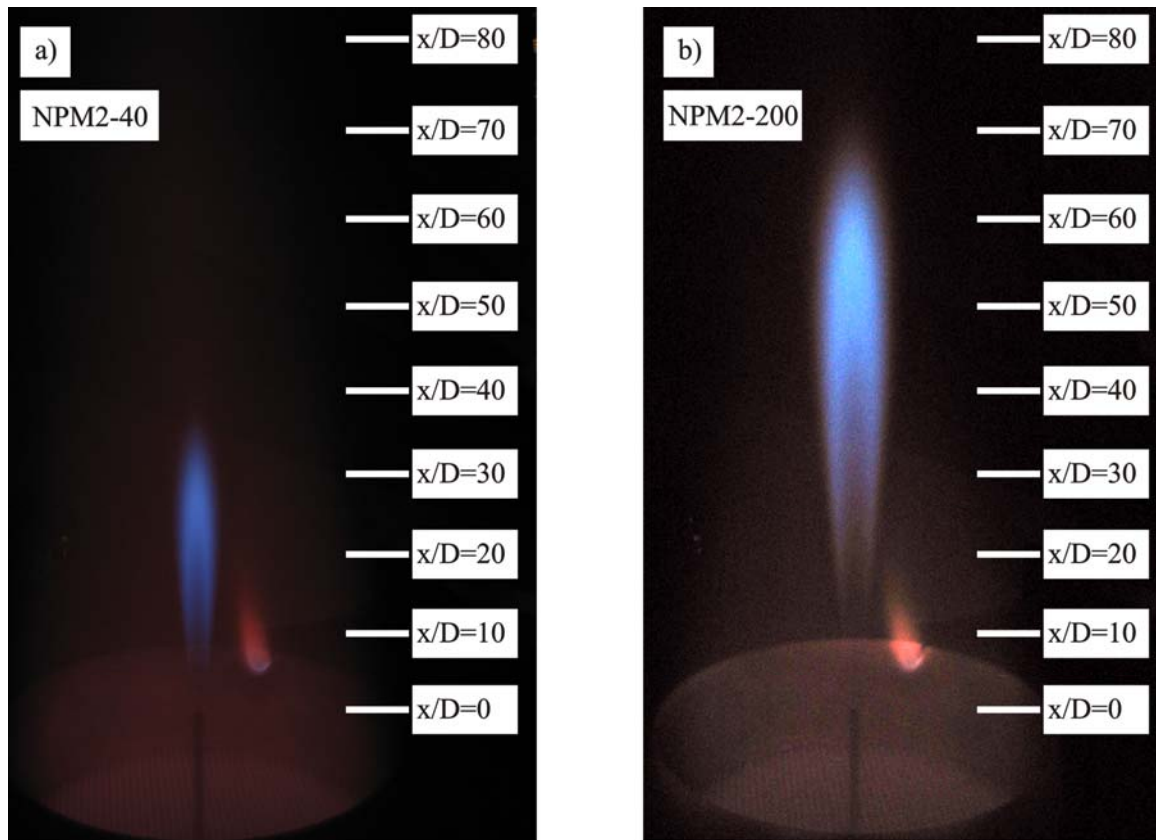


Fig. 3-8. Mean flame luminosity images of the NPM2-40 a), and NPM2-200 b) flames. The small red region to the right of the central jet is the coflow pilot; this pilot flame in way influences the central jet combustion process.

3.2.2 PJB Flow-Field Measurements

LDV measurements have been carried out on the NPM2 flame series (NPM2-40 and NPM2-200). The experimental configuration, processing methodology and expected experimental error is identical to that reported for the LDV measurements for the PM1 flame series reported in Section 3.1.3 of this Chapter is identical to that used for the NPM2 flame series LDV measurements and so will not be repeated here. The only difference to the PM1 measurements reported in Section 3.1.3 is that approximately 50000 samples are typically taken at each data point for the computation of the mean and

RMS velocity statistics for the NPM2 flame series. The results for the LDV measurements are presented in Fig. 3-9 to Fig. 3-10 in the form of normalised mean velocity and turbulent kinetic energy for centreline axial data and radial traverse data. In Fig. 3-9 to Fig. 3-10 the mean total velocity (U_{tot}) is normalised by the bulk exit velocity (U_0) and the turbulent kinetic energy (k) is normalised by the bulk exit velocity squared (U_0^2). The bulk exit velocity used for the normalisation is taken to be the expected value at STP reported in Table 3-1. The turbulent kinetic energy is defined from the measured RMS u and v components velocity using Eq. (3.6).

$$k = \frac{1}{2} \sqrt{(u')^2 + 2(v')^2} \quad (3.6)$$

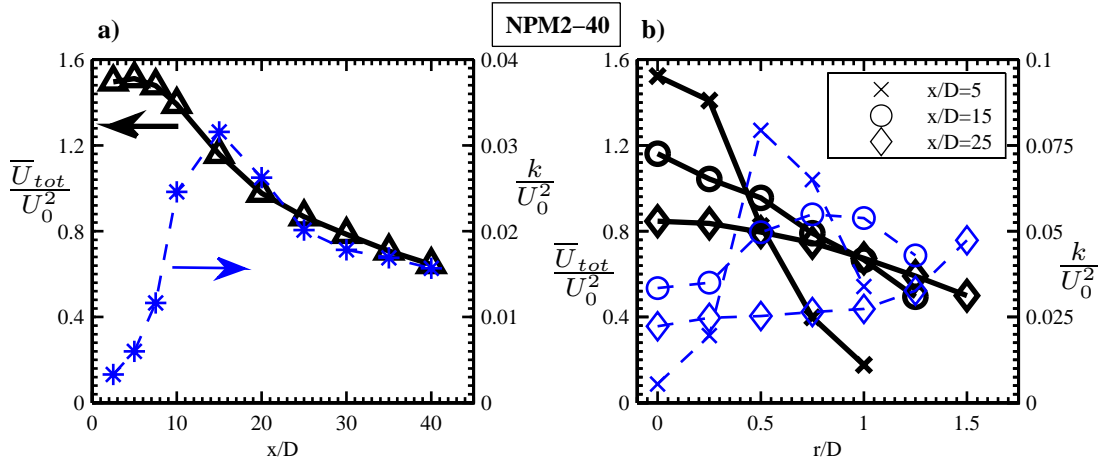


Fig. 3-9. LDV velocity measurements for the NPM2-40 flame. The centreline velocity statistics are presented in a) with the normalized mean velocity shown with a solid black line with data points demarked by triangles and the normalized turbulent kinetic energy is shown with a dashed blue with data points demarked with asterisks. The radial traverse velocity statistics are presented in b) for three axial stations, the solid black line represents the normalized mean velocity data and the dashed thin blue represents the normalized turbulent kinetic energy. All data points in a) and b) are joined with a linear line to guide the eye, it is not implied that intermediate points will lie on this straight line.

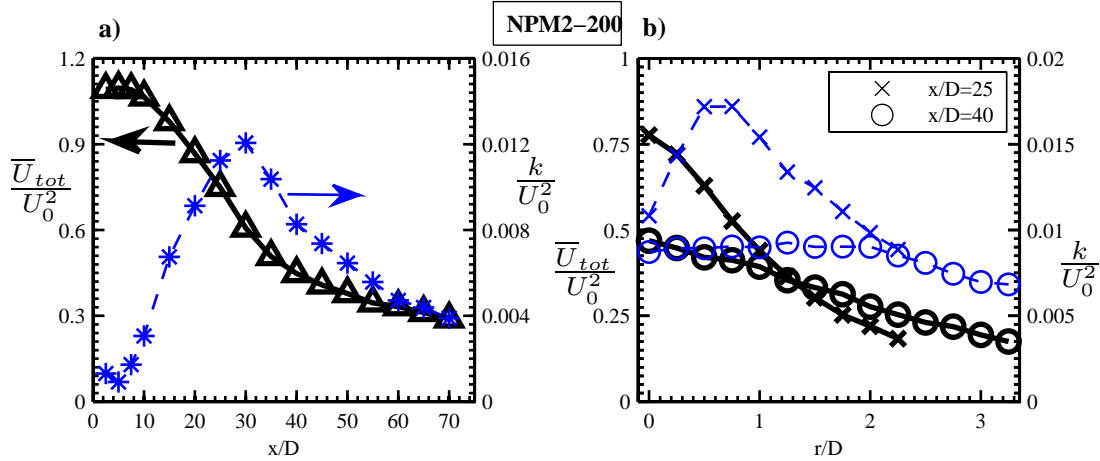


Fig. 3-10. LDV velocity measurements for the NPM2-100 flame. An identical data identification scheme is used in this figure as in Fig. 3-9.

The primary difference between the PJB geometry and the PPJB geometry is the pilot/central jet configuration. In the PPJB the pilot shroud is in direct contact with the hot coflow gases, with heat being transferred from the hot coflow gases through the pilot shroud to the pilot reactants. Even though there is a thermal insulation layer in the pilot shroud to minimise heat transfer it will be shown in Chapter 6 that the pilot gases are preheated to approximately 350K. Although the pilot reactants in the PPJB experience a preheat due to the hot coflow, the central jet reactants are not preheated an appreciable amount as the temperature gradient between the thin central jet tube wall is at most 75K, when combined with the high central jet velocities of the PPJB it will be shown in Chapter 6 that for the low velocity PM1 flames the degree of preheating for the central jet reactants is less than 10K.

The configuration of the PJB central jet tube is much different to the PPJB, the outside of the 0.25mm walled central jet tube is in direct contact with the hot coflow gases and does not feature any thermal insulation to minimise heat transfer like the pilot shroud does in the PPJB. As such, for low central jet velocities in the PJB the central jet reactants experience a significant degree of preheating before the exit plane of the central jet. It will be shown in Chapter 8 from Rayleigh temperature imaging measurements that the degree of preheating for the NPM2-40 flame is approximately 50K. As the central jet mass flow rates for the NPM2-200 flame is much higher than the NPM2-40 flame the

degree of preheating of the central jet reactants is expected to be much lower, being of the order of 10K.

It can be seen from Fig. 3-9a) for the NPM2-40 flame that the mean total velocity normalised by the STP bulk velocity results in a normalised mean velocity of 1.49 on the centreline at $x/D=2.5$ which should be representative of the conditions at the exit plane. By assuming that the flow inside the central jet tube is well developed and that the velocity distribution can well approximated by a power law profile [178], the ratio of the peak centreline velocity to the mean bulk velocity can be approximated using Eq. (3.7).

$$\frac{\bar{U}_{\max}}{\bar{U}_0} = \frac{1}{2}(1 + \sqrt{f})(2 + \sqrt{f}) \quad (3.7)$$

The friction factor term (f) in Eq. (3.7) is determined assuming smooth pipe flow using the relation in Eq. (3.8) developed from the classical Moody diagram [179].

$$\frac{1}{\sqrt{f}} = 0.86 \ln(\text{Re} \sqrt{f}) - 0.8 \quad (3.8)$$

Using the relations given by Eq. (3.7)–(3.8) it is expected that the ratio of the peak centreline velocity to the mean bulk velocity for the NPM2 flame conditions to be 1.28. If a preheat of 50K is accounted before the central jet exit plane the ratio of the expected centreline mean velocity to the STP bulk velocity is found to be 1.50, this corrected value is very close to the measured value of 1.49.

From Fig. 3-9a) and Fig. 3-10a) it can be seen that the centreline velocity decay (mean and k) resembles the form found for the PM1-150 and PM1-200 flames presented in Fig. 3-4 rather than the PM1-100 and PM1-50 flames that has a similar velocity to the NPM2-40 flame in Fig. 3-9a). It is proposed that as the pilot does not have a significant influence for the PM1-150 and PM1-200 flames the flame structure such as the velocity fields

should resemble the structure of the NPM flame series where the jet interacts solely with the hot coflow.

For the lower velocity NPM2-40 flame it can be seen in Fig. 3-9a) that the centreline peak in k occurs around $x/D=15$, whilst for the higher velocity NPM2-200 flame in Fig. 3-10a) the peak value of the centreline k occurs around $x/D=30$. It is believed that this difference is not caused by the difference in the flame lift-off heights between the two but rather the difference in the momentum of the two jets, hence the higher lift-off height of the NPM2-200 flame is a consequence of the peak value of k occurring further downstream in the NPM2-200 flame compared to the NPM2-40 flame rather than being caused by the flame lift-off height.

The three radial velocity profiles for the NPM2-40 flame reported in Fig. 3-9b) show that at $x/D=5$ a thin shear layer exists between the jet fluid and the hot coflow, in the middle of this interface at $r/D=0.5$, the peak turbulence intensity is close to 27%. Further downstream at $x/D=15$ it is apparent that the sharp interface has been smoothed out from both the normalised mean and k profiles. At $x/D=25$ it is apparent that the radial traverse data does not extend radially far enough to capture the peak in the normalised k profile or the half width of the normalised mean velocity profile, however the normalised mean velocity profile is sufficiently smooth to extrapolate a mean velocity half width of $3.4D$.

For the radial traverse data for the NPM2-200 flame reported in Fig. 3-10b) it can be seen that due to the high jet momentum a well defined peak at $x/D=25$ in the normalised value of k exists around $r/D=0.6$, further downstream at $x/D=40$ this well defined peak is not present. It is of interest to note that for the lower velocity NPM2-40 flame the peak in k in the shear layer is prominent at $x/D=5$ and far more distributed at $x/D=15$, the higher momentum effect of the NPM-200 allows the high values of k to persist in the shear layer further downstream. The persistence of the high peaky value of k in the shear layer combined with the larger advection velocities in the NPM2-200 flame are the driving factors that determine the higher lift-off height of the NPM2-200 flame.

CHAPTER 4 LIF QUANTIFICATION

A primary part of this thesis is to experimentally investigate finite-rate chemistry effects in turbulent premixed combustion. It is expected that finite-rate chemistry effects will strongly influence the local minor species concentrations, as such, accurate and if possible quantitative measurements of these species are desirable. Initially, the primary radical that is investigated is the OH radical. Initial investigations showed this to be a promising radical to examine further however several experimental complications were encountered. Essentially most of the issues encountered revolved around the low signal from OH in both the PJB and PPJB flames. In both the PPJB and the PJB the OH concentration levels are much lower than typically found in non-premixed flames. As the spatial scales are quite small in the flames examined a thin laser is highly desirable to maximise the spatial resolution.

To obtain adequate SNR levels for the OH images in both the PJB and PPJB flames it was found that operation in the non-linear regime of LIF was necessary. This meant that a conventional linear LIF regime quantification scheme was no longer valid. This Chapter outlines the development and validation of a non-linear LIF quantification scheme that is crucial for the quantification of the OH images in the PPJB and PJB presented in Chapters 5, 6 and 7.

4.1 Non-Linear LIF Background

Quantitative single-shot planar laser-induced fluorescence (PLIF) imaging of minor species in turbulent combustions flows is a challenging task due to the complex interplay of the various energy transfer mechanisms and the requirement of relatively high signal to noise ratio (SNR) levels. For quantitative PLIF experiments of the important combustion radical OH, the popular excitation strategy $A^2\Sigma^+ \leftarrow X^2\Pi(1,0)$ is typically utilised with irradiance levels near the linear irradiance limit. The requirement of high spatial resolution at large Reynolds numbers necessitates the use of thin laser sheets, when combined with low molecular concentrations operation within the linear regime may not be possible at a satisfactory SNR. The restriction of limiting irradiance levels to within the linear regime is not an experimental equipment limitation, but rather a lack of established models that accurately quantify spectrally integrated non-linear regime laser induced fluorescence (LIF). The development of such a model to quantify both linear and non-linear LIF is the motivation for this study.

The detailed reviews of Daily [180], Kohse-Höinghaus [181] and Eckbreth [182] direct significant attention to reviewing the topic of non-linear LIF both experimentally and theoretically, these reviews highlight that the existing body of work has evolved towards models for quantification of spectrally dispersed point measurements for saturated LIF. Such a detailed review of non-linear LIF is of course not the aim of this background review, however a brief review of the material previously published that is relevant to the material presented in this section is warranted. The term saturated LIF is referred to in this thesis as the LIF regime that the LIF signal is virtually insensitive to laser irradiance, where as non-linear LIF is referred to as a broad term that encompasses the non-linear irradiance dependence regime and the saturated regime. Though termed "non-linear" in this thesis, non-linear regime LIF is not a true non-linear optical technique in the sense that it relies on a non-linear polarisation response, but rather it is termed non-linear because the fluorescence response is non-linearly related to the laser irradiance.

Saturated LIF was first proposed by Omenetto *et al.* [183] and Piepmeier [184] for atomic systems, then for molecular systems by Daily [185], some of the first molecular applications of this technique were applied by Pasternack *et al.* [186]. Saturated LIF was proposed as a method by which quantitative measurements could be made that are insensitive to variations in quenching rates and laser power under the assumption sufficiently high laser irradiance levels to achieve saturation are utilized. The claim of insensitivity to variations in quenching environment and laser power were based on steady state solutions to the governing rate equations for two-level and multi-level systems, representing the population dynamics of relevant atomic or molecular species. The difficulties in applying the saturated LIF approach to systems requiring a greater level of description than the two-level model permits is acknowledged in Daily [185] as very challenging, this is particularly relevant when saturated schemes are applied to multi-level systems where the recorded signal is not spectrally dispersed.

One of the necessary assumptions for saturated LIF is temporal and spatial saturation. By considering a theoretical probe volume that is uniformly spatially irradiated and selectively sampling in time, the non-saturated temporal wings of the LIF signal may be rejected. One of the most challenging facets of saturated LIF is the fact that uniform spatial saturation is difficult to practically achieve, this is primarily due to less than ideal laser beam profiles, lens aberrations and diffraction limitations. Furthermore selectively sampling in time is typically not an option in most PLIF experiments due to equipment and SNR limitations. This means that it is difficult in practice to neglect the spatial and temporal wings of the laser pulse for most non-linear PLIF measurements.

The most successful studies in saturated LIF culminated in the development of the balanced cross rate model to account for the population dynamics under high irradiance conditions and the TOPLIF experimental geometry to account for non-uniform spatial irradiation. The balanced cross rate model [187, 188, 189, 190, 191, 192, 193, 194] is a four-level model that features levels for the laser coupled and bath levels for both the lower state and upper states. By assuming the rate of transfer from the laser coupled levels is equal to the rate of transfer into the two laser coupled levels it becomes possible

to directly relate the temporally integrated LIF signal from the excited state laser coupled level to the total number density using a simple saturated two-level model. By making the assumptions of the balanced cross rate model it is no longer necessary to assume complete steady state as required by the solution of Berg and Shackleford [195]. The balanced cross rate model requires the measured signal to be spectrally resolved such that the measured LIF signal is only from the laser-coupled excited-state level. This degree of spectral resolution in the measured signal is typically not possible in PLIF experiments due to the inherently spectrally integrated nature of PLIF when applied to molecular species. Despite the inherent neglect of the non-uniform spatial variation of irradiance in the balanced cross rate model, point measurement results that compare favourably with absorption measurements have been achieved in Lucht *et al.* [188], using a single spectrometer and appropriate spatial selection. Extensions of the balanced cross rate technique to high pressures by Carter *et al.* [193] and in turbulent flames Lucht *et al.* [189], for absolute concentration measurements has been shown to be possible.

The issue of non-uniform spatial illumination in saturated LIF has been addressed in a number of papers [192, 196, 197, 198, 199]. Solutions that focus on extracting the centreline fluorescence, thus minimising the effects of the spatial wings of the laser beam have been proposed for the spherically focused Gaussian beam in integral form [185, 190, 191, 196] and later in a closed analytic form [199]. These results are based on either steady state or balanced cross rate solutions to the governing rate equations. Experimentally, irrespective of the model used, spatial selection is almost always used in spectrally dispersed point or line measurements. Spatial selection is typically employed by using a horizontal spectrometer slit narrower than the laser beam waist diameter in an attempt to minimise the proportion of the signal obtained from the spatial wings. Utilising two spectrometers the TOPLIF approach of Desgroux and Cottureau [197, 198] and Carter *et al.* [192] is able to correct for non-uniform spatial illumination effects in a more rigorous manner at the expense of additional experimental complexity.

A comparison of wide band and narrow band saturated LIF measurements has been made by Carter and Laurendeau [194]. They obtained encouraging results considering the large

range of pressures, temperatures and quenching environments examined. As expected, limitations for the wide band collection were encountered; at saturated conditions the wideband method still displayed some sensitivity to the quenching environment. Also, different saturation curves and intensities were found for the wide and narrow band collection strategies. The concept of a balanced cross rate or any other steady state method was raised as questionable for wide or even narrow band collection strategies if population bleaching becomes a significant factor.

The aim of this study is to present and validate a comprehensive model for the quantitative interpretation of temporally and spectrally integrated LIF in both the linear and non-linear regimes of LIF. A detailed six-level transient rate equation model is developed in Section 4.2 to examine the important modelling assumptions for the quantification of OH LIF in both the linear and non-linear regimes of LIF. The assumption of steady state and quasi-steady state are examined in Section 4.3, based on the quasi-steady state results the IQSS model is developed as an analytic solution methodology. The IQSS model is numerically validated in Section 4.4 in terms of laser irradiance sensitivity, quenching sensitivity and temperature sensitivity. In Section 4.5 the IQSS is validated against PLIF experimental results in the exhaust gas of a flat flame. A broader discussion of the results is presented in Section 4.6.

4.2 Detailed six-level model

In order to examine the detailed effects of rotational, electronic and vibrational energy transfer (RET, EET and VET respectively) as well as temporally varying excitation, a minimum of a six-level transient rate equation model is required to adequately simulate the transient dynamics for the OH A-X (1,0) system. The rate equation approach has been validated in Daily [200] and also in Settersten and Linne [201] under the assumption that the coherence dephasing time is significantly smaller than the laser time pulse time scale; this is the case for nanosecond excitation and atmospheric pressures examined here.

When combined with the fact that four out of the six levels in the detailed six-level model represent multiple rotational levels or 'lumped' levels, the error introduced by the rate equation approach is negligible. The approach of lumping several rotational levels in this study is justified in the view that the spectrally integrated LIF signal is considered as the validation parameter, whereas the spectrally dispersed signal is not considered.

The results of Daily and Rothe [202] show that a minimum of a six-level model is necessary to adequately study the effects of temperature on OH LIF for (1,0) excitation. By using a six-level model, Daily and Rothe [202] show that important effects such as RET and VET are necessary to be included in any model for accurate predictions, thus predictions utilizing a two-level model can potentially contain significant errors. Daily *et al.* [203] have formed a highly detailed model for NO LIF with over 950 discrete levels included. By forming such a detailed model, the influence of parameters such as RET, pressure, laser irradiance and final state EET under non-stationary conditions may be assessed in great detail. This data can potentially be used to validate reduced NO LIF models and assess the underlying assumptions in great detail. Rahmann *et al.* [204] and Kienle *et al.* [205] describe the LASKIN code for the detailed determination of linear regime LIF spectra from excited state OH. Significant attention has been paid in Brockhinke *et al.* [206, 207] to correctly model and validate the polarisation and spectral dependence of the OH LIF signal using LASKIN code. Generally, the detailed simulation of OH excitation dynamics using the rate equation approach has been utilised in several other studies [208, 209, 210, 211, 212], however simulation of OH excitation dynamics down to the rotational or spin split level for non laser coupled levels is typically not necessary when evaluating the trends of the spectrally integrated LIF signal. It is proposed in this section that a detailed six-level transient rate equation model is adequate for the purpose of validation of the spectrally integrated LIF signal considered in this study.

4.2.1 Model Overview

The detailed six-level model utilised as the reference case for the numerical studies in this section features discrete levels for the laser coupled rotational levels in both the ground state and the excited states. Two lumped levels represent the remainder of the laser coupled vibrational manifolds for $J \neq J'', \nu'' = 0$ and $J \neq J', \nu' = 0$ in the ground and excited states respectively. A lumped level models the population transfer due to VET in the excited state from $\nu' = 1$ to $\nu' = 0$. Population storage in the ground-state non laser-coupled vibrational manifold is modelled by a lumped level representing the $\nu'' = 1$ manifold. Schematically, the energy transfer diagram for the detailed six-level model showing the dominant energy transfer pathways and the numbering of the relevant levels is presented in Fig. 4-1.

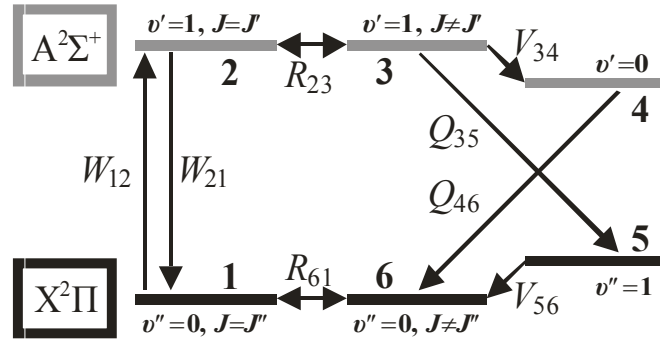


Fig. 4-1. Energy transfer diagram for the six-level detailed model. All spontaneous emission paths from the excited $A^2\Sigma^+$ state as well as EET and VET pathways to and from levels 1 and 2 are not shown in this diagram for clarity.

As both the temporal and spatial variation in the irradiance is relevant, the population levels hence LIF signal will be a function of both space and time. Based on the spatial and temporal dependence of the irradiance the governing equations for the system are essentially a system of six partial differential equations (PDEs). However, this system of six PDEs is separable in space and time. After separation the system of PDEs can be reduced to a system of six ODEs for the temporal variation over a differential element of

the spatial co-ordinate in the laser sheet thickness direction (z) which is represented by Eqs. (4.1)-(4.6). The variation in the LIF signal through the laser sheet thickness is essentially not of interest, but rather the variation of the integrated signal for different irradiance distributions is. Only the integrated value of the LIF signal through the thickness of the laser sheet is considered by Eq.(4.8).

The use of normalized population level fraction N_i , is equivalent to the actual concentration in level i (n_i), divided by the total OH concentration ($N_i=n_i/n_{OH}$). The initial conditions for Eqs(4.1)-(4.6) for all simulations is taken to be equilibrium governed by detailed balance. Equations (4.1)-(4.6) form a coupled system of ODEs and are solved using a high order explicit Runge-Kutta scheme with adaptive time stepping and error control. The absolute solution error is verified to be less than 5×10^{-12} by substituting the computed values of N_i into Eq. (4.7) and examining the residual.

For all of the numerical comparisons made in this Chapter, the bath gas composition is taken to be the equilibrium combustion products of an atmospheric pressure methane-air flat flame at an equivalence ratio of 0.7 and a temperature of 1750K. The selection of this thermo-chemical state for the numerical validation is based on using a consistent bath gas composition with the experimental validation reported in Section 5. The Einstein A_{ji} and B_{ij} , and B_{ji} coefficients are taken from LIFBASE [213]. The mild rotational level dependence of the A_{ij} coefficients has been accounted for by calculating temperature dependant values for the lumped levels. The EET values for $\nu'=0$ are taken from Paul *et al.* [214] and the references contained within, additional values are taken from [215, 216, 217, 218]. The high temperature EET and VET values for $\nu'=1$ are taken from Paul [219], with additional data, particularly at lower temperatures taken from [220, 221]. Broadening of the absorption line width due to homogenous broadening was accounted for using the collisional cross sections reported by Rea *et al.* [222, 223] and Kessler *et al.* [224].

For the detailed six-level model used in this study, an effective rate for RET is calculated such that the predicted RET rate is proportional to the degree of equilibrium departure.

As an example, the functional form for the RET term T_{61} , in Eq. (4.1) is given in expanded form by Eq.(4.9), the T_{23} RET term in Eq. (4.2) can also be expressed in a similar fashion as Eq. (4.9), however with different subscripts for the relevant N_i terms. An important feature of the RET model employed is that detailed balance requirements are satisfied. Although the RET model employed in this study is not as rigorous and universally applicable as RET schemes such as the energy corrected sudden scaling law proposed by Kienle *et al.* [225], for atmospheric pressures and nanosecond excitation combined with the use of a lumped six-level model, the RET model in this study is deemed to be acceptably accurate. Based on the limited data available for RET, the results and values proposed in several studies [204, 212, 216, 226, 227] are combined and used to calculate the RET cross section. For the bath gas composition investigated, a value for the RET cross section of approximately 50\AA is predicted.

The spectrally, temporally and spatially (along the z-axis) integrated fluorescence signal (F) is of primary interest in this study and is defined by Eq.(4.8). In Eq. (4.8) double summation over all the upper states ($i=2,3,4$) and lower states ($j=1,5,6$) is implied. The use of T_{ij} notation in Eqs. (4.1)-(4.6) corresponds to a simplified notation, with each T_{ij} term representing the combined values of RET, EET, VET and spontaneous emission where relevant.

$$\frac{dN_1}{dt} = -N_1W_{12} + N_2(W_{21} + T_{21}) + N_3T_{31} + N_4T_{45} + N_5T_{51} + T_{61} \quad (4.1)$$

$$\frac{dN_2}{dt} = N_1W_{12} - N_2(W_{21} + T_{21} + T_{24} + T_{25}) - T_{23} \quad (4.2)$$

$$\frac{dN_3}{dt} = T_{23} - N_3(T_{34} + T_{35}) \quad (4.3)$$

$$\frac{dN_4}{dt} = N_2 T_{24} + N_3 T_{34} - N_4 (T_{41} + T_{46}) \quad (4.4)$$

$$\frac{dN_5}{dt} = N_2 T_{25} + N_3 T_{35} - N_5 (T_{51} + T_{56}) \quad (4.5)$$

$$\frac{dN_6}{dt} = N_4 T_{46} + N_5 T_{56} - T_{61} \quad (4.6)$$

$$N_1 + N_2 + N_3 + N_4 + N_5 + N_6 = 1 \quad (4.7)$$

$$F = n_{OH} \int_{-\infty}^{\infty} \int_0^{\infty} \int_0^{\infty} \eta(\nu) N_i(t, z) A_{ij}(\nu) d\nu dt dz \quad (4.8)$$

$$T_{61} = 2R_{61} \left[N_1 + N_6 - N_1 / f_B(\nu'', J'') \right] \quad (4.9)$$

The temporal ($f_t(t)$) and spatial ($f_z(z)$) variation functions for the laser pulse as well as the laser, $\varphi_L(\nu)$, and absorption $\varphi_a(\nu)$ line-width functions are normalised to be consistent with the normalisation scheme of Partridge and Laurendeau [228]. The spectral irradiance $I_\nu(\nu, z, t)$ is decomposed into the normalised spectral irradiance (I_ν^0) and the relevant normalised spectral, spatial and temporal variation functions as shown by Eq.(4.10).

$$I_\nu(\nu, z, t) = I_\nu^0 f_z(z) f_t(t) \quad (4.10)$$

As Q -branch transitions are examined experimentally in this study, the degeneracies of the excited and ground state excited rotational levels are equal for the detailed six-level model. An example of the terms involved in the pumping rate term (W_{12}) is given by Eq.(4.11). The ϕ_ν'' term in Eq. (4.11) represents the dimensionless integral overlap term

for the ground state, in the idealised monochromatic laser and absorption limit this term will be unity, however for the real broadened system this term will be less than unity but greater than zero.

$$W_{21} = B_{12} I_L^0 f_z(z) f_t(t) \int_{-\infty}^{\infty} \phi_L(\nu) \phi_a''(\nu) d\nu = B_{12} I_L^0 f_z(z) f_t(t) \phi_\nu'' \quad (4.11)$$

To model the temporal variation of the laser pulse $f_t(t)$, a quadratic exponential function is selected. The quadratic exponential functional form given by Eq. (4.12) is found to be a good functional representation for the temporal variation of a frequency doubled dye laser pumped by a frequency doubled Nd:YAG laser for all time periods during the laser pulse. The value of Δt in Eq. (4.12) is set to a value of $\Delta t = \Delta t_{FWHM} / C_{QE}$ for the simulations, by doing so the FWHM and the integral for $t > 0$ of Eq. (4.12) is equal to Δt_{FWHM} . An explicit analytic expression for the normalising constant C_{QE} is not possible to be derived, therefore C_{QE} is calculated numerically and a value correct to five significant figures is found to be 1.1549. The value of Δt_{FWHM} is set to 8ns, which is the same FWHM as the laser pulse used for the experimental validation in Section 4.4.

$$f_t(t) = C_{QE} \left(4/\sqrt{\pi} \right) (t/\Delta t)^2 \exp \left[-(t/\Delta t)^2 \right] \quad (4.12)$$

4.2.2 Assessment of RET and Final State Effects

For the detailed six level model there is a significant degree of uncertainty in value of the RET cross section, this is due to the large variation in the reported RET cross sections found in literature [204, 206, 207, 212, 216, 226, 227, 229]. As illustrated by Tobai *et al.* [226], the disparities between data sets for RET cross sections are often so large that the agreement between studies is often not possible within the quoted error or uncertainty bars. To assess the potential influence of the uncertainty in the RET rate (R) on the

detailed six-level model results, the relative sensitivity of the spectrally and temporally integrated fluorescence signal F , to the RET rate is computed, this is abbreviated as $S_{F,R}^{rel}$. The value of $S_{F,R}^{rel}$ is computed using the definition $S_{F,R}^{rel} = \partial \ln F / \partial \ln R$, which is effectively the linearised relative sensitivity of F to R , evaluated at the selected RET rate. To evaluate $S_{F,R}^{rel}$ for different irradiance regimes $S_{F,R}^{rel}$ is computed as a function of the normalised spectral irradiance, a plot of $S_{F,R}^{rel}$ vs. I_ν^0 is shown in Fig. 4-2.

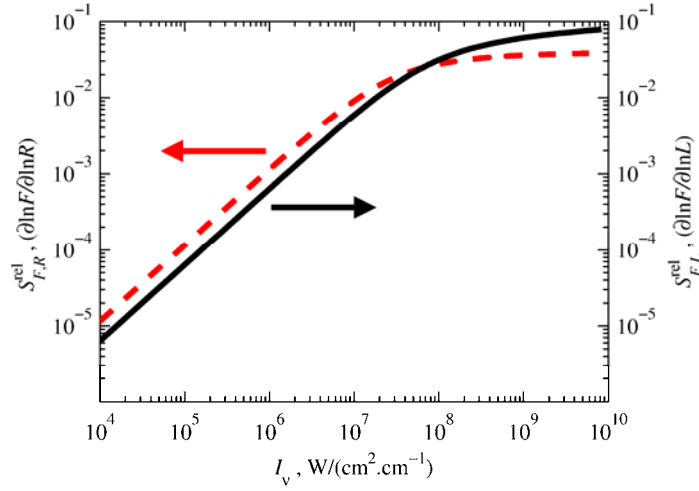


Fig. 4-2. Relative sensitivities of the temporally integrated LIF signal, F , as a function of the normalized spectral irradiance (I_ν^0). Dashed line shows the relative sensitivity of F to the rotational energy transfer rate ($S_{F,R}^{rel}$). Solid line shows the relative sensitivity of F to the quenching loss factor ($S_{F,L}^{rel}$).

From Fig. 4-2, at low irradiance levels where $I_\nu^0 < 1 \times 10^{-6}$, $S_{F,R}^{rel}$ is $< 1 \times 10^{-3}$, hence the sensitivity of F to the RET rate is small and is not a significant factor in this irradiance regime. This low sensitivity at low irradiance levels is caused by there being only a small fraction of the laser coupled level participating in the LIF process, hence replenishment of population in the laser coupled level by RET is not important. For increasingly large laser irradiances, an increased proportion of the laser coupled level participates in the LIF process, RET becomes increasingly important to replenish the population in the laser

coupled level from the other rotational levels ground state $\nu'' = 0$ rovibrational manifold. Hence the normalised sensitivity is larger and increases with increasing irradiance as indicated by the region of constant positive slope for $I_\nu^0 < 1 \times 10^7 \text{ W}/(\text{cm}^2 \cdot \text{cm}^{-1})$ in Fig. 4-2. At very high irradiance levels, Fig. 4-2 shows that the sensitivity of the fluorescence signal to RET remains relatively high, but plateaus around $1 \times 10^8 \text{ W}/(\text{cm}^2 \cdot \text{cm}^{-1})$ rather than continuing to increase with increasing irradiance levels. At these high irradiance levels the limiting factor is no longer the rate at which RET can replenish the laser coupled level from the ground state $\nu'' = 0$ rovibrational manifold, but rather the rate at which population is transferred into the ground state $\nu'' = 0$ manifold. At high irradiance levels depletion of the entire ground state $\nu'' = 0$ rovibrational manifold is the limiting factor minimising any further increase in $S_{F,R}^{rel}$ with increasingly large values of I_ν^0 .

The largest difference in the RET rate reported in literature compared to the value used in this study is approximately 50%. Considering a PLIF experiment that utilises very high normalised spectral irradiance levels such as $1 \times 10^9 \text{ W}/(\text{cm}^2 \cdot \text{cm}^{-1})$, based on the sensitivity results reported in Fig. 4-2, an error of only 2% in the absolute fluorescence signal is predicted. This error would only be realised if an absolute calibration method were utilised such as Rayleigh scattering [190]. If a relative calibration were utilised such as a known OH concentration in a flat flame, a much smaller error due to the RET uncertainty would result. With such a small difference in the absolute LIF signal for a 50% change in the RET rate, the uncertainty in the value of the RET rate derived from literature is not significant for the spectrally integrated results presented in this study.

A possible source of error in the detailed six-level model simulations of the OH LIF process is the uncertainty in the final state after electronic quenching. There are three possible paths that are different to the path presented in Fig. 4-1 that an excited $A^2\Sigma^+$ state molecule can possibly end up at after an electronic quenching event. The implications and assumptions made by neglecting these three paths are discussed below.

After an electronic quenching event the OH molecule can end up in a chemically modified or ionised state, the recovery time from such a state to chemical equilibrium levels is typically of the order of microseconds or more at atmospheric pressure, therefore the molecule is effectively lost from the LIF population cycle during the time scale of the laser pulse. In order to assess the sensitivity of the solution to population loss due to final state quenching, an additional level N_7 , has been added to the system of equations for the detailed six-level model to account for the lost population due to electronic quenching, this equation is given by Eq. (4.13).

$$\frac{dN_7}{dt} = LQ_{25}N_2 + LQ_{35}N_3 + L[Q_{46} + f_B(v' = 0, J = J'')Q_{41}]N_4 \quad (4.13)$$

All quenching values contributing to the T_{ij} terms in Eqs. (4.1)-(4.6) have been changed from the original Q_{ij} form to $(1-L)Q_{ij}$, thus accounting for the quenching population loss factor L . The value of the quenching loss factor L , is taken to be a global factor modelling the rate of quenching loss, the value of L varies from zero for no population loss to unity for all population lost after electronic quenching. The linearised sensitivity of F to the quenching loss factor L ($S_{F,L}^{rel}$), is presented as a function of the normalised spectral irradiance in Fig. 4-2. An approximately similar trend for the loss factor sensitivity $S_{F,L}^{rel}$ as a function of irradiance is found for RET rate sensitivity $S_{F,R}^{rel}$, both of these sensitivities are shown on the same graph in Fig. 4-2. For irradiance levels below 1×10^7 W/(cm².cm⁻¹) Fig. 4-2 shows that there is a steady increase in the sensitivity $S_{F,L}^{rel}$ with increasing irradiance due to the increasing significance of population cycling effects. Although the rate of increase of the sensitivity $S_{F,L}^{rel}$ does reduce at high irradiance levels, there is not the same degree of levelling out as $S_{F,R}^{rel}$ at high irradiance levels. The continued increase in sensitivity of $S_{F,L}^{rel}$ at high irradiance levels is proposed to be due to the large degree of population cycling that occurs at high irradiance levels.

By considering a loss factor of 0.1 and comparing the absolute LIF signal obtained at a normalised spectral irradiance level of $1 \times 10^9 \text{ W}/(\text{cm}^2 \cdot \text{cm}^{-1})$, a 0.1 loss factor will reduce the LIF signal by 12% compared to a loss factor of zero. This is a significant variation and if accurate non-linear LIF measurements are required to be made using absolute calibration methods such as Rayleigh scattering [190], then accurate temperature and species dependant values for the quenching loss factor will be required. Relative calibrations will reduced the uncertainty introduced by the quenching loss factor; however these uncertainties will not be completely mitigated.

Although there have been no published experimental measurements of the quenching loss factor for OH at flame temperatures that the authors are aware of, there has been measurements of final state OH at room temperature by Crosley and Copeland [230] and branching ratios of NO at room temperature by Settersten *et al.* [231]. These studies of small diatomic molecules indicate that some population is lost for room temperature quenching, however there is no theory that describes this process well and extrapolations of the experimental results to flame temperatures is not well justified, particularly as it is known the dominant quenching mechanism is fundamentally different at low and high temperatures for OH. For the detailed six-level model in the remainder of this Chapter a loss factor of zero is assumed. No specific value for the loss factor for OH at flame temperature has been reported experimentally or theoretically. The introduction of a loss factor greater than zero makes it virtually impossible to form detailed reduced analytic models.

A Second possible outcome after an electronic quenching event is that the molecule may end up in a high vibrational level in the ground state such as $\nu'' \geq 2$. If this is the case energy transfer processes maybe too slow to return this molecule to the laser coupled level within the time scale of the laser pulse. Measurements at room temperature of the VET rate for high vibrational levels in the ground state of OH by Dyer *et al.* [232] has shown that this process can be quite slow relative to quenching and excited state VET. No published study that these authors are aware of has explicitly examined VET cross sections or decay rates in the ground state of OH for any vibrational level at flame

temperatures. In a study using a two-colour LIF pump-probe experimental setup to examine ground state RET in a stoichiometric methane-air flame, Chen *et al.* [227] indirectly show that VET from $\nu''=1$ is slow relative to RET. Absolute determination of the ground state VET cross sections or decay rate from $\nu''=1$ cannot be determined from the results presented by Chen *et al.* [227], however a lifetime longer than 3ns can be inferred.

The significance of population in high vibrational levels in the ground state due to final state quenching has been modelled by adding additional levels to the detailed six-level model, each of the additional levels represent a vibrational level in the ground state up to $\nu''=10$. Based on the indirect results of Chen *et al.* [48] we assume that the VET rate for $\nu'' \geq 2$ will be less than or equal to the VET rate from $\nu'=1$ at flame temperatures, thus VET cross sections were assumed to be identical to those from $\nu'=1$ in the absence of any other available data. The high vibrational levels in the ground state are populated by controlling the branching ratio for the final state of quenching; this effectively controls the ratio of the population that arrives in high vibrational levels to the population that arrives in levels where the vibrational quantum number is conserved. A parameter is also used to control the value of the high vibrational level the population is assumed to be populated due to the finite branching ratio value. The results of these simulations vary significantly depending on the selection of the strength of the branching ratio and the selection of the vibrational quantum level for the final state. The main results from such simulations indicate that for branching ratios to high vibrational quantum numbers such as $\nu'' \geq 4$, where the strength of the branching ratio effectively acts as a loss factor. This indicates that population transferred to high vibrational quantum numbers is effectively lost from the population cycle during the laser pulse. For VET to $\nu'' \leq 3$ there is a reduction in the fluorescence yield though not as much as if this population were completely lost from the population cycle, this indicates that for $\nu'' \leq 3$ the population is effectively delayed from re-entering the population cycle but still interacts within the time scale of the laser pulse.

To quantitatively account for high vibrational level ground state effects it would be required to experimentally measure the species and temperature dependant quenching branching ratios and VET cross sections. These detailed experimental results do not presently exist. The checks undertaken to assess the sensitivity of these effects indicate that these effects will only be of significance if the branching ratio is very large with high ν'' being predominately populated. Also, if the ground state VET is significantly slower than VET from $\nu' = 1$ then the sensitivity of final solution to the branching ratio as well as the high ν'' level that is populated will increase.

Although there have been no direct measurements of the quenching loss factor, branching ratio or high vibrational level population after quenching, there is indirect experimental evidence that these factors are not the most dominant parameters in the population dynamics. All of the above three factors effectively decrease the fluorescence yield at high irradiance levels, translating to a more rapid transition to saturation in the fluorescence vs. irradiance curve. Experimental results reported in Section 4 indicate that there is not a significant deviation from the experimentally derived fluorescence vs. irradiance curve when compared to the fluorescence vs. irradiance curve produced by the detailed six-level model with a loss factor of zero. This gives confidence that these effects although possibly present are not dominant factors in determining the spectrally and temporally integrated LIF signal. Further analysis and discussion of the experimental results is left to Sections 4.4 and 4.5 of this Chapter.

From the energy transfer diagram in Fig. 4-1, it is assumed for the detailed six-level model that the vibrational quantum number is conserved after an electronic quenching event. This assumption is not based on any experimental evidence and there is theoretically little reason why the final state after an electronic quenching event should follow Franck-Condon principles. Of a lesser significance to the accuracy detailed six-level model Brockhinke *et al.* [207] has shown that there is some indication that the rotational quantum number is not conserved after VET from $\nu' = 1$, typically the rotational quantum number was shown to increase by assuming some of the excess energy from the VET collision process. Branching after quenching to high vibrational

numbers ($\nu'' \geq 2$) has already been discussed earlier in this Section. Branching is considered here such that the final state after quenching is bound by the energy levels defined by Fig. 4-1, this means that after quenching from $\nu' = 1$, $\nu'' = 1$ and $\nu'' = 0$ are considered as possible final states.

The assumption of conserved vibrational quantum number during electronic quenching has been evaluated by comparing the simulation results from the six-level detailed model assuming three different final state distributions after an electronic quenching event. The first case is the standard assumption of conserved vibrational quantum number, the second case is that the vibrational number is not conserved and the final case is an intermediate case where the final state is split evenly between conserved and non-conserved vibrational quantum numbers. These simulations are carried out with the assumption that no population is lost from the population cycle, hence a zero loss factor. For all cases negligible difference is found in the sensitivity of the fluorescence signal to the irradiance level for $I_{\nu}^0 = 1 \times 10^{10} \text{ W}/(\text{cm}^2 \cdot \text{cm}^{-1})$. This result shows that the assumption of conserved vibrational quantum number after an electronic quenching process that is used for the detailed six-level model is acceptable within the possible outcomes implied by energy transfer diagram in Fig. 4-1. If the assumption of conserved vibrational quantum number after electronic quenching is found to be a poor assumption by future experiments or theory; the sensitivity of this assumption on the presented simulation results in this Chapter is minimal.

4.2.3 Effects of Laser Temporal Pulse Distribution

To examine the effects of different temporal pulse distributions, three different temporal pulse distributions are evaluated using the detailed six-level model. The first temporal distribution is a “Top Hat” profile; this distribution is relevant to the many LIF models that assume a temporally constant “Top Hat” laser irradiance distribution. A realistic temporal pulse distribution for a dye laser pumped by a Q-switched Nd:YAG is modelled

by a quadratic exponential as per Eq. (4.12). The third pulse distribution considered is a triangular pulse distribution given by Eq. (4.14).

$$f_t(t) = \begin{cases} = 0, t < 0 \\ = t / \Delta t, \Delta t \geq t \geq 0 \\ = -t / \Delta t + 2, 2\Delta t \geq t > \Delta t \\ = 0, t > 2\Delta t \end{cases} \quad (4.14)$$

A triangular temporal pulse distribution is evaluated because it will be shown later in Section 4.3 that it is a potential candidate to represent the temporal variation of the laser pulse in an explicit analytic solution. All of the temporal distributions are modelled with a temporal FWHM of 8ns and owing to the normalisation criteria all deliver the same total energy during the pulse. The three temporal distributions are compared by examining the fluorescence yield and sensitivity of the spectrally and temporally integrated LIF signal F , as a function of irradiance in Fig. 4-3. The spatial interpretation of the solution as discussed in Section 4.2.1 can either be considered to be over a uniformly irradiated probe volume or a differential element of a non-uniformly irradiated probe volume.

From the results presented in Fig. 4-3, the assumption of a top hat irradiance distribution predicts the fluorescence vs. irradiance relationship to saturate with respect to laser irradiance for lower values than the realistic quadratic exponential distribution. This has the consequence that the expected fluorescence yield at $I_v^0 = 1 \times 10^{10} \text{ W}/(\text{cm}^2 \cdot \text{cm}^{-1})$ is reduced by 51% compared to the realistic quadratic exponential distribution. This large error at high irradiance levels is to be expected for the top hat temporal distribution as all of the pulse duration is spent at 100% of the maximum irradiance. For the realistic quadratic exponential pulse, only 78% of the pulse energy is spent above 50% of the peak pulse irradiance, allowing the remaining 22% of the pulse energy to be distributed in the temporal wings of the pulse where the fluorescence signal sensitivity to laser irradiance ($\partial F / \partial I_v^0$), hence fluorescence yield is much larger. The triangular pulse distribution

appears to do a far better job at simulating the realistic pulse distribution than the top hat function does. The accurate predictive capability of the triangular temporal function is due to the triangular distribution having a ramp up and a ramp down phase; this emulates the very important temporal wings of the realistic quadratic exponential pulse at high irradiance levels. For an irradiance level of $I_v^0 = 1 \times 10^9 \text{ W}/(\text{cm}^2 \cdot \text{cm}^{-1})$ which is practically achievable in highly saturated PLIF experiments the error in the fluorescence yield between the quadratic exponential and the triangular temporal distributions is less than 7%.

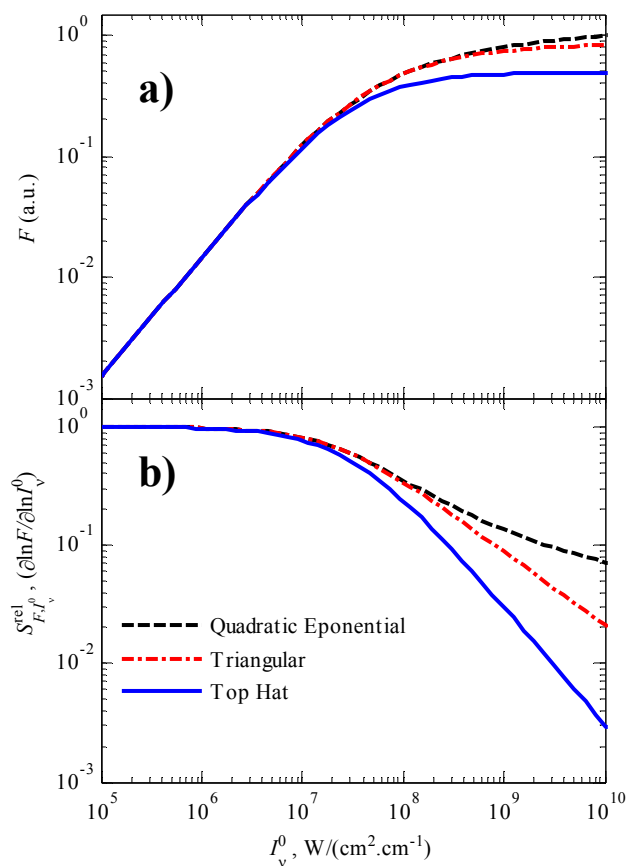


Fig. 4-3. The effect of three different temporal pulse distributions as a function of the normalized spectral irradiance, I_v^0 : a) The variation of the temporally integrated LIF signal F and b) the variation of the relative sensitivity of F to the normalized spectral irradiance ($S_{F,I_v^0}^{rel}$).

4.2.4 Spatial Irradiance Distribution

The effect of different spatial distributions for the laser irradiance is relevant to practical applications of LIF. Many LIF quantification models assume a uniform top hat spatial irradiance distribution, whilst the experimental irradiance distribution is typically far from uniform. The dependence of spatial irradiance distribution is examined numerically using the detailed six-level model using the realistic quadratic exponential of Eq. (4.12) for the temporal variation of $f_i(t)$. The resultant LIF signal F , from the simulations is integrated spectrally, temporally and spatially for the relevant spatial irradiance distribution. Four different spatial distributions are evaluated, these being: top hat, triangular, Gaussian and Lorentzian. In this Chapter the primary concern is PLIF applications, therefore the spatial irradiance distributions are assumed to be a function only of the laser sheet thickness $f_z(z)$ and negligible variation occurs in the laser sheet height direction y , in a single pixel. This is reasonable if the pixel size is much larger than the laser sheet height direction y , this is certainly the case in most PLIF experiments where the sheet height is typically greater than 10mm and projected pixel size is typically of the order of 25-200 μm . If there is significant variation of the spatial irradiance distribution in the y -axis in a single pixel, such as in a spherically focused line imaging LIF experimental setup, then the results presented here cannot be applied and specific simulations to validate and understand this geometry would be required. An additional assumption also needs to be raised, this is the spatial variation of the irradiance in the laser propagation direction x , is this variation negligible over a single pixel? This assumption can be easily assumed experimentally, even for short focal lengths such as 50mm, due to the small projected pixel sizes and the probe volume typically being within the Rayleigh range of the focused beam.

The top hat spatial irradiance distribution case is relevant to many LIF quantification models that assume a uniform spatial irradiance distribution. Experimentally it is almost impossible to practically achieve a uniform spatial irradiance distribution over the entire

PLIF sheet or probe volume; therefore the top hat uniform irradiance distribution is essentially a theoretical idealisation of the experimental process. A triangular spatial distribution is examined as it will be shown later in Section 4.3 that it is a potential candidate to represent the spatial variation of the laser pulse in an explicit analytic solution. The functional form for the triangular spatial irradiance used here is given by Eq.(4.15).

$$f_z(z) = \begin{cases} = 0, z \leq -\Delta z \\ = z / \Delta z + 1, -\Delta z \leq z \leq 0 \\ = -z / \Delta z + 1, \Delta z \geq z > 0 \\ = 0, z > \Delta z \end{cases} \quad (4.15)$$

The Gaussian spatial distribution is selected as it is a typical spatial irradiance profile found experimentally, most beam profiles can be transformed to a near Gaussian distribution through spatial filtering or relay imaging. The Lorentzian distribution is evaluated to examine the effects of large spatial wings in the spatial irradiance distribution, the Lorentzian functional form is an approximation to the spatial irradiance distribution if optical aberrations or beam divergence are significant in an experiment

The four spatial irradiance distributions are compared by examining the fluorescence yield and sensitivity of F to I_v^0 , as a function of irradiance in Fig. 4-4. For all distributions a linear fluorescence regime is predicted for low irradiance values followed by non-linear regime at higher irradiance levels. The fluorescence response in the non-linear regime is significantly different for the different distributions. The triangular distribution function appears to be a promising candidate to approximate the response of the Gaussian spatial distribution as for all irradiance levels the difference in the fluorescence yield with the Gaussian curve is minimal and within an acceptable error. The top hat distribution function predicts a significantly lower fluorescence yield at high irradiance levels and a more rapid transition to saturation compared to the Gaussian profile. The rapid transition to saturation for the top hat profile can be attributed to there being effectively no spatial wings in this profile, this is in contrast to the other three

distributions evaluated. For $I_v^0 = 1 \times 10^9 \text{ W}/(\text{cm}^2 \cdot \text{cm}^{-1})$ the triangular distribution under predicts the absolute fluorescence yield by only 8%, however the top hat distribution at the same irradiance level under predicts the fluorescence yield by 48%, this is assuming the Gaussian distribution is the true spatial distribution. For the Lorentzian spatial distribution it is apparent that even at very high irradiance levels such as $I_v^0 = 1 \times 10^{10} \text{ W}/(\text{cm}^2 \cdot \text{cm}^{-1})$ saturation is not close to being achieved, or indeed ever possible to be achieved.

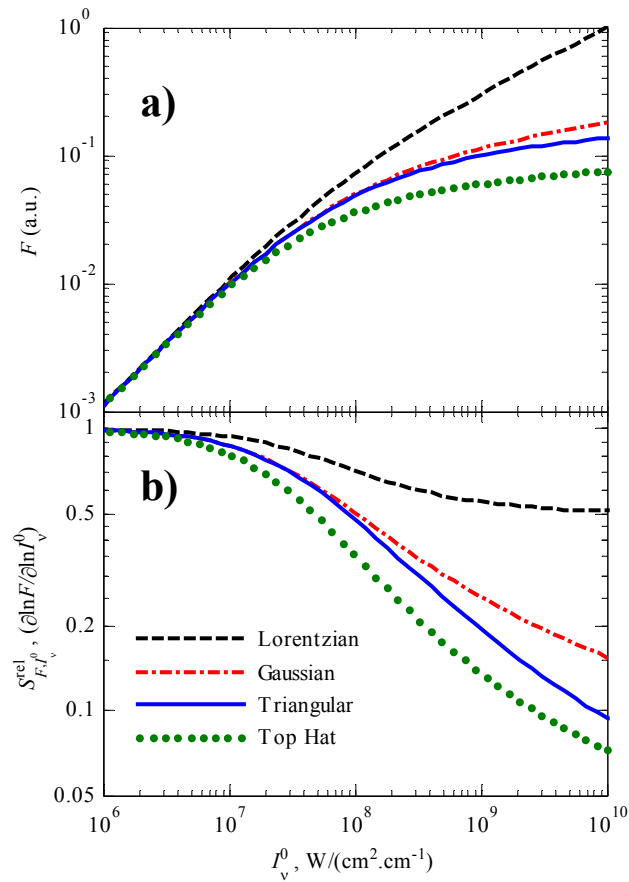


Fig. 4-4. A comparison of the temporally and spatially integrated LIF signals, F , for four different spatial spectral irradiance distributions as a function of the normalized spectral irradiance I_v^0 . The variation of F is given in a) and the variation of the relative sensitivity of F to the normalized spectral irradiance ($S_{F,I_v^0}^{rel}$) is given in b).

Although the Lorentzian spatial distribution is an idealisation, the results in Fig. 4-4 indicate how important accurate description of the spatial profile of the laser beam is required. For example, if an experimentally measured spatial irradiance profile is a Voigt distribution but approximated as Gaussian distribution, significant error could result if the original Voigt profile contains a significant Lorentzian fraction. If it is found that an experimentally measured profile has a significant wing contribution that resembles a Lorentzian profile, to avoid quantification errors the irradiance distribution must be accounted for explicitly or the beam profile improved through spatial filtering techniques to remove the Lorentzian component.

4.3 The Reduced Model

The detailed six-level model presented in Section 4.2 is not practically feasible for processing experimental results as six ODEs are required to be solved for each pixel in each PLIF image. It is desirable to form an explicit formulation for the quantification of the LIF signal without the need to call any significantly time consuming integration or mathematical routines. In this section the underlying assumptions of a reduced LIF model are explored. Basic two-level and four-level models assuming complete steady state and constant spatial and temporal irradiance are developed as reference models. An explicit analytic model is developed that does not assume a constant temporal and spatial irradiance is developed and validated for key parameters against the detailed six-level model simulation results.

4.3.1 Steady State and Quasi-Steady State Assumptions

The set of equations forming the detailed six-level model is too complex to form an explicit LIF model; hence simplifying assumptions are required to form an explicit

model. At atmospheric pressures for typical hydrogen-air or hydrocarbon-air combustion products, RET rates are approximately an order of magnitude larger than EET and VET rates. Based on this information a possible assumption that could be made is to assume that the RET rates are infinitely fast making populations N_1 and N_2 in Fig. 4-1 solely a function of N_6 and N_3 respectively. By making the assumption of infinitely fast RET, only four levels are required to model the population cycle hence Eqs. (4.1)-(4.6) reduce to a set of four ODEs. The energy transfer diagram and new notation for these four levels is given by Fig. 4-5. By assuming infinitely fast RET, rotational equilibrium for all vibrational levels is enforced, this requires the modification of the W_{12} and W_{21} terms introduced by Eq. (4.1) to include a Boltzmann fraction term f_B , to account for the fraction of the population in levels N_1 and N_2 that is coupled directly to the laser irradiance due to absorption or stimulated emission.

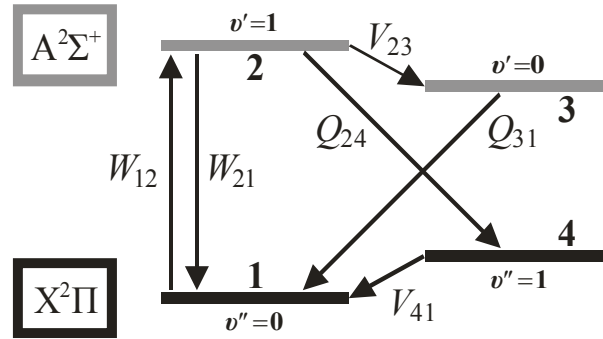


Fig. 4-5. Energy transfer diagram for the four-level model, spontaneous emission pathways from the excited $A^2\Sigma^+$ state are not shown for clarity.

To form a closed explicit solution for the four-level model, the assumption of complete steady state is made implying that all of the dN_i/dt terms will be zero. By assuming steady state it is implicitly assumed that the cross rates are balanced. The assumption of complete steady state may seem to violate some of the knowledge gained about the importance of the population dynamics learnt from the detailed six-level model in Section 2, however it will be subsequently shown that it is possible to incorporate some of the important transient population dynamics into an explicit model that utilises the steady

state solution as a starting point. Solving the steady state equations for the four level system allows a closed form solution for the fluorescence signal at a given normalised laser spectral irradiance, this is given by Eqs. (4.16)-(4.19).

$$F = \eta n_{\text{OH}} \int_{-\infty}^{\infty} \int_0^{\infty} \frac{I_v^0 f_t(t) f_z(z) \tau_1}{\left[I_v^0 f_t(t) f_z(z) \tau_2 + \tau_3 \right]} dt dz \quad (4.16)$$

The simplifying constants τ_1 , τ_2 , and τ_3 in Eq. (4.16) can be expressed by Eqs. (4.17)-(4.19).

$$\tau_1 = B_{12} \phi'' f_B(\nu'', J'') V_{41} \left[Q_{31} (A_{21} + A_{24}) + V_{23} (A_{31} + A_{34}) \right] \quad (4.17)$$

$$\tau_2 = B_{12} \phi'' f_B(\nu'', J'') (Q_{24} Q_{31} + Q_{31} V_{41} + V_{23} V_{41}) + B_{21} \phi' f_B(\nu', J') Q_{31} V_{41} \quad (4.18)$$

$$\tau_3 = Q_{31} V_{41} (Q_{24} + V_{23}) \quad (4.19)$$

It should be noted that although steady state has been assumed, the term representing the temporal variation of the laser irradiance $f_t(t)$ has not been dropped. This term was not eliminated as it is only necessary to assume steady state for the individual population levels to form Eq.(4.16), it is not necessary to assume steady state for any of the other terms that may contain a temporal dependence in the equations governing the four level system.

It is possible to integrate Eq. (4.16) directly if the spatial and temporal dependence functions $f_z(z)$ and $f_t(t)$ are known, this has been carried out successfully in Dunn *et al.* [175]. The method of directly integrating Eq. (4.16) is undesirable in terms of the significant calibration effort required and computational time necessary to process large datasets of PLIF images and will not be considered further in this Chapter.

Under the assumption of steady state with uniform spatial and temporal irradiance distributions it is possible to directly integrate Eq. (4.16) to form a closed solution, this solution is given by Eq. (4.20). To obtain Eq. (4.20) a top hat irradiance distributions with FWHM values of Δz and Δt for the spatial and temporal variations respectively are assumed. The result of Eq. (4.20) is termed the steady state four-level solution.

$$F = \eta n_{\text{OH}} \Delta z \Delta t \frac{I_v^0 \tau_1}{(I_v^0 \tau_2 + \tau_3)} \quad (4.20)$$

For the conditions examined in this study the rate of change of the laser temporal irradiance is of a similar time scale to the VET and EET rates. This shows that the response time of the system (the energy transfer rate) is of a similar time scale as the perturbing function (the laser pulse), for these conditions it is possible to consider that the system or the energy level populations are in a dynamic equilibrium or a Quasi-Steady State (QSS). To test and implement the QSS assumption Eq. (4.16) is integrated in time using the quadratic exponential distribution of Eq. (4.12) for the laser temporal irradiance variation, $f_t(t)$.

A comparison evaluating the sensitivity of the spectrally and temporally integrated fluorescence signal F , to I_v^0 ($S_{F, I_v^0}^{\text{rel}}$), as a function of irradiance is presented in Fig. 4-6, for the QSS assumption, the full SS assumption and the results from the detailed six-level model. The results in Fig. 4-6 do not consider the spatial variation of $f_z(z)$ and can be considered as results for a uniform spatial irradiance distribution or a differential element of a varying spatial irradiance distribution. As shown by Fig. 4-6, the assumption of complete steady state for the four-level model does not predict results accurately for high irradiance levels. In Fig. 4-6 the four-level model using the QSS assumption yields results that are indistinguishable from the detailed six-level model results for all irradiance levels including very high irradiance values. The excellent results for the four-level model using the QSS assumption can be attributed to the fact that at any given instant during the laser pulse, the populations in the LIF producing levels are close to

their equilibrium values for the given irradiance level at the given instant. It should be noted that if the VET and EET rates are significantly decreased or the laser pulse duration significantly decreased by an order of magnitude or more the agreement between the QSS solution and the detailed six-level model solution decreases.

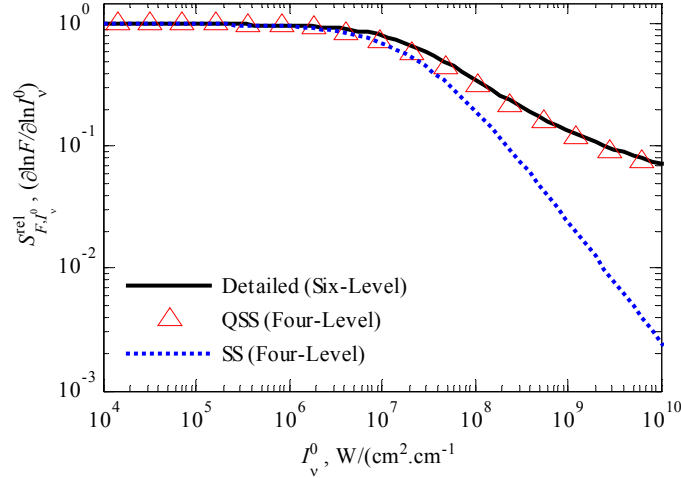


Fig. 4-6. Relative sensitivity of the temporally integrated fluorescence, F , to the normalized spectral irradiance, I_v^0 . Results for the detailed six-level model are compared with the four-level model for two different assumptions: quasi-steady state (QSS) and steady state (SS).

4.3.2 Explicit Model Formulation

Based on the information gained in Section 4.2 for the detailed six-level model, it is clear that any accurate reduced model must account in some way for the temporal and spatial dependence of the laser irradiance. As shown by Fig. 4-6, the assumption of QSS in a four-level model is a reasonable assumption to accurately account for the temporal variation of the laser irradiance for the condition examined. Whilst the QSS assumption is shown to give good results in Fig. 4-6, it is not possible to integrate Eq. (4.16) and obtain an explicit solution if a quadratic exponential distribution is used for the temporal variation, simultaneously considering a Gaussian distribution for the spatial variation of the laser irradiance is clearly not possible.

For certain functional forms it is possible to directly integrate Eq. (4.16) and obtain an explicit solution, this has already been examined for the uniform top hat distribution result in Eq. (4.16). Another functional form that permits an explicit solution to Eq. (4.16) is the triangular functional form for both the spatial and temporal dependence of the laser irradiance. The exact functional forms of the triangular distributions $f_z(z)$ and $f_t(t)$, are given by Eqs. (4.15)-(4.14) respectively. Substituting Eqs. (4.15) and (4.14) into Eq. (4.16) for the distribution of $f_z(z)$ and $f_t(t)$ respectively and subsequently performing the integration yields an explicit functional form for F , which is given by Eq.(4.21). The model formed by Eq. (4.21) is termed the integrated quasi-steady state (IQSS) model.

$$F = \eta n_{\text{OH}} \frac{4\tau_1 \Delta z \Delta t}{\tau_2^2} \left[\tau_2 + \frac{\tau_3}{I_v^0} \text{dilog} \left(-\frac{I_v^0 \tau_2}{\tau_3} \right) \right] \quad (4.21)$$

It should be noted that the dilogarithm notation used here is consistent with $\text{dilog}(z) = -\int_0^z \frac{\ln(1-t)dt}{t}$ and $\text{dilog}(z) = Li_v(z)$ where $v=2$. The dilogarithm is defined here as the polylogarithm (Li_v) of order $v=2$ and argument z . The dilogarithm in Eq. (4.21) can be computed efficiently using one of the many standard algorithms available [233, 234]. The dilogarithm function is also implemented as a standard function in some commercial mathematical packages. As I_v^0 , τ_2 and τ_3 are always positive, the argument of the dilogarithm in Eq. (4.21) will always be negative, this avoids the problem with the singularity of the dilogarithm function at $z=1$. For values of $|z| < 1$, $\text{dilog}(z)$ maybe computed using the power series defined by Eq (4.22).

$$\text{dilog}(z) = \sum_{n=1}^{\infty} \frac{z^n}{n^2} \quad (4.22)$$

For small values of I_ν^0 , a linear dependence of the fluorescence signal on the irradiance should be predicted from Eq. (4.21). To this end a linearised small irradiance solution to Eq. (4.21) is examined. Utilising the first term of the series defined by Eq. (4.22), the trivial solution $F=0$ is recovered, if the first two terms of the series is utilised the following expression for fluorescence F is found:

$$F = \eta n_{\text{OH}} \Delta z \Delta t \frac{I_\nu^0 \tau_1}{\tau_3} \quad (4.23)$$

The result of Eq. (4.23) can be considered a linearised low irradiance solution of Eq.(4.21). It is of interest that by making the standard low irradiance linearisation assumption to Eq. (4.20) requires the $I_\nu^0 \tau_2$ term in the denominator of Eq. (4.20) to be neglected as this term is much smaller than the τ_3 term in the low irradiance limit. By dropping the $I_\nu^0 \tau_2$ term in the denominator of Eq. (4.20) the resultant functional form is identical to Eq. (4.23). By eliminating the τ_2 term from Eq. (4.20) numerous terms are neglected in Eq. (4.23) including stimulated emission. Enough information is still retained in Eq. (4.23) to model all of the relevant collisional and radiation transfer process to quantify the LIF signal; Eq. (4.23) should therefore be an accurate model for the low irradiance level limit.

4.3.3 IQSS Model Numerical Validation

To validate the IQSS model presented in Eq. (4.21) the detailed six-level model is used as a numerical validation tool. The most significant function of a LIF model is quantification of the collected LIF signal to obtain a concentration or mole fraction, to do this variations in three key parameters are required to be accurately accounted for: irradiance, energy transfer rates and temperature. By examining the sensitivities of the fluorescence model to these three key parameters, an assessment may be made for the

absolute and relative predictive capabilities of the model. To simulate realistic experimental parameters the detailed six-level model is used with a quadratic exponential function as per Eq. (4.12) for the temporal irradiance variation and a Gaussian distribution for the variation in the spatial irradiance variation. For evaluation, the model uses the same values for the FWHM of the temporal and spatial distribution as used by the detailed six-level model.

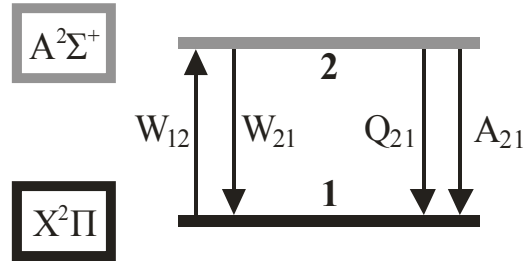


Fig. 4-7. Energy transfer diagram for the two-level model.

It is of interest to not only examine the performance of the IQSS model in Eq. (4.21) to the three parameters but to also the steady state four-level model presented in Eq. (4.20). It also of interest to evaluate the performance of so called two-level models [180], two level models are by the most used LIF model to quantify experimental results. An example energy transfer diagram for the two-level model is given in Fig. 4-7, immediately it can be seen that it is not possible to account for VET effects or the differences in Einstein A coefficients or quenching rates from $\nu'=1$ and $\nu'=0$. By assuming steady state and uniform top hat temporal and spatial distributions for the irradiance it is possible to express the solution for the two-level system by Eq.(4.24).

$$F = \frac{n_{OH} \eta \Delta t \Delta z \phi_v'' f_B(\nu'', J'') B_{12} I_v^0 A_{21}}{I_v^0 (\phi_v'' f_B(\nu'', J'') B_{12} + \phi_v' f_B(\nu', J') B_{21}) + A_{21} + Q_{21}} \quad (4.24)$$

The form of Eq. (4.24) is seldom used in practice, a less accurate linearised small irradiance solution is usually applied, this is given by Eq. (4.25).

$$F = \frac{n_{OH} \eta \Delta t \Delta z \phi_v f_B (\nu'', J'') B_{12} I_\nu^0 A_{21}}{A_{21} + Q_{21}} \quad (4.25)$$

For evaluation purposes Eq. (4.25) will not be examined as essentially the sensitivity of Eq. (4.25) to irradiance and energy transfer rates will not change as a function of irradiance level. The actual sensitivities of Eq. (4.25) although constant with irradiance level, will be identical to the value of the full steady state two-level in Eq. (4.24) at low irradiance levels.

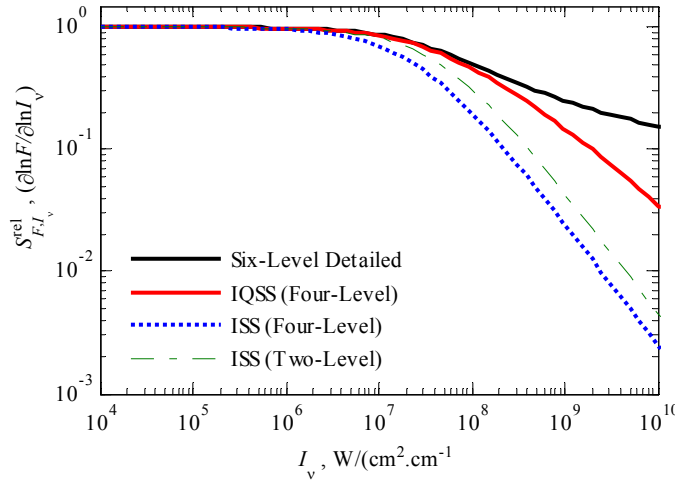


Fig. 4-8. Relative sensitivity of the spatially and temporally integrated fluorescence, F , to the normalized spectral irradiance, I_ν^0 . Results for the detailed six-level model are compared with the four-level model for two different assumptions: quasi-steady state (QSS) and steady state (SS). Also shown are the results for the two-level model assuming steady state (SS).

In Fig. 4-8 the sensitivity of the LIF model to laser irradiance is presented. As expected all models predict an identical linear limit for irradiance levels below $1 \times 10^5 \text{ W}/(\text{cm}^2 \cdot \text{cm}^{-1})$, beyond this irradiance level in the non-linear regime significant differences between the models can be found. Both the steady state two-level and the steady state four-level models predict a rate of transition to saturation and a rate of reduced irradiance sensitivity in the non-linear regime that is much faster than the true detailed six-level model results, this indicates that significant errors occur for both models in the non-linear regime. The

IQSS model adequately predicts the fluorescence sensitivity to irradiance in the non-linear regime, however the error in the predicted sensitivities for very high irradiance levels such as $I_v^0 > 1 \times 10^9 \text{ W}/(\text{cm}^2 \cdot \text{cm}^{-1})$ becomes increasingly large.

In typical LIF experiments the laser energy is monitored on a shot to shot basis and it is one of the roles of the LIF model to correct the signal for the shot to shot irradiance fluctuations. For OH PLIF experiments a relative calibration method is almost exclusively used. The fluctuation in laser energy typical experiments is usually no greater than $\pm 10\%$ from the calibration point.

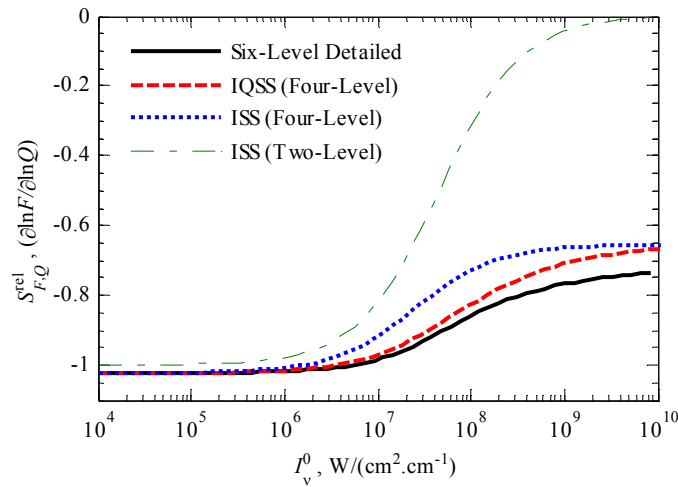


Fig. 4-9. Relative sensitivity of F , temporally and spatially integrated, to the local Electronic quenching rate, Q , as a function of the normalized spectral irradiance, I_v^0 . Results for the detailed six-level model are compared with the four-level model for two different assumptions: quasi-steady state (QSS) and steady state (SS). Also shown are the results for the two-level model assuming steady state (SS).

Assessment of the predictive capability of a LIF model from the predicted fluorescence sensitivity to irradiance is actually a measure with poor sensitivity if relative calibrations are utilised. Take for example an experiment with a relative calibration at an irradiance level of $1 \times 10^9 \text{ W}/(\text{cm}^2 \cdot \text{cm}^{-1})$ and a single shot is taken in the same media as the calibration however with a 10% reduced laser energy. If the fluorescence sensitivity to irradiance were predicted by the LIF model to be an order of magnitude smaller than the

real value, such as with the steady state four-level model, the error in the predicted LIF signal, hence species concentration would only be 2.4%. It is worthy to note for the same situation use of the IQSS model would result in an error of 1.1%. If absolute calibration methods are utilised the sensitivity to the accuracy of the predicted fluorescence sensitivity to irradiance is much larger and accurate prediction of the fluorescence yield vs. irradiance is imperative for the LIF model. Although the predicted fluorescence sensitivity to irradiance has a low sensitivity on the final result for experiments that utilise relative calibration methods, a generalisation can be made that poor prediction of the fluorescence sensitivity to irradiance will indicate a poor general predictive capability of the LIF model for other parameters.

As noted earlier in this section another important function of the LIF model is to correct the collected LIF signal for variations in thermo-chemical state that cause changes in the energy transfer rates. The most relevant energy transfer rates for broadband spectrally integrated LIF are VET and EET, both of these parameters vary strongly with temperature and composition. The relative sensitivity of the fluorescence F , to the local EET rate ($S_{F,Q}^{rel}$), is presented as a function of irradiance level in Fig. 4-9. Generally for all of the model results presented in Fig. 4-9 the fluorescence sensitivity to the EET rate is predicted to be slightly less than -1 for low irradiance levels, at high irradiance levels the absolute sensitivity decreases and then increasing in sensitivity but still remaining negative for large irradiance levels. For low irradiance levels the IQSS model and the steady state four-level model predict an initial sensitivity that is slightly less than -1, the low irradiance level sensitivity less than -1 can be attributed to the quenching that occurs from both the levels in the excited state, further evidence can be found by examining the quenching terms in Eqs. (4.16)-(4.19), particularly worth noting is that there is a quadratic dependence on quenching in the denominator of Eq. (4.16). The quadratic quenching dependence in the denominator of Eq. (4.16) is a feature that the two-level model is unable to capture due to the use of only one upper state level, this limitation of the two-level model is illustrated in Fig. 4-9 by the fact that the two-level model predicts an initial quenching sensitivity that is incorrect even in the low irradiance limit. The low irradiance limit error for the two-level model is only small for the specific conditions

examined in Fig. 4-9, however this disparity is significant from the idea that the two-level model is often claimed to be exact in the low irradiance limit.

The final role of the LIF model examined here is the correction for temperature changes to the LIF signal. Temperature variation has the effect of modifying the partition function for the excited line there by changing the percentage of the population that is directly coupled with the excitation laser. A second effect that temperature has is the variation in the quenching cross section; it is assumed here that the species concentrations do not change with temperature and only the relevant species quenching rates change with temperature. Another effect that can possibly be regarded as a secondary effect is the change of the integral overlap as a function of temperature due to an increase in molecular line broadening with temperature.

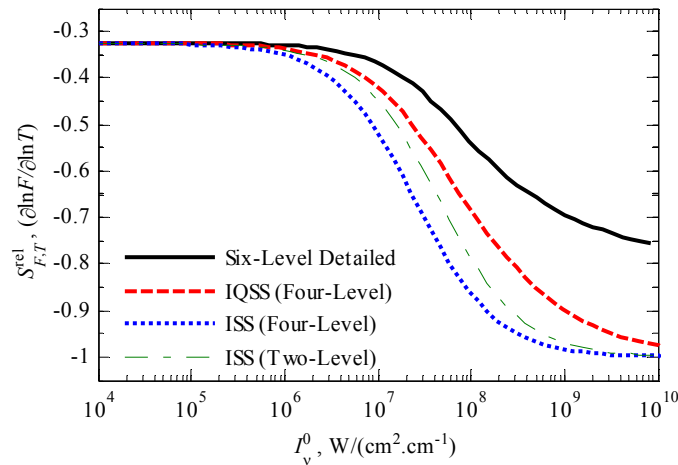


Fig. 4-10. Relative sensitivity of F , temporally and spatially integrated, to temperature as a function of the normalized spectral irradiance, I_v^0 . Results for the detailed six-level model are compared with the four-level model for two different assumptions: quasi-steady state (QSS) and steady state (SS). Also shown are the results for the two-level model assuming steady state (SS).

To examine the LIF model's ability to account for variations in temperature, the relative sensitivity of the fluorescence F , to the local temperature rate ($S_{F,T}^{rel}$), is presented as a function of irradiance level in Fig. 4-10. For low irradiance levels less than 1×10^5 $\text{W}/(\text{cm}^2 \cdot \text{cm}^{-1})$ all of the models predict the same sensitivity which is to be expected in the

linear regime of LIF. Moving beyond the linear regime, the differences between the detailed six-level model and the simplified models become apparent. It also becomes apparent that the ISS two- and four-levels models predict a transition to a -1 power dependence that is too rapid, although the IQSS model also predicts a transition to a -1 power dependence that is too rapid it still performs better for all irradiance levels than the ISS models. As the predicted exponent of the sensitivity is negative the sensitivity to temperature decreases with increasing irradiance levels thus the error in predicting this sensitivity at high irradiance levels should be minimal.

4.4 Experimental Comparison

The fluorescence irradiance predicted using Eq. (4.21) is compared with the experimentally derived fluorescence irradiance and the results are shown in Fig. 4-11. The experiment was carried out in the post flame exhaust of a 0.7 equivalence ratio methane-air premixed flat-flame burner. Simultaneously to the OH LIF measurement the Rayleigh scattering signal from the second harmonic of an Nd:YAG laser was utilised to measure temperature. Based on the Rayleigh scattering measurements, the post flame gas temperature is measured to be $1750 \pm 40\text{K}$. The dye laser fundamental FWHM spectral bandwidth was measured to be $0.075 \pm 0.01\text{cm}^{-1}$. This measurement was done by passing a portion of the fundamental of the dye laser beam through an etalon of high finesse then through a spherical expanding lens to magnify the interference pattern once projected onto a screen. The interference pattern on the screen was then imaged at high resolution with a CCD camera, the spacing and intensity of the interference fringes was then related to the spectral bandwidth.

The temporal response of the laser was monitored by a high-speed photodiode and an oscilloscope, the temporal response is found to best be represented by a quadratic exponential form of Eq. (4.12), with a FWHM of 8ns. To measure the sheet thickness and energy distribution a thin sheet of BK7 glass was placed at the focal plane of the laser sheet. After significantly attenuating the laser energy with a Fresnel type attenuator [235]

the resultant fluorescence from the UV excited BK7 glass was found to be linearly proportional to the laser energy. By imaging this fluorescence at high fidelity on a CCD camera a functional form of a Gaussian profile with FWHM of $80\mu\text{m}$ was found to be an acceptable fit.

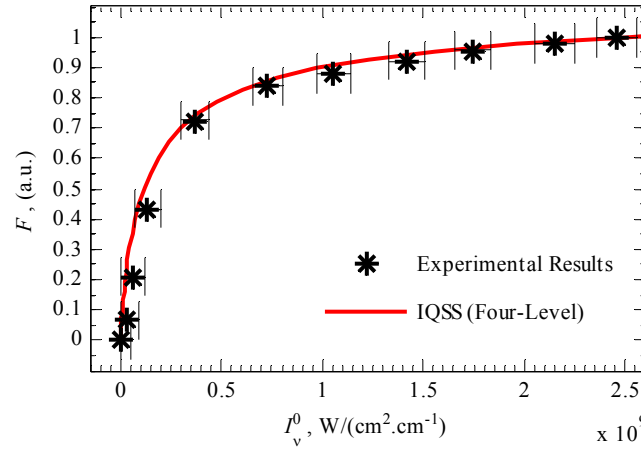


Fig. 4-11. Comparison of the IQSS model predictions and experimental measurements for the relationship between F , spatially and temporally integrated, and the normalized spectral irradiance, I_v^0 .

The collection efficiency and quantum efficiency of the fluorescence collection system were not evaluated, thus a relative calibration is required. This calibration was undertaken in a known OH concentration field on a flat flame burner. By varying the laser beam attenuation with the Fresnel type attenuator the laser energy was changed whilst not significantly changing the beam irradiance distribution at the focus. The η factor in Eq. (4.21) is taken to be the total calibration factor and was evaluated at the maximum irradiance value. To examine the correlation between the experimental results and the model predictions a small region of a PLIF image is extracted and the fluorescence-irradiance relation monitored. As the calibration is conducted at the maximum irradiance of $1.1 \text{ GW/(cm}^2\text{cm}^{-1}\text{)}$ the correlation in Fig. 4-11 by default at this value is 1. It can be seen in Fig. 4-11 that the model qualitatively predicts the experimentally observed

fluorescence-irradiance trend very well for all irradiance levels, including in the linear irradiance limit.

4.5 Discussion

In partially premixed and non-premixed turbulent combustion a useful imaging diagnostic method is to combine 2D Rayleigh scattering with OH PLIF to obtain temperature and OH mole fraction fields respectively, as reported by Kelman and Masri [32, 236]. A significant limitation to the quantitative measurement of the OH PLIF is the uncertainty of the quenching environment. The non-linear PLIF scheme presented in this Chapter reduces the effective sensitivity to quenching environment variations as well as the overall uncertainty in the predicted OH mole fraction. Combined with the increased quantitative nature of the measurements the single shot SNR would be increased due to the increased signal levels available when operating in the non-linear LIF regime.

The application of the non-linear LIF technique presented in this Chapter to other molecules or excitation schemes could be feasible to implement in a semi detailed model. Additional levels to model other electronic or vibrational states and loss mechanisms such as pre-dissociation would need to be judiciously added. A complete reduction of the semi detailed model such as the six-level model used in this Chapter to an explicit analytic expression for the LIF interpretation may not always be possible for other molecules or excitation schemes.

Semi detailed modelling with a transient six-level model has revealed that near the limit of the so called “linear regime” where the LIF signal can be well approximated with a linear irradiance dependence, the dependence on quenching environment is no longer linear as predicted by low irradiance linear limit two-level models typically used for linear LIF interpretation. Even under linear irradiance dependence conditions the reduced model presented in this Chapter would be advantageous to use as the dependence on

quenching environment would be more accurately predicted when compared with predictions with linear limit two-level models.

In summary, a non-linear LIF quantification technique has been developed and presented in this Chapter. The primary LIF model developed is termed the IQSS model which will allow quantification of OH in experiments such as the PJB and PPJB where non-linear LIF irradiance levels are required to obtain acceptable signal levels.

CHAPTER 5 PPJB 2D IMAGING RESULTS

The instantaneous spatial structure of flames in the PPJB is examined in this chapter through the use of a number of simultaneous planar imaging techniques. A significant advantage of planar imaging techniques over point or line measurements is that the instantaneous image maybe given a two dimensional spatial context for a given realisation. An example of this is that the measured data maybe conditioned on the local gradient of the scalar, this is something that is just not possible in point measurements. Furthermore qualitative spatial structure descriptors such as island, pocket and peninsula formation relevant to premixed combustion maybe readily identified. More advanced quantitative analysis of the spatial structure of planar images is also possible including the identification of fractal length scales, curvature and inner and outer cut-off length scales. These are additional examples of quantities that are particularly relevant to premixed combustion.

Although planar imaging techniques have the potential to reveal significant insight into the spatial structure of the relevant flow or flame, some ambiguity still does remain. This ambiguity originates from both finite spatial resolution of the measurement and the unaccounted third dimensional effects, or so called "out of plane motions". The finite spatial resolution of a measurement system may be quantified as is done for the experiments reported in this thesis, however the interplay of this finite spatial resolution value with the various flow field scales such as the Kolmogorov and Batchelor scales is a complex issue that has yet to be definitively resolved. The claim of "well resolved experimental results" or "sufficient spatial resolution" is always a topic of great

controversy in turbulent combustion or indeed fluid mechanics in general. In premixed turbulent combustion, the minimum resolution requirement is even more ambiguous due to chemical length scales being of the order of the smallest flow fields scales in certain circumstances.

The issue of quantifying three dimensional effects on two dimensional measurements of layer thicknesses, gradient magnitudes and scalar dissipation rate measurements is a complex task. Ideally if three dimensionally corrected realisations or statistics are desired dual or multiple sheet imaging techniques are required. If only a single sheet image is recorded, interpretation of single images must be treated with caution. The use of certain statistical measures that are not significantly sensitive to out of plane motions is one method that the complications of out of plane motions maybe overcome. In flows with a large bulk flow direction such as free jet flows where one of the image axes is aligned with the bulk flow direction the correction for three dimensional effects for the conditional mean scalar gradient does not significantly change the shape of the conditional mean, but mainly scales the conditional mean by a factor that can be of the order of 20%. In flows such as strongly swirled flows the correction for three dimensional effects is significant for both the magnitude (50% or more) and shape of the conditional mean. Simple magnitude scaling corrections for the conditional mean in these flows may not be possible for these flows. If the example of the free jet is again considered, the PDF of an iso-scalar surface for the out of plane angle is not expected to change significantly as a function of Reynolds number for sufficiently high Reynolds numbers in the turbulent regime. This allows parametric investigations using two dimensional proxies to be used for the full three dimensional measurements for certain measures such as scalar gradients which are inherently sensitive in magnitude to out of plane effects.

In this Chapter results from three major experimental campaigns are presented. In Section 5.1 a wide image region experiment of simultaneous Rayleigh OH PLIF is reported. The idea here is that the Rayleigh field is used to calculate the temperature with minimal error in a premixed flame. This temperature field will be useful in understanding the reaction

progress structure of the flame: for example answering the question: does the particular flame examined display thin flame fronts or thickened flame fronts? The spatial distribution of the OH mole fraction field will be a valuable indicator of finite rate chemistry effects on the minor species field. An emphasis is placed on identifying qualitative structures and descriptors of the instantaneous temperature and OH fields. Even though the data is processed to be quantitative both in terms of temperature and OH mole fraction this feature of the experiment is not emphasised. In Section 5.2 a simultaneous Rayleigh OH PLIF experiment is again reported, however the imaging region is much smaller than that the experiment reported in Section 5.1. Significant attention is paid to making the experiment quantitative and minimising the experimental uncertainties. Care is also taken to quantify and maximise the image spatial resolution. Section 5.3 reports the results of a simultaneous Rayleigh, OH PLIF and CH_2O PLIF experiment. The product of the CH_2O and OH mole fractions is shown to be a very good marker for the global heat release and reaction rates, thus this experiment can reveal insight into the spatial structure simultaneously for both the temperature and reaction rate fields.

5.1 Large Image Region Rayleigh OH PLIF Imaging

The aim of conducting the large image region experiment is to examine the planar spatial structure of both the temperature and OH fields. What is referred to here as large image region is in fact an image area approximately $5D$ high and $7D$ wide. Some of the experimental description, data quantification method and results presented in this section have been reported in a previous publication [175]. The experimental setup and description is discussed in Section 5.1.1, while Section 5.1.2 details the processing and accuracy of the data. Selected imaging results are presented in Section 5.1.3 including a brief discussion. A more extensive discussion of the results in terms of global finite-rate chemistry effects is left until Chapter 8.

5.1.1 Experimental Setup

The experimental setup essentially consists of forming and overlapping a visible Rayleigh laser sheet and a UV laser sheet at the probe volume, filtering the appropriate signal and collection of the signal on a digital detector. A 3D overview of this experimental setup is presented in Fig. 5-1.

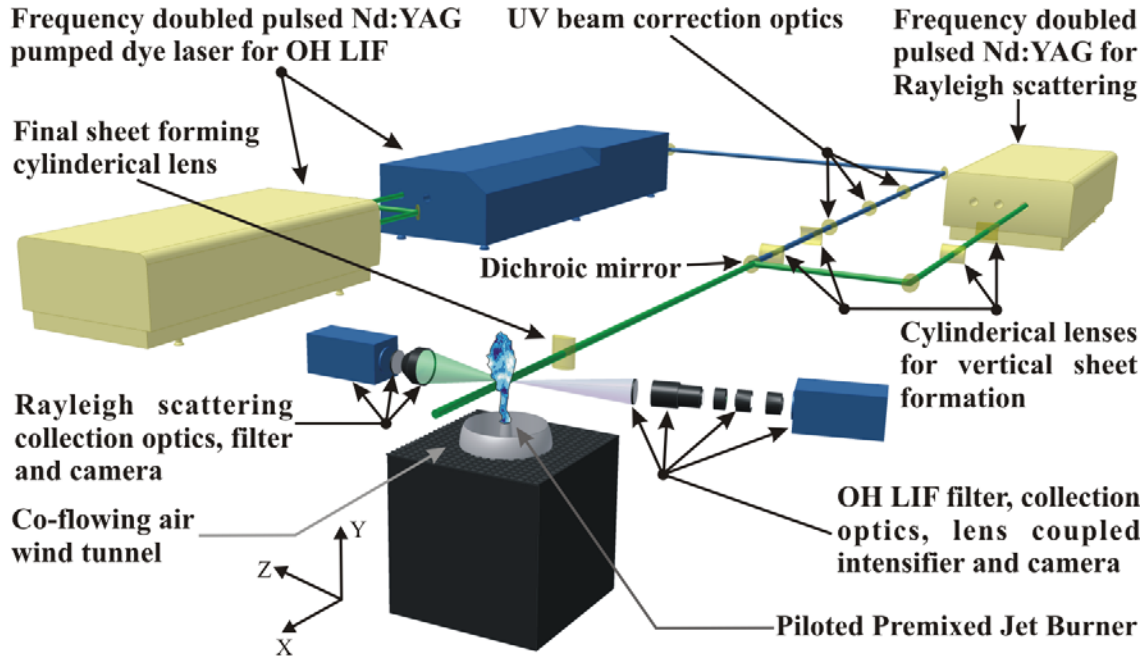


Fig. 5-1. An overview of the experimental layout for the large image region Rayleigh OH PLIF experiment including lasers, optics and signal collection.

The Rayleigh laser sheet is generated from the second harmonic of an Nd:YAG (Spectra Physics Pro350), operating at an energy of 1.4J/pulse at 532nm. The 532nm beam is expanded in the y-axis by a pair of plano-concave and plano-convex cylindrical lenses to produce a sheet height of 25mm.

The UV beam for the OH PLIF, is generated by the second harmonic of an injection seeded Nd:YAG (Spectra Physics Pro350) pumping a dye laser (Sirah PrecisionScan) with Rhodamine 6G in ethanol as the lasing medium. The fundamental of the dye laser at 566nm is then doubled in a Potassium Dihydrogen-Phosphate (KDP) crystal to produce

UV radiation at 283.2nm, corresponding predominately to $Q_1(7)$ excitation for the $A^2\Sigma^+ - X^2\Pi(1,0)$ system of OH. The UV is spectrally isolated from the dye laser fundamental by use of a four Pellin-Broca prism unit. The UV is then spherically expanded through a Keplerian spatial modulator by a pair of plano-convex lenses and an iris, the beam is then cylindrically expanded in the y-axis through a pair of plano-concave and plano-convex lenses to produce a collimated beam in the sheet height axis (y-axis) direction of 25mm. The UV beam is then combined with the 532nm beam by use of a dichroic mirror. The combined UV and visible beams are then focused cylindrically in the z-axis by a 300mm focal length plano-convex fused silica lens to form a thin sheet at the probe volume.

If both the visible and UV beams are collimated in the z-axis propagation direction before the final cylindrical lens a focal plane miss-match will occur. The cause for the focal point miss-match between the UV and the visible beams is that the index of refraction for most optically transparent materials changes from the visible to the UV (typically increasing refractive index with smaller wavelengths) to cause a smaller focal length for the UV compared to the visible beam assuming a single element lens is used. The focal point of the UV beam at the probe volume is made to coincide with the 532nm focal point by allowing a small divergence in the beam to remain after the initial spatial filtering of the UV beam. The divergence in the y-axis direction of the UV beam is corrected by the subsequent cylindrical expansion after the spatial modulator. The divergence of the UV beam in the z-axis direction is not corrected after the spatial modulator, allowing the UV beam focal point to coincide with the visible.

The 532nm Rayleigh scattered light is collected at 90 degrees by an f/1.4, 85mm visible camera lens onto a Peltier cooled interline-transfer CCD detector. Flame luminescence and interferences due to UV laser scattering and OH LIF is rejected totally with a 532nm 10nm bandwidth filter and a 500ns camera gate time. The OH LIF signal is collected at 90 degrees with an f/4.5, 105mm UV lens, which focuses the collected OH LIF onto a UV sensitive generation two intensifier. The intensifier rear phosphor screen is lens coupled to an interline transfer CCD camera with a magnification of unity by a pair of f/1.2, 45mm camera lenses. Resonant UV light, flame luminosity and 532nm scattering is

rejected from the OH LIF signal with a band-pass filter centred at 313nm with a 10nm FWHM bandwidth combined with a 1 μ s gate time on the intensifier multi-channel plate (MCP).

The laser beam waist thicknesses at the focal point are measured to be less than 100 microns and 80 microns FWHM for the 532nm and UV beams respectively. The mean beam width was measured by rotating the final cylindrical optic by 90 degrees and imaging the resulting Rayleigh scattering signal at high resolution. An estimate of the spatial over-lap accuracy of the two beams at the waist is approximately 20 microns; this was done by examining burn marks on photosensitive paper under a microscope. Although the accuracy of the burn mark method cannot be relied on for absolute measurements of beam thickness, for the purpose of assessing beam overlap it is deemed to be adequate. Due to the reduced waist of the UV beam, the overall focal waist envelope for the two beams remains below 100 microns despite the 20 micron uncertainty in beam overlap. The beam waist at the edges of the images was measured to be 130 microns and 95 microns FWHM for the 532nm and UV beams respectively, although at the edges of the image the beam was well outside the Rayleigh range the relatively small beam thickness at such a distance from the focal plane can be attributed to the optical aberrations induced by the final cylindrical lens and the non-Gaussian profile of both the 532nm and UV beams.

5.1.2 Data Processing

The approach taken for the image collection of the Rayleigh signal on a non-intensified CCD detector is based on the improved spatial Modulation Transfer Function (MTF), reduced noise and improved signal linearity possible when compared to intensified approaches. For intensified CCD signal collection strategies the shot noise and noise introduced by the intensifier is typically convoluted over a number of pixels and only CCD readout noise contributes significantly to the local inter-pixel SNR. It is possible that using intensified approaches the local inter-pixel SNR can be quite high whilst the

global image SNR can be quite poor. By removing the intensifier the noise the intensifier introduces is removed, however shot noise is no longer convoluted over a number of pixels, thus it is quite possible that the local inter-pixel SNR can be lower than in intensified approaches. Of course only if the signal level is sufficiently high and well above the CCD readout noise floor, will the global image SNR be higher in the non-intensified CCD case compared to the intensified CCD case.

To reduce inter-pixel noise in the Rayleigh measurements, a contour aligned smoothing algorithm similar to that presented by Dunn *et al.* [175] is utilised. The contour smoothing algorithm was originally devised for non-premixed combustion experiments to increase the Signal to Noise Ratio (SNR) of Raman images using the Rayleigh image as a high quality contour reference image. In the current premixed configuration, the OH and Rayleigh images do not adequately correspond, so a reference image is created from the original noisy Rayleigh image. The high SNR Rayleigh reference image is created by applying a low pass Fourier Transform filter to remove inter-pixel noise and then applying a conventional 5x5 pixel linear filter. The application of the contour smoothing algorithm is found to reduce noise and preserve gradient information better than any other linear, Gaussian or spectral filtering scheme. The SNR of the pre-smoothed Rayleigh images in the 1500K hot coflow combustion products is typically 15, this is achieved with a projected pixel size of 50 μ m. Post smoothing the SNR approaches an upper limit of 50, which is primarily constrained by uncertainties in correcting each image for fluctuations in the laser beam profile.

Once the normalised Rayleigh images were corrected for background and laser energy fluctuations, the contour smoothing algorithm was applied, followed by a correction for cross section variation, temperature was then obtained using the ideal gas law. The Rayleigh cross section variation with collected Rayleigh signal was taken from the line of best fit from data obtained using laminar freely propagating flames, opposed flow strained laminar flames and mixing limit simulations using the codes of Stårner *et al.* [237] and Kee *et al.* [238]. GRI 3.0 Goodwin [177] was used as the kinetic mechanism with multi component transport properties in all simulations. The relevant Rayleigh

scattering cross sections were taken from literature [239, 240]. For the opposed flow simulations, combinations of compositions that represented the central jet CNG-air, coflow and pilot combustion products were simulated. The maximum cross section error from the line of best fit is 4% ($\pm 60\text{K}$) close to 1500K due to the large range of compositions possible from the pilot, coflow and central jet streams at this temperature. The line of best fit for the cross section is shown in Fig. 5-2, it is found to be computationally advantageous for the cross section to be cast in terms of the relative Rayleigh signal as opposed to the temperature.

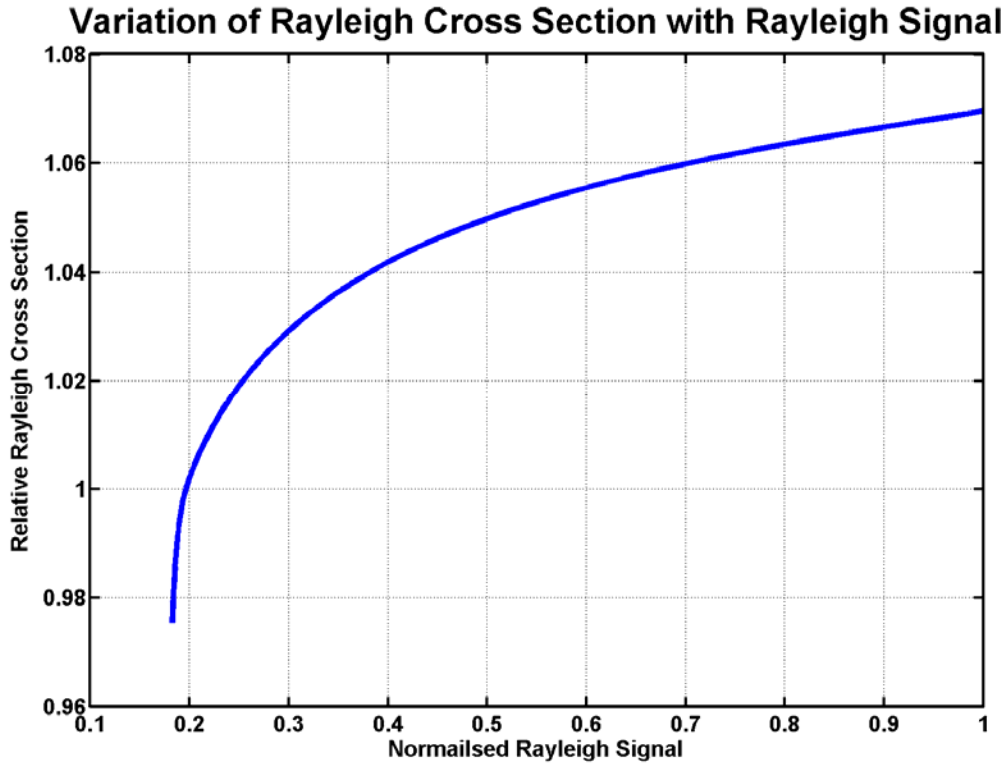


Fig. 5-2. Variation of the line of best fit for the relative Rayleigh cross section as a function of the normalised Rayleigh signal.

The OH PLIF strategy used in this study is to operate with laser spectral irradiance levels sufficiently high to operate in the non-linear regime of LIF. The advantages of operating in the non-linear regime are numerous such as reduced sensitivity to quenching corrections, reduced influence of beam energy fluctuations shot to shot, reduced

sensitivity to spatial beam energy fluctuations and near maximisation of the possible fluorescence signal level. The most pressing challenge for non-linear PLIF is the lack of well established models for LIF quantification. If the reasonable assumption is made that negligible attenuation of both the laser energy and the LIF signal occurs, even detailed multi level rate equation models that account for temporal and spatial variations will predict a linear dependence of the OH concentration with collected LIF signal [180]. The challenge for the LIF model is to correct the collected LIF signal for variations in quenching environment, temperature and laser energy fluctuations. In order to quantify the LIF signal in this study, the methodology first presented by Dunn *et al.* [241] then expanded by Dunn and Masri [242] is used. This method utilises a steady state solution to the rate equations [180] based on a four level model of the OH molecule as outlined by Dunn and Masri [242] to interpret the measured LIF signal. Equation (5.1) gives the relation of OH mole fraction (X_{OH}) to the measured fluorescence signal level (F_{OH}). As temperature (T) is measured simultaneously to the OH fluorescence, the variation of Boltzmann fraction, electronic and vibrational energy transfer rates with temperature are incorporated directly in Eq. (5.1).

$$X_{OH} = \eta \int_{-\infty}^{\infty} \int_0^{\infty} \frac{F_{OH} [\tau_1(T) + I_v^0(z, t) \tau_2(T, z, t)]}{I_v^0(z, t) \tau_3(T)} dz dt \quad (5.1)$$

The simplifying constants $\tau_1(T)$, $\tau_2(T)$, and $\tau_3(T)$ in Eq. (5.1) involve Einstein A and B coefficients, the integral overlap correction, ideal gas correction, Boltzmann fraction correction, temperature and composition dependant electronic and vibrational energy transfer rate terms and are given in Chapter 4. The Einstein A_{ji} , B_{ji} and B_{ij} coefficients are taken from LIFBASE [213]. Similarly to the Rayleigh cross section variation with temperature, the vibrational and electronic energy transfer rate variation with temperature and composition has been calculated using the equation of best fit derived from results of freely propagating, opposed flow and mixing limit laminar simulations using quenching coefficients from Paul [219] and Tamura *et al.* [218]. The line of best fit gives a maximum quenching rate error of 3% at 1500K, again due to the large range of

compositions possible at this temperature. An example graph showing the lines of best fit derived from the laminar calculations for the electronic energy transfer and vibrational energy transfer rates as a function of temperature is given in Fig. 5-3.

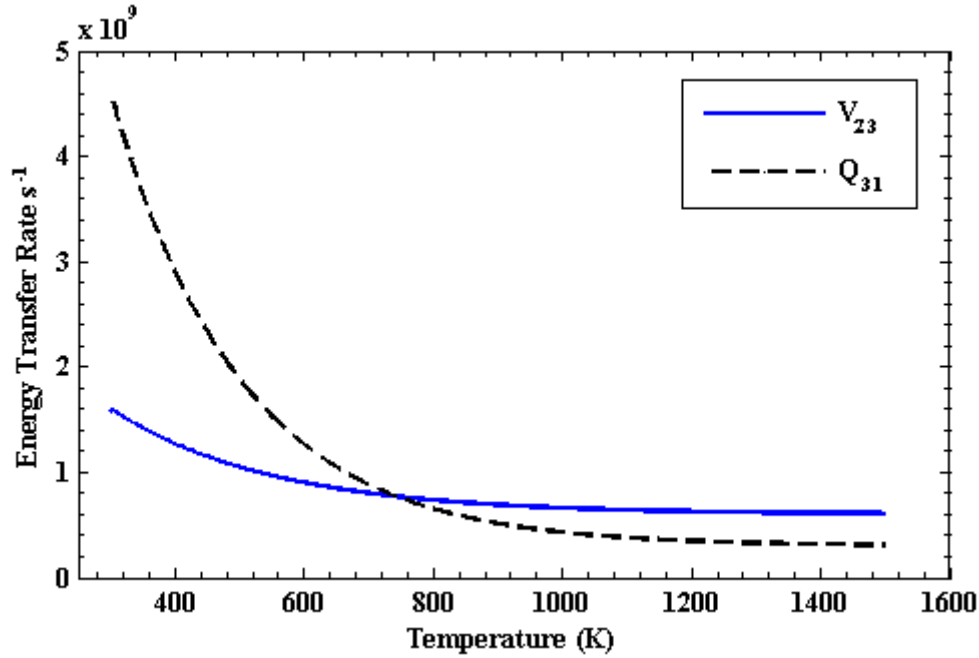


Fig. 5-3. Variation of lines of best fit for the electronic energy transfer (Q_{13}) and vibration energy transfer (V_{34}) in the temperature range 300K to 1500K.

As the LIF strategy in this experiment is implemented as a relative method, a source of known concentration OH is required for calibration. The system calibration constant η was determined from calibration in the post flame exhaust gas of a premixed flat flame with an equivalence ratio of 0.8. If the laser spatial profile is assumed to be approximately constant between calibration images then the temporal and spatial wing effects that complicate analysis of absolute calibration methods [191], will not be a significant source of error. The three spatial components of the laser intensity matrix I_v^0 are determined by the 283nm Rayleigh scattering from room temperature propane in the conventional planar configuration and in the 90 degree rotated configuration discussed in Section 5.1.1; signal collection was enabled by temporarily removing the 313nm

interference filter. Although computationally intensive, Eq. (5.1) was evaluated directly using the measured spatial and temporal profiles of I_{ν}^0 .

Neglecting single shot noise, the OH measurement accuracy is subject to two primary error sources: the calibration uncertainty of the OH concentration in the post flame gas required to determine η , uncertainty in the measurement of I_{ν}^0 and systematic LIF model error. The temperature of the post flame gas in the premixed flat flame calibration burner is measured with the Rayleigh scattering technique. The Rayleigh scattering signal is measured in both the unburnt and reacting configurations to confirm the composition of the reacting flow minimising the impact of flowmeter error. Noise effects due to shot noise and read out noise are virtually eliminated by averaging over one thousand images. Averaging to reduce noise is possible in this calibration flame as the flow is both laminar and steady. The resulting temperature of the calibration flame of 1810K is measured with an uncertainty of +/-1.5%, which is predominately due to uncertainties in the relative values of the Rayleigh cross sections for the hot gas products and detector readout non-linearity. The estimated OH calibration uncertainty from the premixed flat flame burner is +/- 4%, assuming OH is close to the equilibrium value. This is verified with laminar flame simulations with an assigned temperature profile identical to the experimentally measured temperature profile.

An assessment of the combined systematic model error and calibration error for OH is carried out by measuring the OH mole fraction in the hot coflow. This is a quenching and temperature environment different from the calibration flame that is again uniform, steady and close to equilibrium. This measurement is made 100mm downstream from the coflow base plate, where chemical equilibrium at the measured temperature can be safely assumed. The measured OH mole fraction is 6.05×10^{-5} which is 8% greater than that predicted by thermodynamic equilibrium at 1453K of 5.61×10^{-5} . In a single image realisation for a turbulent flow field, the error in the measured temperature and noise (shot and read out) further contribute to the OH uncertainty, we consider that the OH quantification method presented here has an uncertainty for the OH mole fraction of +/-

15% for the present experimental setup. Further discussion of the quantitative nature of the OH algorithm is explored by Dunn and Masri [242] and in Chapter 4.

5.1.3 Results and Discussion

Sample joint images of temperature and OH are presented in Fig. 5-4 and Fig. 5-5 for a range of axial locations in the four flames examined. For consistency, the false colour bars do not change within each figure and use the same peak values of temperature and OH mole fractions. The flow is from bottom to top and the physical space covered by each image is 29 mm (wide) by 19 mm (high) centred on the referred axial location. The images are selected to be representative realisations from the collected dataset of the particular flow and location. The results are not analysed here in a deep statistical quantitative fashion, rather the representative images presented are used to illustrate and describe qualitatively the structure of the four flames in the PM1 series.

The effect of parametrically increasing the central jet velocity on the instantaneous flame structure for a constant axial location is shown in Fig. 5-4a-d for the axial location of $x/D=15$. The results of Fig. 5-4a show that for flame PM1-50 a relatively thin flame front thickness occurs based on the temperature image. Some small peninsula structures of partially reacted gas at temperatures of 800-1100K are evident. Generally these peninsula-like structures point towards the fresh reactants and are possibly caused by the compression of two large-scale counter rotating eddies. The step like nature of the OH field in the reaction zone correlates well in terms of curvature and general structural features with the high ($>1400\text{K}$) temperature contour. The imaging results for the PM1-50 flame indicates a consistent flame structure to that which could be qualitatively described as being in the “complex strain flame-front” regime of Chen and Bilger [9]. The presence of the pilot is highlighted in the PM1-50 case and also in the PM1-100 case by a sheath of 1800K gas around the central jet. This is due to the fact that a constant pilot velocity was used in all the selected flames, yielding a high heat release ratio

between the central jet and pilot for low central jet velocities. This is particularly prominent for the PM1-50 flame.

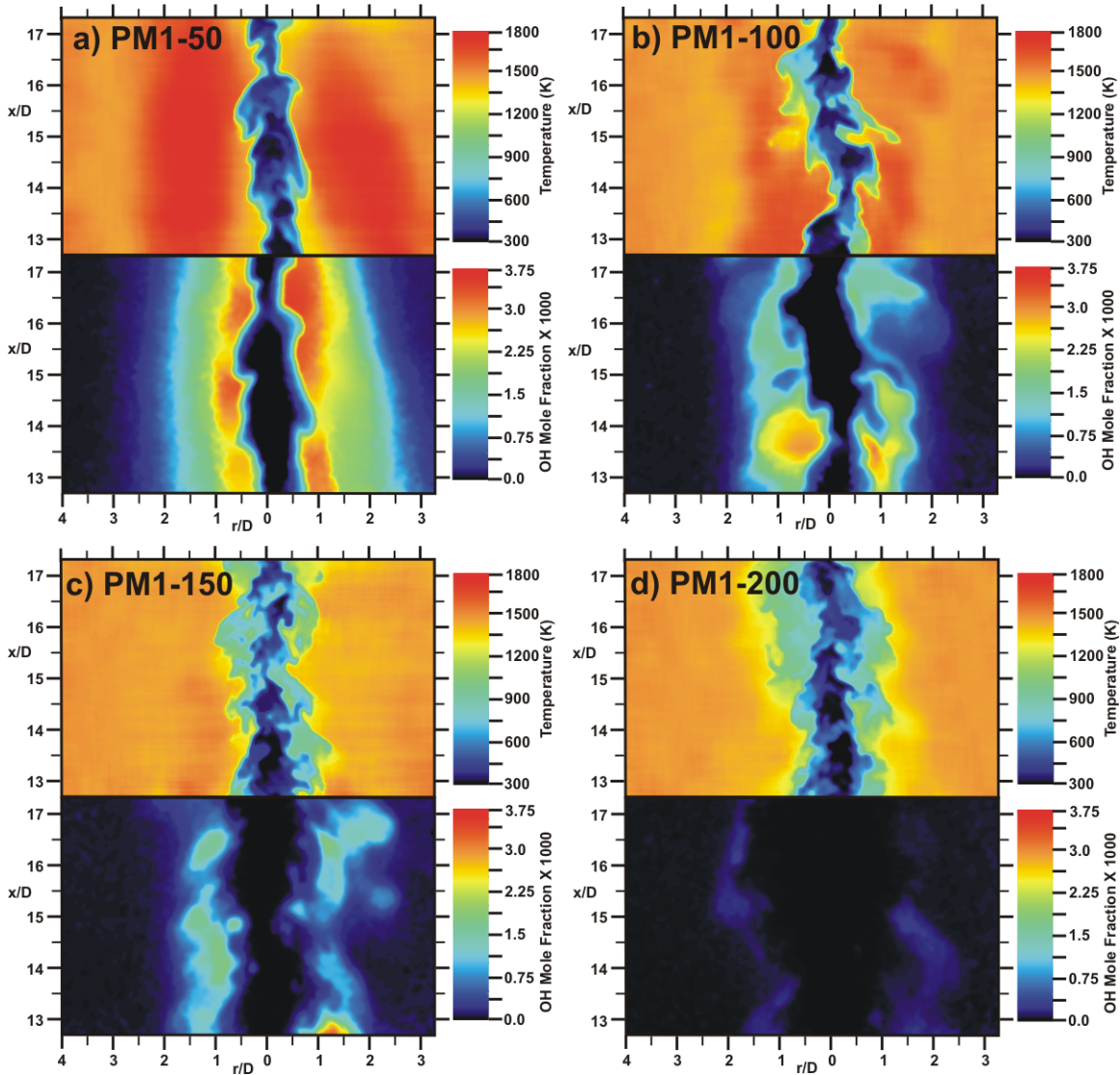


Fig. 5-4. Simultaneous temperature (top image) and OH mole fraction images (bottom image) centred at $x/D=15$ and $r/D=0$ for increasing central jet velocities. a) PM1-50, b) PM1-100, c) PM1-150, d) PM1-200.

A trend of progressive thickening of the thermal flame front for intermediate temperatures with increasing central jet velocities can be observed in Fig. 5-4a-d. This trend gives evidence that the increased turbulence intensity (Fig. 5-4a-d) increases the degree of thickening which is essentially the interaction of the turbulence with the

instantaneous reaction zone. The PM1-100 flame as seen from Fig. 3-2 and Fig. 3-3 in Chapter 3 is one of the transition flames (from regime B to regime C): this is well illustrated in Fig. 5-4b as the OH contour although correlating well with the thermal flame front, becomes non-uniform in thickness with peninsulas and pockets of partially reacted gas well into the OH layer appearing. As with the PM1-50 case, peninsula like structures of partially reacted gas do form in the PM1-100 flame. The orientation of these structures towards the fresh reactants is possible however, it is also apparent that peninsula like structures of partially reacted fluid can also be oriented towards the hot coflow. Flame PM1-150 as seen in Fig. 5-4c again has a highly distributed temperature field around the 500-1200K region. It is interesting to note that from the mean chemiluminescence image for the PM1-150 flame in Fig. 3-3C in Chapter 3 for the just above $x/D=15$ a reduction in luminosity is found, this corresponds well with the isolated patchy regions of OH found near $x/D=15$ in Fig. 5-5b indicating localised extinction is occurring. Flame PM1-200 around $x/D=15$ has virtually no flame luminescence indicating extinction, from Fig. 5-4d the extinction hypothesis at this axial location is well validated due to the very low levels and patchy distribution of OH. The thermal flame front in Fig. 5-4d shows some signs of turbulent mixing penetrating into the reaction layer (1300-1500K); as in many locations no sharp well-defined reaction or mixing layer can be defined.

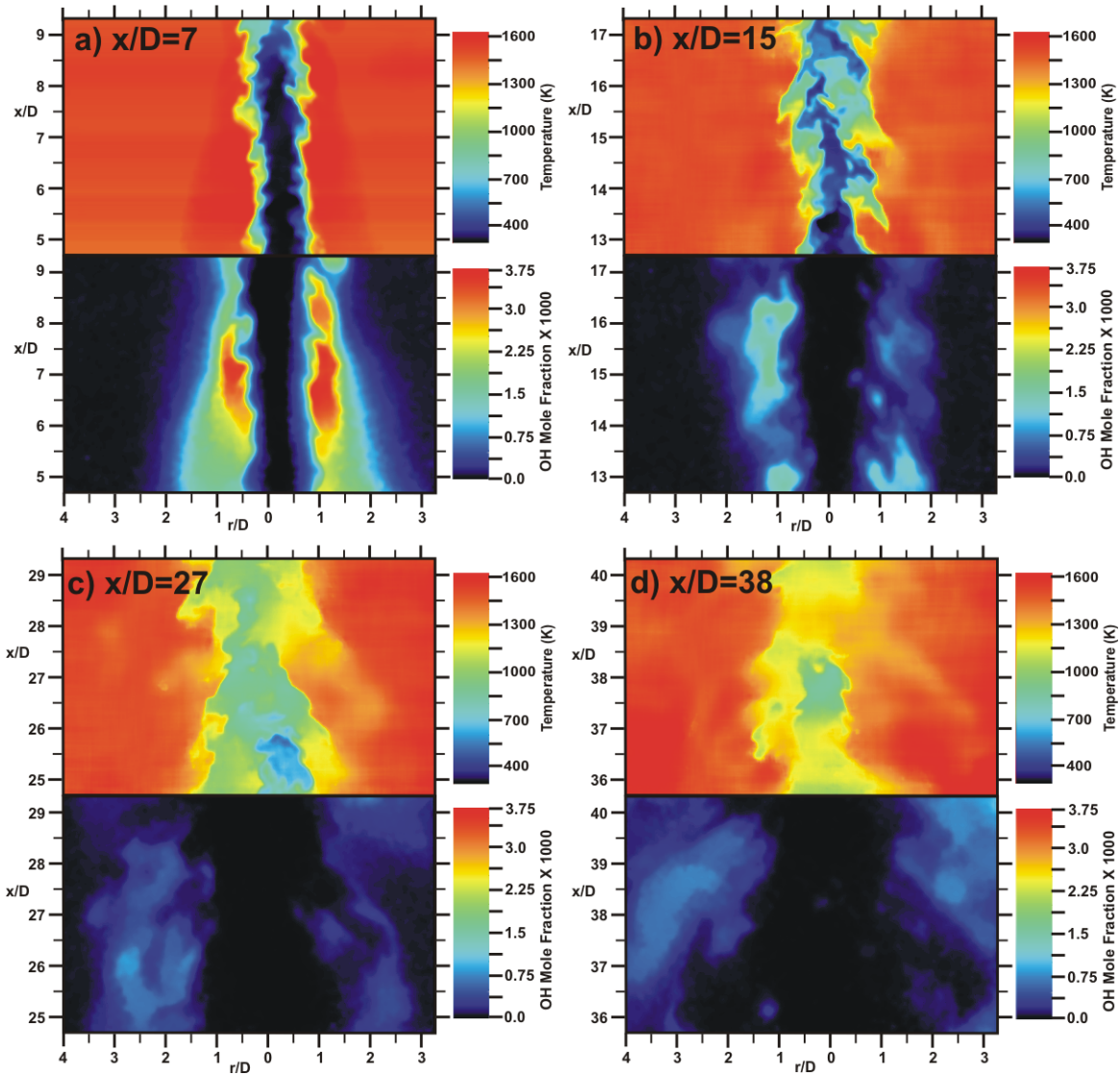


Fig. 5-5. Simultaneous temperature (top image) and OH mole fraction images (bottom image) at for flame PM1-150 (150 m/s central jet velocity) at four axial locations, centred at $r/D=0$. a) $x/D=7$, b) $x/D=15$, c) $x/D=27$, d) $x/D=38$. Note the temperature colour scale is different to the one used in Fig. 5-4.

In the stability diagram presented in Fig. 3-2 in Chapter 3, flame PM1-150 lies in region C where the occurrence of extinction and subsequent re-ignition is present. This flame is used here to illustrate how these phenomena are affected by the axial location along the length of the flame. In Fig. 5-5a-d four image pairs of simultaneous temperature and OH, collected at four axial locations centred at $x/D=7$, 15, 27 and 38 are presented for the PM1-150 flame. At $x/D=7$ in Fig. 5-5a, a radial layer of OH radicals due to the pilot

exists up to $x/D=7$; the beginnings of thinning and breakages in the OH layer start to occur around $x/D=8$ to 9. At $x/D=15$ in Fig. 5-5b, the same conclusions of extinction beginning to occur as those made for Fig. 5-4c hold, as these images are different realisations of identical flames and locations. At $x/D=25$ and 38, where a large reduction in flame luminosity has occurred and extinction is expected, both Fig. 5-5c and d show signs of extinction; low values of peak OH concentration occur at these locations, with up to a four-fold decrease when compared to the $x/D=7$ image. In both Fig. 5-5c and Fig. 5-5d the OH iso-contours do not correspond well with the temperature iso-contours, contrary to what is normally expected in a premixed flame. Apparent in this progression of images (Fig. 5-5a-d), are the decreased gradients of the thermal flame front as a function of downstream distance, displaying the regions in the flame of reduced conditional temperature gradients indicating a distributed flame front.

5.2 High Resolution Rayleigh OH PLIF Imaging

The primary aim of the large image region results presented in Section 5.1 is to obtain a qualitative understanding of the instantaneous flame structure in the PPJB. The experimental setup in Section 5.1 was not optimised for spatial resolution and SNR, but rather these effects were weighted with the desire for a large image region. In this section the requirement for a large image region is no longer a restraint since only a "sufficiently large" image region is required and the primary focus is to maximise spatial resolution and SNR for quantitative analysis of the results. Again as in Section 5.1, the Rayleigh-OH PLIF technique is used to examine the flame structure. Because of the effort to increase the spatial resolution and SNR of the measurements presented in this section (relative to the experimental results presented in Section 5.1) are the high resolution measurements of temperature and OH. Some of the material presented here has been presented by Dunn *et al.* [243]. The experimental setup and description is discussed in Section 5.2.1, in Section 5.2.2 the experimental data processing and accuracy are discussed. Selected imaging results are presented in Section 5.2.3 together with some statistical analysis of the results, a brief discussion is also presented. Further discussion of

the results in terms of further understanding the mechanisms of global finite-rate chemistry effects is left until Chapter 8.

5.2.1 Experimental Setup and Characterisation

There are significant synergies between the experimental setup presented in this section for the high resolution imaging experiment and the experimental setup presented for the large image region experiment in Section 5.1.1. There is however a number of modifications to almost each element of the experimental setup to improve the results. For this reason the experimental setup is again described with all of the improved or modified elements outlined. Again because of the synergies between the experimental setup in Section 5.1.1 there will be some repetition of the experimental description in this section.

An overview of the experimental setup for the high resolution imaging experiment is presented in Fig. 5-6 this includes the lasers, optical layout, and signal collection. The Rayleigh scattering signal was generated by the frequency doubled output of a pulsed Nd:YAG laser (Spectra Physics Pro 350) at 532nm, yielding 1.325J at the probe volume. The Rayleigh beam was focused by a 300mm focal length fused silica lens into a sheet 13mm high. The laser sheet thickness of the Rayleigh beam was measured by rotating the final cylindrical lens by 90 degrees and subsequently imaging the flat beam via Rayleigh scattering. Fitting a Gaussian function to the results at the focal plane resulted in a Full Width Half Maximum (FWHM) measurement of $80 \pm 12\mu\text{m}$ on the centreline of the image. This small beam waist was only possible by renewing the flash lamp in the oscillator and amplifier pump chambers and careful adjustment of the oscillator cavity mirrors.

The methodology of measuring the mean beam width using the 90 degree rotated beam imaging technique was checked by using the scanning knife edge technique [244, 245, 246]. Essentially the 532nm Rayleigh was attenuated using a Fresnel type attenuator

[235], as the 1.4J of energy at 532nm would quickly vaporise and damage the scanning knife edge if the full energy was utilised. Some degradation of the fidelity of the knife edge was still observed during the experiment, this degradation was balanced with the minimum amount of energy able to be measured by the power meter after the knife edge. Attenuating the energy of the beam by changing the Q-switch delay or flash lamp voltages was found to be undesirable as only at full power is the beam divergence minimised and pointing stability maximised. The knife edge scanning technique relies on the transform of the error function like scanning response to the true functional form. To do this an original functional form of a Gaussian or more generally a radially symmetric function must be assumed. The intensity distribution of the 2D laser sheet at the probe volume can neither be assumed to be Gaussian nor radially symmetric. It is possible to convert the scanning knife edge data to a mean intensity distribution without resorting to the Radon transform if an elliptically symmetric distribution is assumed and the following form of the inverse Abel transform presented in Eq. (5.2).

$$F(r) = \frac{1}{\pi} \int_r^{\infty} \frac{d^2 E(x)/dx^2}{\sqrt{x^2 - r^2}} dx \quad (5.2)$$

In Eq. (5.2), $F(r)$ represents a radially average intensity, r can be considered as an equivalent radially symmetric co-ordinate, $E(x)$ is the energy of intensity distribution from the knife edge scan along the x -axis. It is found that the transform derived by Eq. (5.2) is particularly sensitive to noise this has been previously noted in Abramson *et al.* [247]. To reduce the effects of noise a number of measures have been taken. The non-linearity and noise from the power meter after the knife edge was compensated for by a complementary measurement of the laser energy using a CCD camera measuring the resultant Rayleigh scattering and irradiance on a surface after the knife edge attenuation. Noise predominately introduced by the imprecise incrementing of the knife edge by fitting a smoothing function to the data points before inversion. After the analysis of the knife edge scanning the resultant beam thickness at the probe volume was determined to be approximately Gaussian with a FWHM of $92 \pm 16\mu\text{m}$. The larger value and uncertainty determined using knife edge scanning technique is deemed to be caused by

the inherent larger experimental noise of the knife edge scanning technique and the small additional beam divergence caused by the Fresnel like attenuation [235] of the beam.

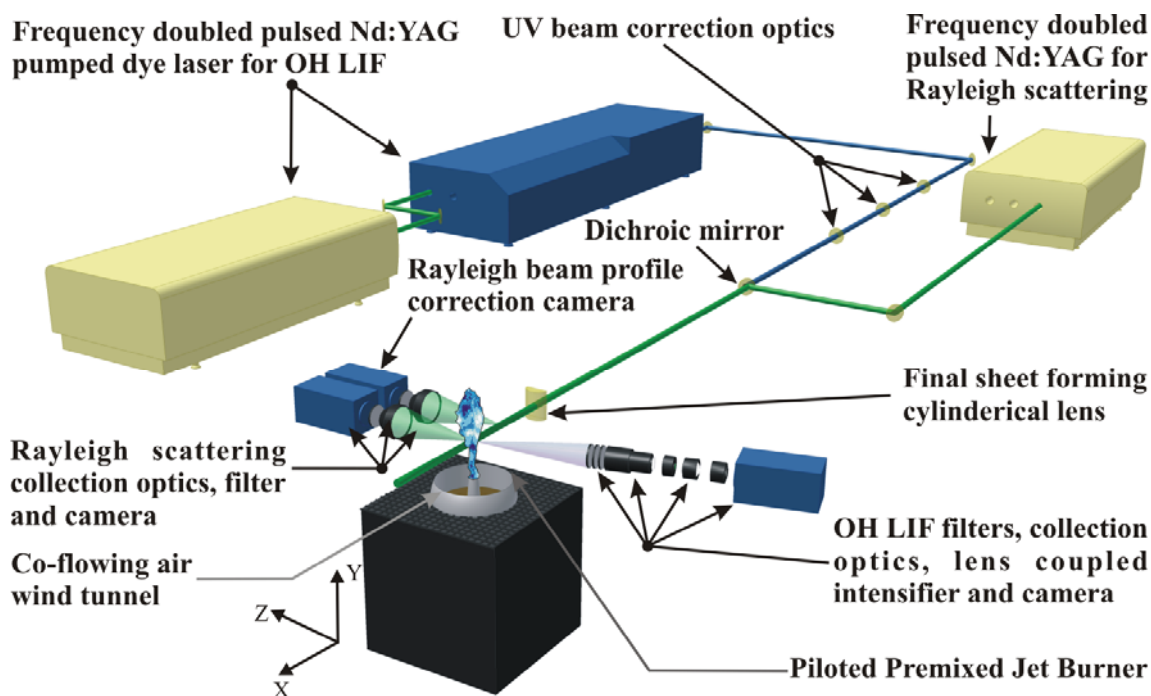


Fig. 5-6. An overview of the experimental setup for the high resolution imaging setup.

The OH LIF was generated by the frequency doubled output of a pulsed Nd:YAG laser (Spectra Physics Pro 350) pumping a Syrah dye laser using Rhodamine 6G in ethanol then subsequently doubling the output to produce an Ultra Violet (UV) laser beam at 283.01nm exciting predominately the $Q_1(6)$ band-head of OH for excitation of the excitation for the $A^2\Sigma^+-X^2\Pi(1,0)$ system. The $Q_1(6)$ band-head of OH is found to be advantageous in terms of signal levels for this experiment, although the integral overlap calculation is slightly more complex due to the overlapping $Q_2(1)$, $Q_{12}(3)$ and $Q_{12}(1)$ bands for the finite laser bandwidth. An enhanced beam profile capillary cell is used in the final amplifier of the dye laser; this addition enhances the beam profile and the pulse to pulse stability of the beam profile through the course of an experiment. The UV is spectrally isolated from the dye laser fundamental by use of a four Pellin-Broca prism unit.

The spatial profile of the UV beam after the exit of the dye laser was significantly improved by the use of a spatial modulator, which is essentially a Galilean beam expander with an iris at the focal point. The focal plane of the Galilean beam expander is essentially the Fourier transform of the spatial frequency of the laser beam, by placing an aperture at the focal point higher order modes of the beam are suppressed. By using a hard aperture in the form of an iris or pin hole it would be expected that some degree of ringing be introduced, to remedy this problem a soft apodising aperture in the form of a serrated aperture is typically used. It was found that it was not necessary to use a soft apodising aperture as there was no significant ringing present on the beam once it was refocused at the probe volume; this enabled the use of a much simpler aperture setup. The lack of any ringing effect was probably due to the fact that the beam was only weakly spatially filtered and the combination of diffraction and optical element aberrations convoluted any ringing effects, effectively smoothing the beam profile.

After the UV beam was expanded and passed through a spatial modulator to improve beam quality, a slight divergence was left on the UV beam to allow the focal length of the UV beam waist at the probe volume coincide with the 532nm beam waist. The UV beam waist thickness was measured by again rotating the final optic and imaging the LIF produced from acetone vapour, a value of $80 \pm 12\mu\text{m}$ was obtained. This measurement was again checked using the knife edge scanning technique and Gaussian function with a FWHM of $90 \pm 20\mu\text{m}$ was obtained. The energy of the 13mm high laser sheet at the probe volume was 20mJ with a line width of 0.15cm^{-1} in the UV.

The 532nm Rayleigh scattering signal was collected by an 85mm $f_{\#}1.4$ lens then passed through a 532nm 10nm FWHM interference filter, when combined with a 500ns camera gate, interferences from flame luminosity and OH LIF were eliminated. An un-intensified inter-line transfer Charge Coupled Device (CCD) camera (LaVision FlowMaster) was used for the Rayleigh signal. This camera has 1280 x 1024 pixels with individual pixel sizes of $6.7\mu\text{m} \times 6.7\mu\text{m}$ and a Quantum Efficiency (QE) of 36% at 532nm. On-chip

binning of 2x2 was utilised, yielding an effective probe volume to projected super-pixel pixel size of $34\mu\text{m}$. The Rayleigh imaging system Step Response Function (SRF) was measured using the scanning knife edge method outlined by Wang and Clemens [248] and references contained within. From the SRF the Line Spread Function (LSF) was calculated and a FWHM of $40\mu\text{m}$ was predicted. Utilising the analysis of Wang and Clemens [248] with the computed LSF resolution, dissipation structures with measured widths greater than $134\mu\text{m}$ an error contribution of less than 10% on the peak measured dissipation value can be attributed due to the finite spatial resolution of the imaging system. The single shot Signal to Noise Ratio (SNR) of the Rayleigh imaging system was found to be 40, measured in a uniform field of 300K air.

The OH LIF collection system is based on a lens coupled intensified CCD system. Interferences on OH LIF signal from Flame luminosity, 532nm and 283nm Rayleigh scattering was rejected totally by two 2mm thick UG11's and a 2mm thick WG305 Schott coloured glass filters combined with a $2\mu\text{s}$ intensifier gate time. A 105mm $f_{\#4.5}$ UV lens was coupled to an 18mm 2nd generation UV sensitive intensifier and subsequently lens coupled by two 50mm $f_{\#1.2}$ lenses to a CCD camera. The LSF for the OH collection system was found to be $127\mu\text{m}$ FWHM; this value of the LSF is much larger than the Rayleigh system due to the inclusion of the intensifier.

5.2.2 Data Processing

To determine the sensitivity of the Rayleigh cross section and OH quenching rate to composition and temperature variations freely propagating, opposed flow and mixing limit laminar flow simulations were conducted using the code of Goodwin [177]. It was found to be advantageous to cast these dependencies with respect to the normalised Rayleigh signal as opposed to temperature, as shown by Fig. 5-7 and Fig. 5-8. A maximum error of 3% is predicted for the Rayleigh cross section based on these calculations; however as can be seen from Fig. 5-7 the average error in cross section over

the entire temperature range is closer to 1%. The Rayleigh images were converted to temperature by assuming an ideal gas and applying the normalisation and background correction schemes developed in Dunn *et al.* [241].

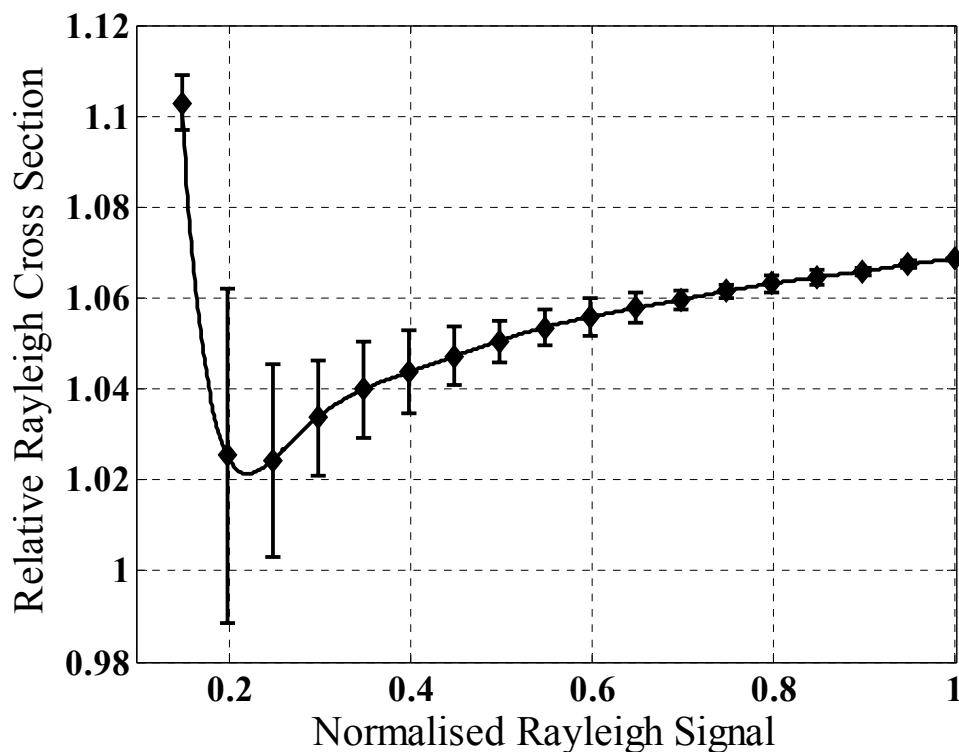


Fig. 5-7. Relative Rayleigh cross section vs. Rayleigh signal normalised by air for the PM1 flame series.

The OH LIF quenching rate variation with temperature and composition is shown in Fig. 5-8 however no error bars are shown for clarity due to the maximum error being less than 2%. The OH electronic and vibrational energy transfer rates and calculation method were taken from Dunn *et al.* [241] and references contained within.

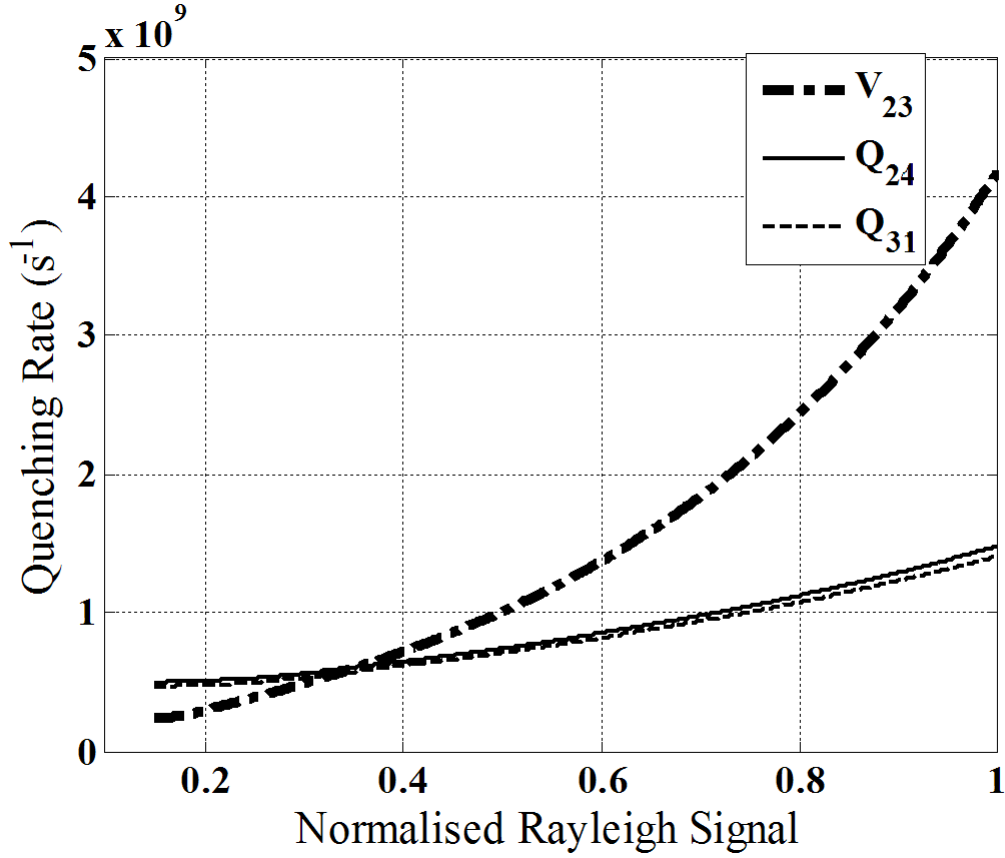


Fig. 5-8. OH quenching rates vs. Rayleigh signal normalised by air.

Due to the low OH mole fractions that occur in lean premixed combustion the OH LIF SNR can typically be very low if linear LIF and laser sheet thicknesses less than 250 μ m are employed. To obtain an acceptable SNR for the OH LIF we have employed non-linear OH LIF and further developed the quantification method presented by Dunn *et al.* [241]. Assuming a four level model and steady state the OH mole fraction may be expressed in terms of the collected fluorescence F_{OH} as:

$$X_{OH} = \eta \int_{-\infty}^{\infty} \int_0^{\infty} \frac{F_{OH} [\tau_1(T) + I_v^0(z,t) \tau_2(T,z,t)]}{I_v^0(z,t) \tau_3(T)} dz dt \quad (5.3)$$

The simplifying parameters in Eq.1 $\tau_1(T)$, $\tau_2(T)$, and $\tau_3(T)$ involve Einstein coefficients, and temperature dependant electronic and vibrational transfer rates. The Einstein A_{ji} , B_{ji} and B_{ij} coefficient values necessary for Eq. (5.3) were taken from LIFBASE [213]. Both the optical system efficiency η and the laser intensity matrix I_v^0 were determined from calibrations of various premixed flames on a premixed flat flame burner.

To investigate the effects of different image smoothing algorithms the computed temperature dissipation from a temperature image (PM1-150 at $x/D=10$ from Fig. 5-10) before and after the application of noise and filtering algorithm has been compared. The noise was added to the image in a similar distribution that occurs in single shot image data, taking the uniform field coflow SNR from 149 to 21. A number of filter kernel sizes and filter algorithms were trialled such as: Gaussian, adaptive Gaussian, anisotropic Gaussian and the anisotropic contour aligned algorithm presented by Dunn *et al.* [243]. The results for three illustrative filters are shown in Fig. 5-9, this figure shows how small kernel filters (5x5 Gaussian) preserve some high frequency information but do not remove enough noise at low dissipation values. Very large filter kernels (15x15 Gaussian) are effective in reducing noise for low dissipation areas, however the rise in error above 3200 (K/Pixel)^2 is due the smearing effect the large filter kernel has on high gradient structures. The anisotropic contour aligned algorithm is shown to give the best results out of all the algorithms tested. The results from Fig. 5-9 show that on average an error of 30% is introduced in measurements of temperature dissipation, for the particular structure length scales and amplitudes in the considered image. It should be considered that the corresponding mean error introduced into temperature gradient measurements using the anisotropic contour aligned algorithm is 5%, a much smaller error.

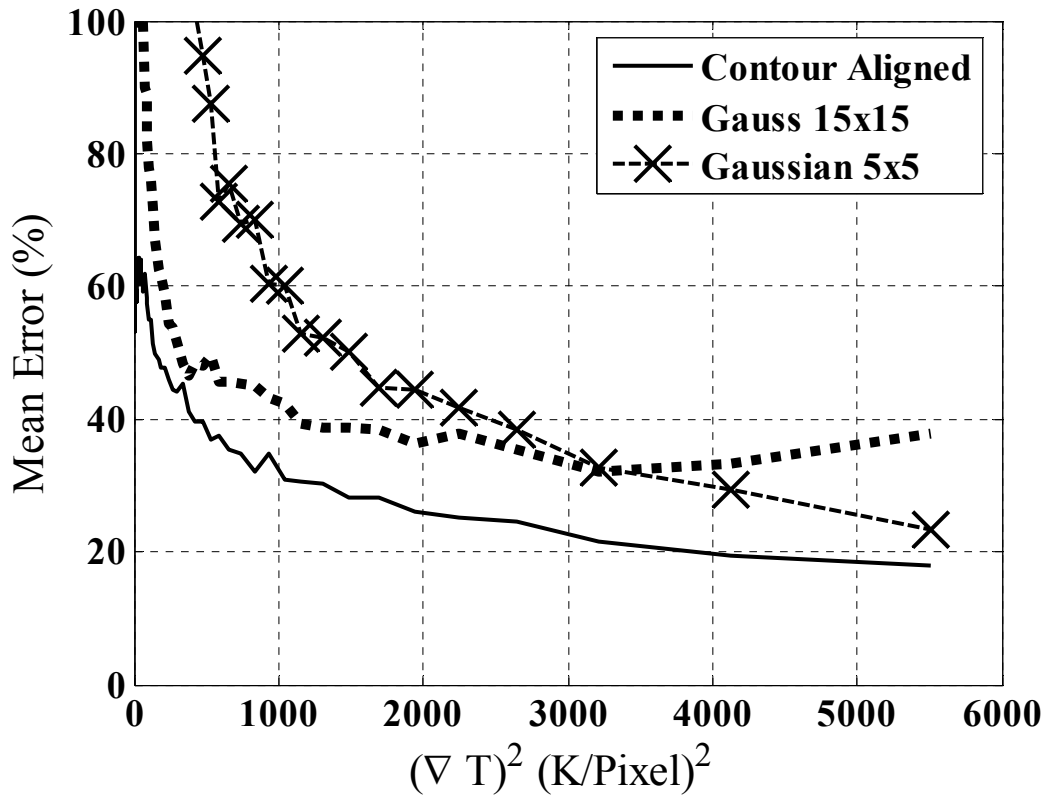


Fig. 5-9. Comparison of mean temperature dissipation error using three different image smoothing schemes.

5.2.3 Results and Discussion

This section shows sample results for an axial location of $x/D=10$ at jet velocities of 50, 100 and 150 m/s. Results for other axial locations in these flames are shown elsewhere by Dunn *et al.* [175, 243]. Simultaneous images of OH and temperature and the corresponding computed 2D temperature gradient image are shown in Fig. 5-10 for each of the central jet velocities investigated. For all of the images at $x/D=10$ the pilot has some degree of influence and as such the mechanics cannot be simply regarded as straining and mixing against combustion products that are similar to the central jet

composition. At $x/D=10$ we expect no significant extinction events such as those presented by Dunn *et al.* [175] at $x/D \geq 15$ for the PM1-150 and PM1-200 cases.

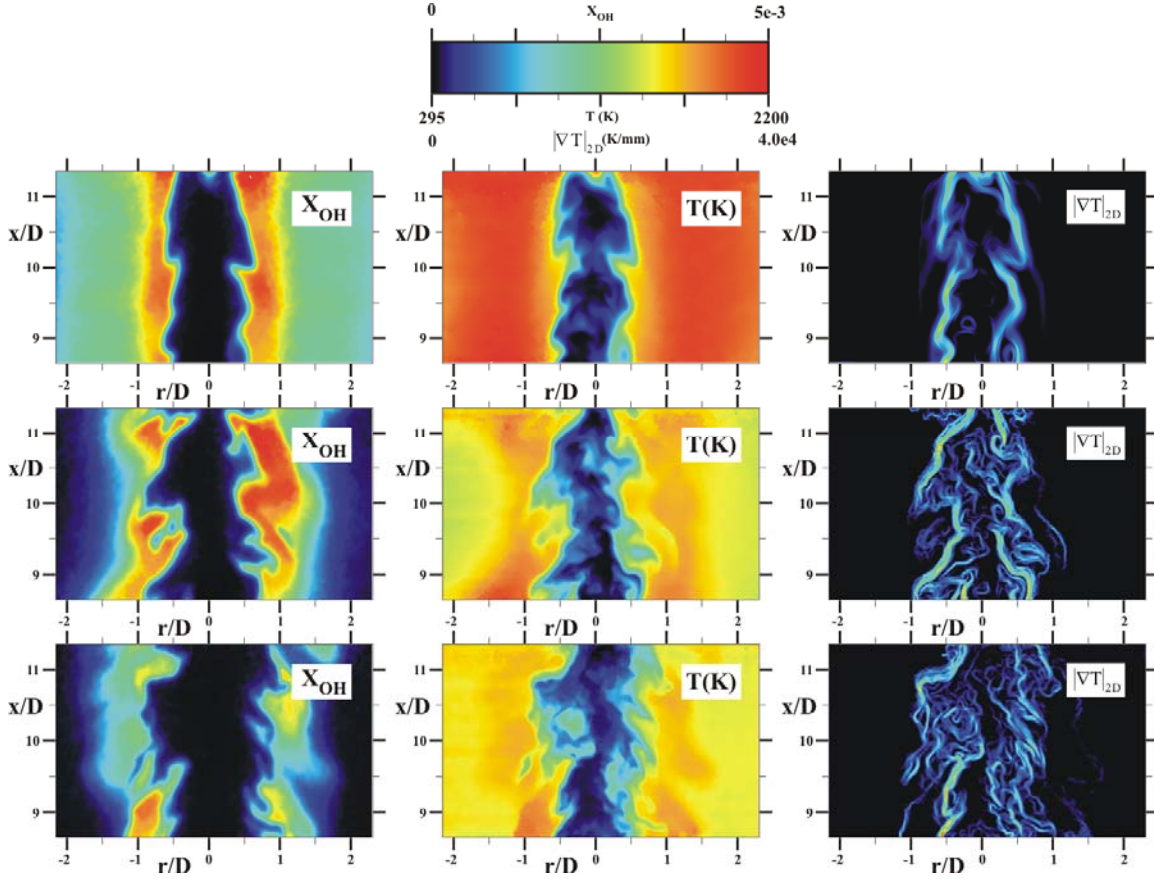


Fig. 5-10. Simultaneous imaging results of OH, temperature and $|\nabla T|_{2D}$ for PM1-50 (top row), PM1-100 (middle row) and PM1-150 (bottom row).

To illustrate the transition from a thin laminar like flame front to a thickened flame front, Fig. 5-11 shows the progression of the mean 2D temperature gradient conditional on temperature for increasing velocities. It should be noted that changes in the out of plane flame orientation PDF as a function of jet velocity could influence the results reported in Fig. 5-11 as they are based on a 2D measurement, this issue is addressed in Chapter 8 with 3D corrected gradient measurements, the results of these measurements are that any possible changes in the out of plane flame angle PDF as a function of central jet velocity

do not influence the relative comparison of 1D (or 2D) scalar gradients between flames in the PM1 flame series for a given fixed axial location. The trend of the conditional mean decreasing with increased central jet velocities is seemingly contradictory as to what would be expected from strained opposed flow simulation of unburnt vs. burnt reactants. In the laminar opposed flow geometry the trend of increasing temperature gradient with strain rate is qualitatively similar if either coflow products at 1500K or if pilot products at 2200K are applied. The reduction in mean temperature gradient with temperature is an indication that the premixed combustion regime is no longer flamelet like and is possibly an example of what has been conceptually described in the premixed combustion regime diagram as the thickened flame-front Dunn *et al.* [175], or distributed flame front regime.

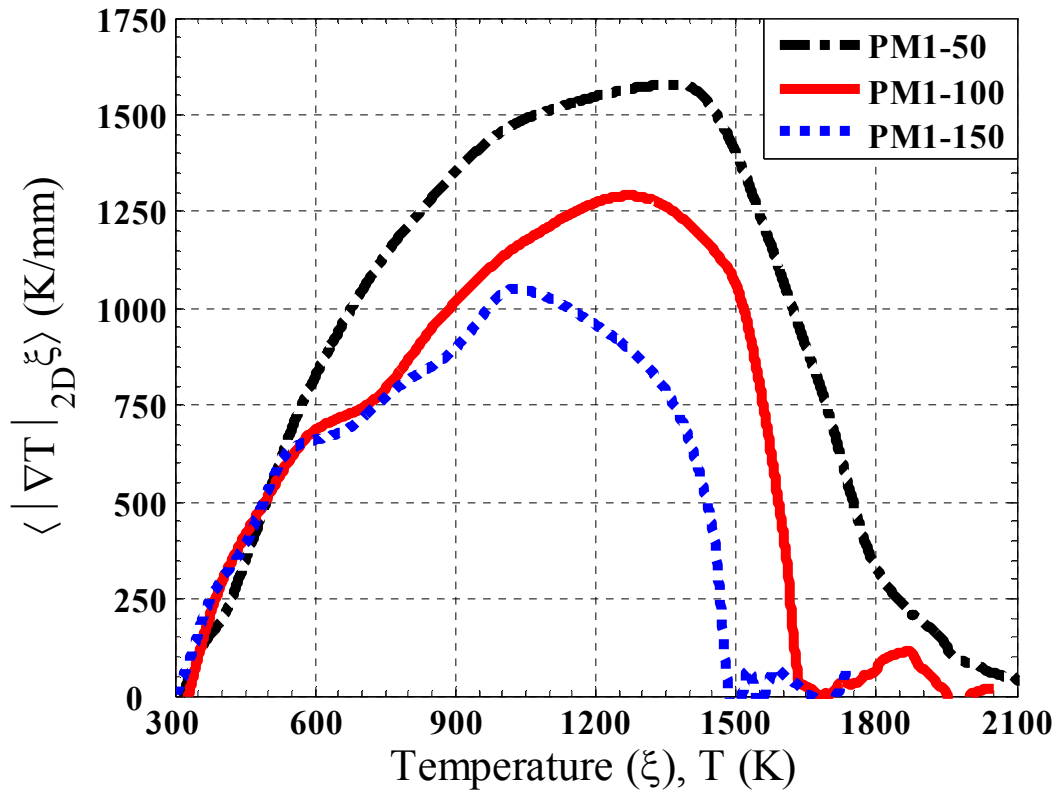


Fig. 5-11. Temperature gradient conditional on temperature for flames PM1-50, PM1-100 and PM1-150, data taken at $x/D=10$.

To contrast the trend found for conditional temperature gradient in the turbulent PM1 flame series reported in Fig. 5-11, a series of laminar flame simulation results are presented in Fig. 5-12. For the laminar simulations temperature gradient vs. temperature for freely propagating flames and opposed flow simulations of fresh central jet reactants vs. hot coflow products for a range of strain rates are examined. As expected from the laminar flame simulations reported in Fig. 5-12 for increasingly large strain rates the temperature gradient increases, this is in contrast to the trend of decreasing temperature gradient as a function of jet velocity found for the turbulent case reported in Fig. 5-11. Further graphs illustrating the structure of laminar opposed flow flames can be found in Appendix E of this thesis.

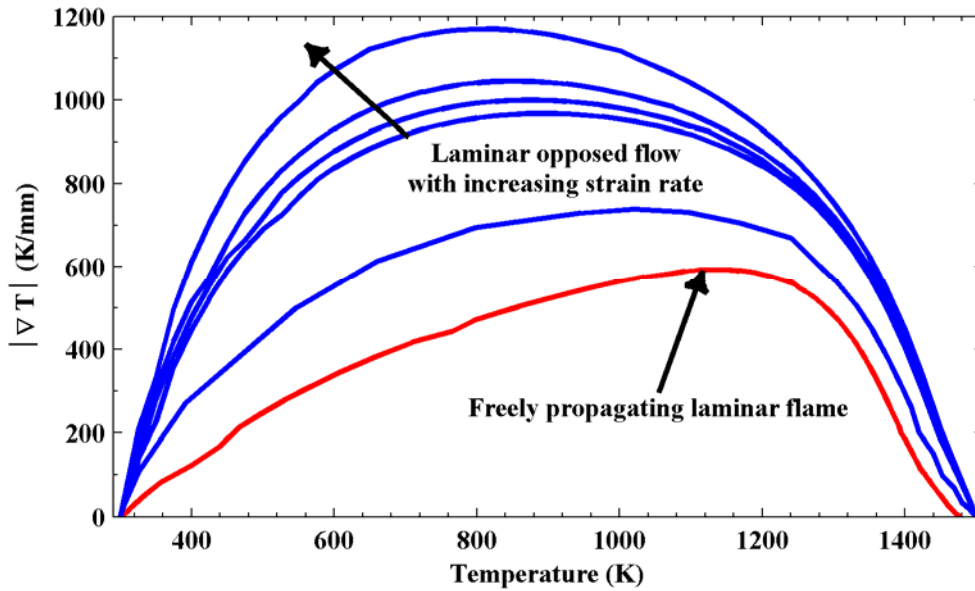


Fig. 5-12. Laminar flame temperature gradient vs. temperature data for freely propagating central jet reactants and opposed flow simulations of fresh central jet reactants vs. hot coflow products for a range of strain rates.

As reported by Dunn *et al.* [175] both the mean chemiluminescence images and simultaneous images of the PM1-150 flame exhibit an extinction region or reduced reaction rate region at around $x/D=15$. Although only images taken at $x/D=10$ are examined here, the PM1-150 data at $x/D=10$ should show some signs that extinction

further downstream is imminent. As OH was utilised as indicator of reaction rate by Dunn *et al.* [175], the mean OH concentration conditional on temperature in the temperature range 900-1500K is found to be reduced by up to 41% in Fig. 5-13 when compared to the values found in the PM1-50 and PM1-100 cases. For data presented in Fig. 5-13 at temperatures above 1500K the high OH concentration peak found in all of the flames is due predominately to the mixing and straining with the hot stoichiometric pilot combustion products that has high OH concentrations.

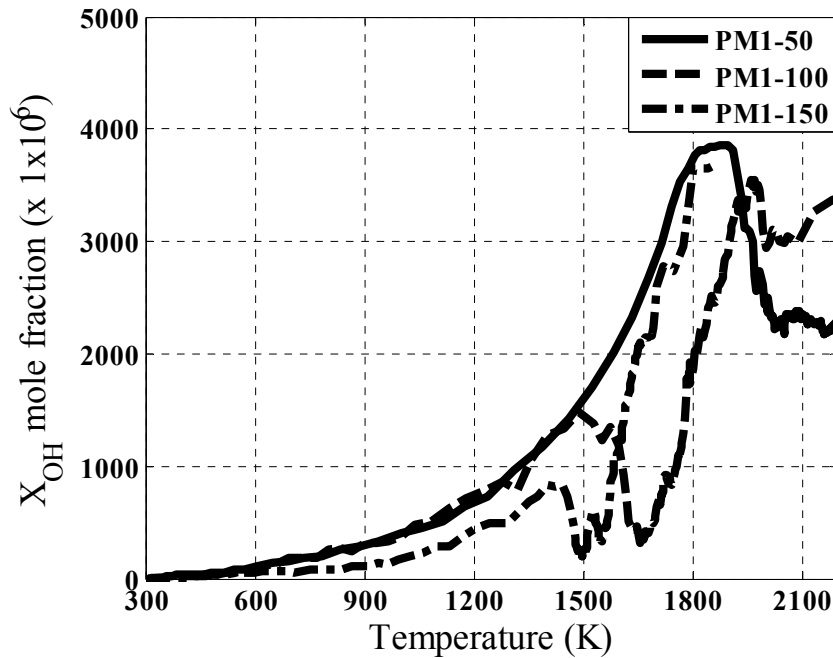


Fig. 5-13. Conditional mean X_{OH} for flames PM1-50, PM1-100 and PM1-150. The results presented here are data taken at $x/D=10$.

An examination of the mean OH mole fraction conditional on the local temperature gradient for the PM1 flame series is presented in Fig. 5-13. From Fig. 5-13 it can be generally claimed that with increasing central jet velocity, hence strain rate, that the conditional mean OH value will decrease. For temperature gradient values in the range 750-2250 (K/mm) it is found that the conditional mean OH value is relatively insensitive to variations in temperature gradient. It is found for the three flames that for high

temperature gradient values, the conditional mean OH levels increase. It is possible this is caused by the sharp interface between the high OH concentration pilot products straining against the fluid central jet fluid. Conditioning the temperature gradient on a specific value of temperature will confirm if this is a fluid mechanical straining effect or a genuine production mechanism for OH at high strain rates which would be highly unlikely.

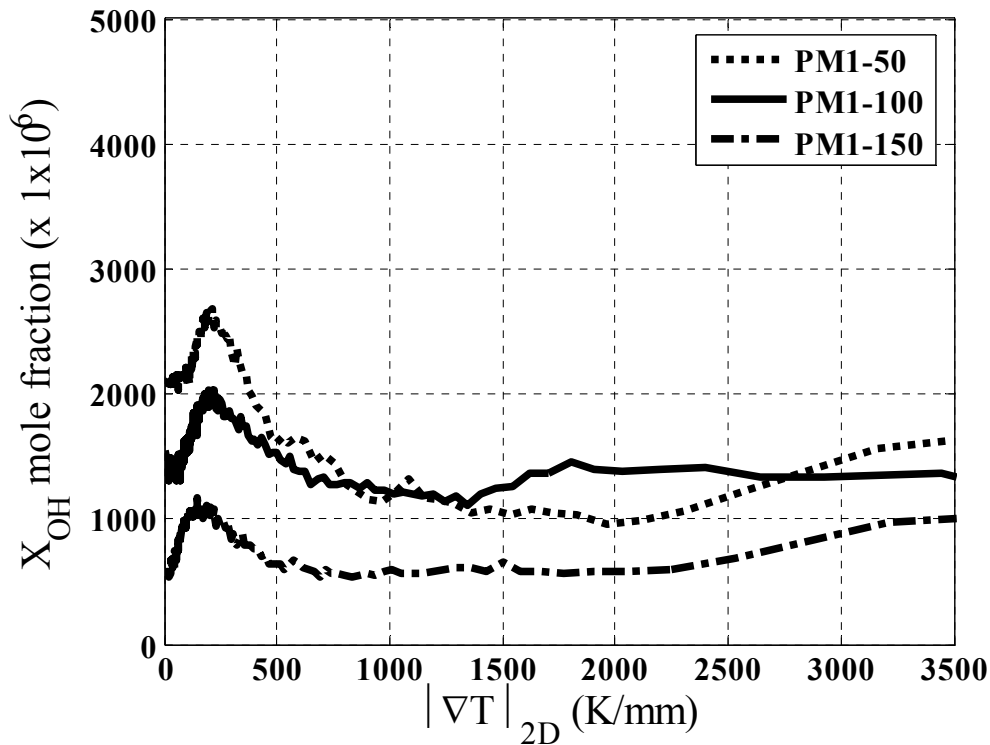


Fig. 5-14. Conditional mean X_{OH} conditioned on the local value of the 2D temperature gradient for flames PM1-50, PM1-100 and PM1-150. The results presented here are data taken at $x/D=10$.

It is found for the highly turbulent flames investigated a number of phenomena that are indications of the so called “distributed reaction zone regime”. Instantaneous imaging indicates a progressive broadening of the flame front with increasing jet velocity. The instantaneous images for the high velocity flames indicate the presence of eddies that are of the order of the inertial range embedded in the instantaneous flame front, this provides

insight into the flame broadening mechanism. To unambiguously define the flame structure, statistical measures based on the imaging results are examined. The mean temperature gradient conditional on temperature is shown to decrease with increasing strain rate, contrary as to what would be predicted by strained laminar flame simulations. For the highest velocity case examined, the mean OH conditional on temperature shows a decrease from the values found in the lower velocity cases and laminar flame simulations indicating a reduction in reaction rate is occurring.

In this section the laser diagnostic setup that enables high resolution Rayleigh scattering and OH LIF experiment with reliable statistics of the measured scalars (and their gradients) to be examined is reported. The limitation for the temperature gradient (and temperature dissipation) is found to be the post acquisition smoothing to remove the instrument and shot noise. A fundamental limitation of the OH LIF measurements is the poor MTF of the image intensifier which limits accurate joint statistics of temperature and OH in regions of high gradients and generally any examination of the OH gradient and dissipation.

5.3 Simultaneous Rayleigh, OH and CH₂O PLIF Imaging

The use of the simultaneous Rayleigh OH PLIF imaging technique in Sections 5.1 and 5.2 of this Chapter has provided valuable insights into the flame structure of the PPJB PM1 flame series. The local flame thickness and gradients has been examined using the temperature images, whilst the state of the local radical pool, hence an indication of the reaction rate has been estimated using the OH images. Whilst OH can be used as an approximate indicator of the local reaction rate, it is not possible to definitively correlate the local OH concentration to the local reaction rate or heat release rate if temperature is the only other scalar that is simultaneously measured.

In a study by Najm *et al.* [249] it was shown that the HCO correlates quite well with the local heat release in numerical simulation for a vortex flame interaction, HCO was also

measured experimentally in a perturbed laminar V-flame to measure the heat release layer however the HCO LIF signal is very weak with an SNR of 2 after phase averaging over 50 shots. This low SNR of HCO LIF signal relegates the measurement technique to laminar flows only and shows this particular implementation of the technique is clearly unsuitable for single shot images in turbulent flows. The CH_3O radical has also been examined by Najm *et al.* [250] however the CH_3O LIF signal was found to be of a similar level to HCO and CH_3O was found to be inferior to HCO as a reaction rate indicator which has a similar signal level. The CH radical has been proposed to be a flame front marker and possibly a reaction rate indicator by Nguyen and Paul [251] however Vagelopoulos and Frank [252] show that this assumption is highly dependent on the local flame composition and strain rate.

The work by Paul and Najm [253] has shown that by simultaneously imaging OH and formaldehyde (CH_2O) it is possible to use the product of the two species concentrations to obtain an indicator that is proportional to the local heat release rate and reaction rate. Paul and Najm [253] make the assumption that the raw LIF signals of OH and CH_2O once normalised for laser sheet energy variations are proportional to the concentrations of these two species and any error that is incurred by such an assumption is minimised by the fact that the two species only ever occur simultaneously within a very small temperature band, thus the influence of neglecting temperature dependant corrections such as the Boltzmann fraction and quenching variation will be minimised. The use of the product of OH and CH_2O is becoming a popular technique to examine the instantaneous heat release and reaction rate flame structure in premixed [254, 255, 256], partially-premixed [257, 258] and non-premixed combustion [55].

The simultaneous measurement of OH, CH_2O and temperature is reported in this section to examine finite-rate chemistry effects in the PM1 flame. One of the primary features of the PM1 flame series is the occurrence of an extinction region and re-ignition region for the PM1-150 and PM1-200 flames, this extinction and re-ignition region or variation in the reaction rate as a function of axial location is an ideal candidate to be studied using the reaction rate indicator OHxCH_2O technique examined in this section.

5.3.1 Experimental Setup

The experimental setup was primarily governed by the excitation scheme selected for the CH₂O LIF, therefore a brief discussion and justification of the selected scheme is explored below. There are numerous excitation strategies for CH₂O LIF that has been reported in literature, each of the particular schemes have particular advantages and disadvantages. One of the more popular excitation strategies is excitation via the 4_0^1 transition that occurs near 353nm, excitation is typically achieved with a tuneable XeF excimer laser [38, 254, 259] or a tuneable frequency doubled dye laser pumped by a frequency doubled Nd:YAG laser [255, 260]. This scheme features a relatively strong absorption cross section and good LIF yields as the transition is not predissociative, however PAH and other species such as C₂ may interfere with the resultant LIF signal. It is possible to estimate this degree of interference by tuning the laser off-resonance however the 4_0^1 absorption band is quite broad requiring tuning of several nanometres to avoid any possible CH₂O sideband absorption. For 353nm excitation depending on the laser energy, mixture composition and LIF filtering scheme certain Raman transitions (such as H₂) can interfere with resultant CH₂O LIF signal complicating the signal interpretation.

An alternative to 4_0^1 excitation is to excite the 4_0^3 transition with radiation near 339nm as demonstrated by Shin *et al.* [261], Paul and Najm [253] and also Schiebl *et al.* [262]. Although the absorption cross section for this transition is approximately an order of magnitude larger than the 4_0^1 absorption cross section at 353nm, the 4_0^3 transition is predissociative resulting in a LIF yield for the 4_0^3 transition that is comparable to 4_0^1 excitation at 353nm [253]. As the excitation wavelength for 4_0^3 excitation is blue shifted compared to 4_0^1 excitation, the degree of Raman interferences if present will be further minimised. Interferences due to PAH and other species such as C₂ are still present for

339nm excitation, detuning for 339nm excitation is simpler compared to 353nm excitation as the 4_0^3 absorption transition is spectrally much narrower than the 4_0^1 transition.

Excitation via 4_1^0 the transition using so called hot bands near 370nm has been shown to be possible by Luque *et al.* [263, 264] however the resultant absorption cross section and LIF yield are found to be approximately an order of magnitude smaller than 4_0^1 and 4_0^3 excitation. Potential Raman interferences will be exacerbated using 370nm excitation however potential interferences due to PAH and other species such as C_2 are likely to be minimised. The utility of the 4_1^0 excitation scheme is questionable in turbulent flames when other more favourable schemes are available, the 4_1^0 scheme seems to be of real value only if other species such as CH or CN are desired to be excited simultaneously with the same laser source as demonstrated by Bombach and Käppeli [265].

The 4_0^1 transition centred on 353nm has a very broad absorption band of approximately ± 2 nm. It is quite fortuitous that the output of a frequency tripled Nd:YAG at 28188.9 cm^{-1} overlaps with the sidebands of the 4_0^1 transition ($\tilde{A}^2A_1 \leftarrow \tilde{X}^1A_1, 4_0^1pQ$) of CH_2O . This excitation scheme for CH_2O LIF was examined in detail by Harrington and Smyth [260] and has been used as an excitation scheme in many subsequent investigations [266, 267, 268]. Excitation with frequency tripled Nd:YAG can be considered to be one of the most prevalent excitation schemes owing to the fact that a tuneable dye laser is not required.

In a review of CH_2O excitation using frequency tripled Nd:YAG by Brackmann *et al.* [269], some of the most important issues for 355nm excitation scheme are addressed. As the laser wavelength is essentially fixed it is not possible to tune the laser off the relevant transition enough with intracavity etalons or injection seeding to examine possible interferences due predominately to PAH and C_2 . As a compromise to this issue Brackmann *et al.* [269] and also Harrington and Smyth [260] propose that the resulting LIF from PAH will quickly saturate relative to the CH_2O LIF thus for the higher energy

required for 355nm excitation compared with the 353nm excitation, the resulting PAH LIF component of the signal should be much lower. As higher energies are typically employed for 355nm excitation compared to 353nm excitation, potential Raman interferences on the resulting LIF signal must be carefully monitored for 355nm excitation. For comparative purposes it has been found in a preliminary test in a laminar Bunsen flame that between two to four times (depending on the local flame temperature and composition) the energy at 355nm is required for a comparative CH₂O LIF yield compared to 353nm excitation.

For the CH₂O LIF experiments presented in this thesis a frequency tripled Nd:YAG has been exclusively selected as an excitation source. The selection of the excitation scheme for CH₂O LIF using a frequency tripled Nd:YAG is based primarily on the fact that the same laser source can be used for Rayleigh scattering to derive temperature. As noted above the use of 355nm excitation is favourable in terms of LIF yields and features no fundamental problems for lean premixed combustion environments. The use of a single laser as an excitation source for the measurement of two scalars is particularly advantageous in terms of simplifying the experimental setup and partially addressing the beam alignment issues that can occur in multi-beam experiments.

Two lasers and three cameras are utilised for the simultaneous measurement of OH, CH₂O and temperature, an overview of this experimental setup including the lasers, beam path and beam optics, the burner, collection optics and cameras is presented in Fig. 5-15. The output from an Nd:YAG (Spectra Physics Pro 350) is frequency tripled to produce 700mJ of energy per pulse at the probe volume at a wavelength of 354.85nm (this is referred to as the 355nm beam). This beam was used for both Rayleigh scattering and excitation for CH₂O PLIF. For excitation of OH PLIF (283nm beam) the standard approach of a frequency doubled Nd:YAG pumped dye laser is used. Further details of the Nd:YAG and dye laser setup for the OH excitation that is identical to that used here can be found in Section 5.2 and will not be repeated here. The two UV beams are overlapped using dichroic mirrors and focused at the probe volume using a 300mm focal length fused silica cylindrical lens. The 283nm beam is up-collimated after spatial

modulation so that the focal point coincides with that of the 355nm beam at the probe volume. Before and after each experiment the beam overlap of the 355nm and 283nm beams were checked using burn marks on photosensitive paper. The out of plane uncertainty in the alignment is estimated to be 30 μ m. The beam waists at the focal plane is measured using the scanning knife edge technique outlined in Section 5.2.1, Fresnel attenuation was necessary for the 355nm beam to prevent damage to the scanning edge. FWHM values of 80 μ m and 100 μ m are found for the 283nm and 355nm beams respectively.

A non-intensified inter-line transfer Charge Coupled Device (CCD) camera (LaVision FlowMaster) is used to record the Rayleigh signal. This camera has 1280 x 1024 pixels with individual pixel sizes of 6.7 μ m x 6.7 μ m and a Quantum Efficiency (QE) of 48% at 355nm. On-chip binning of 2x2 is utilised, yielding an effective probe volume to projected super-pixel pixel size of 32 μ m. Commercial camera lenses feature anti-reflection coating that absorb very strongly at wavelengths below 400nm, for this reason it is not possible to collect the Rayleigh signal with a low $f_{\#}$ commercial camera lens as is done for the experiments reported in Sections 5.1 and 5.2 of this Chapter. A 105mm f/4.5 UV lens is used to collect the Rayleigh scattering signal at 355nm. Flame luminosity and any CH₂O LIF signal is rejected by use of a 500ns gate time and a 1mm black glass coloured filter (Schott glass UG11). Tests for a range of laminar flames indicate that OH LIF does not interfere on the Rayleigh camera, this is probably due to the weak OH LIF signal relative to the 355nm Rayleigh signal and the sharp spectral drop off in quantum efficiency of the camera that occurs after 340nm, ($\eta@310\text{nm}=12\%$).

The OH LIF collection system is based on a lens coupled intensified CCD system. Flame luminosity, 355nm and 283nm Rayleigh scattering is rejected using a 310nm centre wavelength interference filter 10nm bandwidth combined with a 2 μ s gate time. A 105mm f/4.5 UV lens is coupled to an 18mm 2nd generation UV sensitive intensifier and subsequently lens coupled by two 50mm f/1.2 lenses to a CCD camera. It should be noted that the through-put of this system for the OH LIF is significantly lower than the configurations reported in Section 5.1 and 5.2 of this Chapter for the OH PLIF. This

lower efficiency of the OH system is almost exclusively because of the low transmissivity of the interference filter compared to coloured glass filtering scheme used in Section 5.2.

The CH₂O LIF signal is recorded using a lens coupled intensified CCD system. The CH₂O LIF signal is collected with an 85mm focal length f/1.4 visible camera lens. This camera lens has a visible anti reflection coating that strongly absorbs UV light at wavelengths below 400nm such as 355nm Rayleigh. Additional rejection of UV light is afforded by a 400nm high pass filter. As only lean premixed flames are examined, interference issues such as PAH and C₂ LIF that complicate the CH₂O LIF signal in non-premixed are not present. Interferences due to CH₄, N₂, H₂O and H₂ Raman are possible due to the high 355nm energies used in this experiment. Raman scattering from N₂ (2330cm⁻¹) in a pure N₂ cold flow is found to be negligible even without the 400nm high pass filter. To reject CH₄ Raman scattering (2915, 3017cm⁻¹) in a pure CH₄ cold flow it is found the 400nm band pass filter was necessary to completely reject this signal. Raman scattering from H₂O (3657cm⁻¹) and H₂ (4160cm⁻¹) is possible to not be completely rejected using the presented filtering scheme. The peak mass fraction of H₂ in the premixed methane-air flames examined is expected to be less than 0.1% therefore H₂ does not occur in sufficient concentrations to cause an interference problem. By imaging the post flame gases of a stoichiometric methane-air on a flat flame calibration burner it is found that the combination of any miscellaneous interference combined with possible H₂O Raman interference is negligible. By gating the CH₂O intensifier for 500ns flame luminosity is rejected totally from the LIF signal.

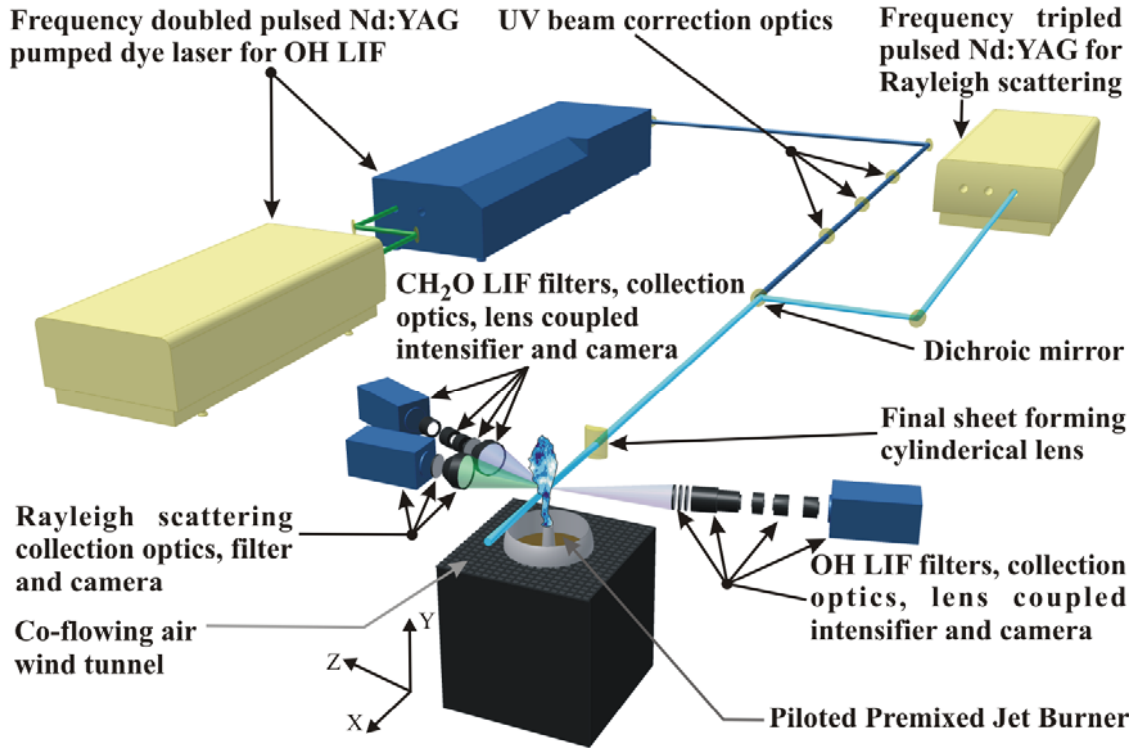


Fig. 5-15. An overview of the experimental setup showing lasers, beam paths, beam optics, burner, signal collection optics and cameras used for the simultaneous imaging of temperature, OH and CH_2O .

Even though the experimental resolution in terms of pixel size ($20\mu\text{m}$) and beam thickness ($<100\mu\text{m}$) is quite good, the limiting resolution factors are the low SNR of the images and the poor MTF of the CH_2O and OH intensifiers. Quantification of resolution degradation due to noise is very difficult to quantify, however a conservative estimate for the spatial resolution is $250\mu\text{m}$.

5.3.2 Data Processing

The three cameras were spatially matched by imaging a calibration grid placed at the laser sheet focal plane, using a PIV like algorithm the image sizes and distortions were corrected typically to sub-pixel accuracy. The accuracy of this mapping technique was tested using Mie scattering from the dust in air with the relevant camera filters removed

and applying a sub-pixel accuracy PIV algorithm to the data once calibrated with the grid, typically the mapping was accurate to within one pixel, with a maximum error of 2.8 pixels.

The data processing and quantification methodology for the Rayleigh and the OH PLIF signals to obtain temperature and the OH mole fraction follows identically from the method presented in Section 5.2 of this Chapter and is not repeated here. The processing and quantification of the CH₂O PLIF signal has not been previously discussed and will be explored below.

The correction of the CH₂O LIF signal to yield CH₂O concentrations involves three primary corrections: partition function correction, quenching correction and laser energy correction. The correction for the variation of the partition function of CH₂O as a function of temperature follows standard detailed balance principles; however definition of the energy levels is somewhat more complicated than standard diatomic molecules. CH₂O is a polyatomic molecule that has many overlapping rovibrational bands at atmospheric pressures and non-cryogenic temperatures. To determine the rotational level energy two rotational quantum numbers are required ($J=15$ and $K=5$). Kyritsis *et al.* [267] show that for 355nm excitation the vibrational and rotational partition functions may be expressed by Eq. (5.4) and Eq. (5.5) respectively.

$$f_v = 1 - \exp(-1680.5/T) \quad (5.4)$$

$$f_R = \frac{40.2 \exp(-740/T)}{(1 + 0.134/T + 0.037/T^2) T^{3/2}} \quad (5.5)$$

The correction of CH₂O due to quenching is difficult as species and temperature dependant cross sections do not exist for CH₂O. Paul and Najm [253] suggest a general $T^{-0.5}$ dependence on quenching, this method is partially validated by Kyritsis *et al.* [267], the general $T^{-0.5}$ quenching dependence is assumed for this study.

For the very high irradiance levels used in this study it is found that the CH₂O LIF is partially saturated or at least not in the linear LIF regime. A general non-linear two level LIF model is assumed to be valid for CH₂O which is given by Eq. (5.6).

$$F_{CH_2O} = \frac{n_{CH_2O} C_1 I_v^0 A_{21}}{I_v^0 f_v f_R C_2 + A_{21} + Q_{21}} \quad (5.6)$$

In Eq. (5.6) C_1 and C_2 are experimentally determined calibration coefficients. Eq. (5.6) allows the inclusion of both quenching and partition function corrections to be included in the correction frame work. The calibration of the CH₂O PLIF signal is achieved using two methods. Firstly, a flat field of CH₂O is used to determine I_v^0 , this flat field was created by flowing air through a heated sample of paraformaldehyde then flowing this mixture through a cold flow calibration burner. Absolute values were calibrated using a laminar Bunsen flame with known CH₂O concentrations from laminar flame calculations.

5.3.3 Results and Discussion

The imaging results for simultaneously measured CH₂O, OH, temperature and OHxCH₂O, a reaction rate indicator is examined in this section. It is of specific interest to examine the instantaneous flame structure for flames that exhibit strong finite-rate chemistry effects using this measurement technique, therefore images of only the PM1-150 flame are examined. Similar results and image trends to PM1-150 flame are found for the PM1-200 flame which also features strong finite-rate chemistry effects but example images the PM1-200 flame are not presented here. The statistical analysis of the results from the imaging experiments reported in this section for the entire PM1 flame series is examined in Chapter 8.

The primary focus of this section is the presentation of PM1-150 flame images for a series of axial locations shown in Fig. 5-16 and in Fig. 5-17. The range of axial locations is large enough to cover the initial ignition region ($x/D=5$) through to the extinction region ($x/D=30$) then to the re-ignition region ($x/D=60$). The selected image realisations for each location have been selected at random to avoid investigator bias, generally the presented images can be considered to be representative of the features, structures and concentrations of other image realisations at the same location.

As Rayleigh scattering is a resonant technique it is susceptible to interferences due to scattering and reflections from solid surfaces. For the images taken at $x/D=5$ it was not possible to adequately correct the Rayleigh image for reflections from the burner, as such the temperature image in Fig. 5-16 for $x/D=5$ has been cropped to a larger extent than Rayleigh images at other axial locations. The CH_2O and OH PLIF images at $x/D=5$ do not suffer from this issue as they are relatively immune to reflection issues due to the LIF process being a non-resonant process.

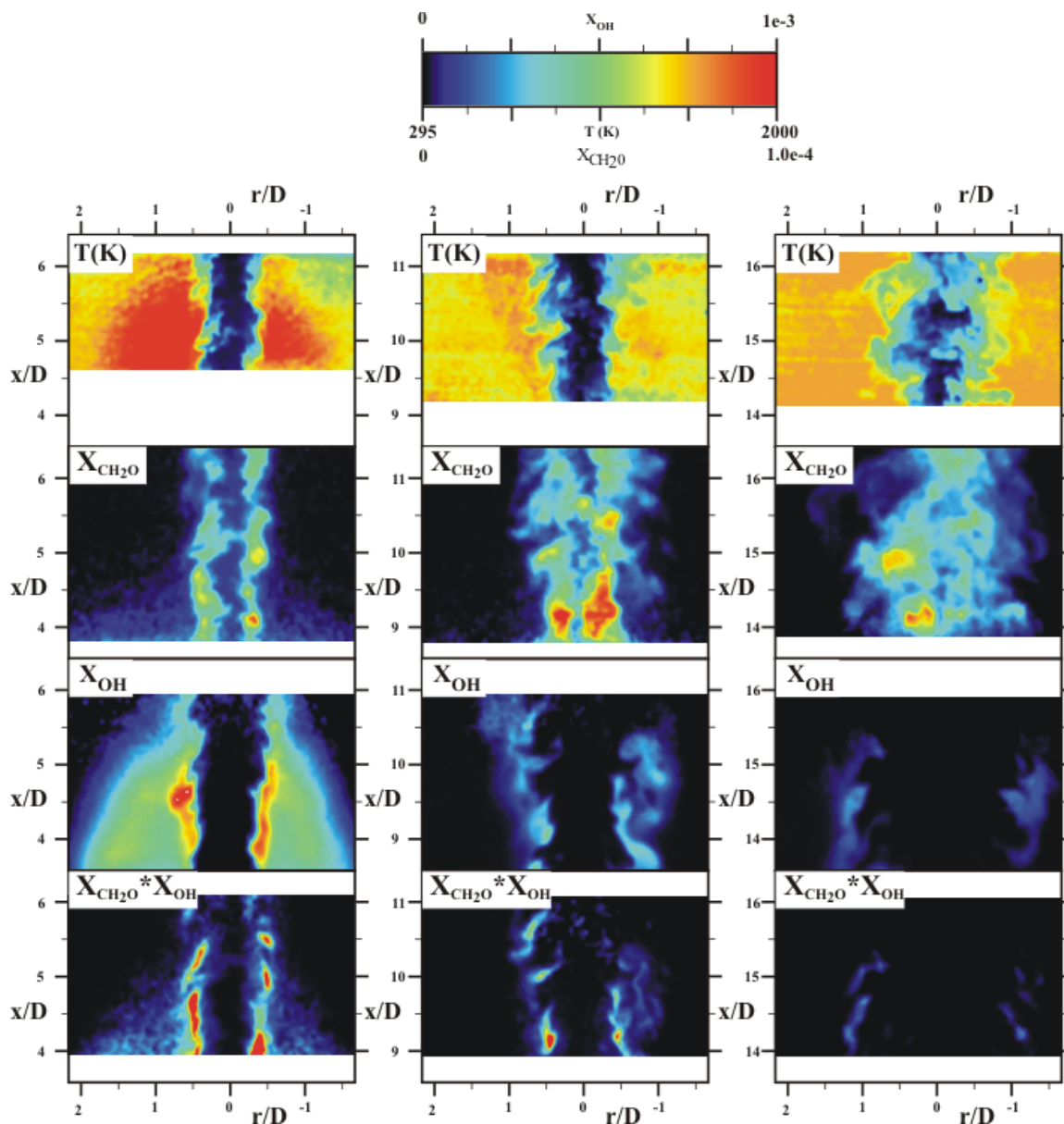


Fig. 5-16. Randomly selected instantaneous imaging of temperature, CH_2O , OH and the reaction rate indicator $\text{CH}_2\text{O} \cdot \text{OH}$ for the PM1-150 flame at $x/D=5$ (left column), 10 (middle column) and 15 (right column).

In Fig. 5-16 for $x/D=5$ the shrouding effect of the stoichiometric pilot is apparent in the OH image by the large region of high OH levels surrounding the central jet up to $x/D=5.5$ and in the temperature image by the high $\sim 2000\text{K}$ region surrounding the central jet. It can be seen from the temperature image that even very early on at $x/D=5$ that the flame structure is not thin and step like, it can be seen that corresponding to the regions of

partially reacted fluid in the temperature image CH_2O exists in two thickened vertical bands following the flame front. It is apparent that very early on for the PM1-150 flame that reaction zone is not a continuous structure of uniform high reaction rate, breakages and patchiness in the reaction layer is beginning to be apparent even at $x/D > 5$.

At locations further downstream ($x/D=10$ and 15) it is apparent from the images in Fig. 5-16 that as expected evidence of extinction becomes apparent. The magnitude of the reaction rate in the reaction layer is decreased by almost an order of magnitude at $x/D=15$ compared with values found at $x/D=5$. This quantitatively proves that the global reaction rate has decreased at this location, confirming that extinction or a reduced reaction rate is occurring, this finding confirms the initial hypothesis of the extinction region beginning around $x/D = 15$ based on the mean chemiluminescence images.

Progressing from $x/D=5$ to 10 then to 15 the generalised observation can be made that the instantaneous flame front based on the temperature image broadens as a function of increasing axial location. This flame broadening process creates large regions of intermediate temperatures in the flame front, although this feature has already been found with the Rayleigh OH imaging earlier in this Chapter it is interesting to examine the CH_2O concentrations at these locations and intermediate temperatures. It is found that the CH_2O concentration in these intermediate regions is very high and the structure of the CH_2O field is more akin to being described as a well stirred reactor than the thin CH_2O structure expected for typical turbulent premixed flames. The breakdown of the thin CH_2O layer structure in the reaction zone for laminar and low turbulence premixed flames to a thickened CH_2O layer in the reaction zone has also been reported by Böckle *et al.* [254]. The degree of thickening of the CH_2O layer was not as large as that found here as much lower turbulence intensities are examined by Böckle *et al.* [254], yet the turbulence intensity was sufficiently high for turbulent eddies to penetrate and stir the preheat zone in their flame.

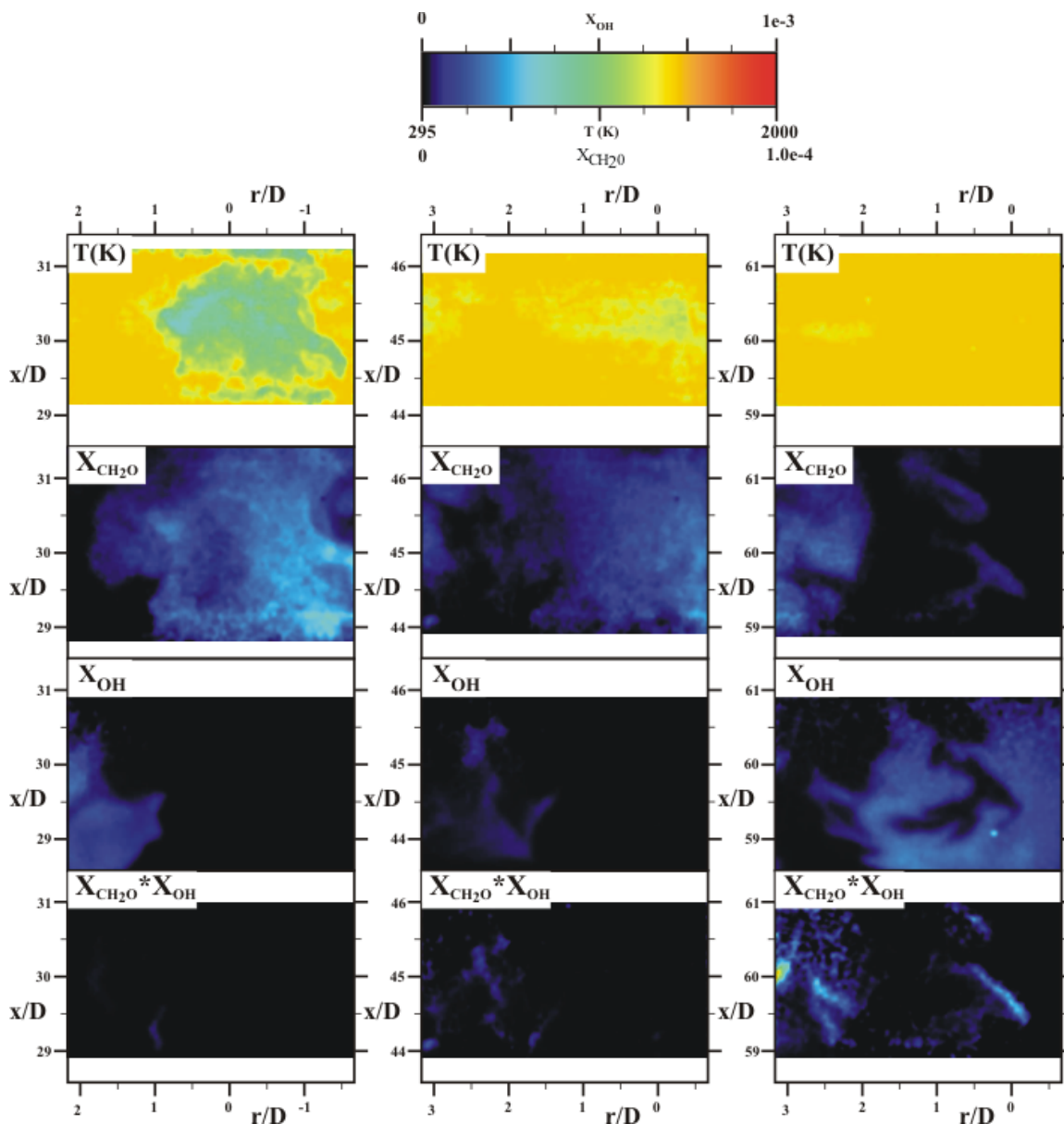


Fig. 5-17. Randomly selected instantaneous imaging of temperature, CH_2O , OH and the reaction rate indicator $\text{CH}_2\text{O}^*\text{OH}$ for the PM1-150 flame at $x/D=30$ (left column), 45 (middle column) and 60 (right column).

Further downstream at $x/D=30$, 45 and 60 shown in Fig. 5-17 the progression from the extinction region to the re-ignition region is established. At $x/D=30$ the reaction rates remain very low and the CH_2O occurs in large patches that are almost uniform in concentration. At $x/D=45$ a small increase in the reaction rates are found over $x/D=30$ which is typically of the order of 30%. Further downstream at $x/D=60$ higher reaction

rates are found, combined with higher OH concentrations. Generally the reaction rates at $x/D=60$ are found to be high in thin stripes at temperatures that are very close to the coflow temperature. It is interesting to note that in the re-ignition region the regions of high reaction rate occur essentially at constant temperatures or at least at temperatures very close to those expected at reaction completion.

A difficult but interesting question arises when examining the images presented in this section and other images (e.g. Rayleigh OH in Sections 5.1 and 5.2 in this Chapter) is: What is the mechanism for the re-ignition region? Addressing this question quantitatively based on the available experimental data is not possible; however a couple of observations and possible hypothesis are worth outlining.

It is known that the propensity for auto-ignition increases in regions of lean equivalence ratios with low scalar dissipation rates. Large amounts of hot coflow fluid (for experimental proof see Chapter 6) are mixed with the central jet reactants before the re-ignition region, ensuring the mixture to be diluted and above the critical temperature of 1300K so that chain branching reactions can dominate and produce a cascade effect (auto-ignition). Also it has been shown by the velocity measurements and confirmed by the low gradients in the temperature images that the local scalar dissipation rate is expected to be small which favours auto-ignition.

If auto-ignition is the dominant mechanism for the re-ignition region then it would be expected that small kernels of high OH concentration would be found before the re-ignition region, further downstream the small OH kernels would grow to become part of the reaction zone in the re-ignition region. These tell tale patches of high OH concentration are however not found. The images reveal that large patches of OH gradually increasing in OH concentration as they move through the re-ignition region. Although not based on imaging evidence it is found experimentally that there is no audible popping or audible transition of the flame from the PM1-50 to the PM1-200 flames. Such an audible transition occurs for the progression from seated flames to auto-igniting flames in the Cabra burner flame series.

By studying numerous realisations a common trend can be found in the axial progression from the extinction region to the re-ignition region. The driving factor that increase the reaction rate indicator $\text{OH} \times \text{CH}_2\text{O}$ is the fact that the peak OH and CH_2O layer become closer as a function of axial distance past $x/D=30$. Essentially, similar OH and CH_2O levels are found at $x/D=30$ and $x/D=45$ however these two layer have moved closer together allowing the reaction rate to increase. Based on this observation it is hypothesised that the re-ignition region is caused by the axial decay in the strain rates allowing regular premixed flame oxidisation to continue as opposed to an auto-ignition process.

Through the use of the CH_2O , OH and Rayleigh imaging technique the instantaneous flame structure of the PM1-150 flame has been examined in detail for a large range of axial locations. It has been shown that by use of the reaction rate indicator $\text{OH} \times \text{CH}_2\text{O}$ a description of the flame reaction rate as a function of axial location is able to be constructed that compares favourably with previous findings using the mean chemiluminescence images and Rayleigh OH images to confirm the existence of an extinction region and a re-ignition region.

Generally all of the images reported in this section feature a much lower SNR compared to images presented in the other sections of this Chapter. The simultaneous measurement of OH and CH_2O is typically a very demanding measurement even in non-premixed combustion where CH_2O can be in high concentrations. For the lean premixed PM1 flames in PPJB CH_2O and OH concentrations are very low relative to non-premixed flames placing further difficulties in obtaining quality measurements. The measurement of CH_2O is typically the source of the largest error and noise, however in this study the SNR of the CH_2O LIF has been made acceptable by using very high excitation energies. Further optimisation and improvement of the results could be obtained by producing OH PLIF images that are of the same quality as those presented in Section 5.2. This would be possible if the interference filter were replaced with the coloured glass filters used in

Section 5.2, however to reject 355nm scattered light an intensifier with a gate time less than 100ns would be required.

CHAPTER 6 PPJB RAMAN-RAYLEIGH-LIF RESULTS

The line Raman-Rayleigh-LIF experimental technique is used to investigate a number of flames stabilised in the PPJB. The line Raman-Rayleigh-LIF experimental results reported in this Chapter were conducted in collaboration with Dr R. S. Barlow in the Turbulent Combustion Laboratory (TCL) at the Combustion Research Facility (CRF), Sandia National Laboratories (SNL), CA. The data acquired at SNL is referred to as the "Sandia measurements" or the "line Raman-Rayleigh-LIF measurements" where appropriate in this Chapter and more generally in this thesis.

The line Raman-Rayleigh-LIF technique in the implementation reported here allows the simultaneous measurement of all major species and temperature combined with simultaneous CO via two-photon laser-induced fluorescence and OH via crossed-plane planar laser-induced fluorescence (PLIF). Using the cross-plane OH PLIF, it is possible to correct the one dimensional line measurement for three dimensional effects; such corrections allow unambiguous determination of scalar layer thicknesses and scalar gradients on an instantaneous measurement basis. Significant amounts of new information can be obtained from the Raman-Rayleigh-LIF measurements that cannot be obtained from the planar imaging measurements reported in Chapters 5 and 7 making the Raman-Rayleigh-LIF measurements a valuable tool to further understanding the flame structure in the PPJB.

There are several distinguishing differences between the data obtained from the line Raman-Rayleigh-LIF facility at the CRF and the planar imaging data obtained at The

University of Sydney reported in Chapters 5 and 7. In all of the imaging experiments reported in this thesis, temperature is almost exclusively determined by converting the Rayleigh signal to temperature through the use of Rayleigh cross sections derived from the curve of best fit obtained from laminar flame simulations. Although the error introduced by this assumption is small and is nowhere near the error introduced by a constant Rayleigh cross section assumption in non-premixed combustion, a small uncertainty remains in the temperature calculation. By measuring all major species in the line Raman-Rayleigh-LIF technique the uncertainty in the determined temperature from the Rayleigh cross section is virtually eliminated. Although the spatial resolution of the temperature measurements using the line Raman-Rayleigh-LIF measurements is approximately twice as large as the imaging measurements, the SNR of the line Raman-Rayleigh-LIF measurements much higher. The Line Raman-Rayleigh-LIF measurements have much higher SNR due to a number of factors such as: a 75 times higher laser irradiance level per unit area, faster collection optics and lower read out noise and increased dynamic range of the read out camera. In fact, the Rayleigh signal level is so large in the line Raman-Rayleigh-LIF experiments the signal needs to be attenuated by neutral density (ND) glass filters to prevent saturation of the detection camera.

The line Raman-Rayleigh-LIF experiments measure all major species simultaneously with temperature. As each of the three streams (coflow, pilot and central jet) have unique elemental mass fractions, the measurement of the major species allows the determination of a mixture fraction for each of the three streams. The measurement of mixture fraction is useful in understanding the spatial and conditional mixing patterns of the three streams. The conditioning of measurements on the mixture fraction of the three streams is not possible using the imaging data reported in this thesis or any other imaging techniques in general at a comparable SNR level.

In addition to the measurement of the major species and temperature measurements, the minor species CO and OH are simultaneously measured along the same line as the Raman-Rayleigh measurements. The CO measurements are made using a two-photon LIF technique that has superior SNR, Signal to Background Ratio (SBR) and spatial

resolution compared to Raman CO measurements. Comparable measurements of CO using planar techniques are possible and preliminary CO PLIF experiments have been conducted at The University of Sydney. The SNR of the imaging measurements was found to be much lower than the Sandia measurements, also only temperature was simultaneously measured in the imaging measurements restricting the utility of these measurements in comparison to the many other species measured in the Sandia CO LIF experiments. For these reasons the Sandia CO LIF experimental measurements of CO are exclusively reported in this thesis.

The OH radical is measured in the Sandia measurements using the crossed plane OH PLIF technique, with the intersection of the two crossed planes corresponding to the line Raman-Rayleigh measurement volume. As with the CO measurements, OH can be used in combination with the other measured species to determine the local forward reaction rates of certain individual reactions. The local 3D flame orientation can also be determined using the crossed plane OH PLIF, allowing not only determination of the flame orientation PDF but a correction to be made for the one dimensionality of the measurements to yield the full 3D value for the measured scalar layer thickness, scalar gradient and scalar dissipation. The utility of this correction is of course limited to where OH is present and sufficient gradients of OH exist. The measurement of the flame orientation is also possible using a planar two sheet Rayleigh approach in the cross plane configuration as shown by Knaus *et al.* [270], or in the parallel configuration as shown by Mansour [271]. In Chapters 5 and 7 using the PLIF technique the local OH concentration has been imaged with higher accuracy, precision and spatial resolution compared to the Sandia OH measurements, the utility of the Sandia measurements is that OH is measured simultaneously with temperature, major species, CO and three dimensional flame orientation, this is something that is of course not done in the imaging work.

A detailed description of the Sandia experimental setup is given in Section 6.1. In Section 6.2 the experimental data quality is examined. In Section 6.3, the experimental results for the line Raman-Rayleigh measurements are presented. Detailed analysis and discussion of the experimental results presented in this Chapter in terms of flame structure and

finite-rate chemistry effects is left until Chapter 8. A comprehensive data presentation of all of the relevant measured and calculated parameters presented as spatial scatter plots including the spatial mean and RMS combined with conditional scatter plots including the conditional mean and RMS for the PM1 flame series is presented in Appendix C.

6.1 Experimental Setup

A detailed description of the Sandia experimental setup is given in this Section. This includes a general overview of the experimental facility in Section 6.1.1, a summary of the lasers and excitation optics used for the experiments in Section 6.1.2, a review of the signal collection optics and cameras in Section 6.1.3, modifications to the PPJB for the Sandia experiments in Section 6.1.4 and the calibration regime for the Sandia measurements in Section 6.1.5

6.1.1 Experimental Facility Overview

The current configuration of the TCL at Sandia is a by-product of the gradual evolution of the many Raman-Rayleigh experimental campaigns studying turbulent flames at Sandia over approximately the last 25 years. This evolutionary process of the Raman-Rayleigh experimental setup at Sandia has had one large evolutionary step in this 25 year period, this being the replacement of the turbulent diffusion laboratory (TDL) with the TCL as summarised by Barlow and Karpetis [272]. This step from the TDL to the TCL essentially moved from point Raman-Rayleigh measurements to 1D line Raman-Rayleigh measurements, allowing the measurement of spatial scalar correlations.

Initial Raman-Rayleigh measurements in the TDL by Dibble *et al.* [273, 274, 275] were focused on hydrogen-air non-premixed jet flames delivering point measurements of major species, mixture fraction and temperature. These initial measurements utilised a

flash lamp pumped dye laser and PMT for signal acquisition. This system was also extended to examine scalar fluxes by simultaneously measuring velocity at the measurement location using LDV as reported by Dibble *et al.* [273]. The use of hydrogen-air flames presented minimal difficulties in terms of major species Raman cross talks and minor species interferences on the collected Raman signals. The application of the TDL experimental setup to hydrocarbon flames where significant spectral interferences and cross-talks occur has been detailed by Dibble *et al.* [276] and in number of publications by Masri *et al.* [54, 55, 56, 57] and by Stårner *et al.* [277, 278, 279, 280]. Extensions and improvements to the original Raman-Rayleigh system in the TDL have also been reported. Barlow *et al.* [281] reports the addition of a quantitative OH LIF system for simultaneous OH and Raman-Rayleigh measurements. The further addition of simultaneous quantitative NO LIF to the measurements has been detailed by Carter and Barlow [282]. The replacement of CO Raman measurements with CO LIF measurements for higher accuracy and precision of the CO measurements as well as the replacement of dye laser based excitation to pulse stretched Nd:YAG excitation for the Raman-Rayleigh measurements is detailed by Nguyen *et al.* [283].

The TCL evolved out of the need for measurements of scalar dissipation in non-premixed combustion. One dimensional (1D) line Raman-Rayleigh measurements of species and temperature using a rotating shutter based signal collection was first conceptually described for Raman only diagnostics in SI engines by Miles [284] and then later in laminar diffusion flames by Barlow and Miles [285, 286]. This Raman technique was combined with simultaneous Rayleigh and CO LIF by Karpetis and Barlow [287]. The rotating shutter based signal collection for the Raman signal collection forms the cornerstone for Raman signal collection in the TCL. A further improvement to the TCL Raman-Rayleigh system was outlined in Karpetis and Barlow [288] who describe the ability to correct the 1D measurements for three dimensional (3D) effects by using a crossed plane correction based on two crossed plane OH PLIF sheets.

6.1.2 Excitation Laser Setup and Optics

The excitation source for the Raman-Rayleigh system is based on the output of four frequency doubled Nd:YAG lasers at 532nm that are spatially overlapped to form a 1.8J macro pulse, this macro pulse is then pulse stretched to avoid optical breakdown at the probe volume. Schematically the setup of the four lasers, beam path and pulse stretcher are shown in Fig. 6-1.

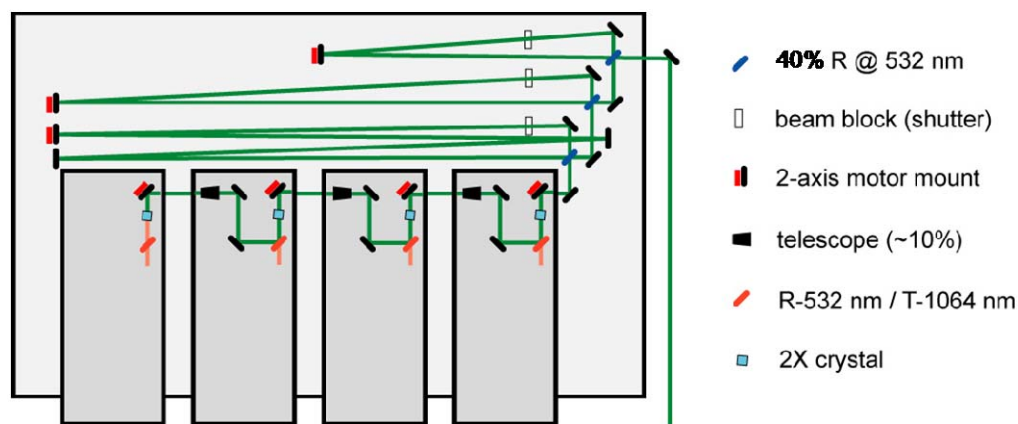


Fig. 6-1. Schematic diagram of the four frequency doubled Nd:YAG lasers and pulse stretcher used for the Raman-Rayleigh system. This figure is used with permission from Dr. R. S. Barlow.

The combination and collimation of the four beams from the four lasers is achieved using a successive chain of dichroic optics and beam telescopes. The fundamental from the first laser is frequency doubled and the second harmonic separated from the fundamental by the use of a dichroic mirror that reflects 532nm at 45° and passes 1064nm, for alignment purposes this dichroic mirror is mounted on a two axis computer controlled piezoelectric mirror mount. The frequency doubled output from the first laser then passes through a collimating telescope to allow the focal point to coincide with the other laser beams that might have slightly different divergence and beam profiles. The frequency doubled output from the first laser is then overlapped with the fundamental of the second laser and passed through the frequency doubling crystal of the second laser and then to a 45° 532nm reflecting mirror similar to the first laser. The fundamental from the second laser

is separated and only the overlapping second harmonics from the first and second lasers remain. This process of collimating, combining with the laser fundamental, frequency doubling and second harmonic separation is continued for the third and fourth lasers. At the end of this chain of four lasers a collimated overlapping pulse train of four 532nm beams exits.

If the output from the Nd:YAG cluster were to be focused spherically a gas breakdown event would occur, this would create an intensely luminous plasma plume that would render the Raman-Rayleigh measurements useless. To minimise the probability of a gas breakdown event, the pulse output from the four lasers is staggered by 150ns intervals, this alone is not enough to stop gas breakdown and must be combined with a three legged pulse stretcher to minimise the probability of gas breakdown. The use of the Nd:YAG pulse stretching system is discussed by Nguyen *et al.* [283], with the design features and optimisation of the pulse stretching systems detailed in Kojima and Nguyen [289].

Each leg of the pulse stretcher essentially consists of a partially reflecting mirror and two high reflecting mirrors one of which is mounted on a precision piezoelectric 2 axis mirror mount. As the pulse enters one leg of the stretcher 40% of the pulse energy passes directly out of the stretcher leg and into the next pulse stretcher leg, the other 60% makes a round trip around the pulse stretcher leg then 40% of the 60% of laser energy that enter the pulse stretcher leg (24% of the original) leaves the pulse stretcher leg while the remaining energy (36% of the original) does another loop of the pulse stretcher leg and so on. This process is repeated for each of the other two pulse stretcher legs. The pulse stretcher results in an individual pulse temporal FWHM of ~84ns, being significantly increased from the original individual pulse duration of 10ns FWHM. The ensemble pulse train last approximately 600ns. A temporal recording of the temporal variation of the energy at the exit of the pulse stretcher with a fast photodiode and oscilloscope is given in Fig. 6-2. Examining the Fig. 6-2 it is tempting to suggest that an additional pulse stretcher leg could be added and the inter pulse time of 150ns could be reduced to reduce the total pulse train time. There are a number of additional constraints that prevent this from occurring, additional optical elements and additional beam reflections increase the

losses of the pulse stretching systems however more importantly additional pulse path lengths decrease the quality of the beam profile due to divergence.

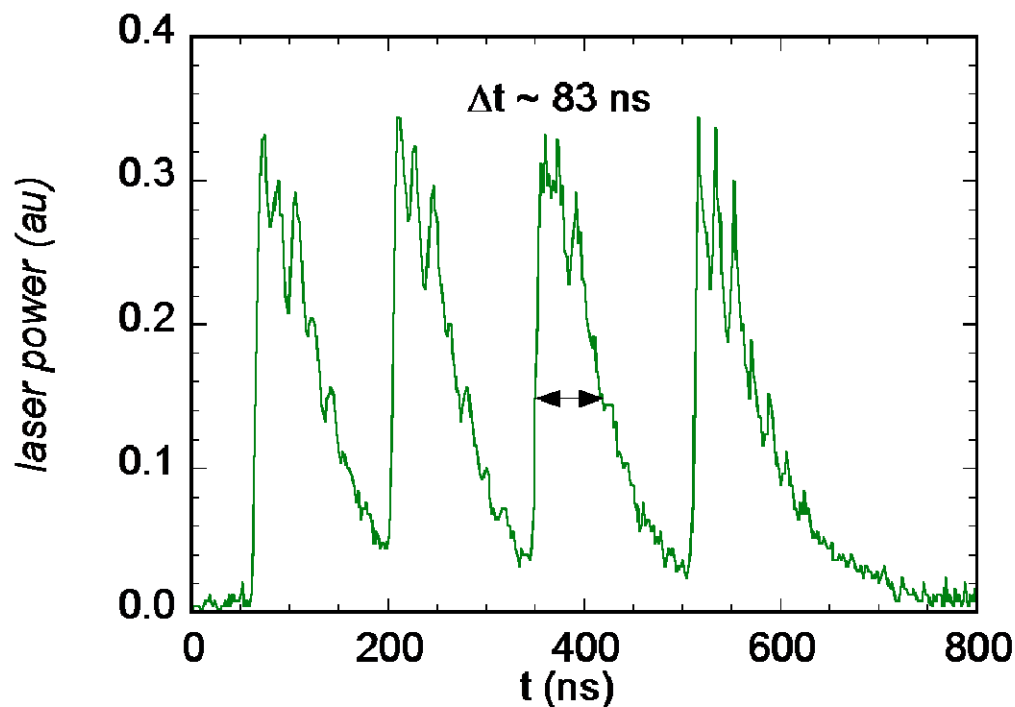


Fig. 6-2. Temporal variation of the laser power at the exit of the Nd:YAG pulse stretcher. This figure is used with permission from Dr. R. S. Barlow.

Major alignment of the pulse stretcher was necessary before every experiment, this was done after the four Nd:YAG Raman-Rayleigh lasers had warmed up for at least two hours. This alignment was crucial to obtain a small beam waist at the probe volume and avoiding intermittent gas breakdown events in the probe volume. During experiments, at approximately hourly intervals, minor adjustments to the pulse stretcher were necessary, after a number of hours running major adjustments were often found to be necessary.

The 532nm beam was focused to the probe volume with a 500mm focal length spherical lens; essentially the beam waist along the 7mm probe volume is in the Rayleigh range so the beam waist changes by a negligible amount along the probe volume, this can be seen

in a Rayleigh image of the beam presented in Fig. 6-3a). As the Rayleigh camera essentially takes a planar image of the 532nm beam at the probe volume the beam FWHM can be directly measured to aid the pulse stretcher alignment and to monitor any misalignment that may be developing during an experiment. Typically, the beam FWHM at the probe volume ranged from 110 μ m to 190 μ m. If the beam waist went above 180 μ m in an experiment typically further runs were stopped until a minor alignment of the pulse stretcher was carried out to minimise the beam waist. A characteristic image of the 532nm beam for a single shot in air is presented in Fig. 6-3 a), with profile of the intensity distribution through the beam presented in Fig. 6-3 b). The intensity distribution presented in Fig. 6-3 b) is not well modelled with a Gaussian distribution however a $1/e^2$ value maybe assigned; using the 0.135 of peak method yields a $1/e^2$ value of 225 μ m for this particular image.

Some of the advantages of measuring CO with the two-photon LIF method compared to Raman measurement are highlighted by Dally *et al.* [290] and more generally the advantages of CO LIF based measurement methods over Raman based methods is examined by Dally *et al.* [290] for non-premixed flames. Excitation of CO through the B-X system of CO using two-photon LIF at 230nm is found to be a near optimal scheme for measurements in turbulent hydrocarbon flames although interferences from photo-dissociated hot band CO₂ and C₂ spectral interferences must be carefully managed.

To generate the 230nm radiation for CO LIF in the TCL the output from an Nd:YAG is frequency doubled, the frequency doubled output is used to pump a dye laser using a mixture of Rhodamine 6G and Rhodamine 590 in methanol producing an output of 590nm. The 590nm output from the dye laser is doubled to 293nm, which is then frequency mixed with the 1064nm fundamental of the Nd:YAG to produce the 230nm radiation. At room temperature a spectral scan of CO LIF vs. wavelength indicates that the operational wavelength for combustion diagnostics is approximately 75% below the peak found for the cold flow maxima. No obvious rotational level spectral structure can be defined in the cold CO LIF scan; this is probably due to the spectrally dense absorption spectra of CO in the region of 230nm combined with homogenous Doppler

and non-homogenous collisional (Lorentzian) broadening convoluted with the two photon process absorption integral and laser bandwidth. At higher temperatures this absence of rotational level structure in the spectrum is expected to be exacerbated due to the increased broadening effects at high temperatures and the increased number of energy states populated by the CO molecule at higher temperatures.

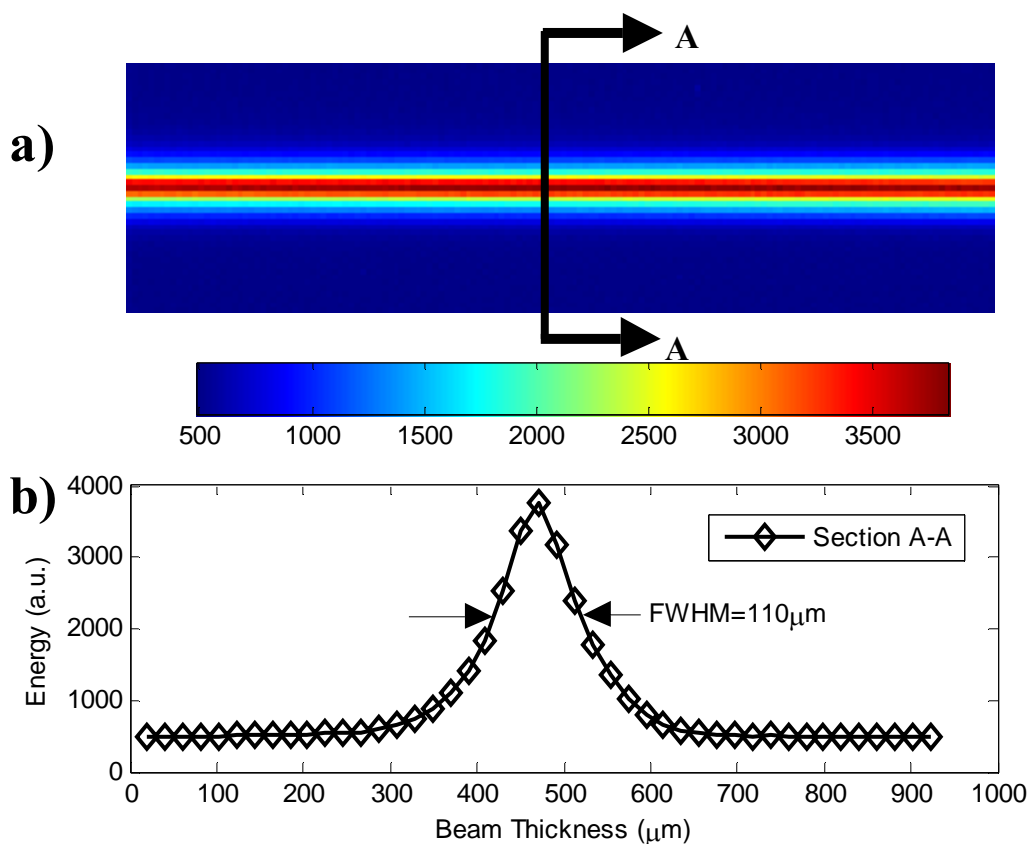


Fig. 6-3. a) Example image of the 532nm Raman-Rayleigh beam for a single realization in a uniform medium, note this image is not to scale, the vertical height of the image is approximately 1mm and the length 7mm. b) Sectional profile of the imaged beam intensity distribution through the section A-A shown in a), note the FWHM for this profile is 110 μ m and the $1/e^2$ width is 225 μ m.

The CO LIF signal is related in a non-linear fashion to the CO LIF laser intensity primarily because the CO LIF excitation strategy used is a two-photon process. A characteristic image of the CO LIF signal for a single shot in the methane-air flat flame burner used for calibrations is presented in Fig. 6-4a), a vertical profile of the LIF signal through the image is presented in Fig. 6-4b). The intensity distribution presented in Fig.

6-4 b) is not well modelled with a Gaussian distribution however a $1/e^2$ value maybe assigned; using the 0.135 of peak method yields a $1/e^2$ value of $320\mu\text{m}$ for this particular image.

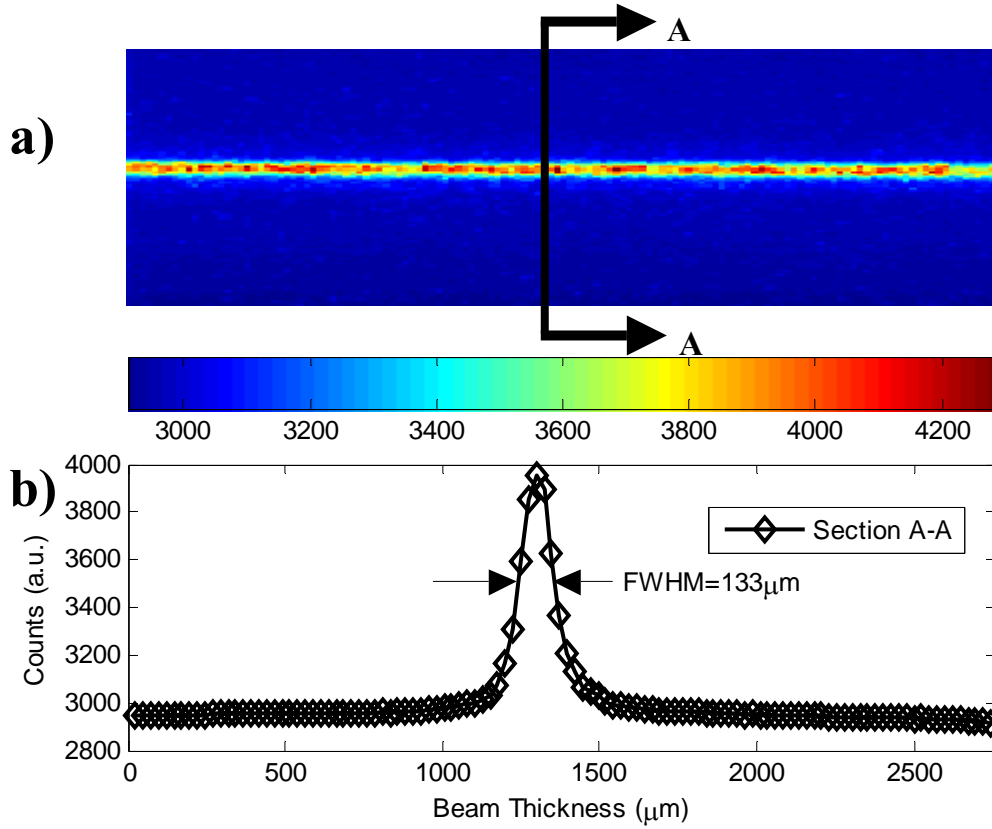


Fig. 6-4. a) Example image of the resultant single-shot CO LIF signal in a uniform medium of post flame gases, note this image is not to scale as the vertical height of the image is approximately 2.8mm and the length 6.5mm. b) Sectional profile of the imaged beam intensity distribution through the section A-A shown in a), note the FWHM for this profile is $133\mu\text{m}$ and the $1/e^2$ width is $320\mu\text{m}$.

Profiling of the two OH PLIF laser sheets using a pinhole and a photo-diode with a micrometer traverse has been carried out for both laser sheets. Fitting a Gaussian profile to the measured energy profiles at the focal plane yields a FWHM sheet thickness of $250\mu\text{m} \pm 50\mu\text{m}$. At the edges of the images $\pm 3\text{mm}$ away from the focal plane (along the axis of the laser propagation), the measured FWHM sheet thickness becomes $350\mu\text{m} \pm 50\mu\text{m}$. Typical energies for each of the two OH PLIF sheets are of the order of 2-3mJ.

To gain an appreciation for Sandia laboratory where the Raman-Rayleigh-LIF measurements were made Fig. 6-5 shows the layout of the lasers, optical tables and test section.

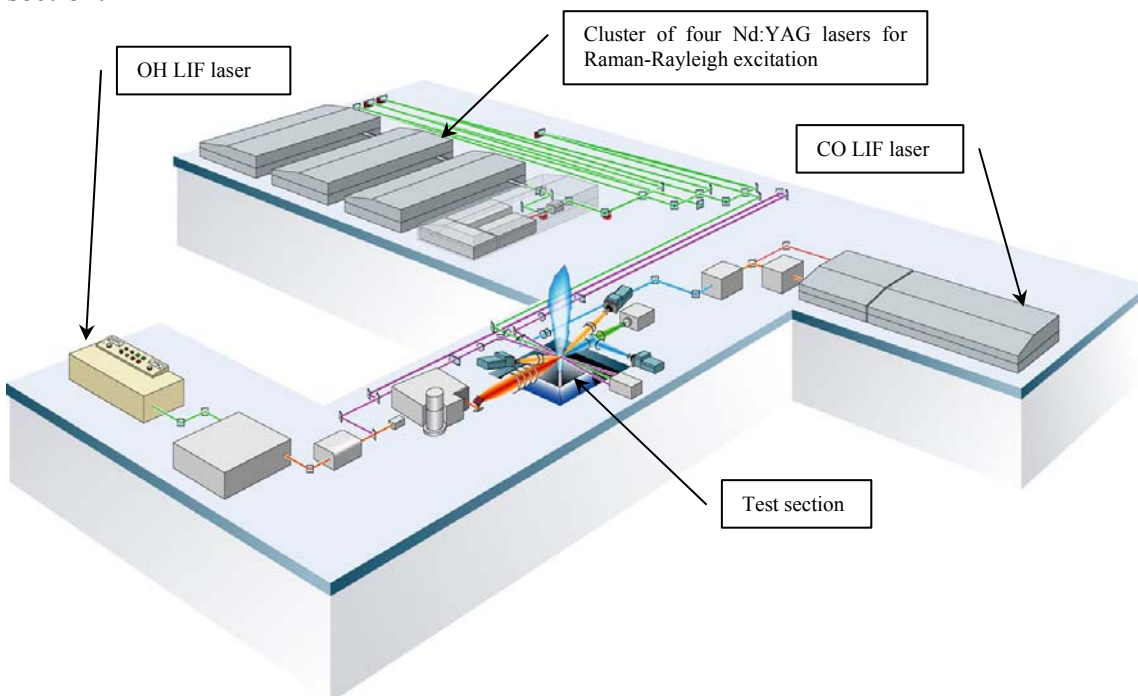


Fig. 6-5. A pictorial overview of the TCL at Sandia showing the six lasers, beam paths, test section and five cameras. This figure is used with permission from Dr. R. S. Barlow.

6.1.3 Signal Collection

The Raman signal is collected with a pair of 150mm diameter achromats ($f/2$ and $f/4$) which were mounted face to face to achieve a magnification of 2.0. Effectively this allowed the Raman collection optics to collect photons from the probe volume at $f/2$. The rear $f/4$ lens was matched to the entrance aperture of a 27cm imaging spectrometer (SPEX 270M). Flame luminosity is rejected from the Raman signal by the use of a high speed rotating shutter arrangement; the gate time of this rotating shutter arrangement is approximately $9\mu\text{s}$. The spectrally dispersed Raman lines are then recorded by a cryogenically-cooled CCD camera (Roper Scientific CryoTiger), the use of such a high

performance camera is crucial to obtain adequate SNR on the weak Raman signals at high temperatures.

The Rayleigh signal is collected with a pair of $f/3.7$ achromatic lenses. Flame luminosity is rejected through the use of a 532nm interference filter and a mechanical leaf shutter. The Rayleigh signal is recorded on a back illuminated CCD camera (Roper Scientific Spec-10 400B). Typically the Rayleigh camera was binned 3×1 in the vertical and horizontal directions allowing a possible resolution of $20\mu\text{m}$ in the beam propagation direction. CO LIF from the $B^1\Sigma^+(\nu''=0) \rightarrow A^1\Pi^+(\nu'=1)$ band is collected with a pair of $f/3.7$ achromatic lenses and recorded on an ICCD camera. Spectral interferences onto the CO LIF due primarily to PAH and C_2 LIF are minimised by the use of an interference filter centred at 484nm with a 10nm bandwidth.

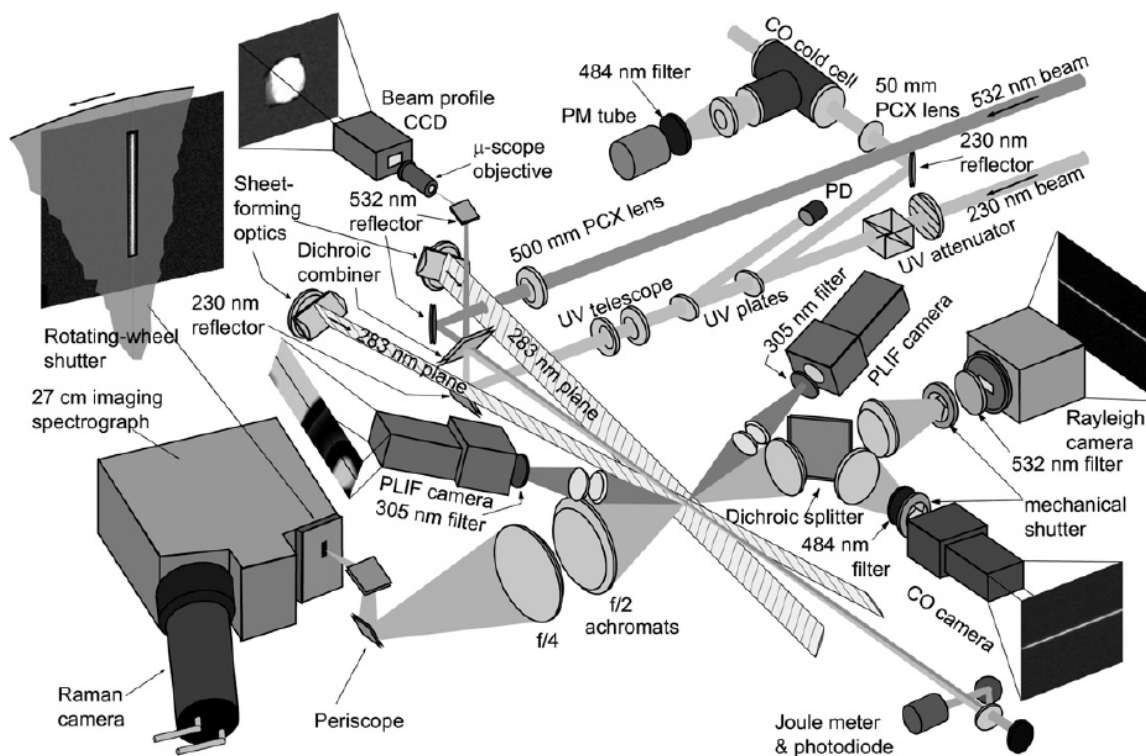


Fig. 6-6. An overview of the Sandia Raman-Rayleigh-LIF measurement system focusing on the final laser sheet formation, signal collection optics and signal recording cameras. This figure is used with permission from Dr. R. S. Barlow.

The cross plane addition to the Raman-Rayleigh and CO LIF experimental setup is described and characterised by Karpetis and Barlow [291, 292]. The cross plane OH signal collection was based on collecting the OH PLIF signal using two 3" plano-convex collection lens pairs for each OH PLIF ICCD. This collection system provided large OH PLIF signal levels and near optimal magnification, however the spatial resolution of this configuration was quite poor. The spatial resolution of the OH PLIF system produced a blur spot of around 1mm. This may be acceptable for measurements in non-premixed combustion where the spatial gradients are relatively low however for measurements in turbulent premixed combustion this spatial resolution for OH is not adequate.

To address the issue of spatial resolution in the OH PLIF measurements the plano-convex lens pairs have been replaced by CERCO 45mm $f/1.8$ UV camera lenses hence reducing the optical blur from around 1mm to less than $175\mu\text{m}$. The new OH PLIF lens configuration operates with a magnification of 0.16 and a projected pixel resolution of $150\mu\text{m}$. This magnification is less than optimal; however it is an acceptable compromise considering the improvement in spatial resolution gained with the revised lens combination. Compared to the previous setup, the new configuration allows the OH spatial resolution to be acceptable for measurements in premixed flames and thus permitting quantitative OH measurements in turbulent premixed combustion.

An overview of the laser sheet formation and signal collection setup for the Raman-Rayleigh-LIF measurements is given in Fig. 6-6. This figure highlights the numerous beams and signals that must be simultaneously managed for such an experiment.

6.1.4 PPJB Burner

A copy of the PPJB was constructed in Sydney and taken to Sandia for the detailed measurements. Prior to shipping to Sandia the replica Burner was tested in Sydney to check the stability characteristics were identical to the original version, no differences between the two burners were found. Different from previous studies by Dunn *et al.*

[175], pure methane is used in the Sandia experiments, instead of compressed natural gas (CNG). It is worth noting that no discernable changes in the flame behaviour or stability limits were found with the use of pure methane, justifying the comparability of the present measurements with previous velocity and imaging experiments [175].

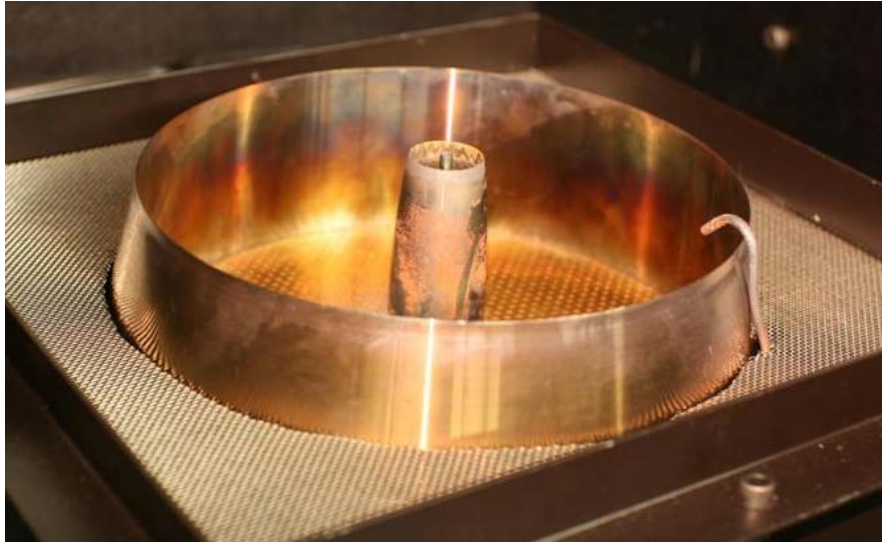


Fig. 6-7. Photograph of the PPJB in the Sandia measurement test section. Surrounding the burner is the filtered air wind tunnel adapter that was made specifically for the PPJB. Also note the burner in this image features the standard height collar (65mm).

To adapt the PPJB to the Sandia wind tunnel test section, a purpose built connector for the wind tunnel was built. This allowed filtered air at approximately 1m/s to be co-flowing with the burner to maximise the potential core of the hot coflow as well as to provide additional cooling to the outer parts of the burner. A photograph of the PPJB in the Sandia test section is presented in Fig. 6-7.

The collection optics for the Raman system at Sandia collects light at $f/2$, therefore with the standard collar configuration measurements are only able to be collected for $x/D > 7$ to prevent partially obscuring the Raman collection optics. Such obscuration would invalidate the calibrations and therefore the correction matrix. It is highly desirable to take measurements below $x/D = 7$ but equally it is undesirable to correct the Raman signal for the obscuration. Specifically for the Raman measurements at Sandia for $x/D < 7.5$ a

custom coflow collar has been manufactured. This allows measurements down to $x/D > 2$ without obscuration occurring. This revised coflow collar sits only 25mm in total from the coflow base-plate. As the revised collar is not as well streamlined as the original collar the interface between the coflow and the wind tunnel is far more turbulent and a greater degree of beam steering occurs. It is for this reason that the revised collar is only used for the reported measurements at $x/D = 2.5$.

Digital mass flow rate meters were used to control the flow rates for all streams in the burner and calibration flows. The digital mass flow rate meters were calibrated to an accuracy of 1.0% using a variety of laminar flow elements that have traceable calibration certificates.

6.1.5 Calibrations

Rather than calculate the cross talk terms for the Raman species from first principles using quantum mechanics based simulations, the approach is taken to experimentally calibrate the cross talk terms using a range of flows with known compositions and temperatures. The calibration flows that are used can be categorised into four categories: cold flows, heated flows, flat flames and Bunsen flames.

The cold flow and the flat flame calibrations are conducted using a honeycomb matrix flat flame calibration burner. This burner consists of a 50mm diameter central flow with a 0.9mm pitch stainless steel hexagonal honeycomb to stabilise the flame and prevent flash back. Surrounding the main central region is an 89mm OD, 52mm ID annular region that a coflow of N_2 is fed through, this coflow minimises the effects of ambient air drafts disturbances to the central flow and maximises the potential core of the central flow.

To generate the temperature dependant calibration curves in the region of 300K-550K for all of the Raman species and the relevant cross talk terms an electrically heated flow configuration is utilised. The flow rates and flow compositions used for the cold and

heated flows are given in Table 6-1 as well as an indication of the primary terms that are resolved in the calibration matrix by the particular calibration measurement. The heated flows were conducted at the beginning of the experimental campaign and served the purpose to generate the temperature dependant calibration matrix terms at low temperatures, the most important one of these being the cross talk between O_2 and CO_2 . Cold flow calibrations were conducted at the beginning and end of every experiment. The cold flows were used as an approximate base-line check for the individual Raman species gain as well as a being a global check for the major cross talk terms. Subtle adjustment of these terms throughout the experimental campaign was found to be desirable to compensate for the small changes in the beam profile that occur between each experiment.

Table 6-1. Cold flow and heated flow calibrations flow rates and primary calibration purpose for the Sandia experiments.

Flow rates (slm)	Primary Calibration Purpose
Dry air: 60	O_2 , $O_2 \rightarrow CO_2$, $O_2 \rightarrow C_2$, $O_2 \rightarrow CO$, $O_2 \rightarrow \text{background}$.
N_2 : 60	N_2 , $N_2 \rightarrow CH_4$, $N_2 \rightarrow CO$, $N_2 \rightarrow C_2$, $N_2 \rightarrow \text{background}$.
N_2 : 45, CO_2 : 5	CO_2 , $CO_2 \rightarrow O_2$, $CO_2 \rightarrow C_2$, $CO_2 \rightarrow \text{background}$.
N_2 : 40, CH_4 : 10	CH_4 , $CH_4 \rightarrow N_2$, $CH_4 \rightarrow H_2O$, $CH_4 \rightarrow \text{background}$.
N_2 : 40, H_2 : 10	H_2 , $H_2 \rightarrow H_2O$, $H_2 \rightarrow CO_2$, $H_2 \rightarrow O_2$, $H_2 \rightarrow C_2$, $H_2 \rightarrow \text{background}$, $H_2 \rightarrow N_2$, $H_2 \rightarrow CH_4$, $H_2 \rightarrow CO$.
Humid ambient air: 50	H_2O , $H_2O \rightarrow H_2$, $H_2O \rightarrow CH_4$, $H_2O \rightarrow \text{background}$.

To calculate the high temperature dependence of Raman channel cross talks, nine methane-air flame are investigated. These nine flames are run at the start and end of each day's experiments. The flow rates, equivalence ratios and measured temperatures of these flames are given in Table 6-2. The temperature of these flames has been previously measured very precisely using N_2 CARS thermometry; this technique has an approximate uncertainty of $\pm 20K$. By knowing the original composition and the temperature at the probe volume precisely, all major species including CO and OH can be calculated by assuming chemical equilibrium with a high degree of accuracy.

Table 6-2. Summary of the methane-air flat flames used for high temperature Raman-Rayleigh-LIF calibrations.

Flame #	1	2	3	4	5	6	7	8	9
CH ₄ (slm)	4.76	5.04	5.31	5.59	5.85	6.26	6.67	6.31	4.71
Air (slm)	55	55	55	55	55	55	55	50	35
T (K)	1997	2063	2122	2171	2197	2189	2139	2100	2029
ϕ	0.824	0.872	0.919	0.967	1.012	1.083	1.154	1.201	1.281

A laminar diffusion flame of methane-air is used as a source of PAH LIF and C₂ interference for these terms in the correction matrix. The degree of uncertainty involved in these corrections is much higher than other terms in the correction matrix as the concentration of PAH and C₂ is not known in these flames and must be estimated. A hydrogen-air laminar diffusion flame is used to correct H₂ cross talks at high temperatures that occur over almost all of the channels at high temperatures.

6.2 Data Processing and Experimental Characterisation

In this Section the experimental data quality is examined. This includes the data processing methodology in Section 6.2.1, the spatial resolution of the Sandia Raman-Rayleigh-LIF measurement system in Section 6.2.2 and the accuracy and precision of the Sandia measurements in Section 6.2.3.

6.2.1 Processing methodology

The data reduction scheme for the Raman-Rayleigh-LIF data has evolved over time, just as the experimental setup has evolved over time at the TDL and TCL at Sandia. Initially

the Raman channel for each species was corrected using a temperature dependant calibration coefficient as outlined by Dibble *et al.* [273, 276]. A significant development in the processing of Raman-Rayleigh data was made by Dibble *et al.* [34] detailing the conceptual frame work for the matrix inversion method for Raman-Rayleigh signal quantification. The matrix inversion method allows it to be possible to implement temperature dependant species cross-sections and most significantly temperature dependant species, background and interference corrections.

The OH PLIF signal was processed using the non-linear LIF quantification scheme presented by Dunn and Masri [242]. CO LIF was treated as species in the matrix inversion process with a temperature dependant gain and cross talks. The laser power dependence exponent for CO LIF used to correct for shot to shot fluctuations in the laser energy was set to 1.2, this was based on laser power dependence test. As the laser energy dependence was significantly less than 2, this indicates that photo-ionisation was the predominant loss mechanism compared to electronic quenching.

6.2.2 Spatial Resolution

Accurate determination of the global experimental spatial resolution is complicated by the many different beam diameters, blur spots and pixel resolutions involved. In Dunn *et al.* [293] the spatial resolution of the measurement system was partially verified for measurements in turbulent premixed combustion. This was done by comparing the experimental results obtained in a lean premixed Bunsen flame to numerically computed results using a two-dimensional, axisymmetric configuration combined with detailed kinetics and multi-component transport. Using the method outlined by Dunn *et al.* [293] it was shown to be possible to measure the gradient of temperature in a 0.94 equivalence ratio methane-air Bunsen flame within an accuracy of $\sim 7\%$ in the peak gradient magnitude.

Due to the high spatial resolution required for measurements in turbulent premixed combustion relative to non-premixed combustion, the estimated spatial resolution of 0.3mm for the measurements presented by Barlow and Karpets [294] may not be adequate. Insufficient spatial resolution can introduce errors and bias the results, particularly when quantification of scalars such as CO and OH require temperature and major species to be simultaneously measured. These errors not only affect instantaneous measurements, they can bias the mean scalar fields, such as the mean fields presented in results section of this section. The $1/e^2$ blur spot size for the Rayleigh, Raman and CO LIF optical collection system has been evaluated using ZEMAX [295] and found to be approximately 40 μ m, 200 μ m and 40 μ m respectively. The projected pixel sizes on the Rayleigh, Raman and CO LIF are found to be to be 41 μ m, 228 μ m, and 98 μ m respectively.

The estimated spatial resolution of 0.3mm reported by Barlow and Karpets [294] is based on the fact that in non-premixed flames mixture fraction is potentially a multi-valued function of collected Rayleigh signal, thus it would not seem to be immediately possible to interpolate the low resolution Raman measurements to the high resolution Rayleigh measurements in a rigorous manner. In premixed combustion a different scalar namely temperature, is of primary interest. Although temperature is still a function of the Rayleigh cross section in premixed flames, it can be shown that the Rayleigh cross section variation through a premixed flame is very small. Therefore, interpolating the Raman signal to the higher resolution Rayleigh signal to determine the local cross section only introduces a small error.

The approach of interpolating the Raman to the Rayleigh resolution has been partially validated by taking measurements in a laminar lean premixed Bunsen flame with the results compared at Raman and interpolated Rayleigh resolution to a computed Bunsen flame. The laminar lean premixed Bunsen flame is computed using the commercial CFD code (Fluent v6.3.26 [296]). The flame is modelled in an axisymmetric configuration using a steady, laminar solver. The kinetic mechanism DRM22 developed by Kazakov and Frenklach [297] as a skeletal mechanism based on GRI 1.2, is selected to be an

acceptable balance between computational time and kinetic mechanism accuracy. Full multi-component species and thermal diffusion transport are utilised for the simulations. To further reduce the computational time *In Situ* Adaptive Tabulation (ISAT) is employed. The simulation results are found to be independent of the ISAT error tolerance (e_{tol}) for a value of $e_{\text{tol}} \leq 5 \times 10^{-6}$, a value of $e_{\text{tol}} = 5 \times 10^{-6}$ is used for this simulation. Extensive grid refinement is applied around the reaction zone to achieve a grid independent solution. Radiation losses are not included in the simulation.

A stringent test for the degree of accuracy and resolution for the measurements in turbulent premixed combustion is the measurement of temperature gradients. By comparing measurements of temperature gradients in a laminar premixed Bunsen flame with computations, an assessment may be made with regards to the accuracy and resolution of the measurements. The justification for interpolating the Raman to Rayleigh resolution measurements is presented in Fig. 6-8, since the Rayleigh resolution data correlates well with the simulation results, with a peak error of $\sim 7\%$. The fluctuations in temperature gradient for the Rayleigh resolution measurements at positions 1.25mm and above are due to the increased noise floor occurring in regions with high temperature and low temperature gradients. This fluctuation is not as prominent in the Raman resolution measurements due to the stronger noise smoothing effect at lower spatial resolution. If the Raman resolution is used for calculating the temperature gradient, the error in the peak value is estimated to be much higher, e.g. close to 24%. Not only is the peak value under estimated by using the Raman resolution, the width of the temperature gradient structure is broadened with an increased FWHM compared to both the simulation and the Rayleigh resolution results.

To remove as much noise as possible from the signal whilst not decreasing the spatial resolution is a delicate balance that is highly dependent on the filtering scheme used. Numerous finite difference and spectral filtering schemes have been trialled in an attempt to minimise noise and maintain acceptable spatial resolution, whilst many of these schemes display favourable characteristics they typically feature a significant phase error. This phase error can cause significant problems when applied to region of high gradients

when examining the data conditioned on a variable other than a spatial one. A filtering method that has the ability to effectively remove noise and that typically features considerably lower phase errors than spectral methods are wavelet methods. A wavelet filtering scheme using a 3 level Daubechies wavelet decomposition with soft thresholding has been selected to be a near optimal filtering scheme for the data. The threshold for the reconstruction for each of the wavelet levels was optimised manually by examining an example dataset of laminar Bunsen flames. An example of the success of the wavelet filtering scheme can be found in Fig. 6-8 where the high temperature noise apparent in the “Rayleigh Resolution” data has been removed in the “Filtered Rayleigh” data.

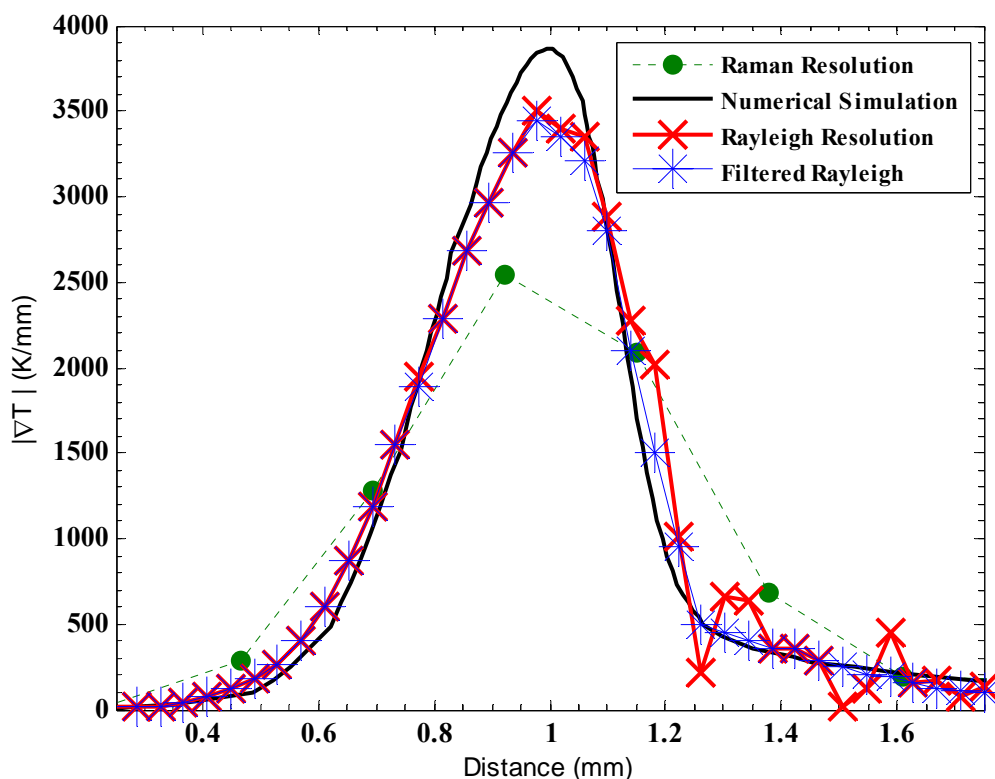


Fig. 6-8. An example realisation of temperature gradient through the reaction zone of a lean-premixed laminar Bunsen flame. The experimental results using different processing techniques are compared with the numerically calculated profile.

6.2.3 Accuracy and Precision

The measurements presented in this Chapter for temperature in a uniform field at 2200K have an estimated precision of $<1\%$ and an accuracy of 2% . For the CO in a uniform field at a temperature of 2000K the precision is 5% whilst the systematic error is estimated to be 10% . For OH the precision in a uniform field is 10% whilst the potential for systematic error is estimated to be 20% on average, however systematic errors higher than this are possible in regions of high OH gradients, particularly in the temperature range of 800K-1200K. The error in determining the flame orientation is examined in Karpetis and Barlow [291, 292].

6.3 Results and Discussion

In this Section the experimental results for the line Raman-Rayleigh measurements are presented. This includes an examination of the mean and RMS temperature profiles in Section 6.3.1, an examination of the utility of the major species radial profiles in Section 6.3.3 and the mixing patterns of the three streams are examined through the definition of individual stream mixture fractions in Section 6.3.3

6.3.1 Mean and RMS Temperature Profiles

Radial profiles of the Reynolds mean and RMS temperature have not previously been reported for the entire PM1 flame series and are presented here for the first time. Radial profiles are reported for all flames at $x/D = 2.5, 7.5$ and 15 , for the PM1-50 flame additional data is reported at $x/D = 15$, for the remaining three flames further data at $x/D = 30$ and 45 is also reported. Each radial traverse consists of 300 realizations taken at 4mm increments so that an overlap of 2mm occurs between each radial traverse increment due to the total measurement length being 6mm. The Radial profiles of the

Reynolds mean temperature is reported in Fig. 6-9a)-d) and the Reynolds RMS temperature is reported in Fig. 6-10a)-d).

The results in Fig. 6-9a) for the PM1-50 flame indicate that there is a very strong influence of the pilot gases to $x/D = 15$ and beyond. At $r/D=0.5$ for all axial traverse locations the mean temperature is close to the adiabatic temperature of the central jet (T_{ad}) 1480K, indicating a mean flame brush structure that is similar to a vertical shear layer of fresh jet reactants vs. a mixture of hot jet, pilot or coflow products, the ratio of which depending on the axial location. This near vertical reaction zone structure is consistent with the mean flame brush shape reported for the PM1-50 flame [175].

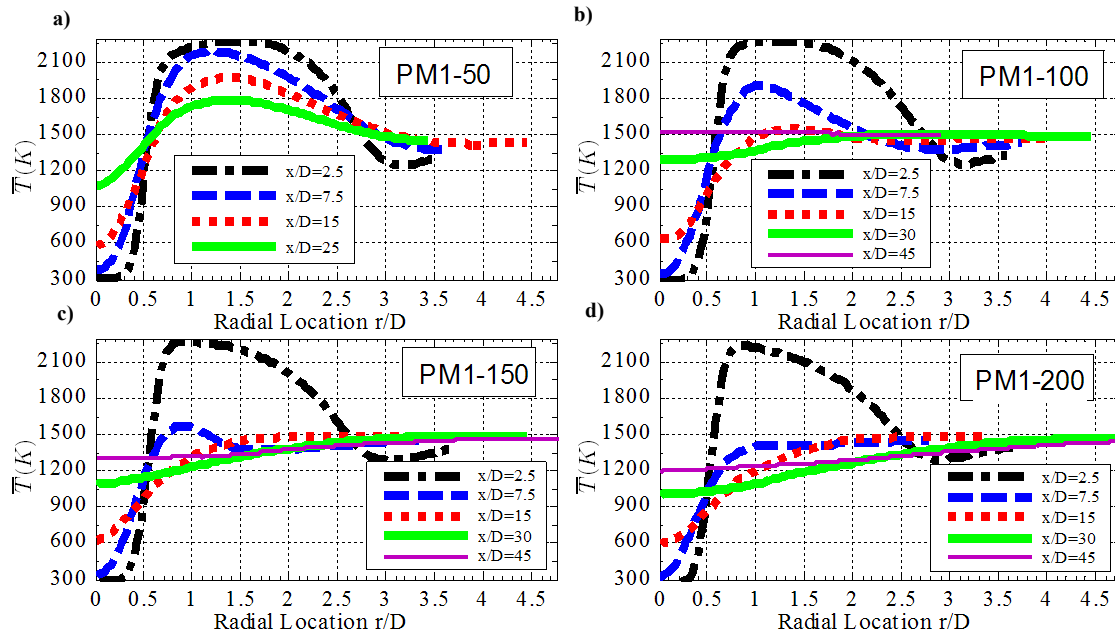


Fig. 6-9. Radial profiles at a number of axial locations of the Reynolds mean temperature for the four PM1 flames ((a) PM1-50, b).PM1-100, c) PM1-150 and PM1-200).

In Fig. 6-9a)- d) at $x/D=2.5$ for $r/D>2.7$ a drop in the mean temperature drops below the coflow temperature of 1500K can be observed for all four flames. This drop in temperature is due to the thermal boundary layer that develops in the hot coflow around the stainless steel pilot shroud in the 70mm vertical distance between the coflow base plate and the central jet exit plane. As a consequence of the heat transfer from the hot

coflow to the pilot shroud, the pilot reactants are preheated to approximately 400K, resulting in a mean pilot exhaust temperature of approximately 2275K at $x/D=2.5$. No significant preheating of the central jet reactants is observed.

The results reported for the PM1-150 and PM1-200 flames in Fig. 6-9c)-d) feature a number of similarities, both show that the mean temperature fields are quite different compared to the PM1-50 flame. The region of complete reaction progress for the central jet close to 1480K does not occur at a constant r/D value like in the PM1-50 flame but rather the mean flame brush contour is diverging, resembling an inverted conical shape up to $x/D=45$. This correlates well with the flame brush shape reported by Dunn *et al.* [175] for the mean chemiluminescence image of the PM1-150 and PM1-200 flames. The high temperature >1500K pilot products that are prominent in the PM1-50 measurements show only a small increase over the coflow temperature at $x/D=7.5$ for the PM1-150 flame, whilst at $x/D=7.5$ for the PM1-200 flame no mean rise above the coflow temperature is reported. No temperature increase above the coflow temperature at or above $x/D=15$ is observed for both of the flames, this indicates that the pilot products are completely entrained and mixed by $x/D=15$. The thermal boundary layer that forms in the coflow around the pilot shroud is evident at $x/D=2.5$, $r/D>2.6$ and $x/D=7.5$, $r/D>1.2$ for the PM1-150 flame, whilst no evidence of the thermal boundary layer is present for the PM1-200 flame past $x/D=2.5$. However at $x/D=15$ and beyond the sub-1500K coflow temperatures are not present. It is believed that the most significant differences (such as the decay of the pilot) between the PM1-50 and the high velocity PM1-150 and PM1-200 flames is primarily due to the increased entrainment rate of the PM1-150 and PM1-200 flames compared to the PM1-50 flame. For all of the high velocity flames the effects of compressibility close to the exit plane of the central jet at $x/D=2.5$ are minimal, with only a 10K decrease in the mean static temperature measured for the PM1-200 flame at $x/D=2.5$ on the centreline.

The radial profile of RMS temperature Fig. 6-10 show that a very similar temperature hence scalar fluctuation level of around 400K occurs initially at $x/D=2$ between the central jet and the pilot gases for all of the flames. This high fluctuation level persists

axially along the flame brush for the PM1-50 flame, however for all of the other flames this fluctuation level decays with axial location.

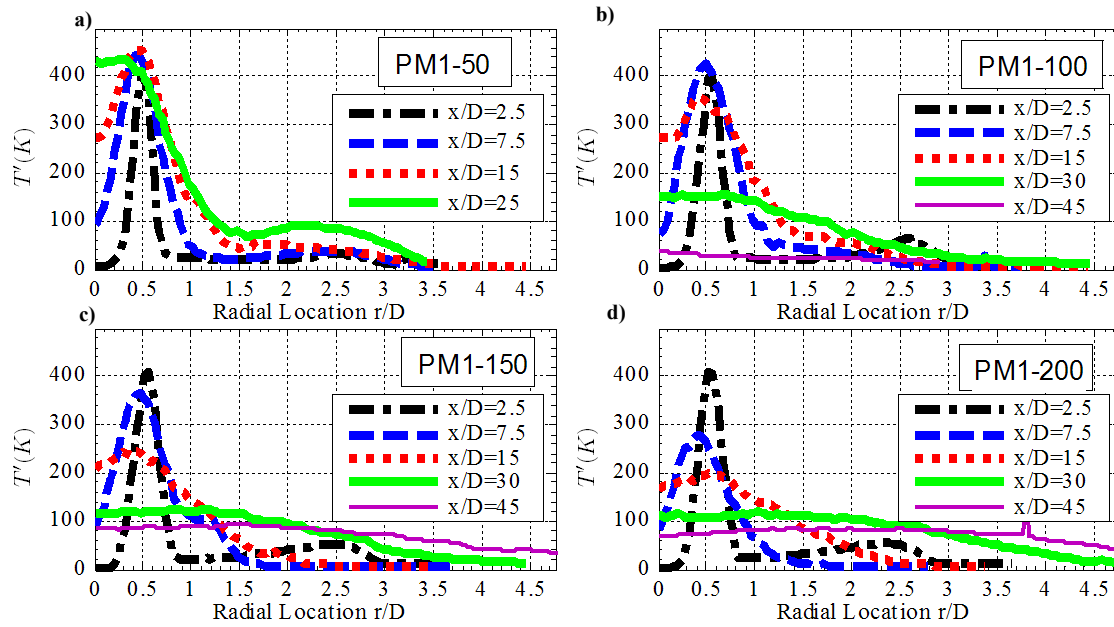


Fig. 6-10. Radial profiles at a number of axial locations of the Reynolds RMS temperature for the four PM1 flames ((a) PM1-50, b).PM1-100, c) PM1-150 and PM1-200).

6.3.2 Scalar Profiles

For premixed combustion of fresh reactants vs. hot products the difference between the non-reacting mixing line and the unstrained laminar flame in a plot of any major species vs. temperature is very small. In fact this difference is so small that it is not possible to discern using the measurements reported here as the noise levels although relatively small are larger than this difference. This essentially means that the trends displayed by any of the major species will follow temperature quite well. This is demonstrated by Fig. 6-11a)-d) where the radial profiles of Reynolds mean CO_2 mass fraction are presented. Essentially the same trends and information as those found for the mean temperature reported in Fig. 6-9 are found in Fig. 6-11. For this reason further radial profiles of the

major species are not presented here but are presented in appendix C for reference purposes.

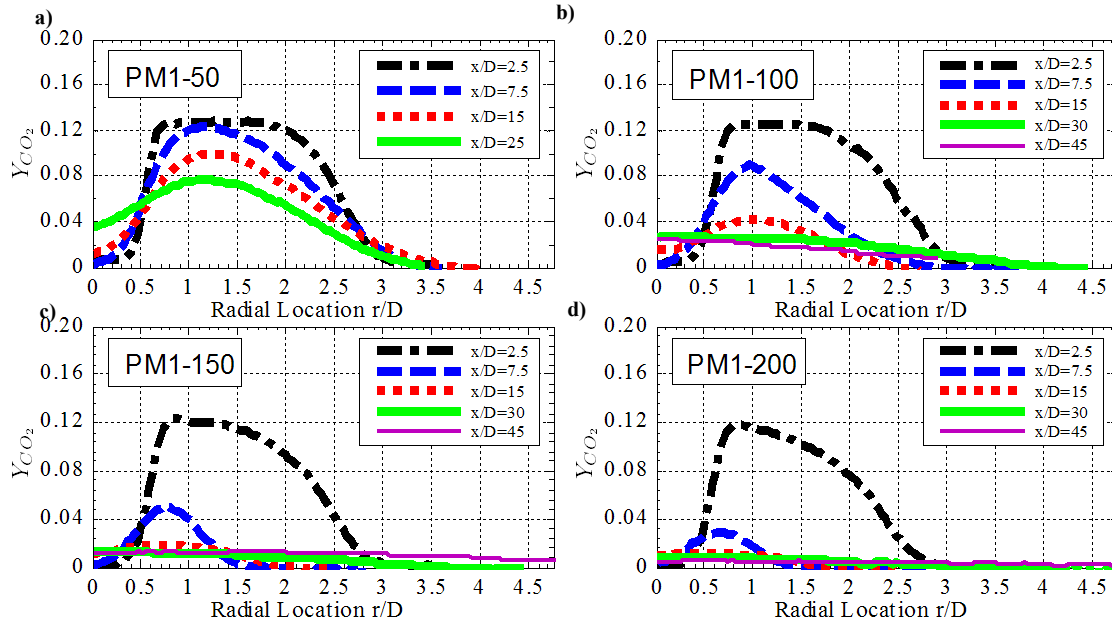


Fig. 6-11. Radial profiles at a number of axial locations of the Reynolds mean CO_2 mass fraction for the four PM1 flames ((a) PM1-50, b).PM1-100, c) PM1-150 and PM1-200).

6.3.3 Mixture Fraction Profiles

Due to the multi-species nature of the presented measurements, conserved scalar mixture fractions for the pilot (ξ_{pilot}), coflow (ξ_{coflow}) and central jet (ξ_{jet}) based on the elemental mass fractions originating from the respective streams may be defined. Making the assumption of unity Lewis number, the equations governing the three mixture fractions for the three stream mixing problem may be implicitly expressed by Eqs.(6.1)-(6.5).

$$Z_C = \xi_1 Z_{C,1} + \xi_2 Z_{C,2} + \xi_3 Z_{C,3} \quad (6.1)$$

$$Z_H = \xi_1 Z_{H,1} + \xi_2 Z_{H,2} + \xi_3 Z_{H,3} \quad (6.2)$$

$$Z_O = \xi_1 Z_{O,1} + \xi_2 Z_{O,2} + \xi_3 Z_{O,3} \quad (6.3)$$

$$Z_N = \xi_1 Z_{N,1} + \xi_2 Z_{N,2} + \xi_3 Z_{N,3} \quad (6.4)$$

$$\xi_1 + \xi_2 + \xi_3 = 1 \quad (6.5)$$

Where Z_i ($i = C, H, N$ or O) is the elemental mass fraction that can be calculated at each point based on the Raman measurements of the major species. ξ_j ($j=1,2,3$) is the mixture fraction of the respective stream, where the arbitrary assignment has been made $\xi_1 = \xi_{\text{Jet}}$, $\xi_2 = \xi_{\text{Pilot}}$ and $\xi_3 = \xi_{\text{Coflow}}$. The constants Z_{ij} are the elemental mass fractions at the exit plane for each of the three streams and are known constants for each experiment.

To solve this system of five equations in three unknowns a least squares method or a reduction in the number of equations is required. Molecular oxygen (O_2) is the most difficult to deal with in terms of the Raman corrections due to the strong sensitivity of the cross talk with CO_2 to temperature and beam steering, thus the atomic oxygen mass fraction is a candidate to be dropped from Eq. (6.3). Molecular nitrogen (N_2) although featuring in large concentrations in all streams has a poor dynamic range due to near identical mass fraction of N_2 in all streams and can be considered another candidate to be dropped from Eq. (6.1). The $Z_{C,3}$ term in Eq. (6.1) represents the elemental carbon mass fraction in the hydrogen-air hot coflow at the exit plane, this term is zero for all cases examined. Historically for the two-stream mixture fraction problem in non-premixed hydrocarbon flames the oxygen terms have been dropped so there is no conflict with previous methods if it is dropped. Neglecting the atomic oxygen and nitrogen terms leaves three equations in the three unknown mixture fraction variables. Solving these three equations results in Eqs. (6.6)-(6.8).

$$\xi_1 = \frac{Z_C(Z_{H,3} - Z_{H,2}) + Z_{C,2}(Z_H - Z_{H,3})}{Z_{C,1}(Z_{H,3} - Z_{H,2}) + Z_{C,2}(Z_{H,1} - Z_{H,3})} \quad (6.6)$$

$$\xi_2 = \frac{Z_C(Z_{H,1} - Z_{H,3}) + Z_{C,1}(Z_{H,3} - Z_H)}{Z_{C,1}(Z_{H,3} - Z_{H,2}) + Z_{C,2}(Z_{H,1} - Z_{H,3})} \quad (6.7)$$

$$\xi_3 = \frac{Z_C(Z_{H,2} - Z_{H,1}) + Z_{C,1}(Z_H - Z_{H,2}) + Z_{C,2}(Z_{H,1} - Z_H)}{Z_{C,1}(Z_{H,3} - Z_{H,2}) + Z_{C,2}(Z_{H,1} - Z_{H,3})} \quad (6.8)$$

Example values for the constants Z_{ij} for a hydrogen-air hot coflow temperature of 1500K with $\Phi=0.43$, a stoichiometric methane-air pilot and a $\Phi=0.5$ methane-air central jet are given in Table 6-3.

Table 6-3. Elemental mass fractions for each of the three streams at the exit plane for all of the flames examined.

	C	H	O	N
1 (Jet)	0.02127	0.00709	0.2263	0.74534
2 (Pilot)	0.041272	0.013767	0.220172	0.72478
3 (Coflow)	0	0.012373	0.230087	0.75754

Radial profiles of the Reynolds mean and RMS mixture fractions for the coflow, pilot and central jet are presented in Fig. 6-12-Fig. 6-17 for the PM1 flame series. These figures complement many of the conclusions derived from the radial temperature profiles presented in Fig. 6-9 and Fig. 6-10.

For the PM1-50 flame it is clear from the measured values of $\bar{\xi}_{\text{coflow}}$ and $\bar{\xi}_{\text{pilot}}$ that in the central jet flame brush ($r/D < 0.5$) there is a low degree of entrainment of coflow and pilot products for all axial stations. This is due to the low shear rate at the interface between the pilot and coflow exhaust products. When the very slow mixing rate between the pilot and the coflow is combined with the relatively low entrainment rate of the central jet in the PM1-50 flame the resultant mean coflow mixture fraction at $r/D=0.5$, $x/D=25$ is only 0.1. This indicates from a mixture fraction perspective that the central jet combustion process has minimal interaction with the hot coflow.

Entrainment and mixing of coflow products into the central jet flame brush is a significant feature of the PM1-100,150 and 200 flames. For the PM1-150 flame on the centreline at $x/D=30$, which is in the middle of the identified extinction zone, $\bar{\xi}_{\text{coflow}}$ is 0.42 and in the re-ignition region at $x/D=45$, $\bar{\xi}_{\text{coflow}}$ increases to 0.65, this shows that a large fraction of coflow fluid is entrained into the central jet flame brush. Even though it is evident that significant entrainment of coflow fluid occurs at $x/D=30$, the extinction region is not caused by reaction dilution or quenching effects from the entrained coflow fluid. The coflow gas that is entrained is close to 1500K, the adiabatic temperature of the central jet, effectively eliminating the reaction quenching effects that would occur if cold ambient air were being entrained. Secondly the coflow product gases are at a similar equivalence ratio to the central jet, thus mixing between the two streams does not cause significant “leaning out” of the central jet mixture, but rather the mixing process should be considered as mixing with exhaust products.

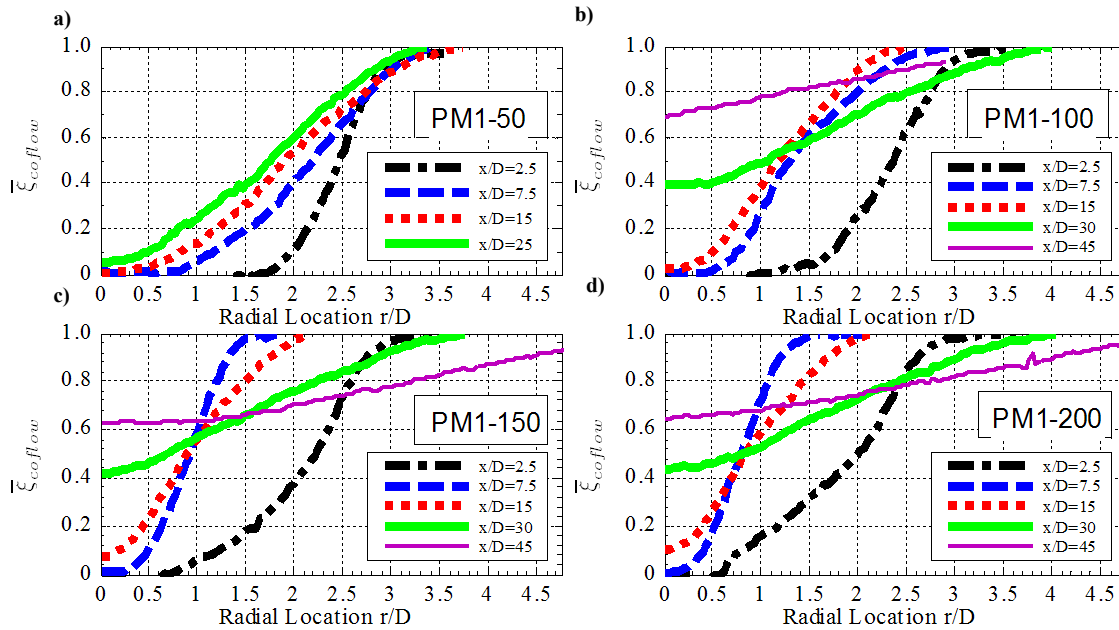


Fig. 6-12. Radial profiles at a number of axial locations of the Reynolds mean coflow mixture fraction for the four PM1 flames ((a) PM1-50, b).PM1-100, c) PM1-150 and PM1-200).

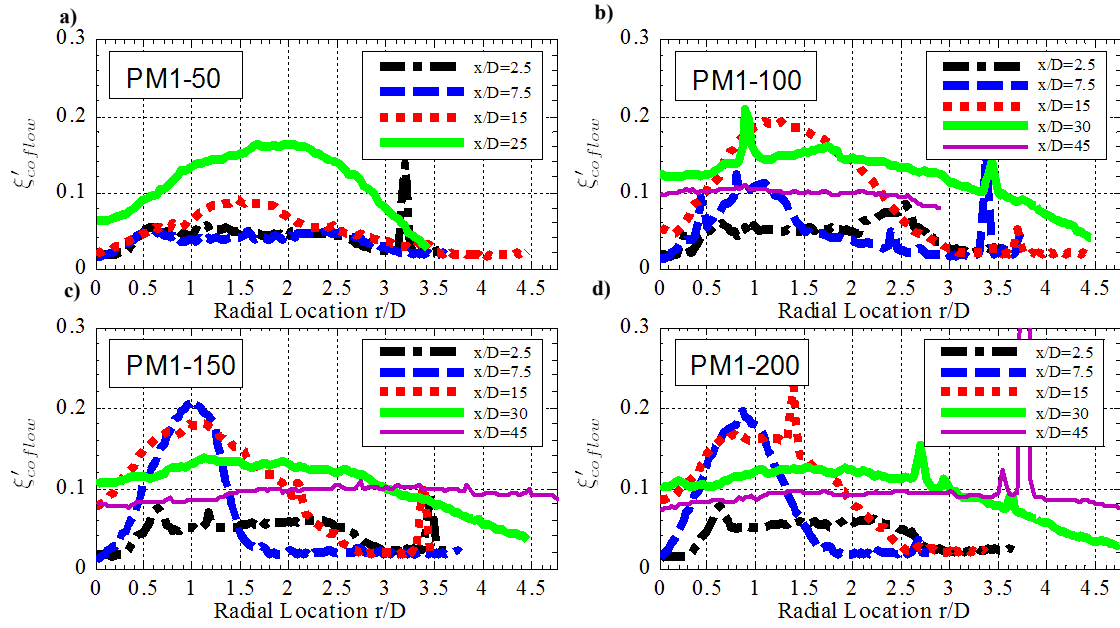


Fig. 6-13. Radial profiles at a number of axial locations of the Reynolds RMS coflow mixture fraction for the four PM1 flames ((a) PM1-50, b).PM1-100, c) PM1-150 and PM1-200).

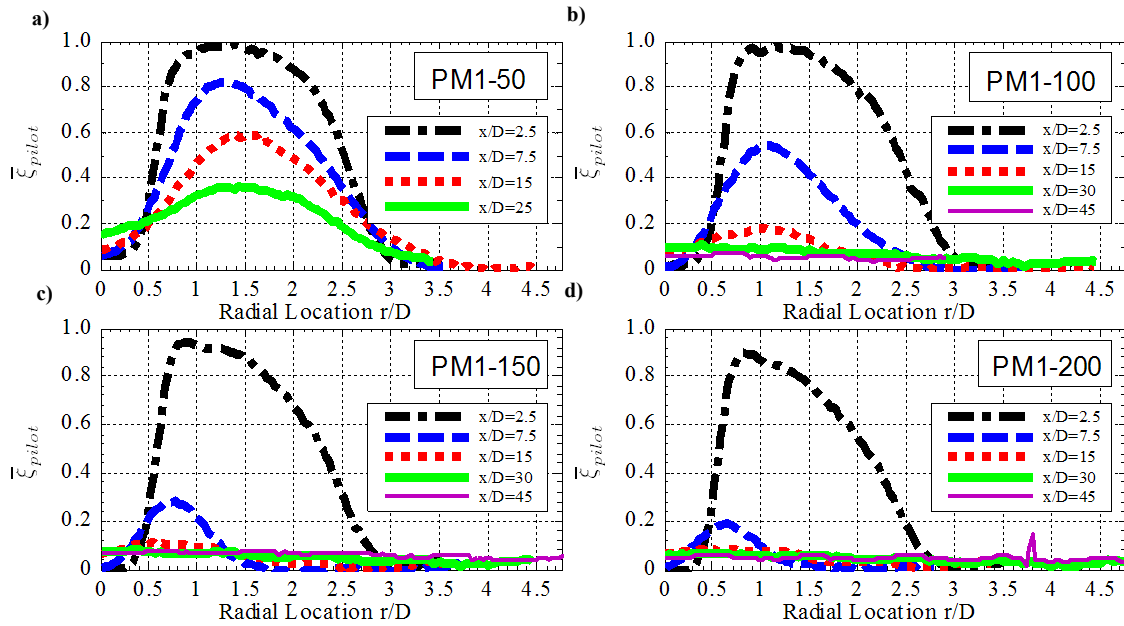


Fig. 6-14. Radial profiles at a number of axial locations of the Reynolds mean pilot mixture fraction for the four PM1 flames ((a) PM1-50, b).PM1-100, c) PM1-150 and PM1-200).

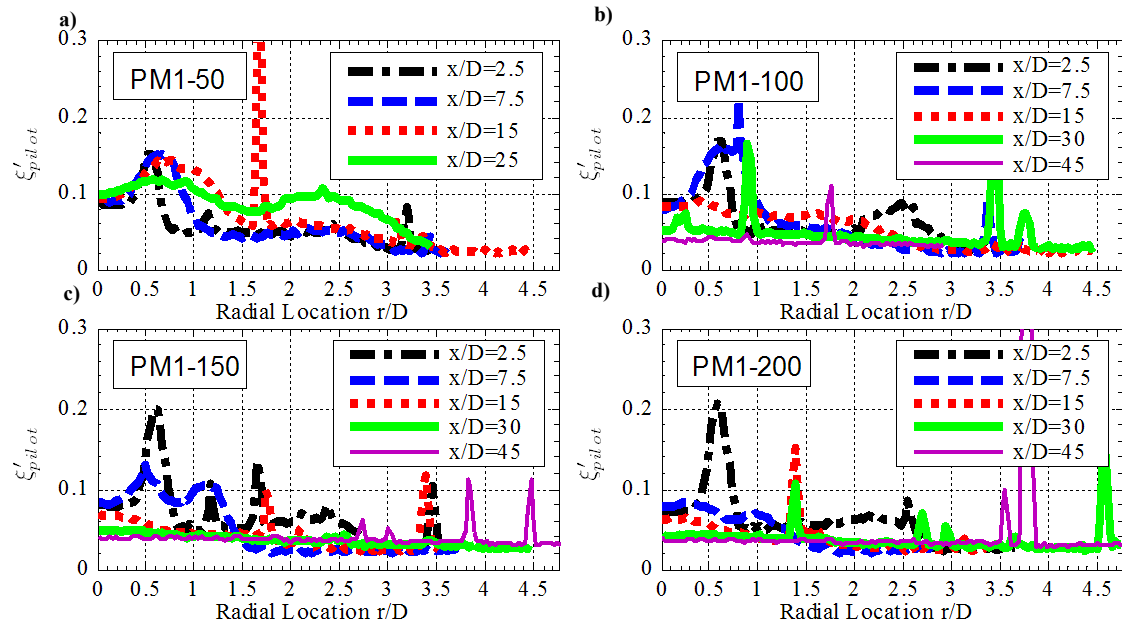


Fig. 6-15. Radial profiles at a number of axial locations of the Reynolds RMS pilot mixture fraction for the four PM1 flames ((a) PM1-50, b).PM1-100, c) PM1-150 and PM1-200).

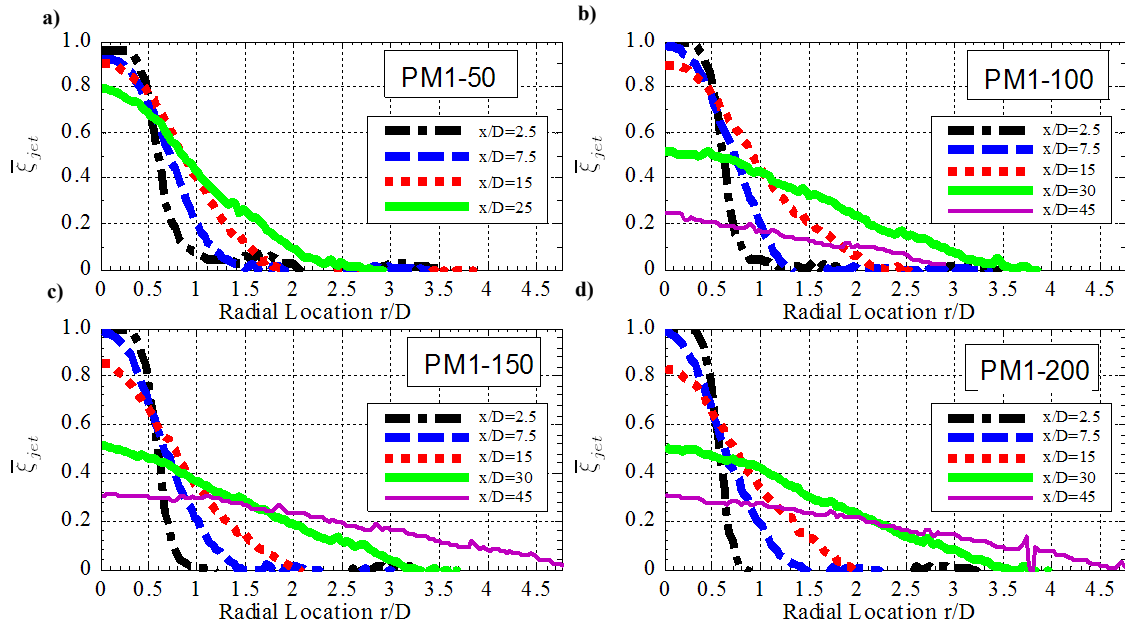


Fig. 6-16. Radial profiles at a number of axial locations of the Reynolds mean central jet mixture fraction for the four PM1 flames ((a) PM1-50, b).PM1-100, c) PM1-150 and PM1-200).

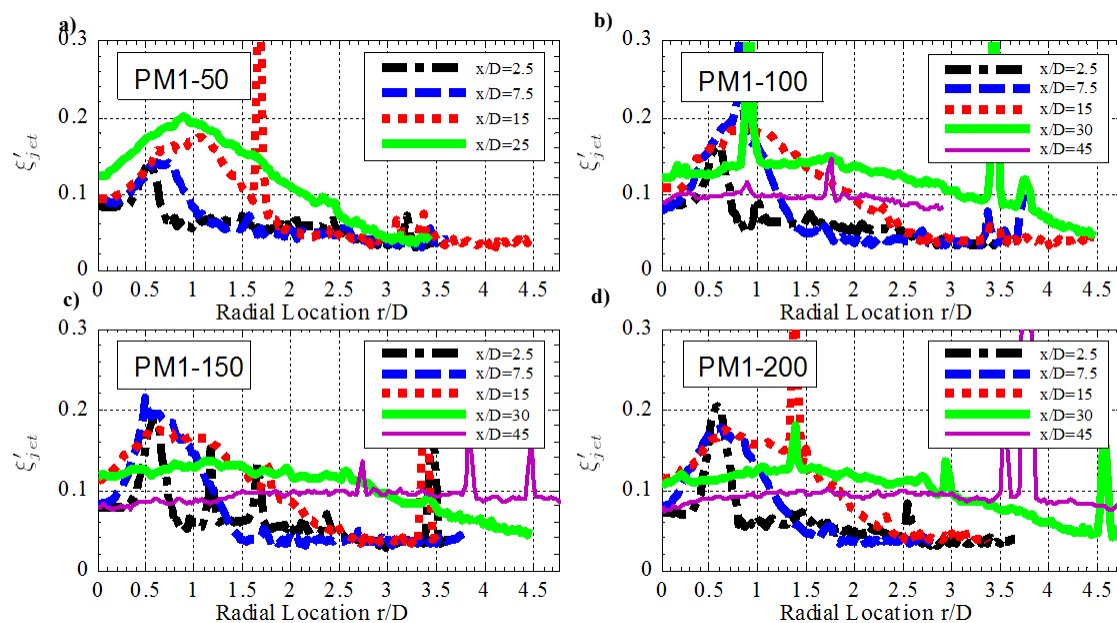


Fig. 6-17. Radial profiles at a number of axial locations of Reynolds RMS central jet mixture fraction for the four PM1 flames.

CHAPTER 7 PJB 2D IMAGING RESULTS

The structure of four flames from the PM1 flame series has been examined through the use of a number of experimental techniques such as: mean chemiluminescence images and LDV in Chapter 3, a variety of planar imaging techniques in Chapter 5 and line Raman-Rayleigh measurements in Chapter 6. These results highlight the large variation of the flame structure both as a function of axial location for a single flame and the significant differences between flames in the PM1 flame series. In order to delineate the effect of the pilot on the structure of the PM1 flame series, the PJB is introduced in Chapter 3 as a complementary experimental platform to the PPJB. It is shown in Chapter 3 that the stoichiometric pilot is crucial to obtain an initial ignition region for PPJB flames, none of the PJB flames feature an initial ignition region for the same jet and coflow conditions as the PM1 flames in the PPJB. By not having a stoichiometric pilot the PJB flames feature a chemiluminescent mean flame brush that is lifted from the nozzle exit, the downstream position of which increases with increasing jet velocity.

The lifted premixed flames produced by the PJB are deserving of study in their own right within the context of turbulent premixed combustion, this is particularly so because no other published paper to this author's knowledge has examined the configuration of lifted turbulent purely premixed flames supported by hot combustion products. It is not the aim in this thesis to study the PJB flames in the broad context of turbulent premixed combustion, but rather in the context of the finite-rate chemistry and the PPJB flames. The PJB flames are a very valuable aid in isolating certain phenomena to further understanding relevant concepts and ideas pertinent to the PPJB and finite-rate chemistry

effects. The flames of the PJB are lifted in nature, however unlike normal lifted non-premixed flames the fresh reactants start to mix with and strain against hot combustion products immediately at the nozzle exit. The position of the flame brush should be governed by an ignition delay time (thus a finite-rate chemistry effect) rather than being purely limited by mixing as with the lifted non-premixed case. Mixing will of course interact and modify the lift-off height however it is not a necessity for a flame to occur as with the non-premixed case. The comparative structure of the PJB flames upstream from the mean flame brush and inside the mean flame brush is of particular interest in light of the flame structure results obtained in Chapter 5 for the PPJB flames. The PM1-150 and PM1-200 flames in the PPJB feature a re-ignition region downstream from the extinction region; it is of interest if similarities or differences can be found between the flame structure in the re-ignition region of relevant PPJB flames and the flame base of the PJB flames.

Based on these motivations, it is sufficient to study two PJB flames denoted NPM2-40 and NPM2-200, a low lift-off and a high lift-off flame respectively. Both of the selected flames feature constant coflow temperatures and jet equivalence ratios, the jet Reynolds number is the only parameter that is changed. The most immediately relevant experimental technique to qualitatively and quantitatively study the mean and instantaneous PJB flame structure is proposed to be simultaneous planar imaging of temperature and OH, in a similar configuration and being complementary to the high resolution Rayleigh OH imaging experiment in Chapter 5, Section 5.2. OH will be a valuable indicator of the radical pool before the mean flame front; also the levels of OH concentration inside the mean flame brush will be of interest. Temperature measurements using Rayleigh scattering are of interest to determine the instantaneous and mean flame spatial structure relative to those of the PPJB in Chapter 5, Section 5.2. The temperature measurements must be of high resolution as there is particular interest in how the conditional PDF of the instantaneous flame front thickness changes as a function of downstream location for a single flame and also relative to different flame conditions. Of particular interest is how the flame structure for the high velocity NPM2-200 case near the location of the mean flame brush stabilisation point compares with the re-ignition

region in both the PM1-150 flame and the PM1-200 flames. This comparison is significant because at this location the advection time scales and turbulence intensity are of a similar magnitude and based on the mean chemiluminescence at this region a rapid axial increase in reaction rate occurs.

An overview of the experimental setup and the flame conditions examined in this Chapter is presented in Section 7.1, followed by an outline of the data reduction method in Section 7.2. The experimental results and a discussion in terms of the flame structure is presented in Section 7.3, however just as in Chapters 5 and 6 detailed discussion of the results in terms of finite-rate chemistry effects is left until Chapter 8. Some of the material presented in this Chapter has been previously published by Dunn *et al.* [298].

7.1 Experimental Setup

In order to investigate the instantaneous temperature and local radical pool concentrations, simultaneous Rayleigh scattering and OH Laser Induced Fluorescence (LIF) has been conducted. An overview of the entire laser diagnostic experimental setup is given in Fig. 7-1. The Rayleigh scattering signal is generated by the frequency doubled output of a Q-switched Nd:YAG laser (Spectra Physics Pro 350) at 532nm, yielding 1.33 J at the probe volume. The Rayleigh beam is focused by a 300mm focal length fused silica lens into a sheet 13mm high. The laser sheet thickness of the Rayleigh beam is measured by rotating the final cylindrical lens by 90 degrees and subsequently imaging the flat beam via Rayleigh scattering. By fitting a Gaussian function to the resultant beam profile at the focal point results in a full width half maximum (FWHM) measurement of the beam thickness of $80 \pm 12\mu\text{m}$.

The OH LIF is generated by the frequency doubled output of a pulsed Nd:YAG laser (Spectra Physics Pro 350) pumping a Syrah dye laser using Rhodamine 6G in ethanol. The fundamental of the dye laser is subsequently doubled to produce an Ultra Violet

(UV) laser beam at 283.01nm for $A^2\Sigma^+-X^2\Pi$ (1,0) excitation of OH, predominately pumping the $Q_1(6)$ line. The UV energy at the probe volume is measured to be 11mJ with a pyroelectric joule meter. The FWHM line width of the fundamental of the dye laser was measured to be 0.075cm^{-1} , this measurement was made by passing a weak reflection of the dye laser beam through a high finesse etalon and expanding the resultant diffraction pattern through onto a white screen. The diffraction pattern was subsequently imaged and the intensity of the light in each circular band being proportional to the energy in the particular spectral band. This measurement of the bandwidth was also confirmed in the UV (although with a greater uncertainty) by deconvolution of a spectral scan over the spectrally isolated $P_1(1)$ line to be $0.15\pm 0.03\text{cm}^{-1}$. The UV beam is expanded and passed through a spatial modulator to improve beam quality, with the focal length being adjusted so as to make the beam waist at the probe volume coincide with the 532nm beam waist. The UV beam is formed into a sheet 12mm in height with an $80\mu\text{m}$ FWHM sheet thickness at the waist. The UV beam waist is measured by again rotating the final cylindrical lens and imaging the LIF produced from acetone vapour.

The 532nm Rayleigh scattering signal is collected at 90° by an 85mm f/1.4 lens, imaging the Rayleigh signal directly onto a Charge Coupled Device camera at a magnification of 0.20. The inter-line transfer CCD camera for the Rayleigh signal collection (LaVision FlowMaster 3S) has 1280×1024 pixels with individual pixel sizes of $6.7\mu\text{m} \times 6.7\mu\text{m}$ and a quantum efficiency of 36% at 532nm. Flame luminosity and OH LIF signal are totally suppressed from the Rayleigh camera by a 532nm 10nm FWHM interference filter combined with a 500ns camera gate time. On chip binning of 2x2 is selected to be the best compromise between spatial resolution and signal to noise ratio (SNR). This gives an effective probe volume to projected super-pixel pixel size of $34\mu\text{m}$. The single shot SNR of the Rayleigh imaging system prior to image smoothing is found to be 40, measured in a uniform field of 298K filtered air.

The Rayleigh imaging system Step Response Function (SRF) is measured using the scanning knife edge method outlined by Wang and Clemens [248] and references

contained within. From the SRF the Line Spread Function (LSF) is calculated and a FWHM of $40\mu\text{m}$ is predicted. Utilising the analysis of Wang and Clemens [248] with the computed LSF resolution, dissipation structures with measured widths greater than $134\mu\text{m}$ an error contribution of less than 10% on the peak measured dissipation value can be attributed due to the finite spatial resolution of the imaging system.

The OH LIF collection system is based on a lens coupled intensified CCD system. Flame luminosity, 532nm and 283nm Rayleigh scattering is rejected to sub-pixel count levels by two 2mm thick UG11 and a single 2mm thick WG305 Schott coloured glass filters combined with a $2\mu\text{s}$ gate time. A 105mm f/4.5 UV lens is coupled to an 18mm 2nd generation UV sensitive intensifier and subsequently lens coupled by two 50mm f/1.2 lenses to a CCD camera. The LSF for the OH collection system is found to be $127\mu\text{m}$ FWHM; this value of the LSF is much larger than the Rayleigh system due to the inclusion of the intensifier.

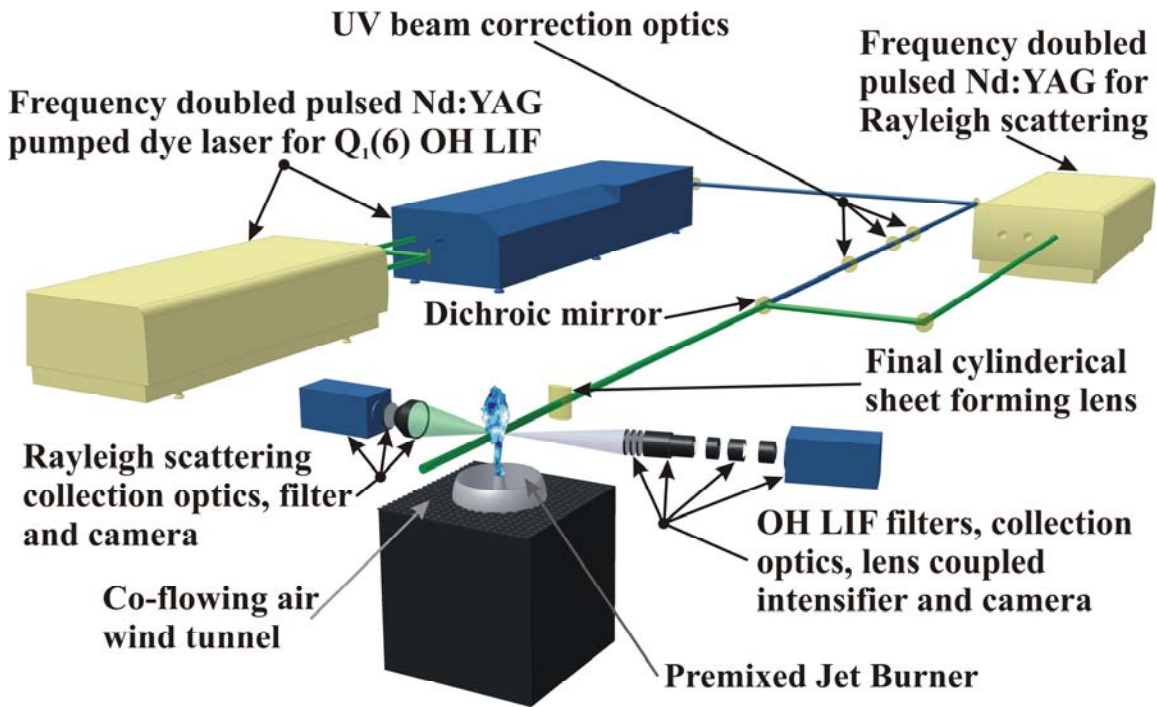


Fig. 7-1. Experimental schematic showing lasers, laser beam paths, laser and collection optics, imaging collection system and the PJB.

7.2 Data Reduction

To determine the sensitivity of the Rayleigh cross section and OH quenching rate to composition and temperature variations, laminar flame simulations are conducted for freely propagating, opposed flow and mixing limit using the Cantera code developed by Goodwin [177]. It is found to be advantageous in terms of data processing to cast the Rayleigh cross section and quenching rate dependencies with respect to the normalised Rayleigh signal as opposed to temperature. A maximum error of 2% is predicted for the Rayleigh cross section based on these calculations; however as can be seen from Fig. 7-2 the average error in cross section over the entire temperature range is smaller than this. The Rayleigh images were converted to temperature assuming an ideal gas and corrected for background reflections and normalised using the scheme developed by Dunn *et al.* [241]. Although the Rayleigh cross section error the actual temperature measurement uncertainty is larger than 2% particularly at high temperatures, a preliminary estimate if the temperature uncertainty at 1600K is 6% considering effects such as readout noise, shot noise, errors in beam sheet correction and cross section error.

The OH LIF quenching rate variation with temperature and composition follows a similar trend for data spread and uncertainty than the Rayleigh cross section does, with a maximum error of 2%. The OH electronic and vibrational energy transfer rates and calculation method were taken from Dunn *et al.* [241] and references contained within. Due to the low OH mole fractions that occur in lean premixed combustion, the OH LIF SNR can typically be very low if linear LIF techniques and laser sheet thickness less than 250 μ m are employed. To obtain an acceptable SNR for the OH PLIF a non-linear OH LIF regime has been employed in the experiment, based on a further development of the quantification method presented in Dunn *et al.* [175] the non-linear OH PLIF signal has been quantified using the technique presented by Dunn and Masri [242]. Using this

quantification method the collected fluorescence F can be related to the OH concentration (n_{OH}) by Eq. (7.1).

$$F = \eta n_{OH} \frac{4\tau_1 \Delta z \Delta t}{\tau_2^2} \left[\tau_2 + \frac{\tau_3}{I_v^0} \text{dilog} \left(-\frac{I_v^0 \tau_2}{\tau_3} \right) \right] \quad (7.1)$$

The simplifying parameters in Eq. (7.1) τ_1 , τ_2 , and τ_3 involve Einstein coefficients, Boltzmann fraction, and temperature dependant electronic and vibrational transfer rates. The Einstein A_{ji} , B_{ji} and B_{ij} coefficient values necessary for Eq. (7.1) were taken from LIFBASE [213]. Determination of the optical system efficiency η is determined from a calibration in the post flame gasses of a premixed flat flame burner.

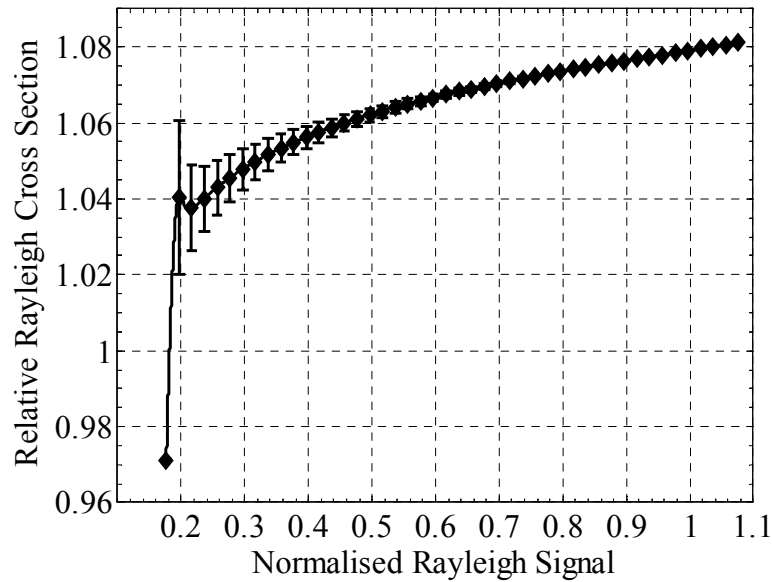


Fig. 7-2. Numerical simulation results for the Rayleigh cross section variation vs. normalised Rayleigh signal. The normalised Rayleigh signal is taken to be the numerically calculated Rayleigh signal divided by the corresponding Rayleigh signal of ambient air. The error bars show the bounds for low strain and high strain rate simulations.

7.3 Results and Discussion

The primary results that are discussed and analysed in this section centre around the images presented in Fig. 7-3 and Fig. 7-4 for the NPM2-40 and NPM2-200 flames respectively. Representative realisations of OH, temperature and temperature gradient are presented in Fig. 7-3 and Fig. 7-4 as well as computed Reynolds mean temperature and OH images. As the NPM2-40 is regarded as a low lift-off flame the analysis of this flame focuses on three axial locations $x/D=5$, 15 and 25 corresponding to pre-lift-off, stabilisation point and in the middle of the flame brush. The high lift-off NPM2-200 flame is examined at $x/D=5$, 25 and 50 with these regions again corresponding to pre-lift-off, stabilisation point and in the middle of the flame brush.

Mean radial profiles of OH for the NPM2-40 and NPM2-200 flames are presented in Fig. 7-5 and Fig. 7-6. Earlier chemiluminescence images in Chapter 3, Fig. 3-8 show that for the NPM2-40 flame the mean flame base initially occurs close to $r/D=5$; Fig. 7-5 as well as Fig. 7-3a show that there is a small increase in the mean OH above the equilibrium levels of OH occurring in the coflow, this indicates that the flame is undergoing some level of reaction at $x/D=5$. Further downstream at $x/D=15$ it is evident from Fig. 7-3b that a reaction zone is present due to the elevated levels of OH, close to the levels found in laminar opposed flow simulations. At $x/D=25$ from Fig. 7-5 the mean temperature profile is close to equilibrium and that super equilibrium levels of OH occur in post flame oxidation zone where slow oxidation reactions limit the rate at which OH is reduced to thermal equilibrium levels. The mean flame luminosity images indicate that the mean flame brush is conical in shape, similar to an elongated Bunsen shape tapering to a tip around $x/D=20-25$. This description ties in well with the results for the mean temperature and OH profiles in Fig. 7-5, with the mean temperature profile at $x/D=25$ indicating a closed mean flame brush.

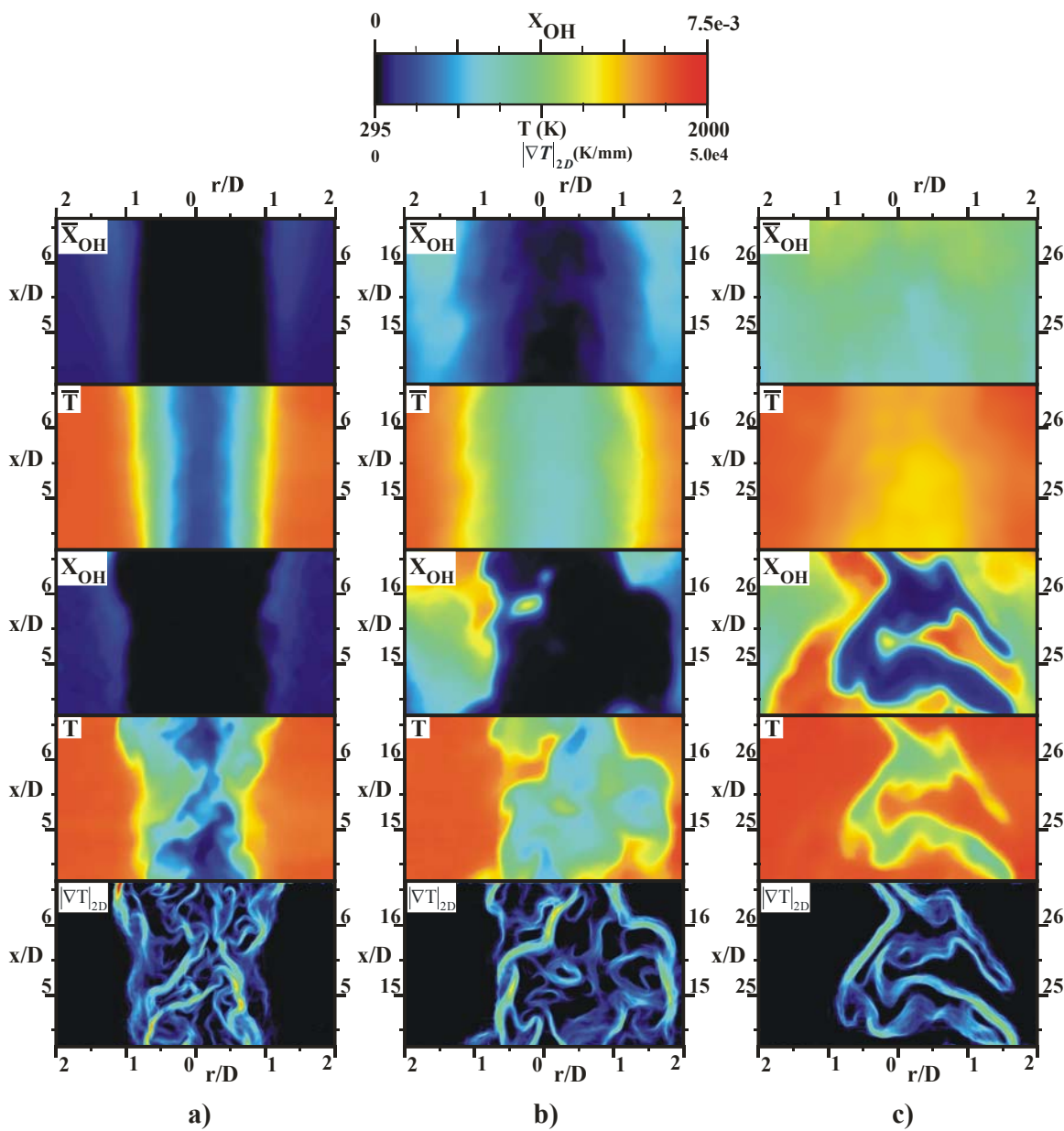


Fig. 7-3. Mean Temperature and OH images combined with a representative instantaneous realisation of temperature, OH and the computed temperature gradient for the NPM2-40 flame a) centred at $x/D=5$ a), $x/D=15$ b) and $x/D=25$ c).

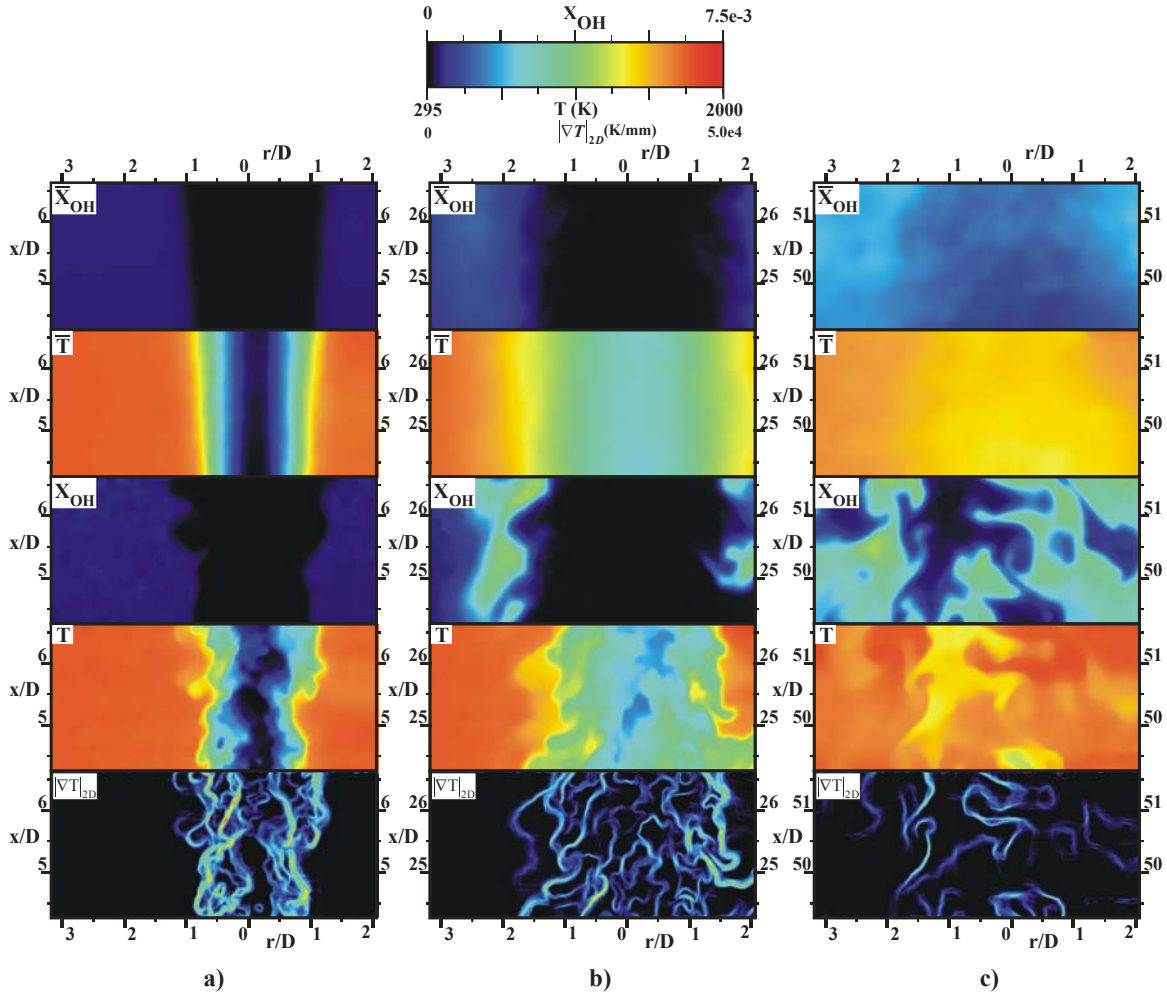


Fig. 7-4. Mean Temperature and OH images combined with a representative instantaneous realisation of temperature, OH and the computed temperature gradient for the NPM2-200 flame a centred at $x/D=5$ a), $x/D=25$ b) and $x/D=50$ c).

For the NPM2-200 there is no indication that any reaction at all is occurring at $x/D=5$, as the mean OH radial profile at this location does not increase above the coflow levels. Instantaneous images of OH at this location backup this finding as only $\sim 4\%$ of the realizations from the large data set could small regions of OH level just above the coflow level are found. The instantaneous realisation presented in Fig. 7-4a) is a representative example of an image in which no OH can be above the coflow levels. Even the few images where regions of OH above the coflow level can be found, the OH magnitude is so small that it is indiscernible using the colour map employed in Fig. 7-4. At $x/D=25$ it is evident from both Fig. 3-8 and Fig. 7-6 that the mean flame brush walls have not

merged like they have at this axial location for the NPM2-40 flame. Fig. 7-4 reveals that the instantaneous flame front undergoes a significant degree of mixing and thickening to the point where large regions of partially reacted gas are present.

The flame structure for the NPM2 is quite unlike what would be expected from the results of a strained laminar premixed flamelets where straining compresses the instantaneous flame front reducing the instantaneous flame front thickness. From the results shown for NPM2-200 flame the conditions are not consistent with laminar flamelets. This is based on the observation that the high central jet velocity in the NPM2-200 produces very high turbulence intensities such that both NPM2 flames would fall into what is classified as the “Distributed Reaction Zone Regime”.

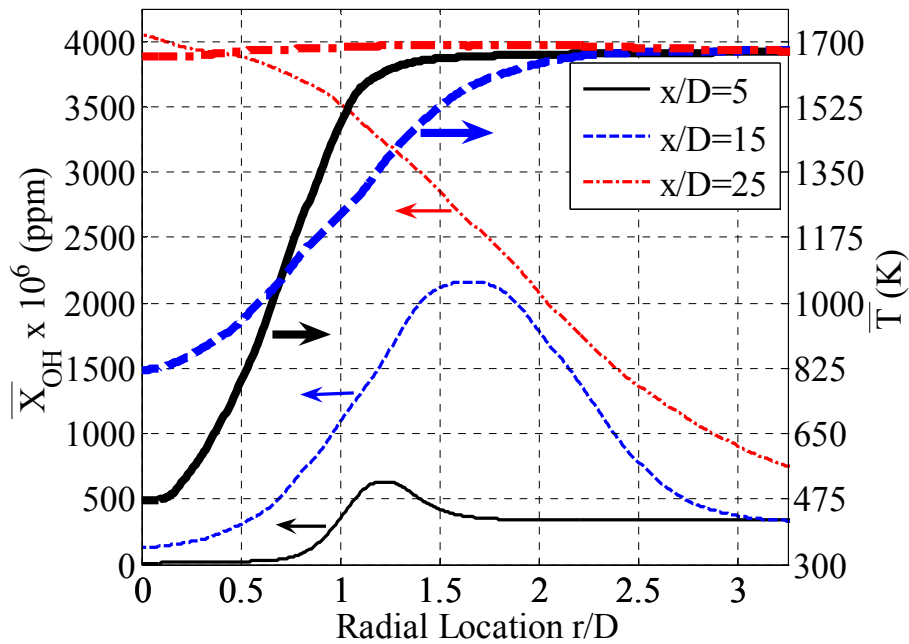


Fig. 7-5. Radial Profiles of the Reynolds mean OH and temperature at $x/D=5, 15$ and 25 for the NPM2-40 flame.

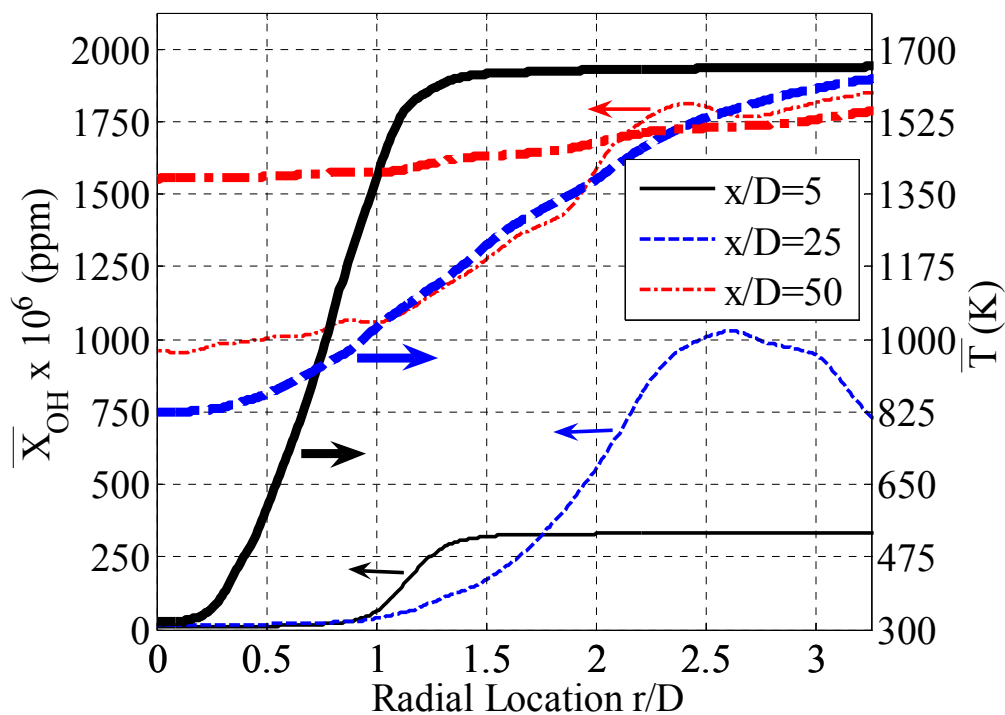


Fig. 7-6. Radial Profiles of the Reynolds mean OH and temperature at $x/D=5$, 25 and 50 for the NPM2-200 flame.

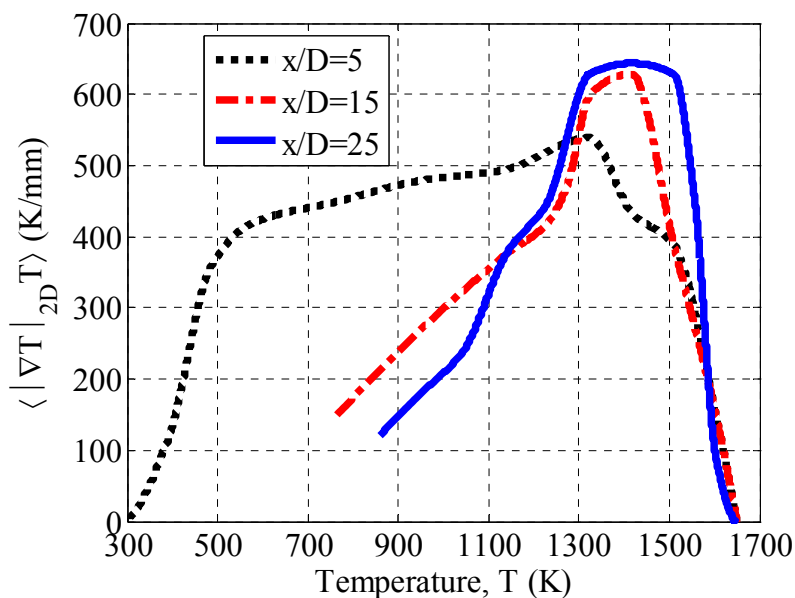


Fig. 7-7. Comparison of the ensemble Reynolds mean 2D temperature gradient conditional on temperature for the NPM2-40 flame computed from images at $x/D=5$, 15 and 25.

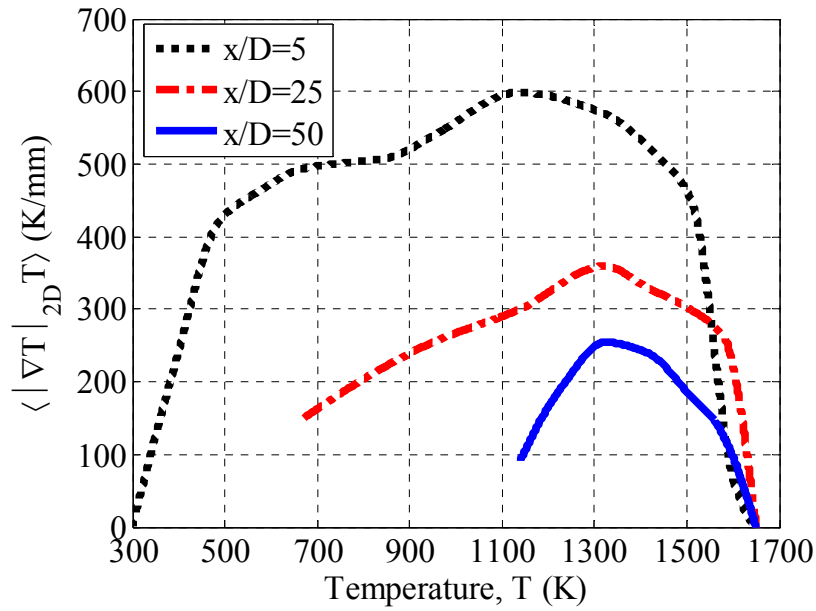


Fig. 7-8. Comparison of the ensemble Reynolds mean 2D temperature gradient conditional on temperature for the NPM2-200 flame computed from images at $x/D=5$, 25 and 50.

Statistically validating the idea of increased thickening of the instantaneous flame front beyond the single realisations presented in Fig. 7-3 and Fig. 7-4 are the plots of mean 2D temperature gradients conditional on temperature as presented in Fig. 7-7 and Fig. 7-8. The simulated unstrained laminar premixed gradient peaks at close to 1400 K/mm at 1200K, both the NPM2 flames have mean temperature gradients that are well below this value, by at least by a factor of 2. Due to the nature of the geometry and previous investigations of free jets into a hot coflow Dunn *et al.* [175] it is reasonable to expect that the jet turbulence intensity will decay with axial location. From Fig. 7-7 the increase in the mean temperature gradient with axial location at $x/D=15$ and 25 from the value at $x/D=5$ can possibly be attributed to the decrease in turbulence intensity with axial location found in Chapter 3, Fig. 3-9 allowing less interaction and embedding of turbulence in the flame front and flame reaction to progress at a rate closer to the laminar value. This explanation, it would seem, is contradicted by the results for the NPM2-200 in Fig. 7-8, here the conditional mean temperature gradient decreases with increasing axial location. It is proposed that the continued decrease in conditional mean temperature gradient is due to the inherently high turbulence intensities reported in Chapter 3, Fig.

3-10 for the NPM2-200 flame that persist to continue finite rate chemistry effects well down stream. As an additional effect, the chemical time scale will also increase as a function of downstream location due to entrainment and dilution with hot combustion products.

CHAPTER 8 FINITE RATE CHEMISTRY

In this Chapter finite-rate chemistry or the turbulence chemistry interaction is examined with respect to the experimental results presented in Chapters 3, 5, 6 and 7. In Chapter 5 through the use of 2D imaging techniques the structure of the flame has been examined. In Section 5.1 an increase in the instantaneous 2D flame thickness with increased Reynolds number for the PM flame series was qualitatively observed. The qualitative observations of increased flame thickness have been quantified in Section 5.2 by examining the conditional mean temperature gradient variation for different flames. The quantitative results in Section 5.2 confirms that statistically, the PM1 flame series displays a decrease in the conditional mean 2D temperature gradient as a function of increasing Reynolds number.

In this Chapter, a number of experimental measurands are used to further understand the interaction between turbulence chemistry or otherwise termed finite-rate chemistry effects. The interaction of turbulence on the flame front in terms of the spatial temperature structure is quantitatively examined in Section 8.1 through the use of the temperature gradient, primarily through the use of the temperature gradient derived from the cross-plane corrected Sandia line imaging data essentially a 3D measurement of flame thickness. In Section 8.2 minor species are examined conditional on temperature and then as product with other simultaneously measured minor species such as $[\text{CO}][\text{OH}]$ in Section 8.2.3. The conditional value of the quantity $[\text{CO}][\text{OH}]$ is proportional to the net CO_2 production rate for certain temperature ranges. The product of $[\text{CH}_2\text{O}][\text{OH}]$ is used in Section 8.2.4 as an indicator of the net reaction rate and heat release. A discussion the

characterisation of the flames examined in terms of premixed combustion regime diagrams is examined in Section 8.3.

8.1 Flame Thickness

In order to demonstrate the mean degree of instantaneous flame thickening, the three-dimensional (3D) temperature gradient is examined Fig. 8-1 and Fig. 8-2. By using the two OH PLIF cross-plane sheets, in a similar manner to Barlow and Karpetsis [294], the one dimensional Raman-Rayleigh-LIF line measurement have been corrected flame orientation according to Eq. (8.1). The derivation of Eq. (8.1) and further discussion of the cross plane correction to scalar thicknesses, gradients and dissipation measurements is discussed in Appendix A.

$$\Delta T_{3D} = \Delta T_{1D} \sqrt{1 + \frac{4}{3} \left(\frac{n_{gv} + n_{fu}}{n_{fx} + n_{gx}} \right)^2 + 4 \left(\frac{n_{fu} - n_{gv}}{n_{fx} + n_{gx}} \right)^2} \quad (8.1)$$

The application of the cross plane correction minimises any ambiguities that can potentially arise due to variations in the flame orientation PDF that could occur as a function of axial location or increased central jet velocity. The results presented in Fig. 8-1 are conditioned at a temperature of $\xi=1200\text{K}$ and presented function of axial position for all of the PM1 flames. By presenting the conditional mean value at only one temperature, no information can be inferred on how the shape of the conditional temperature gradient changes with axial position or increased turbulence levels. This information is left to be presented in Fig. 8-2. However, Fig. 8-1 succinctly displays how a representative value of $\langle \nabla T_{3D} | \xi \rangle$ varies with axial distance and over different flames, hence turbulence levels.

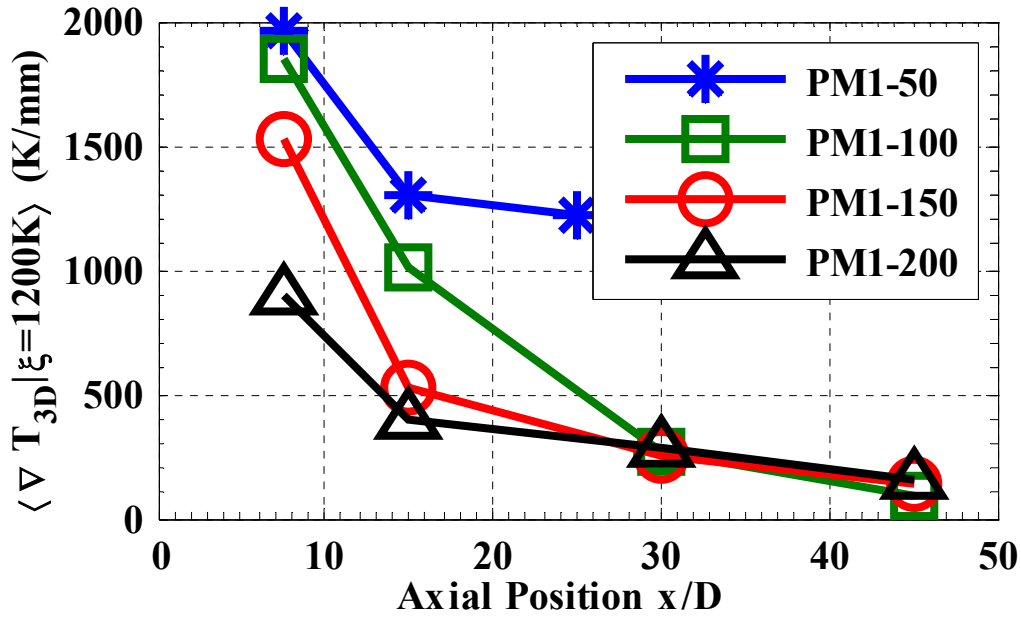


Fig. 8-1. Conditional mean temperature gradients taken at $\xi=1200K$ for the PM1 flame series at a number of axial stations.

From Fig. 8-1 it can be seen that all of the PM1 flame series exhibit a monotonic decrease in $\langle \nabla T_{3D} |_{\xi} \rangle$ with increasing values of x/D . Furthermore, a trend of decreasing values of $\langle \nabla T_{3D} |_{\xi} \rangle$ with increased central jet velocity particularly at $x/D=7.5$ and 15 is observed. Imaging results reported in Chapter 5 and by Dunn *et al.* [175] have indicated that the instantaneous flame front in the PM1-50 flame does not experience a large degree of thickening and remains relatively thin and step like in nature. This is in contrast to the PM1-100, PM150 and PM1-200 flames where thickening of the instantaneous flame front can be observed with increasing x/D and increasing central jet velocities. This picture corresponds well with the results in Fig. 8-1 as the PM1-50 does exhibit some axial decay in $\langle \nabla T_{3D} |_{\xi} \rangle$ but the absolute value at $x/D=25$ is approximately a factor three times larger than the other three flames at $x/D=30$. From freely propagating laminar flame calculations a temperature gradient of 580 K/mm is predicted at 1200K, with increasing strain rates in the laminar opposed flow configuration this value only increases, as seen in Fig. 5-12. It is significant to note that $\langle \nabla T_{3D} |_{\xi} \rangle$ is less than 580K/mm at $x/D \geq 15$ for the

PM1-150 and PM1-200 flames corresponding to the region where the onset of extinction is hypothesized to occur. No increase in the value of $\langle \nabla T_{3D} | \xi \rangle$ is observed for the PM1-150 or PM1-200 flames at $x/D \geq 45$ where re-ignition is hypothesized to occur.

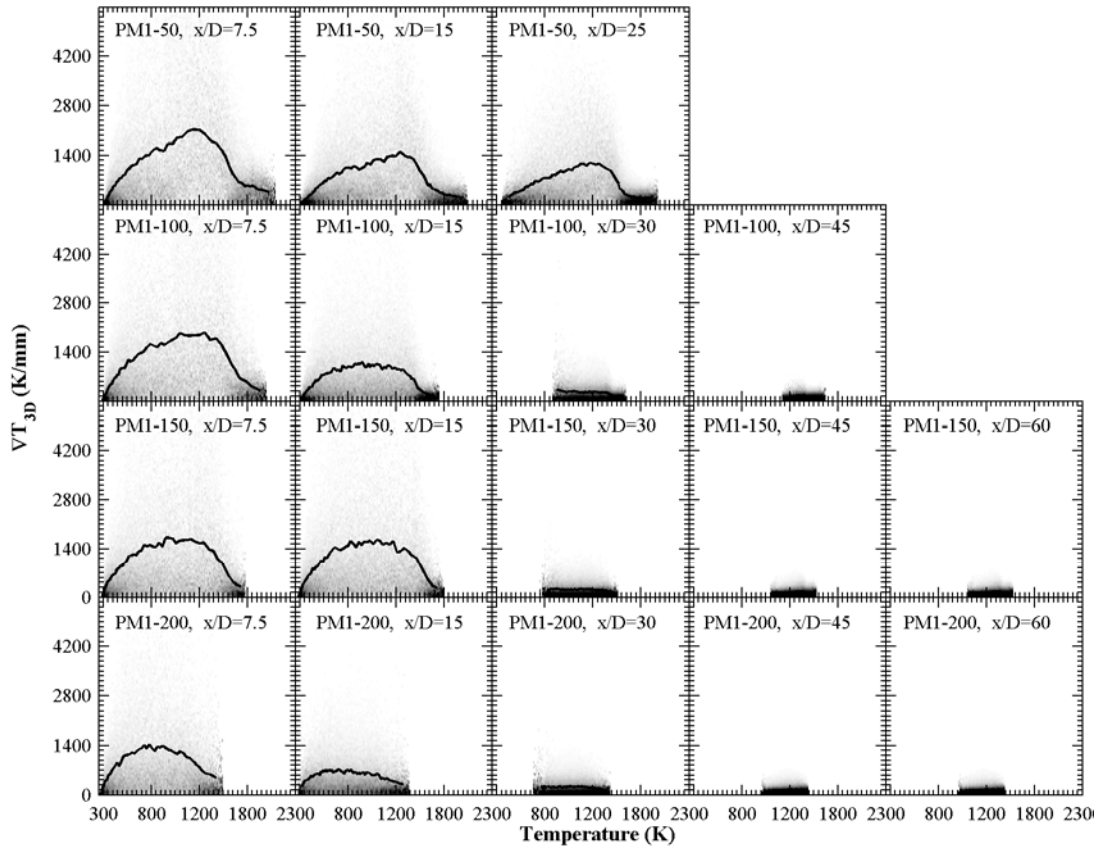


Fig. 8-2. PDF of $\nabla T_{3D} | \xi$ for the PM1 flame series, the probability density is proportional to the shade of grey, light corresponds to a low probability and dark a high probability. The conditional mean is shown as a black solid line.

The results presented in Fig. 8-2 show how the PDF of temperature gradient changes with axial position and increased turbulence intensity through increased jet velocity. For the PM1-50 flame it appears that there is very little change in the PDF shape as a function of axial location, only a small scaling of decreasing magnitude is found. It is to be noted that for the PM1-50 that the PDF displays a skewness towards high temperatures as is found for the laminar freely propagating and low strain rate opposed flow flames in Fig. 5-12.

Generally for the PM1-100 and PM1-150 flames a symmetric distribution for the PDF is found, whilst for the PM1-200 flame a low temperature skewness is found for the PDF for $x/D \leq 15$. From Fig. 8-2 it can be seen that a selection of $\xi = 1200\text{K}$ for Fig. 8-1 is a good general representative value to display the change in the magnitude of the PDF with axial velocity and axial location

8.2 Reaction Rate

The local reaction is examined in this section with respect to the mean flame chemiluminescence in Section 8.2.1, minor species concentrations in Section 8.2.2, the net CO_2 production rate in Section 8.2.3 and in terms of the heat release in Section 8.2.4.

8.2.1 Mean Flame Chemiluminescence

The initial identification of target flames and subsequent characterisation of the PPJB and PJB flames in Chapter 3 was based on the mean flame chemiluminescence images such as those presented in Fig. 3-3. It was also identified in Chapter 3 that the dominant source of the mean flame chemiluminescence is due to spontaneous emission from CH^* . The use of the mean CH^* field will be discussed here as in terms of its utility to be a mean reaction rate field indicator.

At atmospheric pressures the lifetime of CH^* is very short due to the rapid electronic quenching of CH^* to ground state ($X^2\Pi$) CH , this quenching process can be expressed through the reaction $\text{CH}^* + \text{M} \rightarrow \text{CH} + \text{M}$. The production of CH^* is due almost exclusively to the reactions $\text{O} + \text{C}_2\text{H} \rightarrow \text{CH}^* + \text{CO}$ and $\text{C}_2\text{H} + \text{O}_2 \rightarrow \text{CH}^* + \text{CO}_2$, it should be noted that both of these reactions involve C_2H as a reactant and the presence of C_2H is predominately the limiting factor in CH^* production. The C_2H molecule is formed primarily by the decomposition of the C_2H_2 molecule by O or OH , this means that C_2H

and therefore CH^* are not significantly influenced by the C-1 oxidation path of methane but rather the C-2 oxidation path.

As CH^* formation is governed by a different chemical pathway to CH formation, there can be no certainty that the CH and CH^* fields will be correlated. It should also be noted that any measurement of CH field with laser diagnostics such as LIF will be a measurement of the ground state CH field and not the CH^* field. To gain insight into the spatial structure and correlation of CH, CH^* and heat release a freely propagating laminar premixed methane flame has been computed for a 0.5 equivalence ratio atmospheric pressure methane-air flame. To enable the calculation of the CH^* field in the laminar flame additional reactions were added to the chemical mechanism (GRI3.0), these reactions are those proposed by Smith *et al.* [299], Devriendt *et al.* [300] and Tamura *et al.* [218], the specifics of these reactions are examined in greater detail Chapter 10 and the necessary additional reactions are given in Table 10-1. The results of the laminar flame simulation in terms of the spatial structure of the CH, CH^* , heat release and temperature fields is presented in Fig. 8-3.

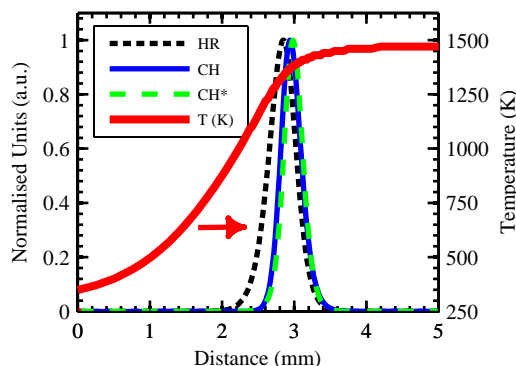


Fig. 8-3. The spatial structure of heat release (HR), CH, CH^* and temperature (T (K)) in a freely-propagating laminar premixed flame of methane-air with an equivalence ratio of 0.5. Curves for the mass fractions of CH and CH^* as well as the heat release have been normalized by their respective peak value.

The results reported in Fig. 8-3 indicate that for the simulated laminar flame, the peak CH and CH^* seem to be spatially well correlated with each other as well as with the flame

heat release. It is not possible from the single flame simulation in Fig. 8-3 to infer that in turbulent flames CH and CH^* are well correlated or that the CH or CH^* fields are correlated with heat release. It has been shown in a number of studies [252, 301, 302] that CH can be an unreliable indicator of the local heat release as it can be sensitive to the local strain rate, the local equivalence ratio and N_2 dilution effects. For a limited range of equivalence ratios and low strain rates Vagelopoulos and Frank [252] are able to show that CH is well correlated to the local heat release. As the formation path of CH^* is quite different to CH, the adequacy of CH^* as a heat release indicator cannot be ruled out based on the findings for CH. By examining a number of strain rates, fuels (including methane), equivalence ratios and pressures in laminar Bunsen flames Nori and Seitzman [303] show that CH^* is a good indicator of the local heat release rate, the extension of the correlation of CH^* to the local heat release rate in turbulent flames is also shown to be valid. The correlation of CH^* with the local heat release rate in laminar and turbulent flows is also confirmed by Panoutsos *et al.* [304].

Based on the results that CH^* is a good indicator of the local heat release rate in turbulent flames, greater confidence can be gained in the characterisation methodology used for PPJB and PJB flames in Chapter 3 in terms of reaction rate and finite-rate chemistry effects. For the PPJB this means that for flames such as the PM1-150 where extinction and re-ignition occur it is valid to claim that in the extinction region the mean heat release rate is reduced compared to re-ignition region further downstream where the CH^* levels are higher. For the PJB the start of the mean heat release region of the flame brush can be thus the lift off height can be well approximated by the CH^* emission.

8.2.2 Minor Species

It has been noted in Chapter 6 that significant signs of finite-rate chemistry effects in turbulent premixed combustion will not be found in the major species but rather in the state of the local radical pool hence inferring the local reaction rate. In this Section the CO and OH concentrations are examined. Some of the material reported in this section is

also reported in a publication by Dunn *et al.* [305]. CO is an important intermediate in the oxidation of hydrocarbon fuels, the concentration of CO will give indications as whether single step chemistry or mixing arguments are valid, flamelet arguments and perhaps finite rate chemistry effects in the PPJB possibly through the investigation of forward reaction rates of individual reactions. Whilst OH persists well past the reaction zone in the hot combustion products due to the water gas shift reactions OH must be present in the reaction zone in order for considerable reaction to be occurring, therefore although the presence of OH does not infer high or low reaction rates are occurring its absence does indicate that the local reaction rate is low.

The results of Fig. 8-4 and Fig. 8-5 show modified scatter plots for the measured mole fraction of CO (X_{CO}) and the mole fraction of OH (X_{OH}) collected at various axial locations in flames PM1-50, PM1-100, PM1-150 and PM1-200. Each axial location presents tens of thousands of data points collected at various radial positions, plotted against the measured temperature. The solid line shown on each plot represents the conditional mean, while the shades of grey represent the density of data collected within the temperature band indicating the conditional probability density. The data for Fig. 8-4 and Fig. 8-5 was taken from radial traverse data from the centreline to where the mean central jet mixture fraction (η_{jet}) has decayed to half of the centreline mixture fraction value ($\eta_{jet} > 0.5\eta_{jet-CL}$). By doing such conditioning, biasing of the PDF due to the entrainment of coflow fluid was minimised.

From Fig. 8-4 for the PM1-50 flame shows that the conditional mean X_{CO} distribution does not change significantly with axial location and the peak value is close to that obtained by opposed flow simulations ($1.6e-2$) of pilot products vs. fresh central jet reactants. For the PM1-50 flame Fig. 8-5 shows that a similar trend of a small progressive decreases in the X_{OH} distribution occurring as a function of axial distance. The constancy of the PM1-50 with laminar predictions supports the validity of using the PM1-50 as a “flamelet-like” reference flame. The X_{OH} and X_{CO} values for the PM1-50 are consistently above the values obtained for the unstrained premixed flame and the coflow products vs.

jet reactants opposed flow simulation. This shows the significant influence the pilot has on the radical pool surrounding and inside the central jet combustion process.

For the PM1-100 flame the conditional mean X_{CO} shows a small decrease as a function of downstream position in Fig. 8-4. However this progressive axial decrease is far more pronounced in the conditional mean values of X_{OH} in Fig. 8-5. Results for X_{CO} in the PM1-150 flame in Fig. 8-4 show that there is reduction in the conditional mean X_{CO} from $x/D=7.5$ to $x/D=15$, however the conditional mean X_{CO} magnitude is relatively similar for $x/D>15$. A similar trend for the X_{CO} in PM1-200 to the PM1-150 flame is observed, though generally at lower values of the conditional mean X_{CO} than in the PM1-150 flame. With the X_{OH} being a general indicator of reaction, the X_{OH} scatter plots in Fig. 8-5 for the PM1-150 and PM1-200 flames highlight the very low levels of X_{OH} that are observed in the extinction region and the increased X_{OH} levels in the re-ignition region compared to the extinction region. These findings for the axial distribution of X_{OH} correlate well with the imaging results reported in Chapter 5 and a previous publication Dunn *et al.* [175].

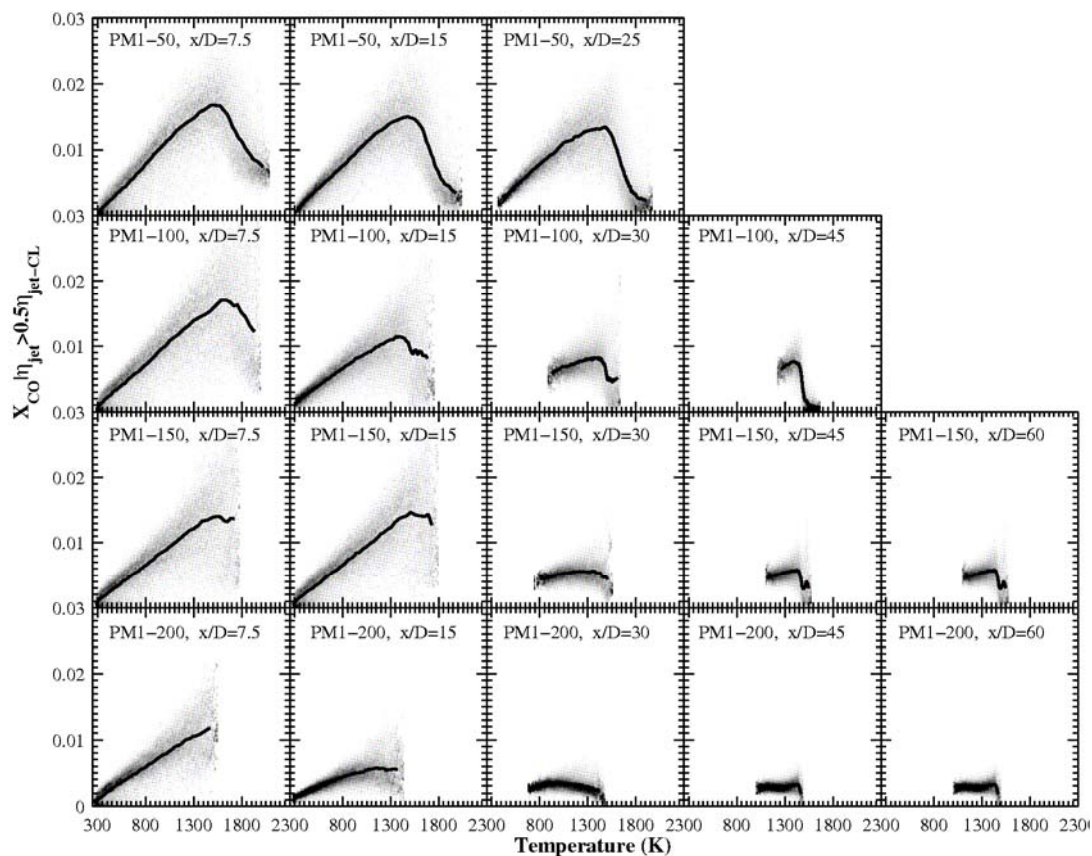


Fig. 8-4. PDF of CO mole fraction for the PM1 flame series, the probability density is proportional to the shade of grey, light corresponds to a low probability and dark a high probability. The conditional mean is shown as a black solid line.

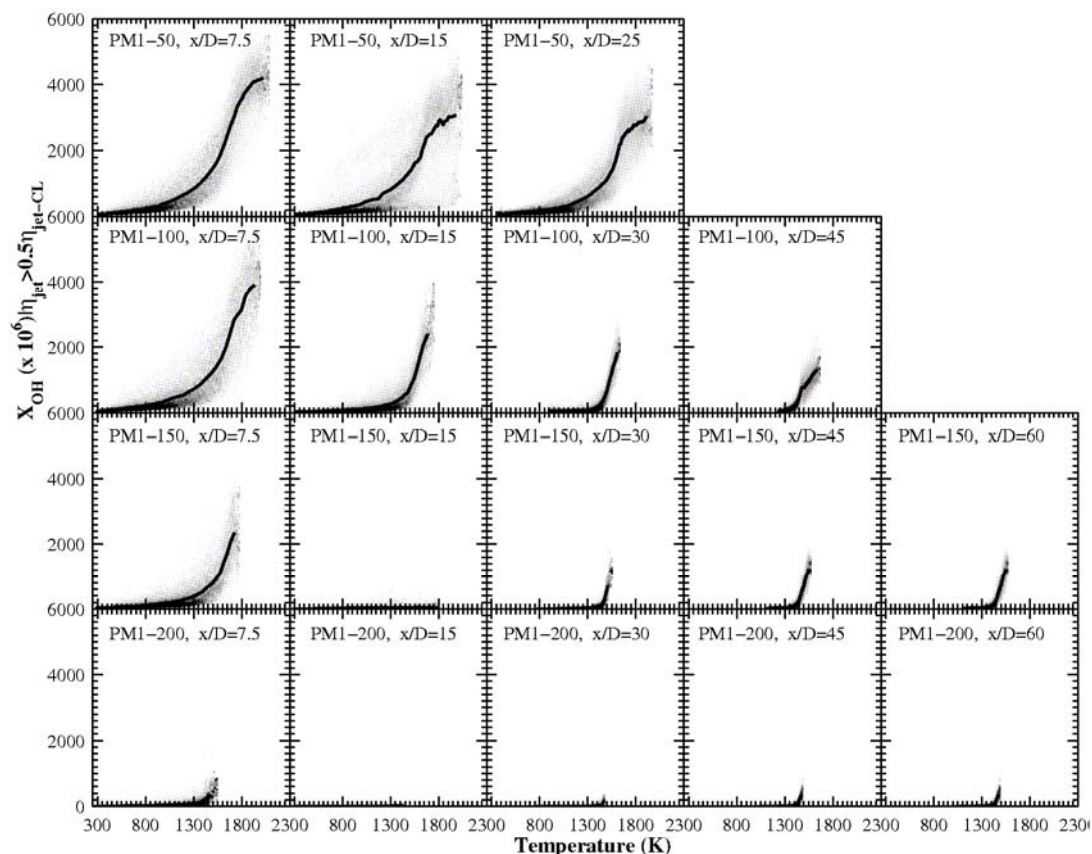


Fig. 8-5. PDF of OH mole fraction for the PM1 flame series, the probability density is proportional to the shade of grey, light corresponds to a low probability and dark a high probability. The conditional mean is shown as a black solid line.

8.2.3 CO₂ Net Production Rate

In order to explore the extent of finite rate chemistry effects, and keeping within the limitation of the species that are measured, the product of CO and OH mole fractions (denoted here as $[\text{CO}][\text{OH}]$) is explored here as an indicator of the net production rate of CO₂. This is under the assumption that the forward reaction $\text{OH} + \text{CO} \rightarrow \text{H} + \text{CO}_2$ plays a significant role in the fuel oxidation process, thus is a significant reaction to study finite-rate chemistry effects. The reverse of this reaction will become significant at high temperatures, thus even for a qualitative examination, in order to correlate $[\text{CO}][\text{OH}]$ to the net CO₂ production rate the reverse reaction and other possible reactions involving

CO₂ are evaluated. The use of simultaneous imaging of CO and OH has previously been used by Rehm and Paul [306] and also by Frank *et al.* [307] as an indicator of the forward rate of reaction for OH + CO → H + CO₂, however the correlation with the net formation rate of CO₂ was not examined in these studies.

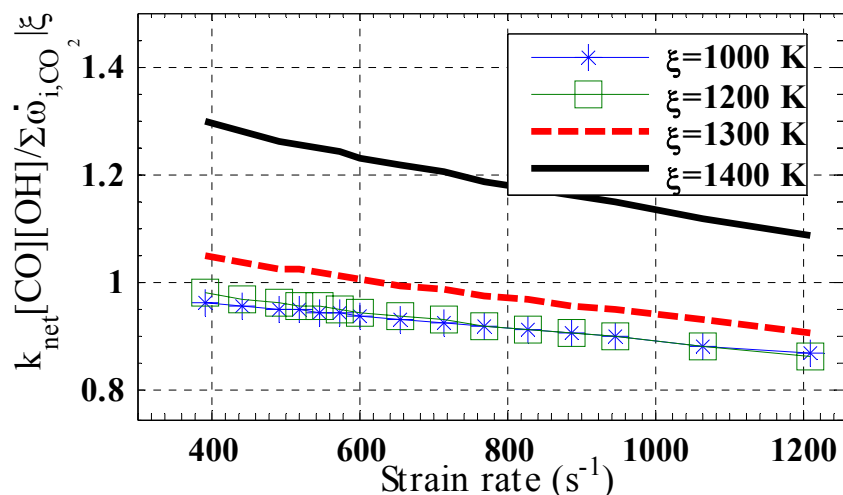


Fig. 8-6. Variation of the ratio of [CO][OH] to the net CO₂ production rate as a function of strain rate. $\sum \dot{\omega}_{i,\text{CO}_2}$ is taken to be the net reaction rate for CO₂ summed over the i^{th} reaction, for all evaluated reactions.

The hypothesis that [CO][OH] correlates with the net CO₂ formation rate tested first using calculations for premixed opposed flow laminar simulations of fresh central jet reactants vs. hot coflow products for various strain rates. In Fig. 8-6 the computed ratio of [CO][OH] to the net CO₂ production rate is plotted for a range of strain rates. For all strain rates examined in Fig. 8-6, it appears that [CO][OH] is a good qualitative indicator of the net CO₂ production rate. At a given temperature there is typically less than a 16% variation in the correlation of [CO][OH] to net CO₂ production rate from the maximum to minimum strain rate simulated. Examination of results obtained with fresh central jet reactants vs. hot pilot products that would be a more realistic simulation for the PM1-50 flame at small x/D , reveals a similar conclusion to those presented in Fig. 8-6. Based on the laminar opposed flow results, it seems reasonable to assume that if the product of CO and OH mole fractions conditional on temperature ($[\text{CO}][\text{OH}]|\xi$) is examined, for the

compositions of the flames investigated the net CO_2 production rate may be qualitatively inferred.

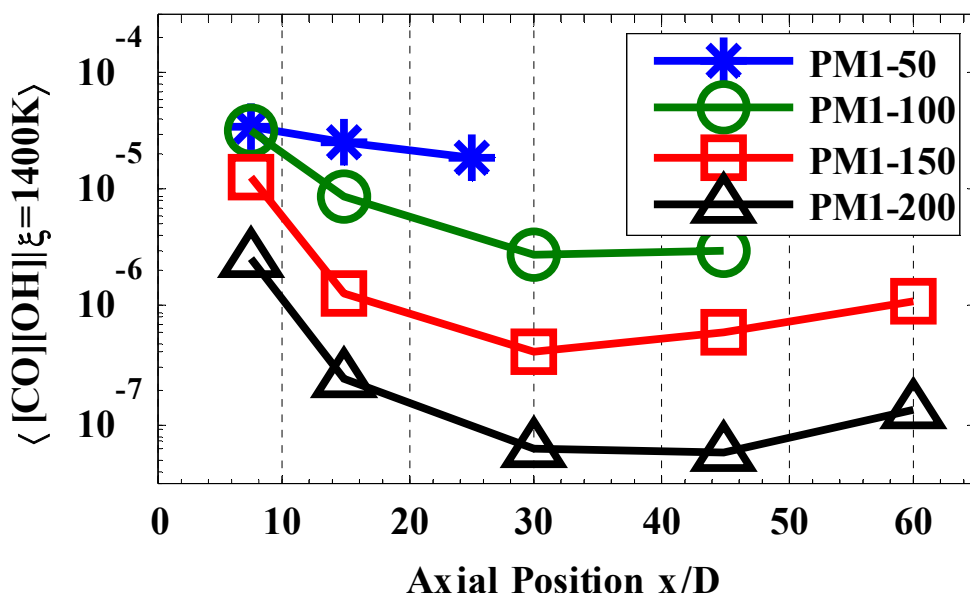


Fig. 8-7. Conditional mean values for the product of CO and OH, taken at $\xi=1400\text{K}$ at a number of axial stations, for the PM1 flame series.

The results presented in Fig. 8-7 and Fig. 8-8 show the results for the product of CO and OH for the PM1 flame series. Fig. 8-7 displays the comparison of $\langle [\text{CO}][\text{OH}] | \xi \rangle$, conditioned at a temperature of $\xi=1400\text{K}$ vs. axial location, thereby condensing the results for the entire flame series onto a single figure. Fig. 8-8 shows the entire PDF as a function of temperature for the entire flame series at all measurement stations. The PM1-50 flame displays a small monotonic decrease in $\langle [\text{CO}][\text{OH}] | \xi \rangle$ with axial distance, the PM1-100 displays a similar monotonic decrease in $\langle [\text{CO}][\text{OH}] | \xi \rangle$ with increasing x/D , although there is a much larger range and the values at $x/D=30$ and 45 are almost identical. The results for the PM1-150 for $[\text{CO}][\text{OH}]$ are relevant in terms of the extinction and re-ignition in this flame. Initially at $x/D=7.5$ there is a region of high values of $\langle [\text{CO}][\text{OH}] | \xi \rangle$, this is followed by a region of rapid decrease up to $x/D=30$, which is in the middle of the proposed extinction region. Beyond $x/D=30$, at $x/D=45$ and 60, an increase in the mean luminosity is observed termed, the re-ignition region. It is a significant result that $\langle [\text{CO}][\text{OH}] | \xi \rangle$ increases at $x/D=45$ and 60 relative to $x/D=30$. The

PM1-200 flame exhibits a very sharp drop to very low levels of $\langle [\text{CO}][\text{OH}] | \xi \rangle$ beyond $x/D=7.5$ which corresponds to the identification that this flame is globally extinguished. Mean luminosity images of this flame indicate that there is a slight increase in the mean luminosity near $x/D=60$. Measurements of $\langle [\text{CO}][\text{OH}] | \xi \rangle$ correlate well with this observation, showing a small increase at $x/D=60$ over the values at $x/D=30$ and 45.

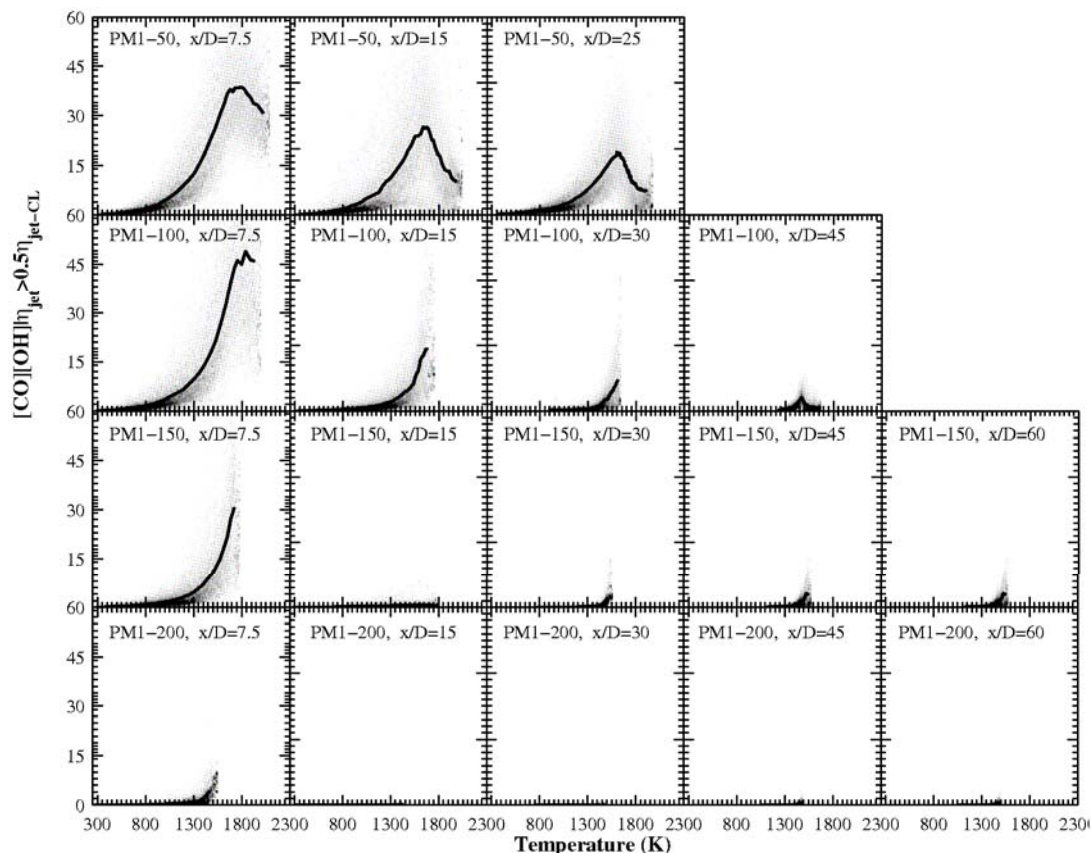


Fig. 8-8. PDF of $[\text{CO}][\text{OH}]$ the PM1 flame series, the probability density is proportional to the shade of grey, light corresponds to a low probability and dark a high probability. The conditional mean is shown as a black solid line.

8.2.4 Heat Release

In Chapter 5, Section 5.3 the use of the product of CH_2O and OH was used as a qualitative indicator of the reaction rate in the images examined. Analysis of the results

with respect to the axial variations of the reaction rate was not presented in Chapter 5 and is presented here. The concept of extinction and re-ignition has been well verified in terms of the net CO_2 production rate by the results presented in Section 8.2.3. The data presented here essentially attempts to verify this assumption in terms of the heat release rate as it has been shown that the product CH_2O and OH corresponds to the heat release rate [253].

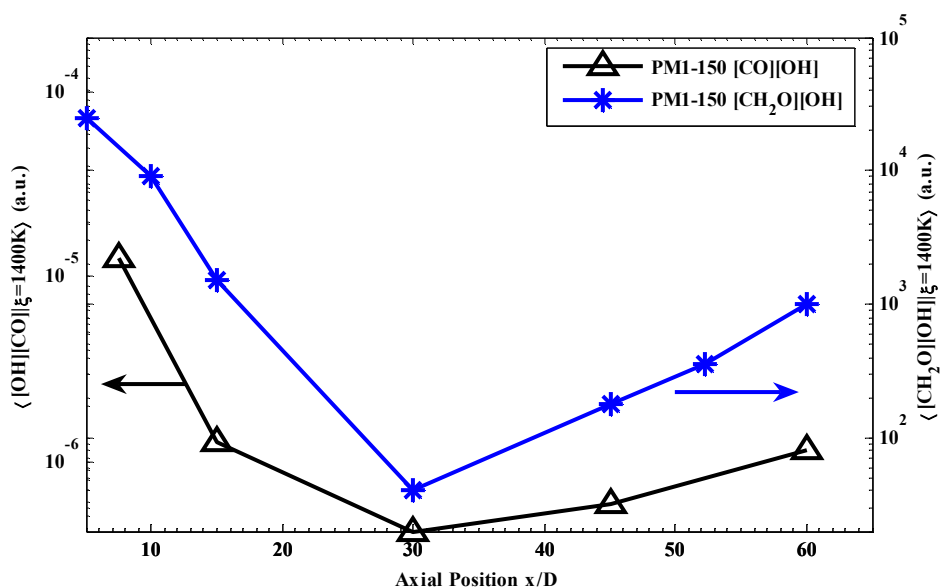


Fig. 8-9. A comparison of the product $[\text{CO}][\text{OH}]$ and $[\text{CH}_2\text{O}][\text{OH}]$ conditional on a temperature of 1400K for the PM1-150 flame.

Specifically in this section the results for the PM1-150 flame are examined. The axial variation of the heat release indicator $[\text{CH}_2\text{O}][\text{OH}]$ is examined in Fig. 8-9. The axial decay of the product of CO and OH has already been examined in Fig. 8-7 and is presented again in Fig. 8-9 for comparative purposes with the CH_2O data. It can be seen that the axial variation of $[\text{CH}_2\text{O}][\text{OH}]$ follows a similar trend to the $[\text{CO}][\text{OH}]$. This is not surprising since the formation of CO_2 is a significant heat release step in the oxidation of methane. The result of Fig. 8-9 is that there can now be claimed to be quantitative evidence of the initial ignition, extinction and re-ignition regions of the PPJB flames both in terms of heat release and net CO_2 formation.

8.3 Discussion: Flame Characterisation

The characterisation and categorisation of turbulent premixed flames is often done with reference to a premixed combustion regime diagram or “Borghi diagram” which was first proposed by Borghi [8], then later developed by Peters [12, 13] and subsequently refined by Chen and Bilger [9]. The philosophy for the construction of the regime diagram adopted here, is similar to that taken by Chen and Bilger [9]. This method is adopted because this regime diagram was theorised and developed not on conceptual interactions of turbulence and premixed flames like the regime diagrams of Borghi [8] and Peters [12, 13], but rather on the experimental evidence of the flame structure from planar imaging experiments. It is this author’s strong belief that for any generalised premixed regime diagram, the diagram must be at least partially on experimental imaging results (scalar and/or velocity) to categorise the flame structure in these regimes. When qualitatively and quantitatively examining such images, effects such as the development of out of front islands and peninsula formation in the turbulent flame front regime or reductions in the scalar dissipation relative to laminar calculations in the complex strain front regime may be readily identified and easily included in the knowledge base of such a regime diagram. Without such data for the justification of the bounds of and testing of the generality of the proposed regime diagram the utility of such a diagram must be questioned.

In order to plot the selected flames on a premixed regime diagram the integral length scale, turbulence intensity, laminar flame speed and thickness are required. From the LDV results the turbulence intensity, q' , and integral length scale, ℓ_0 has been obtained. The relevant values are taken at $x/D=15$, at the radial location where the shear layer occurs ($r/D=0.5$). Utilising the freely propagating unstrained laminar flame code of Goodwin [177] with multi component diffusion and the GRI 3.0 [176] mechanism for methane, the laminar flame speed, S_L , and thermal flame thickness, δ_{th} , has been

computed for a methane-air of equivalence ratio 0.5. The computed properties of the laminar flame are given in Table 8-1.

Table 8-1. Laminar flame characteristics for an unstrained premixed methane-air flame of equivalence ratio (Φ) equal to the central jet composition of the PM1 flames investigated. T_{ad} is the adiabatic flame temperature. S_L is the laminar flame speed. δ_{th} is the laminar flame thermal thickness based on the maximum gradient. t_f is defined as the laminar flame thermal time scale (δ_{th}/S_L).

Φ	T_{ad} (K)	S_L (m/s)	δ_{th} (mm)	t_f (ms)
0.50	1480	0.051	2.0	39

The unstrained laminar flame thickness in Table 8-1 is defined by Eq. (8.2).

$$\delta_{th} = \frac{T_{ad} - T_u}{|\nabla T|_{\max}} \quad (8.2)$$

Where T_{ad} is the adiabatic flame temperature and T_u is the unburnt reactant temperature. Using the results from the unstrained laminar flame calculation the characteristic chemical or flame time-scale, t_f , can be calculated by Eq. (8.3).

$$t_f = \frac{\delta_{th}}{S_L} \quad (8.3)$$

The Damköhler number, Da , in Table 8-2 is defined here as the ratio of the turbulence time-scale to the chemical time-scale. In order to obtain a value for the characteristic turbulence time-scale, t_t , we have approximated the characteristic length scale as ℓ_0 ; hence the turbulence timescale can be approximated by Eq. (8.4).

$$t_t \approx \frac{\ell_0}{q'} \quad (8.4)$$

The Karlovitz number, Ka , in Table 2 has been defined in terms of the flame and Kolmogorov (t_η) time-scales and can be expressed by Eq. (8.5).

$$Ka = \frac{1}{\sqrt{15}} \frac{t_f}{t_\eta} \quad (8.5)$$

The integral length scale is used as an approximation for the characteristic eddy size for the calculation of the kinetic energy dissipation rate, necessary for the calculation of t_η , approximated here by Eq. (8.6).

$$t_\eta = \left(\frac{\ell_0 \nu}{q'^3} \right)^{1/2} \quad (8.6)$$

Table 8-1 and Table 8-2 summarise the relevant combustion parameters for the laminar flame and relevant non-dimensional numbers for the selected flames at $x/D=15$ respectively. The Da and Ka , reported in Table 8-2 for these lean flames are partially influenced by the small laminar flame speed and the large laminar thermal flame thickness relative to stoichiometric values.

Table 8-2. Non-dimensional parameters for the flames examined. q' is the total turbulence intensity, η is the Kolmogorov length scale, ℓ_0 is the integral length scale, Re_t is the turbulent Reynolds number and Da is the Damköhler number.

Flame Code	PM1-50	PM1-100	PM1-150	PM1-200
U_0 (m/s)	50	100	150	200
Re	12500	25000	37500	50000
q'/S_L	48	280	360	460
ℓ_0/δ_{th}	2.4	1.8	1.6	1.8
δ_{th}/η	59	240	290	350
Re_t	720	3100	3700	5200
Ka	140	2300	3500	4900
Da	0.049	0.0063	0.0045	0.0038

On only a qualitative basis from the instantaneous temperature and OH images in Fig. 5-10a), flame PM1-50 would not be expected to be classified as an example of a distributed flame front regime flame. The flame structure observations discussed in detail in Section 5.2.3 for the temperature and OH images are in contradiction to the predictions shown in Fig. 8-10, particularly for the PM1-50 flame that is predicted to be in the distributed flame front regime. Two possible explanations can be provided, one being that the premixed regime diagram has been developed and validated with the concept of a homogenous, moderately turbulent flow-field advecting normally toward the flame front. This is far from the situation encountered in the PPJB with a highly turbulent flow-field being produced through intense shear. Secondly due to the near flammability limit equivalence ratios the unstrained laminar flame velocity and thermal flame thickness are far from those that would be obtained for equivalence ratios in the range 0.7 to 1.0.

For all the selected flames studied the Lewis number of the deficient reactant methane, is less than unity as well as the Markstein number (Ma) less than zero, this is obtained by extrapolating the experimental and numerical data for Ma reported by Hassan *et al.* [308]. Given a negative value of Ma it would be expected from flamelet theory that extinction or near zero turbulent flame speed would not be possible based purely on the flames response to large values of stretch. Two important observations based on Ma and the observed extinction re-ignition needs to be pointed out. As shown in the characterisation diagram in Fig. 3-2 extinction re-ignition is observed for flames with equivalence ratios less than 0.7, where the Ma number is less than zero. A second important result is that for propane flames where the Ma number is always positive, a similar characterisation diagram to Fig. 3-2 is produced, including an extinction re-ignition regime similar to that reported here for the methane case. Based on these findings it would seem that the Ma for a given composition is not a useful parameter in determining if extinction is possible for a premixed flame in the PPJB. This does not mean that flamelet models cannot predict flame extinction, but rather flamelet models that utilise Ma and all of the corresponding assumptions will not predict flame extinction. This means that flamelet models that utilise the Ma number will not be able to predict the extinction and re-ignition effects in the PM1 flame series.

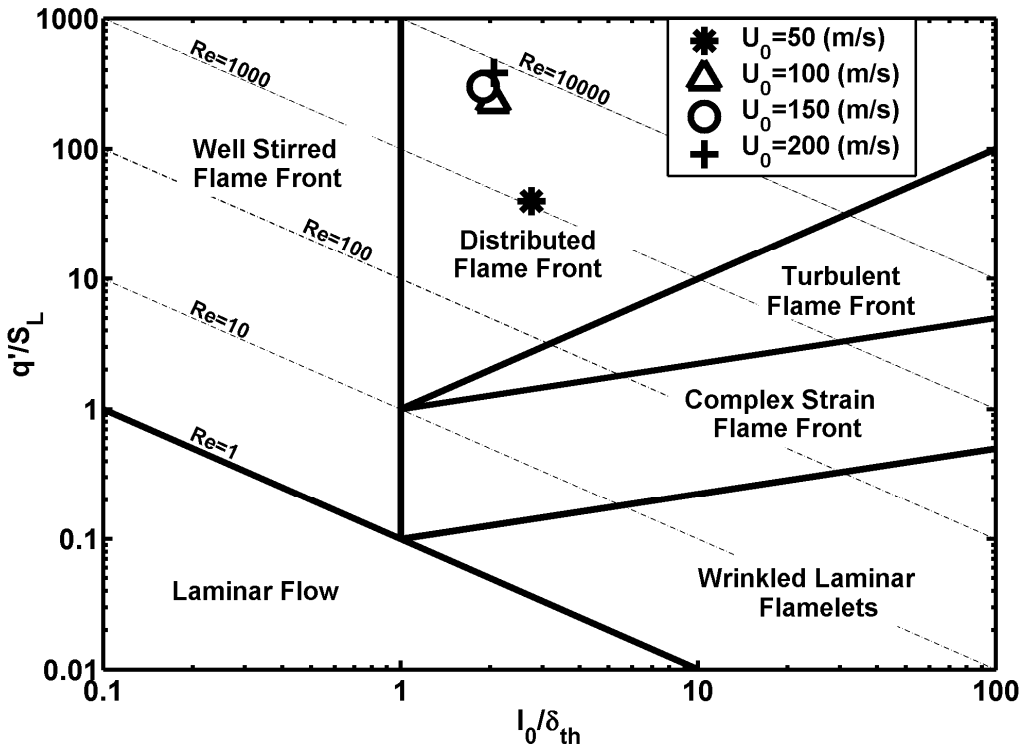


Fig. 8-10. The premixed combustion regime diagram similar to that proposed by Chen and Bilger [9], the locations of the four PM1 flames in terms of the central jet velocity is shown. The integral length scales and turbulence intensity values necessary to locate the selected flames on the regime diagram were taken from the values at $x/D=15$.

CHAPTER 9 EXPERIMENTAL AND NUMERICAL INVESTIGATIONS OF NON-REACTING VARIABLE DENSITY JETS

It is part of the aim of this thesis to investigate the predictive capabilities of the state of the art RANS PDF model in computing finite-rate chemistry effects in the turbulent premixed combustion. The success of the RANS PDF model to simulate finite-rate chemistry effects in model piloted and non-piloted flames in non-premixed combustion has been well established [72, 82]. The extension of the RANS PDF model to premixed combustion using the PPJB would seem like a logical progression. Of the many RANS based models capable of incorporating finite-rate chemistry effects, the PDF method would have almost the best probability of successfully simulating finite-rate chemistry effects.

The RANS TPDF code used for the numerical investigations in this thesis is a hybrid finite-volume Monte Carlo code where the momentum, continuity and turbulence equations are solved using a standard finite volume methodology and the joint temperature-composition PDF is solved using a stochastic Monte-Carlo particle based solution. Further discussion of the PDF implementation and simulation results can be found in Chapter 2 and 10. As a consequence of the PDF solution methodology the turbulence quantities are solved using one of the many standard RANS turbulence models such as the k - ϵ , k - ω or Reynolds stress models as opposed to joint PDF modelling of the velocity frequency composition PDF that could be viewed as a more rigorous approach. As the hybrid RANS TPDF methodology will rely on accurate prediction of the

turbulence quantities to correctly predict the PPJB flames some confidence needs to be obtained in the predictive capabilities of the standard RANS turbulence models for a non-reacting benchmark case that is relevant to the PPJB simulations. The proposed benchmark case for the non-reacting calculations is a non-reacting variable density jet.

Both the PPJB and the PJB configurations feature a low-temperature high-density axisymmetric jet issuing into a high-temperature low-density coflow. This configuration of an axisymmetric jet mixing with a coflow of different density is commonly termed in the non-reacting case as a variable density jet [309, 310, 311]. This is in contrast to the non-reacting constant density jet where the density of the jet and coflow are identical.

It is the aim of this chapter to investigate the predictive capabilities of the standard RANS based turbulence models for the non-reactive variable density jet with conditions such as density ratio and Reynolds numbers that are similar to the PPJB flames. A detailed and exhaustive comparative study of all of the published RANS turbulence models in literature for the variable density jet geometry is not seen as essential. It is also not the aim of this chapter to solve the predictive capability issues of the standard RANS turbulence models. Only some parametric variation of the various turbulence modelling constants is examined although detailed parametric studies for all turbulence models is not conducted. To summarise, the primary aim of this chapter is to gain an appreciation of the predictive capabilities of the standard RANS turbulence models for a variable density jet. Such an understanding will allow a greater appreciation of the simulation results when the PPJB flames are simulated using the coupled PDF RANS simulations in Chapter 10.

To model the piloted and non-piloted non-premixed flames in a RANS framework, the k - ϵ , k - ω and Reynolds stress models are often used due to their successful predictive capabilities and the similarity of the problem with the non-reacting constant density round jet. The predictive capabilities of most RANS turbulence models for non-reacting variable density jets are by in large unknown and untested. As noted by Pope [312] there have been numerous experimental investigations of the constant density round jet

examining the many influencing parameters, reported results range from the scalar fields to the velocity fields. There is unfortunately not the same depth of experimental results published for variable density round jets. In fact most investigations into variable density jets utilise a density ratio (ρ_R) less than unity. In this thesis the density ratio is taken to be the ratio of the density of the jet fluid at the exit plane (ρ_{Jet}) divided by the density of the coflow fluid at the exit plane (ρ_{Coflow}) which is given by Eq. (9.1).

$$\rho_R = \frac{\rho_{Jet}}{\rho_{Coflow}} \quad (9.1)$$

For the PPJB flames with a coflow temperature of 1500K such as the PM1 and PM4 flame series, the density ratio (ρ_R) is approximately equal to 5.4. The only experimental investigations that density ratios of the order of 5 are reported are those reported by Pitts [309]. The investigations by Pitts [309] and Richards and Pitts [311] compare the mean centreline mass fraction and unmixedness of a variable density jet by parametrically varying the Reynolds numbers between 7890 and 11860 at a density ratio of 5.11. Whilst the data of Pitts [309] can be considered to be a valuable first step in the detailed understanding variable density jets, there is still a significant scope for experimental investigations in this area.

The lowest Reynolds number PPJB flame examined in detail in this thesis is the PM1-50 flame which has an exit Reynolds number of 12500 and the highest is the PM4-225 flame with an exit Reynolds number of 56250. Based on the disparity in the Reynolds number between the available data by Pitts [309] at $\rho_R = 5.11$ and the PPJB flames an experimental campaign has been undertaken to measure the axial and radial profiles of the velocity fields using LDV. An advantage of carrying out specific measurements in a non-reacting variable density jet is that the geometry and conditions for the experimental measurements can be tailored to be specifically relevant to the PPJB flames in terms of density ratio, Reynolds number and geometrical configuration.

In Section 9.1 the configuration for the experimental setup for the non-reacting variable density jet measurements is presented. An overview of the numerical model including details such as the grid, numerical convergence and grid resolution that are used for the RANS simulations is presented in Section 9.2. In Section 9.3 the specific details of the implementations of the RANS turbulence models used for the simulations is presented. The results from the numerical simulations and experiments are compared with experimental results for the constant density case in Section 9.4 and in Section 9.5 for the variable density case.

9.1 Selected Cases and Experimental Measurements

To investigate the non-reacting flows experimentally, the PJB geometry has been used to maintain maximum relevance to the reacting cases. For the constant density flows filtered compressed air is used for both the central jet and the coflow. For the variable density cases examined filtered compressed air is again used for the central jet however to achieve a high density ratio between the coflow and the central jet a combusting hot coflow of hydrogen-air is used, this is the same as done for the reacting cases in the PJB and PPJB.

Table 9-1. Summary of the flow conditions examined in this chapter for non-reacting flows of constant and variables densities.

	Jet density (kg/m ³)	Jet velocity (m/s)	Coflow density (kg/m ³)	Coflow velocity (m/s)	Density Ratio	Jet Reynolds Number
NR-50	1.18	50	1.18	1.0	1.0	12579
NR-1500-50	1.18	50	0.218	4.0	5.4	12579
NR-150	1.18	150	1.18	1.0	1.0	37736
NR-1500-150	1.18	150	0.218	4.0	5.4	37736

A summary of the non-reacting cases examined is given in Table 9-1. Two density ratios are examined the standard unity density ratio case (constant density case) and a density

ratio 5.4 (variable density case). This density ratio is the same value that occurs for the PM1 flame series in the PPJB. For each density ratio two Reynolds numbers are investigated ranging from 12600 to 37700.

For each of the four cases LDV measurements are carried out to determine the single point axial and radial velocity fields. In all cases the jet was the only stream that was seeded with particles, thus the reported velocity measurements will be biased towards higher jet mixture fractions. This biasing effect is expected to manifest in the results with the experimental velocity measurements (mean and RMS) being always larger the predicted velocity as the coflow mean and RMS velocity is significantly lower than the jet fluid. The experimental setup and data processing methodology is exactly the same as the PPJB and PJB LDV measurements reported in Chapter 3 and is not repeated here. The LDV derived velocity results are reported in the same figures as the numerical simulation results, for the constant density case this corresponds to Fig. 9-2-Fig. 9-8 and for the variable density case this corresponds to Fig. 9-9-Fig. 9-14.

9.2 Numerical Solution Problem Setup

All computations were carried out on a grid independent mesh that featured $\sim 200k$ cells with 30 cells across the central jet exit. Grid independence to less than 4% of the asymptotic value at a Richardson extrapolated infinite mesh density was found at 15 cells across the central jet exit corresponding to ~ 35000 cells in total. The mesh features a very high mesh density in the areas of high turbulent kinetic energy dissipation such as in the vicinity of the central jet exit; this high mesh density is highlighted by Fig. 9-1a). The area close to the central jet exit also features a near unity aspect ratio quadrilateral mesh to minimise the numerical error. The mesh density decreases away from the central jet exit utilising an unstructured quadrilateral mesh with an attempt to minimise the number and degree of highly skewed quadrilateral cells. The computational domain is 700mm long by 200mm in the radial direction, the central jet velocity inlet is $50D$ upstream from

the central jet exit plane to allow fully developed flow to occur, the domain extends $125D$ from the central jet exit to the outlet.

Due to the numerous turbulence models evaluated in this study, the simulations were implemented in a number of codes, the codes that were used for the simulations were: OPENFOAM [313], a modified version of the code available on the web from the book by Ferziger and Peric [314] and also where possible the turbulence models were also implemented in Fluent [296] as user defined functions if not available as a standard model selection. All simulations utilise the Quadratic Upwind Interpolation for Convective Kinematics (QUICK) advection scheme due to its advantageous boundedness and dissipative properties compared to first order upwind and second order upwind schemes. To monitor convergence the invariance of the scalar and velocity monitors distributed throughout the domain was utilised. All computations take advantage the axisymmetric configuration of the geometry.

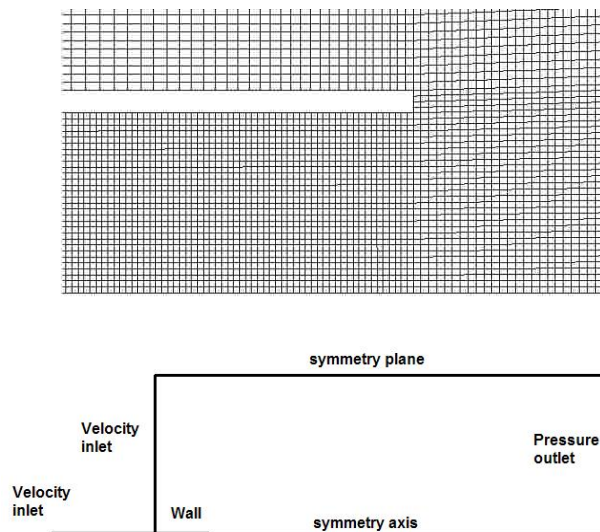


Fig. 9-1. a) (Top) Close up view of the central jet exit highlighting the mesh density and cell aspect ratio, note the jet radius is 2mm making the area of interest for this figure $\sim 7\text{mm} \times 3.75\text{mm}$. b) (Bottom) gives an overview of the computational domain and boundary conditions utilised for the simulations.

To account for density changes due to temperature an incompressible-ideal gas model is utilised combined with an implicit pressure based solver. The 50m/s and 150m/s jet velocity cases have Mach numbers (M) of 0.14 and 0.43. Generally for Mach numbers greater than 0.7 it is considered mandatory to account for compressibility effects through the coupling of the momentum and density equations. To test the assumption of neglecting compressibility, the 150m/s case has been simulated using a compressible formulation with both pressure and density based solvers. The density based solver exhibited good convergence and mass balance characteristics, the results show negligible difference to incompressible calculations when an ideal-gas model is exclusively used to calculate density from temperature. Significant numerical stability issues were found with the pressure based solver, which is to be expected. With a numerically stable solution, poor mass balance was displayed for the pressure based solution. It should be noted that in the numerical implementation of the RANS based transported PDF model reported in Chapter 10 it is not possible to use the density based solver due to the way the Monte-Carlo solution is coupled to the momentum equations, thus it would not seem possible to simulate flows with significant compressibility effects or $M > 0.7$ using the transported PDF method in the reacting case with the present implementation of the transported PDF code as the pressure based solver displays poor convergence and numerical stability properties for the coupled full density variation case.

Variable thermodynamic and transport properties are used for all simulations. A kinetic theory model was used for the specific heat (C_p), thermal conductivity (k) and viscosity (μ). The effect of heat transfer from the hot coflow fluid to the central jet pipe causing a preheating of central jet fluid has been accounted for using a coupled heat calculation.

9.3 RANS Based Turbulence Modelling

For the k - ϵ two-equation turbulence modelling methodology, three k - ϵ based models are examined for their predictive capabilities of a variable density jet. The three k - ϵ based models are referred to as the standard k - ϵ model, the Re-Normalised Group theory (RNG)

k - ε model and the realizable k - ε model. For all of the k - ε based models a transport equation for the turbulent kinetic energy (k) and the turbulent kinetic energy dissipation rate (ε) is utilised. The turbulent kinetic energy (k) for all of the turbulence models (not just the three k - ε turbulence models) is defined by Eq. (9.2).

$$k = \frac{1}{2} \overline{u'_i u'_i} \quad (9.2)$$

The derivations of the standard k - ε model as presented by Launder and Spalding [315, 316] proceeds with an exact unclosed transport equation for the turbulent kinetic energy which is given by Eq. (9.3).

$$\frac{\partial(\rho k)}{\partial t} + \frac{\partial(\rho \bar{u}_j k)}{\partial x_j} = \frac{\partial}{\partial x_j} \left[\frac{\rho}{2} \overline{u'_i u'_j u'_j} + \overline{u'_i P'} - 2\rho \nu \overline{u'_j S_{ij}} \right] - \rho \overline{u'_i u'_j} \frac{\partial(\bar{u}_i)}{\partial x_j} - \rho \varepsilon \quad (9.3)$$

In order for Eq. (9.3) to be solved a number of the terms must be closed by using certain modelling assumptions. Introducing the gradient-diffusion hypothesis allows the first term on the RHS of Eq. (9.3) to be modelled according to Eq. (9.4).

$$\frac{\rho}{2} \overline{u'_i u'_j u'_j} + \overline{u'_i P'} - 2\rho \nu \overline{u'_j S_{ij}} \approx \frac{\nu_t}{\sigma_k} \frac{\partial k}{\partial x_j} \quad (9.4)$$

The turbulent viscosity hypothesis (or sometimes to as the eddy viscosity hypothesis) assumes that the tensor $\overline{u'_i u'_j}$ representing the anisotropy is aligned with the mean rate of strain $\overline{S_{ij}}$. By evoking the turbulent viscosity hypothesis, the second term on the RHS of Eq. (9.3) maybe modelled using Eq. (9.5).

$$\rho \overline{u'_i u'_j} \approx 2\nu_t \overline{S_{ij}} \quad (9.5)$$

With the closure modelling assumptions of Eq. (9.4) and Eq. (9.5) incorporated into Eq. (9.3), the modelled transport equation for the turbulent kinetic energy can be expressed by Eq. (9.6).

$$\frac{\partial(\rho k)}{\partial t} + \frac{\partial(\rho \bar{u}_j k)}{\partial x_j} = \frac{\partial}{\partial x_j} \left[\left(\mu + \frac{\mu_t}{\sigma_k} \right) \frac{\partial k}{\partial x_j} \right] + \mu_t 2S_{ij}S_{ij} - \rho \varepsilon \quad (9.6)$$

The equation for the transport of the turbulent kinetic energy dissipation rate cannot be regarded as an exact equation as can the transport equation for the turbulent kinetic energy in Eq. (9.3). Although an exact transport equation for ε can be derived, there are numerous terms that any kind of rigorous closure at high Reynolds number has not been well validated. Wilcox [317] regards the necessary modelling assumptions to form a closed ε equation from the exact ε transport equation as "drastic surgery" and the resultant equation referred to as "...no more exact than the dimensional analysis of Kolmogorov (1945)". Pope [312] presents the view of the model ε equation in the k - ε model as an entirely empirically based model and as such evaluates the merits and limitations of the model. The resultant model equation for ε can be expressed by Eq. (9.7).

$$\frac{\partial(\rho \varepsilon)}{\partial t} + \frac{\partial(\rho \bar{u}_j \varepsilon)}{\partial x_j} = \frac{\partial}{\partial x_j} \left[\left(\mu + \frac{\mu_t}{\sigma_\varepsilon} \right) \frac{\partial \varepsilon}{\partial x_j} \right] + C_{\varepsilon 1} \frac{\varepsilon}{k} \mu_t - C_{\varepsilon 2} \rho \frac{\varepsilon^2}{k} \quad (9.7)$$

The turbulent viscosity (μ_t) in Eq. (9.6) and Eq. (9.7) is modelled in the standard fashion by Eq. (9.8).

$$\mu_t = \rho C_\mu k^2 / \varepsilon \quad (9.8)$$

The values for the turbulence model constants ($C_{\varepsilon 1}$, $C_{\varepsilon 2}$, C_μ , σ_k , and σ_ε) for standard k - ε model recommended by Launder and Spalding [315] are given by Table 9-2.

Table 9-2. Turbulence model constants used for the standard k - ε model.

$C_{\varepsilon 1}$	$C_{\varepsilon 2}$	C_{μ}	σ_k	σ_{ε}
1.44	1.92	0.09	1.0	1.3

A revision to the standard k - ε as presented by Launder and Spalding [315] is the RNG k - ε model which was developed primarily by Yakhot and Orszag [318]. The RNG k - ε model utilises Re-Normalisation Group theory to analytically derive expression for the closure coefficients directly from the Navier-Stokes equations. Although the end result of the RNG analysis results in equations for k and ε that are very similar to the standard k - ε equation there are some differences. As a result of the RNG procedure a differential equation results for the expression of the turbulent viscosity (ν_t) that is of the form of Eq. (9.9).

$$d\left(\frac{\rho^2 k}{\sqrt{\varepsilon \mu}}\right) / d\nu_t = 1.72 \frac{\nu_t d\nu_t}{\sqrt{\nu_t^3 + 99}} \quad (9.9)$$

In the limit of high Reynolds numbers Eq. (9.9) reduces to Eq. (9.8) which is the standard expression for the turbulent viscosity, however with the value of $C_{\mu}=0.085$ which is derived from RNG theory which is only a 6% difference from the value of C_{μ} for the standard k - ε model.

RNG theory also provides an exact expression for the Prandtl numbers σ_k and σ_{ε} which is given implicitly by Eq. (9.10).

$$\left| \frac{1 - 1.329\sigma_k}{0.3929\sigma_k} \right|^{(1-1/e)} \left| \frac{1 + 2.3929\sigma_k}{3.3929\sigma_k} \right|^{1/e} = \frac{\mu}{\mu_t} \quad (9.10)$$

RNG theory predicts identical values for the turbulent Prandtl numbers, thus the equation defining σ_ε will be identical to the equation for σ_k as given by Eq. (9.10). In the limit of high Reynolds numbers Eq. (9.10) predicts $\sigma_k = \sigma_\varepsilon = 0.7179$.

The k and ε equations for the RNG k - ε model are essentially identical to the k and ε equations for the standard k - ε model which are given by Eqs. (9.6)-(9.7), however the turbulence model constants are different to the standard k - ε model values and there is an additional term in the ε equation for the RNG k - ε model. An additional term is also added by Yakhot and Orszag [318] to the equation for ε that does not appear to be based on RNG theory and can be considered as an *ad hoc* addition. This additional term is given by Eq. (9.11).

$$\frac{C_\mu \rho (2S_{ij}S_{ji})^{3/2} S^3 k^2 (\varepsilon - \sqrt{2S_{ij}S_{ji}} k \eta_0)}{(\varepsilon + \beta \sqrt{2S_{ij}S_{ji}} k)} \quad (9.11)$$

It is interesting to note that after the enormous mathematical effort to apply RNG theory the RANS equations, Pope [312] claims that the *ad hoc* term of Eq. (9.11) "is largely responsible for the difference in performance of the standard and RNG (k - ε) models". Essentially the effect Eq. (9.11) has on the ε equation is to decrease the turbulent viscosity in region of high strain rates. It is also worthy of noting that RNG theory calculates analytic values for turbulence model constants $C_{\varepsilon 1}$ and $C_{\varepsilon 2}$. The turbulence model constants for the RNG model in the high Reynolds number limit are presented in Table 9-3.

Table 9-3. Values for the turbulence model constants for the RNG k - ε model in the high Reynolds number limit.

$C_{\varepsilon 1}$	$C_{\varepsilon 2}$	C_{μ}	σ_k	σ_{ε}	η_0	β
1.42	1.68	0.085	0.7179	0.7179	4.38	0.012

The realizable k - ε model utilises essentially the same model equation for the transport of k as the standard and RNG k - ε models, this being Eq. (9.6). The significant difference between the realizable k - ε model and the standard and RNG k - ε models is the ε equation. The realizable k - ε model was developed and first presented by Shih *et al.* [319] and relies upon an exact transport equation for enstrophy that can be recast as an ε transport equation. The realizable k - ε model is so termed as it is a property of the model that the Reynolds stresses are realizable within the Lumley triangle [320]. Realisability is a property that both the standard and RNG k - ε models do not satisfy.

For the realizable k - ε model, the model equation for the transport of k is given by Eq. (9.6), which is identical to the modelled k equation for the standard and RNG k - ε models. The significant difference for the realizable k - ε model over the standard and RNG k - ε models is in the transport equation for ε which is given by Eq. (9.12).

$$\frac{\partial(\rho\varepsilon)}{\partial t} + \frac{\partial(\rho\bar{u}_j\varepsilon)}{\partial x_j} = \frac{\partial}{\partial x_j} \left[\left(\mu + \frac{\mu_t}{\sigma_{\varepsilon}} \right) \frac{\partial \varepsilon}{\partial x_j} \right] + \rho C_{\varepsilon 1} \sqrt{2S_{ij}S_{ji}} \varepsilon - \rho C_{\varepsilon 2} \frac{\varepsilon^2}{k + \sqrt{\nu_t} \varepsilon} \quad (9.12)$$

The value for the turbulent viscosity in the realizable k - ε model is calculated using Eq. (9.8), however C_{μ} is no longer a constant and is computed according to Eq. .

$$C_{\mu} = \frac{1}{4.04 + \left(\sqrt{6} \cos(\phi) k U^* / \varepsilon \right)} \quad (9.13)$$

The expression for ϕ and U^* in Eq. (9.13) is given by Eq. (9.14) and Eq. (9.15) respectively.

$$\phi = \frac{1}{3} \cos^{-1} \left(\frac{\sqrt{6} S_{ij} S_{jk} S_{ki}}{(S_{ij} S_{ij})^{3/2}} \right) \quad (9.14)$$

$$U^* = \sqrt{S_{ij} S_{ij} + (\bar{\Omega}_{ij} - \varepsilon_{ijk} \omega_k)(\bar{\Omega}_{ij} - \varepsilon_{ijk} \omega_k)} \quad (9.15)$$

The standard values for the turbulence model constants for the realizable k - ε model are given in Table 9-4.

Table 9-4. Turbulence model constants used for the realizable k - ε model.

$C_{\varepsilon 1}$	$C_{\varepsilon 2}$	σ_k	σ_ε
1.44	1.90	1.0	1.2

Three k - ω models are examined, the standard k - ω model outlined by Wilcox [317], the shear stress transport k - ω model as outlined by Menter [321] and the stress transport k - ω model of Wilcox [317]. All of the k - ω models feature a transport equation for k as well as a transport equation for ω which can be termed as the specific dissipation rate or ε/k like term. Pope [312] shows that some k - ω models can be recast as k - ε models, after suitable transformation the resulting new k - ε models feature additional terms.

The standard k - ω model outlined by Wilcox [317] features the model transport equation for k of the form of Eq. (9.16), which has some similarities to Eq. (9.6) for the modelled k transport equation for the k - ε models.

$$\frac{\partial(\rho k)}{\partial t} + \frac{\partial(\rho \bar{u}_j k)}{\partial x_j} = \frac{\partial}{\partial x_j} \left[\left(\mu + \frac{\mu_t}{\sigma_k} \right) \frac{\partial k}{\partial x_j} \right] + \mu_t 2 S_{ij} S_{ij} - \rho \beta_i^* f_{\beta^*} k \omega \quad (9.16)$$

The turbulent viscosity in the standard k - ω model is given by Eq. (9.17) which in the high Reynolds number yields $\alpha^* = 1$ is essentially identical to Eq. (9.8) the turbulent viscosity definition in the k - ε models when ω is related to the k - ε model by $\omega = \varepsilon / (C_\mu k)$.

$$\mu_t = \alpha^* \frac{\rho k}{\omega}, \alpha^* = \left(\frac{\beta_i / 3 + (\rho k / 6 \mu \omega)}{1 + (\rho k / 6 \mu \omega)} \right) \quad (9.17)$$

The β_i^* and f_{β^*} terms that are involved in the term governing the dissipation of k in Eq. (9.16) are given by Eqs. (9.18)-(9.19) respectively.

$$\beta_i^* = \beta_\infty^* \left(\frac{4/15 + (\rho k / 8 \mu \omega)^4}{1 + (\rho k / 8 \mu \omega)^4} \right) \quad (9.18)$$

$$f_{\beta^*} = \begin{cases} 1 & \chi_k \leq 0 \\ \frac{1 + 680 \chi_k^2}{1 + 400 \chi_k^2} & \chi_k > 0 \end{cases}, \chi_k = \frac{1}{\omega^3} \frac{\partial k}{\partial x_j} \frac{\partial \omega}{\partial x_j} \quad (9.19)$$

The transport equation for ω in the standard k - ω model is given by Eq. (9.20).

$$\frac{\partial(\rho \omega)}{\partial t} + \frac{\partial(\rho \bar{u}_j \omega)}{\partial x_j} = \frac{\partial}{\partial x_j} \left[\left(\mu + \frac{\mu_t}{\sigma_\omega} \right) \frac{\partial \omega}{\partial x_j} \right] + \alpha \frac{\omega}{k} \mu_t - \rho \beta_i f_{\beta \omega} \omega^2 \quad (9.20)$$

The last term on the RHS of Eq. (9.20) governs the dissipation of ω , this term contains $f_{\beta \omega}$ which is given by Eqs.(9.21).

$$f_{\beta\omega} = \frac{1+70\chi_\omega}{1+80\chi_\omega}, \chi_\omega = \left| \frac{\Omega_{ij}\Omega_{jk}S_{ki}}{(\beta_\omega^*\omega)^3} \right| \quad (9.21)$$

The constants for the standard k - ω model are given in Table 9-5.

Table 9-5. Turbulence model constants used for the standard k - ω model.

β_i^*	σ_k	σ_ε	β_ω^*	α_0	R_ω
0.072	2.0	2.0	0.09	1/9	2.95

The shear stress transport (SST) k - ω model is the second k - ω model that is evaluated. The general model form of the SST k - ω model proposed by Wilcox [317] is followed. A strong feature of the SST k - ω model is the use of blending functions so that the SST k - ω model performs asymptotically correctly in the wall bound and free stream limits. The use of blending function in the SST k - ω model makes the equations considerably lengthier to present as well as making the SST k - ω model rely on more model constants than most established turbulence models. The equation for the transport of k in the SST k - ω model given by Eq. (9.22) is similar to the k equation for the standard k - ω model given by Eq(9.16), however there are some modifications to the terms governing the production and dissipation k , these being the last two terms on the RHS of Eq. (9.22).

$$\frac{\partial(\rho k)}{\partial t} + \frac{\partial(\rho \bar{u}_j k)}{\partial x_j} = \frac{\partial}{\partial x_j} \left[\left(\mu + \frac{\mu_t}{\sigma_k} \right) \frac{\partial k}{\partial x_j} \right] + \min(\mu_t 2S_{ij}S_{ij}, 10\rho\beta_i^{*4}k\omega) - \rho\beta_i^*k\omega \quad (9.22)$$

The second term on the RHS of Eq. (9.22) governs the production of k and is a significant source of difference in the k transport equation between the standard and SST k - ω models. The β_i^* term is given by the same relation as in the standard k - ω model, this being Eq.(9.18). The expression governing the turbulent viscosity μ_t , is given by Eq. (9.23).

$$\mu_t = \frac{\rho k}{\omega} \frac{1}{\max\left(1/\alpha^*, \sqrt{2S_{ij}S_{ij}}F_2/\alpha_1\omega\right)} \quad (9.23)$$

The α_1 term in Eq. (9.23) is a model constant, whilst the F_2 and α^* terms are given by Eqs. (9.24)-(9.17) respectively.

$$F_2 = \tanh\left(\left[\frac{2\sqrt{k}}{0.09\omega y}, \frac{500\mu}{\rho y^2\omega}\right]^3\right) \quad (9.24)$$

The last term on the RHS of Eq. (9.22) governs the dissipation of k , it is of similar form to the same term in Eq (9.16) for the standard k - ω model, but with the piece wise function f_{β^*} removed.

The turbulent kinetic energy Prandtl number σ_k , contained in the first term on RHS of Eq. (9.22) is given by Eq. (9.25) where σ_{k1} and σ_{k2} are model constants.

$$\sigma_k = \frac{\sigma_{k1}\sigma_{k2}}{F_1\sigma_{k2} + \sigma_{k1}(1 - F_1)} \quad (9.25)$$

The F_1 blending term in Eq. (9.25) is given by Eq.(9.26).

$$F_1 = \tanh\left\{\left[\min\left(\max\left[\frac{2\sqrt{k}}{0.09\omega y}, \frac{500\mu}{\rho y^2\omega}\right], \frac{4\rho k}{\sigma_{\omega 2}D_{\omega}^+ y^2}\right)\right]^4\right\} \quad (9.26)$$

The D_{ω}^+ term in Eq. (9.26) is given by Eq. (9.27), with $\sigma_{\omega 2}$ being a model constant.

$$D_{\omega}^{+} = \max \left[\frac{2\rho}{\sigma_{\omega 2} \omega} \frac{\partial k}{\partial x_j} \frac{\partial \omega}{\partial x_j}, 10^{-10} \right] \quad (9.27)$$

The transport equation for ω in the SST k - ω model is given by Eq. (9.28).

$$\frac{\partial(\rho\omega)}{\partial t} + \frac{\partial(\rho\bar{u}_j\omega)}{\partial x_j} = \frac{\partial}{\partial x_j} \left[\left(\mu + \frac{\mu_t}{\sigma_{\omega}} \right) \frac{\partial \omega}{\partial x_j} \right] + \alpha_{\infty} \rho 2S_{ij}S_{ij} - \rho\beta_i\omega^2 + \frac{2(1-F_1)\rho\sigma_{\omega 2}}{\omega} \frac{\partial k}{\partial x_j} \frac{\partial \omega}{\partial x_j} \quad (9.28)$$

The second term on the RHS of Eq. (9.28) governing the production of ω contains α_{∞} which is given by Eq. (9.29).

$$\alpha_{\infty} = F_1\alpha_{\infty,1} + (1-F_1)\alpha_{\infty,2} \quad (9.29)$$

The $\alpha_{\infty,1}$ and $\alpha_{\infty,2}$ terms in Eq. (9.29) are given by Eqs. (9.30) and (9.31) respectively.

$$\alpha_{\infty,1} = \frac{\beta_{i,1}}{\beta_{\infty}^{*}} - \frac{\kappa^2}{\sigma_{\omega 1} \sqrt{\beta_{\infty}^{*}}} \quad (9.30)$$

$$\alpha_{\infty,2} = \frac{\beta_{i,2}}{\beta_{\infty}^{*}} - \frac{\kappa^2}{\sigma_{\omega 2} \sqrt{\beta_{\infty}^{*}}} \quad (9.31)$$

In Eqs. (9.30)-(9.31) $\beta_{i,1}$, $\beta_{i,2}$, β_{∞}^{*} , κ , $\sigma_{\omega 1}$ and $\sigma_{\omega 2}$ are all model constants. The β_i term for the SST k - ω model in Eq. (9.28) is different to the standard k - ω model, with β_i in the SST k - ω model given by Eq. (9.32) where $\beta_{i,1}$ and $\beta_{i,2}$ are model constants.

$$\beta_i = F_1\beta_{i,1} + (1-F_1)\beta_{i,2} \quad (9.32)$$

The required constants for the SST k - ω are given in Table 9-6.

Table 9-6. Turbulence model constants used for the k - ω SST model.

$\sigma_{k,1}$	$\sigma_{\omega,1}$	$\sigma_{k,2}$	$\sigma_{\omega,2}$	α_1	$\beta_{t,1}$	$\beta_{i,2}$	α_0	β_∞^*
1.176	2.0	1.0	1.186	0.31	0.075	0.0828	1/9	0.09

The third k - ω model to be evaluated is the stress- ω model outlined by Wilcox [317]. In the stress- ω model equations for the transport of the Reynolds stresses an equation for ω are solved. The equation for the transport of ω is given by Eq. (9.33).

$$\frac{\partial(\rho\omega)}{\partial t} + \frac{\partial(\rho\bar{u}_j\omega)}{\partial x_j} = \frac{\partial}{\partial x_j} \left[\left(\mu + \frac{\mu_t}{\sigma_\omega} \right) \frac{\partial \omega}{\partial x_j} \right] + \frac{\alpha\rho\omega}{k} \tau_{ij} \frac{\partial u_i}{\partial x_j} - \rho\beta_0 f_{\beta\omega} \omega^2 \quad (9.33)$$

In Eq. (9.33) τ_{ij} represents the Reynolds stress tensor, α , β_0 and σ_ω are constants, $f_{\beta\omega}$ is given by Eq. (9.21) which is the same definition as the standard k - ω model. The turbulent viscosity μ_t , is given by Eq. (9.34).

$$\mu_t = \frac{\rho k}{\omega} \quad (9.34)$$

The Reynolds stress transport equation in tensor form is given by Eq. (9.35).

$$\frac{\partial(\rho\tau_{ij})}{\partial t} + \frac{\partial(\rho\bar{u}_j\tau_{ij})}{\partial x_k} = \frac{\partial}{\partial x_k} \left[\left(\mu + \frac{\mu_t}{\sigma_\tau} \right) \frac{\partial \tau_{ij}}{\partial x_k} \right] - \frac{\rho}{2} P_{kk} - \rho P_{ij} + \frac{2\rho}{3} \beta_0^* f_{\beta^*} \omega k \delta_{ij} - \rho \Pi_{ij} \quad (9.35)$$

The σ_τ term in Eq. (9.35) is a model constant that can be interpreted as the Prandtl number for the Reynolds stresses. The Π_{ij} term in Eq. (9.35) represents the pressure-strain correlation and is given by Eq.(9.36).

$$\Pi_{ij} = \beta_0^* f_{\beta^*} C_1 \omega \left(\tau_{ij} + \frac{2k\delta_{ij}}{3} \right) - \hat{\alpha} \left(P_{ij} - \frac{\delta_{ij} P_{kk}}{6} \right) - \hat{\beta} \left(D_{ij} - \frac{\delta_{ij} P_{kk}}{3} \right) - \hat{\gamma} k \left(S_{ij} - \frac{S_{kk} \delta_{ij}}{3} \right) \quad (9.36)$$

In Eq. (9.36) C_1 , $\hat{\alpha}$, $\hat{\beta}$ and $\hat{\gamma}$ are all model constants. The P_{ij} and D_{ij} tensor abbreviations in Eq. (9.36) are given by Eqs. (9.37) and (9.38) respectively.

$$P_{ij} = \tau_{im} \frac{\partial u_j}{\partial x_m} + \tau_{jm} \frac{\partial u_i}{\partial x_m} \quad (9.37)$$

$$D_{ij} = \tau_{im} \frac{\partial u_m}{\partial x_j} + \tau_{jm} \frac{\partial u_m}{\partial x_i} \quad (9.38)$$

The f_{β^*} term in Eq. (9.36) is given by Eq. (9.39) which is similar (but not identical) to the expression given by Eq. (9.19) for the standard k - ω model.

$$f_{\beta^*} = \begin{cases} 1 & \chi_k \leq 0 \\ \frac{1+640\chi_k^2}{1+400\chi_k^2} & \chi_k > 0 \end{cases}, \chi_k = \frac{1}{\omega^3} \frac{\partial k}{\partial x_j} \frac{\partial \omega}{\partial x_j} \quad (9.39)$$

The model constants for the stress- ω model are given in Table 9-7.

Table 9-7. Turbulence model constants used for the stress- ω model.

C_1	σ_ω	σ_τ	$\hat{\alpha}$	$\hat{\beta}$	$\hat{\gamma}$	C_1	α	β_0^*	β_0
9/5	1/2	1/2	213/275	54/275	136/275	9/5	13/25	9/100	9/125

The final turbulence model that is evaluated is the Reynolds stress model, the implementation that is used here follows that presented by Launder [322] for the

Reynolds stress equations and corresponding ε equation. The quadratic pressure strain model proposed by Speziale *et al.* [323] is utilised in the simulations. The equation governing the transport of ε is given by Eq. (9.40).

$$\frac{\partial(\rho\varepsilon)}{\partial t} + \frac{\partial(\rho\varepsilon u_i)}{\partial t} = \frac{\partial}{\partial x_j} \left[\left(\mu + \frac{\mu_t}{\sigma_\varepsilon} \right) \frac{\partial \varepsilon}{\partial x_j} \right] + C_{\varepsilon 1} \frac{\rho\varepsilon}{k} \tau_{ij} \frac{\partial u_i}{\partial x_j} - C_{\varepsilon 2} \frac{\rho\varepsilon^2}{k} \quad (9.40)$$

In Eq. (9.40) σ_ε , $C_{\varepsilon 1}$ and $C_{\varepsilon 2}$ are model constants and τ_{ij} is the Reynolds stress tensor.

The turbulent viscosity is modelled in the same fashion as with the standard k - ε model and can be expressed as per Eq. (9.8).

The Reynolds stress transport equation is given by Eq. (9.41).

$$\frac{\partial(\rho\tau_{ij})}{\partial t} + \frac{\partial(\rho u_k \tau_{ij})}{\partial x_k} = \frac{\partial}{\partial x_k} \left[\left(\mu + \frac{\mu_t}{\sigma_\tau} \right) \frac{\partial \tau_{ij}}{\partial x_k} \right] - \rho P_{ij} + \frac{2\rho}{3} \varepsilon \delta_{ij} \rho \Pi_{ij} \quad (9.41)$$

In Eq. (9.41) σ_τ is a constant, with P_{ij} and Π_{ij} are defined by Eq. (9.42) and (9.43) respectively.

$$P_{ij} = \tau_{ik} \frac{\partial u_j}{\partial x_k} + \tau_{jk} \frac{\partial u_i}{\partial x_k} \quad (9.42)$$

$$\begin{aligned} \Pi_{ij} = & -\left(C_1 \rho \varepsilon + C_1^* P\right) b_{ij} + C_2 \rho \varepsilon \left(b_{ik} b_{kj} - \frac{b_{mn} b_{mn} \delta_{ij}}{3} \right) + \left(C_3 - C_3^* \sqrt{b_{ij} b_{ij}} \right) \rho k S_{ij} + \\ & + C_4 \rho k \left(b_{ik} S_{jk} + b_{ik} S_{ik} - \frac{2 b_{mn} S_{mn} \delta_{ij}}{3} \right) + C_5 \rho k \left(b_{ik} \Omega_{kj} + b_{jk} \Omega_{ik} \right) \end{aligned} \quad (9.43)$$

In Eq. (9.43) the quadratic pressure strain correlation, C_1 , C_1^* , C_2 , C_3 , C_3^* , C_4 and C_5 are model constants, with the b_{ij} , S_{ij} and Ω_{ij} terms given by Eqs. (9.44), (9.45) and (9.46).

$$b_{ij} = \frac{\rho\tau_{ij} - \frac{2}{3}\rho k\delta_{ij}}{2\rho k} \quad (9.44)$$

$$S_{ij} = \frac{1}{2} \left(\frac{\partial u_j}{\partial x_i} + \frac{\partial u_i}{\partial x_j} \right) \quad (9.45)$$

$$\Omega_{ij} = \frac{1}{2} \left(\frac{\partial u_i}{\partial x_j} - \frac{\partial u_j}{\partial x_i} \right) \quad (9.46)$$

The necessary model constants for the Reynolds stress turbulence model are given in Table 9-8.

Table 9-8. Turbulence model constants used for the quadratic pressure strain Reynolds stress turbulence model.

σ_ε	$C_{\varepsilon 1}$	$C_{\varepsilon 2}$	C_1	C_1^*	C_2	C_3	C_3^*	C_4	C_5
1.0	1.44	1.92	3.4	1.8	4.2	0.8	1.3	1.25	0.4

9.4 Constant Density Case Results

The velocity results for the numerical simulations and experimental LDV measurements are reported in this Section for the constant density case. The constant density data is used as a reference point particularly as the constant density free jet issuing into a small velocity co-flowing fluid is a well studied problem both experimentally and numerically.

For the axial variation of the mean and RMS velocity reported in Fig. 9-2 and Fig. 9-9 it can be seen that generally most of the turbulence models adequately simulate these quantities with respect to the experimental data. Exceptions to this trend are the stress- ω and the standard k - ω models, both predict a potential core that too long and both predict a peak RMS velocity that is lower than the predictions of the other models and the experimental data. In this simple non-reacting constant density case the implication of changing $C_{\varepsilon 1}$ in the standard k - ε model can be seen, increasing $C_{\varepsilon 1}$ from 1.44 to 1.6 results in a slower decay of the mean velocity but this is at the expense of decreasing the predicted RMS velocity that is predicted quite well with a standard value of 1.44. Generally all of the simulations over predict the mean spreading rate compared to the measurements in Fig. 9-3-Fig. 9-6 and Fig. 9-8, however radial predictions for the RMS velocity appear to better for the stress- ω and the standard k - ω models than the other models. For the standard k - ε model $C_{\varepsilon 1} = 1.44$ produces better results for the mean radial velocity, whilst $C_{\varepsilon 1} = 1.60$ produces better results for the RMS radial velocity.

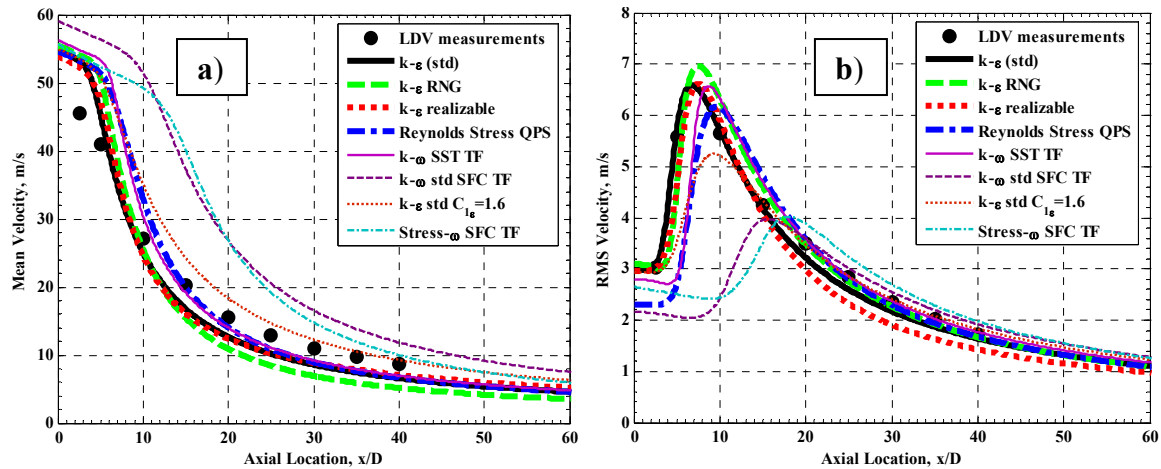


Fig. 9-2. a) Mean axial velocity and RMS velocity b) (right) at $r/D=0$ for the cold flow case with a central jet velocity of 50m/s.

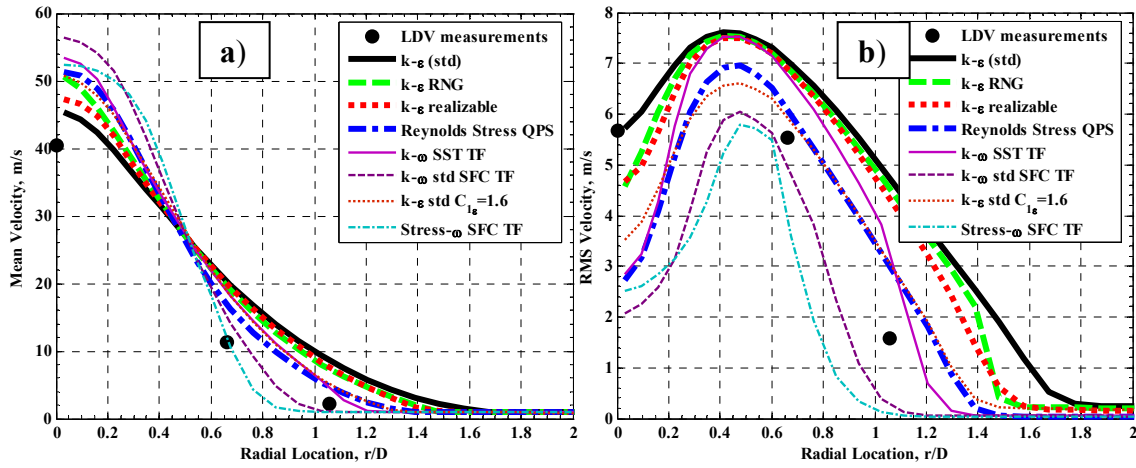


Fig. 9-3. a) Mean axial velocity and RMS axial velocity b) (right) at $x/D=5$ for the cold flow case with a central jet velocity of 50m/s.

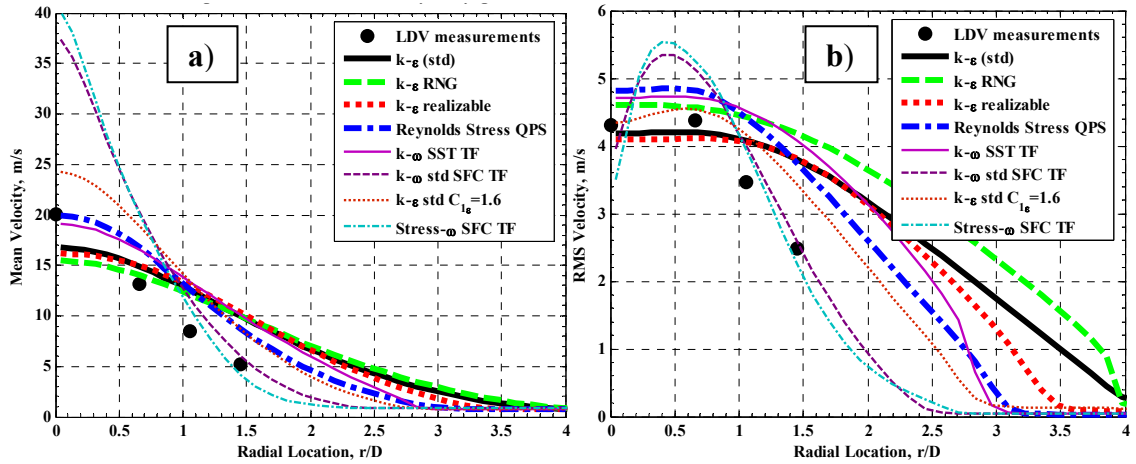


Fig. 9-4. a) Mean axial velocity and RMS axial velocity b) (right) at $x/D=15$ for the cold flow case with a central jet velocity of 50m/s.

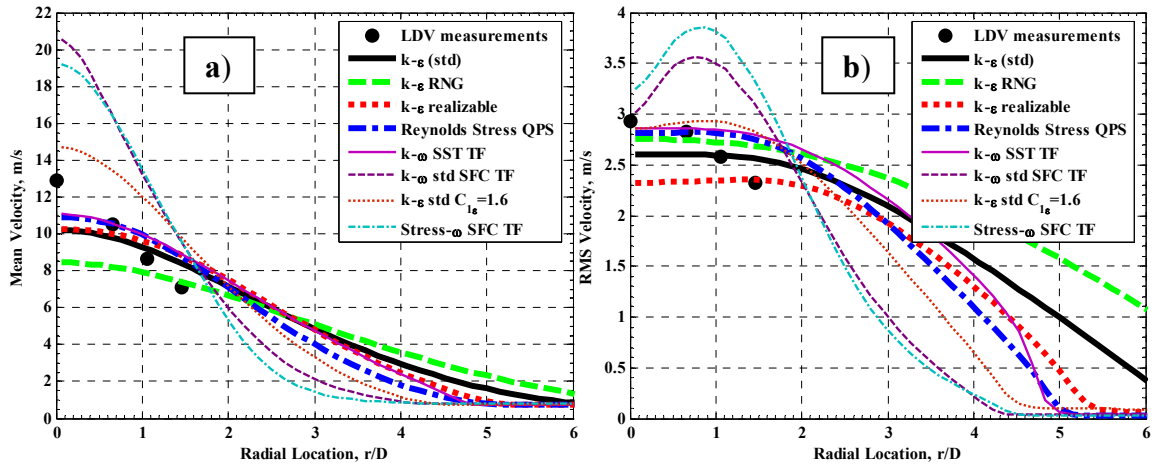


Fig. 9-5. a) Mean axial velocity and RMS axial velocity b) (right) at $x/D=25$ for the cold flow case with a central jet velocity of 50m/s.

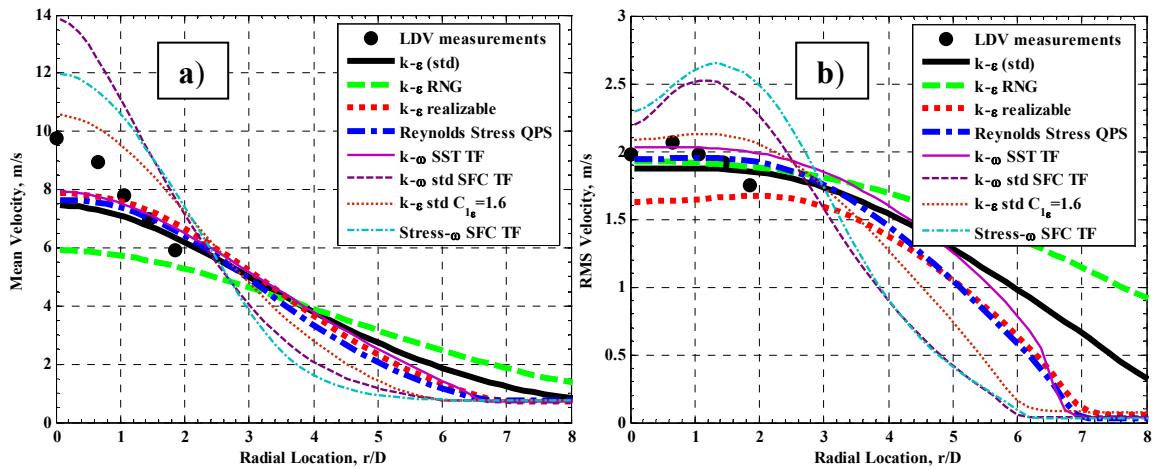


Fig. 9-6. a) Mean axial velocity and RMS axial velocity b) (right) at $x/D=35$ for the cold flow case with a central jet velocity of 50m/s.

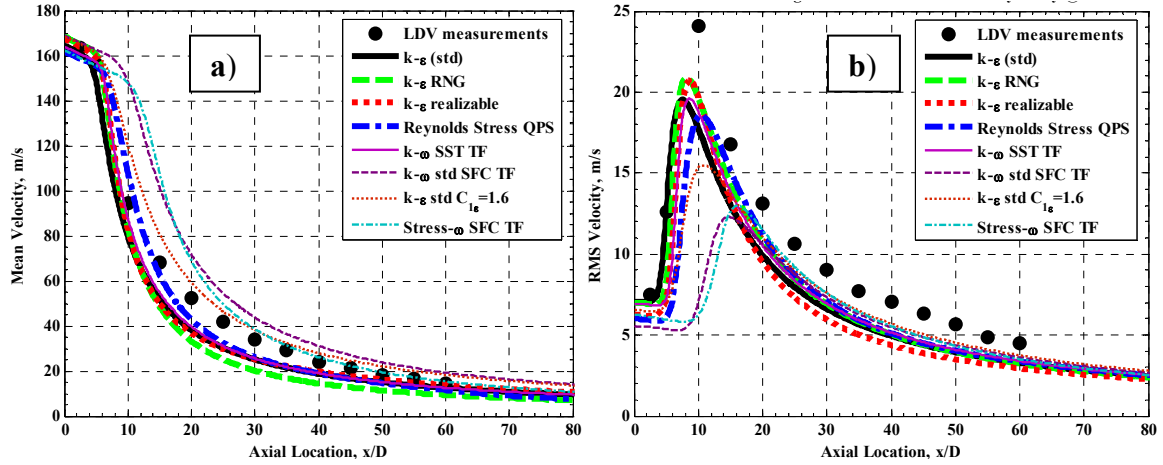


Fig. 9-7. a) Mean axial velocity and RMS axial velocity b) (right) at $r/D=0$ for the cold flow case with a central jet velocity of 150 m/s.

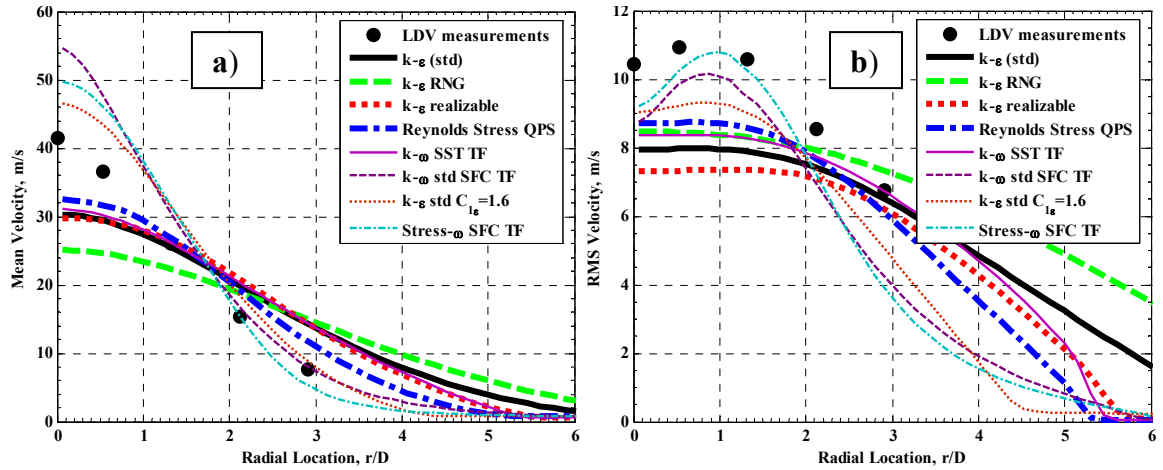


Fig. 9-8. a) Mean axial velocity and RMS axial velocity b) (right) at $x/D=25$ for the cold flow case with a central jet velocity of 150 m/s.

9.5 Variable Density Case Results

The velocity results for the numerical simulations and experimental LDV measurements are reported in this Section for the variable density case. The variable density data is used

as a reference point particularly as the constant density free jet issuing into a small velocity co-flowing fluid is a well studied problem both experimentally and numerically.

In Fig. 9-9 for the low velocity case and in Fig. 9-12 for the high velocity case it can be seen that none of the RANS turbulence models predict the axial variation of the mean velocity accurately. Acceptable results can be claimed for most of the turbulence models (with the exception of the stress- ω and the standard k - ω models) for the low velocity case for the RMS velocity in Fig. 9-9b). Poor prediction for all of the turbulence models of the RMS velocity for the location and the magnitude of peak RMS velocity is found for the high velocity case in Fig. 9-12b). As with the constant density cases the spreading rate in Fig. 9-10-Fig. 9-11 and Fig. 9-13-Fig. 9-14 for the mean velocity is found to be predicted to be too large and the radial profile for the RMS velocity are found to be under predicted compared to the measurements.

As a general conclusion from the non-reacting simulations it has been shown that there are several RANS models that perform *adequately* for both the constant density and variable density jet simulations. No single model stands out as calculating all of these flows better than others, typically a balance is struck between predicting the mean and the RMS velocity acceptably. A general recommendation for an adequate turbulence model for the reacting PDF calculations in Chapter 10 are the standard k - ϵ model with $C_{1\epsilon}=1.60$ and the shear stress transport k - ω model. For all of the flows examined changing $C_{1\epsilon}$ from the standard value of 1.44 to 1.6 generally improvement were realised in the mean velocity fields at the expense of decreased predictive capabilities for the RMS velocity fields.

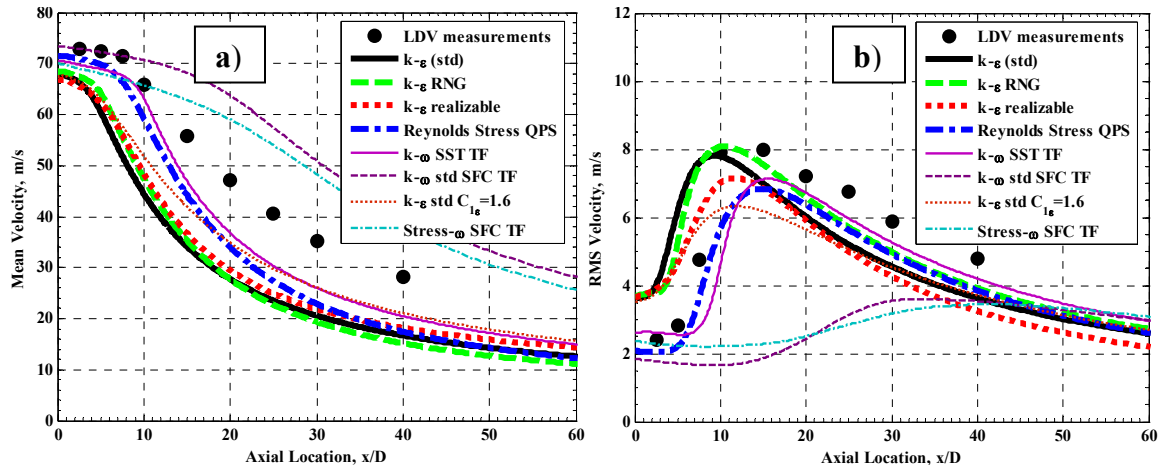


Fig. 9-9. a) Mean axial velocity and RMS axial velocity b) (right) at $r/D=0$ for the 1500K coflow case with a central jet velocity of 50m/s.

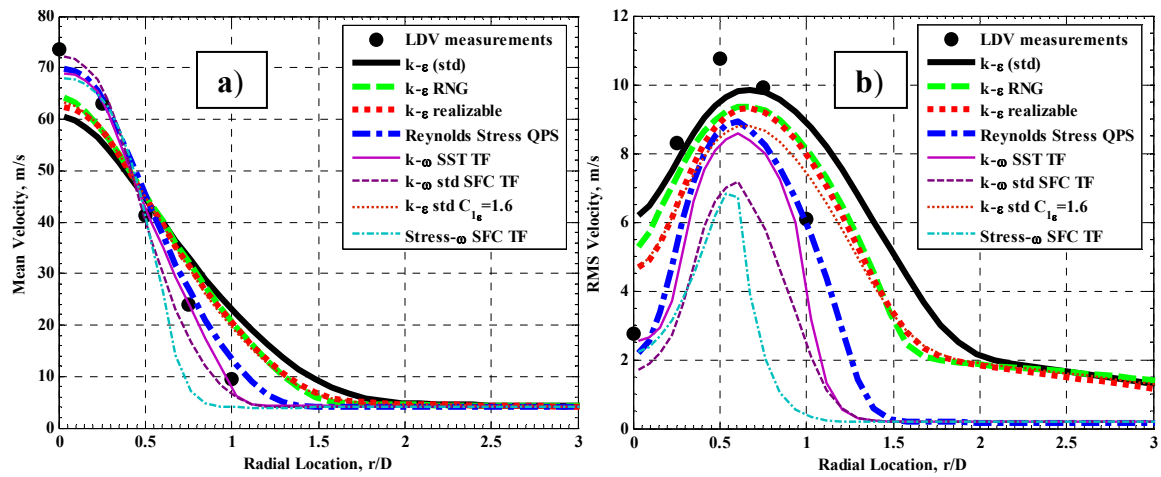


Fig. 9-10. a) Mean axial velocity and RMS axial velocity b) (right) at $x/D=5$ for the 1500K coflow case with a central jet velocity of 50m/s.

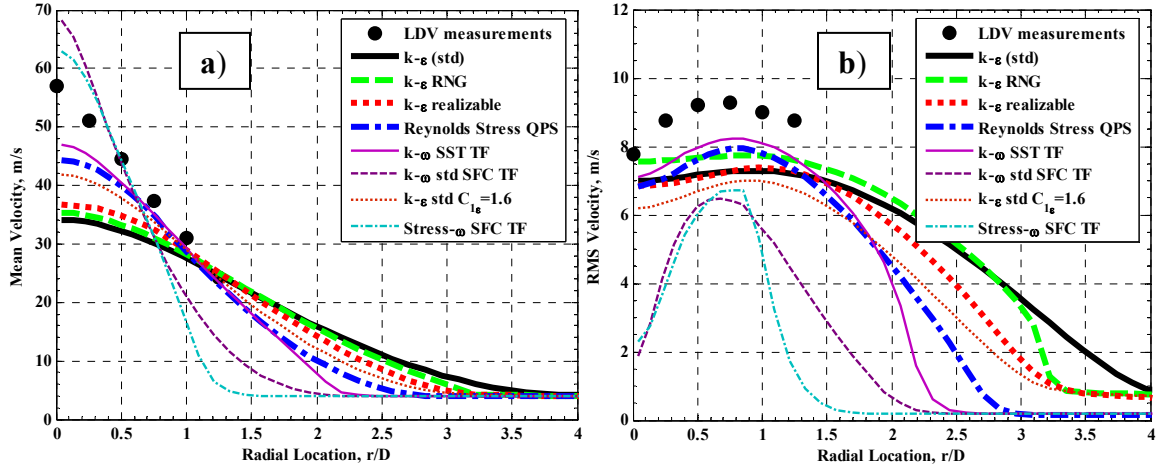


Fig. 9-11. a) Mean axial velocity and RMS axial velocity b) (right) at $x/D=15$ for the 1500K coflow case with a central jet velocity of 50m/s.

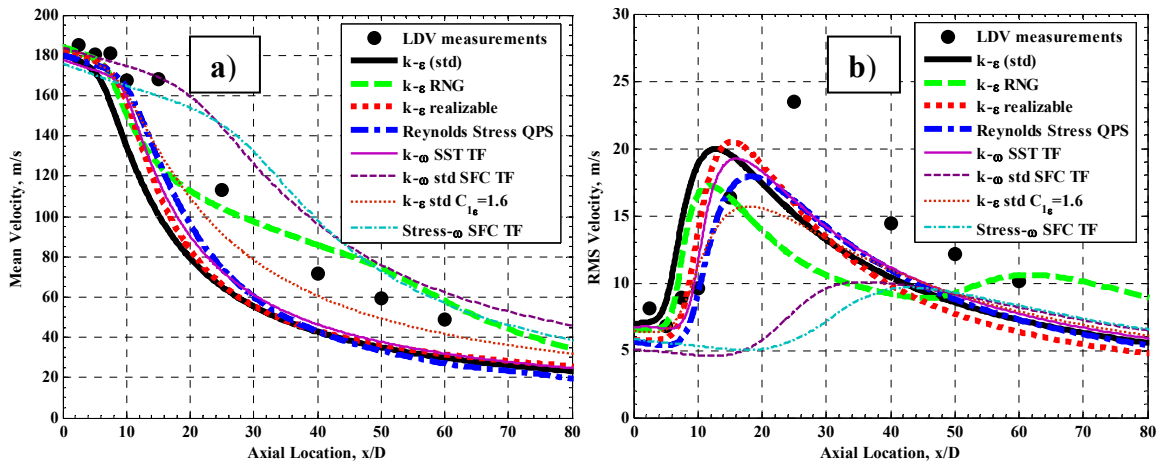


Fig. 9-12. a) Mean axial velocity and mean RMS axial velocity b) (right) at $r/D=0$ for the 1500K coflow case with a central jet velocity of 150m/s.

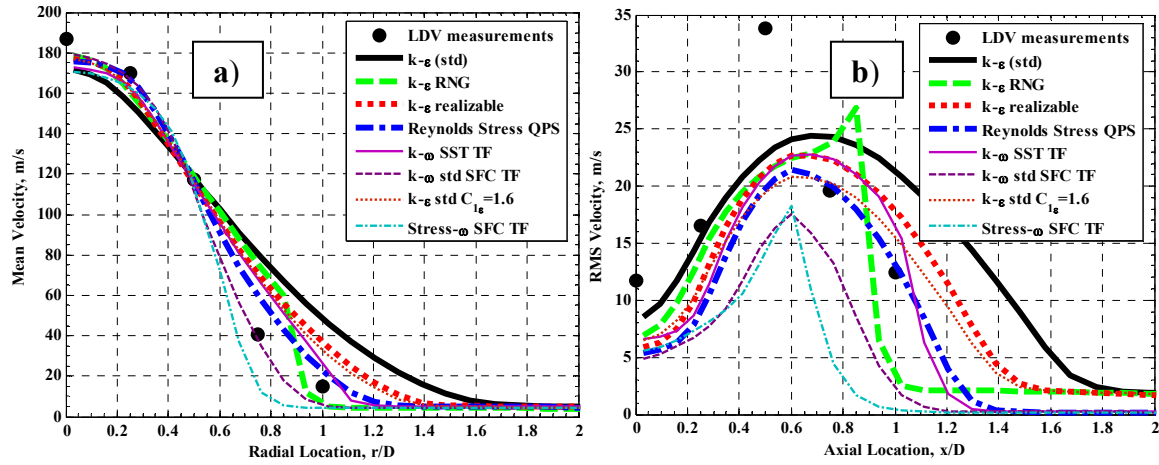


Fig. 9-13. a) Mean axial velocity and RMS axial velocity b) (right) at $x/D=5$ for the 1500K coflow case with a central jet velocity of 150m/s.

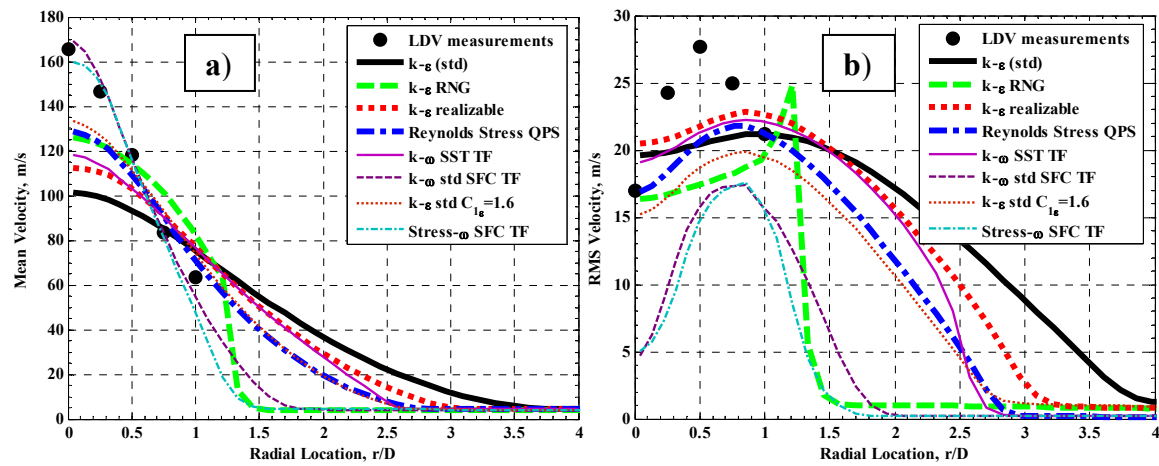


Fig. 9-14. a) Mean axial velocity and RMS axial velocity b) (right) at $x/D=15$ for the 1500K coflow case with a central jet velocity of 150m/s.

CHAPTER 10 RANS TPDF SIMULATION RESULTS

As highlighted in Chapter 3, a significant feature of the PM1 flame series is that finite-rate chemistry effects become more significant as the jet velocity is increased. For the PM1-150 and PM1-200 flames finite-rate chemistry effects become so strong that distinct regions of extinction and re-ignition occur. The main aim of this thesis is to examine finite-rate chemistry effects in turbulent premixed combustion, whilst the PPJB has been developed and studied extensively experimentally in Chapters 3 to 8; it is in this Chapter that finite-rate chemistry effects in turbulent premixed combustion are examined numerically. There has been a large number of numerical models for premixed combustion proposed, some of these models are summarised in various review articles [13, 324, 325, 326]. It is simply not possible to examine and evaluate all of the possible turbulent premixed combustion models in this thesis.

To model the PM1 flame series either a RANS or LES based methodology needs to be applied. For an LES simulation to calculate flames that feature significant finite-rate chemistry effects the following requirements should be considered as a minimum: the model should not assume any precomputed form for the chemistry such as a flamelet table, detailed chemistry schemes should be able to be implemented, the transport equations for several species should be solved (at least more than the one or two characteristic scalars commonly used in LES). The only LES model that immediately satisfies these requirements is the LES/FDF model. The LES/FDF model although providing promising results for piloted diffusion flames in the results reported by Raman and Pitsch [327], is yet to be conclusively validated parametrically for a series flames that

feature finite-rate chemistry effects. A second drawback of the LES/FDF method is the enormous computation requirements for high fidelity LES simulations [328]. Based on these reasons the LES methodology is ruled out as a simulation methodology in this thesis.

As finite-rate chemistry effects are the focus of this study, the RANS based PDF method has been selected as the simulation technique. This selection is based on the success of the PDF method in predicting finite-rate chemistry effects in non-premixed combustion, particularly for the piloted diffusion flame series [80, 97, 159].

In this Chapter the PPJB PM1 flames series is simulated numerically using a Reynolds Averaged Navier Stokes (RANS) based transported probability density function (TPDF) methodology. The numerical method uses a finite-volume (FV) RANS approach for the solution of the continuity, momentum and turbulence equations and is coupled with a Lagrangian particle based Monte Carlo solution of the transported probability density function (TPDF) equations for the thermo-chemical composition. The strategy of coupling the finite-volume method and particle methods in this study is termed a hybrid particle-finite-volume scheme, with the specific PDF method termed a TPDF-RANS method.

The numerical results reported indicate that the TPDF method is capable of producing promising results for the velocity, scalar and finite-rate chemistry effects. The weakest link in the modelling methodology is shown to be the turbulence model. In particular, the model equation for the transport of the turbulent kinetic energy dissipation (ε) in the standard k - ε model or its equivalent the specific turbulent kinetic dissipation (ω) in the k - ω model are the weakest link of these turbulence models. Optimal results in terms of the scalar variance and finite rate-chemistry effects are found with values of C_ϕ much larger than those established in previous studies for non-premixed combustion.

A review of previous studies using the PDF method to simulate turbulent premixed combustion is discussed in Section 10.1. An overview of the numerical method including

a detailed discussion of the mixing models, ISAT and sources of numerical errors is presented in Section 10.2. Issues and error analysis regarding the numerical implementation of the TPDF-RANS method to the PPJB flames including discretisation error, statistical error, numerical bias, ISAT/ODE errors and solution/convergence strategies are discussed in Section 10.3. The numerical results for the RANS-TPDF simulations are reported in two Sections. In Section 10.4 the results for the RANS-TPDF simulations of the PM1 PPJB flame series using two different turbulence models are compared with the experimentally obtained fields for the mean and RMS of velocity and temperature. In Section 10.5 the RANS-TPDF simulations results are examined with respect to finite-rate chemistry effects. This is done almost exclusively by examining the product $[\text{CO}][\text{OH}]$ both numerically and experimentally. A general discussion of the results in terms of turbulence models, mixing models, value of the time scale ratio C_ϕ , calculating the mean chemiluminescence for experimental comparison and general predictive capabilities with regards to the TPDF-RANS method as it is implemented in this study is discussed in Section 10.6.

10.1 The PDF Method in Premixed Combustion

A background for the PDF method has already been presented in Chapter 2. Invariably, because of the dominance of non-premixed combustion in the development and demonstrated success the background presented in Chapter 2 primarily focused on application of the PDF method to turbulent non-premixed combustion. An overview of the PDF method specifically focused on turbulent premixed combustion is presented below.

A pioneering work in the application of PDF methods to premixed combustion was presented by Pope [329] in a 1D simulation using a kinetic mechanism that has three independent species that is combined with a joint composition-velocity PDF. The predictive capability for CO and NO was shown for wide range of chemical and

turbulence timescales to be excellent. The increased error for the lean mixtures simulated was expected to be due to the limitations of the three independent species kinetic scheme. A continuation of the work of Pope [329] was presented by Anand and Pope [330] where an equation for the joint velocity and reaction progress variable PDF was formulated and solved. Essentially the results by Anand and Pope [330] showed that the PDF method could predict the turbulent burning velocity well compared to experimental measurements, this is an important validation parameter to predict.

Another early pioneering work in the application of PDF to turbulent premixed combustion was made by Roekaerts [94, 331] who examined a jet stirred reactor. The jet stirred reactor is an idealised geometry in turbulent premixed combustion where a high velocity jet of fresh reactants mixes with partially reacted and completely reacted combustion products at constant equivalence ratio. Although it is difficult to assess the success of the result reported by Roekaerts [94] to the experimental results, the advantage of being able to include the effects of turbulent fluctuations in the mean reaction rate term inherent in the PDF method for premixed is established.

Although not strictly a PDF method Pope and Cheng [332] proposed a stochastic flamelet model that seems to be more closely related to PDF methods than flamelet methods. A further tailoring of the PDF method to turbulent premixed combustion is presented by Pope and Anand [333] where specific terms are reduced to produce a specific PDF model for the flamelet regime and a specific model for the distributed reaction regime. The equations presented by Pope and Anand [333] are far closer to the true PDF equations than those proposed by Pope and Cheng [332] making them more universally applicable particularly with regards to chemistry.

Joint velocity-composition PDF simulation results for a lean-premixed bluff-body combustor bluff-body combustor have been presented by Cannon *et al.* [334] and these results are compared with the limited experimental results reported by Nandula *et al.* [335]. A five step reduced mechanism with the capability of representing NO formation was used in combination with ISAT for chemistry computations. Although globally, the

results of Cannon *et al.* [334] indicate that the correct trend for the single case examined, errors in the mean scalar and velocity radial profiles occurred near the location of the mean reaction zone. Part of this error can be attributed to the deficiencies of the k - ϵ turbulence model in the recirculation region, also errors in the CO and NO predictions can be partially attributed to the limitations of the reduced mechanism. The results reported by Cannon *et al.* [334] also confirm that the PDF method is capable of reproducing at least at a qualitative level the finite-rate chemistry effects that occur at high turbulence intensities for the modelled premixed burner.

Other simulations of the bluff-body combustor geometry reported by Nandula *et al.* [335] using the PDF methodology has been reported by Vicente *et al.* [336] and Fueyo *et al.* [337]. The results of these simulations appear to be slightly improved over those of Cannon *et al.* [334] however significant room for improvement still remains for the minor species CO, OH and NO. Similar to the results by Cannon *et al.* [334] it appears from the results reported by Vicente *et al.* [336] that the mean flame brush width is under predicted. Fueyo *et al.* [337] highlight the significant influence that different turbulence models have on the results for the scalar and velocity profiles after the bluff body.

The application of the PDF method to a well documented turbulent premixed flame has been carried out by Lindstedt and Vaos [338]. The flames simulated are slender Bunsen flames that are supported initially by a moderately large (five jet diameters) hot coflow of combustion products, more details of the burner are reported by Chen *et al.* [10]. A reduced complex chemical mechanism for methane oxidation is utilised that includes NO formation featuring 14 solved and 15 steady state species. As a single pass parabolic marching method was used for the solution scheme, direct integration of the chemical source term was possible although still at considerable computational cost. A common general criticism of PDF methods applied to premixed combustion is their inability to account for a laminar flame speed in the calculations. Based on a fractal based reaction rate closure proposed by Kuan *et al.* [339] it is possible for a laminar flame speed and small-scale turbulence properties to be incorporated into the scalar time-scale ratio. The down side of this approach is that another empirical constant C_ϕ^* is required to be

assigned for closure to be complete. Overall the result reported by Lindstedt and Vaos [338] agree reasonably well with the experimental results however, agreement between the experimental and computed radial profiles for turbulent kinetic energy and flame brush thickness could be improved. Lindstedt and Vaos [338] also note that the prediction of extinction in the flame series is not adequately predicted.

Whilst there can be some agreement for the EMST mixing model that a value of $C_\phi = 1.5$ produces good results in non-premixed combustion there is not the same level of confidence for premixed combustion, in fact little is known about the generality of the scalar time scale of the reaction progress variable in premixed combustion. Lindstedt and Vaos [338] propose a value for $C_\phi = 4.0$ for the Modified Curl mixing model as near optimal with a value of $C_\phi^* = 1.2$ for their proposed fractal based closure [339] for the scalar time scale ratio. From the results presented by Lindstedt and Vaos [338] comparing the effect of C_ϕ for $C_\phi^* = 0.0$ it is not clear in that $C_\phi = 4.0$ is the optimal value of C_ϕ , it could be argued that $C_\phi = 8.0$ yields equally good or better results than $C_\phi = 4.0$ as the mean OH radial profiles have smaller error and the reaction progress variable appears to be predicted in better agreement with the experimental data at $x/D > 8.5$ for $C_\phi = 8.0$, especially for the F1 flame. Generally these values of C_ϕ are considered to be much larger than those accepted for non-premixed combustion.

No PDF simulations published to date has compared the performance of different mixing models in turbulent premixed combustion. Lindstedt and Vaos [338] use the MC mixing model exclusively in their investigation; they claim the modified Curl mixing model performs reasonably well for source term dominated problems, of which premixed combustion is one. Comparative examination of other mixing models such as the EMST and IEM mixing models to see if the MC mixing model is indeed optimal for source term dominated problems has not been reported.

Although almost all applications of the TPDF method to turbulent premixed combustion have been to steady state flows, Hulek and Lindstedt [340] have examined steady and unsteady propagating turbulent premixed flames. The unsteady computations were enabled by computation of a mean pressure at each time step by a finite volume solver. The mean PDF equations were then solved for the corresponding time step. This computational method can be likened to an unsteady RANS (URANS) calculation for the PDF method. Computation of the reaction rate was made computationally tractable by the use of a single step mechanism.

An extension of PDF computations for turbulent premixed combustion from laboratory flames to practical geometries has been examined by James *et al.* [341, 342], who examined a model lean premixed gas turbine combustor. Although in this geometry the air and fuel enter as separate streams into the premixer, at the exit plane of the premixer the mixture fraction PDF is essentially a delta function at the operational air to fuel ratio. To simplify computations an axisymmetric geometry is utilised. Complex chemistry is included in the computations with an augmented reduced mechanism (ARM) for methane-air-nitrogen chemistry that includes NO formation. ISAT tabulation was utilised to accelerate the reaction rate computation with a reported speed up factor of 165 over direct integration. The reported computational results for the mean temperature field are in excellent agreement with experimental measurements, further assessment of the predictive accuracy for minor species and finite-rate chemistry is not possible due to a lack of experimental data. It is interesting to note that one of the few other universal (valid in the premixed and non-premixed limits) RANS models that can incorporate complex chemistry, the eddy break-up (EBU) model, was reported to not be capable of stabilising a flame in this geometry [342]. In summary the results reported by James *et al.* [342] confirm that the PDF method is capable of stabilising a turbulent premixed flame in a practical premixed combustor with detailed chemistry in a geometry where other models fail.

A common criticism of the PDF method in turbulent premixed combustion simulations is that there is no immediate way of incorporating molecular diffusion transport effects that

are important in determining the laminar premixed flame speed, hence turbulent flame speed. One solution to this argument has already been mentioned in the literature review above, this being the time scale ratio modification by Kuan *et al.* [339]. As an alternative to the time scale ratio model by Kuan *et al.* [339] it can be argued that perhaps it is not necessary to include the molecular diffusivity effect for certain flames. Whilst it is of course acknowledged that mixing occurs at the smallest scales which are governed by molecular diffusion, it is proposed in a thickened flame front where the flame front thickness is of the order of the integral length scale the transport of reactants in the flame front will be dominated by turbulent transport rather than molecular transport. The application of this hypothesis is proposed to be justified for the PPJB flames by the observation that significantly reduced scalar gradients in the instantaneous flame front are observed as reported in Chapters 5, 7 and 8. It is also found that the instantaneous flame thickness is so large it is often of the order of the integral length scale for the high velocity cases. It is also important to emphasise that that neglecting molecular transport is not being proposed to be valid for simulating the thin flamelet regime of turbulent premixed combustion where the diffusion length scales can be of the same order of the instantaneous flame thickness, but rather the mechanism is being proposed to be valid for the distributed or well stirred regimes of combustion.

10.2 Numerical Algorithm and Numerical Models

Details of the finite-volume method and the discretisation method that is applied to the continuity, momentum and turbulence equations are detailed in Chapter 2. The specifics of the RANS turbulence models used for this study are outlined in Chapter 9 and are not repeated here. The fundamental equations for the PDF methodology are outlined in Chapter 2 together with an outline of the numerical algorithm for the Monte Carlo particle method. In this section the specific details of the micro mixing model, the ISAT algorithm and the Monte Carlo solution method are examined in detail.

As mentioned previously the stochastic Monte Carlo particle method requires a model to simulate mixing between particles this model is typically termed the mixing model. The three mixing models used in this study are the Modified Curl (MC), Interaction by Exchange with the Mean (IEM) and Euclidean Minimum Spanning Tree (EMST). Whilst there are many desirable features for mixing models as outlined by Pope [312] the above three mixing satisfy the basic minimum requirements of conservation of the mean scalar value and the temporal decay of the scalar variance displays the correct exponential rate. A detailed discussion of the specifics of these mixing models is given in greater detail in Chapter 2. Where possible the value of the mixing model constant C_ϕ is modified in an attempt to obtain an understanding of the optimal value of C_ϕ for the particular mixing model.

As mentioned earlier the stochastic Monte Carlo implementation of the PDF features a number sources of error, the dominant two sources are termed statistical error and statistical bias. There are two controls that are available to control the statistical error and statistical bias: The number of iterations in the time average and the number of particles per cell. The number of particles per cell directly influences the level of statistical error and statistical bias, the use of time averaging directly influences the statistical error and only very weakly influences the error due to bias in an indirect fashion. The error due to statistical bias can be attributed to the statistical fluctuations in the particle fields used in the particle evolution equations, this error term is examined in detail for PDF methods by Pope [127]. The error due to statistical bias is expected to scale as $(N_{ppc})^{-1}$, where N_{ppc} is the number of particles per cell. The error due to the so called statistical error is due to the fact that there are only a finite number of particles representing the joint PDF. The statistical error scales as $(N_{TA}N_{ppc})^{-1/2}$, where N_{TA} is the number of iterations in the time average.

The total error ($\varepsilon_{MC,tot}$) involved in the Monte Carlo implementation of the PDF method can be related to the number of particles per cell (N_{ppc}) and the number of iteration in the time average according to Xu and Pope [343, 344] by Eq.(10.1).

$$\varepsilon_{MC,tot} = \frac{a}{M^2} + \frac{b}{N_{ppc}} + \frac{c}{\sqrt{IN_{ppc}}} \quad (10.1)$$

In Eq. (10.1), M is the mesh density and a , b and c are problem dependant error coefficients for the discretisation, bias and statistical errors respectively.

To accomplish time averaging in the Monte Carlo PDF calculations during the phase of generating a statically stationary solution, the time averaging algorithm proposed by Xu and Pope [343, 344] is used for the calculations. The time averaging algorithm is given by Eq. (10.2).

$$\phi_{TA}^j = \left(1 - \frac{1}{N_{TA}}\right) \phi_{TA}^{j-1} + \frac{1}{N_{TA}} \phi^j \quad (10.2)$$

In Eq. (10.2) N_{TA} is the number of iterations in the time average, ϕ_j is the Monte Carlo realisation of the thermo chemical composition vector at the j^{th} iteration, ϕ_{TA}^{j-1} is the value of the mean the thermo chemical composition vector at the $(j-1)^{\text{th}}$ iteration and ϕ_{TA}^j is the calculated value of the new mean for the thermo chemical composition vector at the j^{th} iteration. If N_{TA} is set too large during the initial stages of the solution convergence will be very slow and likewise if N_{TA} is set too small an unacceptable level of statistical noise will be present in the solution and the approach and achievement of a statistically stationary solution will be difficult to judge. During the phase of building a statistically steady solution, it is found for the present simulations of the PPJB that $N_{TA} = 25$ is an

acceptable compromise to rapidly achieve a statistically stationary solution and an acceptably small level of statistical noise present in the solution.

After a statically stationary solution is achieved it is desirable to minimise the amount of statistical noise in the solution using time averaging according to Eq. (10.3).

$$\phi_{TA}^j = \left(1 - \frac{1}{N_{TA}^j}\right) \phi_{TA}^{j-1} + \frac{1}{N_{TA}^j} \phi^j \quad (10.3)$$

Eq. (10.3) is almost identical to Eq. (10.2) except that N_{TA} in Eq. (10.2) is replaced by N_{TA}^j in Eq. (10.3), N_{TA}^j is defined by Eq. (10.4).

$$N_{TA}^j = N_{TA}^{j-1} + N_{inc} \quad (10.4)$$

In Eq. (10.4), N_{inc} is the increment that the number of iterations in the time average is incremented by at each iteration step. If N_{inc} is too small convergence is reached far too slowly, if N_{inc} is set too large an unacceptably large amount of statistical error may remain in the final converged solution. It is found for the present simulations of the PPJB that setting $N_{inc} = 0.5$ yields acceptable results however this was not optimised and larger values may well be valid and produce faster convergence. Simulations were carried out typically until $N_{TA}^j = 5000$ assuring that any contribution that statistical error makes to the solution is minimised.

10.3 Numerical Error Analysis and Validation

The issues concerning the numerical implementation of the hybrid Monte Carlo finite-volume method is examined in this section. As discussed earlier the hybrid Monte Carlo

finite-volume method uses a standard finite-volume based method for the momentum, continuity and turbulence equations and a stochastic Monte Carlo particle method for the thermo-chemical transport equations. The numerical validation and error can be evaluated individually for all of the relevant components. Although all of the relevant parameters are coupled in their effect on the simulation, they may be isolated to evaluate their effect. An example of this is the number of grid cells and the number of particles per cell. For a sufficiently large number of cells the solution no longer changes significantly from one cell to another, in this situation the optimal number of particles per cell essentially becomes independent of the of the number of cells. The discussion and evaluation of numerical method and validation is examined separately for the finite-volume and stochastic Monte Carlo particle method.

The convergence of velocity and temperature at a specific location is reported in Fig. 10-1 and Fig. 10-2 respectively. Essentially both of these graphs indicate that even for a very coarse grid of 2000 cells the error in velocity would be around 5% and the error in temperature around 3% at the selected monitor points. For all of the simulations a grid size of 35000 was utilised. In Fig. 10-7 some global flame measures of the statistical convergence for the number of particles per cell are examined. All of these indicators appear to be very insensitive to the number of particles indicating that less than 2% error for the flame length and thickness and maximum temperature variance can be obtain with only 10 particles per cell.

The variation at a particular monitor point for temperature and velocity as a function of the number of particles per cell (PPC) is examined in Fig. 10-3 and Fig. 10-4. For these monitor points the $\pm 2\%$ error bound occurs at 4 PPC for temperature and 10 PPC for velocity. An examination of the effect of the number of particles per cell of global flame front measures such as the flame length the mean flame front thickness and the peak axial scalar RMS indicates that 20 PPC is sufficient to remain within a $\pm 2\%$ error bound.

The effect of the ISAT tolerance on several minor species concentrations and some global flame properties is examined in Fig. 10-5 and Fig. 10-6. Both of these figures

indicate that the $\pm 2\%$ error bound maybe adhered to with an ISAT error tolerance less than or equal to 1×10^{-5} .



Fig. 10-1. Convergence of the axial velocity as a function of the inverse number of grid cells at $x/D=60$, $r/D=0$ for the PM1-150 flame.

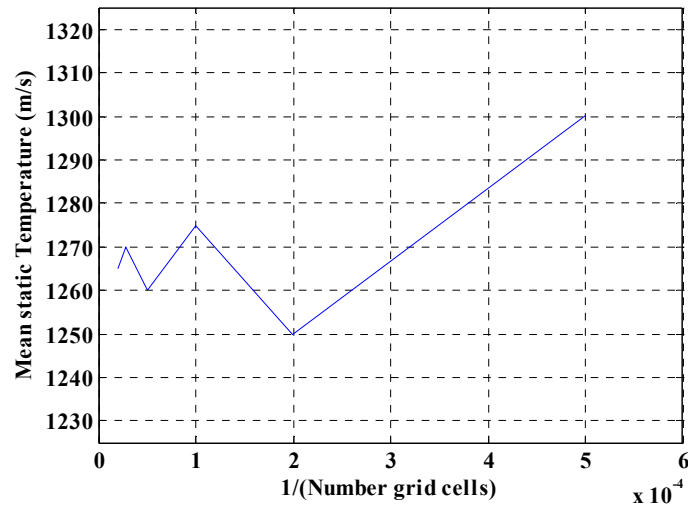


Fig. 10-2. Convergence of the mean static temperature as a function of the inverse number of grid cells at $x/D=22.5$, $r/D=0$ for the PM1-150 flame.

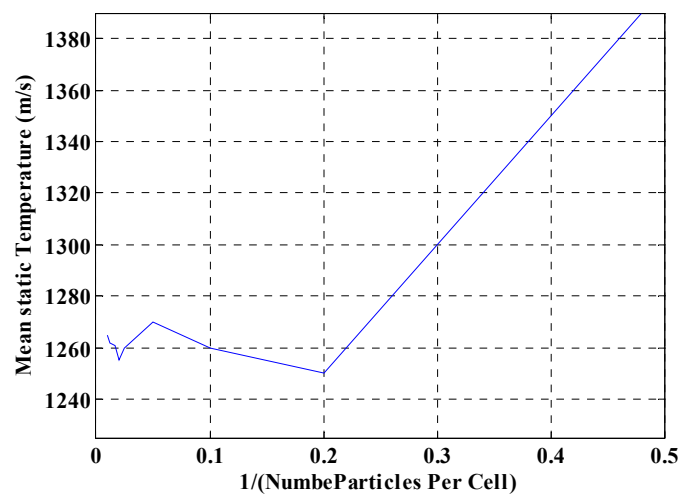


Fig. 10-3. Convergence of the mean static temperature as a function of the inverse number of particles per cell at $x/D=22.5$, $r/D=0$ for the PM1-150 flame.

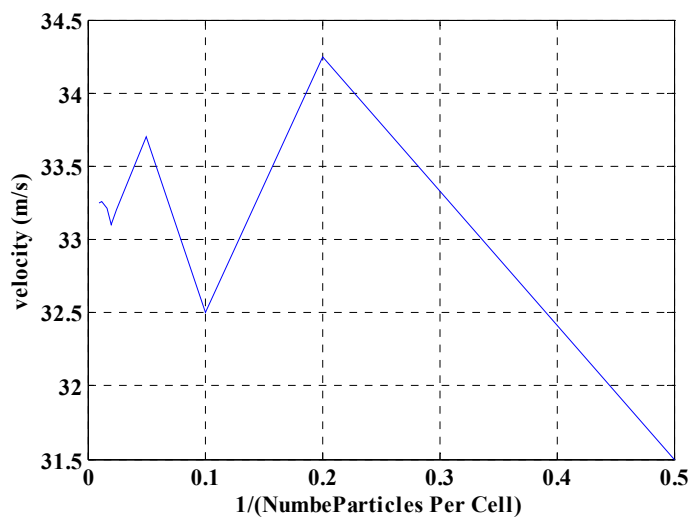


Fig. 10-4. Convergence of the axial velocity as a function of the inverse number of particles per cell at $x/D=60$, $r/D=0$ for the PM1-150 flame.

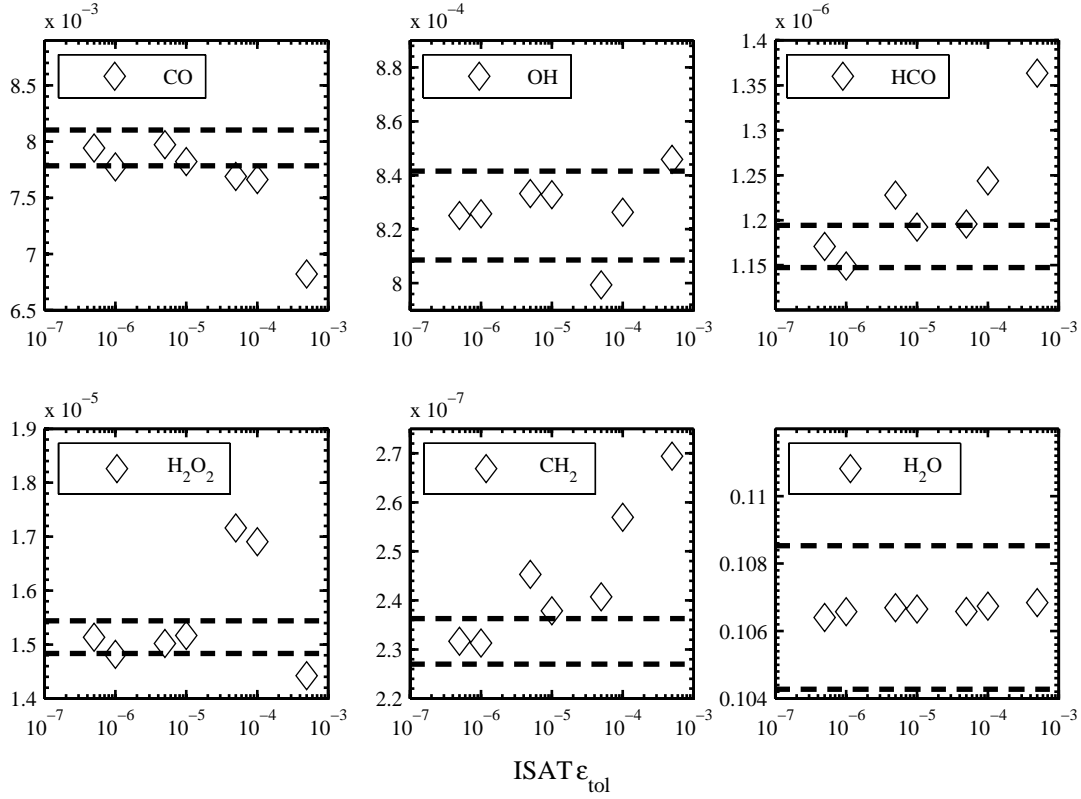


Fig. 10-5. Variation of the peak Favre mean mass fraction for six species along the centreline ($r/D=0$) as a function of the ISAT error tolerance. Data points for each species are shown as diamond symbols, the expected $\pm 2\%$ bounds around the expected error-free value obtained by Richardson extrapolation is shown as two dashed horizontal lines in each figure.

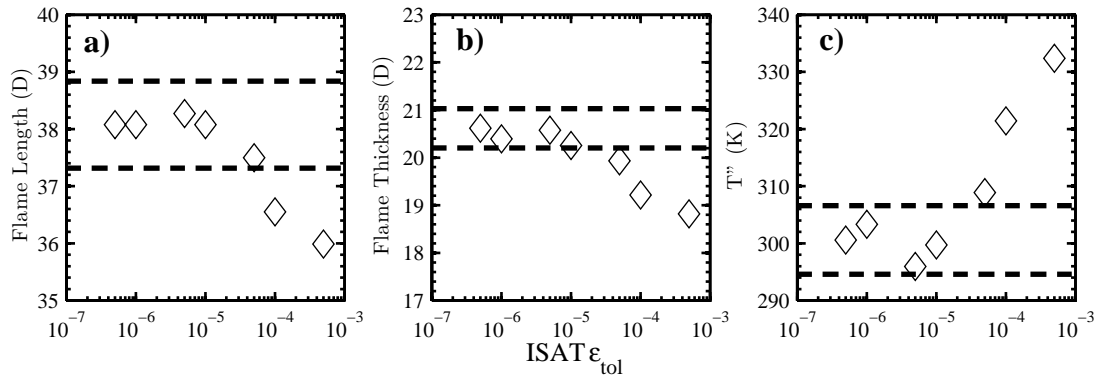


Fig. 10-6. Variation of three flame brush parameters along the centreline ($r/D=0$) as a function of the ISAT error tolerance, a) Favre mean flame brush length in central jet diameters, b) Favre mean flame brush thickness in central jet diameters and c) peak Favre RMS temperature fluctuation. Data points are shown as diamond symbols, the expected $\pm 2\%$ bounds around the expected error-free value obtained by Richardson extrapolation is shown as two dashed horizontal lines in each figure.

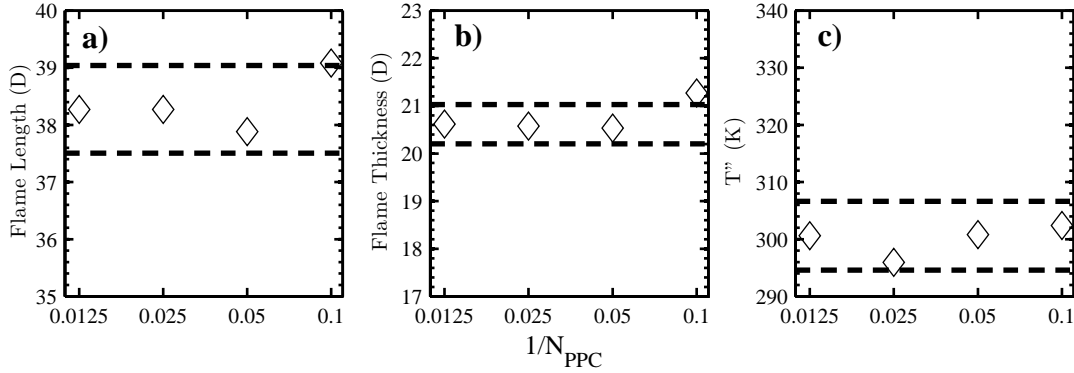


Fig. 10-7. Variation of three flame brush parameters along the centreline ($r/D=0$) as a function of the number of particles per cell, a) Favre mean flame brush length in central jet diameters, b) Favre mean flame brush thickness in central jet diameters and c) peak Favre RMS temperature fluctuation. Data points are shown as diamond symbols, the expected $\pm 2\%$ bounds around the expected error-free value obtained by Richardson extrapolation is shown as two dashed horizontal lines in each figure.

10.4 Velocity and Scalar Predictions

To gain a representative understanding of the predictive capabilities for the velocity fields for the parametric PM1 flame series. Fig. 10-8 - Fig. 10-11 present the mean and RMS axial velocity profiles for the four PM1 flame series flames. The RMS velocity (U_{rms}) has calculated from the u and v components of velocity according to Eq. (10.5), where the inherent assumption of $v' = w'$ that is valid for axisymmetric flows has been made.

$$U_{rms} = \sqrt{\frac{1}{3} \left[(u')^2 + 2(v')^2 \right]} \quad (10.5)$$

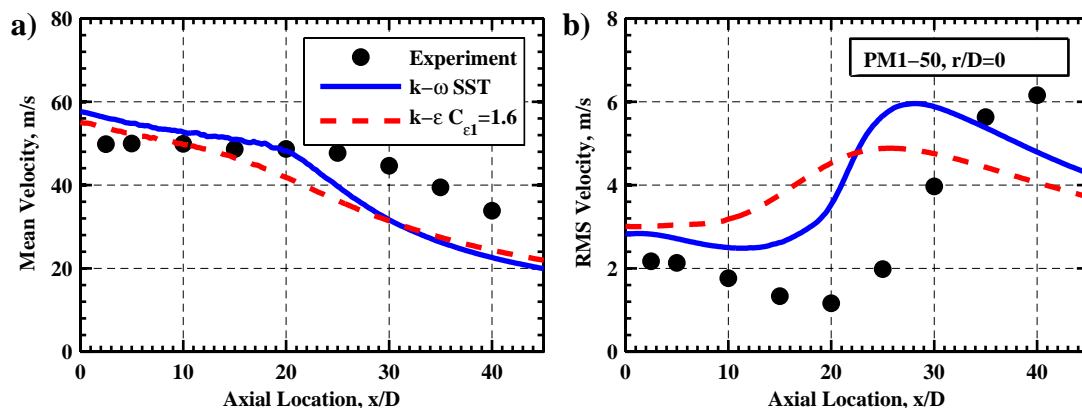


Fig. 10-8. Comparison of LDV measurements with the $k-\omega$ and $k-\epsilon$ model results for the axial velocity statistics along the centreline $r/D=0$ for the PM1-50 flame. The mean velocity profile is reported in a), and the RMS velocity is reported in b).

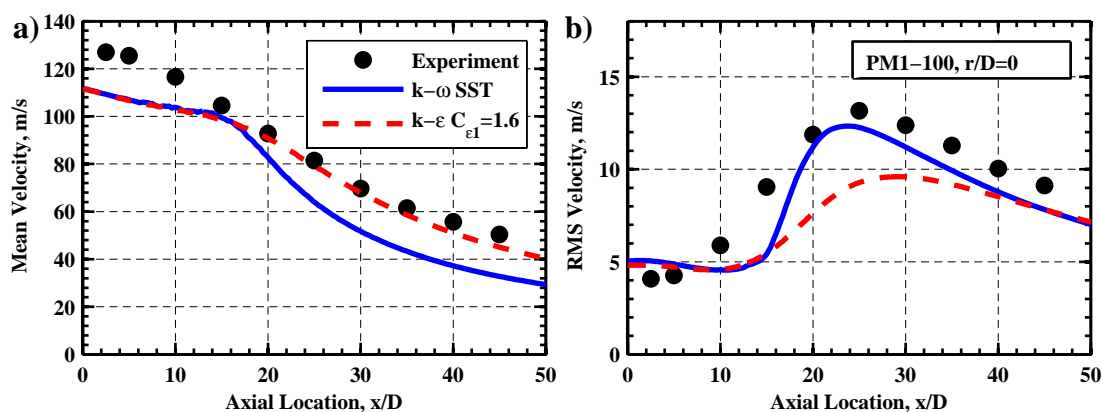


Fig. 10-9. Comparison of LDV measurements with the $k-\omega$ and $k-\epsilon$ model results for the axial velocity statistics along the centreline $r/D=0$ for the PM1-100 flame. The mean velocity profile is reported in a), and the RMS velocity is reported in b).

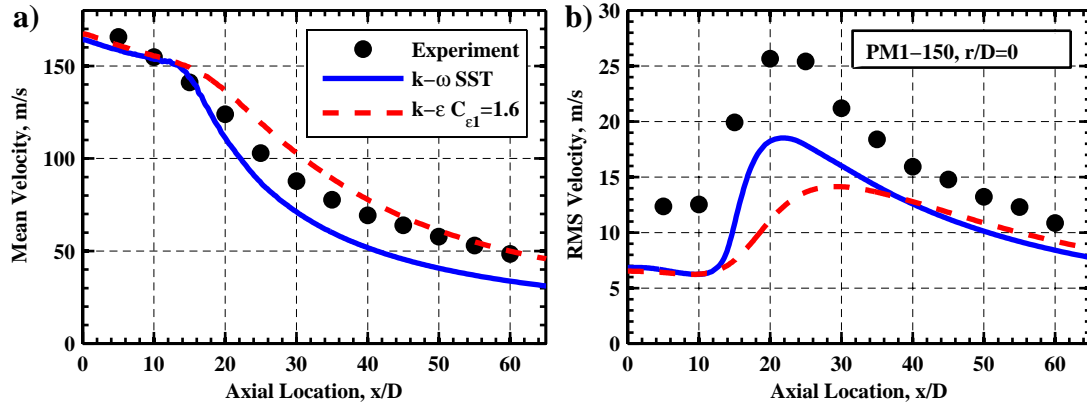


Fig. 10-10. Comparison of LDV measurements with the $k-\omega$ and $k-\epsilon$ model results for the axial velocity statistics along the centreline $r/D=0$ for the PM1-150 flame. The mean velocity profile is reported in a), and the RMS velocity is reported in b).

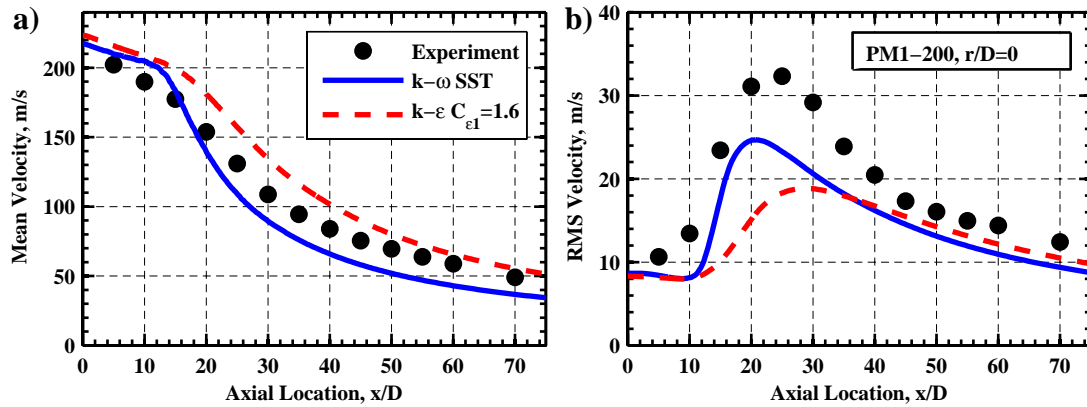


Fig. 10-11. Comparison of LDV measurements with the $k-\omega$ and $k-\epsilon$ model results for the axial velocity statistics along the centreline $r/D=0$ for the PM1-200 flame. The mean velocity profile is reported in a), and the RMS velocity is reported in b).

The predicted mean and RMS centreline velocity is examined in Fig. 10-8-Fig. 10-11 for the entire PM1 flame series and compared to the experimental results. Generally for the mean velocity, the experimental results are bounded by the predictions of the $k-\epsilon$ and $k-\omega$ model results. On average acceptable predictive capability is shown by the turbulence models for the axial decay of the mean velocity. For the RMS velocity for all cases the results of the $k-\omega$ significantly outperform the $k-\epsilon$ model results, although generally the

predicted RMS velocity is too low compared to the experimental results, even for the $k-\omega$ model results.

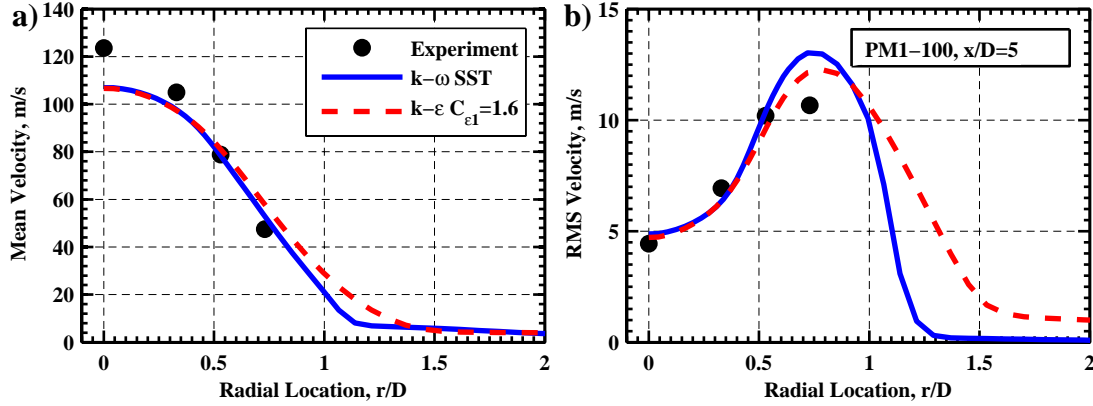


Fig. 10-12. Comparison of LDV measurements with the $k-\omega$ and $k-\epsilon$ model results for the radial velocity statistics at $x/D=5$ for the PM1-100 flame. The mean velocity profile is reported in a), and the RMS velocity is reported in b).

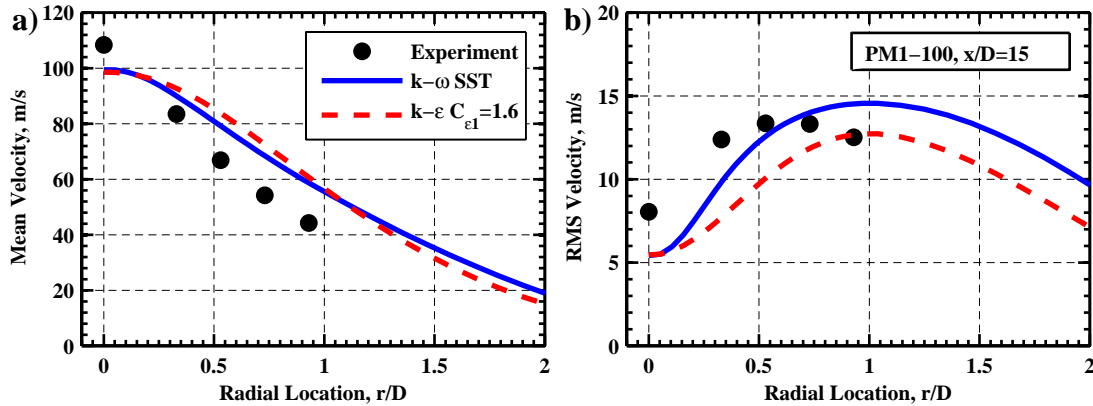


Fig. 10-13. Comparison of LDV measurements with the $k-\omega$ and $k-\epsilon$ model results for the radial velocity statistics at $x/D=15$ for the PM1-100 flame. The mean velocity profile is reported in a), and the RMS velocity is reported in b).

Representative of the results for the PM1 flame series, radial profiles of mean and RMS velocity are displayed for the PM1-100 flame in Fig. 10-12-Fig. 10-15 corresponding to axial measurement stations of $x/D=5, 15, 25$ and 35 . Generally for this flame the mean and RMS fields are relatively well calculated using either the $k-\epsilon$ or the $k-\omega$ model however the $k-\epsilon$ model seems to do a better job of computing the mean velocity field and the $k-\omega$ model seems to do a better job of computing the RMS velocity field. The

corresponding radial profiles of mean and RMS velocity for the entire PM1 flames series is reported in Appendix D.

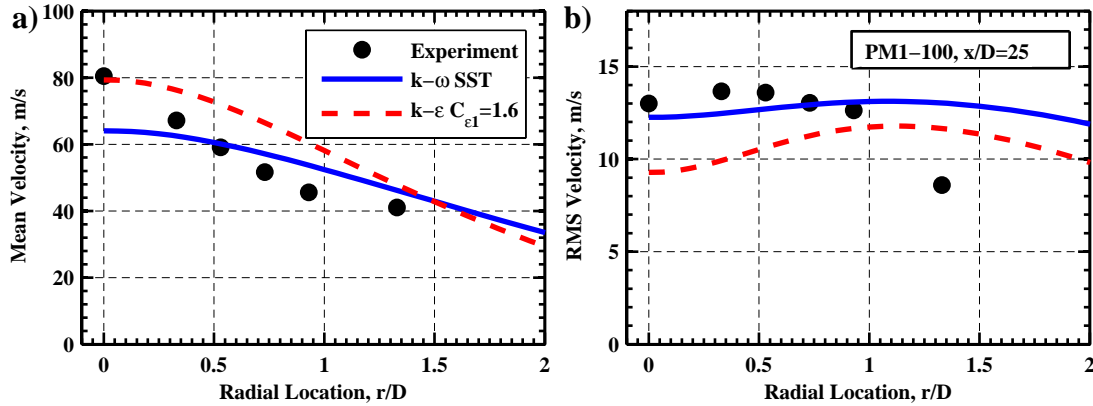


Fig. 10-14. Comparison of LDV measurements with the $k-\omega$ and $k-\epsilon$ model results for the radial velocity statistics at $x/D=25$ for the PM1-100 flame. The mean velocity profile is reported in a), and the RMS velocity is reported in b).

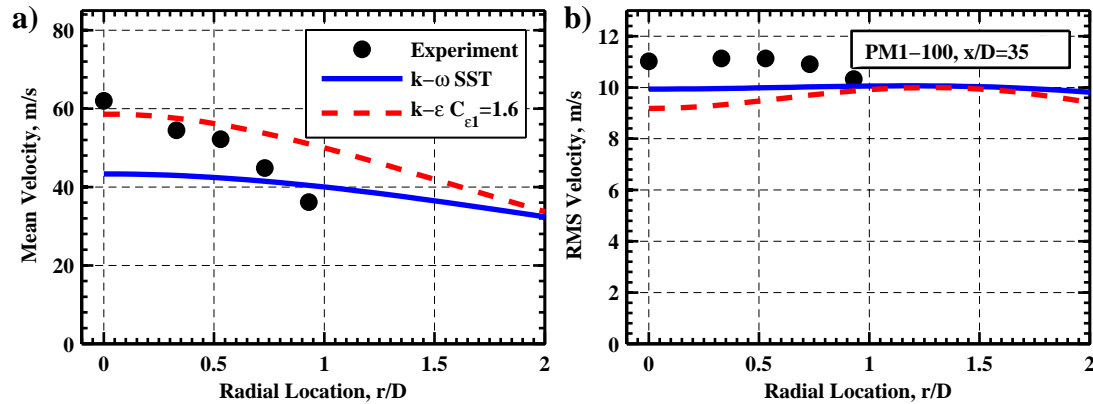


Fig. 10-15. Comparison of LDV measurements with the $k-\omega$ and $k-\epsilon$ model results for the radial velocity statistics at $x/D=35$ for the PM1-100 flame. The mean velocity profile is reported in a), and the RMS velocity is reported in b).

The scalar field predictions for the PM1-150 flame are examined in Fig. 10-16-Fig. 10-20. The scalar radial profiles are of temperature at $x/D=2.5, 7.5, 15, 30$ and 45 . Generally the agreement between the numerical and experimental results for the mean fields are encouraging for $x/D \leq 15$, however because the mean flame length is predicted to be much too short agreement between the experiments and the predictions for $x/D \geq 30$ is quite poor. For all profiles the RMS temperature is over estimated typically by a factor 2.

The simulated RMS temperature profile seems to be approximately the correct shape just the wrong magnitude. Further profiles for the entire PM1 flames series of temperature, OH and CO is including the experimental, $k-\epsilon$ and $k-\omega$ results are reported in Appendix D.

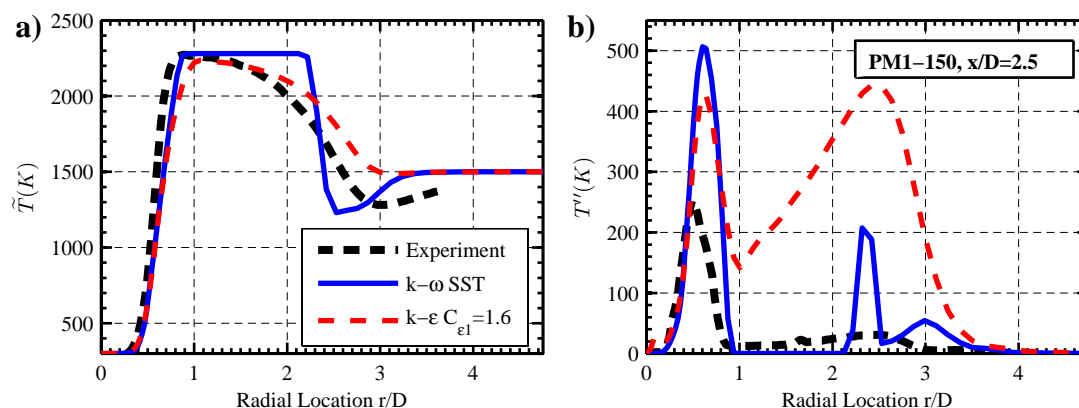


Fig. 10-16. Comparison of Raman-Rayleigh-LIF measurement of temperature with the $k-\omega$ and $k-\epsilon$ model results for the temperature statistics at $x/D=2.5$ for the PM1-150 flame. The Favre mean temperature profile is reported in a), and the Favre RMS temperature is reported in b).

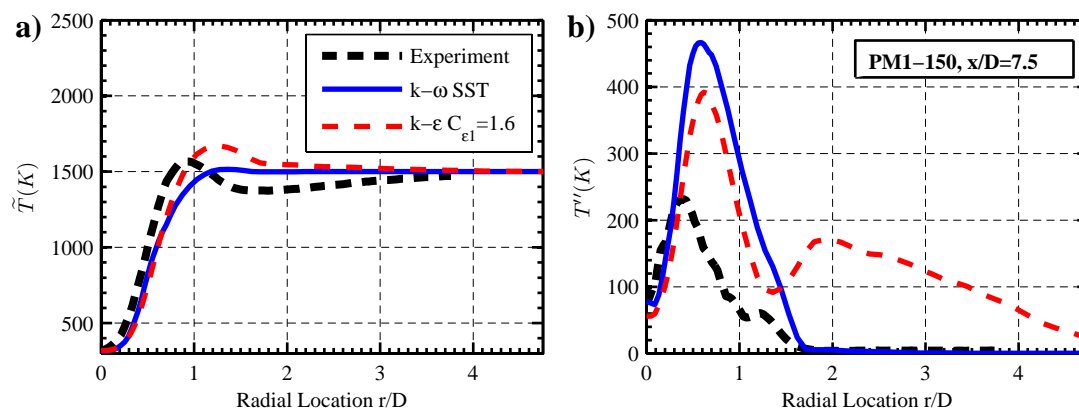


Fig. 10-17. Comparison of Raman-Rayleigh-LIF measurement of temperature with the $k-\omega$ and $k-\epsilon$ model results for the temperature statistics at $x/D=7.5$ for the PM1-150 flame. The Favre mean temperature profile is reported in a), and the Favre RMS temperature is reported in b).

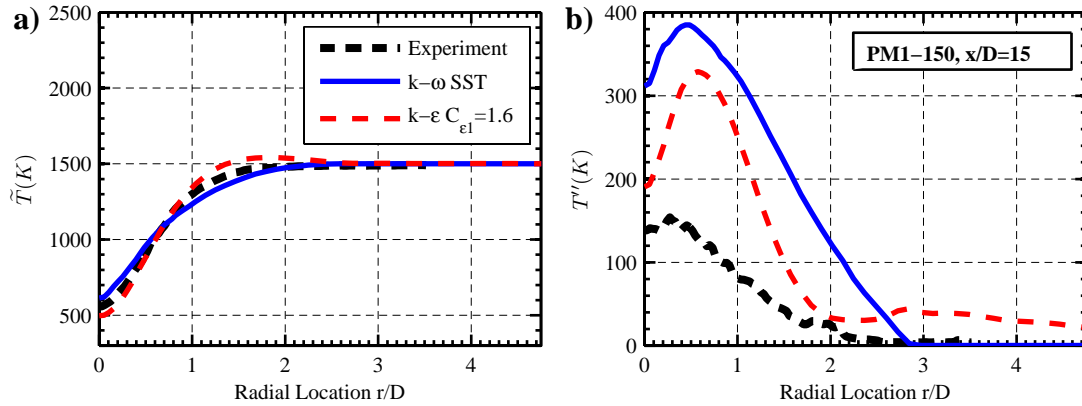


Fig. 10-18. Comparison of Raman-Rayleigh-LIF measurement of temperature with the $k-\omega$ and $k-\epsilon$ model results for the temperature statistics at $x/D=15$ for the PM1-150 flame. The Favre mean temperature profile is reported in a), and the Favre RMS temperature is reported in b).

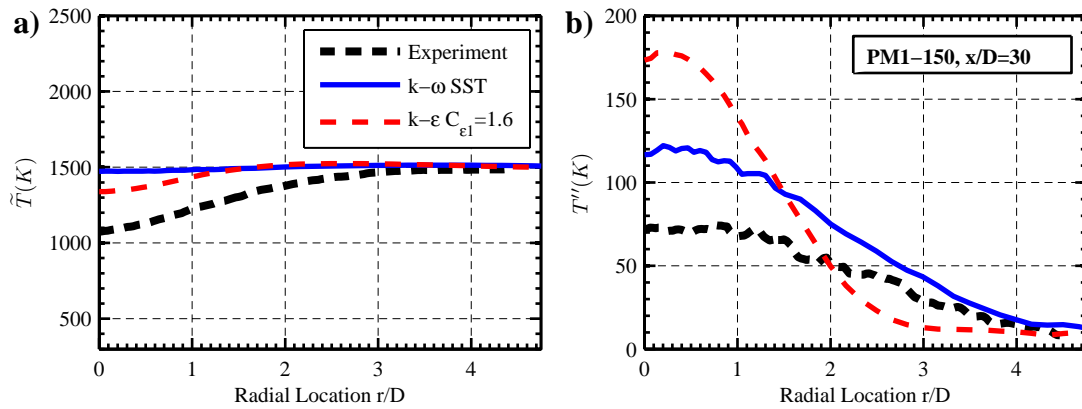


Fig. 10-19. Comparison of Raman-Rayleigh-LIF measurement of temperature with the $k-\omega$ and $k-\epsilon$ model results for the temperature statistics at $x/D=30$ for the PM1-150 flame. The Favre mean temperature profile is reported in a), and the Favre RMS temperature is reported in b).

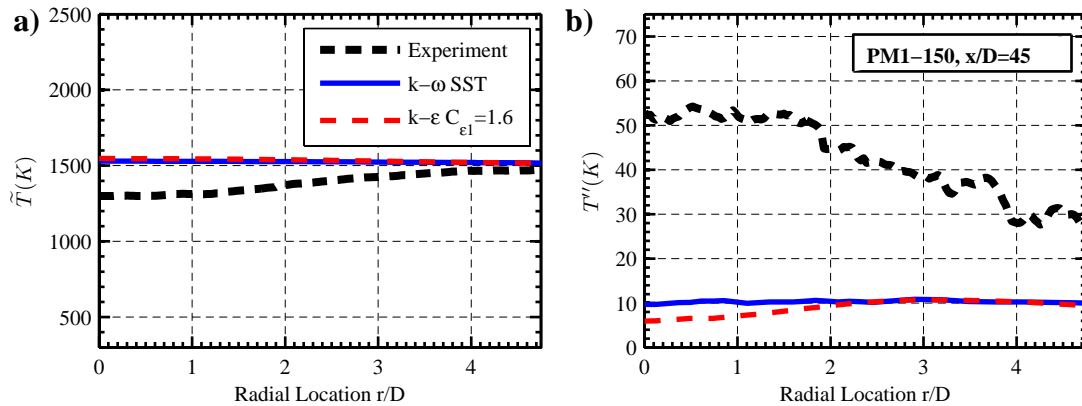


Fig. 10-20. Comparison of Raman-Rayleigh-LIF measurement of temperature with the $k-\omega$ and $k-\epsilon$ model results for the temperature statistics at $x/D=45$ for the PM1-150 flame. The Favre mean temperature profile is reported in a), and the Favre RMS temperature is reported in b).

10.5 Finite-Rate Chemistry Predictions

An essential part of this numerical study of the PPJB in this Chapter is the evaluation of the PDF method to simulate finite-rate chemistry effects in turbulent premixed combustion. The method that is used in this Section to evaluate the degree of finite-rate chemistry effects is the product of CO and OH ($[CO][OH]$) as used in Chapter 8 in the analysis experimental data to discern finite-rate chemistry effects.

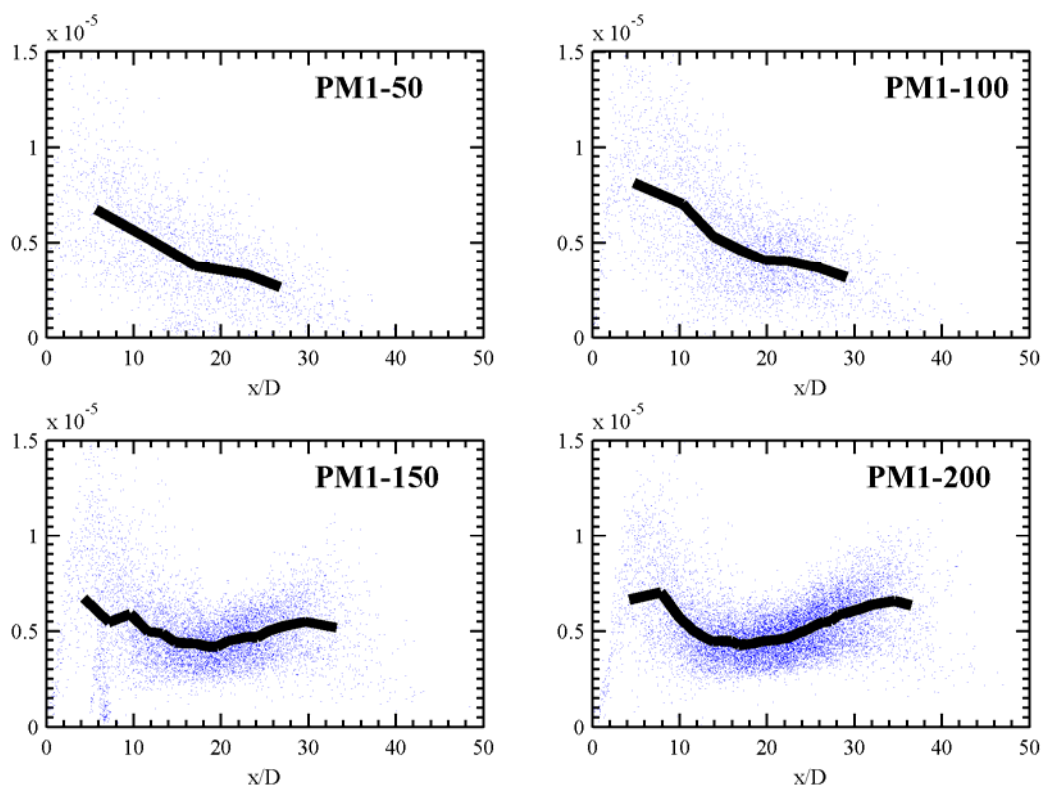


Fig. 10-21. Axial variation of $[CO][OH]_{\xi, 1400 > \xi > 1350 (K)}$ for the PM1 flame series using the k - ϵ turbulence model with $C_{\epsilon 1}=1.6$ and the EMST mixing model with $C_{\phi}=1.5$. Particle data is presented as small blue dots, with the conditional mean being shown as the thick black line.

To analyse the PDF data in terms of all of $[CO][OH]$ firstly the stochastic particles are extracted from a Monte Carlo realisation of the PDF simulation and subsequently only particles that are in the temperature range 1350-1400K are plotted in a scatter plot of

$[CO][OH]$ vs. axial location. Such a scatter plot for the simulated PM1 flame series is presented in Fig. 10-21 for the standard $k-\epsilon$ model and in Fig. 10-22 for the shear stress transport $k-\omega$ model. Both of these figures correspond to data using the EMST mixing model with $C_\phi=1.5$.

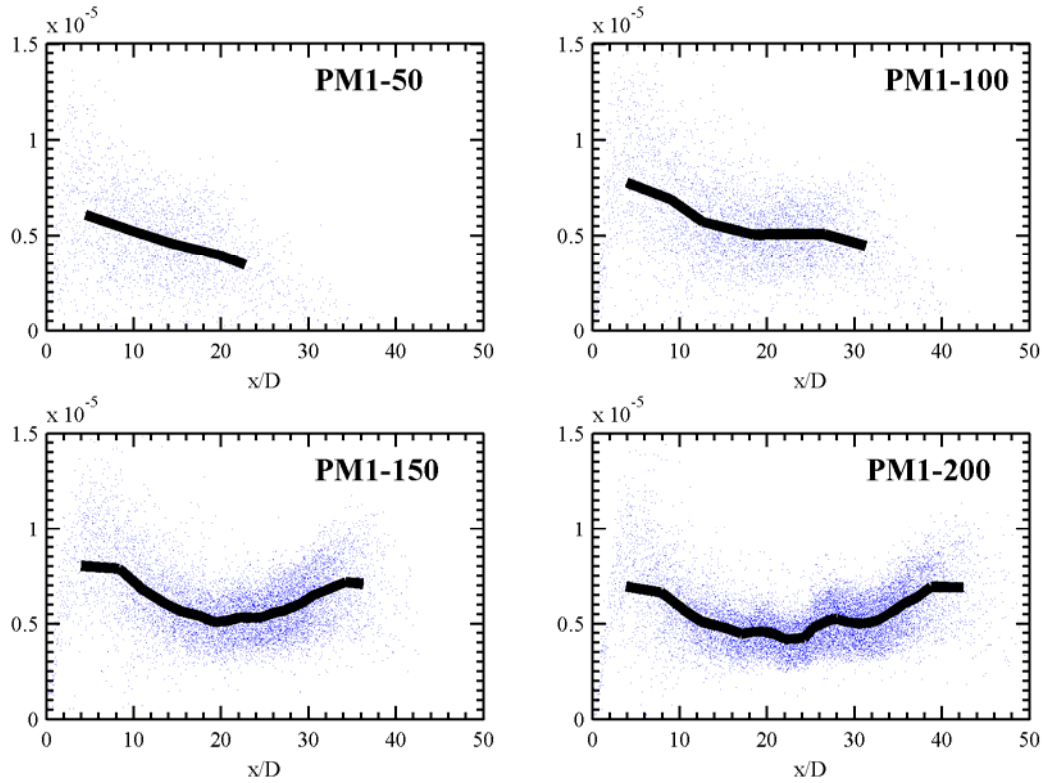


Fig. 10-22. Axial variation of $[CO][OH]_{\xi, 1400 > \xi > 1350 (K)}$ for the PM1 flame series using the $k-\omega$ turbulence model and the EMST mixing model with $C_\phi=1.5$. Particle data is presented as small blue dots, with the conditional mean being shown as the thick black line.

The data presented for both turbulence models in Fig. 10-21 and Fig. 10-22 show that for the simulations of the PM1-150 and PM1-200 flames a dip in the conditional mean value of $[CO][OH]$ occurs after the initial ignition region, further downstream it can be seen that the value of the conditional mean of $[CO][OH]$ increases again corresponding to a re-ignition region. The degree of the extinction and re-ignition regions (measured by the ratio of the maximum value of $[CO][OH]$ in the re-ignition region to the minimum value

of $[\text{CO}][\text{OH}]$ in the extinction region) is nowhere near as large as that measure for the experimental data as presented in Fig. 8-7. The major qualitative finding of Fig. 10-21 and Fig. 10-22 is that the PDF method is predicting *some* degree of finite-rate chemistry effects. In the initial ignition region for $x/D < 10$ the magnitude of $[\text{CO}][\text{OH}]$ correlates well the experimental results indicating that robust burning is occurring experimentally and that this feature is being faithfully reproduced numerically. Where the major deficiency in the numerical results lie is in the region $x/D > 10$ where extinction and a corresponding dramatic reduction in the value of $[\text{CO}][\text{OH}]$ is expected, where as experimentally the drop from the initial ignition region of $[\text{CO}][\text{OH}]$ to the extinction regions value of $[\text{CO}][\text{OH}]$ is expected to be around 20 the numerical prediction for this value is only around 2. It is difficult to reconcile why there is such a disparity between the experimental and numerical results as the predicted RMS velocity in the region $x/D > 10$ is predicted within a nominal accuracy of around 25% as seen in the results reported in Appendix D. Perhaps one indicator that sheds light on this issue is the poor prediction of the OH mass fraction even at small x/D for the PM1-150 flame as shown in Appendix D, typically the numerical value is far too large, the net effect of this would be to promote more robust burning and a greater resilience to extinction at $x/D > 10$.

10.6 Discussion and Further Results

For the data presented in Fig. 10-21 and Fig. 10-22 only a single mixing model and single value of C_ϕ was examined. It is well known that different mixing models and varying the value of C_ϕ changes finite-rate chemistry predictions as well as the predictions of the scalar variance in PDF simulations. By modifying the value of C_ϕ for three mixing models (EMST, MC and IEM) the variation in the degree of the predicted finite-rate chemistry effects is examined in Fig. 10-23-Fig. 10-25 for the $k-\omega$ turbulence model results.

For the EMST mixing model in Fig. 10-23 it is found that the degree of finite-rate chemistry effects with increases with the value of C_ϕ . Increasing the value of C_ϕ also shortens the length of the flame by a small amount as well. For the EMST mixing model encouraging trends for $[CO][OH]$ can be found for $C_\phi \geq 8.0$ from Fig. 10-23. A second general comment specific to the EMST mixing model results is that the envelope that the scatter plot data falls into seems to become increasingly bounded with greater values of C_ϕ , this observation could be quantified for example by examining the reduction in the Kurtosis of $[CO][OH]$ at $x/D=20$ vs. C_ϕ . It is proposed that this trend is a function of the strong localness property of the EMST which increases with larger values of C_ϕ .

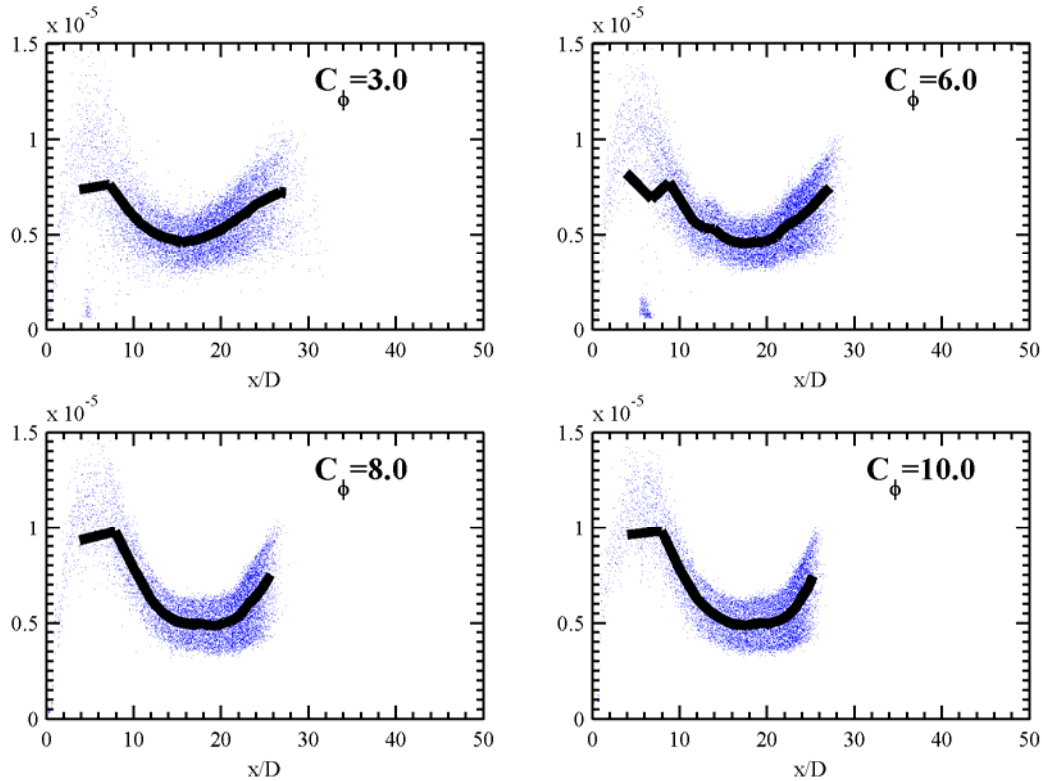


Fig. 10-23. Axial variation of $[CO][OH]_{\xi, 1400 > \xi > 1350 (K)}$ for the PM1-150 flame using the $k-\omega$ turbulence model and the EMST mixing model with different values of C_ϕ . Particle data is presented as small blue dots, with the conditional mean being shown as the thick black line.

The results for the variation of C_ϕ for the MC mixing model in Fig. 10-24 indicate that satisfactory finite-rate chemistry predictions occur with $C_\phi \geq 8.0$ in agreement with the results from the EMST mixing model. For small values of C_ϕ such as 2.0 Fig. 10-24 shows that the MC mixing model predictions for finite-rate chemistry effects are very low.

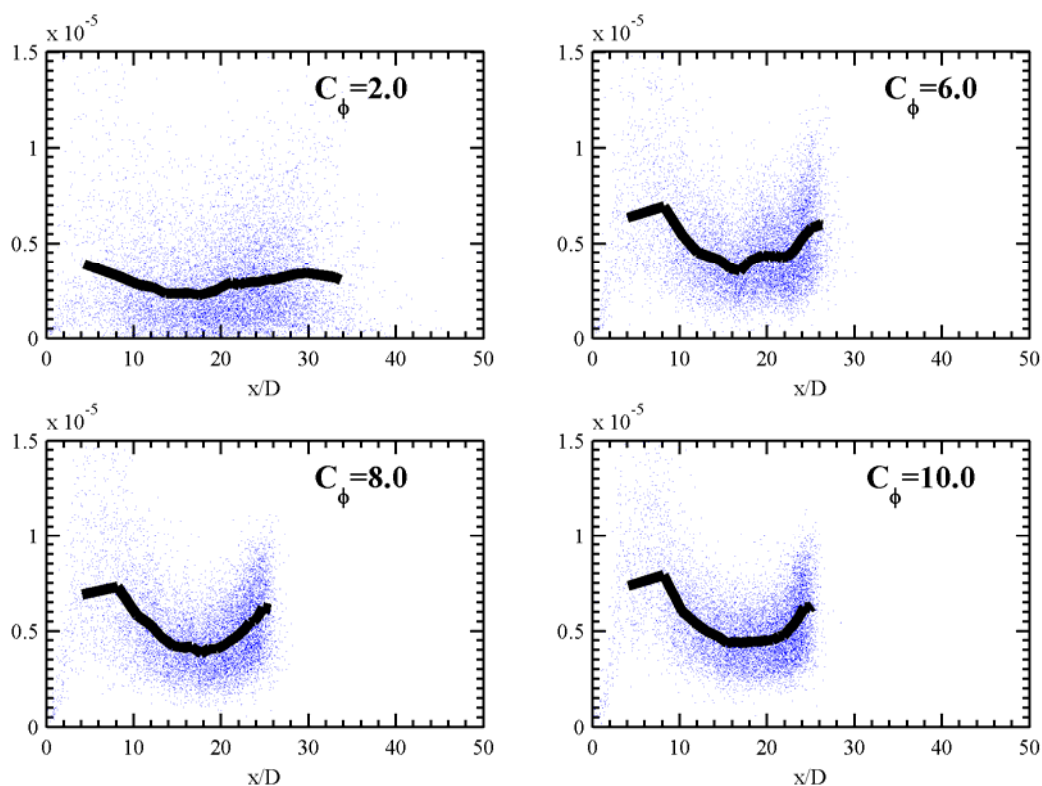


Fig. 10-24. Axial variation of $[CO][OH]_{\xi, 1400 > \xi > 1350 (K)}$ for the PM1-150 flame using the $k-\omega$ turbulence model and the MC mixing model with different values of C_ϕ . Particle data is presented as small blue dots, with the conditional mean being shown as the thick black line.

The results for the variation of C_ϕ for the IEM mixing model in Fig. 10-25 indicate that finite-rate chemistry predictions are not predicted for any value of C_ϕ including $C_\phi \geq 8.0$.

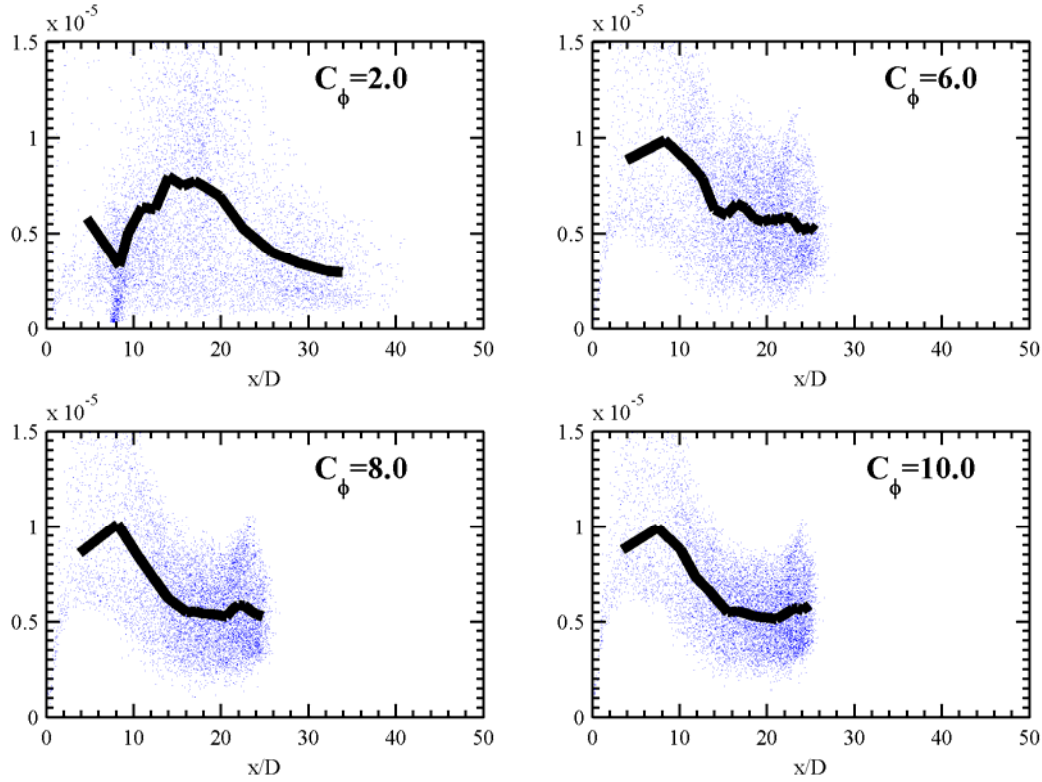


Fig. 10-25. Axial variation of $[CO][OH]_{\xi, 1400 > \xi > 1350 (K)}$ for the PM1-150 flame as a function of C_ϕ using the $k-\omega$ turbulence model and the IEM mixing model. Particle data is presented as small blue dots, with the conditional mean being shown as the thick black line.

As already mentioned not only does the value of C_ϕ change the degree of finite-rate chemistry predictions it also changes the predicted values for the scalar variance. A parametric comparison of the effect of C_ϕ for the PM1-150 flame as a function of axial distance is examined Fig. 10-26 for all three mixing models examined. The characteristic scalar variance value at a particular axial location is found by taking the maximum of the Favre RMS temperature profile. The results in Fig. 10-26 indicates that irrespective of the mixing model a value of $C_\phi \geq 8.0$ (possibly $C_\phi = 8.0$ is optimal) produces better predictions for the scalar variance than the standard value of 1.5 or 2.0. This is important because for the MC and EMST mixing models near optimal prediction of finite-rate chemistry effects were found for values of $C_\phi \geq 8.0$. This leads to the conclusion that for

the particular flames examined a near optimal value of C_ϕ is around 8.0-10.0. If this particular finding is specific for the PPJB simulations or if it is general finding for turbulent premixed combustion remains a topic for further study.

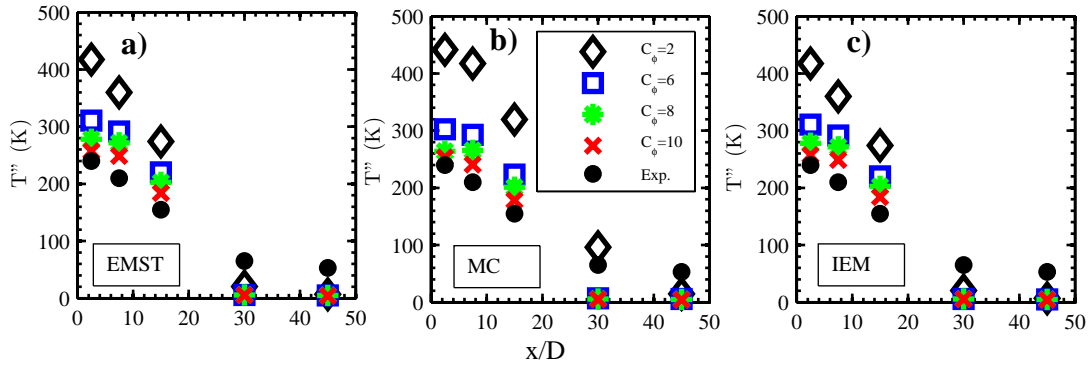


Fig. 10-26. A comparison of the calculated and experimentally measured peak Favre RMS temperature as a function of axial location for the PM1-150 flame using three different mixing models a) EMST, b) MC and c) IEM. The results for each mixing model are reported for values of C_ϕ equal to 2, 6, 8 and 10. The representative peak Favre RMS temperature is determined at each axial location by taking the peak value in the radial profile at the given axial location.

A qualitative experimental measure of the mean reaction rate that was used in Chapter 3 to characterise the PPJB and PJB flames is the mean flame chemiluminescence due to CH^* . It was noted in Chapter 8 and it is emphasised here again that the mean flame CH^* chemiluminescence is not a quantitative measure of the mean reaction rate, but rather it should be considered as a qualitative indicator of the mean reaction rate field and hence mean flame brush structure.

The comparison of the experimentally measured mean flame chemiluminescence with the numerically computed mean flame chemiluminescence has been used to validate the numerically computed reaction rate fields and the flame brush structure with experimental results in a number of studies of laminar flames [345, 346, 347, 348, 349, 350]. The extension to validate numerical results with experimental results for the mean flame chemiluminescence in turbulent combustion has been much more limited, this is possibly because of the requirement that detailed chemistry must be accurately

implemented in the numerical calculations to determine the chemiluminescent species concentrations. Most numerical studies in turbulent combustion that calculate a numerical flame chemiluminescence post-process the chemiluminescent species (e.g. CH^*) field from tabulated chemistry based on flamelet or characteristics scalar principles [351, 352]. By using such tabulated chemistry methods it is possible significant errors are introduced in the kinetic calculation of the CH^* concentration.

As the PDF method treats the chemical source term exactly, it is possible to consider the calculations of the mean flame chemiluminescence if a sufficiently detailed mechanism and appropriate reactions for the chemiluminescent species are utilised. The chemical mechanism used in this study (DRM22) does not include the CH^* and C_2H molecules and their corresponding chemistry. The C_2H_2 (acetylene) molecule is explicitly calculated in the DRM22 mechanism, by making the assumption that C_2H is formed exclusively from the decomposition of C_2H_2 by O or OH and assuming that the destruction rate of C_2H is very fast relative the formation rate, it is possible to consider C_2H as being in quasi-steady state [353]. Similarly by considering that CH^* is exclusively formed by the reaction of C_2H with O or O_2 and that the destruction rate of CH^* is much faster than the formation rate, CH^* maybe considered to be in quasi-steady state. By making such quasi-steady state assumptions it is possible to express the concentrations of C_2H and CH^* in terms of species that are explicitly calculated by the DRM22 mechanism (C_2H_2 , O, O_2 and OH) using Eqs. (10.6)-(10.7).

$$[\text{CH}^*] = \frac{k_1 [\text{C}_2\text{H}][\text{O}] + k_2 [\text{C}_2\text{H}][\text{O}_2]}{\sum_{j=3}^{j=9} k_j [\text{M}_j] + k_{10}} \quad (10.6)$$

$$[\text{C}_2\text{H}] = \frac{k_{11} [\text{C}_2\text{H}_2][\text{O}] + k_{12} [\text{C}_2\text{H}_2][\text{OH}]}{(k_2 + k_{13})[\text{O}_2] + k_1 [\text{O}] + k_{14} [\text{H}_2] + k_{15} [\text{H}][\text{M}]} \quad (10.7)$$

In Eqs. (10.6)-(10.7), k_j corresponds to the forward reaction rate for the j^{th} reaction in Table 10-1. The k_j reaction rates are calculated using the values and sources given in Table 10-1.

Table 10-1. Mechanism details for the additional reactions added to the DRM22 mechanism to calculate the C_2H and CH^* concentrations as well as the CH^* spontaneous emission rate. The forward rate coefficient is assumed to be expressed as $k_j = AT^b \exp(-E_a/R_u T)$. The units for the k_j expression are consistent with standard CHEMKIN notation for chemical mechanisms, that is A (gmol/cm^3) and E_a (cal/gmol).

#	Reaction	A	b	E_a	Reference
1	$\text{C}_2\text{H} + \text{O} \leftrightarrow \text{CH}^* + \text{CO}$	2.50E+12	0.0	0	[176, 300, 354, 355, 356]
2	$\text{C}_2\text{H} + \text{O}_2 \leftrightarrow \text{CH}^* + \text{CO}_2$	3.20E+11	0.0	1600	[176, 355, 356, 357]
3	$\text{CH}^* + \text{N}_2 \leftrightarrow \text{CH} + \text{N}_2$	3.03E+02	3.4	-381	[218, 358, 359, 360, 361, 362]
4	$\text{CH}^* + \text{O}_2 \leftrightarrow \text{CH} + \text{O}_2$	2.48E+06	2.14	-1720	[218, 358, 359, 360, 361, 362]
5	$\text{CH}^* + \text{H}_2\text{O} \leftrightarrow \text{CH} + \text{H}_2\text{O}$	5.30E+13	0.0	0	[218, 358, 361, 362, 363, 364]
6	$\text{CH}^* + \text{H}_2 \leftrightarrow \text{CH} + \text{H}_2$	1.47E+14	0.0	1361	[218, 358, 359, 361, 362, 365]
7	$\text{CH}^* + \text{CO}_2 \leftrightarrow \text{CH} + \text{CO}_2$	2.40E-01	4.3	-1694	[218, 358, 359, 360, 361, 362]
8	$\text{CH}^* + \text{CO} \leftrightarrow \text{CH} + \text{CO}$	2.44E+12	0.5	0	[218, 358, 359, 360, 361, 362]
9	$\text{CH}^* + \text{CH}_4 \leftrightarrow \text{CH} + \text{CH}_4$	1.73E+13	0.0	167	[218, 358, 359, 361, 362, 366]
10	$\text{CH}^* \leftrightarrow \text{CH} + h\nu$	1.86E+06	0.0	0	[213]
11	$\text{C}_2\text{H}_2 + \text{O} \leftrightarrow \text{C}_2\text{H} + \text{OH}$	4.60E+19	-1.4	28950	[176]
12	$\text{C}_2\text{H}_2 + \text{OH} \leftrightarrow \text{C}_2\text{H} + \text{H}_2\text{O}$	3.37E+07	2.0	14000	[176]
13	$\text{C}_2\text{H} + \text{O}_2 \leftrightarrow \text{HCO} + \text{CO}$	1.00E+13	0.0	-755	[176]
14	$\text{C}_2\text{H} + \text{H}_2 \leftrightarrow \text{H} + \text{C}_2\text{H}_2$	5.68E+10	0.9	1993	[176]
15	$\text{C}_2\text{H} + \text{H} + \text{M} \leftrightarrow \text{C}_2\text{H}_2 + \text{M}$	1.00E+17	-1.0	0	[176]

After computing the CH^* field in the numerical simulations using the reactions in Table 10-1 a direct comparison with the experimentally measured mean CH^* chemiluminescence field is not immediately possible. This is because the experimental measurements are effectively a 2D image of projected line of sight measurements from a cylindrically symmetric process (in the mean), whilst the numerical results are a 2D axisymmetric slice through the axis of symmetry of the cylindrically symmetric process. To compare the two different datasets a transformation process is required to be applied to one or both of the datasets.

The mean chemiluminescence images from the experiments are acquired with a commercial colour digital camera, when combined with very low light levels from the flame CH^* emission the recorded images feature a low SNR relative to typical images acquired in laser diagnostics studies using scientific grade CCD. As the experimental measurements are taken from an axisymmetric geometry it is possible to use an inverse Abel transform technique [367] to obtain the radial CH^* emission distribution from the recorded 2D projection. Using such an inverse Abel transform technique on the experimental data would allow direct comparisons with the radial CH^* emission distribution that is computed in the numerical results. This comparison method was not utilised as the inverse Abel transform is highly sensitive to noise in the basis image or profile [368, 369, 370, 371], the low SNR of the experimental images would create additional and unnecessary uncertainties in the comparison of the numerical and experimental data.

A robust, accurate and precise method for experimental and numerical comparison of the experimental and numerical data is to compute a projected line of sight image from the radial CH^* emission distribution derived from the numerical simulations using an Abel transform [367]. The Abel transform is sensitive to noise in the basis image or profile (although to a far lesser extent than the inverse Abel transform), but as the numerical results feature virtually no statistical noise compared to the experimental results, the uncertainty introduced due to statistical noise being amplified in the transformation

process is virtually eliminated. The expression that is used for the data reduction of the axisymmetric numerical data to yield a projected 2D image for direct comparison with the experimental measurements is given by Eq. (10.8).

$$E(z) = 2 \int_{-\infty}^{\infty} \int_x^{\infty} \frac{P(r,z) r dr dx}{\sqrt{r^2 - x^2}} \quad (10.8)$$

In Eq. (10.8) the $P(r,z)$ term represents the radial and axial distribution of the CH^* emission calculated from the numerical results. The net axial variation of the CH^* emission is primarily of interest for the comparison of the experimental and numerical data. By integrating the projected CH^* emission in the radial direction of the projected image for both the numerical and experimental results, a single axial profile can be used for comparative purposes. An advantage of radially integrating the projected images is that the SNR of the experimental data is significantly increased.

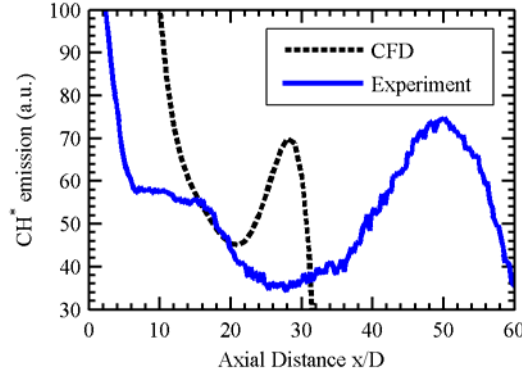


Fig. 10-27. Comparison of the radially averaged CH^* emission for the PM1-150 flame as a function of axial location for the experimental measurements and the numerically calculated CH^* field from the PDF calculations.

A comparison of the axial variation of the experimental and numerically computed CH^* emission for the PM1-150 flame using the EMST mixing model with $C_\phi = 10$ and the k - ω turbulence model is examined in Fig. 10-27. These particular numerical model parameters were selected as they provide the best agreement between the numerical results for the comparison with the axial distribution of $[\text{CO}][\text{OH}]$ in the extinction and

re-ignition regions of the PM1-150 flame. The significant feature of the PM1-150 flame is the occurrence of an extinction and a re-ignition region, this feature is qualitatively apparent in the mean luminosity images and has been quantified using measurements of $[\text{CO}][\text{OH}]$ and $[\text{CH}_2\text{O}][\text{OH}]$. It is of interest if the numerically computed CH^* field features the same extinction and re-ignition regions as the experimental data.

The experimental data for the mean flame CH^* emission can only be considered to be qualitative in nature. Any comparison with experimental values cannot be based on absolute values but rather should be based on trends or a lack thereof between the two datasets. One such a trend relevant to finite-rate chemistry effects is the ‘dip’ in the flame CH^* chemiluminescence in the extinction region of the PM1-150 flame and the corresponding rise of the CH^* chemiluminescence in the re-ignition region further downstream. As a quantitative reference for finite-rate chemistry effects in the PM1-150 flame both experimentally and numerically, the $[\text{CO}][\text{OH}]$ ratio is re-examined. For the experimental measurements of the ratio of the $[\text{CO}][\text{OH}]$ in the extinction region to the re-ignition region a value of 2.7 has been found, whilst for the numerical results using the same numerical parameters as those proposed just above, the ratio was found to be 2.0.

A similar comparison to the $[\text{CO}][\text{OH}]$ ratio is proposed for the CH^* emission using the ratio of CH^* emission between the extinction region and the re-ignition region for the numerically computed and experimentally measured values for the PM1-150 flame. From Fig. 10-27 the ratio of the extinction region to re-ignition region CH^* emission is found to be 2.2, whilst the numerical simulations predict a ratio of 1.6. The numerical results for the ratio of $[\text{CO}][\text{OH}]$ in the extinction region to the re-ignition region was found to be 26% lower than the corresponding experimental measurements, it is quite remarkable that the numerically predicted CH^* emission ratio is a similar value, being 27% lower than the experimental value for the CH^* emission ratio. This is an important result as it shows that the CH^* ratio predicts virtually the same degree of extinction for CH^* emission as $[\text{CO}][\text{OH}]$ in the numerical simulation when compared to the experimental results in regions that exhibit significant finite-rate chemistry effects. Considering the qualitative nature of the experimental CH^* chemiluminescence measurements and the uncertainties

involved in the kinetic modelling of CH^* , the agreement between the numerical and experimental data for the CH^* fields can be considered to be quite promising, particularly for examining flames and regions of flames that exhibit significant finite-rate chemistry effects. Further studies examining the universality of the qualitative relationship between the mean CH^* emission as a measure of the mean reaction rate will of course be required for other geometries and compositions.

It has been noted earlier in this Chapter that the mean flame length based on temperature is significantly under predicted in the numerical simulations compared to the experimental results. This is why the peak CH^* emission in the re-ignition region for the experimental results is around $x/D=50$, whilst the numerical results for re-ignition region peak around $x/D=29$. Therefore part of the utility of the CH^* numerical calculation can be for the validation of the mean flame length of the numerical calculations with experimental data.

Further experimental efforts to qualitatively measure the CH^* emission may be possible if the detection system is calibrated using an absolute technique such as Rayleigh scattering [190]. Such efforts would probably not provide any additional insight into the problem as considerable uncertainty still exists in the numerically computed CH^* concentrations levels, this is primarily due to the uncertainties in the CH^* kinetic formation and destruction rate constants. Future improvement to the measurement of the mean CH^* emission could involve the use of a low noise CCD camera similar to the CCD cameras used for the laser diagnostic imaging reported in Chapter 6. An additional chemiluminescent species not considered here that could also be used for additional mean luminosity validation could be OH^* [372]. The measurement and calculation of OH^* would also allow the numerically computed CH^* to OH^* ratio to be compared with the experimental CH^* to OH^* ratio. The utility of such a ratio is not immediately clear in the context of the premixed PPJB and PJB flames, however for stratified (perhaps the PM4 flame) or non-premixed flows the CH^* to OH^* ratio has been shown to be an indicator of local mean equivalence ratio in both turbulent [373] and laminar flows [163, 348].

Future comparisons of the CH^* level for the entire PM1 flame series would benefit from better predictions of the mean flame length, also analysis of the PM1-200 flame could use the ratio of CH^* emission in the extinction and re-ignition regions as the validation technique in a similar fashion used here for the PM1-150 flame. Analysis of the PM1-50 and PM1-100 flames could use an axial rate of decay parameter for CH^* emission to compare the experiments with the numerical predictions. The extension of the CH^* emission validation method to future PDF calculations of the PM4 (the PM4 flame series features a central jet equivalence ratio of 0.8 in the PPJB) and NPM2 flames will be of interest. Indeed in general, the CH^* and perhaps the OH^* validation technique could prove to be a useful validation technique for turbulent combustion simulations of geometries where only mean luminosity measurements exists and detailed laser diagnostics results either do not exists or are currently in progress.

The accuracy of future investigations that use the calculated CH^* value for validation purposes could benefit from the use of a chemical mechanism that has greater accuracy for C-2 chemistry and includes explicit C_2H (Ethyne) reactions, GRI 3.0 could be considered as a suitable candidate that satisfies these requirements. Further accuracy in the predicted CH^* levels could be gained by adding explicit reactions for C and C_2 chemistry as suggested by Smith *et al.* [355]. The addition of C and C_2 chemistry would allow additional formation routes for ethyne such as $\text{C} + \text{CH}_2 \rightarrow \text{H} + \text{C}_2\text{H}$ and $\text{C}_2 + \text{H}_2 \rightarrow \text{C}_2\text{H} + \text{H}$ to be simulated and also additional CH^* formation reactions via $\text{C}_2 + \text{OH} \rightarrow \text{CO} + \text{CH}^*$. Relaxation of the quasi-steady state assumption for CH^* by adding explicit reactions for the formation and destruction of CH^* would also increase the accuracy of the CH^* predictions.

CHAPTER 11 CONCLUSIONS AND RECCOMENDATIONS

11.1 Conclusions

An experimental and numerical investigation of finite-rate chemistry effects in premixed combustion has been reported in this thesis. A new model premixed burner the PPJB has been developed that exhibits finite-rate chemistry effects. Certain flames exhibit a region of reduced luminosity downstream from the initial ignition region, this region of reduced luminosity has been termed the extinction region. Further downstream where the turbulence intensity and scalar dissipation rates have decayed a region of increased luminosity occurs this region is termed the re-ignition region.

The characterisation of the PPJB and PJB has been presented along with stability plots showing the relevant transitions of the flames as they approach extinction. Four flames are selected from various regions of the stability diagram for further detailed investigations of the PJB. Results presented are based on time averaged chemiluminescence, simultaneous temperature and OH mole fraction imaging and LDV measurements. The initial hypothesis of an extinction region occurring from the time averaged chemiluminescence imaging has been partially validated by the simultaneous temperature and OH mole fraction imaging. In the region of decreased time-averaged luminosity OH concentrations occur in greatly reduced concentrations and in isolated patchy regions that do not conclusively follow an isothermal contour. A significant trend of increased flame front thickening at $x/D=15$ for increased turbulence intensities (via

increasing the central jet velocity) particularly around the 800 to 1000K region is found as illustrated in Fig. 5-11.

LDV measurements for axial profiles of the mean and RMS velocity flow-field for the reacting and non-reacting case are presented. Results indicate that the effect of the pilot is to delay the axial location of peak turbulence intensity in the flame downstream when compared to the non-reacting case. This initial reduction in turbulence generation when combined with the high temperature, combustion radical-rich pilot could explain why an initial ignition process is possible and not a lifted flame brush or blown off flame conditions.

Experimental measurements aiming to further understand the mean and instantaneous compositional flame structure of four premixed flames stabilized on the PPJB burner have been examined in this thesis. The results for the low velocity PM1-50 flame show that the central jet combustion process is significantly influenced by the stoichiometric pilot and that the mean reaction zone can be likened to a vertical shear layer. Mean profiles of temperature indicate that a low temperature ($\sim 1300\text{K}$) boundary layer develops around the pilot shroud. This boundary layer persists further downstream for the PM1-50 case but is rapidly mixed out in the PM1-150 case. The effect of the stoichiometric pilot reduces gradually with increasing jet velocity so that the pilot combustion products are rapidly mixed with the coflow and central jet mixtures past $x/D=2.5$ in the PM1-150 flame.

Conditional mean levels of X_{CO} and X_{OH} are shown to exhibit a significant decrease at $x/D=30$ for the PM1-150 and PM1-200 flames, indicating an overall reduction in reaction progress. The conditional mean temperature gradient decreases significantly for the higher velocity flames, implying a thickening in the reaction zone and increased turbulence interaction with the preheat and reaction zones. For the PM1-150 and PM1-200 flames around $x/D=30$, which is the region where extinction occurs, a trend of a decreasing $\langle [\text{CO}][\text{OH}] | \xi \rangle$ is measured with increasing jet velocity, implying an overall reduction in the conversion to carbon dioxide. Further downstream in flames PM1-150

and PM1-200 as mixing rates are relaxed, $\langle [\text{CO}][\text{OH}] | \xi \rangle$ increases marking the onset of an increase in reaction rate, termed here as the re-ignition region. The reported flame broadening and the confirmation of an extinction and re-ignition zone for certain flames provide a valuable insight into the mechanisms of finite-rate chemistry effects in premixed combustion. In general, images of $[\text{CH}_2\text{O}][\text{OH}]$ concur with the findings of the results for $[\text{CO}][\text{OH}]$ in terms of the extinction region and the re-ignition region for the flames examined.

Numerical simulation of the PM1 flame series using a RANS based PDF method has been examined. Predictions for the turbulence field for even a non-reacting variable density field has proven to be a very challenging task for the turbulence model; no RANS model evaluated clearly displays a universal predictive capability for the non-reacting or reacting cases. The PDF simulation results for the PM1 flame series indicates that generally the mean flame length is calculated to be shorter than the experimental measurements. Finite-rate chemistry effects are examined by the use of the product of OH and CO as was done to evaluate the experimental results, by using this measure it is found that using the EMST or modified Curl mixing model an extinction and re-ignition region is calculated for the relevant flames. Optimal prediction of finite-rate chemistry effects and the scalar variance is found for values of the mixing model constant of 8.0-10.0, this is unusually large compared to accepted values for non-premixed combustion. The fact that both the scalar variance and finite-rate chemistry effects are optimised with this large value of mixing model constant suggests that the value of C_ϕ may need to be reassessed for premixed combustion.

In summary this thesis has developed an experiment to study finite-rate chemistry effects in turbulent premixed combustion and advanced laser diagnostics have been applied to this experiment. The measurements reveal new information in terms of the instantaneous flame structure both in terms of the scalar structure and the reaction rate and minor species structure that indicate finite-rate chemistry effects. Numerical modelling of the developed experimental geometry indicates that it is possible to successfully predict finite-rate chemistry effects in premixed combustion using the RANS PDF method.

11.2 Discussion of Future Work and Recommendations

The definitive conclusions of this thesis have been presented above in Section 11.1. In the following Section a broad discussion of future possible work and recommendations pertaining to the PPJB, PJB and finite-rate chemistry both numerical and experimentally in premixed combustion are discussed.

It is possible to operate the PPJB and the PJB with the hot coflow temperature lower than the adiabatic temperature of the central jet reactants, in this case any possible extinction can be attributed to a combination of shear driven extinction and reaction quenching or dilution. This case could also be viewed as an example of stratified combustion, as it is possible for the reaction to occur in regions where stratifications in the local equivalence ratio occur. Further examination of such flames particularly using the Raman-Rayleigh-LIF method will be valuable in understanding the role of stratification in these flames.

Orientation correction measurements for the line measurements at Sandia have been used to correct one dimensional measurement of gradient and dissipation. The orientation correction is based on a crossed plane OH LIF method. For the orientation correction to be possible OH must be present and a sufficiently large gradient must exist that is relatively noise free to determine the normal vector. OH does not typically exist in measurable quantities below $\sim 1000\text{K}$, also in the post flame oxidation zone although the OH concentration is well within the detection limit the gradients of OH in this region are low and highly susceptible to noise polluting the correction. Another limitation of the cross plane technique is the inability to accurately correct scalar gradient and dissipation measurements to an acceptable accuracy if the local scalar orientation is determined to be at an angle $\theta > 75^\circ$. A possible idea for general improvement of the cross plane technique at the Sandia line imaging would be to replace the cross plane OH with a cross plane Rayleigh technique. This would allow scalar orientations to be measured across all temperatures minimising the limitations of using OH LIF as the marker. Preliminary measurements at The University of Sydney suggest that only 50mJ of energy for each

sheet at 355nm would be sufficient for adequate SNR at high temperatures. Of course replacing the cross plane OH LIF with cross plane Rayleigh does not remove the limitation that the local scalar normal orientation angle be $\theta < 75^\circ$ for an adequately noise free correction be made. The limitation of $\theta < 75^\circ$ for adequate orientation corrections is a fundamental limitation of correcting 1D measurements for orientation on an instantaneous shot to shot basis and is not a limitation of the cross plane technique but rather a limitation of the fact that the Raman-Rayleigh-LIF measurement is only conducted along a 1D segment making the criteria for orientation far more limiting than if the measurements were carried out on a 2D planar basis and corrected for orientation.

It would be interesting to examine the trend of nitric oxide NO formation through the PM1 flame series, particularly as the time scales for NO production are quite slow and undoubtedly are influenced by turbulence-chemistry interaction. One of the significant advantages of lean premixed gas turbine combustion is the dramatically reduced levels of NO and oxides of nitrogen NO_x that are achievable. Although the PJB and PPJB are geometrically quite different to a lean premixed gas turbine combustor there are significant similarities in the combustion process in that lean premixed combustion is supported by hot exhaust gas products understanding NO formation in such a process would be valuable in understanding from a fundamental perspective the formation of NO in such experiments and practical applications. Practically the NO levels in the PJB and PPJB may be below the detection limit of laser based NO LIF measurements.

Preliminary measurements of NO PLIF for the PM1 series of flames in the PPJB using a similar setup as Gounder *et al.* [374] has revealed that NO occurs in levels that are below the system sensitivity for PLIF measurements. Further refinements to the NO PLIF system proposed by Juddoo [375] might increase the system sensitivity for NO PLIF measurements. This however remains an open question and perhaps only point or line measurements may be possible. Also intrusive techniques such as suction probe measurements of NO could be required to attain the required sensitivity for NO in the PPJB or PJB.

The observed transition from initial ignition to extinction to re-ignition for certain flames in the PPJB was observed based on mean chemiluminescence images. This visible chemiluminescence in lean premixed flames is almost exclusively from CH^* , C_2^* does not feature significantly in the mean luminescence signal as it does in stoichiometric and rich flames. Based on this it could be interesting to conduct a CH LIF experiment to examine the CH layer thickness and concentration in the PPJB. CH corresponds only weakly with the local heat release rate unlike the product of $[\text{CH}_2\text{O}][\text{OH}]$ which is strongly correlated with the local heat release. CH also does not correspond well with the formation rate of a major species such as the product $[\text{CO}][\text{OH}]$ correlates well with the formation CO_2 . CH has traditionally been used to demark the location of the reaction zone and extinction regions in partially premixed combustion, if this strategy were to be used in the PPJB it would be very doubtful if adequate sensitivity and SNR would be able to be achieved as CH levels in the PPJB are predicted to be at least three orders of magnitude lower than in partially premixed combustion based on laminar opposed flow calculations. As noted by Vagelopoulos and Frank [252] care must also be taken in interpreting breakages in the CH contour along the flame front as extinction events, as it is not possible to directly correlate CH with the local reaction rate in certain mixtures. The considerable experimental challenges and the questionable utility of CH measurements were the main reason why experiments that utilise $[\text{CH}_2\text{O}][\text{OH}]$ and $[\text{CO}][\text{OH}]$ were used to demark the reaction zone rather than a CH PLIF experiment. It is my view that if a future strong justification for the use of a CH PLIF experiment to significantly advance the understanding of the combustion physics in the PPJB or PJB can be made, then careful experimental equipment choice and layout would be required. An example of such an equipment layout and choice would be the use of a high energy wide bandwidth long pulse length Alexandrite laser, such a laser with low $f_{\#}$ detection has shown to have at least two orders of magnitude improvement in detection limit over conventional Nd:YAG pumped dye laser systems by Li *et al.* [376].

The integral length scales reported in this thesis were derived from single point LDV measurements assuming Taylor's hypothesis. This was shown to give acceptable results only far from the potential core of the jet; even then the uncertainties were estimated to

be large. If a higher degree of accuracy is required in future for length scales then perhaps particle image velocimetry (PIV) should be considered. In previous turbulent premixed combustion studies PIV has been combined with OH PLIF to obtain conditioned velocity statistics based on the burnt or unburnt nature of the local measurement. It is clear from some of the OH PLIF images in certain PPJB flames presented in this thesis that the binarised OH PLIF signal would be an ambiguous and unreliable marker for separating the burnt and unburnt gases. Perhaps a more fruitful avenue for measuring the conditional velocity would be to combine OH PLIF with CH_2O PLIF to have a clear and less ambiguous demarcation of the reaction zone.

A problem for the measurement of conditional velocities in both of the PPJB and the PJB is that the assumption of a thin flame front separating the reactants and products is not strictly true; in fact the instantaneous flame front thickness in some realisations is thicker than the integral length scale. This breakdown in the thin flame assumption may give some weight to the application of Filtered Rayleigh scattering, in this case velocity via PIV and temperature via filtered Rayleigh scattering can be derived. This would allow instantaneous velocities to be measured at intermediate reaction progress variable values. As a general comment, due to the very high values of u'/S_L for all of the flames studied it would be expected that all flames would obey a gradient diffusion law for the reaction progress variable.

It is shown in this thesis that the prediction of a simple non-reacting variable density jet by standard RANS based models for the mean and RMS velocity is quite challenging and no standard RANS model predicts this trend with adequate accuracy. Whilst the area of experimental measurements in variable density jets has received a small amount of attention in literature the numerical predication of such conditions is very sparse this is definitely an area where future model development work could be aimed both in a RANS sense and possibly LES. Accurate prediction of the non-reacting case should be considered a prerequisite for accurate prediction of the reacting cases of the PPJB and PJB.

Numerical modelling of the PPJB flame series has been challenging in part due to the intimate interaction of the turbulent kinetic energy and turbulent dissipation rate in the mixing model of transported PDF calculations. Improvement on the coupled RANS transported PDF model maybe found if the joint velocity frequency composition PDF is considered to obtain improved results in the RANS context. Large eddy simulation of the PPJB should yield improved results over RANS calculations, however the LES model should use a detailed or at least semi detailed chemistry such that the interaction between the resolved turbulence and chemistry is sufficiently accounted for.

A possible further analysis tool to apply to the PDF RANS calculation results that have been reported in Chapter 10 is the species convection, diffusion and reaction (CDR) balance. The CDR balance has been used by Gordon *et al.* [377] as an indicator of how the numerical model is predicting flame stabilisation, either by auto-ignition (convection reaction balance) or by conventional flame stabilisation (combination of all three). It would be of interest to see if the PDF solution is predicting auto-ignition for the re-ignition region of the high velocity PM1-150 and PM1-200 flames.

The key distinguishing feature between the PJB flames and the PPJB flames is that under certain conditions flames in the PPJB displays an ignition, extinction re-ignition behaviour. It is this transition that makes studying flames in the PPJB so rich in features, particularly in terms of finite-rate chemistry. In order to achieve an initial ignition region in the PPJB a stoichiometric pilot is necessary, this introduces the additional complexity of a pilot as well as a third stream that cannot be described with the same reaction progress variable as the central jet and hot coflow. To characterise such a system two reaction progress variables and a mixture fraction would be required. It is desirable from a modelling perspective to be able to describe the premixed system with a single reaction progress variable due to the considerable amount of research that has gone into modelling turbulent premixed combustion with a single reaction progress variable. Essentially the pilot provides a source rich in combustion intermediates and excess enthalpy to promote initial ignition of the central jet reactants. By virtue of there being at high temperature the pilot also reduces the initial shear at the exit plane delaying the spatial location of the

peak turbulence intensity. It would seem that achieving initial ignition followed by extinction and re-ignition region is not possible without a pilot; hence such an extinction re-ignition process is not immediately amenable to be modelled with a single reaction progress variable approach.

Future development and refinement of the premixed PPJB or PJB should focus on a geometrical configuration that produces flames that feature finite-rate chemistry effects probably through an extinction region and re-ignition region and the ability to characterise the flow with a single reaction progress variable. One possible configuration is to replace the pilot in the PPJB with a bluff body to create a re-circulation region that has long residence times to promote an initial ignition region. To create sufficient re-circulation in the bluff body region it may be necessary to surround the bluff body with a small high-speed annular flow of fresh reactants that either replaces or complements the existing central jet. Conceptually this would be similar to the geometry of the non-premixed Sydney Bluff body burner [107] with the central jet and annulus providing fresh premixed reactants rather than non-premixed fuel and the coflow being of hot combustion products instead of filtered cold air.

CHAPTER 12 REFERENCES

1. Hesiod, "Theogony," (Circa 600 BC).
2. J. M. Stillman, *The Story of Alchemy and Early Chemistry* (Dover, New York 1960).
3. P. Joseph, "An Account of Further Discoveries in Air," *Philosophical Transactions* **65**, 384-394 (1775).
4. F. L. Holmes, *Antoine Lavoisier - The next crucial year, or the sources of his quantitative method in chemistry* (Princeton University Press, 1998).
5. J. Kanefshy, and J. Robey, "Steam engines in 18th-Century Britain: A quantitative assessment," *Technology and Culture* **21**, 161-186 (1980).
6. S. Arrhenius, *Das Werden der Welten* (Academic Publishing House, Leipzig, Germany, 1908).
7. J. Fourier, "Remarques générales sur les températures du globe terrestre et des espaces planétaires," *Annales de Chimie et de Physique* **27**, 136-167 (1824).
8. R. Borghi, "On the structure and morphology of turbulent premixed flames," in *Recent Advances in the Aerospace Sciences*, C. Casi, ed. (Plenum Press, New York, 1985), pp. 117-138.

9. Y.-C. Chen, and R. W. Bilger, "Simultaneous 2-D Imaging Measurements of Reaction Progress Variable and OH Radical Concentration in Turbulent Premixed Flames: Instantaneous Flame-Front Structure," *Combust. Sci. and Technol.* **167**, 187-222 (2001).
10. Y.-C. Chen, N. Peters, G. A. Schneemann, N. Wruck, U. Renz, and M. S. Mansour, "The Detailed Flame Structure of Highly Stretched Turbulent Premixed Methane-Air Flames," *Combust. Flame* **107**, 223-244 (1996).
11. F. Dinkelacker, A. Soika, D. Most, D. Hofmann, A. Leipertz, W. Polifke, and K. Döbbeling, "Structure of Locally Quenched Highly Turbulent Lean Premixed Flames," *Proc. Combust. Inst.* **27**, 857-865 (1998).
12. N. Peters, "The turbulent burning velocity for large-scale and small-scale turbulence," *J. Fluid Mech.* **384**, 107-132 (1999).
13. N. Peters, *Turbulent combustion* (Cambridge University Press, University Press, Cambridge, United Kingdom, 2000).
14. R. G. Abdel-Gayed, D. Bradley, and F. K.-K. Lung, "Combustion Regimes and the Straining of Turbulent Premixed Flames," *Combust. Flame* **76**, 213-218 (1989).
15. G. Damköhler, "Der Einfluß der Turbulenz auf die Flammengeschwindigkeit in Gasgemischen," *Z. Elektrochem* **46**, 601-652 (1940).
16. K. N. C. Bray, "Studies of the turbulent burning velocity," *Proc. Roy. Soc. Lond.* **A431**, 315-335 (1990).
17. D. Bradley, A. K. C. Lau, and M. Lawes, "Flame stretch as a determinant of turbulent burning velocity," *Phil. Trans. Soc. Lond.* **338**, 359-387 (1992).

18. F. C. Gouldin, "An application of fractals to modeling premixed turbulent flames," *Combust. Flame* **68**, 249-266 (1987).
19. E. Cintosum, G. J. Smallwood, and Ö. L. Gülder, "Flame Surface Fractal Characteristics in Premixed Turbulent Combustion at High Turbulence Intensities," *AIAA Journal* **45**, 2785-2785 (2007).
20. K. N. C. Bray, and J. B. Moss, "A unified statistical model of the premixed turbulent flame," *Acta Astronautica* **4**, 291-319 (1977).
21. P. A. Libby, and K. N. C. Bray, "Countergradient diffusion in premixed flames," *AIAA Journal* **19**, 205-213 (1981).
22. K. N. C. Bray, P. A. Libby, G. Masuya, and J. B. Moss, "Turbulence production in premixed turbulent flames," *Combust. Sci. and Tech* **25**, 127-140 (1981).
23. P. A. M. Kalt, Y.-C. Chen, and R. W. Bilger, "Experimental investigation of turbulent scalar flux in premixed stagnation-type flames," *Combust. Flame* **129**, 401-415 (2002).
24. K. N. C. Bray, and P. A. Libby, "Passage time and flamelet crossing frequencies in premixed turbulent combustion," *Combust. Sci. and Tech* **47**, 253-274 (1986).
25. A. Trouvé, and T. J. Poinso, "The evolution equation for the flame surface density in turbulent premixed combustion," *J. Fluid Mech.* **278**, 1-31 (1994).
26. S. Candel, D. Veynante, F. Lacas, E. Maistret, N. Darabiha, and T. J. Poinso, "Flame stretch and the balance equation for the flame area," *Combust. Sci. and Tech* **70**, 1-15 (1990).
27. F. A. Williams, "Turbulent Combustion," in *Mathematics of Combustion*, J. Buckmaster, ed. (SIAM, Philadelphia, 1985), pp. 97-131.

28. Y.-C. Chen, and R. W. Bilger, "Experimental Investigation of Three-Dimensional Flame-Front Structure in Premixed Turbulent Combustion—I: Hydrocarbon/Air Bunsen Flames," *Combust. Flame* **131**, 400-435 (2002).
29. Y.-C. Chen, and R. W. Bilger, "Experimental investigation of three-dimensional flame-front structure in premixed turbulent combustion II. Lean hydrogen/air Bunsen flames," *Combust. Flame* **138**, 155-174 (2004).
30. A. Soika, F. Dinkelacker, and A. Leipertz, "Measurement of the Resolved Flame Structure of Turbulent Premixed Flames with Constant Reynolds Number and Varied Stoichiometry," *Proc. Combust. Inst.* **27**, 785–792 (1998).
31. R. W. Dibble, and R. E. Hollenback, "Laser Rayleigh Thermometry in Turbulent Flames," *Proc. Comb. Inst.* **18**, 1489-1499 (1981).
32. J. B. Kelman, and A. R. Masri, "Quantitative imaging of temperature and OH in turbulent diffusion flames by using a single laser source," *Appl. Opt.* **33**, 3992–3999 (1994).
33. F. C. Gouldin, and R. N. Halthore, "Rayleigh scattering for density measurements in premixed flames," *Exp. in Fluids* **4**, 269-278 (1986).
34. R. W. Dibble, S. H. Stårner, A. R. Masri, and R. S. Barlow, "An Improved Method of Data Acquisition and Reduction for Laser Raman-Rayleigh and Fluorescence Scattering from Multispecies," *Appl. Phys. B* **51**, 39-43 (1990).
35. A. R. Masri, R. W. Bilger, and R. W. Dibble, "'Fluorescence' Interferences with Raman Measurements in Nonpremixed Flames of Methane," *Combust. Flame* **68**, 109-119 (1987).
36. W. Meier, and O. Keck, "Laser Raman scattering in fuel-rich flames: background levels at different excitation wavelengths," *Meas. Sci. Technol.* **13**, 741-749 (2002).

37. E. W. Rothe, and P. Andresen, "Application of tunable excimer lasers to combustion diagnostics: a review," *Appl. Opt.* **36**, 3971-4033 (1997).
38. S. Böckle, J. Kazenwadel, T. Kunzelmann, D.-I. Shin, and C. Schulz, "Single-shot laser-induced fluorescence imaging of formaldehyde with XeF excimer excitation," *Appl. Phys. B* **70**, 733-735 (2000).
39. D. J. Clouthier, and D. A. Ramsay, "The spectroscopy of formaldehyde and thioformaldehyde," *Ann. Rev. Phys. Chem.* **34**, 31-58 (1983).
40. D. C. Moule, and A. D. Walsh, "Ultraviolet spectra and excited states of formaldehyde," *Chem. Rev.* **75**, 67-84 (1974).
41. E. P. Hassel, "Ultraviolet Raman scattering measurements in flames by the use of a narrow band XeCl excimer laser," *Appl. Opt.* **32**, 4058-4065 (1993).
42. Q.-V. Nguyen, and P. H. Paul, "Photochemical effects of KrF excimer excitation in laser-induced fluorescence measurements of OH in combustion environments," *Appl. Phys. B* **72**, 497-505 (2001).
43. J. A. Wehrmeyer, T.-S. Cheng, and R. W. Pitz, "Raman scattering measurements in flames using a tunable KrF excimer laser," *Appl. Opt.* **31**, 1495-1504 (1992).
44. W. Reckers, L. Huwel, G. Grunefeld, and P. Andresen, "Spatially resolved multispecies and temperature analysis in hydrogen flames," *Appl. Opt.* **32**, 907-924 (1993).
45. T. S. Cheng, J. A. Wehrmeyer, and R. W. Pitz, "Simultaneous temperature and multispecies measurement in a lifted hydrogen diffusion flame," *Combust. Flame* **91**, 323-345 (1992).

46. S. P. Nandula, T. M. Brown, and R. W. Pitz, "Measurements of scalar dissipation in the reaction zones of turbulent nonpremixed H₂-air flames," *Combust. Flame* **99**, 775-783 (1994).
47. S. P. Nandula, T. M. Brown, and R. W. Pitz, "Single-pulse, simultaneous multipoint multispecies Raman measurements in turbulent nonpremixed jet flames," *Opt. Lett.* **19**, 414-416 (1994).
48. T. S. Cheng, J. A. Wehrmeyer, R. W. Pitz, O. J. Jr., and G. B. Northam, "Raman measurement of mixing and finite-rate chemistry in a supersonic hydrogen-air diffusion flame," *Combust. Flame* **99**, 157-173 (1994).
49. J. H. Grinstead, G. Laufer, and J. J. C. McDaniel, "Rotational Temperature Measurement in High-Temperature Air using KrF Laser-Induced O₂ Fluorescence," *Appl. Phys. B* **57**, 393-396 (1993).
50. P. Andresen, A. Bath, W. Gröger, H. W. Lülff, G. Meijer, and J. J. t. Meulen, "Laser-induced fluorescence with tunable excimer lasers as a possible method for instantaneous temperature field measurements at high pressures: checks with an atmospheric flame," *Appl. Opt.* **27**, 365-378 (1988).
51. P. Andresen, H. Schlüter, D. Wolff, H. Voges, A. Koch, W. Hentschel, W. Oppermann, and E. Rothe, "Identification and imaging of OH ($v'' = 0$) and O₂ ($v'' = 6$ or 7) in an automobile spark-ignition engine using a tunable KrF excimer laser," *Appl. Opt.* **36**, 7684-7689 (1992).
52. A. Arnold, W. Ketterle, H. Becker, and J. Wolfrum, "Simultaneous Single-Shot Imaging of OH and O₂ Using a Two-Wavelength Excimer Laser," *Appl. Phys. B* **51**, 99-102 (1990).

53. A. Brockhinke, A. T. Hartlieb, K. Kohse-Höinghaus, and D. R. Crosley, "Tunable KrF laser-induced fluorescence of C_2 in sooting flame," *Appl. Phys. B* **67**, 659-665 (1998).
54. R. W. Pitz, T. S. Cheng, J. A. Wehrmeyer, and C. F. Hess, "Two-Photon Predissociative Fluorescence of H_2O by a KrF Laser for Concentration and Temperature Measurement in Flames," *Appl. Phys. B* **56**, 94-100 (1993).
55. A. Joedicke, N. Peters, and M. Mansour, "The stabilisation mechanism and structure of turbulent hydrocarbon lifted flames," *Proc. Comb. Inst.* **30**, 901-909 (2005).
56. P. Andresen, G. Meijer, H. Schlüter, H. Voges, A. Koch, W. Hentschel, W. Oppermann, and E. Rothe, "Fluorescence imaging inside an internal combustion engine using tunable excimer lasers," *Appl. Opt.* **29**, 2392-2404 (1990).
57. A. Brockhinke, P. Andresen, and K. Kohse-Höinghaus, "Quantitative one-dimensional single-pulse multi-species concentration and temperature measurement in the lift-off region of a turbulent H_2 /air diffusion flame," *Appl. Phys. B* **61**, 533-545 (1995).
58. M. S. Mansour, Y.-C. Chen, and N. Peters, "Highly Strained Turbulent Rich Methane Flames Stabilized by Hot Combustion Products," *Combust. Flame* **116**, 136-153 (1999).
59. G. Grünefeld, V. Beushausen, and P. Andresen, "Interference-free UV-laser-induced Raman and Rayleigh measurements in hydrocarbon combustion using polarization properties," *Appl. Phys. B* **61**, 473-478 (1995).
60. G. Grünefeld, M. Schütte, and P. Andresen, "Simultaneous multiple-line/Rayleigh/LIF measurements in combustion," *Appl. Phys. B* **70**, 309-313 (2000).

61. G. Grünefeld, V. Beushausen, P. Andresen, and W. Hentschel, "Spatially Resolved Raman Scattering for Multi-Species and Temperature Analysis in Technically Applied Combustion Systems: Spray Flame and Four-Cylinder In-Line Engine," *Appl. Phys. B* **58**, 333-342 (1994).
62. G.-S. Kim, L. M. Hitchcock, E. W. Rothe, and G. P. Reck, "Identification and Imaging of Hot O₂ ($\nu''=2, 3$, or 4) in Hydrogen Flames Using 193nm- and 210nm-range Light," *Appl. Phys. B* **52**, 180-186 (1991).
63. R. Cabra, T. Myhrvold, J. Y. Chen, R. W. Dibble, A. N. Karpetis, and R. S. Barlow, "Simultaneous Laser Raman-Rayleigh-LIF Measurements and Numerical Modeling Results of a Lifted Turbulent H₂/N₂ Jet Flame in a Vitiated Coflow," *Proc. Combust. Inst.* **29**, 1881-1888 (2002).
64. "TNF Workshop web site. Available from <http://www.ca.sandia.gov/TNF>, Sandia National Laboratories," (2003).
65. Z. Ren, and S. B. Pope, "Sensitivity calculations in PDF particle methods," *Combust. Flame* **153**, 202-215 (2008).
66. P. Givi, W. A. Sirignano, and S. B. Pope, "Probability Calculations for Turbulent Jet Flows with Mixing and Reaction of NO and O₃," *Comb. Sci. Tech.* **37**, 59-78 (1984).
67. T. V. Nguyen, and S. B. Pope, "Monte Carlo Calculations of Turbulent Diffusion Flames," *Comb. Sci. Tech.* **42**, 13-45 (1984).
68. H. A. Wouters, P. A. Nooren, T. W. J. Peeters, and D. Roekaerts, "Simulation of a bluff-body-stabilized diffusion flame using second-moment closure and Monte Carlo methods," *Proc. Comb. Inst.* **26**, 177-185 (1996).

69. A. T. Norris, and S. B. Pope, "Modeling of Extinction in Turbulent Diffusion Flames by the Velocity-Dissipation-Composition," *Combust. Flame* **100**, 211-220 (1995).
70. A. R. Masri, and R. W. Dibble, "Spontaneous Raman measurements in turbulent CO/H₂/N₂ flames near extinction," *Proc. Comb. Inst.* **22**, 607-618 (1989).
71. T. W. J. Peeters, P. P. J. Stroomer, J. E. D. Vries, D. J. E. M. Roekaerts, and C. J. Hoogendoorn, "Comparative experimental and numerical investigation of a piloted turbulent natural-gas diffusion flame," *Proc. 25th Int. Symp. on Combustion*, 1241-1248 (1994).
72. P. A. Nooren, H. A. Wouters, T. W. J. Peeters, D. Roekaerts, and U. Maas, "Monte Carlo PDF modelling of a turbulent natural-gas diffusion flame," *Combust. Theory Modelling* **1**, 79-96 (1997).
73. C. Dopazo, and E. E. O'Brien, "Functional formulation of nonisothermal turbulent reactive flows," *Phys. Fluids* **17**, 1968-1975 (1975).
74. J. Janicka, W. Kolbe, and W. Kollmann, "Closure of the transport equation for the pdf of turbulent scalar fields," *Journal Non-Equilibrium Thermodynamics* **4**, 47-66 (1978).
75. H. Chen, S. Chen, and R. H. Kraichnan, "Probability Distribution of a Stochastically Advected Scalar Field," *Phys. Rev. Lett* **63**, 2657-2660 (1989).
76. S. B. Pope, "Mapping Closures for Turbulent Mixing and Reaction," *Theor. Comput. Fluid Dynamics* **2**, 255-270 (1991).
77. R. W. Bilger, and S. H. Starner, "A Simple Model for Carbon Monoxide in Laminar and Turbulent Hydrocarbon Diffusion Flames," *Combust. Flame* **51**, 155-176 (1983).

78. U. Maas, and S. B. Pope, "Simplifying Chemical Kinetics: Intrinsic Low-Dimensional Manifolds in Composition Space," *Combust. Flame* **88**, 239-264 (1992).
79. J. Xu, and S. B. Pope, "PDF Calculations of Turbulent Nonpremixed Flames with Local Extinction," *Combust. Flame* **123**, 281-307 (2000).
80. R. P. Lindstedt, S. A. Louloudi, and E. M. Vaos, "Joint scalar probability density function modeling of pollutant formation in piloted turbulent jet diffusion flames with comprehensive chemistry," *Proc. Comb. Inst.* **28**, 149-156 (2000).
81. R. R. Cao, and S. B. Pope, "The influence of chemical mechanisms on PDF calculations of nonpremixed jet flames," *Combust. Flame* **143**, 450-470 (2005).
82. Q. Tang, J. Xu, and S. B. Pope, "Probability density function calculations of local extinction and NO production in piloted-jet turbulent methane/air flames," *Proc. Comb. Inst.* **28**, 133-139 (2000).
83. R. P. Lindstedt, and S. A. Louloudi, "Joint scalar transported probability density function modeling of turbulent methanol jet diffusion flames," *Proc. Comb. Inst.* **29**, 2147-2154 (2002).
84. S. James, M. S. Anand, and S. B. Pope, "The Lagrangian PDF Transport Method for Simulations of Gas Turbine Combustor Flows," in *38th AIAA/ASME/SAE/ASEE Joint Propulsion Conference & Exhibit*, (Indianapolis, Indiana, 2002), pp. 1-12.
85. R. L. Curl, "Dispersed phase mixing: I. Theory and effects in simple reactors," *AIChE J.* **9**, 175-181 (1963).
86. L. A. Spielman, and O. Levenspiel, "A Monte Carlo treatment for reacting and coalescing dispersed phase systems," *Chem. Eng. Sci.* **20**, 247-254 (1965).

87. C. Dopazo, "Relaxation of initial probability density functions in the turbulent convection of scalar fields," *Phys. Fluids* **22**, 20-30 (1979).
88. S. B. Pope, "An Improved Turbulent Mixing Model," *Comb. Sci. Tech.* **28**, 131-145 (1982).
89. C. Dopazo, and E. E. O'Brien, "An approach to the autoignition of a turbulent mixture," *Acta Astronaut.* **1**, 1239-1266 (1974).
90. A. T. Norris, and S. B. Pope, "Turbulent Mixing Model Based on Ordered Pairing," *Combust. Flame* **83**, 27-42 (1991).
91. S. Subramaniam, and S. B. Pope, "A Mixing Model for Turbulent Reactive Flows based on Euclidean Minimum Spanning Trees," *Combust. Flame* **115**, 487-514 (1998).
92. R. R. Cao, H. Wang, and S. B. Pope, "The effect of mixing models in PDF calculations of piloted jet flames," *Proc. Comb. Inst.* **31**, 1543-1550 (2007).
93. Z. Ren, and S. B. Pope, "An Investigation of the performance of turbulent mixing models," *Combust. Flame* **136**, 208-216 (2004).
94. D. Roekaerts, "Use of a Monte Carlo PDF method in a study of the influence of turbulent fluctuations on selectivity in a jet-stirred reactor," *Applied Scientific Research* **48**, 271-300 (1991).
95. S. Tiang, A. R. Masri, and S. B. Pope, "PDF Calculations of Turbulent Nonpremixed Flames of H_2/CO_2 Using Reduced Chemical Mechanisms," *Combust. Flame* **95**, 133-150 (1993).

96. A. R. Masri, S. Subramaniam, and S. B. Pope, "A mixing model to improve the PDF simulation of turbulent diffusion flames," *Proc. Combust. Inst.* **26**, 49-57 (1996).
97. V. Saxena, and S. B. Pope, "PDF calculations of major and minor species in a turbulent piloted jet flame," *Proc. Comb. Inst.* **27**, 1081-1086 (1998).
98. C. Beguier, I. Dekeyser, and B. E. Launder, "Ratio of scalar and velocity dissipation time scales in shear flow turbulence," *Phys. Fluids* **21**, 307-310 (1978).
99. N. R. Panchapakesan, and J. L. Lumley, "Turbulence measurements in axisymmetric jets of air and helium. Part 2. Helium jet," *J. Fluid Mech.* **246**, 225-247 (1993).
100. A. R. Masri, R. Cao, S. B. Pope, and G. M. Goldin, "PDF calculations of turbulent lifted flames of H_2/N_2 fuel issuing into a vitiated co-flow," *Combust. Theory Modelling* **8**, 1-22 (2004).
101. R. R. Cao, S. B. Pope, and A. R. Masri, "Turbulent lifted flames in a vitiated coflow investigated using joint PDF calculations," *Combust. Flame* **142**, 438-453 (2005).
102. W. Juchmann, H. Latzel, D. I. Shin, G. Pieter, T. Dreier, H.-R. Volpp, J. Wolfrum, R. P. Lindstedt, and K. M. Leung, "Absolute radical concentration measurements and modeling of low-pressure $CH_4/O_2/NO$ flames," *Proc. Comb. Inst.* **27**, 469-476 (1998).
103. V. Sick, F. Hildenbrand, and P. Lindstedt, "Quantitative laser-based measurements and detailed chemical kinetic modeling of nitric oxide concentrations in methane-air counterflow diffusion flames," *Proc. Comb. Inst.* **27**, 1401-1409 (1998).

104. M. P. Meyer, "The Application of Detailed and Systematically Reduced Chemistry to Transient Laminar Flames," (University of London, London, 2001).
105. S. B. Pope, (personal communication, 2008).
106. K. Liu, S. B. Pope, and D. A. Caughey, "Calculations of bluff-body stabilized flames using a joint probability density function model with detailed chemistry," *Combust. Flame* **141**, 89-117 (2005).
107. A. R. Masri, and R. W. Bilger, "Turbulent diffusion flames of hydrocarbon fuels stabilised on a bluff body," *Proc. Comb. Inst.* **20**, 317-323 (1984).
108. A. R. Masri, R. W. Dibble, and R. S. Barlow, "Raman-Rayleigh measurements in bluff-body stabilised flames of hydrocarbon fuels," *Proc. Comb. Inst.* **24**, 317-324 (1992).
109. A. R. Masri, B. B. Dally, R. S. Barlow, and C. D. Carter, "The structure of the recirculation zone of a bluff-body combustor," *Proc. Comb. Inst.* **25**, 1301-1307 (1994).
110. B. B. Dally, A. R. Masri, R. S. Barlow, G. J. Fiechtner, and D. F. Fletcher, "Measurements of NO in turbulent non-premixed flames stabilized on a bluff-body," *Proc. Comb. Inst.* **26**, 2191-2196 (1996).
111. B. B. Dally, "Turbulent nonpremixed flames stabilised on a bluff-body," (The University of Sydney, Sydney, 1997).
112. A. R. Masri, J. B. Kelman, and B. B. Dally, "The instantaneous spatial structure of the recirculation zone in bluff-body stabilized flames," *Proc. Comb. Inst.* **27**, 1031-1036 (1998).

113. B. B. Dally, A. R. Masri, R. S. Barlow, and G. J. Fiechtner, "Instantaneous and Mean Compositional Structure of Bluff-Body Stabilized Nonpremixed Flames," *Combust. Flame* **114**, 119-148 (1998).
114. B. Merci, D. Roekaerts, B. Naud, and S. B. Pope, "Comparative study of micromixing models in transported scalar PDF simulations of turbulent nonpremixed bluff body flames," *Combust. Flame* **146**, 109-130 (2006).
115. B. Merci, and E. Dick, "Predictive Capabilities of an Improved Cubic k - ϵ Model for Inert Steady Flows," *Flow. Turb. Comb.* **68**, 335-358 (2002).
116. B. Merci, E. Dick, and C. D. Langhe, "Application of an Improved ϵ -Equation to a Piloted Jet Diffusion Flame," *Combust. Flame* **131**, 465-468 (2002).
117. B. Merci, E. Dick, J. Vierendeels, D. Roekaerts, and T. W. J. Peeters, "Application of a new Cubic Turbulence Model to Piloted and Buff-Body Diffusion Flames," *Combust. Flame* **126**, 1533-1556 (2001).
118. B. Merci, C. D. Langhe, J. Vierendeels, and E. Dick, "A Quasi-Realizable Cubic Low-Reynolds Eddy-Viscosity Turbulence Model with a New Dissipation Rate Equation," *Flow. Turb. Comb.* **66**, 133-157 (2001).
119. B. Merci, B. Naud, and D. Roekaerts, "Flow and Mixing Fields for Transported Scalar PDF Simulations of a Piloted Jet Diffusion Flame ('Delft Flame III')," *Flow. Turb. Comb.* **74**, 239-272 (2005).
120. B. Merci, B. Naud, and D. Roekaerts, "Impact of Turbulent Flow and Mean Mixture Fraction Results on Mixing Model Behaviour in Transported Scalar PDF Simulations of Turbulent Non-premixed Bluff Body Flames," *Flow. Turb. Comb.* **79**, 41-53 (2007).

121. B. Merci, D. Roekaerts, and B. Naud, "Study of the performance of three micromixing models in transported scalar PDF simulations of a piloted diffusion flame ("Delft Falme III")," *Combust. Flame* **144**, 476-493 (2006).
122. R. O. Fox, *Computational Models for Turbulent Reacting Flows* (Cambridge University Press, Cambridge, UK, 2003).
123. S. B. Pope, "A Monte Carlo Method for the PDF Equations of Turbulent Reactive Flow," *Comb. Sci. Tech.* **25**, 259-174 (1981).
124. S. B. Pope, "PDF methods for turbulent reactive flows," *Prog. Energy Combust. Sci.* **11**, 119-192 (1985).
125. S. B. Pope, "Lagrangian PDF methods for turbulent flows," *Annu. Rev. Fluid Mech.* **26**, 23-63 (1994).
126. R. Cao, and S. B. Pope, "Numerical integration of stochastic differential equations: weak second-order mid-point scheme for application in the composition PDF method," *Journal of Computational Physics* **185**, 194-212 (2003).
127. S. B. Pope, "Particle method for turbulent flows: Integration of stochastic differential equations," *J. Comput. Phys.* **117**, 332-349 (1995).
128. A. R. Masri, and S. B. Pope, "PDF Calculations of Piloted Turbulent Nonpremixed Flames of Methane," *Combust. Flame* **81**, 13-29 (1990).
129. M. D. Smooke, *Reduced Kinetic Mechanisms and Asymptotic Approximations for Methane-Air Flames* (Springer, Berlin, 1991).
130. J. C. Keck, and D. Gillespie, "Rate-Controlled Partial-Equilibrium Method for Treating Reacting Gas Mixtures," *Combust. Flame* **17**, 237-241 (1971).

131. S. H. Lam, and D. A. Goussis, "Understanding complex chemical kinetics with computational singular perturbation," Proc. 22nd Int. Symp. on Combustion, 931-941 (1988).
132. U. Maas, and S. B. Pope, "Implementation of simplified chemical kinetics based on intrinsic low-dimensional manifolds," Proc. 24th Int. Symp. on Combustion, 103-112 (1992).
133. U. Maas, and S. B. Pope, "Laminar flame calculations using simplified chemical kinetics based on intrinsic low-dimensional manifolds," Proc. 25th Int. Symp. on Combustion, 1349-1356 (1994).
134. J.-Y. Chen, W.-C. Chang, and M. Koszykowski, "Numerical Simulation and Scaling of NO_x Emissions from Turbulent Hydrogen Jet Flames with Various Amounts of Helium Dilution," Comb. Sci. Tech. **110**, 505-529 (1995).
135. F. C. Christo, A. R. Masri, and E. M. Nebot, "Artificial Neural Network Implementation of Chemistry with pdf Simulation of H₂/CO₂ Flames," Combust. Flame **106**, 406-427 (1996).
136. F. C. Christo, A. R. Masri, E. M. Nebot, and S. B. Pope, "An integrated PDF/neural network approach for simulating turbulent reacting systems," Proc. 26th Int. Symp. on Combustion, 43-48 (1996).
137. T. Turanyi, "Parameterisation of reaction mechanisms using orthogonal polynomials," Computer Chem. **18**, 45-54 (1994).
138. B. Yang, and S. B. Pope, "An investigation of the Accuracy of Manifold Methods and Splitting Schemes in the Computational Implementation of Combustion Chemistry," Combust. Flame **112**, 16-32 (1998).

139. B. Yang, and S. B. Pope, "Treating Chemistry in Combustion with Detailed Mechanisms-*In Situ* Adaptive Tabulation in Principle Directions-Premixed Combustion," *Combust. Flame* **112**, 85-112 (1998).
140. S. B. Pope, "Computationally efficient implementation of combustion chemistry using *in situ* adaptive tabulation," *Combust. Theory Modelling* **1**, 41-63 (1997).
141. N. Xie, F. Battaglia, and R. O. Fox, "Simulations of multiphase reactive flows in fluidized beds using *in situ* adaptive tabulation," *Combust. Theory and Modelling* **8**, 195-209 (2004).
142. M. A. Singer, and S. B. Pope, "Exploiting ISAT to solve the reaction-diffusion equation," *Combust. Theory Modelling* **8**, 361-383 (2004).
143. M. A. Singer, S. B. Pope, and H. Najm, "Modeling unsteady reacting flow with operator splitting and ISAT," *Combust. Flame* **147**, 150-162 (2006).
144. M. A. Singer, S. B. Pope, and H. N. Najm, "Operator-splitting with ISAT to model reacting flow with detailed chemistry," *Combust. Theory Modelling* **10**, 199-217 (2006).
145. V. Saxena, and S. B. Pope, "PDF Simulations of Turbulent Combustion Incorporating Detailed Chemistry," *Combust. Flame* **117**, 340-350 (1999).
146. L. Lu, Z. Ren, V. Raman, S. B. Pope, and H. Pitsch, "LES/FDF/ISAT computations of turbulent flames," *Center for Turbulence Research Proceedings of the Summer Program 2004*, 283-294 (2004).
147. L. Lu, and S. B. Pope, "An improved algorithm for *in situ* adaptive tabulation," *Journal of Computational Physics* **228**, 361-386 (2009).

148. A. Juneja, and S. B. Pope, "A DNS study of turbulent mixing of two passive scalars," *Phys. Fluids* **8**, 2161-2184 (1996).
149. S. B. Pope, "Consistent modeling of scalars in turbulent flows," *Phys. Fluids* **26**, 404-408 (1983).
150. S. Subramaniam, and S. B. Pope, "Comparison of Mixing Model Performance for Nonpremixed Turbulent Reactive Flow," *Combust. Flame* **117**, 732-754 (1999).
151. Y. El-Banhawy, S. Sivasegaram, and J. H. Whitelaw, "Premixed, Turbulent Combustion of a Sudden-Expansion Flow," *Combust. Flame* **50**, 153-165 (1983).
152. P. Magre, P. Moreau, G. Collin, R. Borghi, and M. Péalat, "Further Studies by CARS of Premixed Turbulent Combustion in a High Velocity Flow," *Combust. Flame* **71**, 147-168 (1988).
153. B. Bedat, and R. K. Cheng, "Experimental Study of Premixed Flames in Intense Isotropic Turbulence," *Combust. Flame* **100**, 485-494 (1995).
154. T. Landenfeld, A. Kremer, E. P. Hassel, J. Janicka, T. Schäfer, J. Kazenwadel, C. Schulz, and J. Wolfrum, "Laser-Diagnostic and Numerical Study of Strongly Swirling Natural Gas Flames," *Proc. Combust. Inst.* **27**, 1023–1029 (1998).
155. D. Bradley, P. H. Gaskell, X. J. Gu, M. Lawes, and M. J. Scott, "Premixed Turbulent Flame Instability and NO Formation in a Lean-Burn Swirl Burner," *Combust. Flame* **115**, 515-538 (1998).
156. D. M. Wicksall, A. K. Agrawal, R. W. Schefer, and J. O. Keller, "The interaction of flame and flow field in a lean premixed swirl-stabilized combustor operated on $H_2/CH_4/air$," *Proc. Combust. Inst.* **30**, 2875–2883 (2005).

157. F. O'Young, and R. W. Bilger, "Scalar Gradient and Related Quantities in Turbulent Premixed Flames," *Combust. Flame* **109**, 682-700 (1997).
158. M. S. Mansour, Y.-C.Chen, and N. Peters, "The reaction zone structure of turbulent premixed methane-helium-air flames near extinction," *Proc. Combust. Inst.* **24**, 461-468 (1992).
159. A. R. Masri, and R. W. Bilger, "Turbulent non-premixed flames of hydrocarbon fuels near extinction: mean structure from probe measurements," *Proc. Combust. Inst.* **21**, 1511-1520 (1986).
160. J. H. Frank, P. A. M. Kalt, and R. W. Bilger, "Measurements of Conditional Velocities in Turbulent Premixed Flames by Simultaneous OH PLIF and PIV," *Combust. Flame* **116**, 220-232 (1999).
161. M. J. Dunn, R. W. Bilger, and A. R. Masri, "Experimental Characterisation of a Vitiated Coflow Piloted Premixed Burner," in *Proceedings of the Fifth Asia-Pacific Conference on Combustion*, G. J. Nathan, B. B. Dally, and P. A. M. Kalt, eds. (The University of Adelaide, 2005), pp. 417-420.
162. "The University of Sydney, thermofluids website. Available from <http://www.aeromech.usyd.edu.au/thermofluids>, The University of Sydney," (2006).
163. J. Kojima, Y. Ikeda, and T. Nakajima, "Basic aspects of OH(A), CH(A), and C₂(d) chemiluminescence in the reaction zone of laminar methane-air premixed flames," *Combust. Flame* **140**, 34-45 (2005).
164. P. Buchhave, W. K. J. George, and J. L. Lumley, "The measurement of turbulence with the laser-Doppler Anemometer," *Annu. Rev. Fluid Mech.* **11**, 443-503 (1979).

165. W. Fuchs, H. Nobach, and C. Tropea, "Laser Doppler anemometry data simulation: Application to investigate the accuracy of statistical estimators," *AIAA Journal* **32**, 1883-1889 (1994).
166. D. K. McLaughlin, and W. G. Tiederman, "Bias correcting for individual realization of laser anemometer measurements in turbulent flow," *Phys. Fluids* **16**, 2082-2088 (1973).
167. W. Hosel, and W. Rodi, "New biasing elimination method for laser-Doppler-velocimeter counter processing," *Rev. Sci. Instrum.*, 910-919 (1977).
168. M. Gaster, and J. B. Roberts, "Spectral analysis of randomly sampled Signals," *J. Inst. Math. Appl.* **15**, 195-216 (1975).
169. M. Gaster, and J. B. Roberts, "The spectral analysis of randomly sampled records by a direct transform," *Proc. R. Soc.* **354**, 27-58 (1977).
170. W. T. Mayo, "A discussion of limitations and extensions of power spectrum estimation with burst counter LDV systems," in *Proc. Second Int. Workshop on Laser Velocimetry*, (Purdue University, 1974), pp. 90-104.
171. M. J. Tummers, and D. M. Passchier, "Spectral estimation using a variable window and the slotting technique with local normalisation," *Meas. Sci. Technol.* **7**, 1541-1546 (1996).
172. H. Nobach, "Local time estimation for the slotted correlation function of randomly sampled LDA data," *Exp. in Fluids* **32**, 337-345 (2002).
173. H. R. E. V. Maanen, H. Nobach, and L. H. Benedict, "Improved estimator for the slotted autocorrelation function of randomly sampled LDA data," *Meas. Sci. Technol.* **10**, L4-L7 (1999).

174. M. S. Wu, S. Kwon, J. F. Driscoll, and G. M. Faeth, "Preferential Diffusion Effects on the Surface Structure of Turbulent Premixed Hydrogen/Air Flames," *Combust. Sci. and Tech.* **78**, 69-96 (1991).
175. M. J. Dunn, A. R. Masri, and R. W. Bilger, "A new piloted premixed jet burner to study strong finite-rate chemistry effects," *Combust. Flame* **151**, 46–60 (2007).
176. G. P. Smith, D. M. Golden, M. S. Frenklach, N. W. Moriarty, B. Eiteneer, M. Gardiner, V. V. Lissianski, and Z. Qin, "GRI-MECH 3.0, http://www.me.berkeley.edu/gri_mech," (1999).
177. D. G. Goodwin, in *Proc. CVD XVI and EuroCVD Fourteenth*, M. Allendorf, ed. (2003).
178. M. C. Potter, and D. C. Wiggert, *Mechanics of fluids* (Prentice-Hall, Inc., Upper Saddle River, NJ 07458, USA, 1997).
179. L. F. Moody, "Friction Factors in Pipe Flow," *Trans. ASME.* **66**, 671-684 (1944).
180. J. W. Daily, "Laser induced fluorescence spectroscopy in flames," *Prog. Energy Combust. Sci.* **23**, 133-199 (1997).
181. K. Kohse-Höinghaus, "Laser techniques for the quantitative detection of reactive intermediates in combustion systems," *Prog. Energy Combust. Sci.* **20**, 203-279 (1994).
182. A. C. Eckbreth, *Laser Diagnostics for Combustion Temperature and Species* (Gordon & Breach, Amsterdam, 1996).
183. N. Omenetto, P. Benetti, L. P. Hart, J. D. Winefordner, and C. T. J. Alkemade, "Non-linear optical behaviour in atomic fluorescence flame spectrometry," *Spectrochim. Acta, part B* **28**, 289-300 (1973).

184. E. H. Piepmeier, "Theory of laser saturated atomic resonance fluorescence," *Spectrochim. Acta*, part B **27**, 431-443 (1972).
185. J. W. Daily, "Saturation effect in laser induced fluorescence spectroscopy," *Appl. Opt.* **16**, 568-571 (1977).
186. L. Pasternack, A. P. Baronavski, and J. R. McDonald, "Application of saturation spectroscopy for measurement of atomic Na and MgO in acetylene flames," *J. Phys. Chem.* **69**, 4830-4837 (1978).
187. R. P. Lucht, D. W. Sweeney, and N. M. Laurendeau, "Balanced cross-rate model for saturated molecular fluorescence in flames using a nanosecond pulse length laser," *Appl. Opt.* **19**, 3295-3300 (1980).
188. R. P. Lucht, D. W. Sweeny, and N. M. Laurendeau, "Laser-Saturated Fluorescence Measurements of OH Concentration in Flames," *Combust. Flame* **50**, 189-205 (1983).
189. R. P. Lucht, D. W. Sweeney, N. M. Laurendeau, M. C. Drake, M. Lapp, and R. W. Pitz, "Single-pulse, laser-saturated fluorescence measurements of OH in turbulent nonpremixed flames," *Opt. Lett.* **9**, 90-92 (1984).
190. J. T. Salmon, and N. M. Laurendeau, "Calibration of laser-saturated fluorescence measurements using Rayleigh scattering," *Appl. Opt.* **24**, 65-73 (1985).
191. J. T. Salmon, and N. M. Laurendeau, "Analysis of probe volume effects associated with laser-saturated fluorescence measurements," *Appl. Opt.* **24**, 1313-1321 (1985).
192. C. D. Carter, G. B. King, and N. M. Laurendeau, "Quenching-corrected saturated fluorescence measurements of the hydroxyl radical in laminar high-pressure C₂H₆/O₂/N₂ flames," *Comb. Sci. Tech.* **78**, 247-264 (1991).

193. C. D. Carter, G. B. King, and N. M. Laurendeau, "Saturated fluorescence measurements of the hydroxyl radical in laminar high-pressure $C_2H_6 / O_2 / N_2$ flames," *Appl. Opt.* **31**, 1511-1522 (1992).
194. C. D. Carter, and N. M. Laurendeau, "Wide- and Narrow-Band Saturated Fluorescence Measurements of Hydroxyl Concentration in Premixed Flames from 1 bar to 10 bar," *Appl. Phys. B* **58**, 519-528 (1994).
195. J. O. Berg, and W. L. Shackleford, "Rotational redistribution effect on saturated laser-induced fluorescence," *Appl. Opt.* **18**, 2093–2094 (1979).
196. J. W. Daily, "Saturation of fluorescence in flames with a Gaussian laser beam," *Appl. Opt.* **17**, 225–229 (1978).
197. P. Desgroux, and M. J. Cottreau, "Local OH concentration measurement in atmospheric pressure flames by a laser-saturated fluorescence method: two-optical path laser-induced fluorescence," *Appl. Opt.* **30**, 90-97 (1991).
198. P. Desgroux, E. Domingues, and M. Cottreau, "Measurements of OH concentration in flames at high pressure by two-optical path laser-induced fluorescence," *Appl. Opt.* **31**, 2831-2838 (1992).
199. M. Marrocco, "Geometric determination of saturation in fluorescence spectroscopy," *Appl. Opt.* **44**, 2879–2886 (2005).
200. J. W. Daily, "Use of rate equations to describe laser excitation in flames," *Appl. Opt.* **16**, 2322-2327 (1977).
201. T. B. Settersten, and M. A. Linne, "Modeling pulsed excitation for gas-phase laser diagnostics," *J. Opt. Soc. Am. B* **19**, 954-964 (2002).

202. J. W. Daily, and P. R. Rothe, "Effect of laser intensity and of lower-state rotational energy transfer upon temperature measurements made with laser-induced fluorescence," *Appl. Phys. B* **68**, 131–140 (1999).
203. J. W. Daily, W. G. Bessler, C. Schulz, V. Sick, and T. B. Settersten, "Nonstationary Collisional Dynamics in Determining Nitric Oxide Laser-Induced Fluorescence Spectra," *AIAA Journal* **43**, 458-464 (2005).
204. U. Rahmann, W. Kreutner, and K. Kohse-Höinghaus, "Rate-equation modeling of single- and multiple-quantum vibrational energy transfer of OH ($A^2\Sigma^+$, $v'=0$ to 3)," *Appl. Phys. B* **69**, 61–70 (1999).
205. R. Kienle, M. P. Lee, and K. Kohse-Höinghaus, "A detailed rate equation model for the simulation of energy transfer in OH laser-induced fluorescence," *Appl. Phys. B* **62**, 583-599 (1996).
206. A. Brockhinke, W. Kreutner, U. Rahmann, K. Kohse-Höinghaus, T. B. Settersten, and M. A. Linne, "Time-, wavelength-, and polarization-resolved measurements of OH ($A^2\Sigma^+$) picosecond laser-induced fluorescence in atmospheric pressure flames," *Appl. Phys. B* **69**, 477–485 (1999).
207. A. Brockhinke, U. Lenhard, A. Bülter, and K. Kohse-Höinghaus, "Energy transfer in the OH $A^2\Sigma^+$ state: The role of polarization and of multi-quantum energy transfer," *Phys. Chem. Chem. Phys.* **7**, 874-881 (2005).
208. C. Chan, and J. W. Daily, "Laser excitation dynamics of OH in flames," *Appl. Opt.* **19**, 1357-1367 (1980).
209. D. H. Campbell, "Vibrational level relaxation effects on laser-induced fluorescence measurements of hydroxide number density in a methane-air flame," *Appl. Opt.* **21**, 2912-2919 (1982).

210. D. H. Campbell, "Collisional effects on laser-induced fluorescence measurements of hydroxide concentrations in a combustion environment. 1: Effects for $v' = 0$ excitation," *Appl. Opt.* **23**, 689-703 (1984).
211. D. H. Campbell, "Collisional effects on laser-induced fluorescence measurements of hydroxide concentrations in a combustion environment. 2: Effects for $v' = 1$ excitation," *Appl. Opt.* **23**, 1319-1327 (1984).
212. A. Jörg, U. Meier, R. Kienle, and K. Kohse-Höinghaus, "State-Specific Rotational Energy Transfer in OH ($A^2\Sigma^+$, $v'=0$) by some Combustion-Relevant Collision Partners," *Appl. Phys. B* **55**, 305-310 (1992).
213. J. Luque, and D. R. Crosley, "LIFBASE: Database and Spectral Simulation Program (Version 1.5)," J.SRI International Report MP 99-009, (1999).
214. P. H. Paul, C. D. Carter, J. A. Gray, J. W. Thoman, and M. R. Furlanetto, "Correlations for the $A^2\Sigma^+$ ($v'=0$) electronic quenching cross-section," Sandia National Laboratories Report No. **SAND 94-8237**, (1995).
215. J. B. Jeffries, K. Kohse-Höinghaus, G. P. Smith, R. A. Copeland, and D. R. Crosley, "Rotational-level-dependent quenching of OH($A^2\Sigma^+$) at flame temperatures," *Chem. Phys. Lett.* **152**, 160-166 (1988).
216. M. P. Lee, R. Kienle, and K. Kohse-Höinghaus, "Measurements of rotational energy transfer and quenching in OH $A^2\Sigma^+$, $v'=0$ at elevated temperature," *Appl. Phys. B* **58**, 447-457 (1994).
217. P. H. Paul, J. J. L. Durant, J. A. Gray, and M. R. Furlanetto, "Collisional electronic quenching of OH $A^2\Sigma^+$ ($v'=0$) measured at high temperature in a shock tube," *J. Chem. Phys.* **102**, 8378-8384 (1995).

218. M. Tamura, P. A. Berg, J. E. Harrington, J. Luque, J. B. Jeffries, G. P. Smith, and D. R. Crosley, "Collisional Quenching of CH(A), OH(A), and NO(A) in Low Pressure Hydrocarbon Flames," *Combust. Flame*. **114**, 502–514 (1998).
219. P. H. Paul, "Vibrational energy transfer and quenching of OH $A^2\Sigma^+$ ($v'=1$) measured at high temperatures in a shock tube," *J. Phys. Chem.* **99**, 8472–8476 (1995).
220. R. J. Cattolica, and T. G. Mataga, "Rotational-level-dependent quenching of OH $A^2\Sigma^+$ ($v'=1$) by collisions with H_2O in a low-pressure flame," *Chem. Phys. Lett.* **182**, 623–631 (1991).
221. A. T. Hartlieb, D. Markus, W. Kreutner, and K. Kohse-Höinghaus, "Measurement of vibrational energy transfer of OH($A^2\Sigma^+$, $v'=1 \rightarrow 0$) in low-pressure flames," *Appl. Phys. B* **65**, 81–91 (1997).
222. E. C. J. Rea, A. Y. Chang, and R. K. Hanson, "Shock-tube study of pressure broadening of the $A^2\Sigma^+ \leftarrow X^2\Pi$ (0,0) band of OH by Ar and N_2 ," *J. Quant. Spectrosc. Radiat. Transfer* **37**, 117-127 (1987).
223. E. C. J. Rea, A. Y. Chang, and R. K. Hanson, "Collisional broadening of the $A^2\Sigma^+ \leftarrow X^2\Pi$ (0,0) band of OH by H_2O and CO_2 in atmospheric-pressure flames," *J. Quant. Spectrosc. Radiat. Transfer* **41**, 29-42 (1989).
224. W. J. Kessler, M. G. Allen, and S. J. Davis, "Rotational level-dependant collisional broadening and line shift of the $A^2\Sigma^+ - X^2\Pi$ (1,0) band of OH in hydrogen-air combustion gases," *J. Quant. Spectrosc. & Radiat. Transfer* **49**, 107-117 (1993).
225. R. Kienle, M. P. Lee, and K. Kohse-Höinghaus, "A scaling formalism for the representation of rotational energy transfer in OH ($A^2\Sigma^+$) in combustion experiments," *Appl. Phys. B* **63**, 403–418 (1996).

226. J. Tobai, T. Drier, and J. W. Daily, "Rotational level dependence of ground state recovery rates for OH $X^2\Pi$ ($v''=0$). in atmospheric pressure flames using the picosecond saturating-pump degenerate four-wave mixing probe technique," *J. Chem. Phys.* **116**, 4030-4038 (2002).
227. X. Chen, B. D. Patterson, and T. B. Settersten, "Time-domain investigation of OH ground-state energy transfer using picosecond two-color polarization spectroscopy," *Chem. Phys. Lett.* **388**, 358-362 (2005).
228. W. P. J. Partridge, and N. M. Laurendeau, "Formulation of a dimensionless overlap fraction to account for spectrally distributed interactions in fluorescence studies," *Appl. Opt.* **34**, 2645-2647 (1995).
229. R. P. Lucht, D. W. Sweeney, and N. M. Laurendeau, "Time-resolved fluorescence investigation of rotational transfer in $A^2\Sigma^+$ ($v=0$) OH," *Appl. Opt.* **25**, 4086-4095 (1986).
230. D. R. Crosley, and R. A. Copeland, "Collisional quenching and energy transfer in OH," *Proc. SPIE-Int. Soc. Opt. Eng.* **742**, 6-15 (1987).
231. T. B. Settersten, B. D. Patterson, H. Kronemayer, V. Sick, C. Schulz, and J. W. Daily, "Branching ratios for quenching of nitric oxide $A^2\Sigma^+$ ($v'=0$) to $X^2\Pi$ ($v''=0$)," *Phys. Chem. Chem. Phys.* **8**, 5328-5338 (2006).
232. M. J. Dyer, K. Knutsen, and R. A. Copeland, "Energy transfer in the ground state of OH: Measurements of OH($v=8,10,11$) removal," *J. Chem. Phys.* **107**, 7809-7815 (1997).
233. E. S. Ginsberg, and D. Zaborowski, "The dilogarithm function of a real argument," *Comm. ACM* **18**, 200-202 (1975).

- 234. R. Morris, "The dilogarithm function of a real argument," *Math. Comp.* **33**, 778-787 (1979).
- 235. K. Bennett, and R. L. Byer, "Computer-controllable wedged-plate optical variable attenuator," *Appl. Opt.* **19**, 2408-2412 (1980).
- 236. J. Kelman, and A. R. Masri, "Quantitative technique for imaging mixture fraction, temperature, and the hydroxyl radical in turbulent diffusion flames," *Appl. Opt.* **36**, 3506–3514 (1997).
- 237. S. H. Stårner, R. W. Bilger, and M. B. Long, "A Method for Contour-Aligned Smoothing of Joint 2D Scalar Images in Turbulent Flames," *Combust. Sci. and Technol.* **107**, 195-203 (1995).
- 238. R. J. Kee, J. F. Grcar, M. D. Smooke, and J. A. Miller, "CHEMKIN II: A Fortran Program for Modelling Steady Laminar One-Dimensional Premixed Flames," Report SAND85-8240, Sandia National Laboratories, (1985).
- 239. M. Snee, and W. Ubachs, "Direct measurement of the Rayleigh scattering cross section in various gases," *J. Quant. Spectrosc. & Radiat. Transfer* **92**, 293-310 (2005).
- 240. I. Namer, and R. W. Schefer, "Error estimates for Rayleigh scattering density and temperature measurements in premixed flames," *Exp. in Fluids* **3**, 1-9 (1985).
- 241. M. J. Dunn, A. R. Masri, and R. W. Bilger, "Joint Quantitative Imaging of Rayleigh and OH LIF Using Saturated and Linear Fluorescence," in *Proceedings of The Fourth Australian Conference on Laser Diagnostics in Fluid Mechanics and Combustion*, Z. T. Alwahabi, B. B. Dally, P. A. M. Kalt, G. J. Nathan, and C. Y. Wong, eds. (The University of Adelaide, McLaren Vale, South Australia, 2005), pp. 41-44.

242. M. J. Dunn, and A. R. Masri, "A comprehensive model for the quantification of linear and non-linear regime laser-induced fluorescence of OH under $A^2\Sigma^+ \leftarrow X^2\Pi$ (1,0) excitation," Appl. Opt. submitted for review, submitted draft available at <http://www.aeromech.usyd.edu.au/thermofluids/papers/AO_Dunn_1.pdf> (2008).
243. M. J. Dunn, A. R. Masri, R. W. Gordon, and R. W. Bilger, "High resolution temperature and OH imaging in highly turbulent premixed flames," in *Proceedings of The Sixth Asia-Pacific Conference on Combustion*, (The Japanese Section of The Combustion Institute, The Nagoya Congress Center, Nagoya, Japan, 2007), pp. 146-149.
244. M. Mauck, "Knife-edge profiling of Q-switched Nd:YAG laser beam and waist," Appl. Opt. **18**, 599-600 (1979).
245. R. M. O'Connell, and R. A. Vogel, "Abel inversion of knife-edge data from radially symmetric pulsed laser beams," Appl. Opt. **26**, 2528-2532 (1987).
246. J. Soto, "Arbitrary-intensity-profiles measurement of laser beams by a scanning and rotating slit," Appl. Opt. **32**, 7272-7276 (1993).
247. M. A. Abramson, T. J. Asaki, J. E. Dennis, R. L. Pingel, and K. R. O'Reilly, "Quantitative Object Reconstruction using Abel Transform X-ray Tomography and Mixed Variable Optimization," in *AIR FORCE INST OF TECH WRIGHT-PATTERSON AFB OH DEPT OF MATHEMATICS AND STATISTICS*, (2007).
248. G. H. Wang, and N. T. Clemens, "Effects of imaging system blur on measurements of flow scalars and scalar gradients," Experiments in Fluids **37**, 194-205 (2004).
249. H. N. Najm, P. H. Paul, C. J. Mueller, and P. S. Wyckoff, "On the adequacy of certain experimental observables as measurements of flame burning rate," Combust. Flame **113**, 312-332 (1998).

250. H. N. Najm, P. H. Paul, and A. Mcilroy, "A numerical and experimental investigation of premixed methane-air flame transient response," *Combust. Flame* **125**, 879-892 (2001).
251. V. Nguyen, and P. H. Paul, "The time evolution of a vortex-flame interaction observed via planar imaging of CH and OH," *Proc. Comb. Inst.* **26**, 357-364 (1996).
252. C. M. Vagelopoulos, and J. H. Frank, "An experimental and numerical study on the adequacy of CH as a flame marker in premixed methane flames," *Proc. Comb. Inst.* **30**, 241-249 (2005).
253. P. H. Paul, and H. N. Najm, "Planar laser-induced fluorescence imaging of flame heat release rate," *Proc. Comb. Inst.* **27**, 43-50 (1998).
254. S. Böckle, J. Kazenwadel, T. Kunzelmann, D.-I. Shin, C. Schulz, and J. Wolfrum, "Simultaneous single-shot laser-based imaging of formaldehyde, OH, and temperature in turbulent flames," *Proc. Comb. Inst.* **28**, 279-286 (2000).
255. B. O. Ayoola, R. Balachandran, J. H. Frank, E. Mastorakos, and C. F. Kaminski, "Spatially resolved heat release rate measurements in turbulent premixed flames," *Combust. Flame* **144**, 1-16 (2006).
256. A. Fayoux, K. Zähringer, O. Gicquel, and J. C. Rolon, "Experimental and numerical determination of heat release in counterflow premixed laminar flames," *Proc. Comb. Inst.* **30**, 251-257 (2005).
257. R. L. Gordon, A. R. Masri, and E. Mastorakos, "Simultaneous Rayleigh temperature, OH- and CH₂O-LIF imaging of methane jets in a vitiated coflow," *Combust. Flame* **155**, 181-195 (2008).
258. R. L. Gordon, M. J. Dunn, A. R. Masri, and R. W. Bilger, "Quantitative Rayleigh imaging in an autoigniting methane flame," in *Proceedings of The Sixth Asia-*

Pacific Conference on Combustion, (The Japanese Section of The Combustion Institute, Nagoya Congress Center, Nagoya, Japan, 2007), pp. 471-474.

259. A. Burkert, D. Grebner, D. Müller, W. Triebel, and J. König, "Single-shot imaging of formaldehyde in hydrocarbon flames by XeF excimer laser-induced fluorescence," *Proc. Comb. Inst.* **28**, 1655-1661 (2000).
260. J. E. Harrington, and K. C. Smyth, "Laser-induced fluorescence measurements of formaldehyde in a methane/air diffusion flame," *Chem. Phys. Lett.* **202**, 196-202 (1993).
261. D. I. Shin, T. Dreier, and J. Wolfrum, "Spatially resolved absolute concentration and fluorescence-lifetime determination of H₂CO in atmospheric-pressure CH₄/air flames," *Appl. Phys. B* **72**, 257-261 (2001).
262. R. Schießl, P. Pixner, A. Dreizler, and U. Mass, "Formaldehyde formation in the endgas of Otto engines: Numerical simulations and quantitative concentration measurements," *Comb. Sci. Tech.* **149**, 339-360 (1999).
263. J. Luque, J. B. Jeffries, G. P. Smith, and D. R. Crosley, "Quasi-simultaneous detection of CH₂O and CH by cavity ring down absorption and laser-induced fluorescence in a methane/air low-pressure flame," *Appl. Phys. B* **73**, 731-738 (2001).
264. R. J. H. Klein-Douwel, J. Luque, J. B. Jeffries, G. P. Smith, and D. R. Crosley, "Laser-induced fluorescence of formaldehyde hot bands in flames," *Appl. Opt.* **39**, 3712-3715 (2000).
265. R. Bombach, and B. Kämpelli, "Simultaneous visualisation of transient species in flames by planar-laser-induced fluorescence using a single laser system," *Appl. Phys. B* **68**, 251-255 (1999).

- 266. T. Kim, and J. B. Ghandi, "Investigation of light load HCCI combustion using formaldehyde planar laser-induced fluorescence," *Proc. Comb. Inst.* **30**, 2675-2682 (2005).
- 267. D. C. Kyritsis, V. S. Santoro, and A. Gomez, "The effect of temperature correction on the measured thickness of formaldehyde zones in diffusion flames for 355nm excitation," *Exp. in Fluids* **37**, 769-772 (2004).
- 268. K. Bijjula, and D. C. Kyritsis, "Experimental evaluation of flame observables for simplified scalar dissipation rate measurements in laminar diffusion flamelets," *Proc. Comb. Inst.* **30**, 493-500 (2005).
- 269. C. Brackmann, J. Nygren, X. Bai, Z. Li, H. Bladh, B. Axelsson, I. Denbratt, L. Koopmans, P.-E. Bengtsson, and M. Alden, "Laser-induced fluorescence of formaldehyde in combustion using third harmonic Nd:YAG laser excitation," *Spectrochim. Acta, Part A* **59**, 3347-3356 (2003).
- 270. D. A. Knaus, S. S. Sattler, and F. C. Gouldin, "Three-dimensional temperature gradients in premixed turbulent flamelets via crossed-plane Rayleigh imaging," *Combust. Flame* **141**, 253-270 (2005).
- 271. M. S. Mansour, "Two-plane two-dimensional Rayleigh thermometry technique for turbulent combustion," *Optics Letters* **18**, 537-540 (1993).
- 272. R. S. Barlow, and A. N. Karpets, "Scalar Measurements for Combustion Model Validation," in *42nd AIAA Aerospace Sciences Meeting and Exhibit*, (American Institute of Aeronautics and Astronautics, Reno, Nevada, 2004).
- 273. R. W. Dibble, W. Kollmann, and R. W. Schefer, "Conserved Scalar Fluxes Measured in a Turbulent Nonpremixed Flame by Combined Laser Doppler Velocimetry and Laser Raman Scattering," *Combust. Flame* **55**, 307-321 (1984).

- 274. P. Magre, and R. Dibble, "Finite Chemical Kinetic Effects in a Subsonic Turbulent Hydrogen Flame," *Combust. Flame* **73**, 195-206 (1988).
- 275. P. Magre, and R. Dibble, "Finite chemical kinetics effects in a subsonic turbulent hydrogen flame," in *AIAA 25th Aerospace Sciences Meeting*, (American Institute of Aeronautics and Astronautics, Reno, Nevada, 1987).
- 276. R. W. Dibble, A. R. Masri, and R. W. Bilger, "The Spontaneous Raman Scattering Technique Applied to Nonpremixed Flames of Methane," *Combust. Flame* **67**, 189-206 (1987).
- 277. S. H. Stårner, R. W. Bilger, R. W. Bilger, and R. S. Barlow, "Piloted Diffusion Flames of Diluted Methane Near Extinction: Mean Structure from Raman/Rayleigh Fluorescence Measurements," *Comb. Sci. Tech.* **70**, 111-133 (1990).
- 278. S. H. Stårner, R. W. Bilger, R. W. Dibble, and R. S. Barlow, "Piloted Diffusion Flames of Diluted Methane Near Extinction: Detailed Structure from Laser Measurements," *Comb. Sci. Tech.* **72**, 255-269 (1990).
- 279. S. H. Stårner, R. W. Bilger, R. W. Dibble, and R. S. Barlow, "Some Raman/Rayleigh/LIF Measurements in Turbulent Propane Flames," *Twenty Third Symposium (International) on Combustion* **23rd**, 645-651 (1990).
- 280. S. H. Stårner, R. W. Bilger, R. W. Dibble, and R. S. Barlow, "Piloted Diffusion Flames of CO/CH₄/N₂ and CO/H₂/N₂ Near Extinction," *Combust. Flame* **83**, 63-74 (1991).
- 281. R. S. Barlow, R. W. Dibble, and R. P. Lucht, "Simultaneous measurement of Raman scattering and laser-induced OH fluorescence in nonpremixed turbulent jet flames," *Opt. Lett.* **14**, 263-265 (1989).

282. C. D. Carter, and R. S. Barlow, "Simultaneous measurements of NO, OH, and the major species in turbulent flames," *Opt. Lett.* **19**, 299-301 (1994).
283. Q. V. Nguyen, R. W. Dibble, C. D. Carter, G. J. Fiechtner, and R. S. Barlow, "Raman-LIF Measurement of Temperature, Major Species, OH, and NO in a Methane-Air Bunsen Flame," *Combust. Flame* **105**, 499-510 (1996).
284. P. C. Miles, "Raman line imaging for spatially and temporally resolved mole fraction measurements in internal combustion engines," *Appl. Opt.* **38**, 1714-1732 (1999).
285. R. S. Barlow, and P. C. Miles, "A Shutter-Based Line-Imaging System for Single-Shot Raman Scattering Measurements of Gradients in Mixture Fraction," *Proc. Comb. Inst.* **28**, 269-277 (2000).
286. P. C. Miles, and R. S. Barlow, "A fast mechanical shutter for spectroscopic applications," *Meas. Sci. Technol.* **11**, 392-397 (2000).
287. A. N. Karpetis, and R. S. Barlow, "Measurement of Scalar Dissipation in a Turbulent Piloted Methane/Air Jet Flame," *Proc. Comb. Inst.* **29**, 1929-1936 (2002).
288. A. N. Karpetis, and R. S. Barlow, "Measurements of flame orientation and scalar dissipation in turbulent partially premixed methane flames," *Proc. Comb. Inst.* **30**, 665-672 (2005).
289. J. Kojima, and Q.-V. Nguyen, "Laser pulse-stretching with multiple optical ring cavities," *Appl. Opt.* **41**, 6360-6370 (2002).
290. B. B. Dally, A. R. Masri, R. S. Masri, and G. J. Fiechtner, "Two-photon laser-induced fluorescence measurement of CO in turbulent non-premixed bluff body flames," *Combust. Flame* **132**, 272-274 (2003).

291. A. N. Karpetis, and R. S. Barlow, "Measurements of flame orientation and scalar dissipation in turbulent partially premixed methane flames," *Proc. Combust. Inst.* **30**, 665–672 (2005).
292. A. N. Karpetis, T. B. Settersten, R. W. Schefer, and R. S. Barlow, "Laser imaging system for determination of three-dimensional scalar gradients in turbulent flames," *Opt. Lett.* **29**, 355–357 (2004).
293. M. J. Dunn, A. R. Masri, R. W. Bilger, G.-H. Wang, and R. S. Barlow, "On the Mean Compositional Structure of Piloted Premixed Flames Issuing into a Hot Coflow," in *Proceedings of the Australian Combustion Symposium 2007*, A. R. Masri, K. Sendt, P. F. Nelson, and P. Yaroshchuk, eds. (The University of Sydney, 2007), pp. 58-61.
294. R. S. Barlow, and A. N. Karpetis, "Measurements of Scalar Variance, Scalar Dissipation, and Length Scales in Turbulent Piloted Methane/Air Jet Flames," *Flow. Turb. Comb.* **72**, 427-448 (2004).
295. "Zemax, <http://www.zemax.com>," (2007).
296. "Fluent 6.3, <http://www.fluent.com/>," (2007).
297. A. Kazakov, and M. Frenklach, "<http://www.me.berkeley.edu/drm/>,"
298. M. J. Dunn, A. R. Masri, and R. W. Bilger, "Lifted turbulent premixed flames issuing into a hot coflow, imaging of temperature and OH," in *Proceedings of the Sixteenth Australasian Fluid Mechanics Conference*, P. Jacobs, T. McIntyre, M. Cleary, D. Buttsworth, D. Mee, R. Clements, R. Morgan, and C. Lemckert, eds. (School of Engineering, The University of Queensland, Gold Coast, Australia, 2007), pp. 1344-1349.

299. G. P. Smith, C. Park, J. Schneiderman, and J. Luque, "C₂ Swan band laser-induced fluorescence and chemiluminescence in low-pressure hydrocarbon flames," *Combust. Flame* **141**, 66-77 (2005).
300. K. Devriendt, H. V. Look, B. Ceursters, and J. Peeters, "Kinetics of formation of chemiluminescent CH(A²S⁺) by the elementary reactions of C₂H(X²S⁺) with O(³P) and O₂(X³S^{-g}): a pulse laser photolysis study," *Chem. Phys. Lett.* **261**, 450–456. (1996).
301. V. Nguyen, and P. H. Paul, "The time evolution of a vortex-flame interaction observed via planar imaging of CH and OH," *Proc. Comb. Inst.* **26**, 357-364 (1996).
302. H. N. Najm, P. H. Paul, A. Mcilroy, and O. M. Kino, "A Numerical and Experimental Investigation of Premixed Methane-Air Flame Transient Response," *Combust. Flame* **125**, 879-892 (2001).
303. V. N. Nori, and J. M. Seitzman, "CH^{*} chemiluminescence modeling for combustion diagnostics," *Proc. Comb. Inst.* **32**, 895-903 (2009).
304. C. S. Panoutsos, Y. Hardalupas, and A. M. K. P. Taylor, "Numerical evaluation of equivalence ratio measurement using OH^{*} and CH^{*} chemiluminescence in premixed and non-premixed methane-air flames," *Combust. Flame* **156**, 273-291 (2009).
305. M. J. Dunn, A. R. Masri, R. W. Bilger, R. S. Barlow, and G.-H. Wang, "The Compositional Structure of Highly Turbulent Piloted Premixed Flames Issuing into a Hot Coflow," *Proc. Comb. Inst.* **32**, 1779-1786 (2009).
306. J. E. Rehm, and P. H. Paul, "Reaction rate imaging," *Proc. Comb. Inst.* **28**, 1775-1782 (2000).

- 307. J. H. Frank, S. A. Kaiser, and M. B. Long, "Multiscalar imaging in partially premixed jet flames with argon dilution," *Combust. Flame* **143**, 507-523 (2005).
- 308. M. I. Hassan, K. T. Aung, and G. M. Faeth, "Measured and Predicted Properties of Laminar Premixed Methane/Air Flames at Various Pressures," *Combust. Flame* **115**, 539-550 (1998).
- 309. W. M. Pitts, "Effects of global density ratio on the centreline mixing behaviour of axisymmetric turbulent jets," *Exp. in Fluids* **11**, 125-134 (1991).
- 310. W. M. Pitts, "Reynolds number effects on the mixing behaviour of axisymmetric turbulent jets," *Exp. in Fluids* **11**, 135-141 (1991).
- 311. C. D. Richards, and W. M. Pitts, "Global density effects on the self-preservation behaviour of turbulent free jets," *J. Fluid Mech.* **254**, 417-435 (1993).
- 312. S. B. Pope, *Turbulent Flows* (Cambridge University Press, Cambridge, 2000).
- 313. "OPENFOAM <http://www.openfoam.uk>," (2007).
- 314. J. H. Ferziger, and M. Peric, *Computational Methods for Fluid Dynamics* (Springer-Verlag, Berlin Heidelberg, 2002).
- 315. B. E. Launder, and D. B. Spalding, *Lectures in Mathematical Models of Turbulence* (Academic Press, London, England, 1972).
- 316. B. E. Launder, and D. B. Spalding, "The Numerical Computation of Turbulent Flows," *Computer Methods in Applied Mechanics and Engineering* **3**, 269-289 (1974).
- 317. D. C. Wilcox, *Turbulence Modeling for CFD* (DCW Industries, 1998).

- 318. V. Yakhot, and S. A. Orszag, "Renormalization Group Analysis of Turbulence: I. Basic Theory," *Journal of Scientific Computing* **1**, 1-51 (1986).
- 319. T.-H. Shih, W. W. Liou, A. Shabbir, Z. Yang, and J. Zhu, "A New - Eddy-Viscosity Model for High Reynolds Number Turbulent Flows - Model Development and Validation," *Computers Fluids* **24**, 227-238 (1995).
- 320. J. L. Lumley, "Computational modeling of turbulent flows.," *Adv. Appl. Mech.* **18**, 123-176 (1978).
- 321. F. R. Menter, "Two-Equation Eddy-Viscosity Turbulence Models for Engineering Applications," *AIAA Journal* **32**, 1598-1605 (1994).
- 322. B. E. Launder, "Second-Moment Closure: Present... and Future?," *Inter. J. Heat Fluid Flow* **10**, 282-300 (1989).
- 323. C. G. Speziale, S. Sarkar, and T. B. Gatski, "Modelling the Pressure-Strain Correlation of Turbulence: An Invariant Dynamical Systems Approach," *J. Fluid Mech.* **227**, 245-272 (1991).
- 324. R. W. Bilger, S. B. Pope, K. N. C. Bray, and J. F. Driscoll, "Paradigms in turbulent combustion research," *Proc. Combust. Inst.* **30**, 21-42 (2005).
- 325. A. N. Lipatnikov, and J. Chomiak, "Turbulent flame speed and thickness: phenomenology, evaluation, and application in multi-dimensional simulations," *Prog. Energy Combust. Sci.* **28**, 1-74 (2002).
- 326. S. B. Pope, "Turbulent premixed flames," *Annu. Rev. Fluid Mech.* **19**, 237-270 (1987).

- 327. V. Raman, and H. Pitsch, "A consistent LES/filtered-density function formulation for the simulation of turbulent flames with detailed chemistry," *Proc. Comb. Inst.* **31**, 1711-1719 (2007).
- 328. J. C. Oefelein, R. W. Schefer, and R. S. Barlow, "Toward Validation of Large Eddy Simulation for Turbulent Combustion," *AIAA Journal* **4**, 418-433 (2006).
- 329. S. B. Pope, "Monte Carlo Calculations of premixed turbulent flames," *Proc. 18th Int. Symp. on Combustion*, 1001-1010 (1981).
- 330. M. S. Anand, and S. B. Pope, "Calculations of Premixed Turbulent Flames by PDF Methods," *Combust. Flame* **67**, 127-142 (1987).
- 331. D. Roekaerts, "Monte Carlo PDF method for turbulent reacting flow in a jet-stirred reactor," *Computers Fluids* **21**, 97-108 (1992).
- 332. S. B. Pope, and W. K. Cheng, "The stochastic flamelet model of turbulent premixed combustion," *Proc. 23rd Int. Symp. on Combustion*, 781-789 (1988).
- 333. S. B. Pope, and M. S. Anand, "Flamelet and distributed combustion in premixed turbulent flames," *Proc. 20th Int. Symp. on Combustion*, 403-410 (1984).
- 334. S. M. Cannon, B. S. Brewster, and L. D. Smoot, "PDF Modeling of Lean Premixed Combustion Using In Situ Tabulated Chemistry," *Combust. Flame* **119**, 233-252 (1999).
- 335. S. P. Nandula, R. W. Pitz, R. S. Barlow, and G. J. Fiechtner, "Rayleigh/Raman/LIF measurements in a turbulent lean premixed combustor," in *AIAA 34th Aerospace Sciences Meeting and Exhibit*, (American Institute of Aeronautics and Astronautics, Inc., Reno, NV Jan 15-18, 1996).

- 336. W. Vicente, M. Salinas, and E. Barrios, "PDF modeling of CO and NO formation in lean premixed methane flames," *Comb. Sci. Tech.* **176**, 585-601 (2004).
- 337. N. Fueyo, W. Vicente, and J. Blasco, "Stochastic Simulation of NO Formation in Lean Premixed Methane Flames," *Comb. Sci. Tech.* **153**, 295-311 (2006).
- 338. R. P. Lindstedt, and E. M. Vaos, "Transported PDF modeling of high-Reynolds-number premixed turbulent flames," *Combust. Flame* **145**, 495-511 (2006).
- 339. T. S. Kuan, R. P. Lindstedt, and E. M. Vaos, "Higher moment based modeling of turbulence enhanced explosion kernels in confined fuel-air mixtures," in *Advances in Confined Detonations and Pulse Detonation Engines*, G. Roy, ed. (Torus, Press, Moscow, 2003), pp. 17-40.
- 340. T. Hulek, and R. P. Lindstedt, "Computations of Steady-State and Transient Premixed Turbulent Flames Using pdf Methods," *Combust. Flame* **104**, 481-504 (1996).
- 341. S. James, M. S. Anand, M. K. Razdan, and S. B. Pope, "In situ detailed chemistry calculations in combustor flow analyses," in *Proceedings of the ASME TURBO EXPO LAND, SEA & AIR '99, The 44th ASME Gas Turbine and AeroEngine Technical Congress*, (Indianapolis, IN, USA, 1999).
- 342. S. James, M. S. Anand, M. K. Razdan, and S. B. Pope, "In Situ Detailed Chemistry Calculations in Combustor Flow Analyses," *ASME Journal of Engineering for Gas Turbines and Power* **123**, 747-756 (2001).
- 343. J. Xu, and S. B. Pope, "Assessment of Numerical Accuracy of PDF/Monte Carlo Methods for Turbulent Reacting Flows," *Journal of Computational Physics* **152**, 192-230 (1999).

- 344. M. Muradogoglu, P. Jenny, S. B. Pope, and D. A. Caughey, "A Consistent Hybrid Finite-Volume/Particle Method for the PDF Equations of Turbulent Reactive Flows," *Journal of Computational Physics* **154**, 342-371 (1999).
- 345. K. T. Walsh, M. B. Long, M. A. Tanoff, and M. D. Smooke, "Experimental and computational study of CH, CH*, and OH* in an axisymmetric laminar diffusion flame," *Proc. Comb. Inst.* **27**, 615-623 (1998).
- 346. J. Luque, J. B. Jeffries, G. P. Smith, D. R. Crosley, K. T. Walsh, M. B. Long, and M. D. Smooke, "CH(A-X) and OH(A-X) Optical Emission in an Axisymmetric Laminar Diffusion Flame," *Combust. Flame* **122**, 172-175 (2000).
- 347. S. W. Yoo, C. K. Law, and S. D. Tse, "Chemiluminescent OH* and CH* flame structure and aerodynamic scaling of weakly buoyant, nearly spherical diffusion flames," *Proc. Comb. Inst.* **29**, 1663-1670 (2002).
- 348. Y. Ikeda, J. Kojima, and H. Hashimoto, "Local chemiluminescence spectra measurements in a high-pressure laminar methane/air premixed flame," *Proc. Comb. Inst.* **29**, 1495-1501 (2002).
- 349. K. T. Walsh, J. Fielding, M. D. Smooke, M. B. Long, and A. Linan, "A comparison of computational and experimental lift-off heights of coflow laminar diffusion flames," *Proc. Comb. Inst.* **30**, 357-365 (2005).
- 350. S. B. Dworkin, B. C. Connelly, A. M. Schaffer, B. A. V. Bennett, M. B. Long, M. D. Smooke, M. P. Puccio, B. McAndrews, and J. H. Miller, "Computational and experimental study of a forced, time-dependant. methane-air coflow diffusion flame," *Proc. Comb. Inst.* **31**, 971-978 (2007).
- 351. A. M. Kempf, "LES Validation from Experiments," *Flow. Turb. Comb.* **72**, (2007).

352. J. Floyd, and A. Kempf, "Optical computed tomography of chemiluminescent flame radicals: a study of self-absorption using LES generated phantoms," in *Proceedings of the Third European Combustion Meeting*, (Chania, Crete, 2007).
353. J. Warnatz, U. Mass, and R. W. Dibble, *Combustion Physical and Chemical Fundamentals, Modeling and Simulation, Experiments, Pollutant Formation 3rd Edition* (Springer-Verlag, Berlin Heidelberg New York, 2001).
354. R. G. Joklik, J. W. Daily, and W. J. Pitz, "Measurements of CH radical concentrations in an acetylene/oxygen flame and comparisons to modeling calculations," *Proc. Comb. Inst.* **21**, 895-904 (1986).
355. G. P. Smith, J. Luque, C. Park, J. B. Jeffries, and D. R. Crosley, "Low Pressure Flame Determinations of Rate Constants for OH(A) and CH(A) Chemiluminescence," *Combust. Flame* **131**, 59-69 (2002).
356. G. P. Smith, C. Park, and J. Luque, "A note on chemiluminescence in low-pressure hydrogen and methane-nitrous oxide flames," *Combust. Flame* **140**, 385-389 (2005).
357. S. Hwang, W. C. Gardiner, and M. Frenklach, "Induction zone exothermicity of acetylene ignition," *Combust. Flame* **67**, 65-76 (1987).
358. N. L. Garland, and D. R. Crosley, "Collisional quenching of CH $A^2\Delta$, $v' = 0$ at 1300 K," *Chem. Phys. Lett.* **134**, 189-194 (1987).
359. K. J. Rensberger, M. J. Dyer, and R. A. Copeland, "Time-resolved CH ($A^2\Delta$ and $B^2\Sigma^-$) laser-induced fluorescence in low pressure hydrocarbon flames," *Appl. Opt.* **27**, 3679-3689 (1988).

360. W. Bauer, B. Engelhardt, P. Wiesen, and K. H. Becker, "Lifetime measurements of GeH and CH in the $A^2\Delta$, $v'=0$ state by laser-induced fluorescence," *Chem. Phys. Lett.* **158**, 321-324 (1989).
361. R. D. Kenner, S. P. Pfannenberger, P. Heinrich, and F. J. Stuhl, "Electronic quenching of methylidyne($A2.DELTA.$), imidogen($A3.PI.$), imidogen($c1.PI.$), and phosphinidene($A3.PI.$) between 240 and 420 K," *J. Phys. Chem.* **95**, 6585-6593 (1991).
362. P. Heinrich, and F. Stuhl, "Electronic quenching of $CH(A^2\Delta)$ and $NH(A^3\Pi)$ between 300 and 950 K," *Chem. Phys.* **199**, 105-118 (1995).
363. P. Heinrich, R. D. Kenner, and F. Stuhl, "Collisional quenching at 300 K: $CH(A^2\Delta)$ by H_2O , NH_3 and other gases and $NH(A^3\Pi)$ by H_2O ," *Chem. Phys. Lett.* **147**, 575-580 (1988).
364. D. E. Heard, J. B. Jeffries, and D. R. Crosley, "Collisional quenching of $A^2\Sigma^+$ NO and $A^2\Delta$ CH in low pressure flames," *Chem. Phys. Lett.* **178**, 533-537 (1991).
365. A. Vegiri, and S. C. Farantos, "Ab initio potential energy surfaces for studying the quenching of $CH(A^2\Delta)$ by $H_2(X\ 1\Sigma_g^+)$," *Chem. Phys. Lett.* **167**, 278-284 (1990).
366. C. J. Nokes, and R. J. Donovan, "Time-resolved kinetic studies of electronically excited CH radicals II. Quenching efficiencies for $CH(A^2\Delta)$," *J. Chem. Phys.* **90**, 167 (1984).
367. N. Abel, "Auflosung einer mechanischen Aufgabe," *J. Für Die Reine und Angewandte Mathematik* **1**, 153-157 (1826).
368. C. J. Dasch, "One-dimensional tomography: a comparison of Abel, onion-peeling, and filtered backprojection methods," *Appl. Opt.* **31**, 1146-1152 (1992).

- 369. V. Dribinski, A. Ossadtchi, V. A. Mandelshtam, and H. Reisler, "Reconstruction of Abel-transformable images: the Gaussian basis-set expansion Abel transform method," *Rev. Sci. Instrum.* **73**, 2634-2642 (2002).
- 370. A. Sáinz, A. Díaz, D. Casas, M. Pineda, F. Cubillo, and M. D. Calzada, "Abel inversion applied to a small set of emission data from a microwave plasma," *Appl. Spectrosc.* **60**, 229-236 (2006).
- 371. S. Ma, H. Gao, and L. Wu, "Modified Fourier-Hankel method based on analysis of errors in Abel inversion using Fourier transform techniques," *Appl. Opt.* **47**, 1350-1357 (2008).
- 372. J. D. Smith, and V. Sick, "High-speed fuel tracer fluorescence and OH radical chemiluminescence imaging in a spark-ignition direct-injection engine," *Appl. Opt.* **44**, 6682-6691 (2005).
- 373. P. G. Aleiferis, Y. Hardalupas, A. M. K. P. Taylor, K. Ishii, and Y. Urata, "Flame chemiluminescence studies of cyclic combustion variations and air-to-fuel ratio of the reacting mixture in a lean-burn stratified-charge spark-ignition engine," *Combust. Flame* **136**, 72-90 (2004).
- 374. J. D. Gounder, A. R. Masri, S. H. Starnner, and R. W. Bilger, "Mixture fraction imaging in a non-reacting spray jet," in *Proceedings of The Sixth Asia-Pacific Conference on Combustion*, (The Japanese Section of The Combustion Institute, The Nagoya Congress Center, Nagoya, Japan, 2007), pp. 713-716.
- 375. M. Juddoo, (personal communication, 2008).
- 376. Z. S. Li, J. Kiefer, J. Zetterberg, M. Linvin, A. Leipertz, X. S. Bai, and M. Alden, "Development of improved PLIF CH detection using an Alexandrite laser for single-shot investigation of turbulent and lean flames," *Proc. Comb. Inst.* **31**, 727-735 (2007).

- 377. R. L. Gordon, A. R. Masri, S. B. Pope, and G. M. Goldin, "A numerical study of auto-ignition in turbulent lifted flames issuing into a vitiated co-flow," *Combust. Theory and Modelling* **11**, 351-376 (2007).
- 378. F. Q. H. Zhao, H. , "The Applications of Laser Rayleigh Scattering To Combustion Diagnostics," *Prog. Energy Combust. Sci.* **19**, 447-485 (1993).
- 379. R. B. Miles, W. R. Lempert, and J. N. Forkey, "Laser Rayleigh scattering," *Meas. Sci. Technol.* **12**, R33-R51 (2001).

APPENDIX A

CROSS-PLANE ORIENTATION CORRECTION

The cross-plane OH data from Sandia can be used to correct a one dimensional measurement of layer width, gradient and dissipation for three dimensional effects on an instantaneous realisation basis. The relation to correct the one dimensional measurement for three dimensional effects based on the measured quantities of the two cross-plane OH sheets is developed in this appendix. The two cross-planes intersect the along the same line that the one dimensional Raman-Rayleigh-CO LIF measurements are made. The pixel intensity in the two sheets f and g are denoted $f(x,v)$ and $g(x,u)$. Note that v is taken to be the local vertical axis in the sheet f just as u is taken to be the local vertical axis in sheet g . To illustrate the orientations of the various local and global co-ordinate systems, the relevant co-ordinate system notation necessary to derive all of the relations developed in this appendix is presented in Fig. A.1. The x-axis in Fig. A.1 is taken to be the intersection axis that one dimensional Raman-Rayleigh-CO LIF measurements and the line of intersection of the two sheets f and g are aligned with.

The assumption that is made here from the beginning is that the angle each sheet is offset from the y-axis of the global Cartesian co-ordinate system θ , is the same for both sheets f and g , as illustrated by Fig. A.1. For ease of derivation, only one measurement point along the measurement probe volume is considered, extensions to all points along the measurement volume is easily made the relation is developed. The local flame normal vector \hat{n}_f can be expressed in the x, y and z global Cartesian co-ordinates as:

$$\hat{n}_f = n_x \hat{i} + n_y \hat{j} + n_z \hat{k}, |\hat{n}_f| = 1 \quad (\text{A.9})$$

The projection of the flame normal vector \hat{n}_f onto the two cross plane sheets f and g can be expressed in terms of the local normal vector in the two sheets f and g as:

$$\hat{n}_f = n_{fx} \hat{i} + n_{fu} \hat{u}, |\hat{n}_f| = 1 \quad (\text{A.10})$$

$$\hat{n}_g = n_{gx} \hat{i} + n_{gv} \hat{v}, |\hat{n}_g| = 1 \quad (\text{A.11})$$

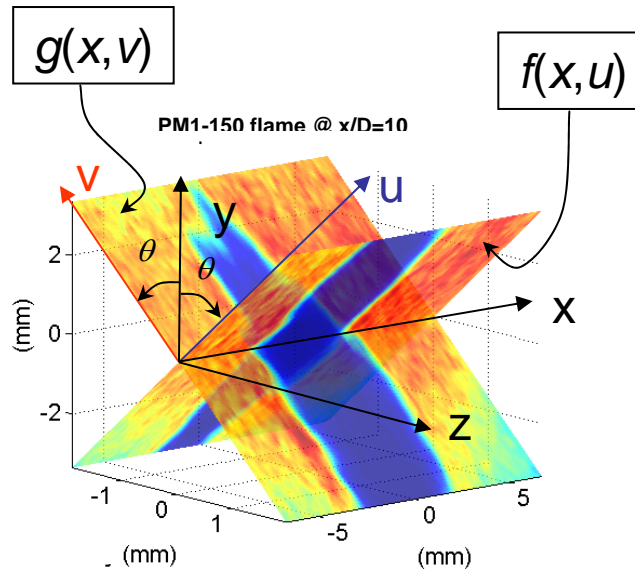


Figure A-1. An example realisation of the OH cross-plane images f and g . This realisation is taken from the PM1-150 flame at $x/D=10$ with the flame approximately centred in the image.

Where the notation for the components of the vectors \hat{n}_f and \hat{n}_g can be expressed as:

$$n_{fx} = \nabla_x f / |\nabla f|, n_{fu} = \nabla_u f / |\nabla f| \quad (\text{A.12})$$

$$n_{gx} = \nabla_x g / |\nabla g|, n_{gv} = \nabla_v g / |\nabla g| \quad (\text{A.13})$$

The local vertical components of the vectors \hat{n}_f and \hat{n}_g (n_{fu} and n_{gv}) may be expressed in terms of the global Cartesian co-ordinate unit vectors \hat{j} and \hat{k} as:

$$n_{fu} \hat{u} = n_y \cos \theta \hat{j} + n_z \sin \theta \hat{k} \quad (\text{A.14})$$

$$n_{gv} \hat{v} = n_y \cos \theta \hat{j} - n_z \sin \theta \hat{k} \quad (\text{A.15})$$

By solving Eqs. (A.14)-(A.15) in terms of the normal vector components of \hat{n}_f and \hat{n}_g allows the n_y and n_z components of the local flame normal vector \hat{n}_f to be expressed as:

$$n_y = \frac{n_{gv} + n_{fu}}{2 \cos \theta} \quad (\text{A.16})$$

$$n_z = \frac{n_{fu} - n_{gv}}{2 \sin \theta} \quad (\text{A.17})$$

The n_x component of \hat{n}_f is measured by both sheets f and g thus it is advantageous to use the average of the two to minimise the influence of noise. The vector \hat{n}_f may now be expressed in terms of the measured quantities from the sheets f and g as:

$$\hat{n}_f = \left(\frac{n_{fx} + n_{gx}}{2} \right) \hat{i} + \left(\frac{n_{gv} + n_{fu}}{2 \cos \theta} \right) \hat{j} + \left(\frac{n_{fu} - n_{gv}}{2 \sin \theta} \right) \hat{k} \quad (\text{A.18})$$

The measurement line is taken to be aligned with the x-axis and here labelled the vector \hat{n}_m which may be trivially defined as:

$$\hat{n}_m = 1\hat{i} + 0\hat{j} + 0\hat{k} \quad (\text{A.19})$$

The main purpose of determining the local flame front vector \hat{n}_{fl} in terms of measured quantities is to determine the local flame front orientation relative to the measurement axis, further it will be shown that it is the secant of this angle ($\sec\alpha$) that will provide the correction. By considering the dot product of the vectors \hat{n}_{fl} and \hat{n}_m defined as:

$$\hat{n}_{fl} \bullet \hat{n}_m = |\hat{n}_{fl}| |\hat{n}_m| \cos \alpha \quad (\text{A.20})$$

The individual terms in Eq. (A.20) may be expressed as:

$$\hat{n}_{fl} \bullet \hat{n}_m = \left(\frac{n_{fx} + n_{gx}}{2} \right) \quad (\text{A.21})$$

$$|\hat{n}_m| = 1 \quad (\text{A.22})$$

$$|\hat{n}_{fl}| = \sqrt{\left(\frac{n_{fx} + n_{gx}}{2} \right)^2 + \left(\frac{n_{gv} + n_{fu}}{2 \cos \theta} \right)^2 + \left(\frac{n_{fu} - n_{gv}}{2 \sin \theta} \right)^2} \quad (\text{A.23})$$

Combining the results of Eqs. (A.20)-(A.23) it is possible to express the cosine of the angle α in terms of measured quantities:

$$\cos \alpha = \left(\frac{n_{fx} + n_{gx}}{2} \right) / \sqrt{\left(\frac{n_{fx} + n_{gx}}{2} \right)^2 + \left(\frac{n_{gv} + n_{fu}}{2 \cos \theta} \right)^2 + \left(\frac{n_{fu} - n_{gv}}{2 \sin \theta} \right)^2} \quad (\text{A.24})$$

Rearranging Eq. (A.24) and expressing in terms of the secant of the angle α yields:

$$\sec \alpha = \sqrt{1 + \left[\frac{n_{gv} + n_{fu}}{(n_{fx} + n_{gx}) \cos \theta} \right]^2 + \left[\frac{n_{fu} - n_{gv}}{(n_{fx} + n_{gx}) \sin \theta} \right]^2} \quad (\text{A.25})$$

For the specific case of $\theta=30^\circ$ which is the case for cross-plane setup at Sandia Eq. (A.25) maybe further simplified to:

$$\sec \alpha = \sqrt{1 + \frac{4}{3} \left(\frac{n_{gv} + n_{fu}}{n_{fx} + n_{gx}} \right)^2 + 4 \left(\frac{n_{fu} - n_{gv}}{n_{fx} + n_{gx}} \right)^2} \quad (\text{A.26})$$

By considering a surface defined by the vectors \hat{n}_m and \hat{n}_{fl} lying on it, the diagram presented in Fig. A.2 maybe formed.

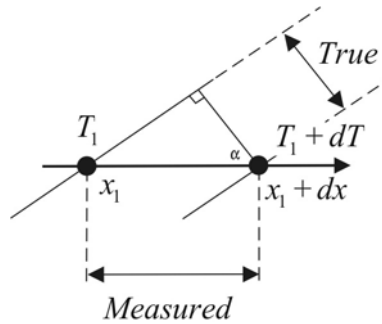


Fig. A.2. A graphical description of the potential bias in the measured value of scalar gradients (or thicknesses) when only a one-dimensional measurement is made.

In Fig. A.2 the variation of the measured value of the scalar gradient and the true value of the scalar gradient is compared. In Fig. A.2 the scalar T , temperature is used for illustrative purposes. The measured temperature gradient can be expressed as:

$$\nabla T_{\text{Measured}} = \frac{(T_1 - dT) - T_1}{(x_1 - dx) - x_1} \quad (\text{A.27})$$

$$\nabla T_{True} = \frac{(T_1 - dT) - T_1}{dx \cos \alpha} \quad (A.28)$$

The relation between the true value and the measured value may now be expressed as:

$$\frac{\nabla T_{Measured}}{\nabla T_{True}} = \frac{1}{\cos \alpha} \quad (A.29)$$

$$\nabla T_{True} = \frac{\nabla T_{Measured}}{\cos \alpha} = \sec \alpha \nabla T_{Measured} \quad (A.30)$$

Where the $\sec \alpha$ term is determined from Eq. (A.26).

If the true measurement of a layer width is desired then a similar relation to Eq. (A.30) is used:

$$\Delta T_{True} = \sec \alpha \Delta T_{Measured} \quad (A.31)$$

Where the $\sec \alpha$ term is derived from Eq. (A.26).

If a correction is to be made to one-dimension measurements of dissipation (N_ξ) for the three dimensional orientation then the relation between the true ($N_{\xi, True}$) and the measured ($N_{\xi, Measured}$) dissipation is expressed as:

$$N_{\xi, True} = \sec^2 \alpha N_{\xi, Measured} \quad (A.32)$$

The $\sec^2 \alpha$ term in Eq. (A.32) is again derived from Eq. (A.26), however the square of the relation developed in Eq. (A.26) is utilised. The correction developed by Eq. (A.32) can be very sensitive to noise effects whether the noise is derived from the measurement

of $N_{\xi, \text{Measured}}$ or more significantly the determination of the angle α . An example the sensitivity of the correction factor $\sec^2 \alpha$ is if α is measured to be 75° and the true value of α is actually 73° this is only an error of 2.7% in α however the resultant error in the correction factor is 28%. This highlights the already well known fact that dissipation measurements are very sensitive to noise, but more significantly in this cross-plane correction experiment that the potential sensitivity to noise increases with increasingly large values of α .

APPENDIX B

RAYLEIGH CALCULATIONS

In combustion environments the Rayleigh scattering signal is proportional to the number density, local Rayleigh cross section and the local laser intensity. The magnitude of the Rayleigh scattering signal received by pixel m , n on the detector from the respective probe volume may be expressed as:

$$R = \eta I_{\text{Laser}} \Omega N \sum_{i=1}^j X_i \sigma_i \quad (\text{B.1})$$

Where η is the collection efficiency of the detection system that includes quantum efficiency of the detector, I_{Laser} is the laser intensity, Ω is the solid collection angle of the detection system, N is the total molecular number density, X_i is the mole fraction of species i and σ_i is the cross section for species i .

In order to process raw Rayleigh images and derive quantitative images for temperature, corrections need to be made for: spatial non-uniformity in the laser irradiance, non-uniform cross-section, the detection system dark background, shot to shot fluctuations in laser power and background reflections. As a start to implementing the said corrections, the raw Rayleigh image ($I_{\text{RawRayleigh}}$), may be expressed as:

$$I_{\text{RawRayleigh}} = I_{\text{Background}} + I_{\text{Reflection}} + I_{\text{Rayleigh}} \quad (\text{B.2})$$

Where both the image components $I_{\text{Reflection}}$ and I_{Rayleigh} are both linearly proportional to the individual shot's laser power. The image component $I_{\text{Background}}$ which represents the background due to detection system dark-noise is easily evaluated for identical camera gate timing and gain settings without the laser pulse. Utilising the relation developed in (B.2) and two ensemble average Rayleigh images taken in a known medium such as air and helium, the following Eqs. (B.3)-(B.4) may be developed.

$$I_{\text{Air}} = I_{\text{Background}} + L_{\text{Avg}} K_{\text{Reflection}} + C_0 N_{\text{Air}} L_{\text{Avg}} \sigma_{\text{Air}} \quad (\text{B.3})$$

$$I_{\text{He}} = I_{\text{Background}} + L_{\text{Avg}} K_{\text{Reflection}} + C_0 N_{\text{He}} L_{\text{Avg}} \sigma_{\text{He}} \quad (\text{B.4})$$

The calibration constant C_0 is determined experimentally. Equations (B.3)-(B.4) may be rearranged to obtain an equation for the extrapolated zero Rayleigh cross section signal, which represents the laser reflection constant $K_{\text{Reflection}}$ for an average laser power.

$$K_{\text{Reflection}} = \frac{(I_{\text{He}} - I_{\text{Air}} \sigma_R)}{(1 - \sigma_R)} - I_{\text{Background}} \quad (\text{B.5})$$

$$\sigma_R = \sigma_{\text{He}} / \sigma_{\text{air}} \quad (\text{B.6})$$

In a review of Rayleigh scattering measurements Zhao [378] discusses the evaluation of the background reflections however doesn't extend this concept to include fluctuations in the background reflections with laser power as proposed in Eqs. (B.3)-(B.4).

In order to compensate for fluctuations in $I_{\text{Reflections}}$ and I_{Rayleigh} due to laser power fluctuations in the flame shot ($I_{\text{FlameShot}}$), the shot laser power (L_{Shot}) needs to be evaluated. This is done by taking the average of a small area in each image near the laser beam centreline, and comparing the same area in the ensemble average of flame image. Close to the edge in the image the coflow composition can be considered to be uniform

and not to fluctuate or be influenced by the central jet combustion process. The values in the area of the coflow in the individual and ensemble average images can be expressed as:

$$I_{FlameAvg} = I_{Background} + L_{Av} K_{Reflection} + C_0 L_{Av} \sigma_{Coflow} \quad (B.7)$$

$$I_{FlameShot} = I_{Background} + L_{Shot} K_{Reflection} + C_0 L_{Shot} \sigma_{Coflow} \quad (B.8)$$

The individual Rayleigh shot image laser power may be evaluated as:

$$\frac{L_{Shot}}{L_{Avg}} = \frac{(I_{FlameShot} - I_{Background})}{(I_{FlameAvg} - I_{Background})} \quad (B.9)$$

Assuming that constant pressure can be applied and the ideal gas equation can be used to relate the molecular number density to the temperature of the flame, the following relation can be formed:

$$\frac{T_{Flame}}{T_{Air}} = \frac{I_{AirRayleigh} L_{Shot} \left(\sum_{i=1}^j X_i \sigma_i \right)_{flame}}{I_{Flame-Rayleigh} L_{Avg} \sigma_{Air}} \quad (B.10)$$

The only unknown that remains in Eq. (B.10) is the flame shot cross section. The Rayleigh scattering cross section (σ_r), which for a gas in vertically polarised light may be expressed according to Miles *et al.* [379] as:

$$\frac{\partial \sigma_r}{\partial \Omega} = \frac{3\sigma}{8\pi} \left(\frac{2 - \rho_0}{2 + \rho_0} \right) \quad (B.11)$$

$$\sigma = \frac{32\pi^3 (n-1)^2}{3\lambda^4 N^4} \left(\frac{6+3\rho_0}{6-7\rho_0} \right) \quad (\text{B.12})$$

The bracketed term in Eq. (B.12) involving ρ_0 is the King correction factor. Many investigators neglect the King correction factor term which introduces an error in each species cross section. An example of the possible error is if the King correction factor is ignored for CO₂, an error of up to 15% can be made in the total Rayleigh cross section (Sneep and Ubachs [239]), the error in the differential cross section will be smaller than this. Due to values for the King correction factor being readily available for combustion relevant species using the data of Sneep and Ubachs [239]), the King correction factor has been accounted for in the Rayleigh cross section calculations in this thesis.

APPENDIX C

Additional Raman-Rayleigh-LIF Results

In this Appendix additional results from the Sandia measurement campaign are presented. The data from each radial traverse is presented spatially and conditional on temperature. The conditional mean and conditional variance are presented on each graph combined with a scatter plot of the data.

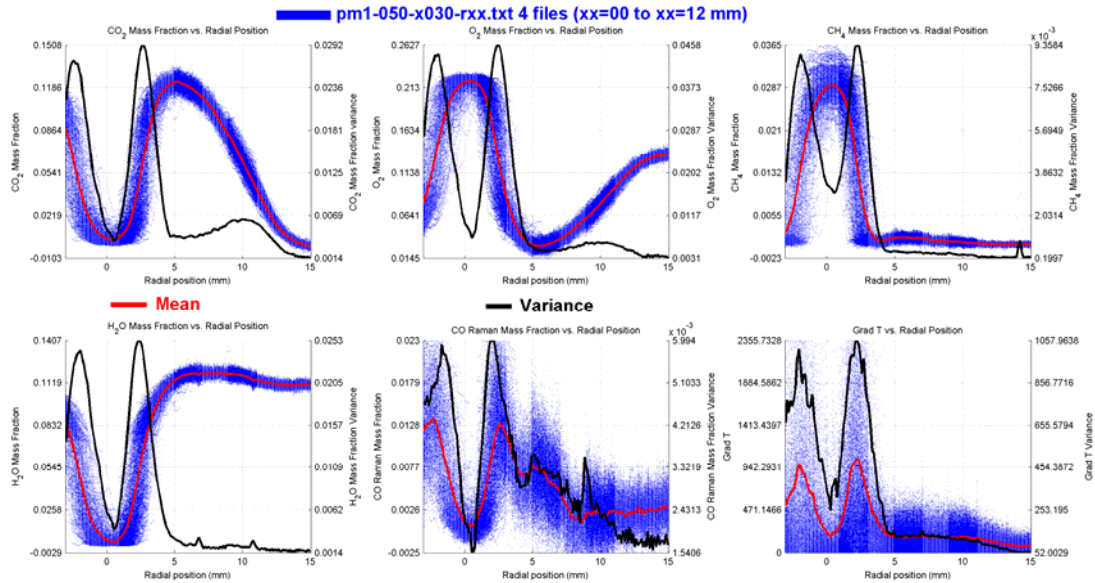
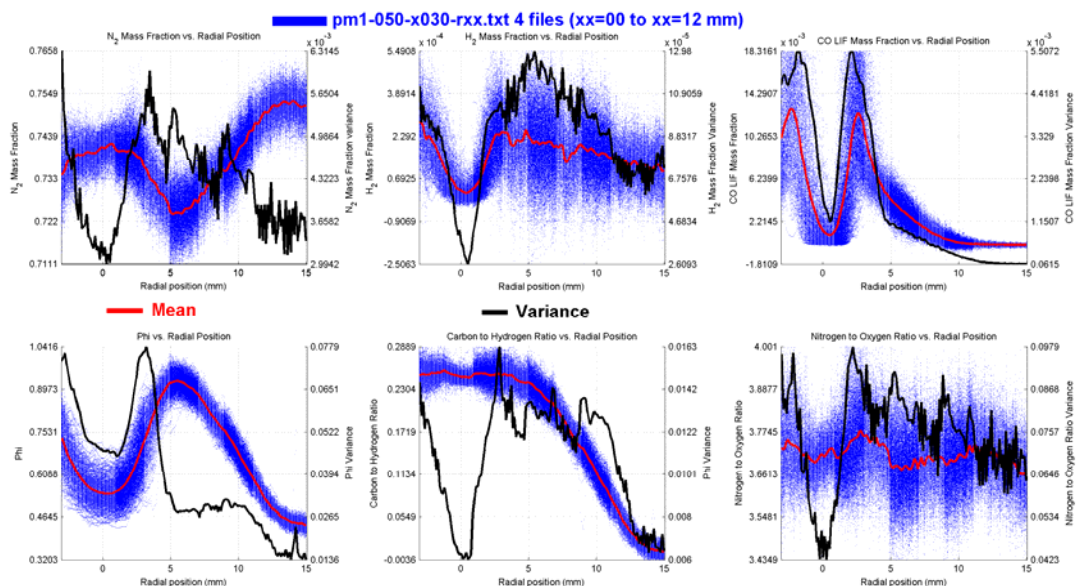
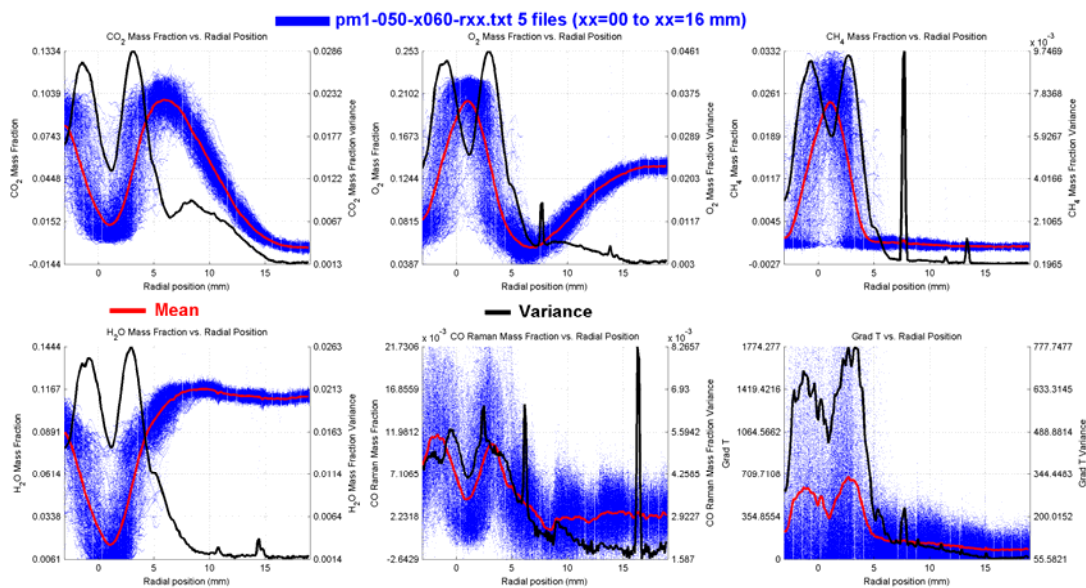
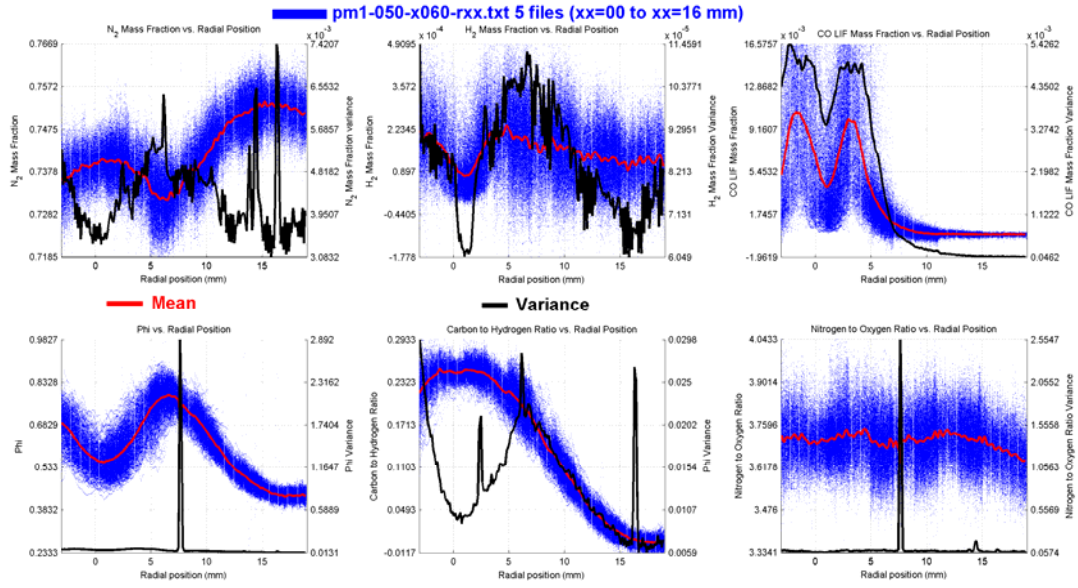
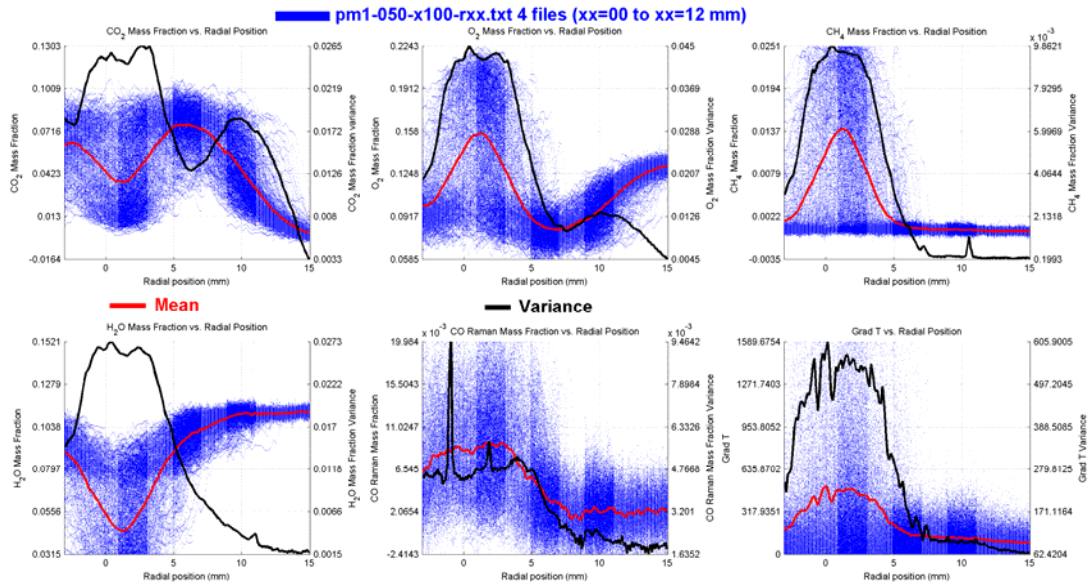
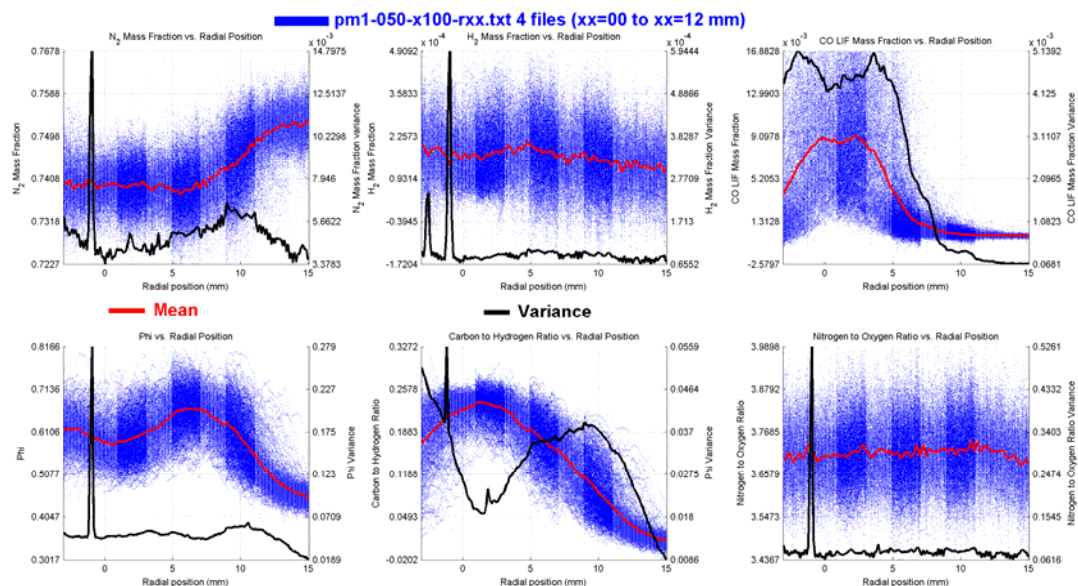
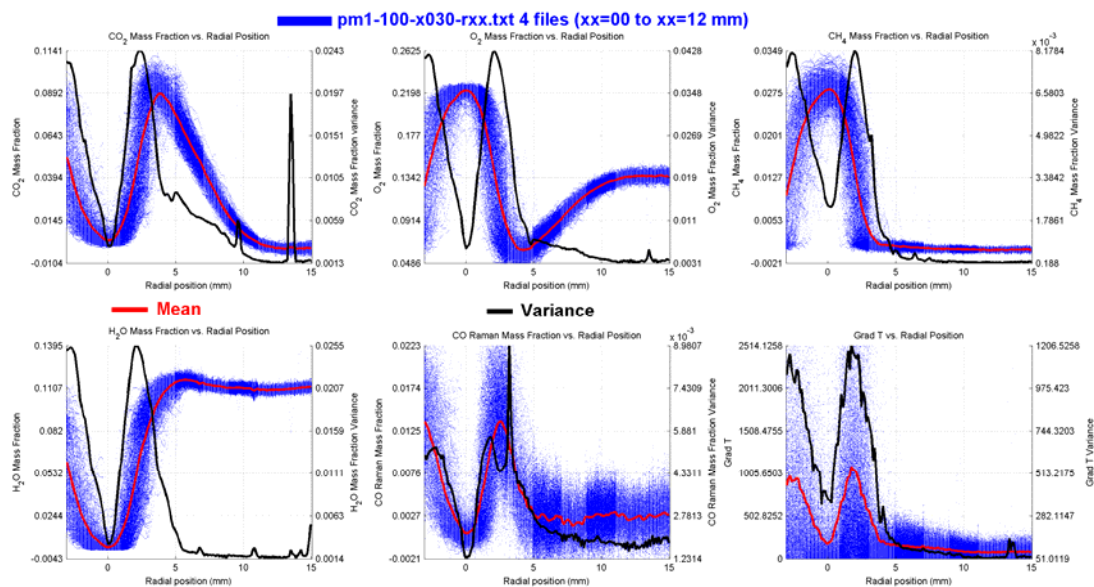
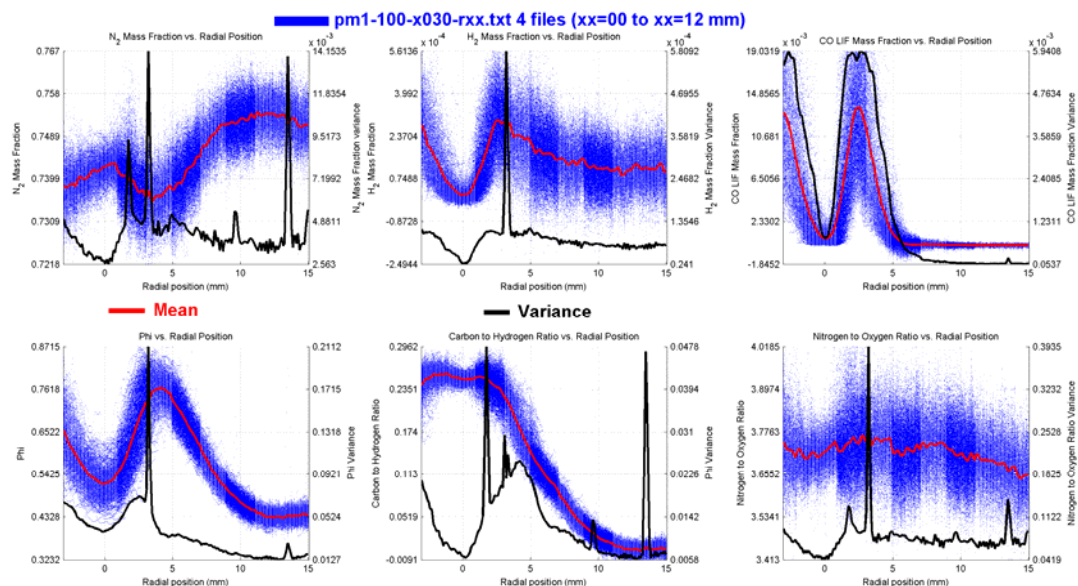
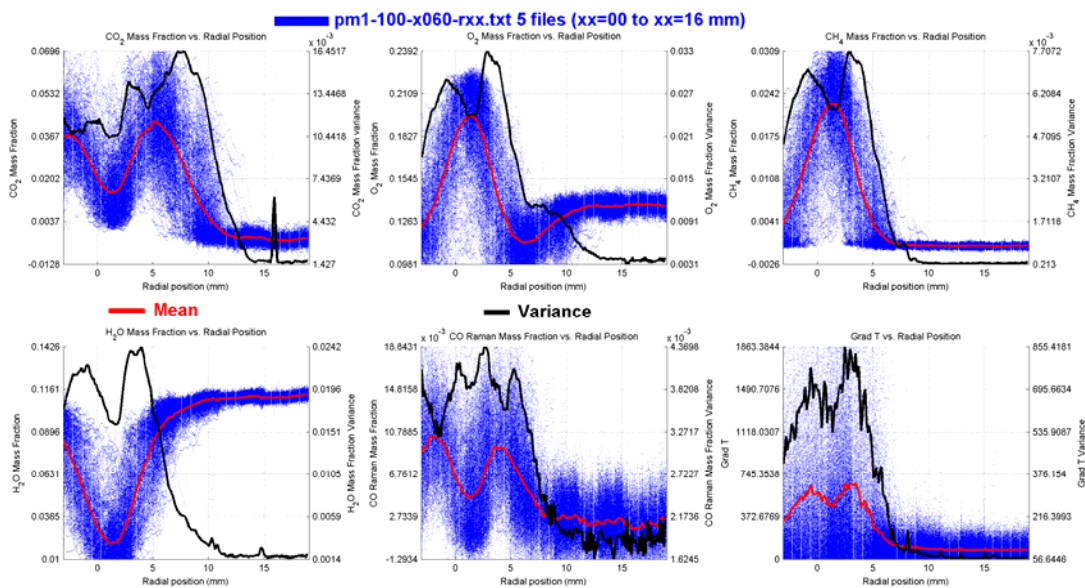


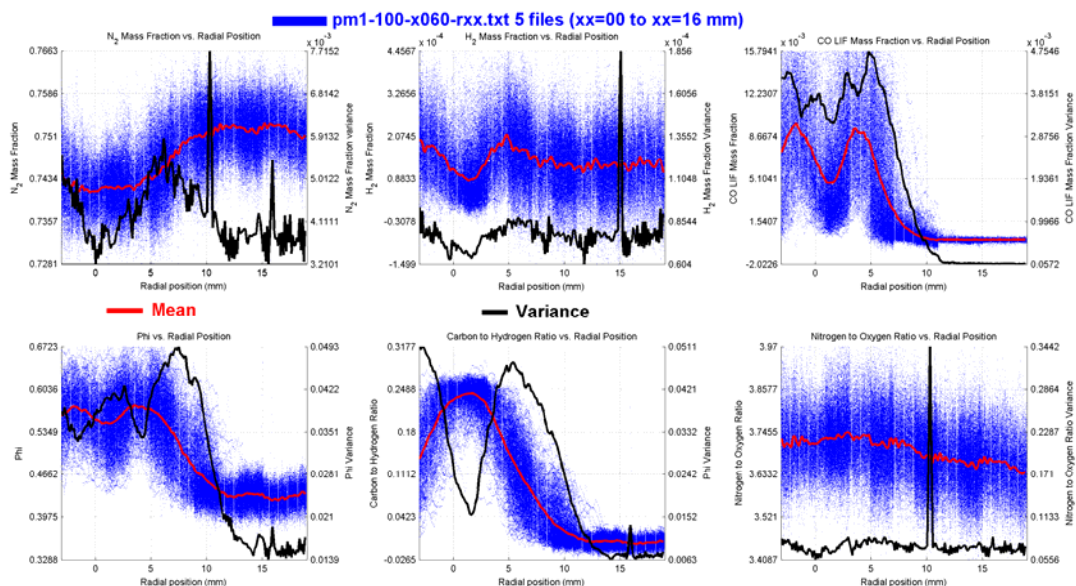
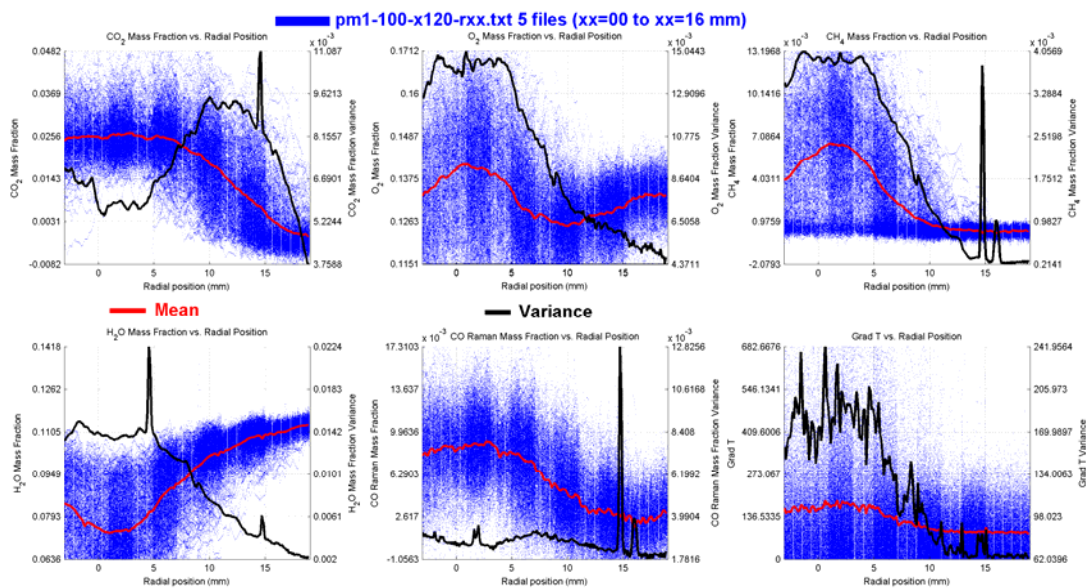
Figure C-1. Spatial profiles for the PM1-50 flame at $x/D=7.5$.

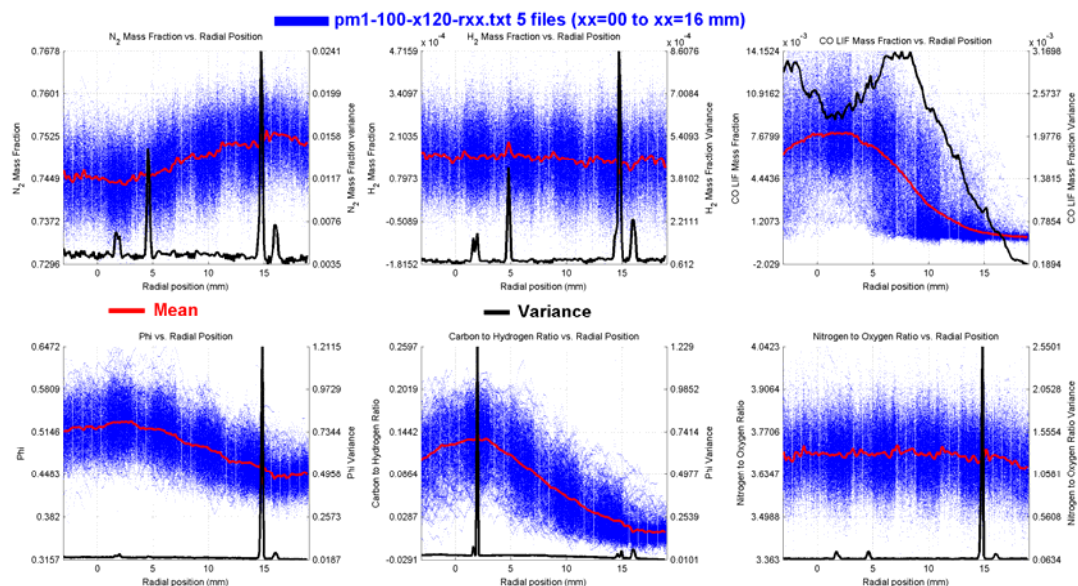
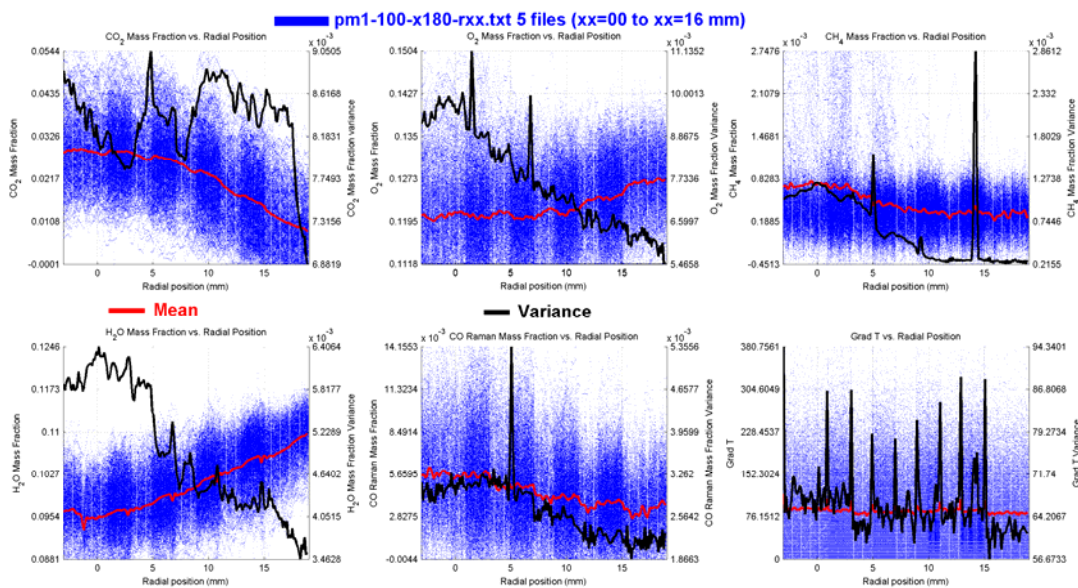
Figure C-2. Spatial profiles for the PM1-50 flame at $x/D=7.5$.Figure C-3. Spatial profiles for the PM1-50 flame at $x/D=15$.

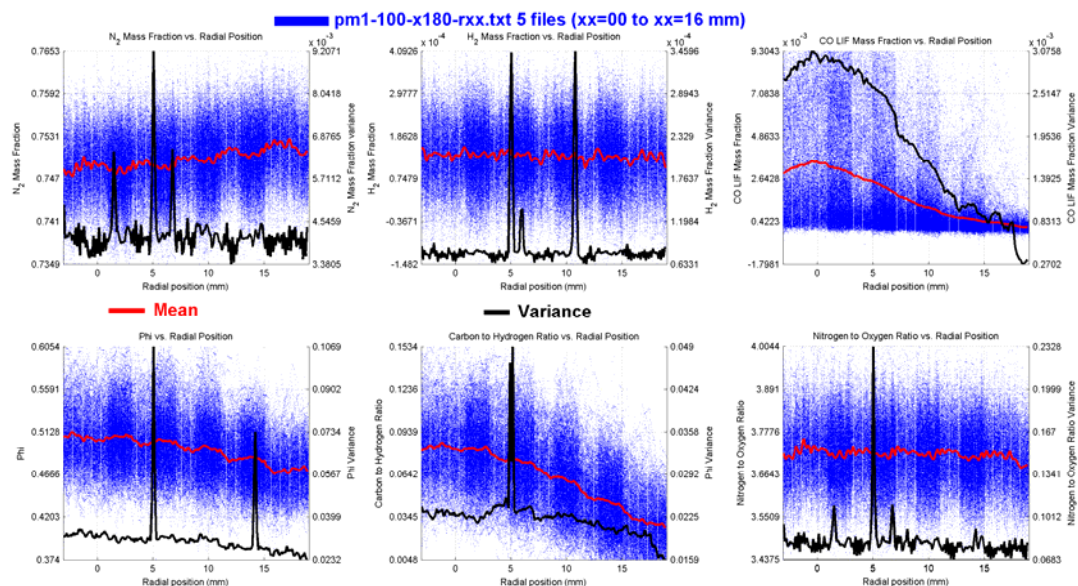
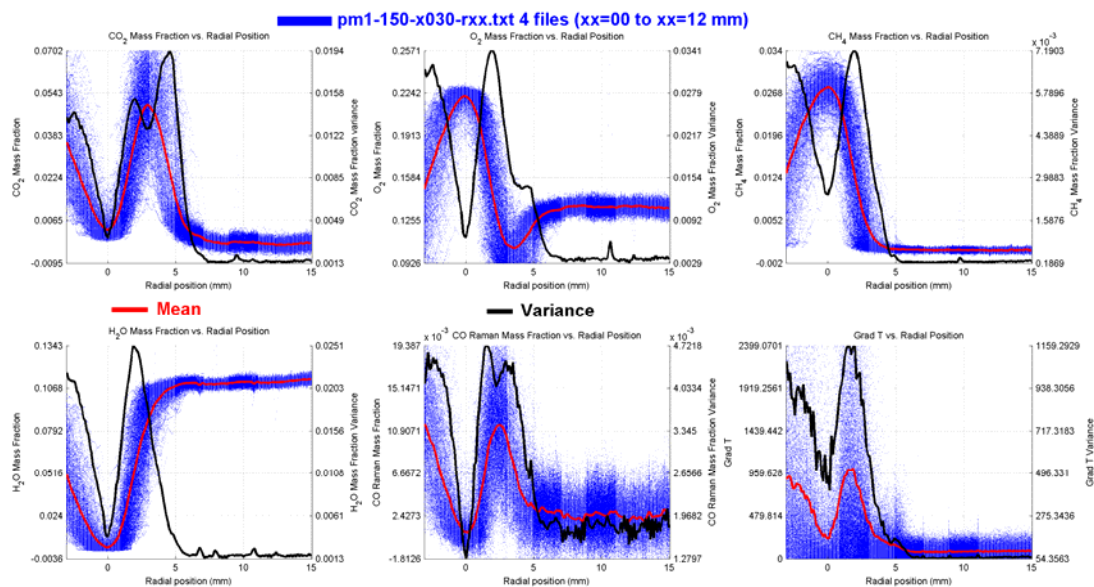
Figure C-4. Spatial profiles for the PM1-50 flame at $x/D=15$.Figure C-5. Spatial profiles for the PM1-50 flame at $x/D=25$.

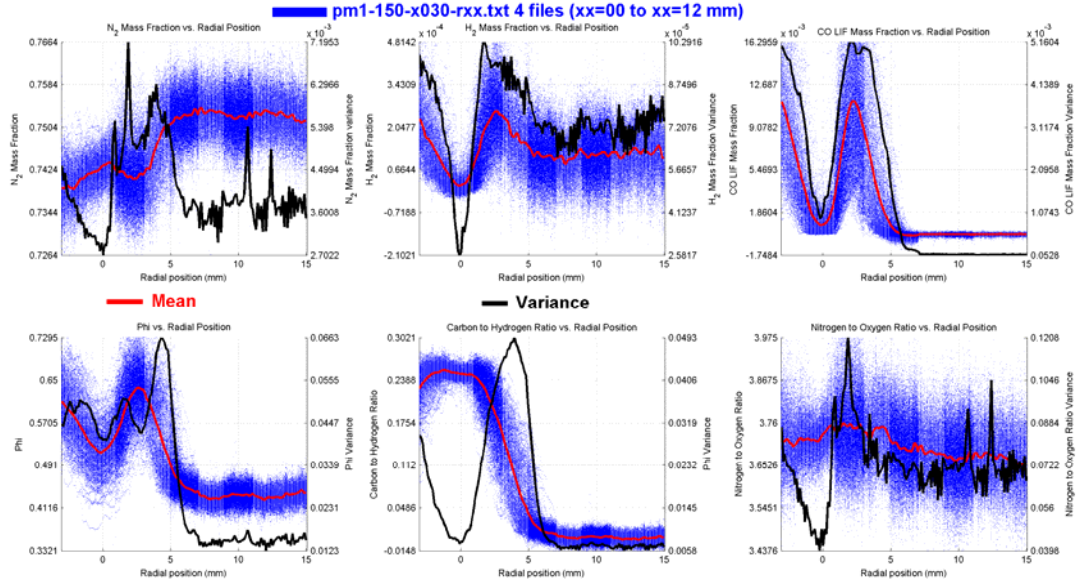
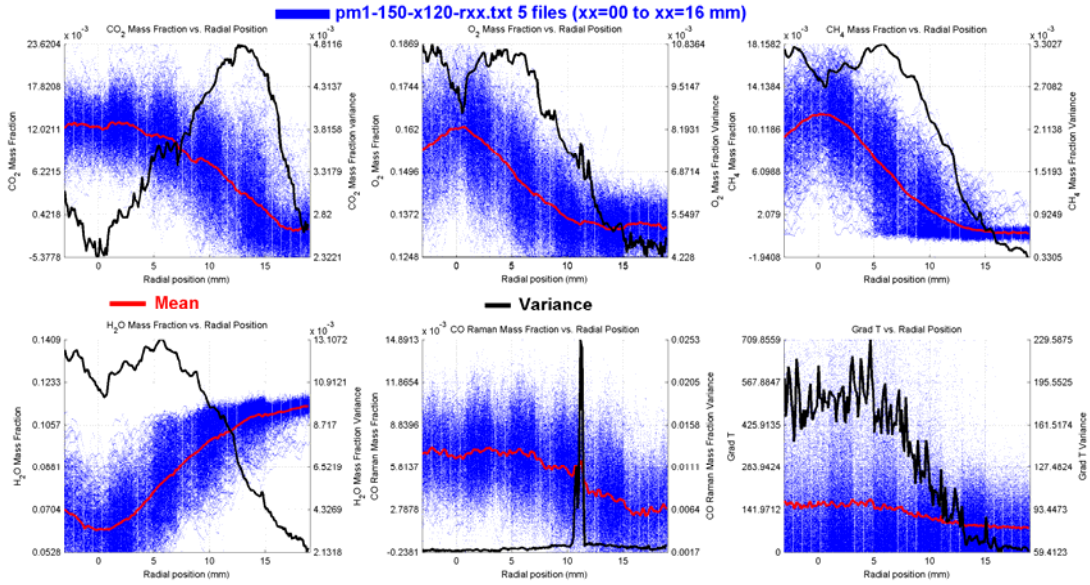
Figure C-6. Spatial profiles for the PM1-50 flame at $x/D=25$.Figure C-7. Spatial profiles for the PM1-100 flame at $x/D=7.5$.

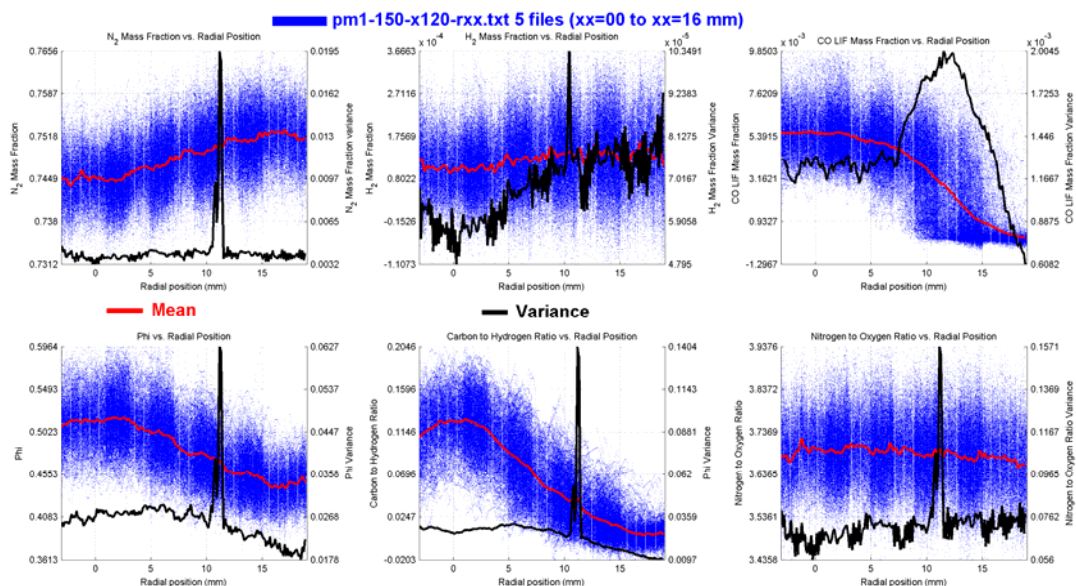
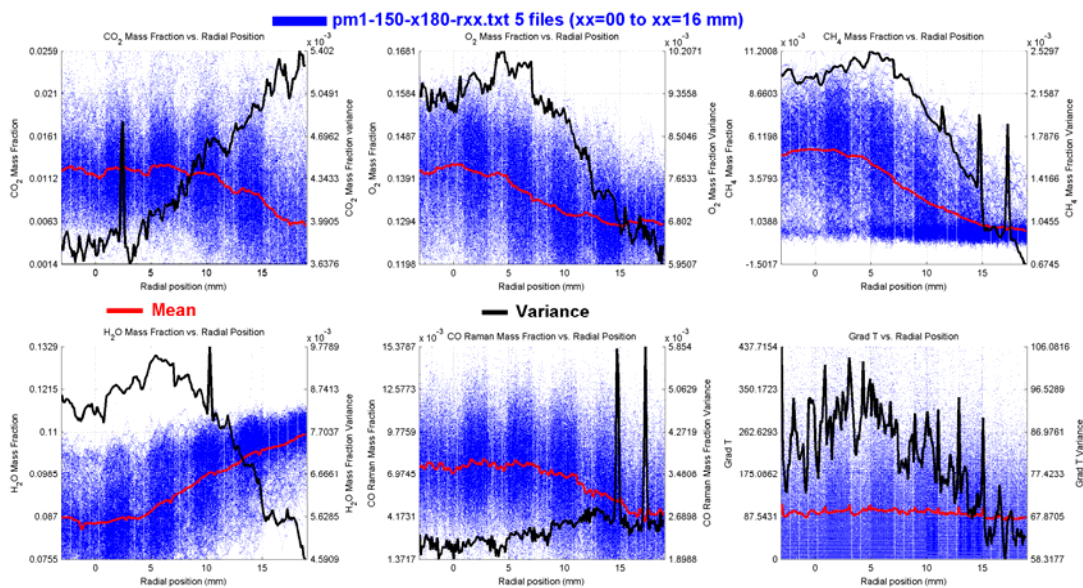
Figure C-8. Spatial profiles for the PM1-100 flame at $x/D=7.5$.Figure C-9. Spatial profiles for the PM1-100 flame at $x/D=15$.

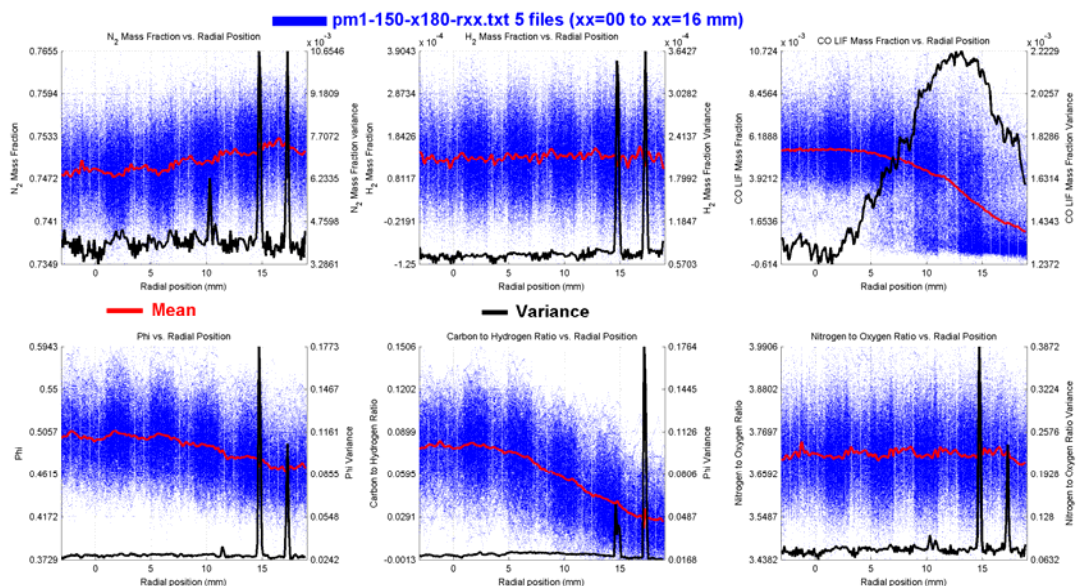
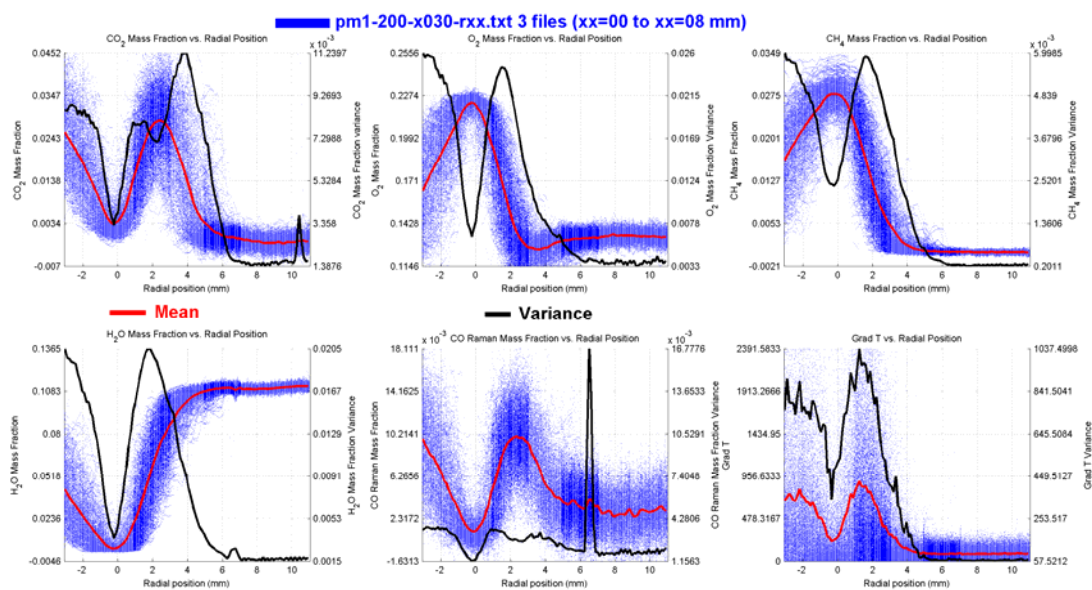
Figure C-10. Spatial profiles for the PM1-100 flame at $x/D=15$.Figure C-11. Spatial profiles for the PM1-100 flame at $x/D=30$.

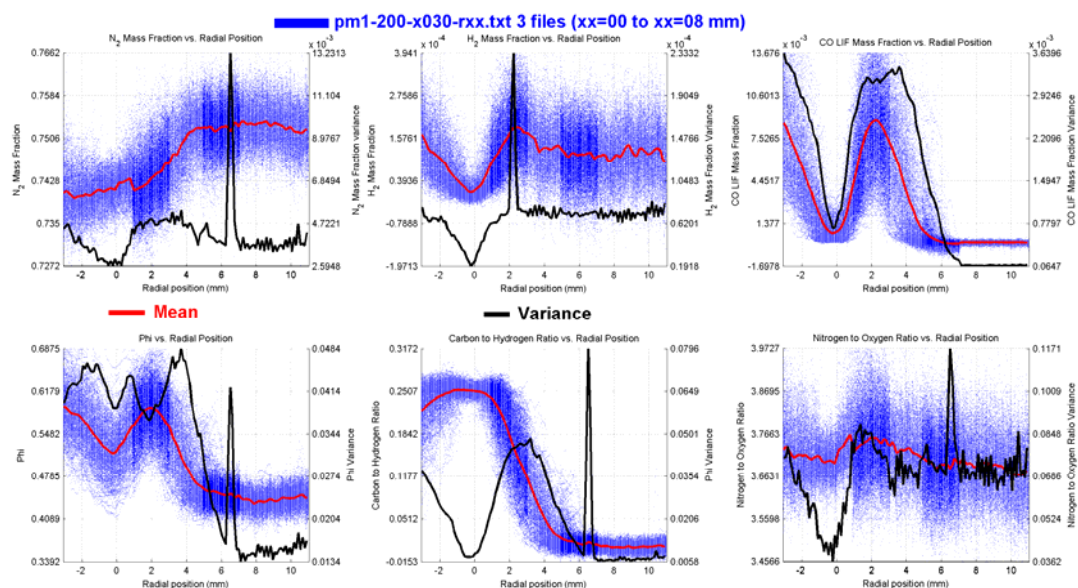
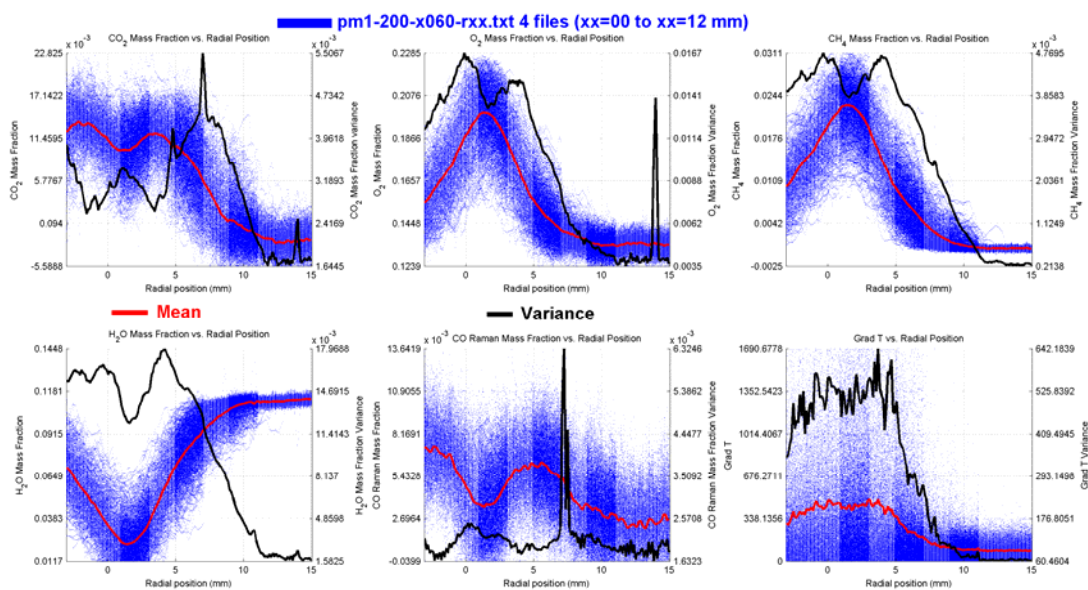
Figure C-12. Spatial profiles for the PM1-100 flame at $x/D=30$.Figure C-13. Spatial profiles for the PM1-100 flame at $x/D=45$.

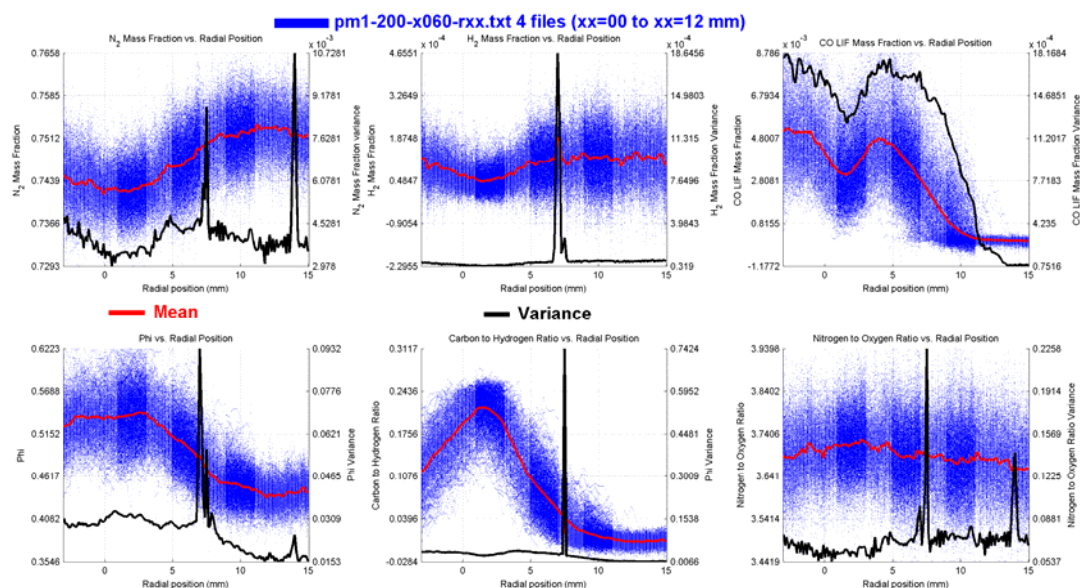
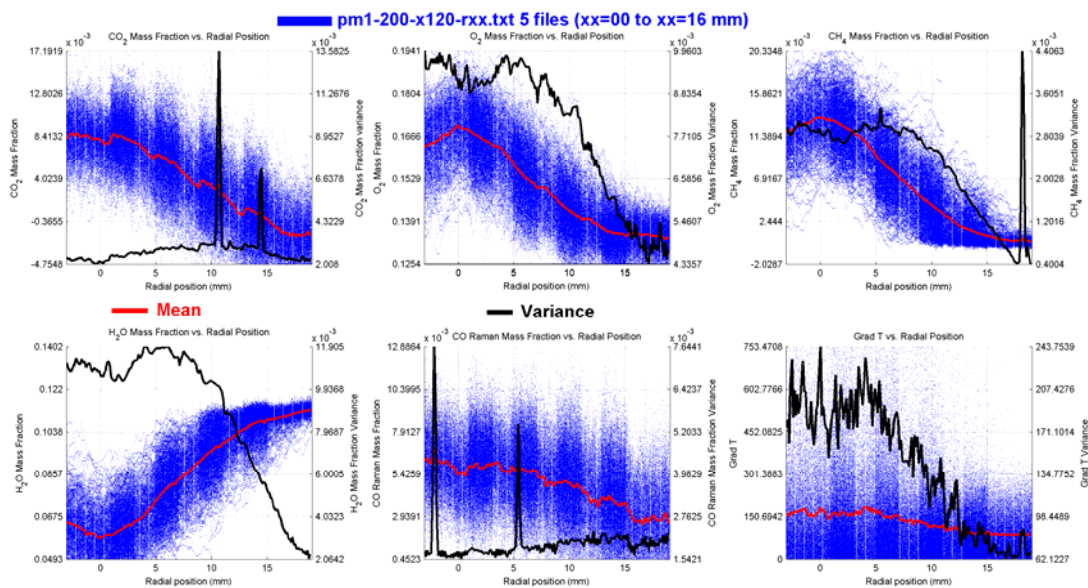
Figure C-14. Spatial profiles for the PM1-100 flame at $x/D=45$.Figure C-15. Spatial profiles for the PM1-150 flame at $x/D=7.5$.

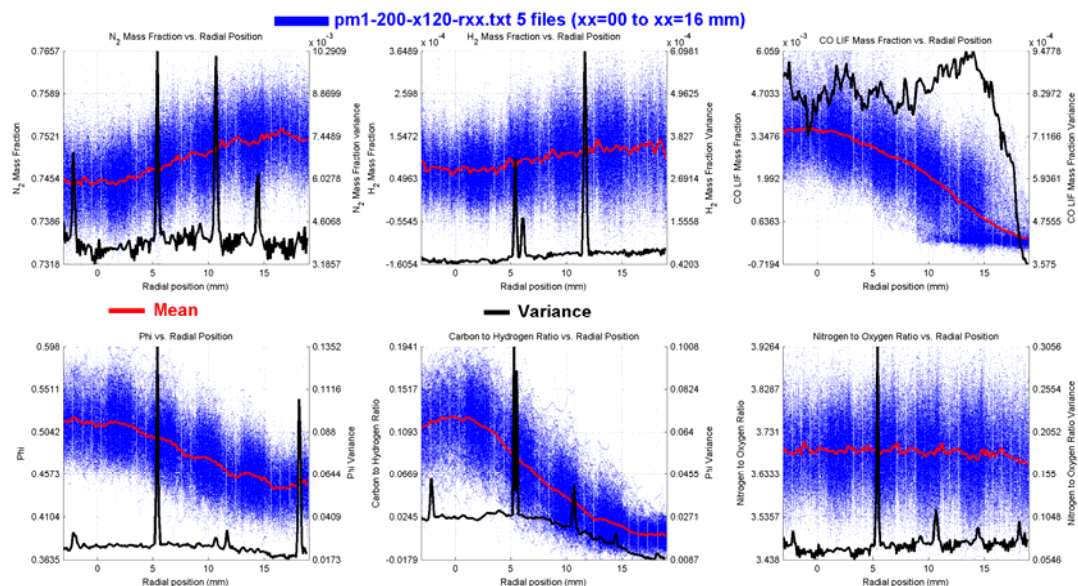
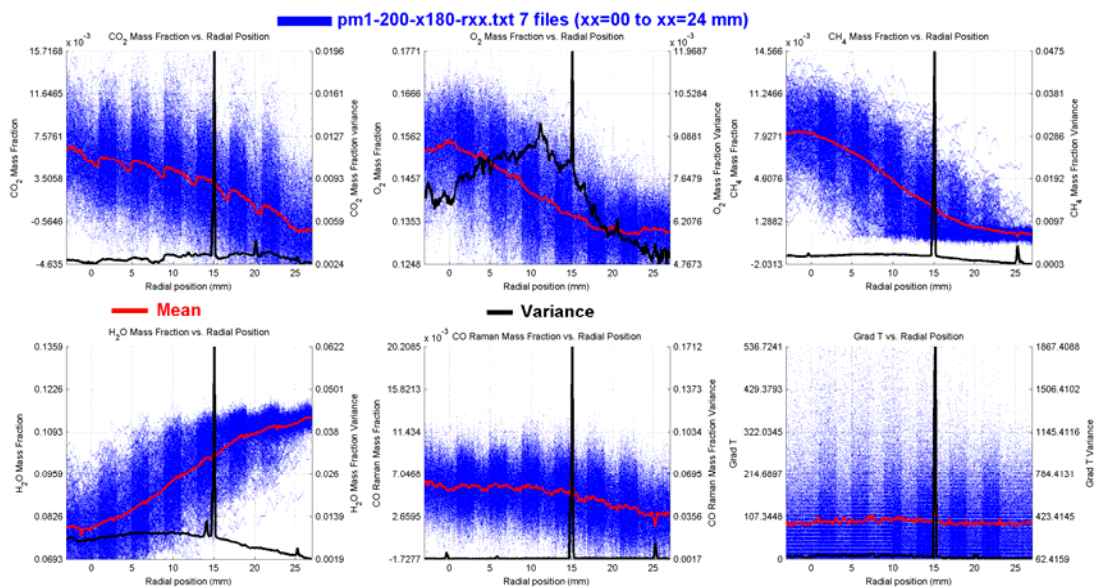
Figure C-16. Spatial profiles for the PM1-150 flame at $x/D=7.5$.Figure C-17. Spatial profiles for the PM1-150 flame at $x/D=30$.

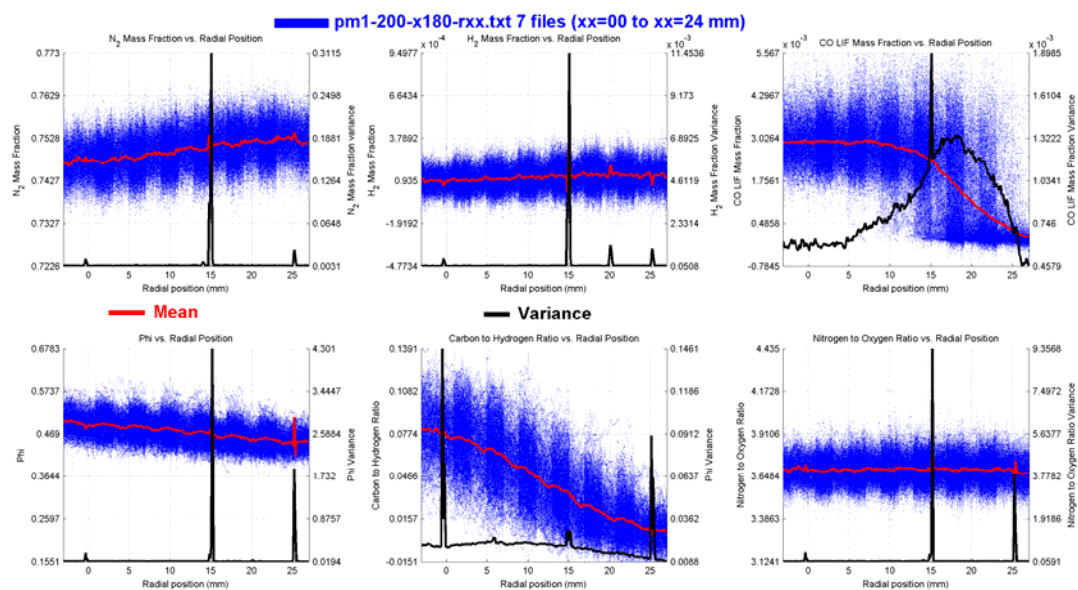
Figure C-18. Spatial profiles for the PM1-150 flame at $x/D=30$.Figure C-19. Spatial profiles for the PM1-150 flame at $x/D=45$.

Figure C-20. Spatial profiles for the PM1-150 flame at $x/D=45$.Figure C-21. Spatial profiles for the PM1-200 flame at $x/D=7.5$.

Figure C-22. Spatial profiles for the PM1-200 flame at $x/D=7.5$.Figure C-23. Spatial profiles for the PM1-200 flame at $x/D=15$.

Figure C-24. Spatial profiles for the PM1-200 flame at $x/D=15$.Figure C-25. Spatial profiles for the PM1-200 flame at $x/D=30$.

Figure C-26. Spatial profiles for the PM1-200 flame at $x/D=30$.Figure C-27. Spatial profiles for the PM1-200 flame at $x/D=45$.

Figure C-28. Spatial profiles for the PM1-200 flame at $x/D=45$.

APPENDIX D

Further PDF Results

In this Appendix the comprehensive comparative results for the PDF simulations with the experimental measurements are presented. Only samples of the comparative results are presented in Chapter 10 due to the volume of the data, presentation of all of the available data in Chapter 10 would be excessive and important features would not be able to be given adequate weight. The data presented in this Appendix is for the PM1 flame series which include: axial and radial traverse data for the mean and RMS velocity, radial profiles at a number of axial stations for the Favre mean and Favre RMS temperature, CO and OH.

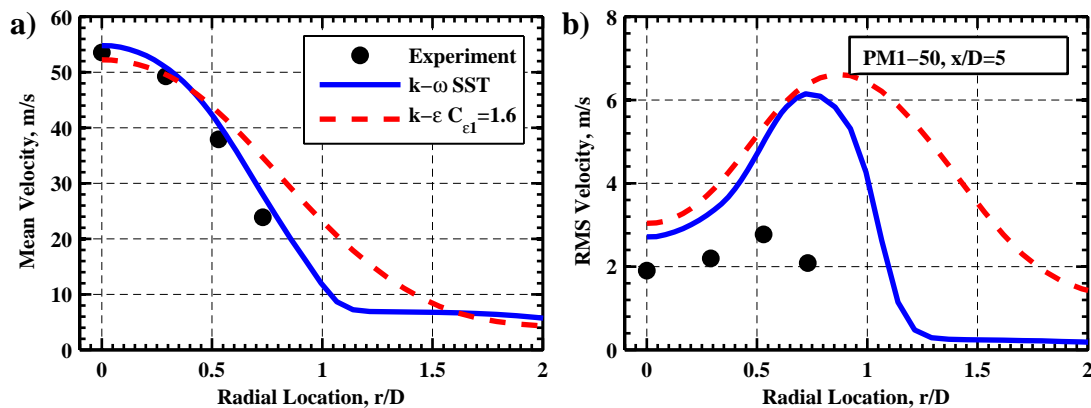


Figure D-1. Comparison of the Reynolds mean a) and RMS b) velocity statistics at $x/D=5$ for the PM1-50 flame.

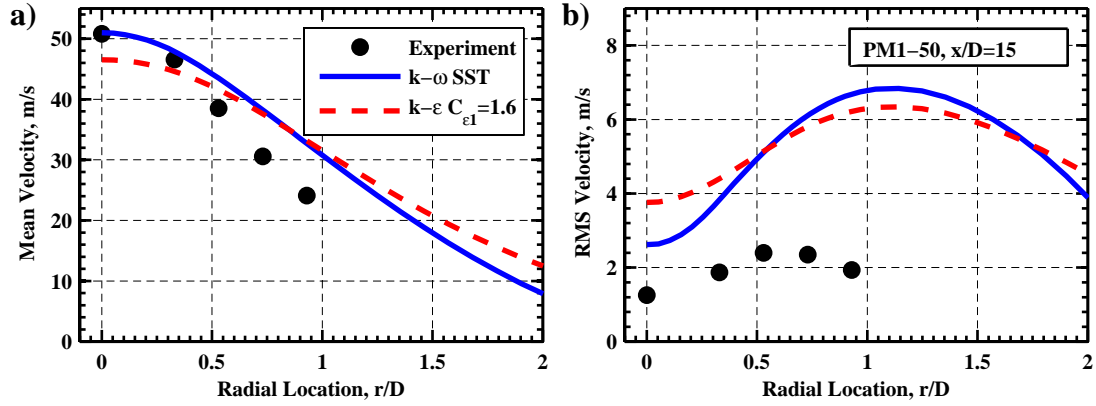


Figure D-2. Comparison of the Reynolds mean a) and RMS b) velocity statistics at $x/D=15$ for the PM1-50 flame.

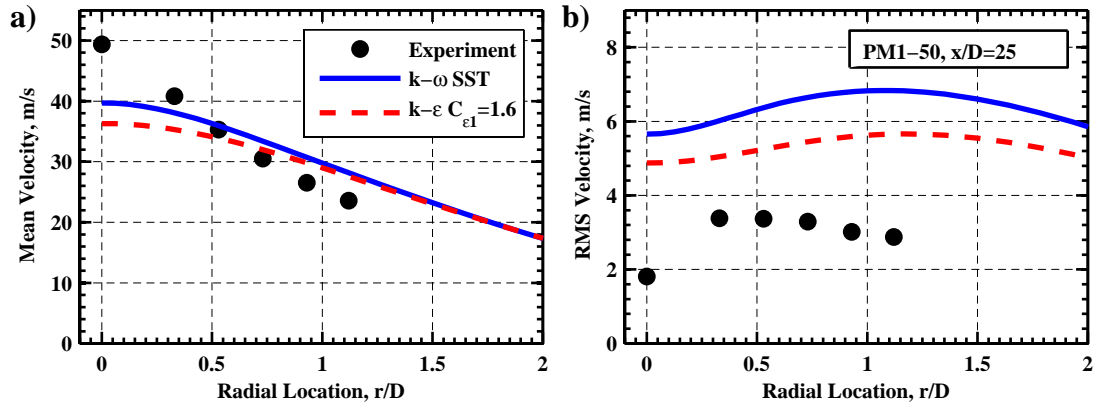


Figure D-3. Comparison of the Reynolds mean a) and RMS b) velocity statistics at $x/D=25$ for the PM1-50 flame.

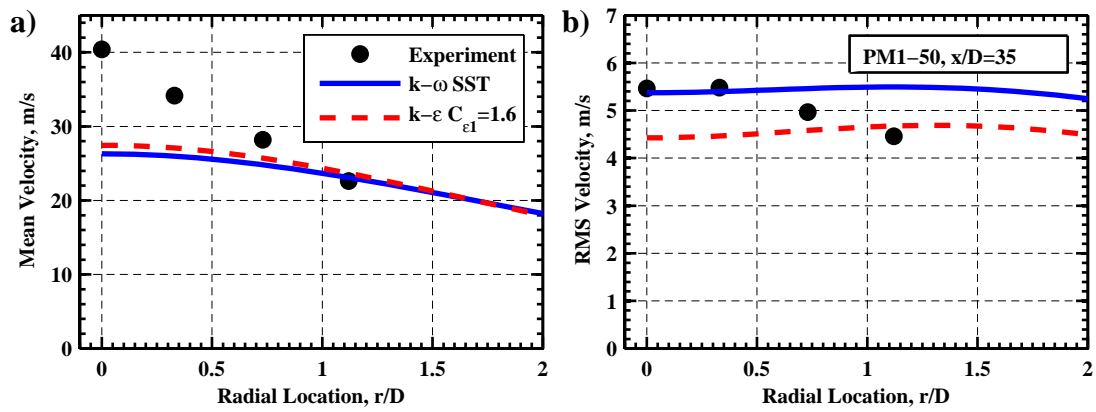


Figure D-4. Comparison of the Reynolds mean a) and RMS b) velocity statistics at $x/D=35$ for the PM1-50 flame.

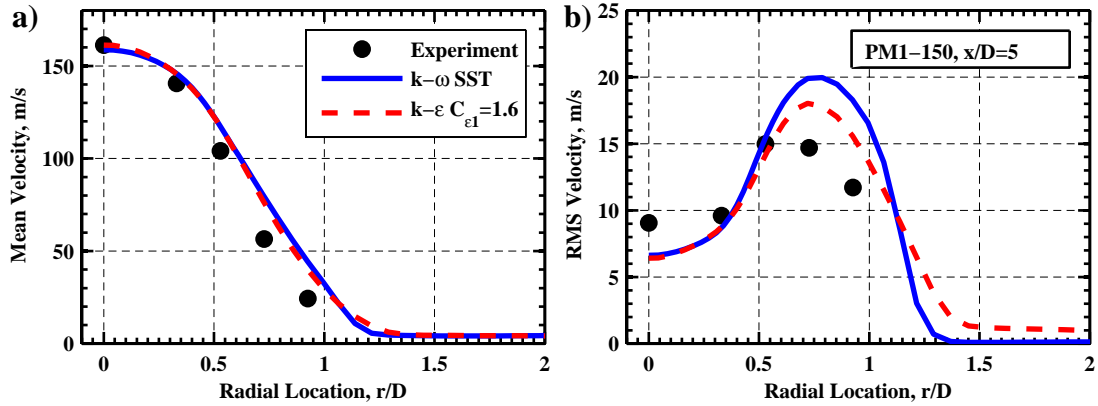


Figure D-5. Comparison of the Reynolds mean a) and RMS b) velocity statistics at $x/D=5$ for the PM1-150 flame.

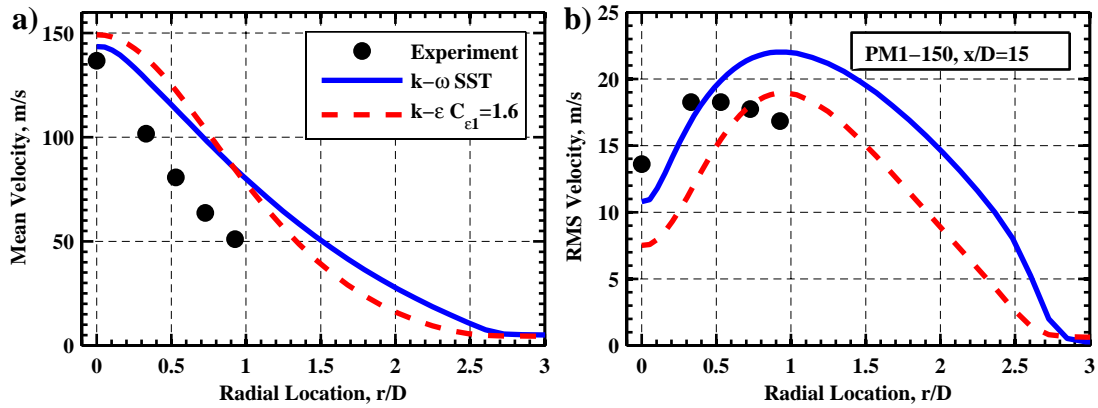


Figure D-6. Comparison of the Reynolds mean a) and RMS b) velocity statistics at $x/D=15$ for the PM1-150 flame.

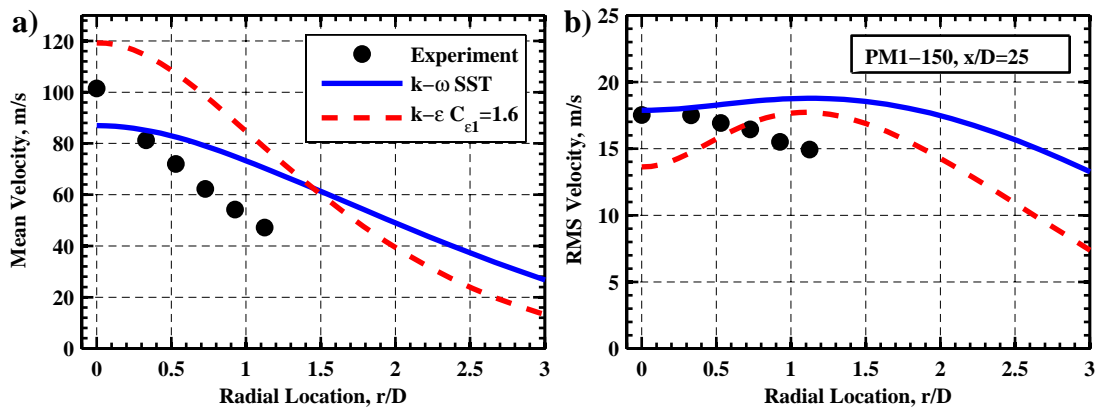


Figure D-7. Comparison of the Reynolds mean a) and RMS b) velocity statistics at $x/D=25$ for the PM1-150 flame.

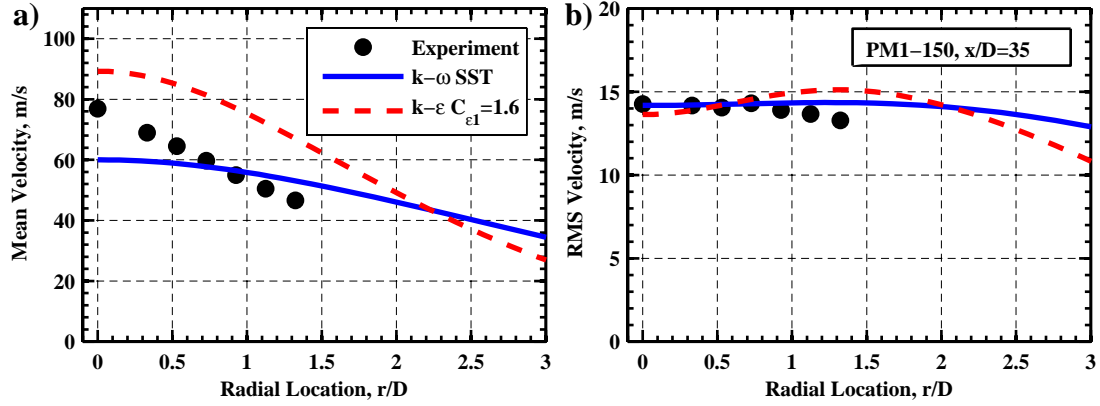


Figure D-8. Comparison of the Reynolds mean a) and RMS b) velocity statistics at $x/D=35$ for the PM1-150 flame.

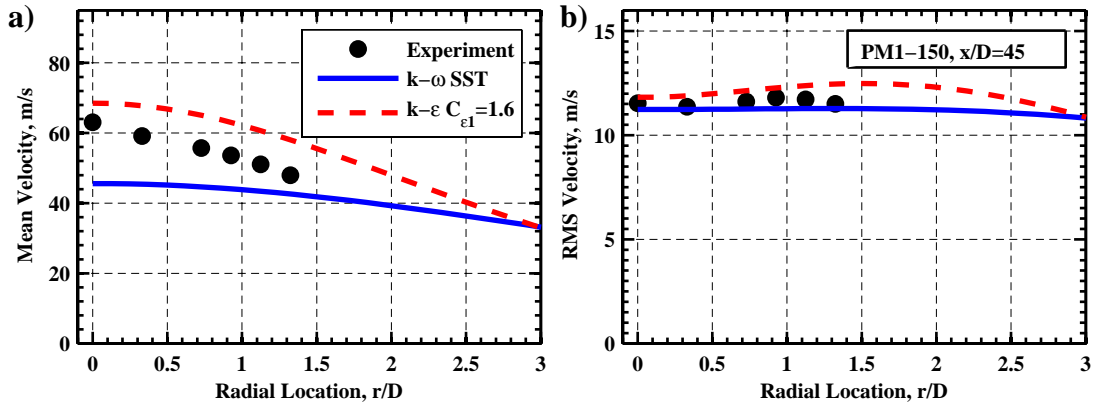


Figure D-9. Comparison of the Reynolds mean a) and RMS b) velocity statistics at $x/D=45$ for the PM1-150 flame.

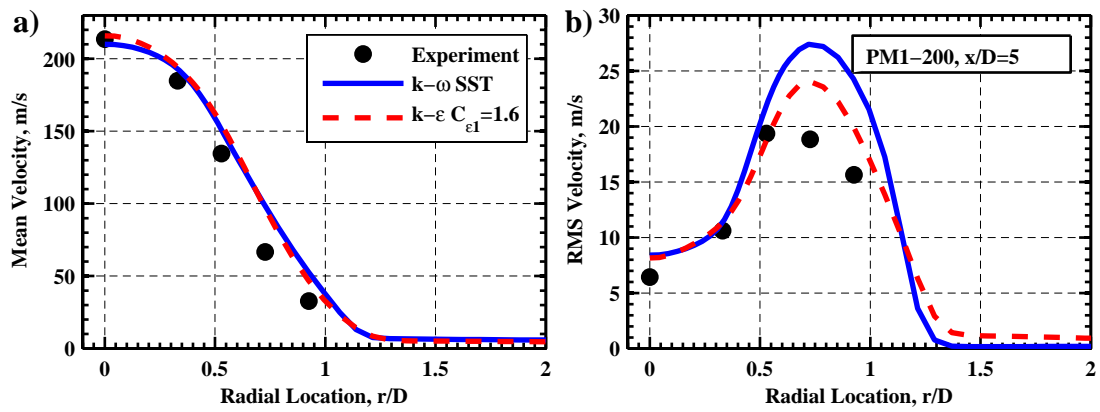


Figure D-10. Comparison of the Reynolds mean a) and RMS b) velocity statistics at $x/D=5$ for the PM1-200 flame.

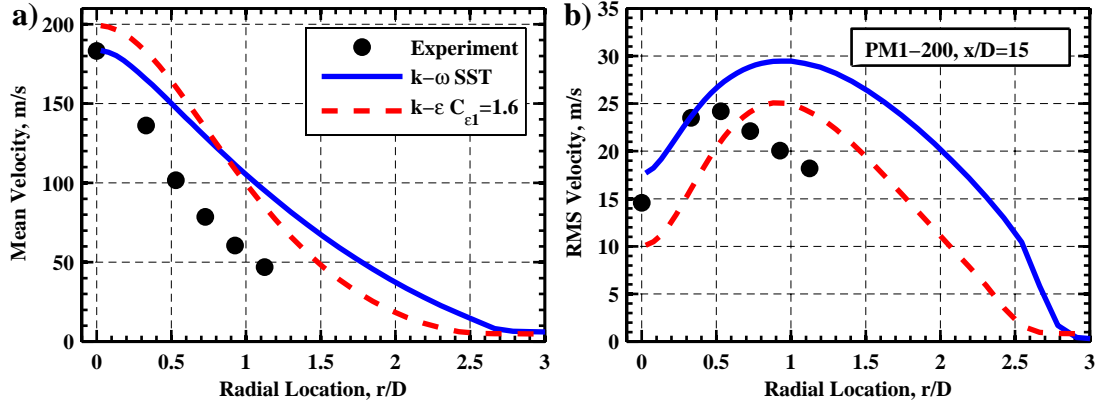


Figure D-11. Comparison of the Reynolds mean a) and RMS b) velocity statistics at $x/D=15$ for the PM1-200 flame.

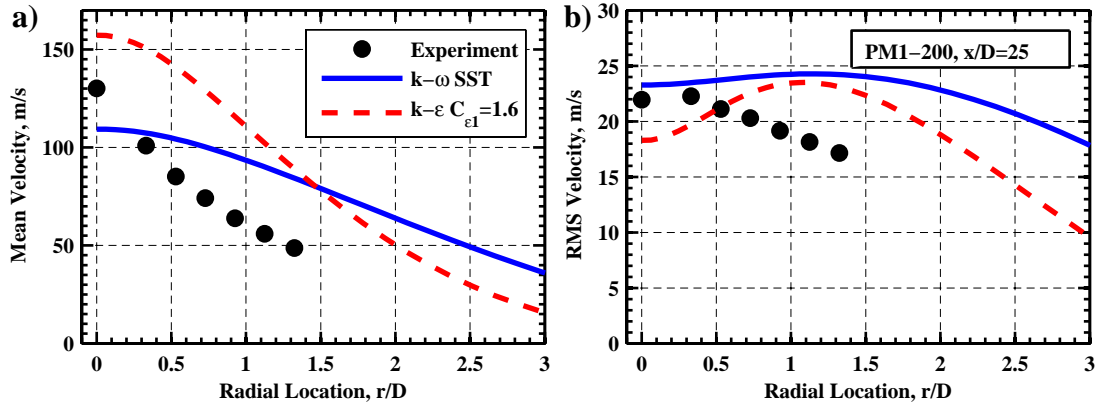


Figure D-12. Comparison of the Reynolds mean a) and RMS b) velocity statistics at $x/D=25$ for the PM1-200 flame.

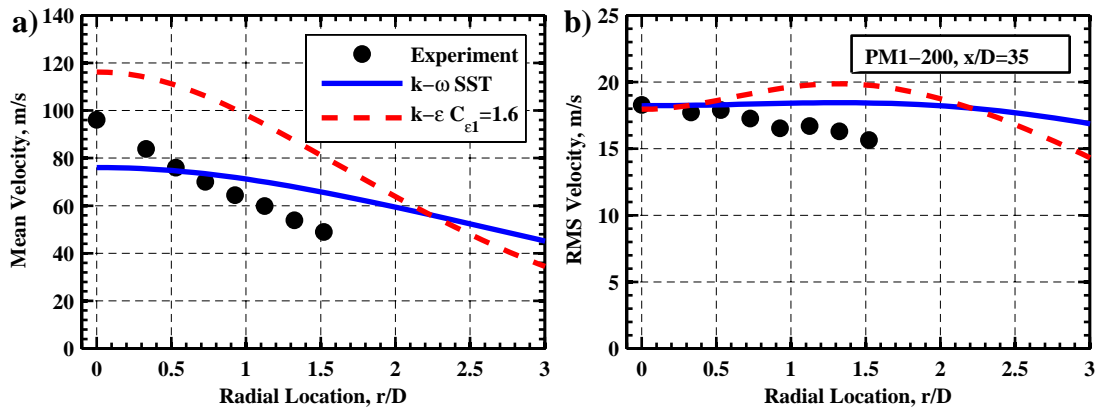


Figure D-13. Comparison of the Reynolds mean a) and RMS b) velocity statistics at $x/D=35$ for the PM1-200 flame.

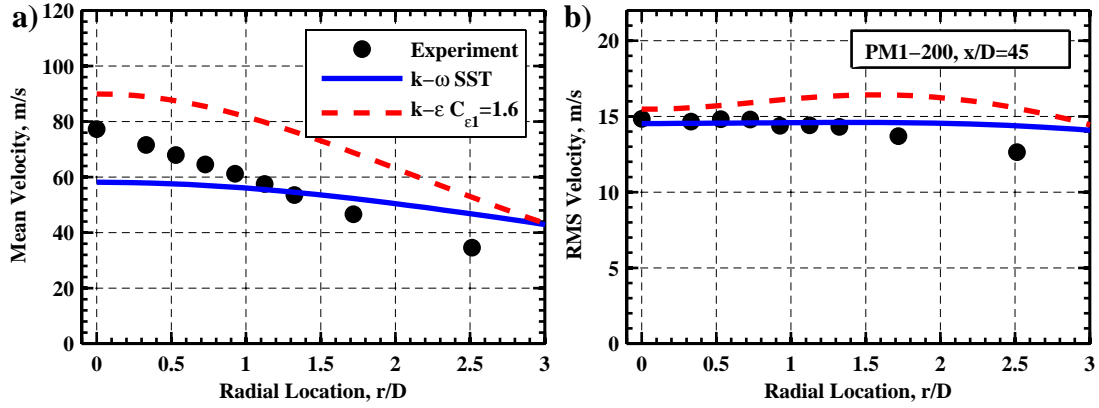


Figure D-14. Comparison of the Reynolds mean a) and RMS b) velocity statistics at $x/D=45$ for the PM1-200 flame.

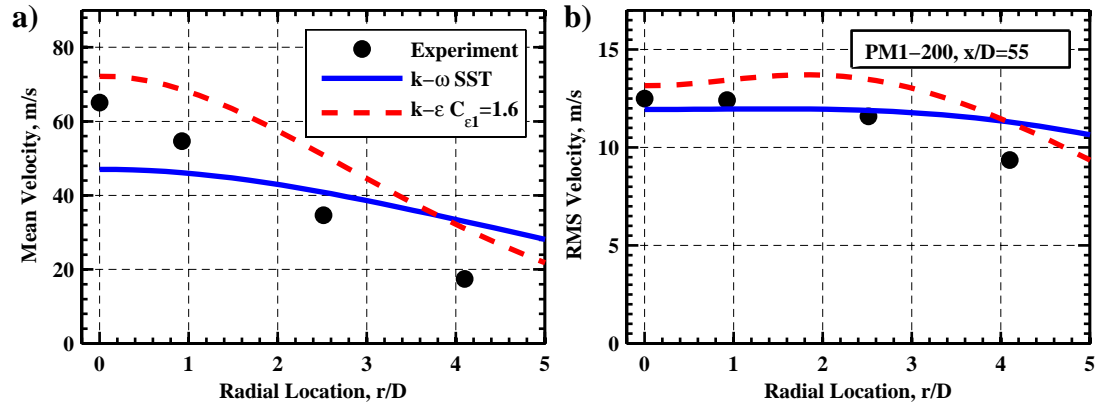


Figure D-15. Comparison of the Reynolds mean a) and RMS b) velocity statistics at $x/D=55$ for the PM1-200 flame.

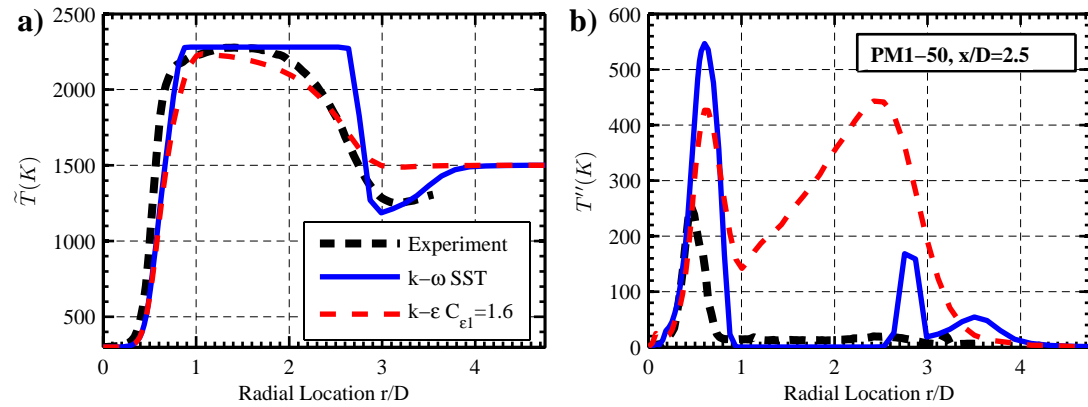


Figure D-16. Comparison of the Favre mean a) and RMS b) temperature statistics at $x/D=2.5$ for the PM1-50 flame.

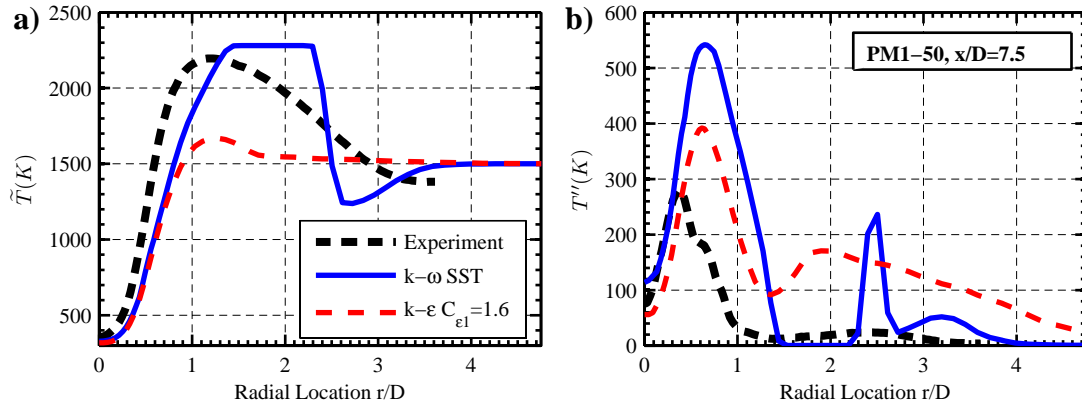


Figure D-17. Comparison of the Favre mean a) and RMS b) temperature statistics at $x/D=7.5$ for the PM1-50 flame.

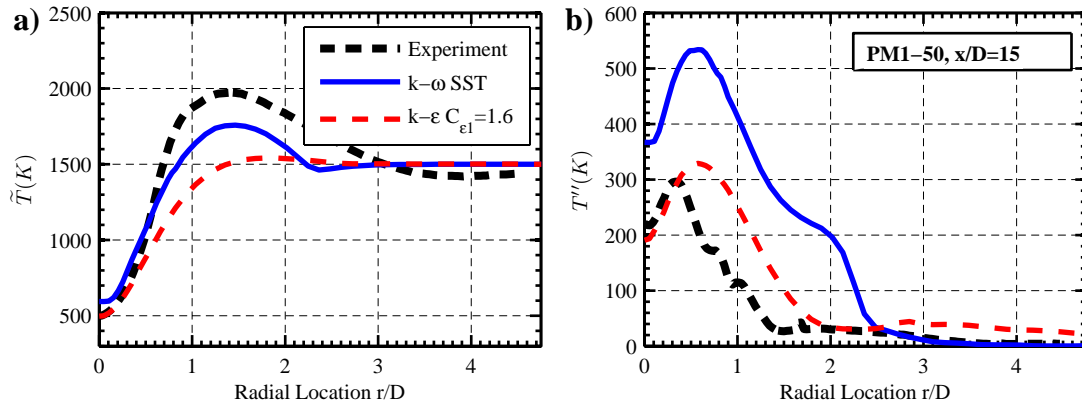


Figure D-18. Comparison of the Favre mean a) and RMS b) temperature statistics at $x/D=15$ for the PM1-50 flame.

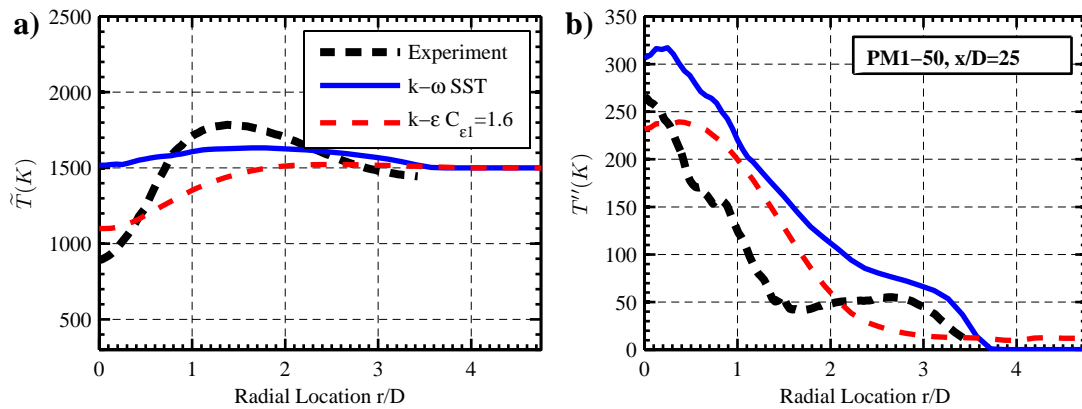


Figure D-19. Comparison of the Favre mean a) and RMS b) temperature statistics at $x/D=25$ for the PM1-50 flame.

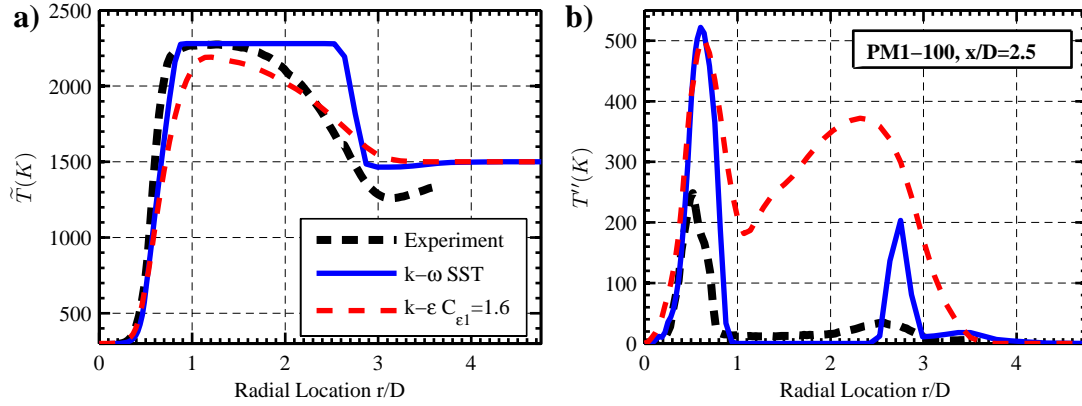


Figure D-20. Comparison of the Favre mean a) and RMS b) temperature statistics at $x/D=2.5$ for the PM1-100 flame.

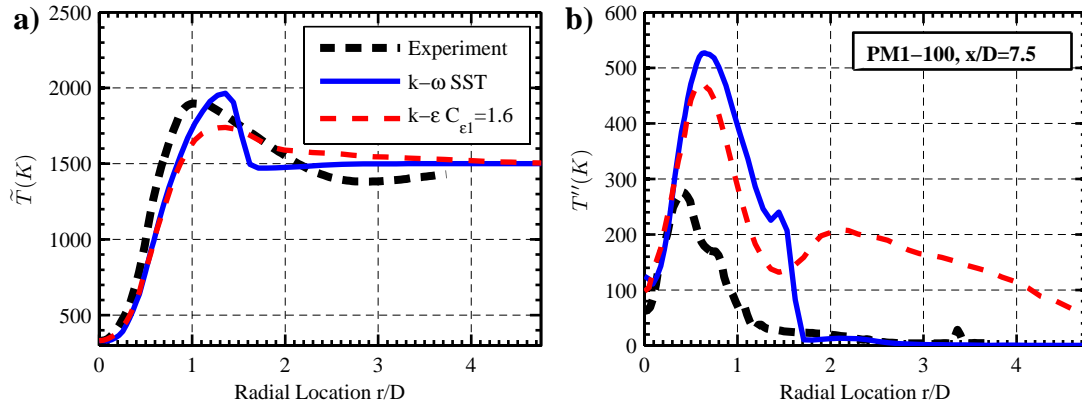


Figure D-21. Comparison of the Favre mean a) and RMS b) temperature statistics at $x/D=7.5$ for the PM1-100 flame.

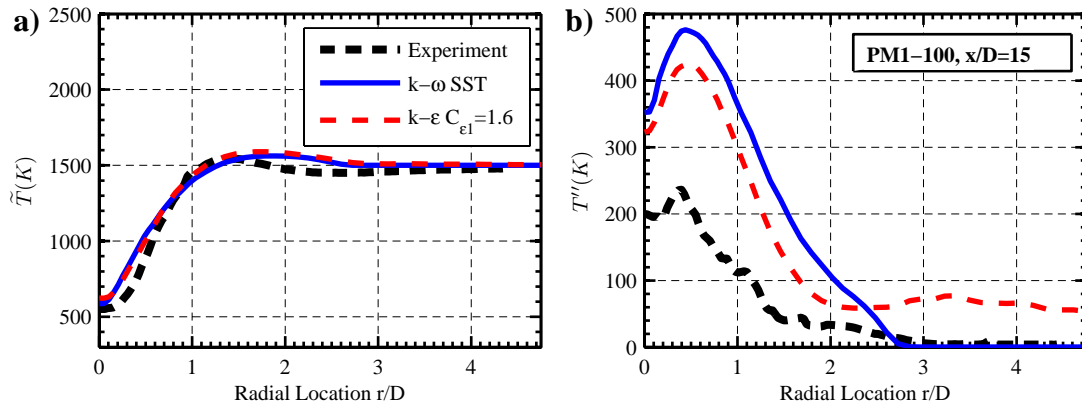


Figure D-22. Comparison of the Favre mean a) and RMS b) temperature statistics at $x/D=15$ for the PM1-100 flame.

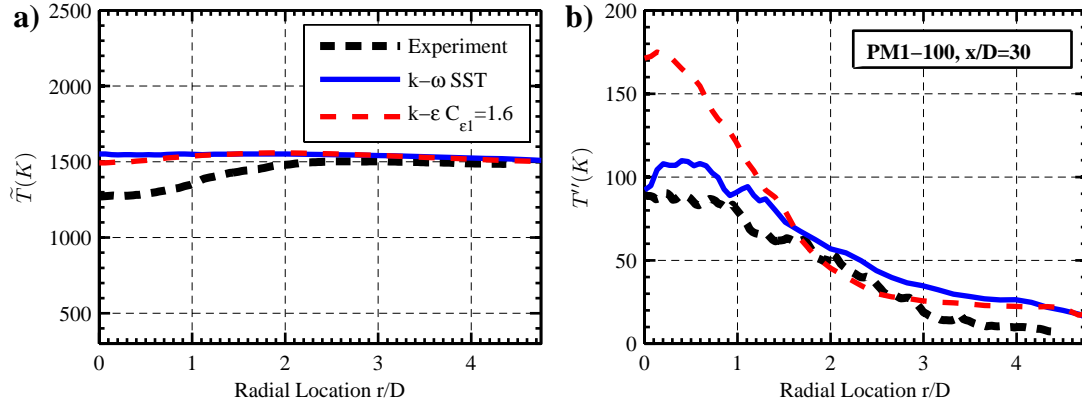


Figure D-23. Comparison of the Favre mean a) and RMS b) temperature statistics at $x/D=30$ for the PM1-100 flame.

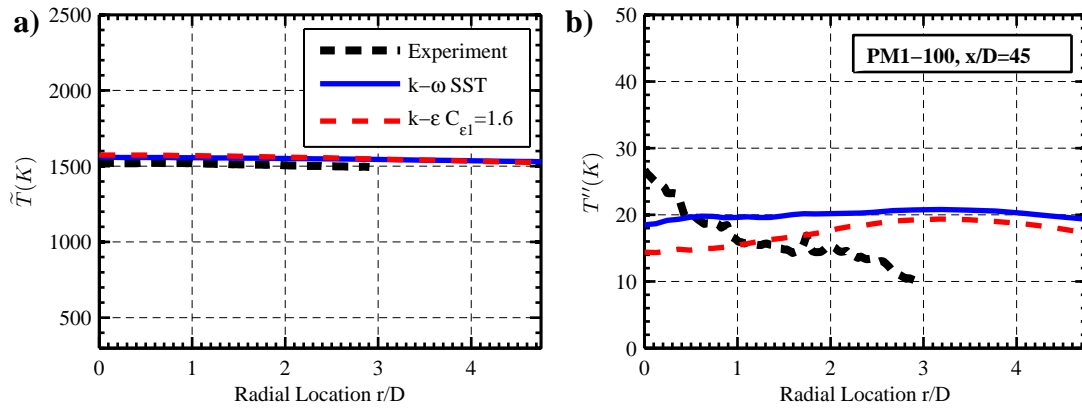


Figure D-24. Comparison of the Favre mean a) and RMS b) temperature statistics at $x/D=45$ for the PM1-100 flame.

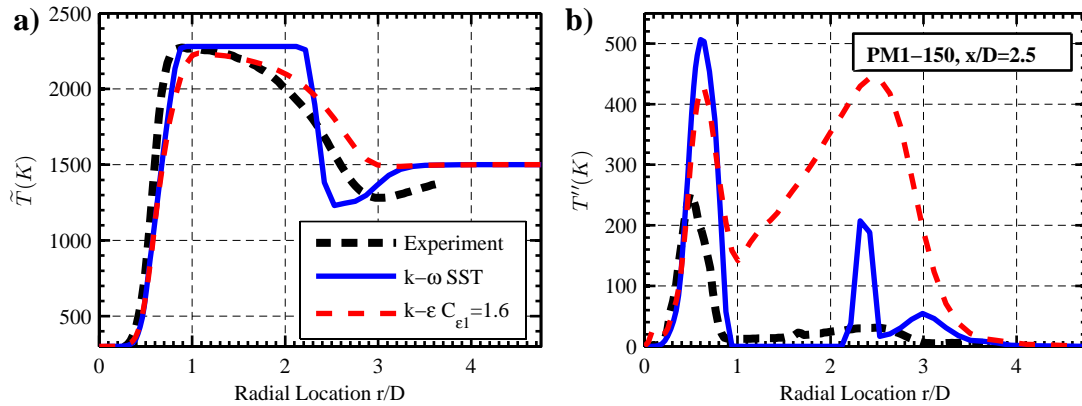


Figure D-25. Comparison of the Favre mean a) and RMS b) temperature statistics at $x/D=2.5$ for the PM1-150 flame.

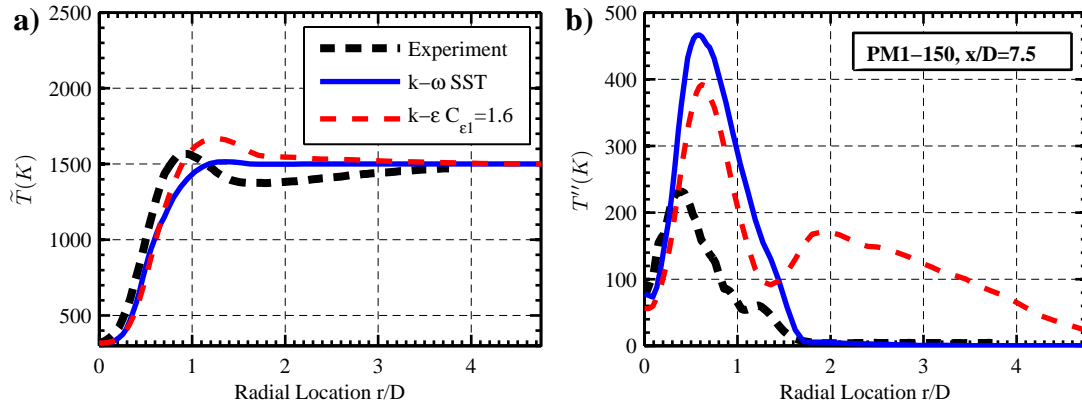


Figure D-26 Figure D-27. Comparison of the Favre mean a) and RMS b) temperature statistics at $x/D=7.5$ for the PM1-150 flame.

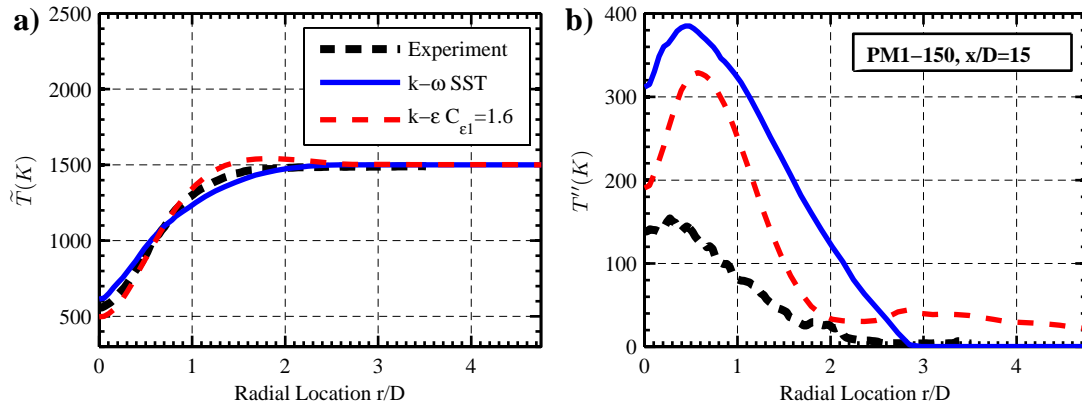


Figure D-28 Figure D-29. Comparison of the Favre mean a) and RMS b) temperature statistics at $x/D=15$ for the PM1-150 flame.

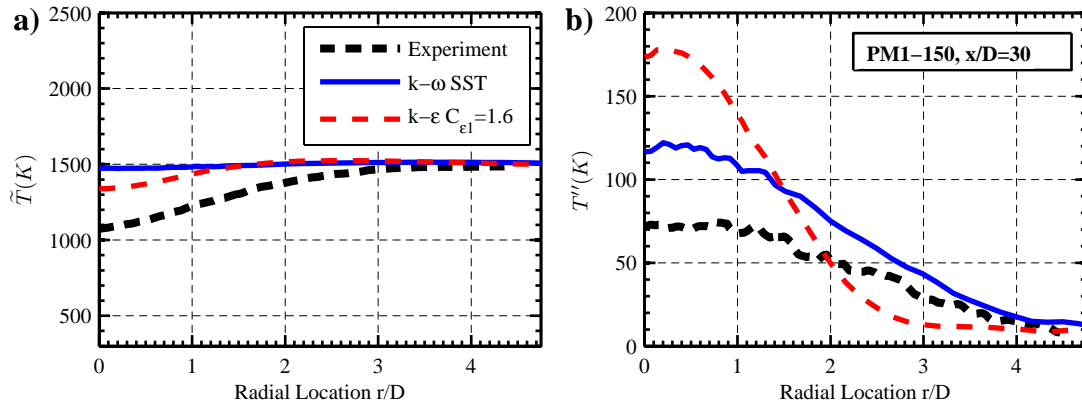


Figure D-30. Comparison of the Favre mean a) and RMS b) temperature statistics at $x/D=30$ for the PM1-150 flame.

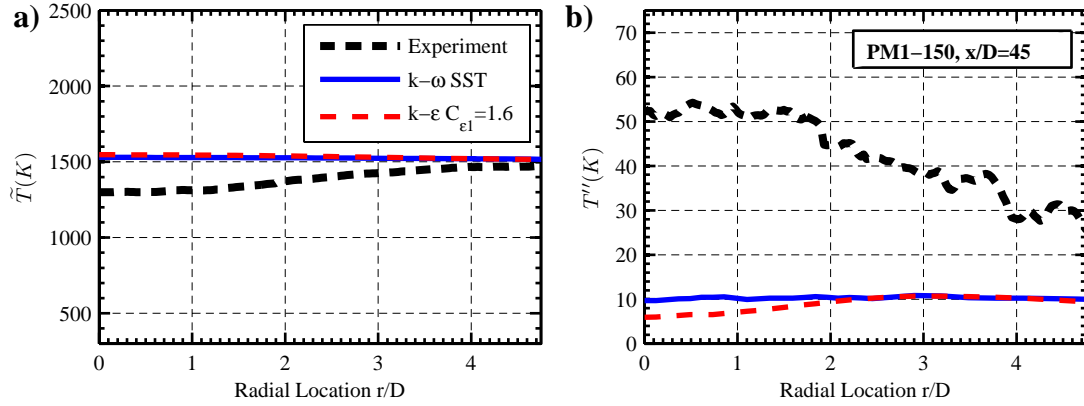


Figure D-31. Comparison of the Favre mean a) and RMS b) temperature statistics at $x/D=45$ for the PM1-150 flame.

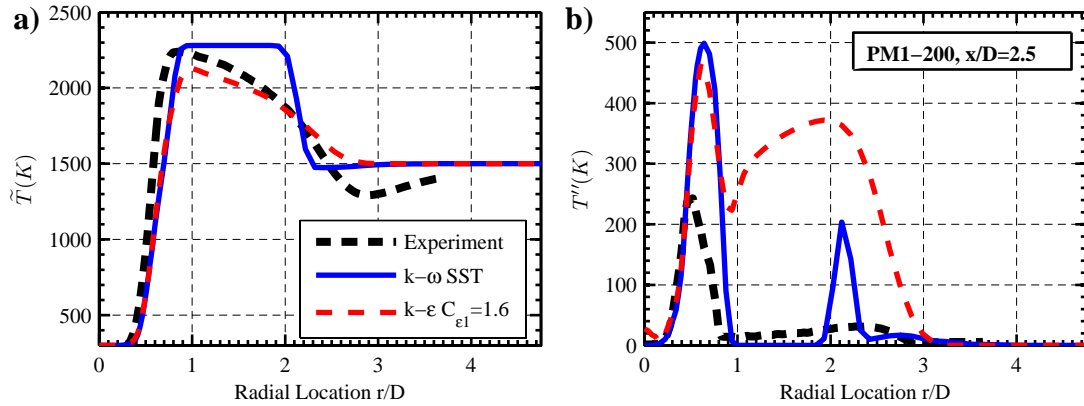


Figure D-32. Comparison of the Favre mean a) and RMS b) temperature statistics at $x/D=2.5$ for the PM1-200 flame.

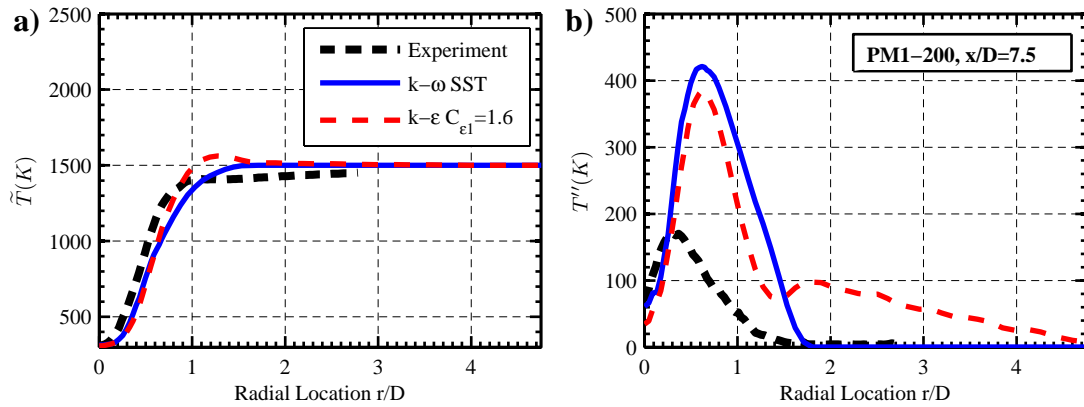


Figure D-33. Comparison of the Favre mean a) and RMS b) temperature statistics at $x/D=7.5$ for the PM1-200 flame.

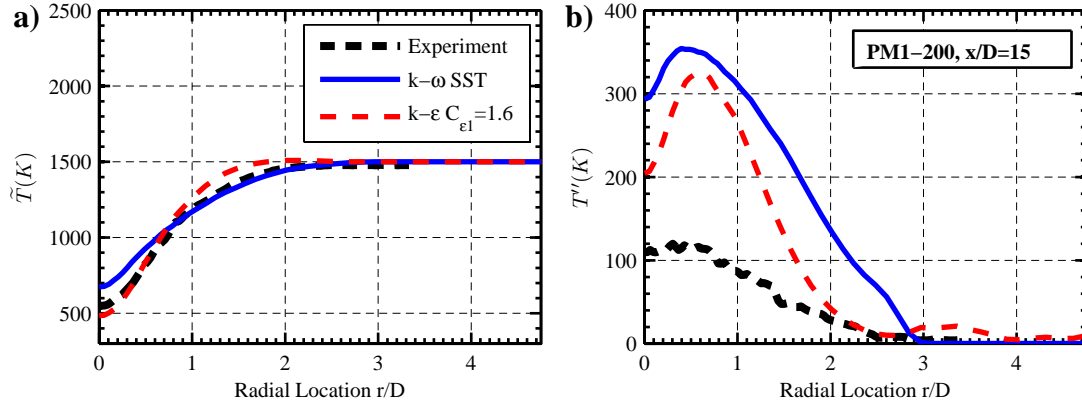


Figure D-34. Comparison of the Favre mean a) and RMS b) temperature statistics at $x/D=15$ for the PM1-200 flame.

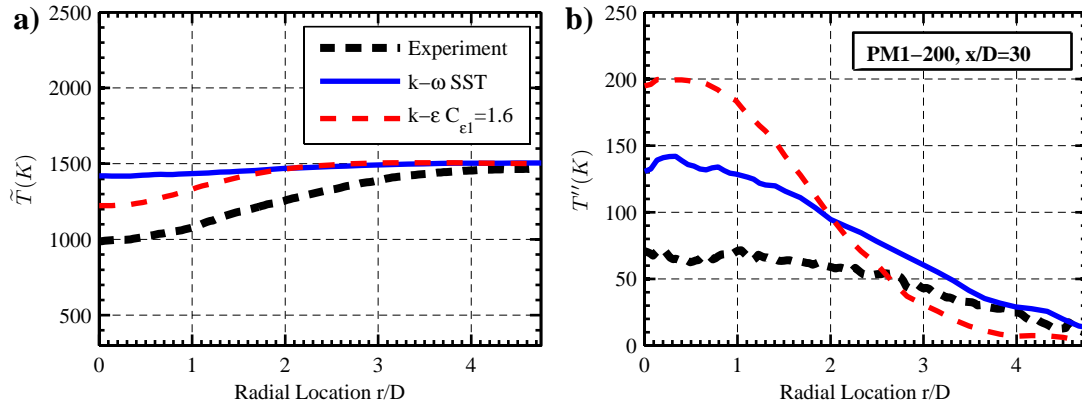


Figure D-35. Comparison of the Favre mean a) and RMS b) temperature statistics at $x/D=30$ for the PM1-200 flame.

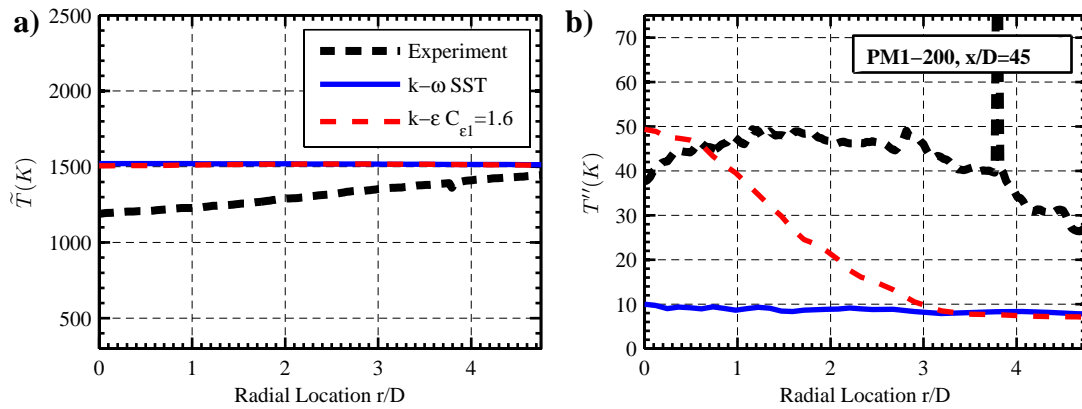


Figure D-36. Comparison of the Favre mean a) and RMS b) temperature statistics at $x/D=45$ for the PM1-200 flame.

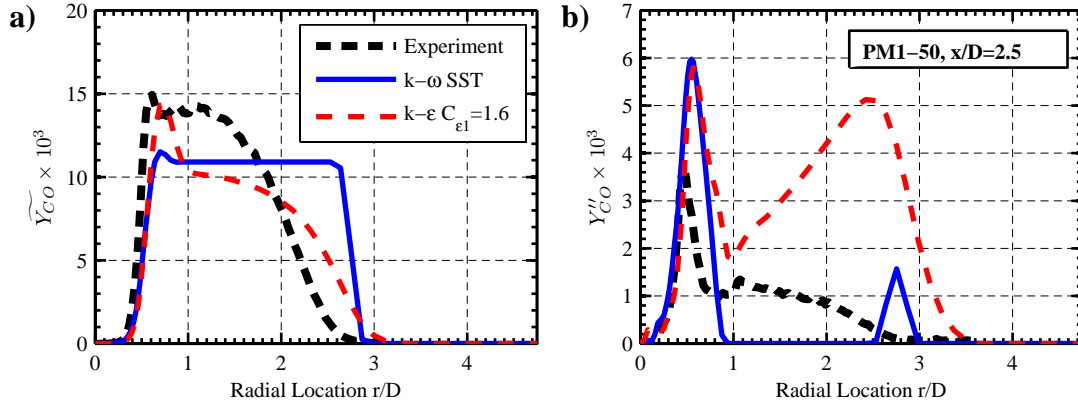


Figure D-37. Comparison of the Favre mean a) and RMS b) CO mass fraction statistics at $x/D=2.5$ for the PM1-50 flame.

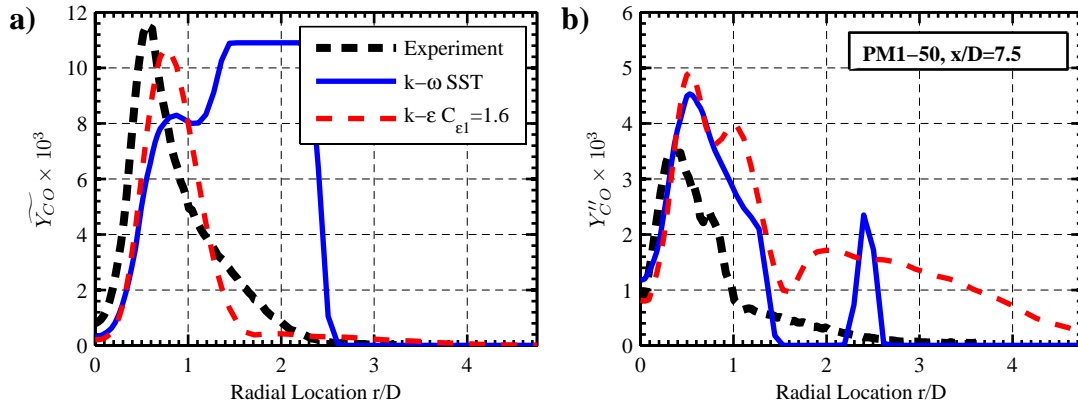


Figure D-38. Comparison of the Favre mean a) and RMS b) CO mass fraction statistics at $x/D=7.5$ for the PM1-50 flame.

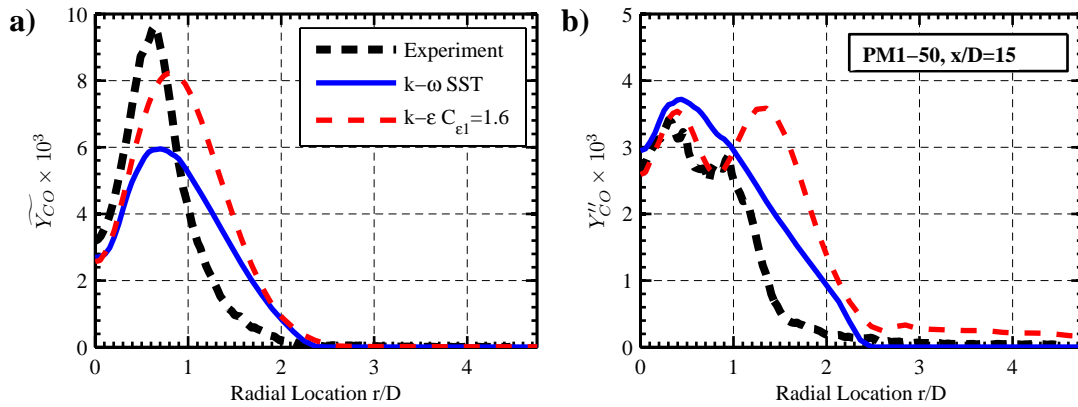


Figure D-39. Comparison of the Favre mean a) and RMS b) CO mass fraction statistics at $x/D=15$ for the PM1-50 flame.

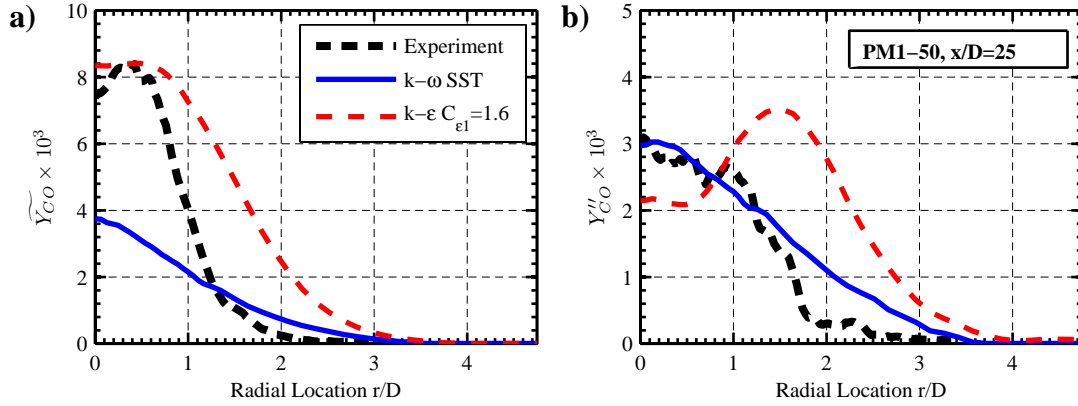


Figure D-40. Comparison of the Favre mean a) and RMS b) CO mass fraction statistics at $x/D=25$ for the PM1-50 flame.

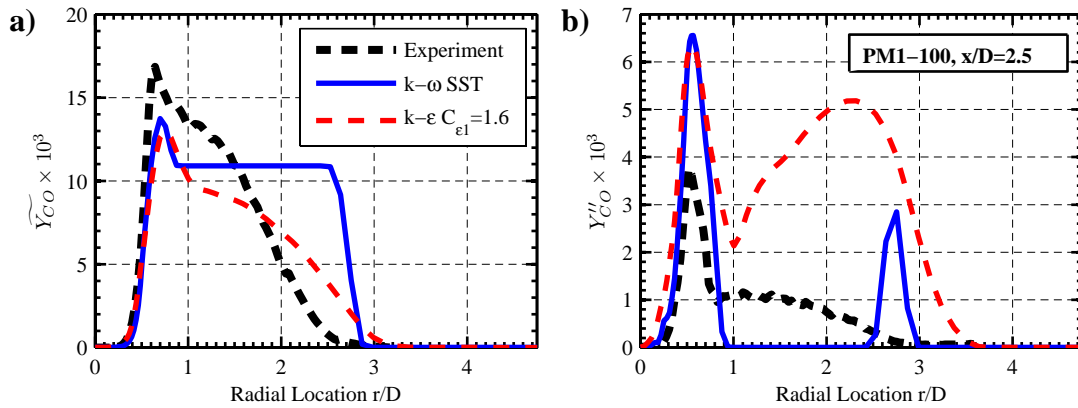


Figure D-41. Comparison of the Favre mean a) and RMS b) CO mass fraction statistics at $x/D=2.5$ for the PM1-100 flame.

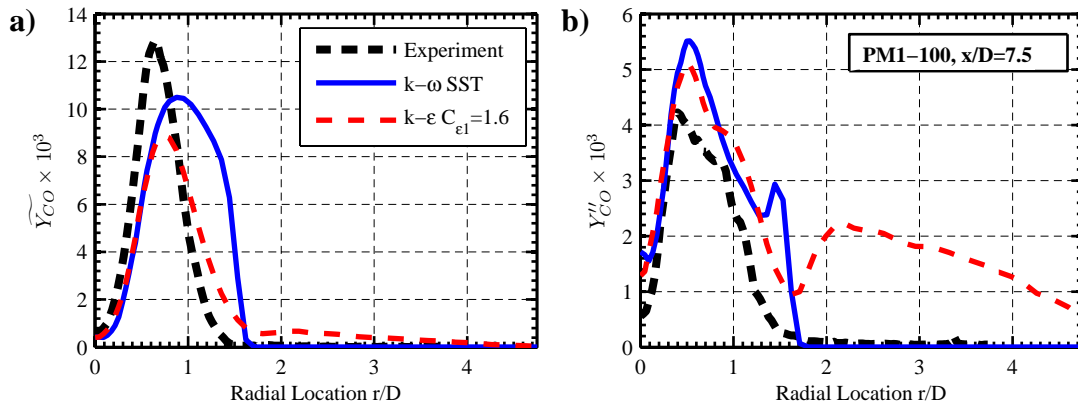


Figure D-42. Comparison of the Favre mean a) and RMS b) CO mass fraction statistics at $x/D=7.5$ for the PM1-100 flame.

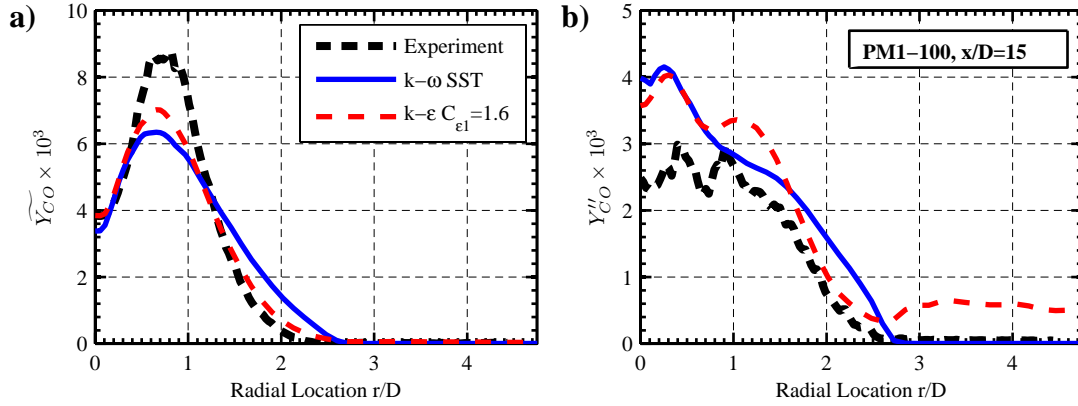


Figure D-43. Comparison of the Favre mean a) and RMS b) CO mass fraction statistics at $x/D=15$ for the PM1-100 flame.

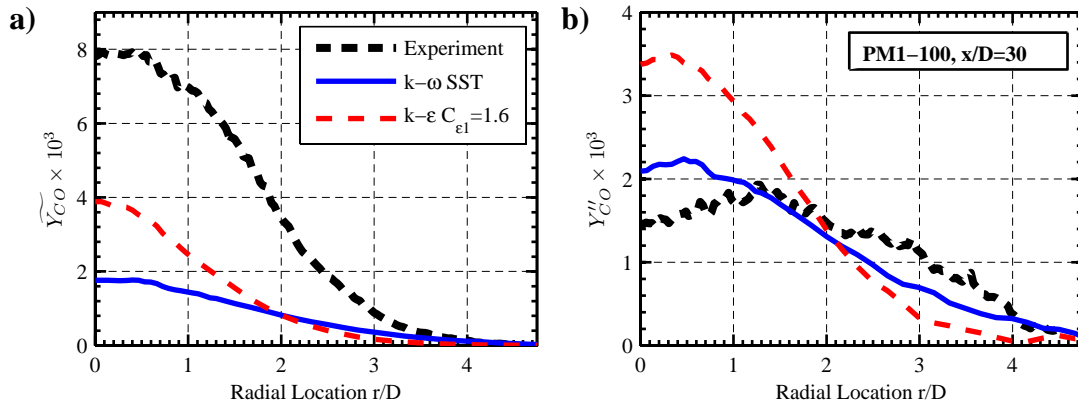


Figure D-44. Comparison of the Favre mean a) and RMS b) CO mass fraction statistics at $x/D=30$ for the PM1-100 flame.

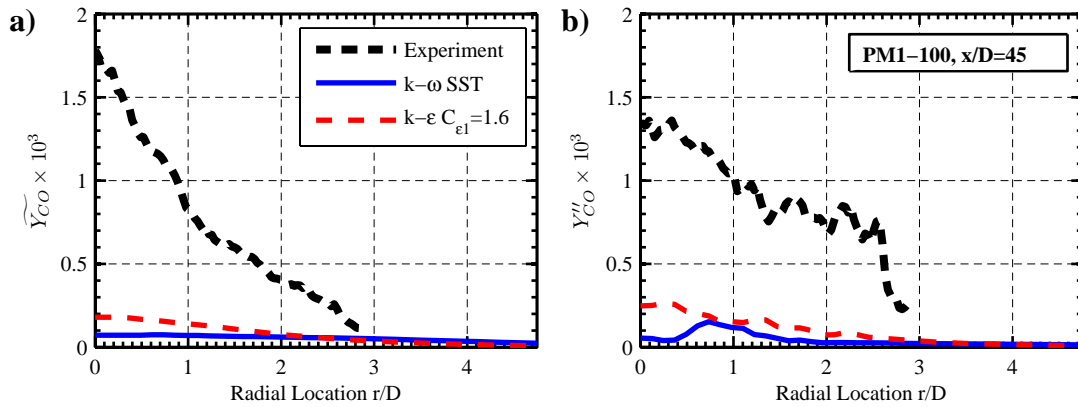


Figure D-45. Comparison of the Favre mean a) and RMS b) CO mass fraction statistics at $x/D=45$ for the PM1-100 flame.

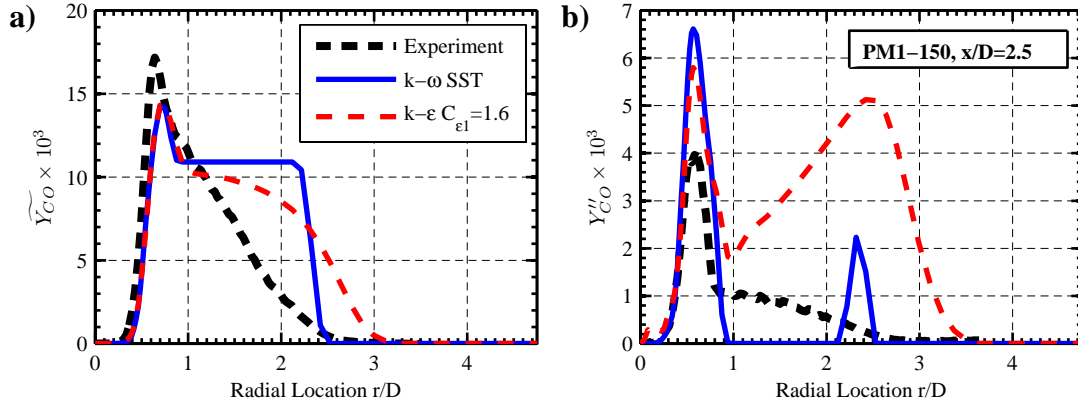


Figure D-46. Comparison of the Favre mean a) and RMS b) CO mass fraction statistics at $x/D=2.5$ for the PM1-150 flame.

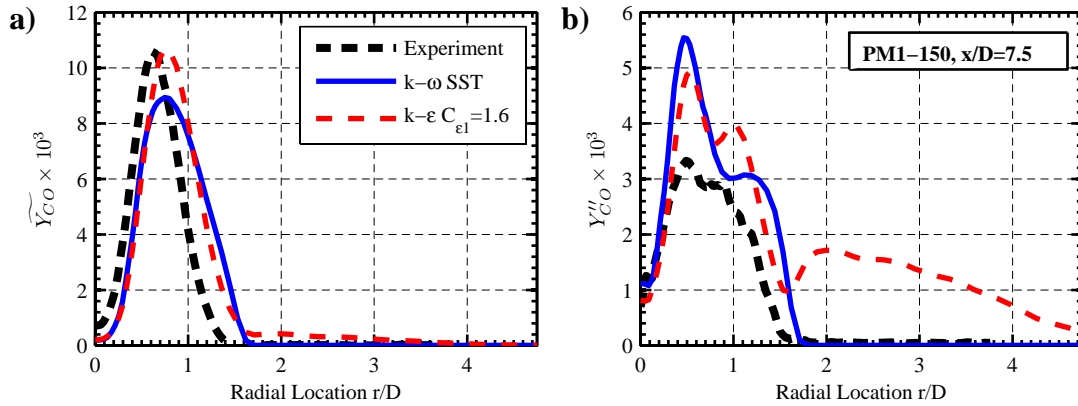


Figure D-47. Comparison of the Favre mean a) and RMS b) CO mass fraction statistics at $x/D=5$ for the PM1-150 flame.

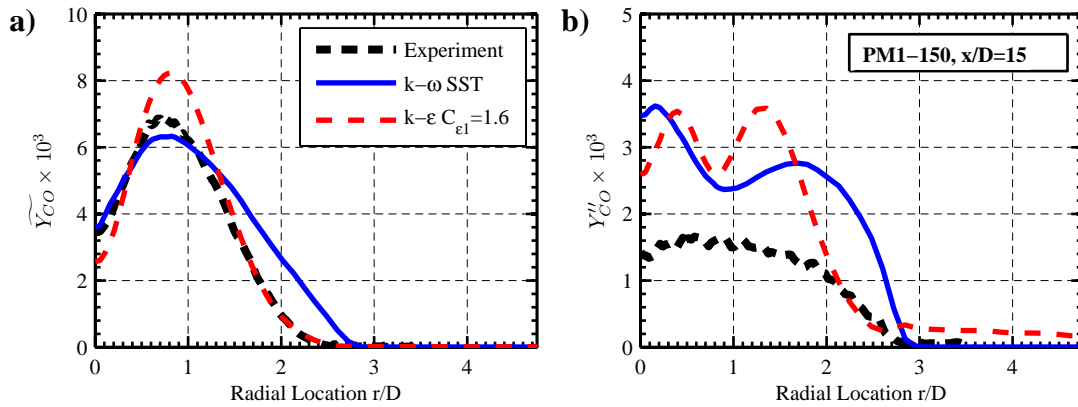


Figure D-48. Comparison of the Favre mean a) and RMS b) CO mass fraction statistics at $x/D=15$ for the PM1-150 flame.

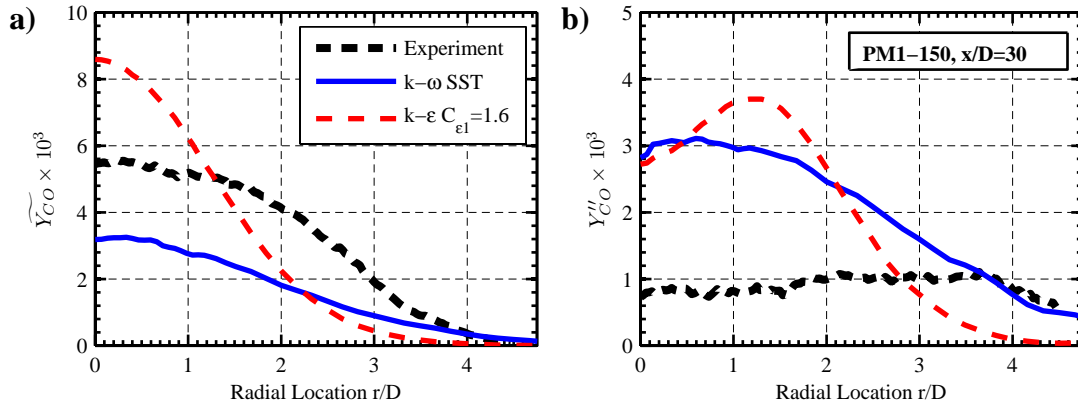


Figure D-49. Comparison of the Favre mean a) and RMS b) CO mass fraction statistics at $x/D=30$ for the PM1-150 flame.

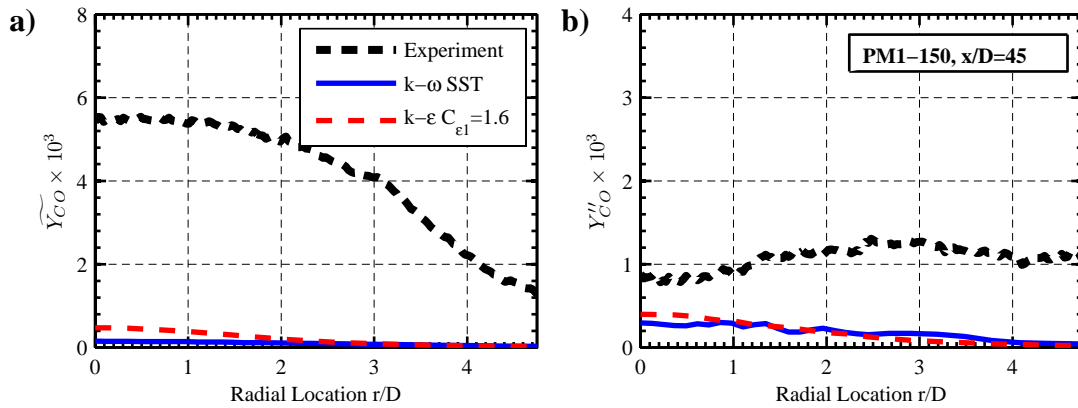


Figure D-50. Comparison of the Favre mean a) and RMS b) CO mass fraction statistics at $x/D=45$ for the PM1-150 flame.

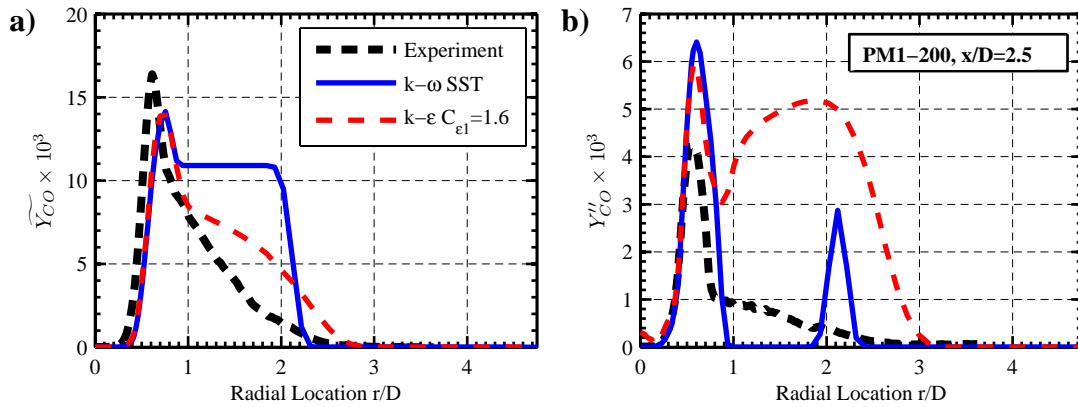


Figure D-51. Comparison of the Favre mean a) and RMS b) CO mass fraction statistics at $x/D=2.5$ for the PM1-200 flame.

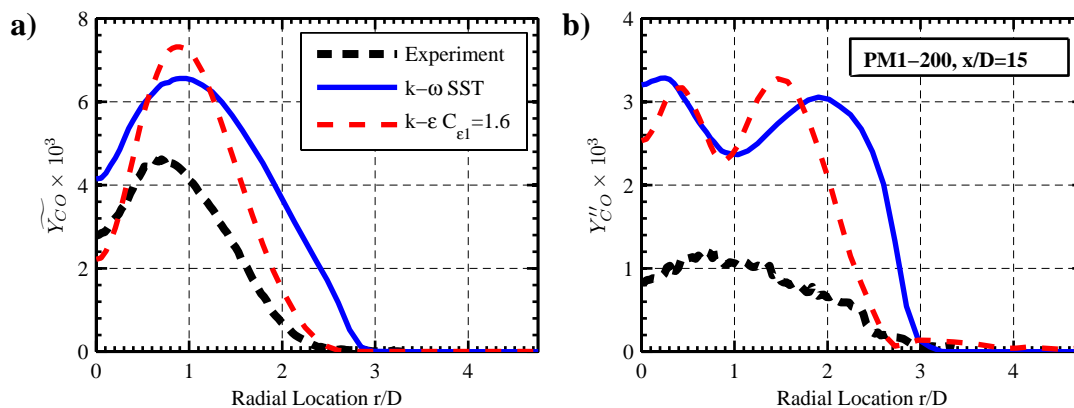


Figure D-52. Comparison of the Favre mean a) and RMS b) CO mass fraction statistics at $x/D=15$ for the PM1-200 flame.

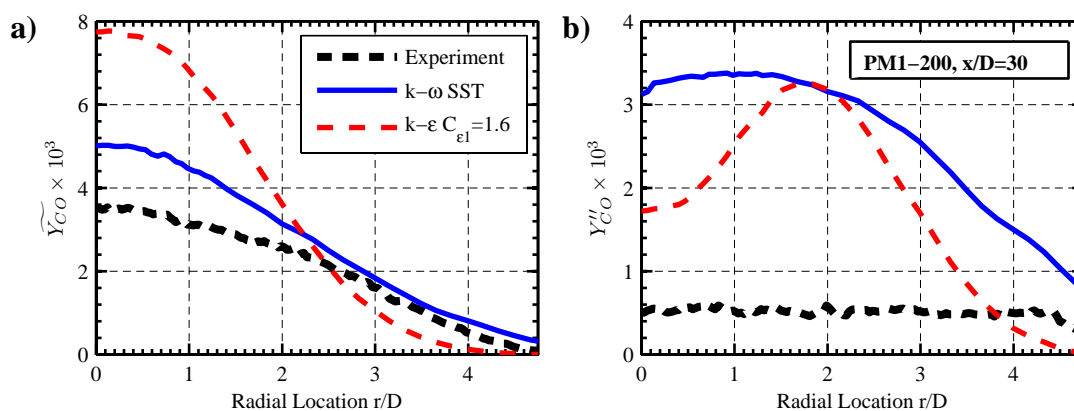


Figure D-53. Comparison of the Favre mean a) and RMS b) CO mass fraction statistics at $x/D=30$ for the PM1-200 flame.

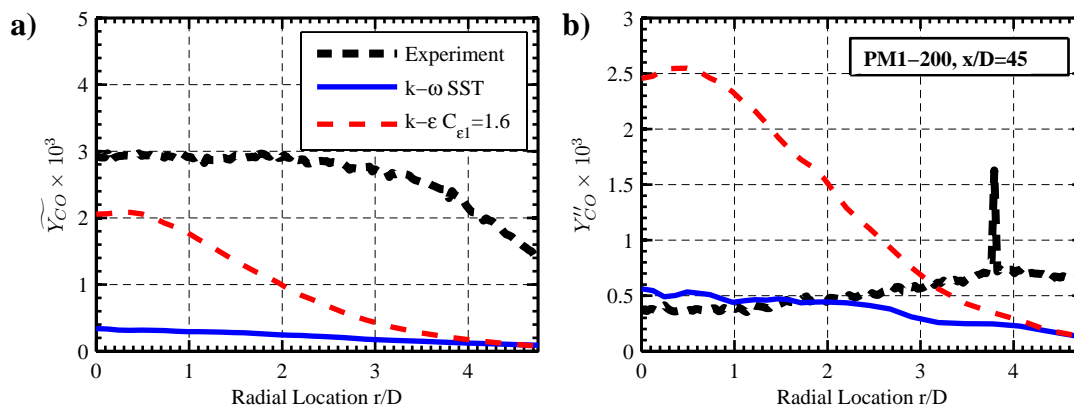


Figure D-54 Comparison of the Favre mean a) and RMS b) CO mass fraction statistics at $x/D=45$ for the PM1-200 flame.

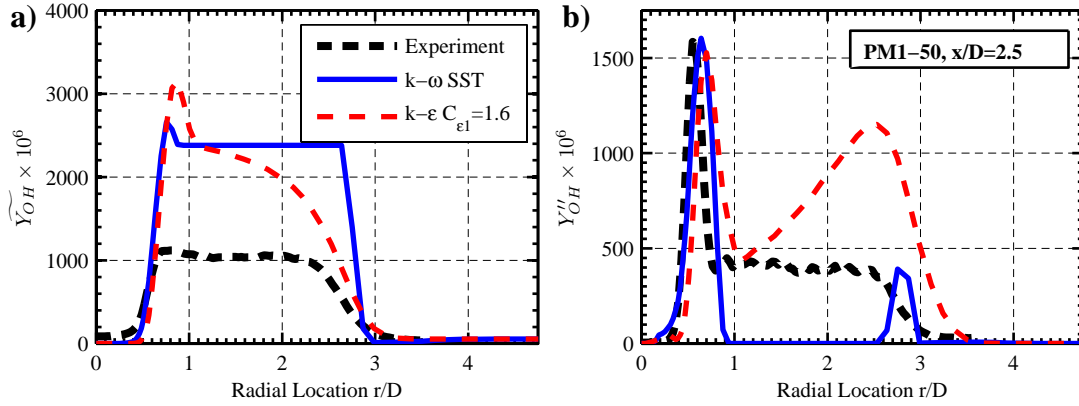


Figure D-55. Comparison of the Favre mean a) and RMS b) OH mass fraction statistics at $x/D=2.5$ for the PM1-50 flame.

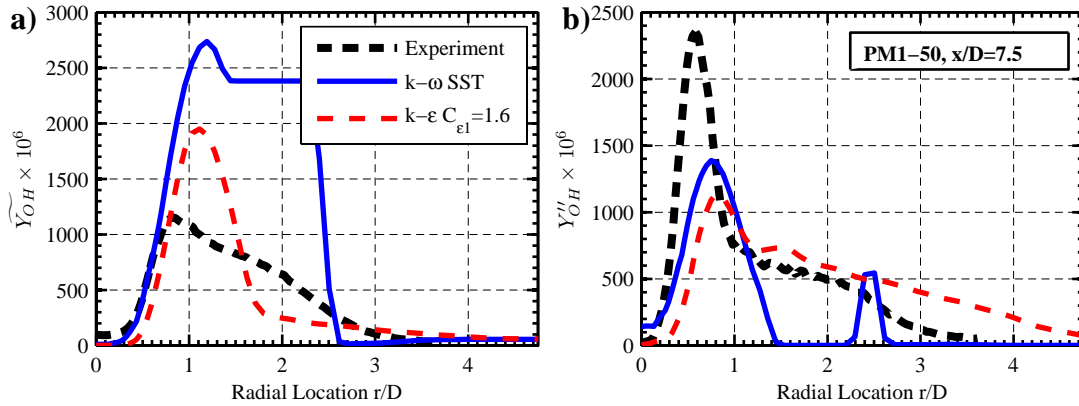


Figure D-56. Comparison of the Favre mean a) and RMS b) OH mass fraction statistics at $x/D=7.5$ for the PM1-50 flame.

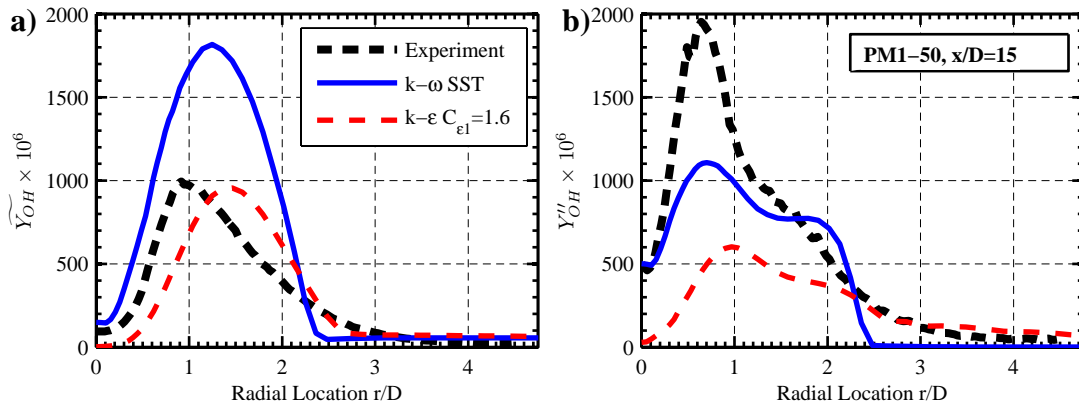


Figure D-57. Comparison of the Favre mean a) and RMS b) OH mass fraction statistics at $x/D=15$ for the PM1-50 flame.

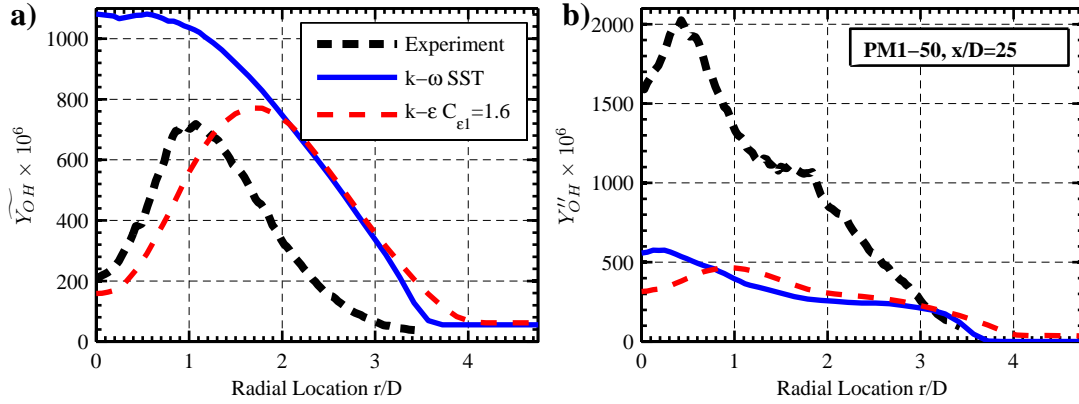


Figure D-58. Comparison of the Favre mean a) and RMS b) OH mass fraction statistics at $x/D=25$ for the PM1-50 flame.

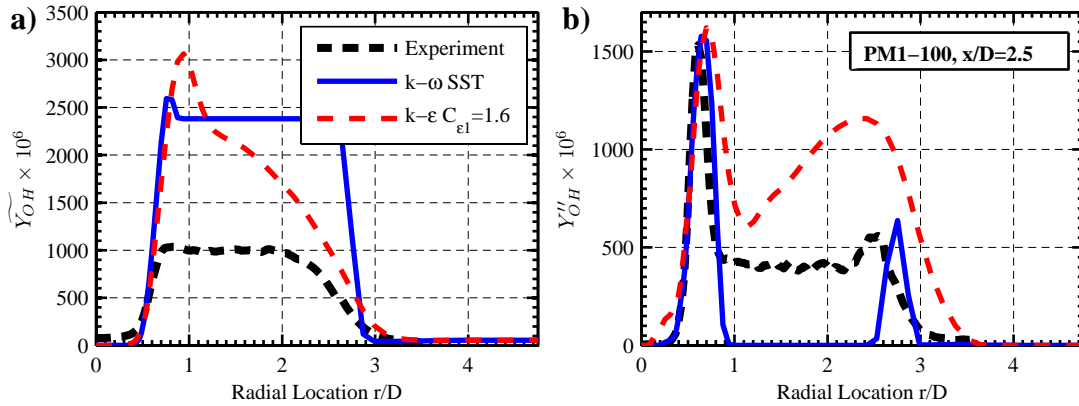


Figure D-59. Comparison of the Favre mean a) and RMS b) OH mass fraction statistics at $x/D=2.5$ for the PM1-100 flame.

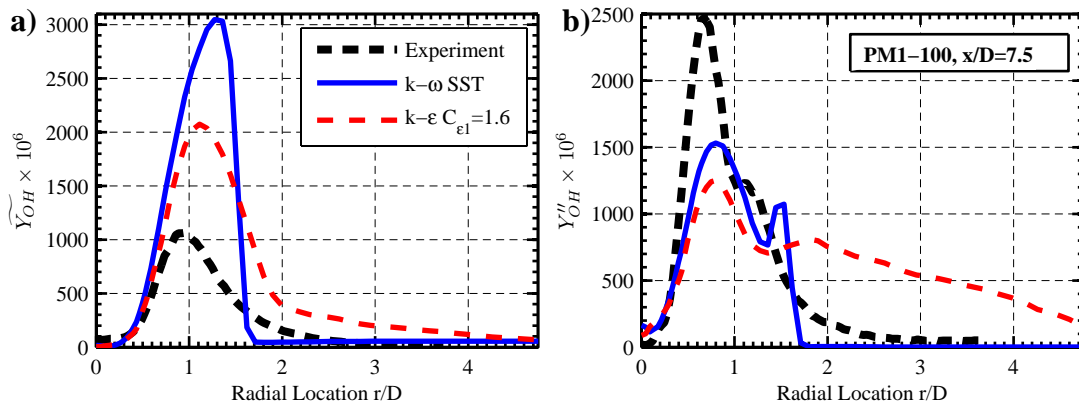


Figure D-60. Comparison of the Favre mean a) and RMS b) OH mass fraction statistics at $x/D=7.5$ for the PM1-100 flame.

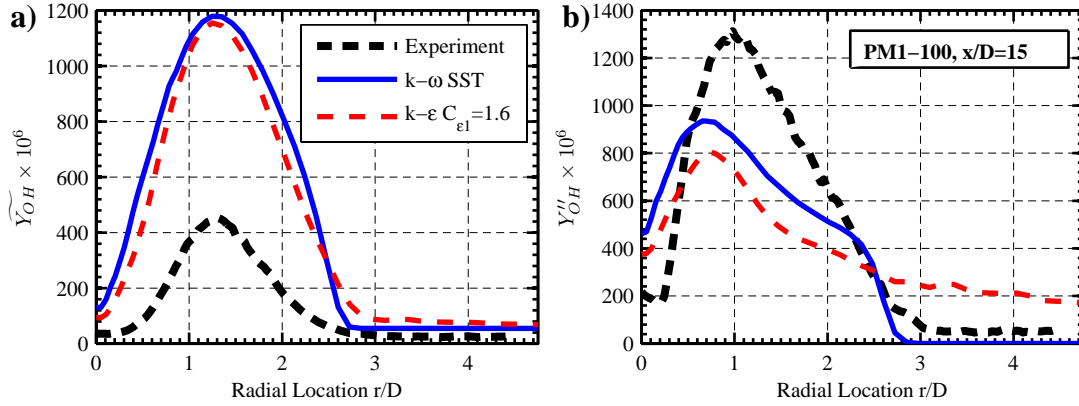


Figure D-61. Comparison of the Favre mean a) and RMS b) OH mass fraction statistics at $x/D=15$ for the PM1-100 flame.

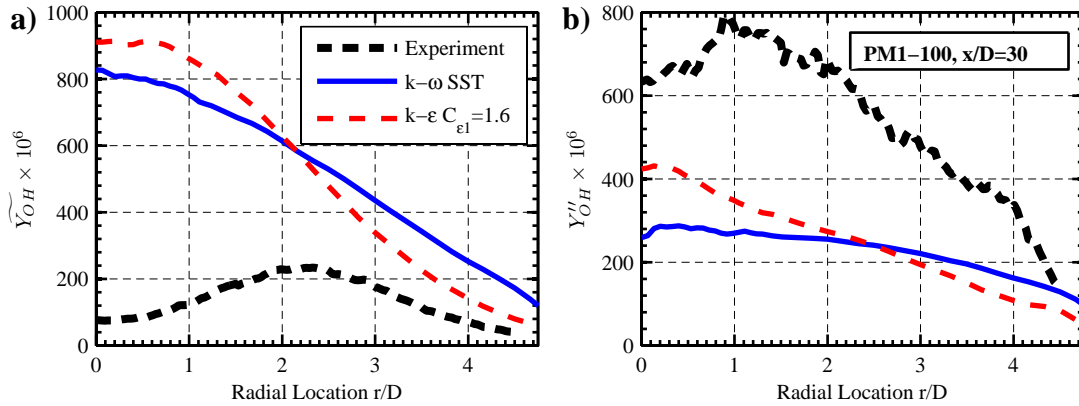


Figure D-62. Comparison of the Favre mean a) and RMS b) OH mass fraction statistics at $x/D=30$ for the PM1-100 flame.

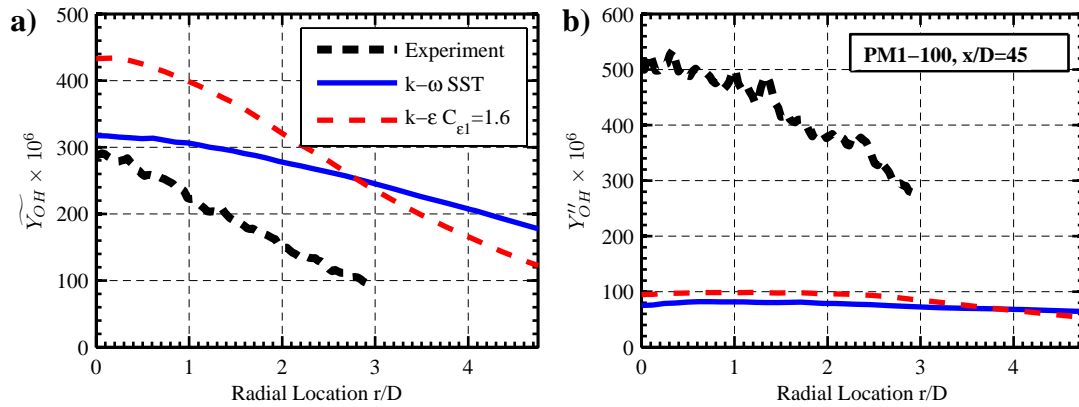


Figure D-63. Comparison of the Favre mean a) and RMS b) OH mass fraction statistics at $x/D=45$ for the PM1-100 flame.

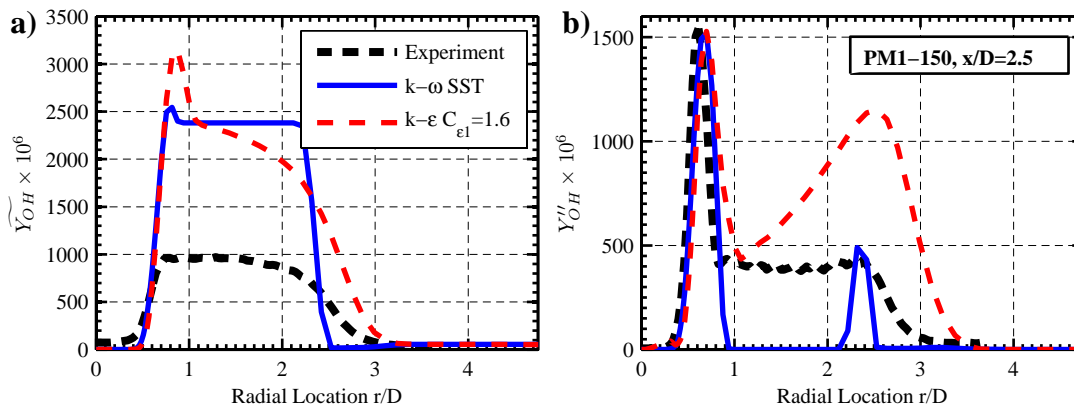


Figure D-64. Comparison of the Favre mean a) and RMS b) OH mass fraction statistics at $x/D=2.5$ for the PM1-150 flame.

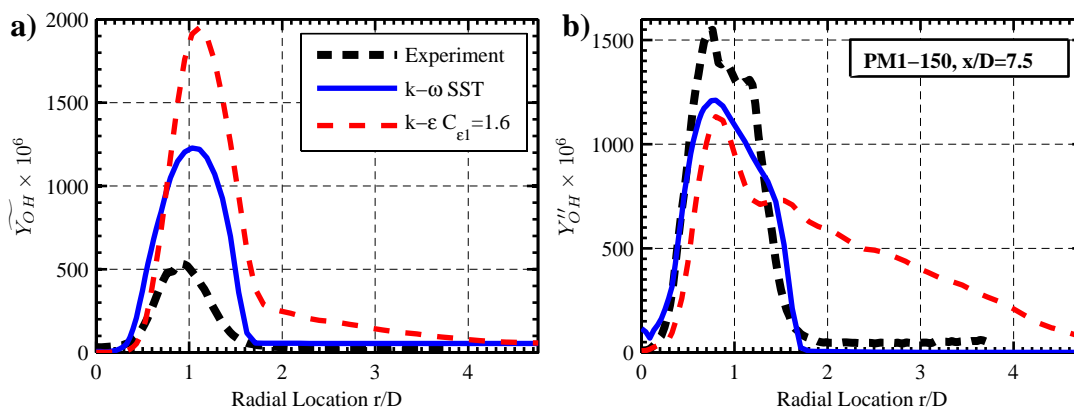


Figure D-65. Comparison of the Favre mean a) and RMS b) OH mass fraction statistics at $x/D=7.5$ for the PM1-150 flame.

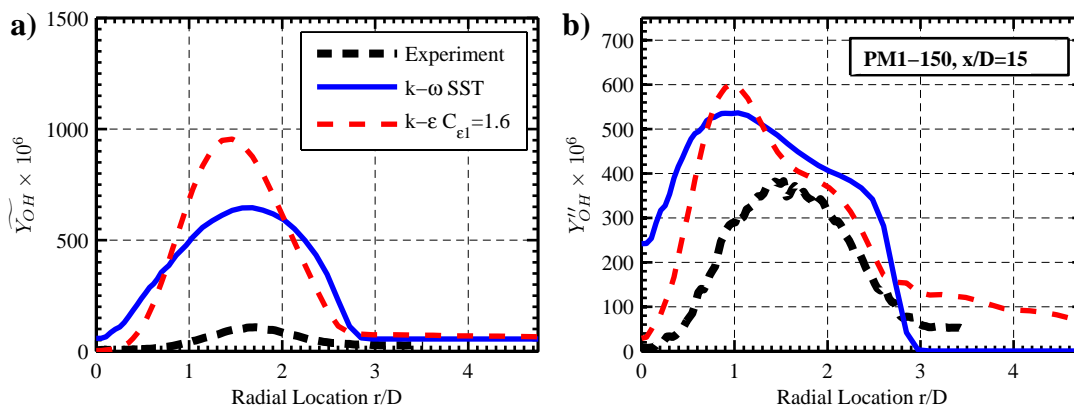


Figure D-66. Comparison of the Favre mean a) and RMS b) OH mass fraction statistics at $x/D=15$ for the PM1-150 flame.

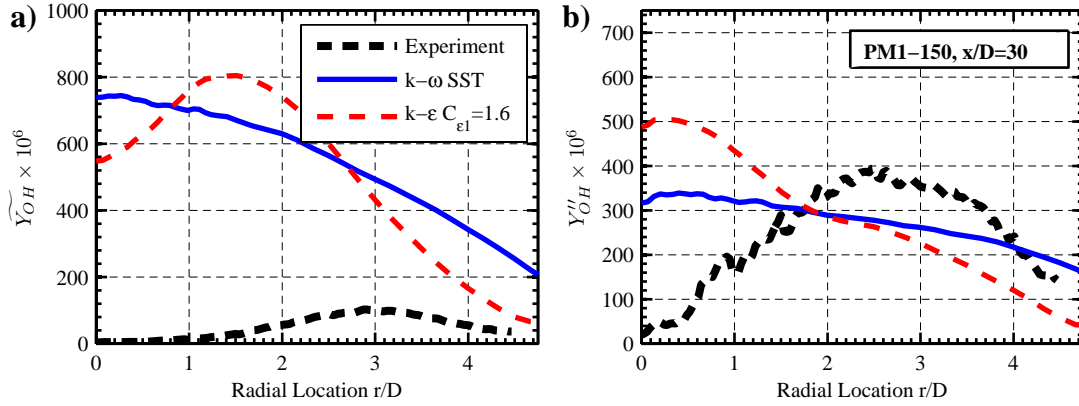


Figure D-67. Comparison of the Favre mean a) and RMS b) OH mass fraction statistics at $x/D=30$ for the PM1-150 flame.

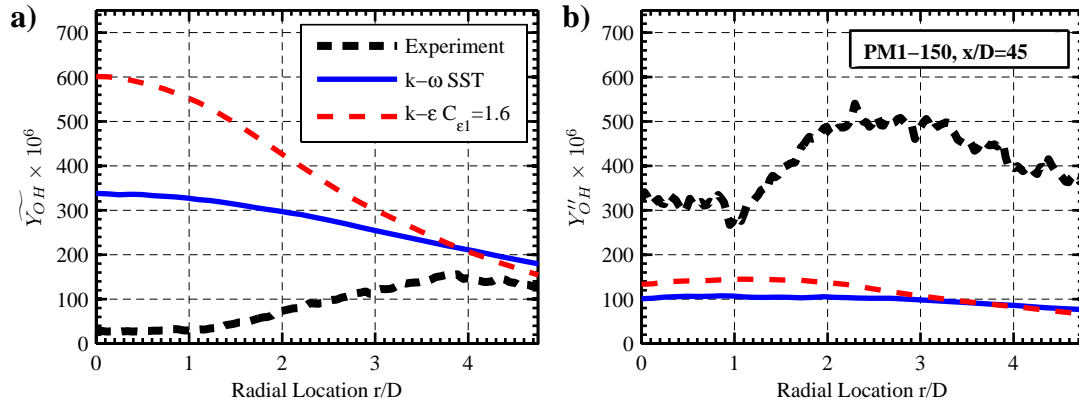


Figure D-68. Comparison of the Favre mean a) and RMS b) OH mass fraction statistics at $x/D=45$ for the PM1-150 flame.

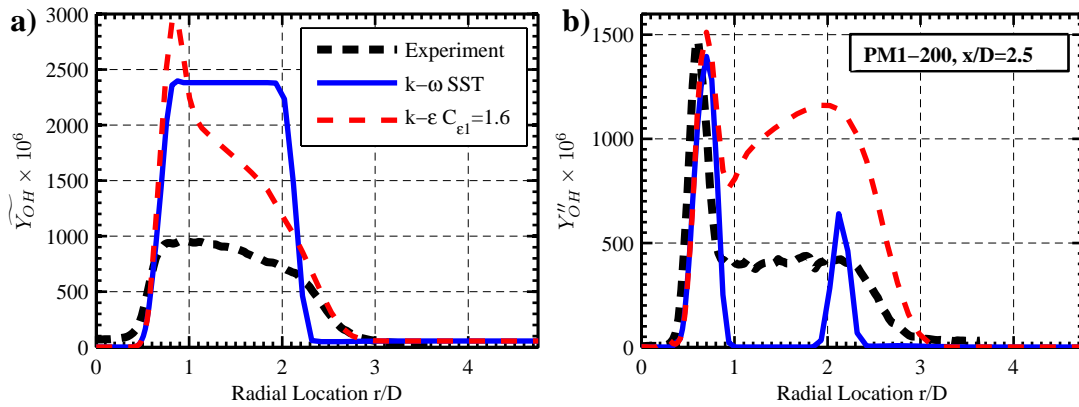


Figure D-69. Comparison of the Favre mean a) and RMS b) OH mass fraction statistics at $x/D=2.5$ for the PM1-200 flame.

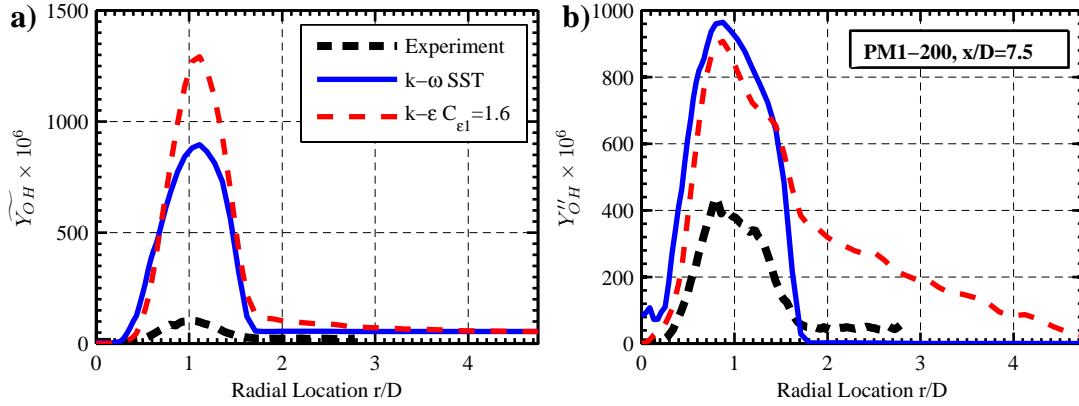


Figure D-70. Comparison of the Favre mean a) and RMS b) OH mass fraction statistics at $x/D=7.5$ for the PM1-200 flame.

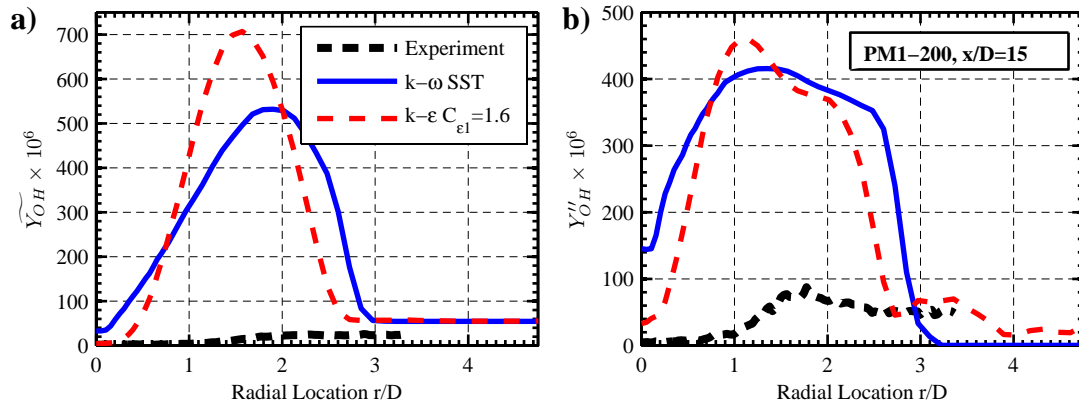


Figure D-71. Comparison of the Favre mean a) and RMS b) OH mass fraction statistics at $x/D=15$ for the PM1-200 flame.

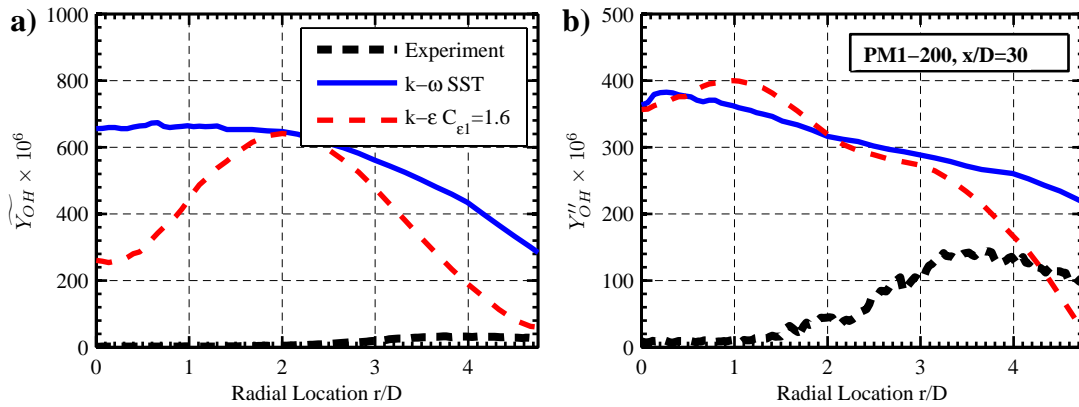


Figure D-72. Comparison of the Favre mean a) and RMS b) OH mass fraction statistics at $x/D=30$ for the PM1-200 flame.

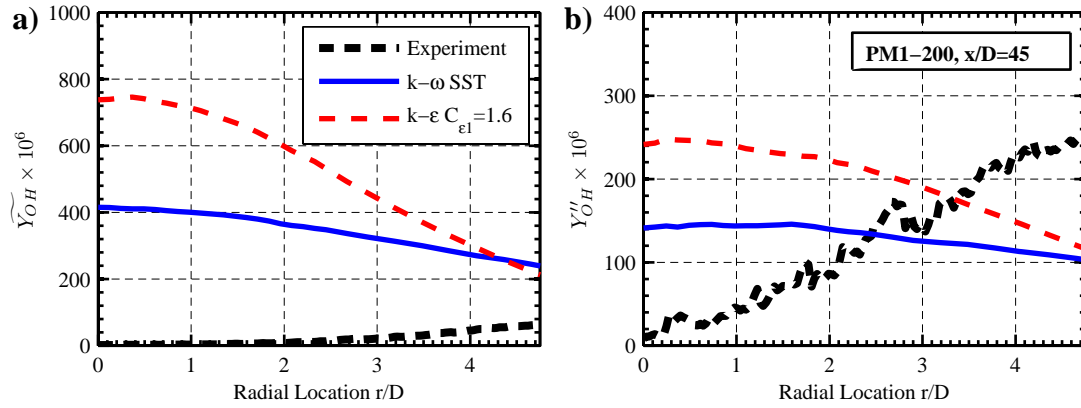


Figure D-73. Comparison of the Favre mean a) and RMS b) OH mass fraction statistics at $x/D=45$ for the PM1-200 flame.

APPENDIX E

Laminar Flame Simulation Results

In this Appendix representative laminar flame simulation results are presented for the canonical twin jet or opposed flow configuration. The primary aim of presenting this data is to have reference source for strained laminar calculations when referring to laminar flamelet trends in the analysis of predominately experimental. The boundary conditions for these simulations use a fresh mixture of 0.5 equivalence ratio methane-air at 300K at one boundary representing the fresh central jet reactants. The second boundary inlet conditions are equilibrium products of a 0.43 equivalence ratio hydrogen-air flame at 1500K. The boundary conditions are selected to relevant to the PM1 flame series conditions. The GRI 3.0 kinetic mechanism and multi-component transport properties are used for the simulations for the particular results presented in this Appendix. The CANTERA code is used for all calculations presented.

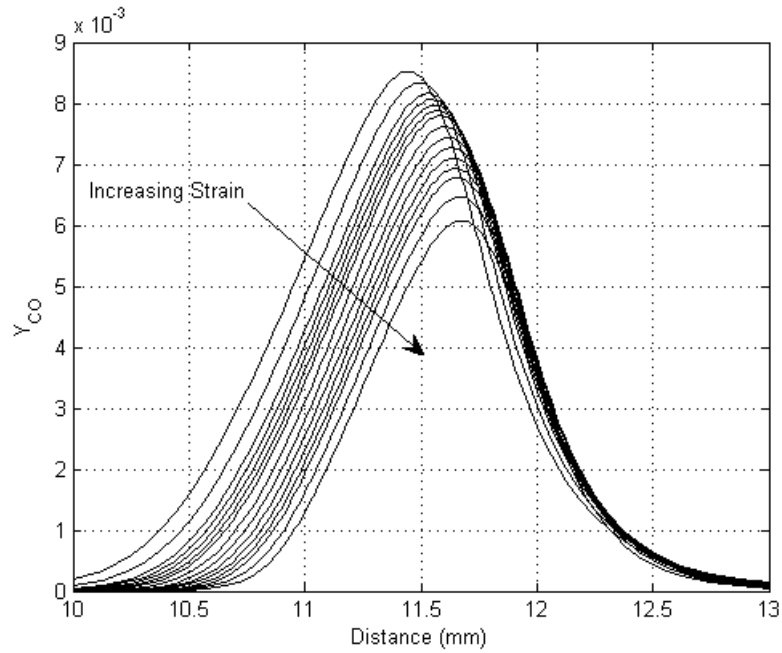


Figure E-1. Spatial variation of CO mass fraction in opposed flow simulations for a number of strain rates.

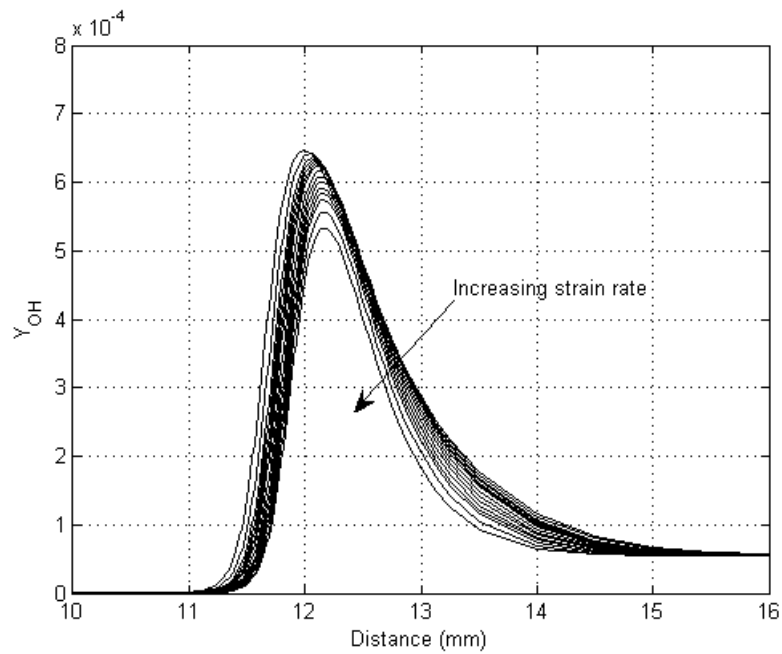


Figure E-2. Spatial variation of OH mass fraction in opposed flow simulations for a number of strain rates.

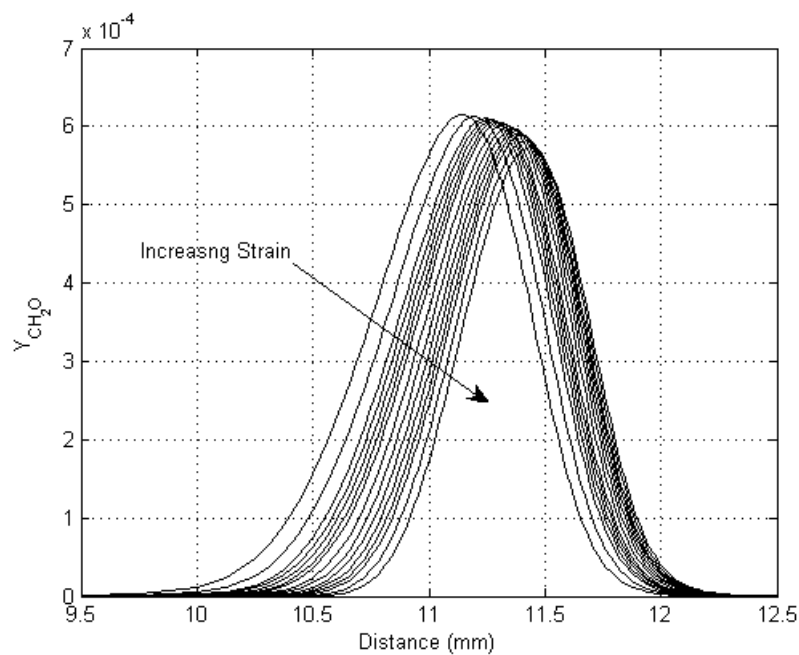


Figure E-3. Spatial variation of CH_2O mass fraction in opposed flow simulations for a number of strain rates.

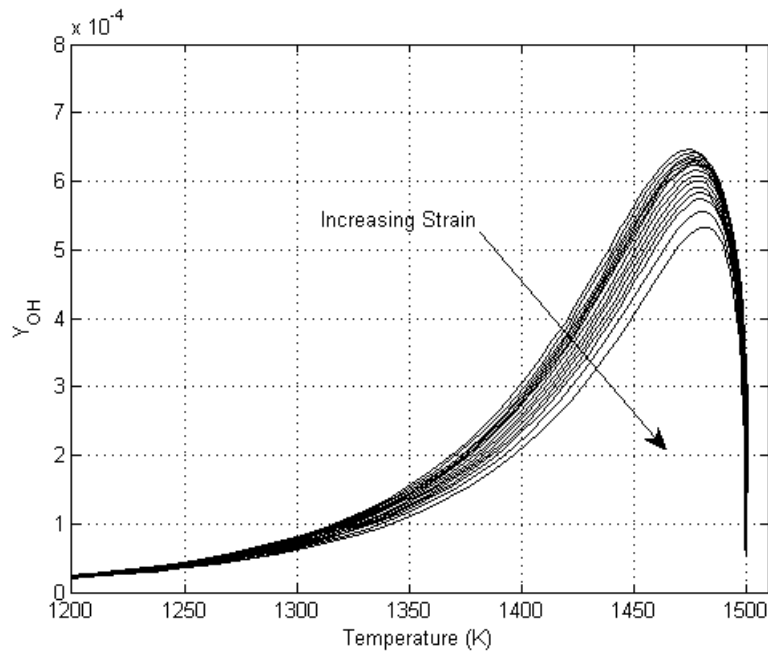


Figure E-4. Variation of OH mass fraction as a function of temperature in opposed flow simulations for a number of strain rates.

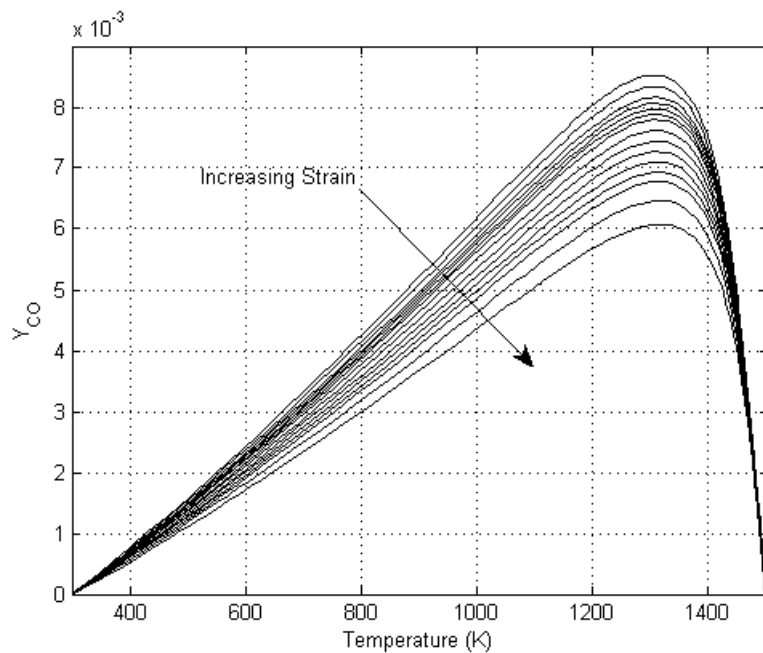


Figure E-5. Variation of CO mass fraction as a function of temperature in opposed flow simulations for a number of strain rates.

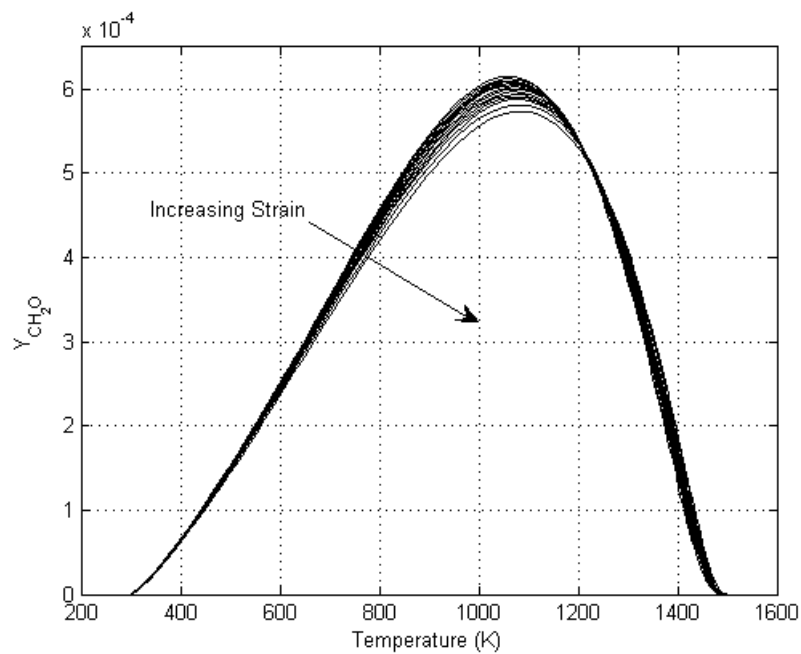


Figure E-6. Variation of CH₂O mass fraction as a function of temperature in opposed flow simulations for a number of strain rates.